TEM of neutron, proton and self-ion irradiation damage in FeCr alloys

Jack C. Haley

Trinity College
University of Oxford

A thesis submitted for the degree of
Doctor of Philosophy

Trinity Term 2018

Abstract

In the absence of a high-flux fusion-neutron irradiation source, the microstructural and mechanical changes expected within materials exposed to a nuclear-fusion environment must be replicated by fission-neutron and other surrogate-particle irradiations. This study uses transmission electron microscopy (TEM) to compare the microstructural defects produced in FeCr alloys during exposure to neutrons, protons, and self-ions.

Alloys of Fe6Cr and Fe9Cr were irradiated using fission-neutrons, 2.0MeV Fe+ ions and 1.2MeV protons at similar temperatures (~300°C) and similar doses (~2.0dpa). The neutron-irradiated alloys contained a population of interstitial dislocation loops with **b**=<111> (>70%) and **b**=<100>. The visible dislocation loops were on average ~5nm in size, and the density varied from $2\pm1x10^{14}cm^{-3}$ in the matrix to $1.2\pm0.3x10^{17}cm^{-3}$ close to helical dislocation lines. Dislocations loops were mostly clustered around sub-grain boundaries and helical-dislocations. Helical-dislocations formed from initially straight screw dislocations experiencing radial-climb in response to a vacancy-biased defect flux. Small chromium clusters were identified in the neutron-irradiated Fe6Cr, and chromium α'-phase precipitates were identified in the Fe9Cr.

Self-ion irradiation produced mostly homogeneously distributed dislocation loops (6-7nm on average), but with a greater fraction of <100> loops (~40%) than was seen in the neutron-irradiated alloys. The self-ion irradiated Fe6Cr and Fe9Cr contained only vacancy-type loops, unlike the neutron or proton irradiated sample which contained only interstitial loops. Chromium remained in solution in both ion-irradiated samples.

Proton-irradiated Fe9Cr contained dislocation loops close to helical-dislocation segments, similar to the neutron-irradiated sample. Chromium α'-phases were also identified. The proton-irradiated Fe6Cr contained much larger loops (~13nm on average) than the neutron or ion-irradiated alloys, and chromium was shown to have segregated on and around these loops. Both proton-irradiated alloys contained large voids (>4nm and up to 12nm) at a density greater than $10^{16}cm^{-3}$. In the neutron and ion-irradiated alloys, voids were mostly <2nm.

Preface

The research described in this thesis was carried out by the author in the Department of Materials at the University of Oxford between October 2014 and September 2018, under the supervision of Prof Steve Roberts and Prof Sergio Lozano-Perez. All the work is original, and where work from others has been included it has been clearly referenced and acknowledged. No part of this thesis has been submitted or accepted for any other degree at this university or elsewhere.

This thesis was funded by EPSRC grant number EP/L01663X/1 and as part of the Fusion Centre for Doctoral Training. The work at the Centre for Advanced Energy Studies was supported by the U.S. Department of Energy, Office of Nuclear Energy under DOE Idaho Operations Office Contrast DE-AC07-051D14517 as part of a Nuclear Science User Facilities experiment. Research conducted in the Materials Research Facility (UKAEA) was supported by equipment funded by National Nuclear Users Facility and the Henry Royce Institute under EP/P021727/1. Irradiation experiments at the Dalton Cumbria Facility and Surrey Ion Bean Centre were funded through the UK National Ion Beam Centre.

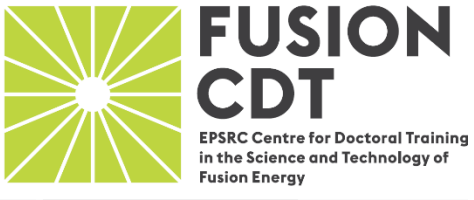

Journal Publications and conference presentations

Parts of this thesis will be written up as papers to be published in peer-reviewed journals. Listed below are the working titles for a selection of papers that are being worked on at the time of submission of this thesis.

- *"Helical dislocations from vacancy defects in FeCr alloys under neutron irradiation" J C. Haley, G. R. Odette, E. Tarleton, F. Liu, S. Lozano-Perez, S. G. Roberts*
  Target journal: Acta Materialia 2019
- *"A TEM comparison of neutron, proton and self-ion damage in FeCr alloys" J. C. Haley, P. Wady, S. de Moraes Shubeita, A. London, G. R. Odette, S. Lozano-Perez, S. G. Roberts*
  Target journal: Journal of Nuclear Materials 2019
- *"On Surprising Dose Rate Effects on the Precipitation of α' phases in Neutron Irradiated Fe9Cr" J. C. Haley, G. R. Odette, S. Lozano-Perez, S. G. Roberts*
  Target journal: Journal of Nuclear Materials 2019
- *"A Simple Method to Determine the Composition of Precipitates within a Foil from the 2D EELS or EDX map" J. C. Haley, S. Lozano-Perez, S. G. Roberts*
  Target journal: Microscopy 2019

Selected oral and poster presentations

- *"Radiation Damage with a Twist: A study of helical dislocations in irradiated FeCr alloys" J. C. Haley, G. R. Odette, S. Lozano-Perez, S. G. Roberts*
  *Oral presentation at **Nuclear Materials** October 2018, Seattle*
- *"Radiation Damage with a Twist: A study of helical dislocations in neutron irradiated FeCr alloys" J. C. Haley, S. Lozano-Perez, S. G. Roberts*
  *Poster presentation at the **International Microscopy Conference** September 2018, Sydney*
- *"A TEM comparison of radiation damage in neutron, proton, and heavy ion irradiated FeCr" J. C. Haley, G. R. Odette, S. Lozano-Perez, S. G. Roberts*
  *Poster presentation at the **International Conference on Fusion Reactor Materials** November 2017, Aomori*

Acknowledgements

First, I would like give my most sincere thanks to my supervisors, Prof Steve Roberts and Prof Sergio Lozano-Perez, for their support and guidance throughout these past four years. I am incredibly thankful for the large amount of independence given to me during this project, and the many interesting discussions we've shared over the years.

I would like to thank Prof Bob Odette of UCSB, without whom, a substantial part of this thesis would not have been possible. I am grateful for his help toward accessing the alloys he irradiated with neutrons back in 2009, and for helpful email exchanges discussing the results I obtained from them.

I would also like to thank the staff at Idaho National Laboratory for polishing the radioactive samples and the staff at the Centre for Advanced Energy Studies (CAES) in Idaho Falls for providing access to their active FIB facility. I am very thankful to Dr Chris Hardie, Miss Alex Cackett, Mrs Kate Breach and Mr Jon Claridge for assistance with the active material at the Materials Research Facility.

I'd like to thank Mr Nick Mason and Dr Andrew Smith of the Dalton Cumbria Facility (DCF) for assistance with the proton irradiation experiments. Also, thank-you to Dr Paul Wady and Dr Samir de Moraes Shubeita (DCF), and Dr Andrew London (UKAEA) for helping me to attend the main proton irradiation experiment throughout the days and nights. Many thanks are also due to Dr Luke Antwiss of the Surrey Ion Beam Centre (SIBC), for assistance with the heavy-ion irradiations, and for assembling a new irradiation stage and vacuum chamber specifically for my experiments.

For many interesting discussions, help on the TEM, and help with defect analysis, I would like to thank Dr Samuel Briggs, Dr Philip Edmondson, Dr Kevin Field, Mr Guanze He, Dr Mike Jenkins, Dr Zhao Shen and Dr Xiaoou Yi. Mike Jenkins in particular has been incredibly helpful with my analysis

of dislocation loops, and I am very thankful to him for taking time out of his retirement to sit with me and discuss results and micrographs.

Similar thanks are also due to members of the department and elsewhere for the support, training and assistance with the instruments used in this work: Miss Alex Cackett, Mrs Gabriella Chapman, Mr Peter Flaxman, Mrs Jennifer Holter, Dr Yina Huang, Dr Gareth Hughes, Dr Mimi Nguygen, Mr Laurie Walters, Mr Graham Wyatt and Dr Neil Young.

I have had the pleasure of many interesting and helpful discussions with the following people, to whom I very thankful: Dr Sergei Dudarev, Dr Mark Gilbert, Dr Daniel Mason, Dr Andrea Sand, and Dr John Titchmarsh.

To my friends from the department, I would like to thank-you for not only interesting and helpful discussions, but also (importantly) keeping me sane and sociable over the years: Dr Thomas Aarholt, Mr Robbie Abernethy, Mrs Rebecca Bradford, Mr Daniel Celis Garza, Dr Katie Collet, Dr Sarah Connolly, Mr Thomas Davis, Mr Glenn Jones, Dr Anna Kareer, Mr Thomas Lapington, Mr Alex Leide, Dr Bo-Shiuan Li, Miss Carmen Makepeace, Mr Julian Malisano, Miss Helen Pratt, Mr Edd Rowe and Mr John Waite.

Last, but not least, thank-you to my family for your eternal support, and to Catherine for your patience, support and comfort throughout the last four years.

Contents

1 Introduction to thesis 1

1.1 Introduction 1

1.2 Nuclear Fusion Power 2

1.3 Materials problems for advanced nuclear reactors 3

1.4 Reduced Activation Ferritic Martensitic steel 5

1.5 Pure iron and Fe-Cr alloys 6

2 Literature Review 7

2.1 The collision cascade 7

2.2 Defect clusters in iron and ferritic alloys 13

2.3 The nature of dislocation loops in iron and iron-based alloys 16

2.4 The Burgers vector of dislocation loops in iron and iron-based alloys 18

2.5 Dislocation loop growth and movement 22

2.6 Dislocation loop interactions with dislocations 24

2.7 Dislocation loops at high doses 27

2.8 Voids and transmutation gases 28

2.9 Effects of chromium (6-14at%) on radiation damage in FeCr alloys 31

2.10 Replicating neutron irradiation damage using ion-beams 36

2.10.1 Displacements per atom 37

2.10.2 Recoil effects and damage differences due to the irradiating particle 39

2.10.3 Dose-rate effects 47

2.11 Summary of key literature elements and thesis goals 55

3 Experimental methods 57

3.1 Introduction 57

3.2 Material fabrication 57

3.3 Irradiation damage experiments and calculations 60
3.4 Sample preparation prior to irradiation 64
3.5 Sample preparation for TEM 66
3.5.1 TEM foil preparation by twin-jet electropolishing 67
3.5.2 FIB methods for TEM preparation 69
3.6 Transmission electron microscopy techniques 74
3.6.1 Indexing convention and calibrations 74
3.6.2 Foil thickness measurements 77
3.6.3 Dislocation loop imaging 80
3.6.4 Dislocation loop characterisation 85
3.7 Imaging voids 91
3.8 Electron Energy Loss Spectroscopy 91
4 Neutron Damage in FeCr 97
4.1 Introduction 97
4.2 Irradiation experiment 97
4.3 Sample preparation 100
4.4 Microstructure of neutron irradiated Fe6Cr 101
4.4.1 Burgers vectors and number density of irradiation-induced dislocation loops in the neutron irradiated Fe6Cr 106
4.4.2 Nature analysis of loops in the neutron irradiated Fe6Cr 110
4.4.3 Size distributions of loops in the neutron irradiated Fe6Cr 112
4.4.4 Voids in neutron irradiated Fe6Cr 115
4.4.5 Redistribution of chromium in neutron irradiated Fe6Cr 119
4.5 Microstructure of neutron irradiated Fe9Cr 123
4.5.1 Burgers vectors and number density of irradiation-induced dislocation loops in the neutron irradiated Fe9Cr 129
4.5.2 Nature analysis of loops in neutron irradiated Fe9Cr 133

4.5.3 Size distributions of loops in the neutron irradiated Fe9Cr 135
4.5.4 Helical dislocations in neutron irradiated Fe9Cr 137
4.5.5 Voids in neutron irradiated Fe9Cr 142
4.5.6 Redistribution of chromium in neutron irradiated Fe9Cr 144
4.6 Summary of neutron irradiated FeCr 150
5 Discussion of neutron damage in FeCr 151
5.1 Introduction 151
5.2 Effect of composition on neutron irradiated FeCr 151
5.3 Inhomogeneity of loops in neutron irradiated FeCr 156
6 Replicating neutron damage with heavy ions and protons 161
6.1 Introduction 161
6.2 Irradiation experiments 161
6.2.1 Irradiation of FeCr alloys with protons 162
6.2.2 Irradiation by self-ions 169
6.3 Microstructure of proton and ion irradiated Fe6Cr 171
6.3.1 Burgers vectors and number density of irradiation-induced dislocation loops in proton and self-ion irradiated Fe6Cr 178
6.3.2 Comparison of loop number density and Burgers vectors of neutron, proton and self-ion irradiated Fe6Cr 182
6.3.3 Nature analysis of loops in proton and self-ion irradiated Fe6Cr 183
6.3.4 Size distributions of loops in proton and self-ion irradiated Fe6Cr 187
6.3.5 Voids in proton and self-ion irradiated Fe6Cr 193
6.3.6 Redistribution of chromium in proton and self-ion irradiated Fe6Cr 201
6.4 Microstructure of proton and ion irradiated Fe9Cr 212
6.4.1 Burgers vectors and number density of irradiation-induced dislocation loops in proton and self-ion irradiated Fe9Cr 219
6.4.2 Nature analysis of loops in proton and self-ion irradiated Fe9Cr 222

6.4.3 Size distributions of loops in proton and self-ion irradiated Fe9Cr 227

6.4.4 Voids in proton and self-ion irradiated Fe9Cr 230

6.4.5 Redistribution of chromium in proton and self-ion irradiated Fe9Cr 244

6.5 Summary of proton and self-ion irradiated FeCr 251

7 Discussion of the differences between neutron, proton and self-ion irradiation 255

7.1 Introduction 255

7.2 Discussion of the as-conducted experiments and the effects of systematic errors on the results 255

7.2.1 Discussion of dose-measurement errors 256

7.2.2 Discussion of temperature measurement errors 258

7.2.3 Discussion of recoil spectra and dose rate effects 261

7.3 The effect of irradiating particle on the irradiation-induced dislocation loops 264

7.4 The effect of irradiating particle on the irradiation induced voids 268

7.5 The effect of irradiating particle on the redistribution of chromium 270

8 Conclusions 273

8.1 Summary of key results 273

8.2 On the use of protons and self-ions for replicating neutron damage 276

8.3 Future work 277

9 References 279

List of figures reprinted with permissions 293

APPENDICES

APPENDIX A **298**

APPENDIX B **299**

APPENDIX C **301**

APPENDIX D **305**

APPENDIX E **310**

APPENDIX F **311**

APPENDIX G **314**

APPENDIX H **317**

Chapter 1: Introduction to thesis

1.1 Introduction

The Paris climate deal of December 2015 concluded with 195 nations agreeing to limit global warming to no more than 2^{o}C above pre-industrial levels by the 22nd century [1]. In order to achieve this, there must be a radical shift away from fossil fuel-based energy production in order to reduce the level of greenhouse gases polluting the atmosphere [2]. As global population rises, electricity consumption is also expected to rise from ~14TW to 25-60TW in the next 35 years [3]. New nuclear concepts are capable of delivering high capacity low-carbon energy that could be used to replace the base-loading coal and gas plants that are rife today.

Advanced nuclear power plants are being researched to improve on the technology currently in use. The so-called “Generation IV” (or simply “Gen-IV”) fission power plants will have improved efficiency, safety, sustainability and at reduced cost. Meanwhile, nuclear fusion is being developed as a means of delivering nuclear energy that has many advantages over fission [4]. Nuclear fusion is sustainable, emits no greenhouse gases, produces no long-term radioactive waste and is impossible to “meltdown” like a fission reactor.

The challenges faced in developing a fusion power plant, and gen-IV fission power plants, are many. This thesis has an overall focus on the radiation-induced damage that materials inside such reactors are prone to, which causes severe embrittlement of steel (and other materials). This can lead to component failure, cracking, and will ultimately limit the lifetime and economic viability of fusion and fission power [4]. This thesis investigates radiation damage from a nuclear fusion perspective, but the work is equally relevant to modern and future fission power plants.

1.2 Nuclear Fusion Power

Nuclear fusion is the joining of two nuclei to make a new element. For a power-producing reactor, the most favoured reaction is between deuterium and tritium (Equation 1.1) due to it having the lowest fusion cross-section of all reactions, whilst also having a high Q-value (the energy-gain of the reaction) [5].

Equation 1.1:

$$D + T \rightarrow 3.6MeV\ \alpha + 14.0MeV\ n$$

A fusion reactor would use this reaction to generate heat, and convert this to electricity just like a conventional power station. Tokamaks are a promising reactor type that are capable of heating a deuterium-tritium (DT) plasma up to over 100 million ^{o}C, which is necessary for deuterium and tritium to overcome the electrical repulsion of the nuclei and fuse. Tokamaks keep the plasma confined within the doughnut-shaped chamber using a sophisticated magnetic configuration for long enough and with a high enough containment pressure for nuclei to collide and fuse [5,6].

A new experimental tokamak called ITER (Figure 1.1) is currently being built in France and when complete will be the world's largest [7]. The primary aim of ITER is to demonstrate the feasibility of fusion as a viable power source, particularly by being the first to prove it is possible to get more energy out than was put in using a magnetic-confinement device. ITER aims to achieve 10-times the energy output that was input over short runs (up to ~30 minutes), and will test various technologies that will be essential for a power-producing device. The first fusion power plant to produce electricity continuously and contribute to the grid is expected by the year 2050, and will be one of several "DEMO" designs [6].

© ITER Organization

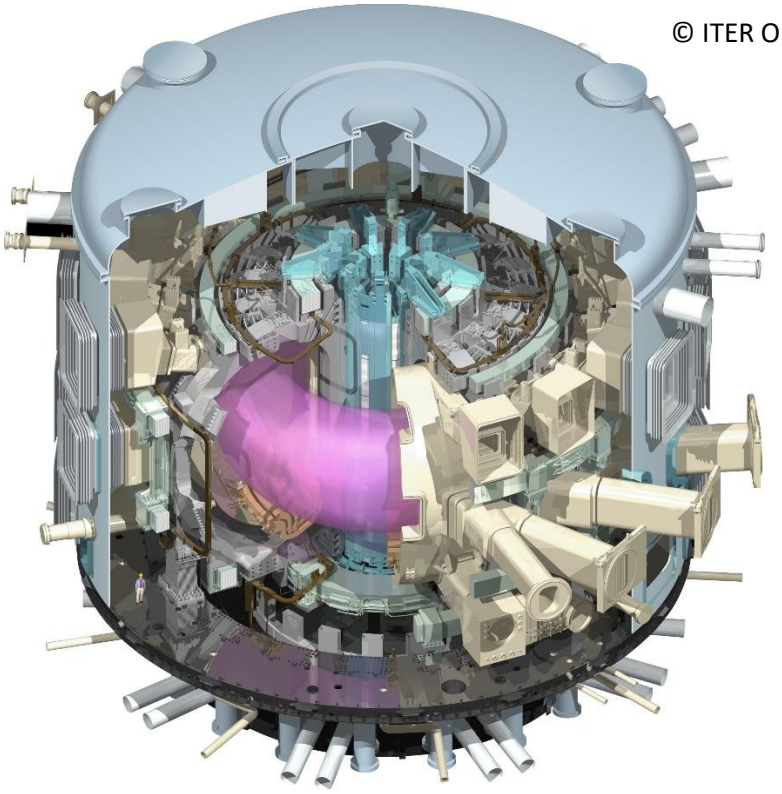

Figure 1.1: The experimental reactor, ITER, from [7]*. When complete it will be the largest Magnetic Confinement Fusion (MCF) device in the world, with an aim of generating more fusion energy than the energy it consumes.*

Although the tokamak is probably the most promising design for a fusion power plant, other concepts are also being studied, such as stellarators [8,9], magnetic bottles [10], or laser-driven inertial confinement devices [11]. Regardless of how the fusion reaction is produced, radiation damage is a serious concern for all of these concepts, especially when translating the technology from an experimental device to a power-producing reactor.

1.3 Materials problems for advanced nuclear reactors

The structural materials that will make up a DEMO fusion reactor will be subject to a harsh environment unlike any other. Plasma facing materials (e.g. W, Be, C) will be subject to severe gas-embrittlement and thermal loading in the surface that can lead to bubbling, fracture and even melting [12]. The temperature within the core of a tokamak is over 100 million ^{o}C, and though this *should* be kept away from any materials via the magnetic fields, the temperatures the materials deal with still present a significant scientific and engineering challenge.

Structural materials will be exposed to high temperatures (~300-600°C), large fluences of high energy neutrons (over 150dpa[1], Figure 1.2) and a highly corrosive environment in the cooling and breeding channels (liquid metals, super-critical water and gas) [4].

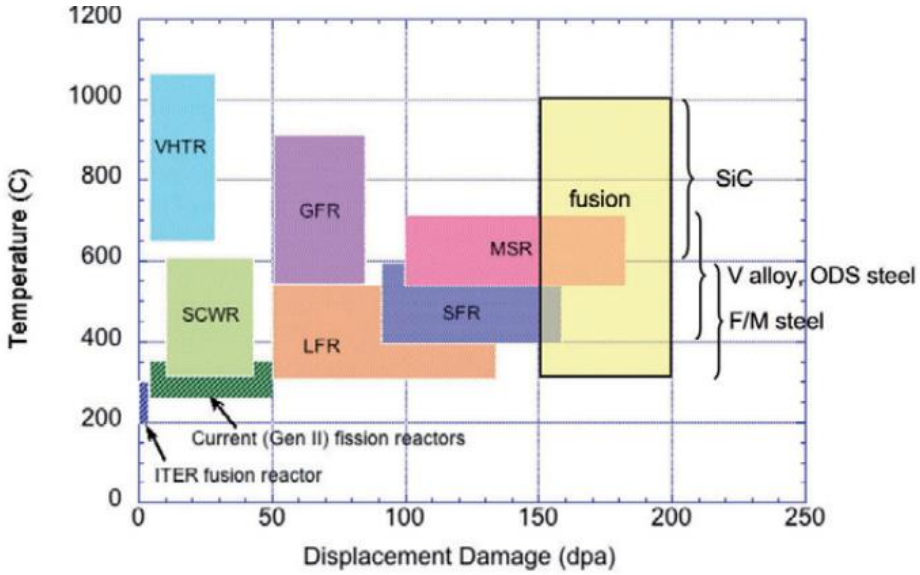

Figure 1.2: Overview of operating temperatures and neutron dose regimes for structural materials in current generation II and potential generation IV fission plants, plus fusion devices ITER and DEMO, from [4].

There are several designs proposed for extracting the energy from a tokamak which all revolve around heating a blanket containing a mixture of neutron-breeding material (e.g. lead) and lithium. The former is required to produce more neutrons than there are fusion reactions occurring within the core, and the latter is to trigger a nuclear reaction that produces tritium, which can then be used in the fusion fuel cycle. Some coolant is then pumped through pipes dispersed in this blanket which extracts the heat away from the reactor [13].

The operational environment of fusion structural materials is a major obstacle to producing an economically viable fusion power plant. The success of nuclear fusion depends primarily on whether the materials challenges can be successfully overcome.

[1] displacements-per-atom (dpa) is a measure of the irradiation damage a material receives.

1.4 Reduced Activation Ferritic Martensitic steel

Ferritic-Martensitic (FM) steels with chromium content 7-10wt% are prime candidates for fusion structural steels [4,13]. These body-centred-cubic (BCC) steels are preferred over face-centred-cubic (FCC) austenitic steels due to their excellent resistance to void swelling, having been observed to exhibit no swelling up to 150dpa at 400-550°C in a fast fission-neutron spectrum [13]. They have good creep resistance and corrosion/oxidation resistance, but suffer irradiation-embrittlement at low temperature and have a low long-term creep rupture strength (~550-600°C) [13]. The chromium content strongly affects the embrittlement induced by neutron irradiation, but the changes to the ductile-to-brittle transition temperature (DBTT) is minimised when the chromium content is ~9wt% [14], as shown by Figure 1.3.

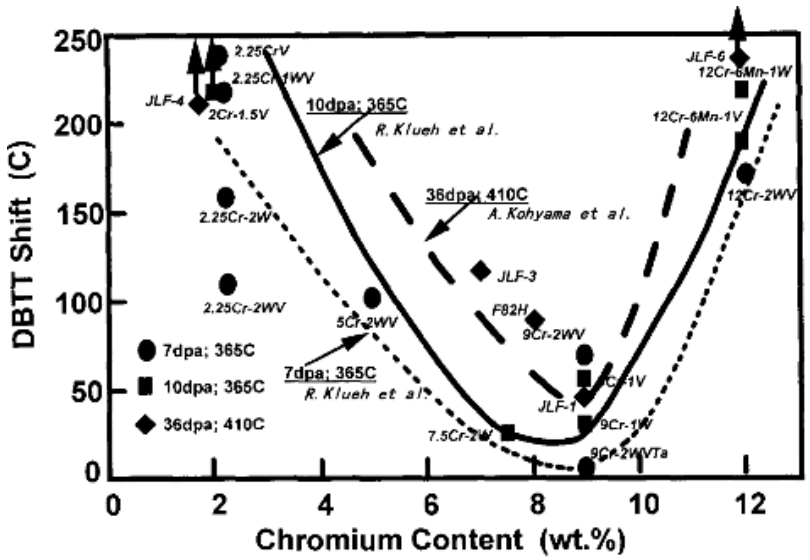

Figure 1.3: Effect of chromium content on the change in DBTT of RA steels and alloys by neutron irradiation, from [14].

An objective of nuclear fusion power production is to produce no long-lived radioactive waste. This means the materials used to construct a nuclear fusion power plant must contain no highly radioactive elements ~100 years after the operational lifetime of the component (for example, Eurofer [13,15], as shown by Figure 1.4). Such steels are known as Reduced-Activation (RA and RAFM[2]) steels. To produce RA steels, common carbide forming elements, like molybdenum and

[2] Reduced Activation Ferritic-Martensitic

niobium, must be replaced by elements that do not form long-lived isotopes after irradiation, such as tungsten and tantalum. Furthermore, impurities including nickel, copper, cobalt, and aluminium must be minimised [13].

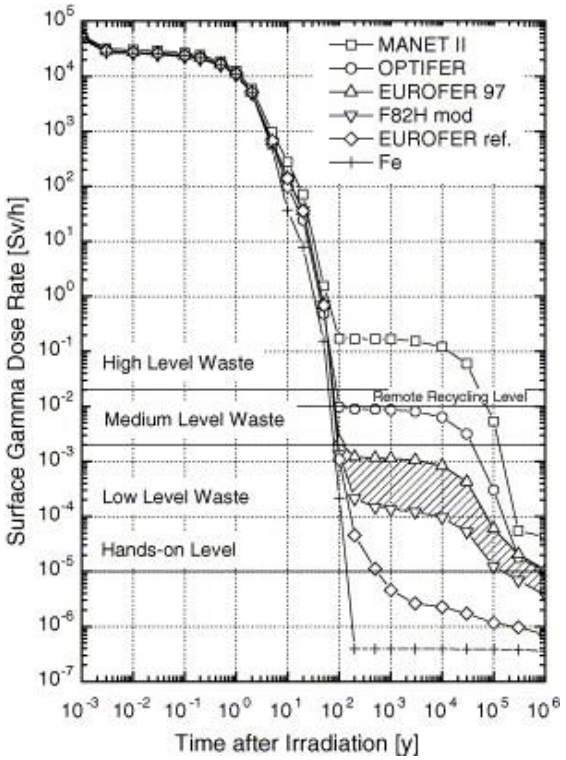

Figure 1.4: Calculated decay of surface dose-rate in iron and ferritic–martensitic steels after irradiation (12.5 MW/m^2) in a first wall DEMO spectrum, from [16].

1.5 Pure iron and Fe-Cr alloys

The complex microstructure and chemistry of steels make comparisons difficult. The study of radiation damage in one candidate steel does not necessarily explain much about the radiation damage response of a different candidate steel, as it is hard to identify the fundamental mechanisms responsible for certain radiation induced phenomena. Therefore, in order to understand the influence of a particular element, it is common to study simple binary alloys with a controlled level of impurities. Pure Fe and Fe-Cr alloys are examples of such model materials for RAFM steels and their study has been particularly important in the development of the more complex variants. This thesis focusses on the radiation damage that accumulates in such FeCr alloys.

Chapter 2: Literature Review

Irradiation damage by neutrons is a main cause of long-term degradation of mechanical properties of reactor materials. Sustained irradiation will lead to hardening and embrittlement via the production of irradiation induced defects, which will leave components prone to cracking and failure.

In order to understand the experimental observations and models of radiation damage, a complete understanding of the damage process is required. This literature review will first discuss the different stages of defect production and evolution, with a focus on iron and iron-based alloys. The various defect types that are produced in such materials will then be discussed, and how these are affected by chromium content. The review will lastly discuss charged-particle irradiations and their use toward replicating neutron-irradiation induced defects.

2.1 The collision cascade

Irradiated particles lose energy as they propagate through a material by three different mechanisms [17]:

- Elastic and inelastic collisions with atomic nuclei, e.g. for neutrons
- Elastic and inelastic collisions with atoms, e.g. for charged-particles
- Ionisation of atoms by passing charged-particles.

If the energy transferred in such a collision is greater than the displacement threshold energy E_d, then the atom will be knocked off its lattice site. The displacement threshold energy for iron and iron-based materials, including FeCr binary alloys and steel, is 40eV [18].

If after the collision, the kinetic energy of the displaced atom (the primary knock-on atom, or PKA) is greater than E_d, then the displaced atom will have enough energy to displace another atom.

If the kinetic energy of the PKA is much greater than E_d, then it may cause a cascade of damage, where many atoms are displaced. Each of these additionally displaced atoms can displace more atoms, which can then displace more atoms, and so on. This chain of events will continue until all the energy has been dispersed (i.e. each atom has energy $<E_D$) [17].

The Kinchin-Pease (KP) model of radiation damage [17] says that above twice the displacement energy, the number of displacements that occur will scale linearly with the damage energy, T_{dam}, which is the portion of the PKA-energy that gets dissipated in elastic collisions [18]. This is shown in Figure 2.1. Above some critical damage energy, the number of displacements will remain constant with damage energy, since PKAs will lose their energy primarily via electronic losses, while energy losses from elastic collisions will saturate [17].

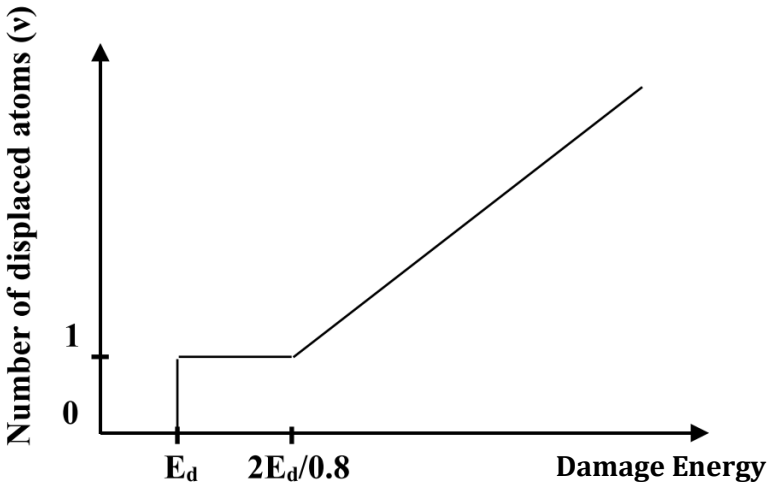

Figure 2.1: Number of vacancies created in a cascade as a function of the damage energy, from [17]

The relation shown by Figure 2.1 is a simplification for the sake of the KP model. In reality, the damage energy will scale approximately linearly with PKA-energy for low energies, but non-linear at high PKA-energy where it follows a log-like scaling, see Figure 2.2 [19].

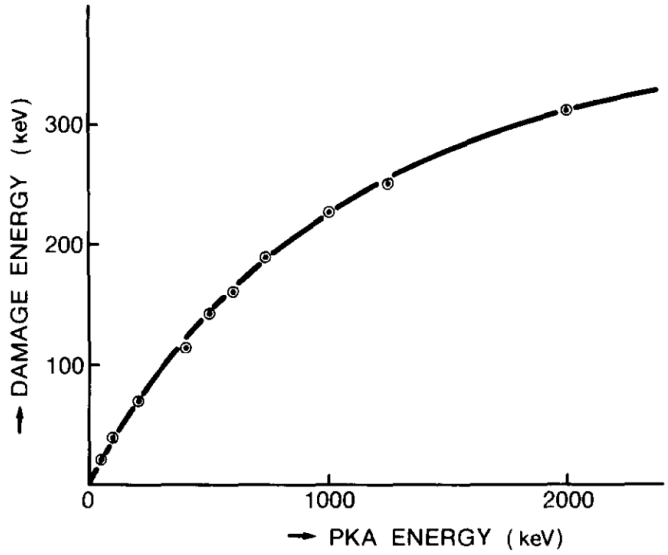

Figure 2.2: Damage energy as a function of PKA energy, from [19]

The displacement of atoms during a cascade means vacancy and interstitial pair (Frenkel pair) production. The majority of such pairs will recombine, but a portion will survive and go on to form extended defects. If an interstitial lies within the spontaneous recombination volume around a vacancy, their accompanying strain fields will be sufficient to attract the two together, allowing recombination to occur. Outside this volume, the Frenkel pair will remain separate [17,20]. For α-iron and chromium, the spontaneous recombination volumes for Frenkel pairs are 105 at.vol. (4.9 nm^3) and 95 at.vol (4.4 nm^3) respectively [21,22], which corresponds to ~6 atoms separation, or ~1nm (neglecting crystallographic effects).

The 14MeV neutron produced inside a fusion reactor produces PKAs with much greater energy than the threshold displacement energy of the target material, so it is capable of displacing many atoms in a material. The recoil-spectrum is the energy spectrum of PKA-energies that are produced by an irradiating particle. Figure 2.3 shows the neutron energy-spectra for a "DEMO" fusion reactor and the corresponding PKA-spectra for iron in a DEMO blanket component [23].

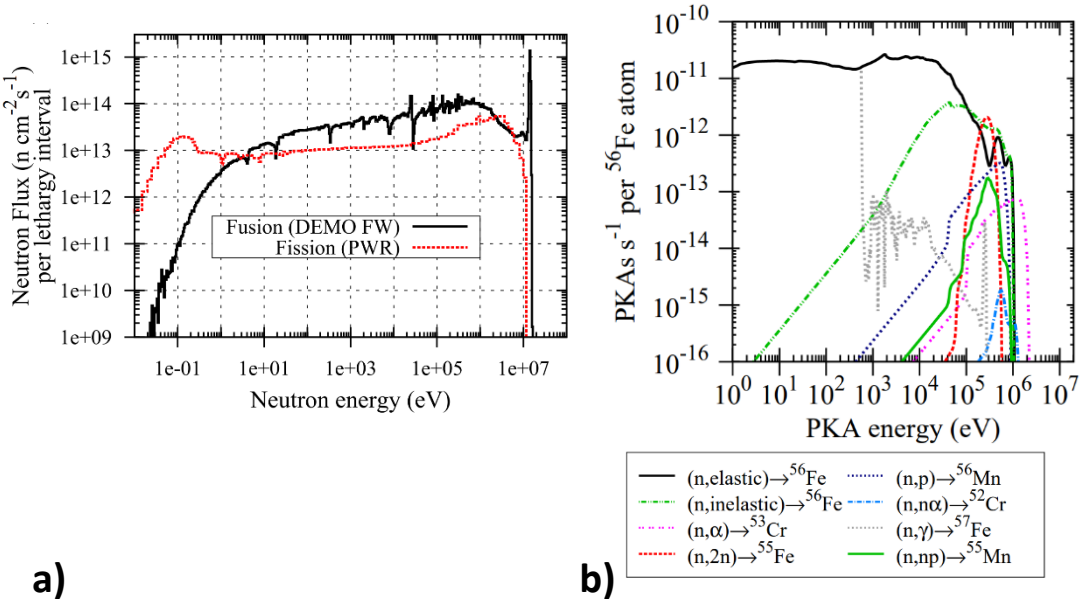

Figure 2.3: a) Neutron energy spectra for a nuclear fusion DEMO first wall, and for a Fission pressurised water reactor (PWR) from [23]*. b) The PKA energy spectra for the various neutron-PKA reactions in iron exposed to a DEMO neutron spectrum* [23]*. The spectra for (n, elastic) is for hard-sphere ballistic displacements, whereas (n, inelastic) is the spectrum for all reactions involving transmutation.*

The collision cascade behaves more like a liquid than a solid for a few pico-seconds as the energy is dissipated between the atoms [17,24]. In this "ballistic phase" of the collision cascade, the core of the cascade will be rich in vacancies, and the displaced atoms, carrying the momentum, are flung away from the centre of the cascade (Figure 2.4). The cascade will then enter a "relaxation phase" and try to collapse back into an ordered array of atoms [17]. This happens so quickly (pico-seconds) that some atoms cannot return to a position in the crystal lattice. The misplaced atoms and holes in the lattice are the interstitial and vacancy point defects [17].

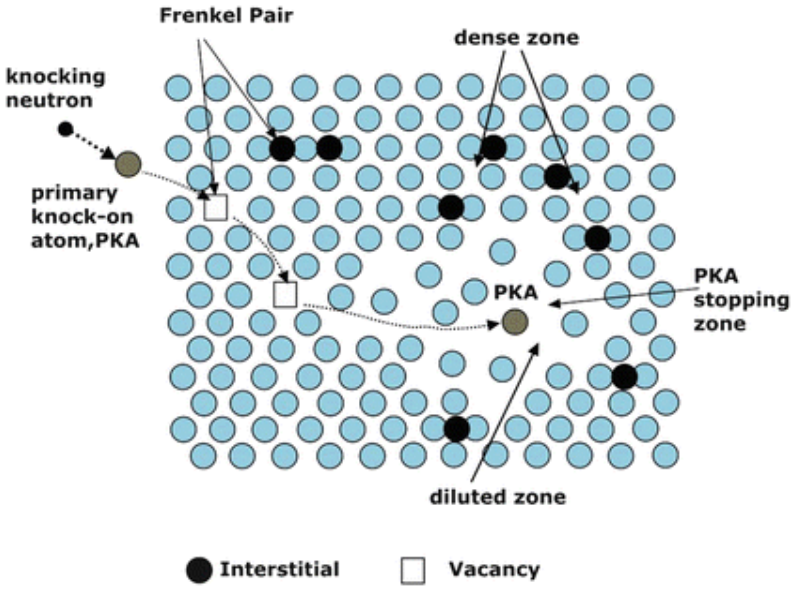

Figure 2.4: Diagram of a collision cascade occurring. A vacancy rich region forms in the centre and interstitials at the edge of the cascade, from [25].

PKAs with energy ~1 MeV predominantly lose energy through inelastic collisions with electrons, which do not cause atomic displacements, but do heat up the matrix. The elastic collisions that do occur will produce highly energetic cascades where PKAs can travel far beyond the core of the cascade and form sub-cascade branches.

It has been shown that the frequency of defect clusters produced by cascades as a function of cluster size follows a power-law [26–28]. Sand et al. [29] used molecular dynamics (MD) to model cascades and fragmentation into sub-cascades, and the defects that are produced by single PKAs. Sand et al. identified a power-law relation that describes the size distribution of primary defect clusters in tungsten, which were later found to match well with experiment [26].

De Backer et al. [27] later used a computationally cheaper approach to model sub-cascades using a binary collision approximation (BCA) approach and by considering the total energy deposition within finite element voxels. Voxels were grouped according to whether the energy deposited within a given voxel was sufficient to melt the material contained. This allows the cascade to be split into sub-domains, representing sub-cascades. The cluster size distribution was then estimated by De Backer et al. from the sub-domain size distribution (Figure 2.5).

The same scaling law shown by Sand et al. [29] applies to the clusters modelled by De Backer et al. [27]. Such an approach could be used for iron, but this has additional complications due to magnetic effects.

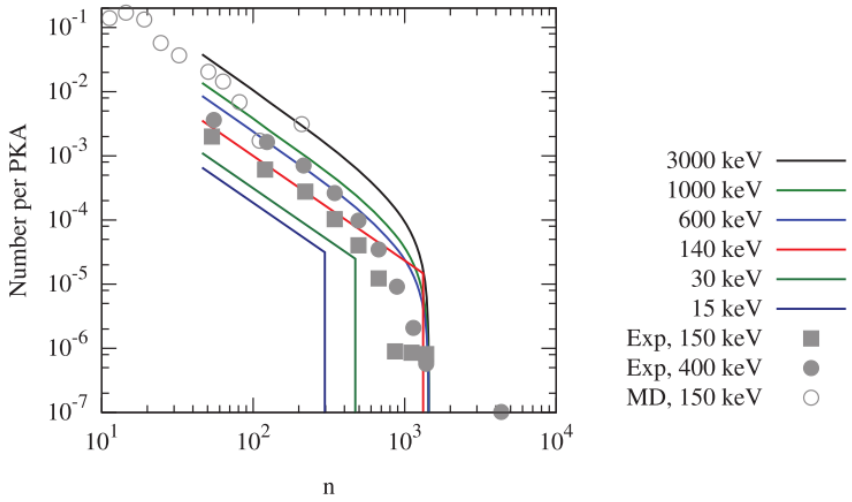

Figure 2.5: Cluster size distribution of primary interstitial defects, for various PKA energies in tungsten, from [27].

After many cascade events, it will be likely for subsequent cascades to overlap with a previously damaged region of material. This will cause coarsening of defect clusters, in addition to coarsening via thermally assisted agglomeration of defects. Coarsening, recombination, and further defect nucleation will cause the overall size distribution in a material to deviate from this power-law, leading to a more complex summation of many power-laws. Thermal annealing can also occur, resulting in a decline in the frequency of small clusters, and the size distribution may be better represented as, for example, a Weibull distribution [30,31].

2.2 Defect clusters in iron and ferritic alloys

In this section and following sections, the formation and evolution of dislocation loops is described. In section-2.8, the evolution of voids alongside gas production during neutron irradiation will be discussed.

Dislocation loops are the "fingerprint" that shows radiation damage has occurred. They are useful features to study as they tell the observer information about the implanted damage, and how this has accumulated and evolved. Dislocation loops are produced in cascades and during cascade-overlap. They are a major source of hardening as they act as pinning points throughout the matrix thereby restricting the movement of dislocations [17,32], and subsequently the material's ability to deform plastically.

Dislocation loops form from the clustering of defects on a common plane - a platelet of defects. For an interstitial platelet, the surrounding lattice must swell and distort to fit the extra atoms in place. A vacancy platelet can cause the surrounding atoms to collapse inwards to the vacant space, distorting the lattice (Figure 2.6).

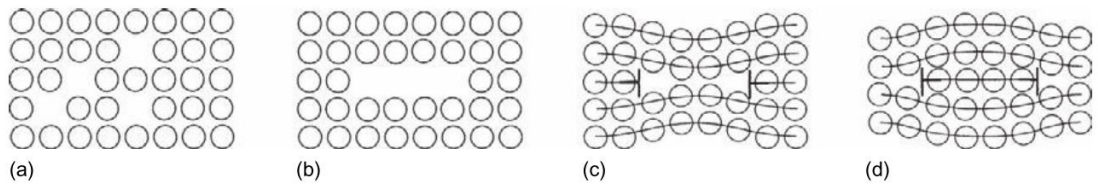

Figure 2.6: Formation of prismatic dislocation loops. a) represents a crystal with a large number of vacancies dispersed throughout the matrix. In b) the vacancies have migrated on to a common plane, and in c) the matrix has collapsed to form a pure edge dislocation loop. d) is an interstitial dislocation loop formed by an equivalent process. From [32].

Prismatic loops (also called pure edge loops) can move via glide along the "glide cylinder" perpendicular to the plane of the loop. Non-prismatic loops (also called non-edge loops) are where the habit plane of the loop is not perpendicular to the Burgers vector, and so the dislocation loop is of mixed character with both screw and edge components [32,33]. The glide plane of a non-edge

loop could therefore exist on any plane [32,34]. Loops can also move within their habit plane via conservative climb [32].

The type of dislocation loops predominantly observed in Fe and FeCr are prismatic or close to prismatic, for example [35–38]. Gao et al. [39] highlighted that the non-prismatic loop population can be significant, and showed observations of loops on {111}, {110}, {200} and {211} type planes. Gao et al. suggested that non-edge loops could be metastable configurations during the transition of a loop from one Burgers vector to another, a schematic illustration of which is shown in Figure 2.7.

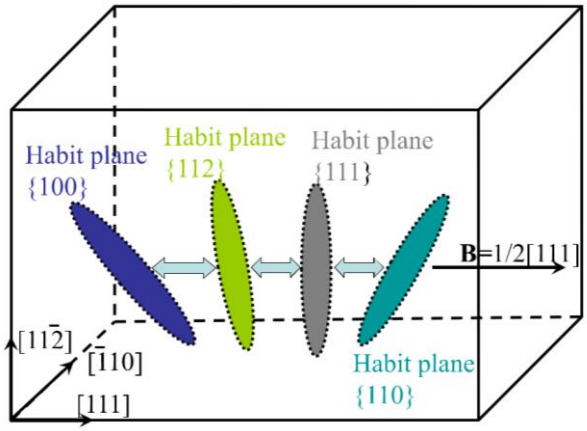

Figure 2.7: Dislocation loop habit planes and the proposed transformation from <100> to <111> Burgers vector, from [39].

Though in many materials (e.g. tungsten) loop nucleation can occur during the collapse of single cascades [40,41], this is not always observed in iron. Robertson et.al [42] showed a threshold dose effect exists in iron. Robertson et al. found no visible damage in iron irradiated at 80°C using neutrons at doses below a fluence of $4x10^{23}$ neutrons/m^2.

English et al. [43] also observed no visible loops in pure Fe below a 80keV self-ion irradiation dose of ~0.01dpa at room temperature [3]. Robertson et al. and English et al.'s observations show that no dislocation loops form in iron before cascade overlap can occur. However, when English et al. [43]

[3] Displacements per atom (dpa) is a measure of irradiation dose. It indicates the average number of times each atom in a material has been displaced during irradiation. This is discussed in detail in section 2.10.1.

implanted heavier ion (80keV W+) irradiations into iron, up to the same dose implanted using 80keV self-ions (Fe+), dislocation loops were observed. This would suggest that cascade collapse is occurring in the heavier-than-iron irradiation, but not from self-ion. This was attributed to the energy density being higher in cascades produced by the 80keV tungsten than cascades produced by 80keV iron [43].

The observations by Robertson et al. [42] and English et al.[43] imply that vacancy clusters are produced in iron from the depleted zone at cascade sites, but they rarely spontaneously collapse to form a dislocation loop as seen in, for example, copper [44]. Instead, visible loops are only observed above a certain 'threshold dose' at which cascade overlap becomes significant and vacancy and/or interstitial clusters can aggregate to form loops [45,46].

Although this threshold dose effect has been observed in other studies of Fe and FeCr alloys (for example, [37,46]), Schäublin et al. [47] have shown that higher energy self-ion irradiations do produce dislocation loops before cascade overlap can occur in Fe and FeCr, as speculated by English et al. [43] and Sand et al. [28]. This suggests that vacancy loop nucleation is possible in iron via cascade collapse. This would be more common (though still rare due to sub-cascade branching) at higher PKA-energies from cascades that are sufficiently energy-dense to produce a large vacancy supersaturation in the cascade core [28]. Sand et al.'s MD observations of interstitial loop cluster formation also indicated that no TEM-visible loops can originate from PKAs (as modelled for PKAs up to 150keV). It should be noted that although English et al. and Schäublin et al. observed loop formation before cascade overlap, neither author actually measured the nature of these loops.

Gilbert et al. [24] showed that although vacancy loop formation may occur in iron, the more stable configuration for a vacancy cluster is as a spherical void. Gilbert et al. showed that spherical voids are more stable than a prismatic vacancy loop of any size. This means that a vacancy loop is probably only an intermediate stage of the damage evolution, and that given enough time and thermal activation, most loops will evolve into a void [24].

Voids in Fe often go unreported in the literature, but this might be because small voids (below ~2nm in diameter) are trickier to image and more difficult to find in the TEM than dislocation loops [48]. However, small dislocation loops are also very difficult to measure the nature of [48], so modelling is usually relied upon to explain the origin of loops below ~2nm in diameter.

2.3 The nature of dislocation loops in iron and iron-based alloys

As discussed in section-2.2, vacancy loops can be produced by cascade collapse in iron. In general, vacancy loops are rarely seen in iron or ferritic alloys. This is likely due to clusters preferentially forming spherical voids rather than loops; existing vacancy loops being too small to be observable in the microscope; and dislocation bias, which describes the preference for interstitials to be absorbed by dislocation loops, rather than recombination with vacancies [49]. Interstitials are much more mobile than vacancies, with point defect migration energies in pure iron of 0.34eV and 0.67eV respectively [50]. Loop evolution is therefore more likely to be dominated by the movement of interstitials than vacancies.

It is usually only possible to measure with confidence the nature of the largest loops in a foil (minimum of ~5nm in diameter). Since it is more likely for interstitial loops to have grown to such sizes, it is not surprising that loops are usually reported to be interstitial in Fe and Fe-based materials. The nature of loops <5nm in size is much more difficult to measure, and usually only possible if the loop depth within a TEM foil is known. Until recently, dislocation loops in tungsten were only thought to be interstitial, but Yi et al. showed that the irradiation-induced loop population in tungsten could comprise both interstitial and vacancy loops [51].

Loop nature analysis is also very difficult, and should always be scrutinised. One mistake in the analysis will change the result from interstitial to vacancy, or vice versa [52,53]. Dislocation loops in irradiated iron and FeCr are most often found to be interstitial, for example [36,42,54]. However, vacancy loops can also be produced. Vacancy loops in Fe-11%Cr were reported by Yao et al. [37], which were produced by 30kV Ga+ beam irradiation at room temperature (i.e. irradiation in a

focussed ion beam microscope). The damage was contained mostly within 30nm of the surface, so Yao et al. argued the presence of vacancy loops is due to the loss of interstitials to the surface. Such interstitial losses are supported by modelling by Sand et al. [55]. Yao et al's observation of vacancy loops at least shows that vacancy loops less than 5nm in diameter are possible in FeCr.

Large vacancy loops have been seen in hydrogen-implanted iron during annealing experiments [56,57]. The authors both used high-energy electrons to introduce Frenkel pairs to the foil. Interstitials are much more mobile than vacancies, so growing loops indicate an interstitial nature, since they should receive a bias of interstitial defects. Similarly, shrinking loops indicates they are vacancy loops.

Both authors [56,57] report a transition from majority interstitial, to majority vacancy-loop population above 700K, which was attributed to the temperature at which vacancy movement becomes significant being around 700K. However, this also means the nature analysis technique using high-energy electrons becomes unreliable around this temperature, because vacancy defects may begin to significantly contribute to the defect flux onto dislocation loops, perhaps aided by an increase in the fraction of interstitial loss to a foil surface or other sinks. This would make interstitial loops look like vacancy.

The paper by Wan et al. [56] also includes nature analysis by the inside-outside contrast techniques, which is more often the approach used to determine nature. After 50keV proton irradiation, and annealing at 400^{o}C, Wan et al. identified only large interstitial loops, but after annealing at 500^{o}C found only large (up to 100nm) vacancy loops. It was suggested that hydrogen trapping at vacancy sites could be encouraging vacancy loop growth, though a more likely explanation could be due to interstitial defect loss at foil surfaces.

To summarise, the dislocation loops produced by neutron and by ion irradiation in ferritic materials are thought to be mostly interstitial, though the nature of small loops is much more

uncertain. Large loops are most commonly reported to be interstitial, but there are examples in the literature of large vacancy loops forming in iron. The difficulty in measuring the interstitial or vacancy nature of a loop means it is rarely performed in irradiation studies.

2.4 The Burgers vector of dislocation loops in iron and iron-based alloys

The Burgers vector of a dislocation loop is highly influential on the displacement field and strain associated with the loop, its direction of movement, and its mobility [58]. The loop Burgers vector is therefore an important parameter that will affect the hardening in a material. Both a<100> and a/2<111> type Burgers vectors[4] can be observed in Fe and Fe-based (ferritic) alloys, but the populations of each are highly dependent on the irradiation conditions.

Eyre and Bartlett [59] conducted a study of iron irradiated with neutrons at 60°C which was then annealed in-situ with TEM up to 500°C. The annealed foil only contained <111> type loops. A study by Masters [60] of self-ion and proton-irradiated iron at 550°C also reported loops with Burgers vector <100>. Later studies have shown either or both <111> loops and <100> loops can be present in irradiated iron, for example [37,61–63]. The presence of <100> loops was initially puzzling, as the <111> loops should be the more energetically favourable geometry of the loops [62]. This is what is observed in other BCC metals, such as tantalum, molybdenum and tungsten [33].

Gelles et al [64] showed that the increased presence of <100> loops is significant, since they are weaker barriers to dislocation slip than <111> loops. This means a greater concentration of <100> loops should have a lesser hardening effect on the matrix.

Eyre and Bullough proposed a mechanism [62] for <100> and <111> loop formation in iron. Their paper proposes that each type originates from a common loop nucleus containing a platelet of interstitials on a {110} plane. This configuration would contain a stacking fault, which would encourage the lattice to reconfigure itself via two possible dislocation reactions:

[4] As a convention in this thesis, the “a” and “a/2” terms are dropped from the Burgers vector notation.

Equation 2.1

$$\text{a)} \quad \frac{a}{2}[110] + \frac{a}{2}[00\bar{1}] \rightarrow \frac{a}{2}[11\bar{1}]$$

$$b) \quad \frac{a}{2}[110] + \frac{a}{2}[\bar{1}10] \rightarrow a[010]$$

Eyre and Bullough's reasoning for the inconsistency of documented <100> and <111> populations in iron is that the production of <100> type loops requires a higher energy to form than <111> loops from the reaction in Equation 1.1. Hence, <100> loops are only observed at higher temperatures [62].

Marian et al. [65] disagreed with the Eyre and Bullough mechanism on <100> loop formation [62], claiming that the high stacking fault energy in BCC metals discounts the formation and stability of faulted loops, suggesting that the Eyre and Bullough mechanism cannot be plausible. Marian et al. [65] approached the problem using MD simulations and demonstrated that small interstitial <111> clusters could form in collision cascades. Pairs of such clusters can then interact to form <100> clusters on a {110} plane, and rotate onto a {200} plane as the cluster grows.

Equation 2.2

$$\frac{a}{2}\langle 111\rangle + \frac{a}{2}\langle 111\rangle \rightarrow \frac{a}{2}\langle 100\rangle$$

It was also shown by TEM and simulation that these <100> loops are immobile and metastable compared to the <111> loops [65,66], allowing the <100> loops to grow via the absorption of smaller <111> clusters. Since Marian et al.'s [65] reasoning that collisions between <111> clusters are responsible for <100> loop formation, this should hold true for other BCC metals with similar <111> mobility. However, <100> loops are almost never observed in such metals [33].

Xu et al. [67] showed via atomistic kinetic Monte Carlo modelling that two <111> loops can produce a <100>, as predicted by Marian et al. [65], however this work only considered the interaction of similar sized loops colliding perfectly. Although Xu et al. showed this mechanism is

possible, without further simulation of various interaction paths and different loop sizes, this cannot confirm that this is the dominant mechanism for <100> formation.

It has been shown that small dislocation loops can transform from one Burgers vector to another, without the need for interaction with other defects. During simple heating, Arakawa et al. [58] observed <111> loops in iron spontaneously changing to <100> loops. It was also observed that <111> loops could change to another <111> loop configuration, and <100> loops could change back to <111> loops.

Dudarev et al. [33] suggested that spin fluctuations in iron are responsible for an elastic instability around the alpha-gamma phase transition temperature. Dudarev et al. showed that this instability is responsible for a dramatic reduction in the shear modulus and this has strong effect on the stability of <100> and <111> loops.

Dudarev et al. predict a strong relation between temperature and loop-type stability, with <100> loops becoming increasingly favourable as the temperature increases beyond 300^{o}C (Figure 2.8). Yao et al. confirmed that the frequency of <100> loops increases with temperature [35] (Figure 2.9) .

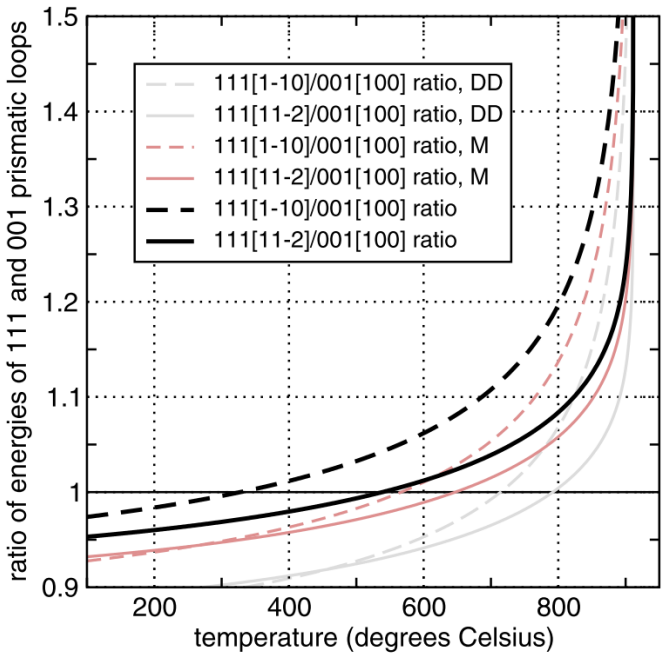

Figure 2.8: Prediction of the ratio of energies required to form a/2<111> and a<100> loops in iron (red lines), a prediction based on a different simulation method (light lines) and a prediction "best fit" in relation to experimental observations (black lines), from [33]

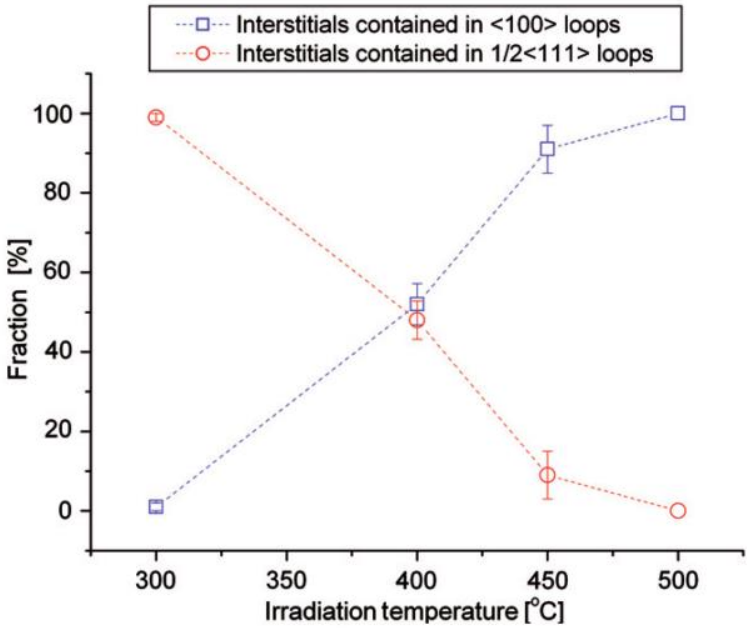

Figure 2.9: Experimental observations by Yao et al [35] *of changes in populations of interstitials in a<100> and a/2<111> loops in iron. From* [35]

Observed increases in <100> loop population are often correlated with increased mobility of defects, for example [47,68]. This would support the idea that the loops are being produced due to an increase in frequency of loop-loop coalescence, which, from the work of [67], could imply that

this is the dominant mechanism behind <100> loop formation. However, these cases may also always correlate with an increased likelihood of spontaneous transformation, such as that observed by Arakawa et al. [58] and the temperature dependence predicted by Dudarev et al. [33] and shown by Yao et al. [35]. Since loop-loop coalescence has never been shown experimentally to produce <100> loops, the dominant mechanism behind <100> loop formation is still an outstanding question.

Schäublin et al. [47] used TEM in-situ with 0.5 MeV self-ion room-temperature irradiation to show that <111> loops constitute the primary damage formed during the initial stages of cascade overlap in iron and FeCr, but <100> loops begin to dominate after a dose of 0.5-1.0dpa. Chromium was shown to reduce the population of <100> loops at the same dose as iron (0.5 and 1.0dpa). Schäublin et al. argued that this supports the loop-loop coalescence mechanism for <100> loop formation. However, at 0.05dpa, Schäublin et al. also saw a higher fraction of <100> loops in alloys of Fe-5Cr, -10Cr and -14Cr than in pure iron. This implies that although <111> loop mobility is reduced in these alloys, <100> loops can form via a different mechanism to the loop-loop coalescence mechanism, and this is favoured by the presence of chromium [47].

2.5 Dislocation loop growth and movement

Dislocation loops and voids act as defect sinks. They have a defect flux in, and a flux out (due to thermal effects). Defects will exhibit growth if the flux in is greater than the flux out. In iron, self-interstitials introduce a much larger lattice distortion than vacancies [69], and therefore have a greater influence on other distortions to the lattice. The consequence of this is that interstitial-type dislocation loops exhibit a stronger attraction for mobile interstitial defects than a vacancy dislocation loop has on mobile vacancy defects [17]. In short, this means interstitial dislocation loops grow faster than vacancy dislocation loops and voids when there are equal numbers of interstitials and vacancies, though this can change in the presence of transmutant gas [47,70].

This explains why interstitial loops are predominantly seen in TEM images of α-iron and FeCr [34,37,71]; most vacancy loops have either not yet grown large enough to be measurable as such, or have evolved into small voids that are not easily visible in the microscope.

Dislocations can move by either glide or climb. Dislocation loops which are able to move by glide in the loop plane are *glissile*, and those which cannot are *sessile*. Prismatic dislocation loops can glide only in directions perpendicular to the projection of the loop and parallel with the Burgers vector. Loops with screw and edge components glide in the direction normal to their line direction. Pure screw dislocation loops have no defined glide plane.

Climb allows prismatic loops to move within their habit plane by extending or retracting an extra half plane of atoms via absorption or emission of vacancies or interstitials [32]. Therefore, growth or shrinkage is a purely climb process. Alternatively, vacancies can diffuse around a dislocation loop causing positive climb on one side and negative climb on the other, allowing the loop to move sideways via "conservative climb" [32].

Dislocation climb is usually mediated by the diffusion of thermal vacancies, leading to a strong temperature dependence in the macroscopically observed creep [17,72]. For irradiated material however, the point-defect mediated climb will dominate, leading to irradiation induced creep dependence on the irradiation dose and dose-rate [72].

Although interstitials are usually considered to play a negligible role in climb, work by Thompson [72] showed that in the presence of equal concentrations of interstitial and vacancy super-saturations, as is the case within neutron-damaged materials (equal numbers of vacancies and interstitials), the resultant loop climb is actually dominated by the absorption of interstitials at the dislocations.

Bacon et al. [73] conducted a series of MD simulations to study the glissile and sessile nature of dislocation loops in BCC, FCC and HCP materials. It was shown that for BCC metals at 100K and

600K, <100> and <111> loops are glissile and can exhibit glide and climb movement. Marian et al. [66] later showed that, although they are intrinsically glissile, interstitial prismatic <100> loops are actually highly immobile in α-iron, requiring a high activation energy of >2.5eV to glide. Marian et al. argue that this means they can be treated as stationary defect sinks that grow by absorption of not only point defects, but also <111> clusters and loops. However, point-defect mediated climb could be significant.

2.6 Dislocation loop interactions with dislocations

Dislocation loops will affect the movement of dislocations and hence the material's ability to deform. Similarly, the dislocations (and grain boundaries) will affect the movement and growth of dislocation loops.

Pre-existing defect sinks can alter the spatial distribution of dislocation loops in a material. Robertson [34] saw loops initially decorating grain boundaries and dislocations in iron after low dose-rate neutron irradiation at 80°C. English [74] provided a review of neutron damage in copper, molybdenum, and iron, and observed an inhomogeneous distribution of the damage in all materials irradiated with neutrons at 80°C. Dislocation loops were found clustered around dislocation lines and sub-grain boundaries, and so it was concluded that such in-grown dislocations and sub-boundaries are necessary precursors to the development of an inhomogeneous spatial distribution of radiation damage.

Such clustering around dislocations was also observed recently by Chen et al. [75] in pure iron irradiated with neutrons up to 1.0dpa at 300°C, with no damage observed in the matrix. Chen et al. observed that the damage was homogeneous in Fe10Cr and Fe14Cr. Hernandez-Mayoral et al. [76] observed the opposite trend. After irradiating FeCr alloys from 2.5 to 12at%Cr with neutrons to 0.6dpa at 300°C, it was observed that dislocation loops were distributed uniformly in the matrix of Fe-2.5Cr, but loops were found only close to grain boundaries and dislocations in the other higher-chromium alloys (Figure 2.10).

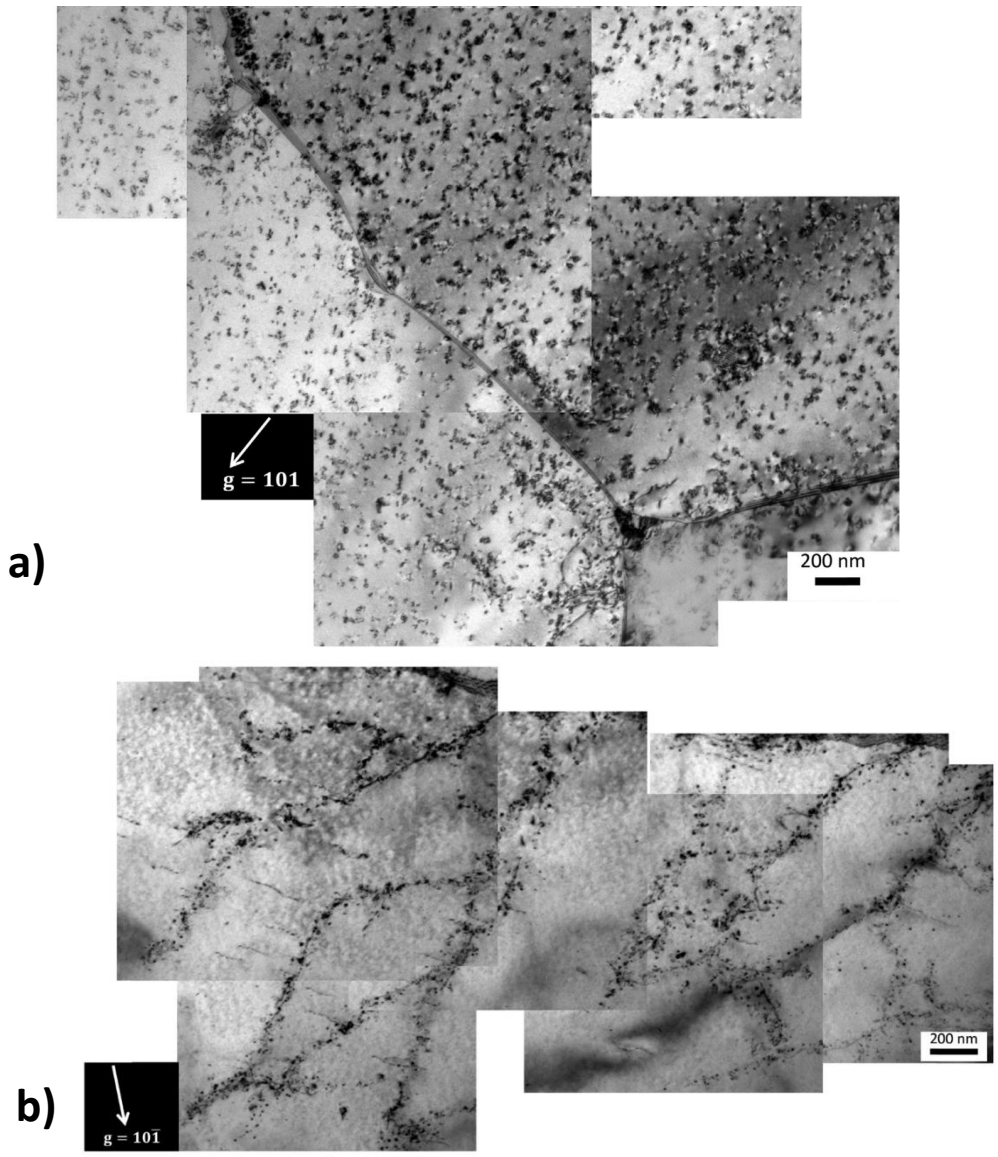

Figure 2.10: Bright field micrographs of homogeneous and heterogeneous dislocation loop damage in FeCr irradiated with neutrons to 0.6 dpa at 300°C. a) Fe2.5Cr and b) Fe5Cr, from [76]

There is clear inconsistency here, and the main arguments made by Chen et al. and Hernandez-Mayoral et al. [76] conflict with each other. Chen et al. suggested that low mobility due to chromium suppresses defect migration, so loops nucleate and grow homogeneously in higher chromium-containing alloys; whereas Hernandez-Mayoral et al. observed that regions dense with dislocation loops correlated with regions free of chromium α' precipitates, and vice versa. Hernandez-Mayoral et al. therefore suggested chromium α' precipitates may change the loop

homogeneity. This explanation is doubtful though, since Chen et al. also observed chromium α' precipitates in the >9%Cr alloys, and even Hernandez-Mayoral et al. reported no chromium α' precipitates in the Fe5%Cr, which also contained only heterogeneously-distributed dislocation loops. Though there is surely some compositional effect on the spatial homogeneity of dislocation loop damage, it is unclear what this may be.

Dislocations are well known to act as sinks for dislocation loops and point defects. For edge dislocations, interstitial clusters tend to appear on the dilational side of the dislocation due to a higher migration efficiency (product of mobility and point defect concentration) [77]. Due to the tendency for vacancy loops to stay small or cluster as immobile voids in iron, dislocation loops will be observed primarily on the dilational side of an edge dislocation [77].

Screw dislocations do not have a compressional or dilational "side" like edge dislocations, so they should act as a sink for both interstitial and vacancy defects. Defects reaching the dislocation core will cause the screw dislocation to jog-out via climb, and gain some edge-component [32,78]. Dislocation loops are easily trapped near screw dislocation cores, so can cluster near such dislocations and even rotate Burgers vector to align with the dislocation [79,80]. If there is a bias of one defect type (interstitial or vacancy), the dislocation will continue to climb out radially from the initial dislocation core [78]. The resulting structure is a helical structure. Helical dislocations are frequently observed in quenched materials due to the super-saturation of vacancies that are frozen-in by the quench [78]. Helical dislocations are observed in irradiated materials [74,80–82], which shows that screw dislocations must bias one defect type. Schäublin et al. [80] assumed this to be interstitial bias, but this has never been experimentally verified.

It is unclear how dislocation loops come to decorate dislocations. Trinkhaus [83,84] considered two mechanisms:

- Point defects migrate towards the dislocation, causing enhanced clustering and eventual loop nucleation in the strain field of the dislocation.
- Loops nucleate homogeneously in the material and glide towards the dislocation, before becoming trapped in the strain field.

Which of these causes loop decoration of dislocations in iron (and other materials) is an unresolved question.

2.7 Dislocation loops at high doses

Dislocation loop densities and size cannot increase forever with increasing dose. The density is well known to reach a peak and plateau with increasing dose (for example, [85]) and can be said to be saturated. At doses approaching the loop population/size saturation dose and above it (typically from a few dpa to 10s of dpa), the microstructure becomes complicated as loops interact with each other more prominently due to the reduced inter-loop spacing.

Hernandez-Mayoral et al. [38] studied Fe and FeCr in-situ with TEM at room temperature and 300^{o}C and studied loop evolution with increasing dose. It was shown that interstitial <111> loops will initially approach each other, agglomerating as strings (1-dimensional cluster) or rafts (2-dimensional cluster) of loops. Loop strings were suggested to be the early stages of raft formation, which may be harder to form during in-situ experiments due to interactions with the foil surfaces (which act as large sinks). Such clusters may experience climb and coalesce as the dose increases. At room temperature, strings were seen in Fe between 3-4dpa, but remained as such up to the end dose of ~5dpa. At 300^{o}C, loop strings were visible from ~3dpa, with some coalescence already apparent. Long “finger-loops” were seen between 3dpa and 5dpa.

These loop strings and finger loops are thought to form due to differences in loop mobility. The glissile <111> loops compared to the sessile <100> loops cause the microstructure to evolve in preference of the direction of the collective movements of the <111> loops. The result is that they align into strings, and eventually coalesce into <111> finger loops [86].

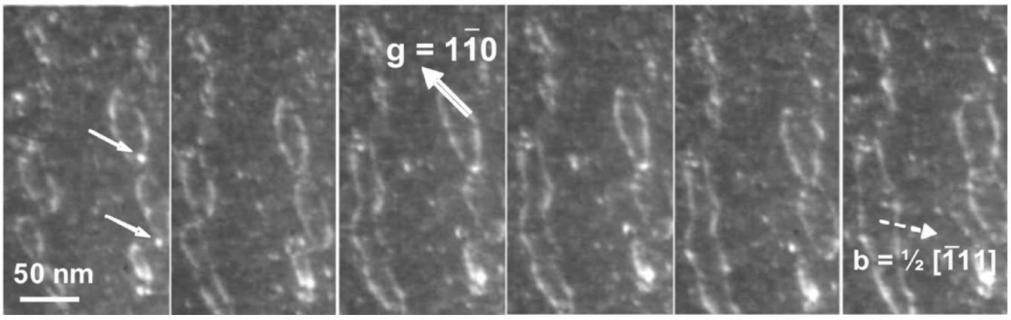

Figure 2.11: A series of video frames of a recording of loops coalescing into long finger-like structures.in ultra-high purity iron, from ~3dpa (far left) to ~5dpa (far right), from [38].

Yao et al [38] carried out irradiations on Fe at higher temperatures from 400°C to 500°C. Below 500°C, the microstructural evolution was observed to be similar to that seen by Hernandez-Mayoral et al. Small strings of <111> loops were seen to coalesce into large finger loops (Figure 2.11), and a steady increase in population of <100> loops with increasing temperature was seen.

2.8 Voids and transmutation gases

Voids or cavities are spherical clusters of vacancies. In iron they are a more stable configuration for vacancy clusters than vacancy loops [24], especially if stabilised by the presence of transmutant gas [87]. The presence of voids can play a large role in the macroscopic material properties because their nucleation and growth causes a change in volume of a material i.e. swelling (Figure 2.12) [88]. Austenitic nickel-containing steels are highly prone to swelling due to the high neutron-capture cross-section of nickel, leading to excessive helium production. Ferritic and ferritic-martensitic steels exhibit less swelling, though Garner et al [89] has shown that swelling in such materials at ultra-high doses (100s of dpa) is still significant.

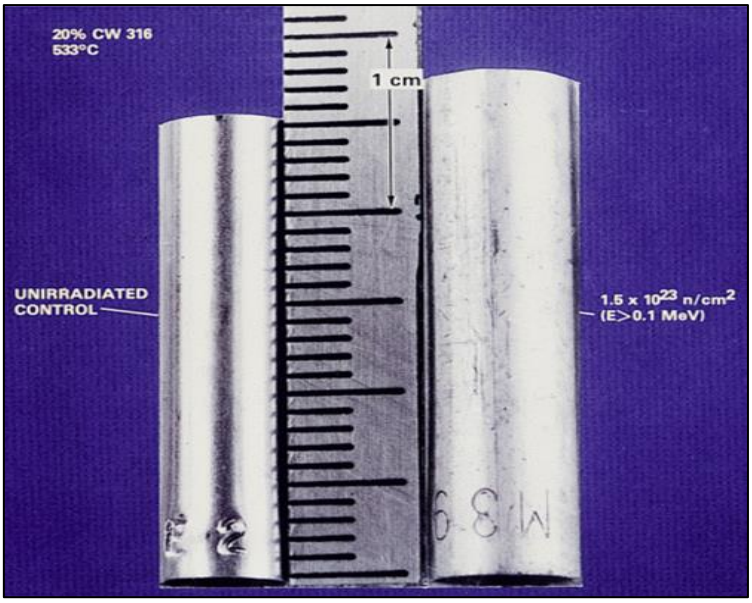

Figure 2.12: Austenitic stainless steel unirradiated and irradiated with neutrons, from [88]

Vacancies are less mobile than interstitials [50], as discussed earlier in 2.3. In comparison to interstitial dislocation loops, voids either need a longer time, require a higher dose (so more vacancies are available to cluster) or a higher temperature (so that mobility is increased) to develop to sizes visible in the TEM (>1-2nm). Void development is also highly dependent on the crystallography, initial dislocation microstructure, composition and level of impurities in the material [90,91].

A consequence of neutron irradiation is the nuclear reactions taking place during inelastic collisions causing new elements to be produced in a material. For ferritic materials, perhaps the most significant compositional change by transmutation is the production of gaseous elements, hydrogen and helium (Equation 2.3).

Equation 2.3

a) $^{56}Fe + n \rightarrow {}^{53}Cr + \alpha$

b) $^{56}Fe + n \rightarrow {}^{52}Cr + n + \alpha$

c) $^{56}Fe + n \rightarrow {}^{56}Mn + \mathrm{p}$

d) $^{56}Fe + n \rightarrow {}^{55}Mn + \mathrm{n} + \mathrm{p}$

Vacancies can agglomerate around hydrogen and helium, with the gaseous impurity acting as new nucleation points for voids while increasing their stability [17]. Given that spherical voids are already the preferred geometry of vacancy clusters [24], voids can be expected to be more populous after fusion-neutron irradiation than after fission-neutron or ion-irradiation. If a cavity contains a gas, such as helium, it is considered a bubble if the pressure inside is sufficient to exert compressive strain on the surrounding matrix [17].

Stewart et al [92] demonstrated that above a certain pressure, helium bubbles grow in iron via emission of interstitial atoms in order to increase the available volume and relieve the pressure inside. The consequence of this is that a build-up of interstitials can eventually form a new dislocation loop. The equilibrium condition for a bubble is reached when the force due to the outward pressure of the gas, p, is equal to the inward-acting force due to the surface tension, as shown by Equation 2.4, where γ is the surface energy and R is the radius of the bubble [17].

Equation 2.4

$$p = \frac{2\gamma}{R}$$

Tanaka et al. [87] showed that the production of helium and hydrogen is much more significant for ferritic alloys in a fusion-neutron spectrum than a fission-neutron spectrum. It was shown that heavy-ion irradiation in-situ with hydrogen has little or no effect on void evolution. Heavy-ion damage in-situ with helium implantation was found to slightly enhance void growth by 0.4%, but when helium and hydrogen were used together with heavy-ions, void growth was significantly enhanced by 5%. These results imply hydrogen's role on swelling may be significant in ferritic materials, despite a large quantity diffusing out [93].

The presence of helium and hydrogen can also effect the dislocation loop evolution. Thin-foil irradiations by Schäublin et al. [47] suggest helium suppresses the movement of <111> dislocations, though this work was conducted for 1000appm/dpa (of helium), which is ~100 times the amount expected during irradiation in a fusion-neutron spectrum. Schäublin et al.'s conclusions were also

inferred from the increased proportion of <111> loops in the foils irradiated in the presence of helium compared to the foils without helium, and reasoned if <111> coalescence is the dominant source of <100> loops, this must imply that <111> loop mobility is reduced. If <111> coalescence is not the dominant mechanism behind <100> formation, then this reasoning fails. The reason for Schäublin et al.'s observations could alternatively indicate that the spontaneous transition from <111> to <100> type, as observed by Arakawa et al. [58], is suppressed by helium.

2.9 Effects of chromium (6-14at%) on radiation damage in FeCr alloys

Ferritic-martensitic alloys with high chromium content are the common basis of many steels being developed for nuclear fusion. The chromium content has numerous advantages, including;

- Improved resistance against corrosion and oxidation
- Reduction in diffusion rates
- Reduced creep rates
- Easier formation of the Martensite phase

In the fusion operating environment of 300-500^{o}C for structural steels, alloys containing ~9wt% Cr experience the least irradiation hardening and are most resistant to erosion corrosion. It also has the lowest change in DBTT after irradiation [4,14,94]. These factors make chromium-containing steels ~9wt% very attractive for fusion application.

The effects of chromium on the dislocation loops produced during irradiation has been studied extensively. Fe-Cr alloys have many similarities to iron in terms of radiation damage. Yao et al. [37] showed the threshold dose effect exists in FeCr as it does for pure iron, which shows that cascade overlap is required for interstitial loop nucleation, and Schäublin et al. [47] showed that cascade collapse can also occur from high energy density cascades. Loop mobility is reduced in FeCr in comparison to pure iron [20,37], which leads to smaller loops and greater loop number densities with respect to iron [54,76,95,96], and increase in fraction of <111> loops [76]. Additionally, chromium can segregate on dislocation loops during irradiation, causing additional strengthening and impedance to dislocation loop motion [97,98].

Through the increased concentration of mobile defects brought on by radiation, diffusion is enhanced which can cause alloying elements to "un-mix" from the matrix. Radiation Induced Segregation (RIS) is the driving of alloying and impurity elements to (or from) extended sinks such as grain boundaries, surfaces and dislocations, caused by the increased diffusion during irradiation. The increased diffusion will also increase the likelihood of the local concentration of chromium in the matrix to increase above the solubility limit of chromium in iron – the composition of chromium above which α' phases form. Such regions can catalyse the formation of α' phases. This is Radiation Induced Precipitation (RIP). Such precipitates (typically 2-4nm in diameter) are significant causes of hardening and embrittlement.

The phase diagram for Fe-Cr is shown in Figure 2.13 and shows four stable solid phases. The BCC α-phase in the iron-rich region and the BCC α'-phase in the chromium-rich region are within the operational temperature range for ferritic-steel components in fission and fusion reactors (300-500^{o}C). These phases are separated on the phase diagram by an α+α' "miscibility gap". This is where chromium and iron are effectively insoluble within the matrix of each other. The more energetically favourable configuration in chromium-containing steels will be chromium rich precipitates contained by a matrix with a composition that lies close to the boundary between α and α+α' phases (the solubility limit).

Prime candidate RAFM steels have chromium content typically 7-14at%, which lies close to and beyond this solubility limit. Above this limit, phase separation by nucleation and growth will occur. This process occurs without irradiation in high chromium steels (>12%) thermally aged at 475^{o}C ("475 embrittlement") [99]. Above ~550 ^{o}C, the chromium remains in the α-phase (Figure 2.13). Below ~300 ^{o}C, chromium tends to stay in solution despite residing in the α+α' miscibility gap. This indicates that the phase separation process is too slow for it to become significant. However, irradiation can accelerate this precipitation [99].

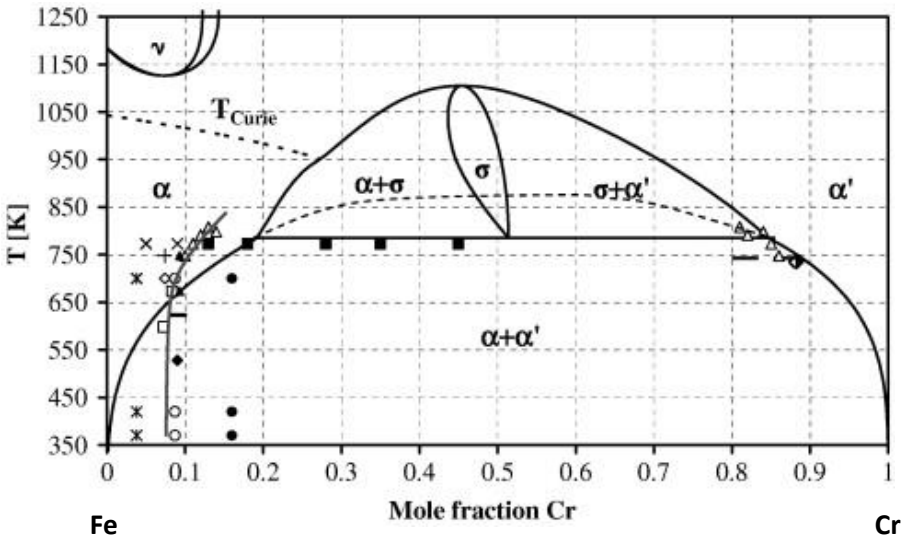

Figure 2.13: Fe-Cr phase diagram, from [100]

Bachhav et.al. studied a series of FeCr binary alloys irradiated with neutrons to a dose of 1.82dpa at 290°C [97,101,102]. Bachhav et al. [101] showed RIP of chromium from α to α' phase for alloy compositions Fe-9Cr to Fe-18Cr, and a uniform Cr distribution in Fe-3Cr and Fe-6Cr (Figure 2.14). This supports previous work by Bonny et al. [99], Cara et al. [103] and Pareige et al. [104] that the solubility limit of chromium at this temperature in iron lies close to 9%. Where α'-phases were observed, the matrix composition ranged from 8.9at% to 10at% chromium. No α' phases were identified in the Fe6Cr alloy by Bachhav et al., but in a separate paper, Bachhav et al. [101] identified chromium clustered around dislocation loops in the same Fe6Cr.

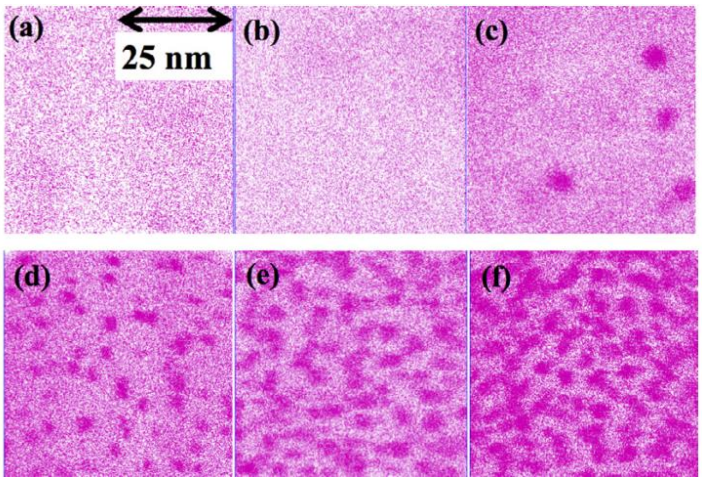

Figure 2.14: Atom Probe Tomography data showing chromium distribution in FeCr alloys neutron irradiated to 1.8 dpa at 325°C . a) Fe-3Cr, b) Fe-6Cr, c) Fe-9Cr, d) Fe-12Cr, e) Fe-15Cr, f) Fe-18Cr. α' precipitates (the dense clusters of chromium) form in Fe-9Cr, but not in Fe-6Cr, implying a solubility limit between 6 and 9at%. From [101].

Since chromium has been seen to cluster at dislocation loops in an alloy with chromium content below the solubility limit [101], this could be evidence that dislocation loops act as nucleation sites for α' precipitates. In the higher chromium alloys, the density of precipitates is too great to infer that each is associated with a loop (much larger than the visible loop population), but early loops or defect clusters may have started the α' nucleation process before evolving into larger and less populous defects.

Pareige et al. [104] studied heavy-ion and neutron-irradiated low-purity Fe-9Cr and Fe-12Cr. Both alloys showed α' precipitation after neutron irradiation at 0.6dpa. However, the heavy-ion irradiated alloys showed no signs of any chromium precipitation. More recently, Tissot et al. [105] showed that chromium precipitates can form from low dose-rate heavy-ion irradiation at 300°C in Fe15Cr, but this is suppressed by the dose-rate effect via ballistic dissolution and, importantly, the injected self-interstitial population[5]. Tissot et al. [106] has also shown that α' precipitates form during electron irradiation in the same Fe15Cr alloys, irradiated at a similar dose-rate and temperature to the self-ion implantation [105]. Electron irradiation produces only single Frenkel-pairs [17], and produced much richer chromium precipitates (>90at% from electron irradiation, and <50at% from heavy-ion irradiation. Since self-ions produce large cascades in iron [17], these works show that cascades can disrupt the formation of the α' phase.

[5] The effect of the implanted ion population is discussed later in section 2.10.2

Hardie et al. [107] has seen evidence of chromium precipitates in heavy-ion irradiated ultra-high purity Fe-5Cr at 290°C (Figure 2.15). Though the precipitates observed were not as chromium-rich as those seen by Bachhav et al. [101] or Tissot et al. [105], Hardie et al.'s results [107] imply that some sort of un-mixing can still occur below the accepted solubility limit of chromium in the presence of radiation damage, and by using heavy-ions. This could be attributed to chromium segregation of dislocation loops [97], though there does not appear to be an accepted standard for when a cluster of chromium atoms may be designated as an α'-phase.

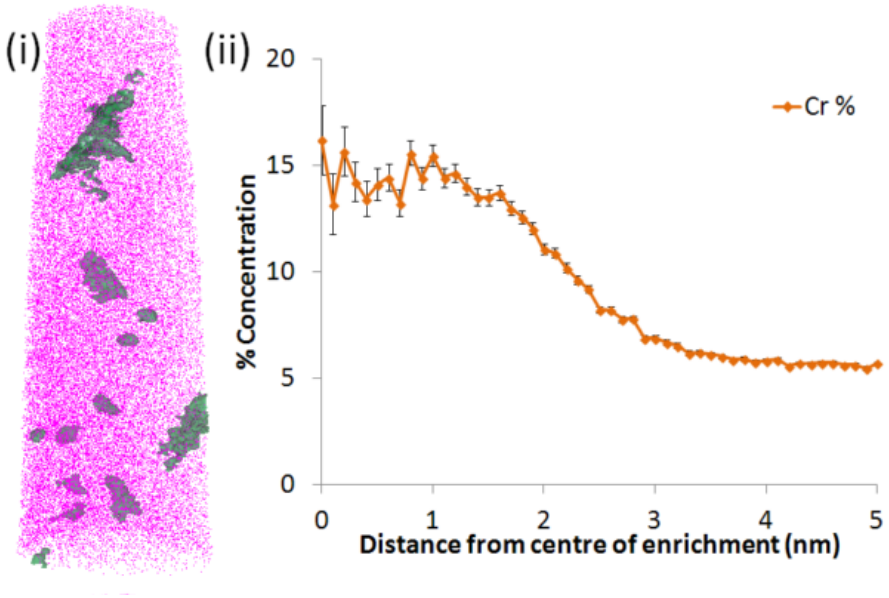

Figure 2.15: Atom Probe Tomography data showing chromium distribution in an ultra-high purity Fe-5Cr alloy irradiated at 400°C with heavy ions at 0.6dpa, from [107].

2.10 Replicating neutron irradiation damage using ion-beams

With no high flux source of fusion-neutrons available for materials testing, the fusion-neutron damage must be studied using surrogate particles and with modelling. A commonly used analogue to fusion-neutrons are fission-neutrons from commercial pressurised-water reactors (PWRs) or dedicated fast-spectrum materials-testing reactors [108]. Correlating fusion and fission-neutron damage is not trivial due to differences in neutron energy spectra and the damage rates, and is further complicated given that much of the early literature on this does not fully document the radiation conditions used. For example, dose-rate, energy-spectra and thermal history of neutron irradiation experiments often go unreported.

Neutron irradiation sources induce harmful levels of radioactivity in samples. This makes handling and studying the samples considerably more complicated. The use of a hot cell and remote handling facilities is generally required for storage, and instruments dedicated to working with such materials are needed for post-irradiation analysis. This considerably adds to the expense of working on neutron-irradiated materials.

Charged-particle irradiations, such as heavy-ions or protons, are much easier to use compared with neutrons. They can be used to probe a wide range of conditions with a degree of flexibility not attainable by fission-neutron sources. Furthermore, they induce little or no radioactivity at the energies typically used[6], unlike neutron sources, and are able to reach high doses in a fraction of the time. Ion accelerators are far more numerous than materials-testing reactors, and much cheaper to build – thus ion beams are cheaper and more convenient to use, which are the main reasons for their appeal.

[6] Heavy-ions are used at energies from a few keV up to tens of MeV, which is insufficient to cause transmutation. Protons are used up to a few MeV, which can induce some low level radioactivity, but much less than what can be expected from neutrons at equivalent dpa-dose. This is particularly true for <2.5MeV proton irradiation of iron.

Self-ion irradiations are attractive as they do not change the chemistry of the material, can generate high levels of damage in a relatively short time and are thought to effectively mimic the PKA from a neutron collision. Protons are also attractive for producing ballistic damage in materials as they have a smoother and deeper damage profile than heavy-ions, as discussed in section-2.10.2.

2.10.1 Displacements per atom

The fluence of irradiation is a bad measure to use as a constant when comparing neutron irradiation to charged-particle irradiations. The accepted alternative dose measure is the "displacements-per-atom" (dpa), which is a prediction of the average number of times each atom in a material has been displaced during irradiation.

Although dose is almost certainly related to the observable damage, the two are not trivial to correlate as the latter is affected by many other variables such as dose-rate and temperature. This is complicated further when comparing damage across different material compositions, or materials irradiated with different particles. Nonetheless, dpa is the most widely adopted unit of displacement-dose.

The accepted industry standard method for calculating dpa is using the Norgett, Robinson and Torrens (NRT) model of displacement damage [18,109]. The SRIM code [110] is a convenient tool that can simulate vacancy creation and energy losses (via various mechanisms) as an ion propagates through a material, and apply the NRT method to calculate the displacements-per-atom.

The NRT model requires the damage energy T_d to be calculated via Equation 2.5.

Equation 2.5

$$T_d = E_{ion}^{p} + E_{recoil}^{p} = E_{recoil}^{a} - E_{recoil}^{i}$$

$$where\ T_d = damage\ energy, \quad E_{ion}^{p} = phonons\ by\ ion, \quad E_{recoil}^{p} = phonons\ by\ recoils,$$
$$E_{recoil}^{a} = Energy\ absorbed\ by\ recoils, \quad E_{recoil}^{i} = Energy\ lost\ by\ ionization\ by\ recoils$$

The average number of vacancies produced by a single PKA is then given by Equation 2.6, which, when scaled by the fluence, can be used to calculate the total number of vacancies produced, and hence the average number of displacements-per-atom.

Equation 2.6

$$v = 0.8 \times \frac{T_d}{2E_d}$$

$$where\ v = vacancies, \quad E_d = displacement\ energy = 40eV\ in\ iron$$

The use of dpa and SRIM to calculate radiation doses is convenient, but far from ideal. Many flaws exist with the model:

- SRIM is unable to predict the number of replacement collisions, where one atom replaces another in the lattice. Replacement collisions affects the number of surviving defects after a cascade, which can vary for different temperatures, materials and different incident particles. SRIM only considers a temperature of 0K.
- SRIM makes no distinction between crystal types, and so does not account for channelling effects (where the mean free path of an ion is longer along crystallographic zone axes). Nor will it consider that the displacement energy of an ion is different for different crystallographic directions.
- It cannot account for dose-rate effects (these will be discussed later), or the damage history of a material.

The most accurate way to predict the damage received by a material is using MD modelling, though this not practical for calculating doses involving many thousands of cascades. SRIM is therefore the most widely adopted program used to simulate vacancy production. For a critical review of SRIM, and guidelines for its use, see reference [18]. The practicalities of calculating dpa will be discussed in section-3.1.

2.10.2 Recoil effects and damage differences due to the irradiating particle

The recoil-spectrum produced by neutrons, self-ions, protons and electrons are all different, and so irradiation by each of these particles will produce a different distribution of cascade sizes, and thus there will be differences to the primary-defects produced by the cascades [17].

Fusion and fission environments have very different neutron spectra that will cause large differences in damage production. The predicted PKA-spectra for structural materials in DEMO suggest over 95% of Frenkel defects will be produced by knock-on atoms with energy of 5-200keV [23]. Collision cascades produced by knock-on atoms <200keV are the dominant source of primary damage production in fusion-neutron irradiation.

The main difference between a fission and fusion energy spectrum is the high flux of higher energy neutrons (~14MeV) produced from the DT-fusion reaction (Figure 2.16). These higher energy neutrons will produces a larger number of transmutations [23,111] and so helium and hydrogen are produced in greater quantities for equivalent displacement damage [112–115] (Table 2.1). The added presence of gas also impacts on the migration of vacancies, void production and defect stability, as well as being a major source of hardening and embrittlement [17].

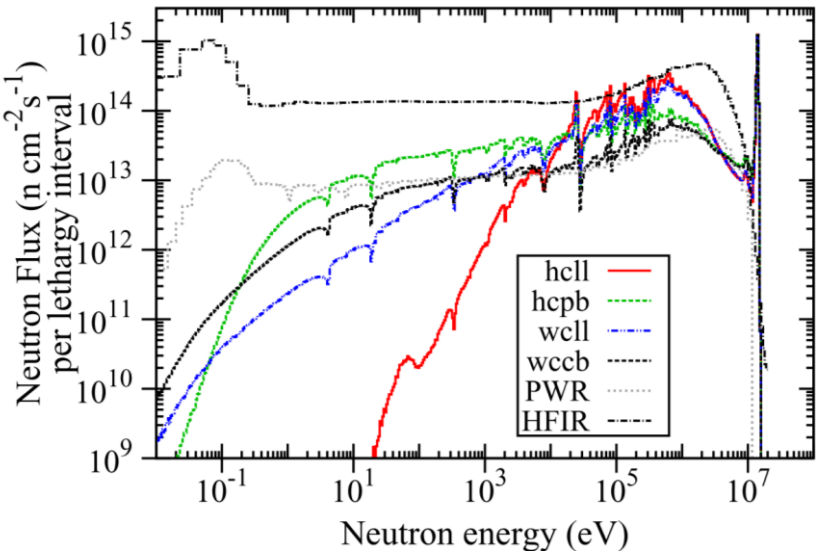

Figure 2.16: Neutron spectra for various DEMO concepts, a typical pressurised water reactor (PWR) and the HIFR experimental fission reactor, from [23].

Spectrum	Gas by-product	APPM per dpa in Iron
DEMO	H	9
	He	17
Fission (ATR)	H	4
	He	0.2

Table 2.1: Production of hydrogen and helium in iron after 1 dpa of a typical DEMO spectrum and fission spectrum (Advanced Test Reactor). These values were calculated using FISPACT-II with help from Dr Mark Gilbert.

As discussed in section-2.1, the number of displaced atoms per cascade approaches a constant function of damage energy above some critical energy [19,116–118]. This threshold represents the energy at which electronic losses dominate PKA-energy losses.

Stoller [117] used MD simulations to study the number of surviving defects as a function of PKA-energy, which was quantified as the fraction of the NRT prediction of vacancies produced by a given PKA (the defect production efficiency). Stoller found this fraction of surviving defects decreases with damage energy up to ~10keV in iron, which indicates that, although a greater number of atoms are displaced in large cascades, this allows for a greater proportion of the interstitials and vacancies to interact, and hence recombine. The defect production efficiency remains roughly constant above 10keV at ~30%, indicating cascade sizes approach a maximum. Above 10keV, sub-cascade formation will become increasingly common and recombination frequency will plateau, though Zarkadoula et al. [119] observed differences in defect production up to a much higher energy of 0.5MeV.

The consequence of this is that for self-ions of energy greater than this threshold PKA-energy, the type of defects produced should be the same as if it were the PKA from a neutron collision [117,119]. This is often used to justify self-ions as a suitable analogue for neutron ballistic damage, since the heavy-ion itself may be treated as a PKA. De Backer [27] has shown that the size

distribution of sub-cascades (which can be considered a PKA-spectrum of sorts) does not change significantly for ion energies of 600keV and above, only changing noticeably in the overall frequency of each sub-cascade volume, so the primary displacement damage should be comparable to neutrons for such high-energy ions.

Since defect production efficiency decreases with PKA-energy [117], defect production by light ions and electrons will be more "efficient". Electrons do not produce cascades, only single Frenkel pairs [17]. This therefore equates to 100% production efficiency, since none recombine (at least initially). Protons produce lower energy recoils than self-ions or neutrons [23,110,117,120], so proton-induced cascades will be smaller on average, yet will produce a higher fraction of surviving defects. This should lead to a greater fraction of surviving defects from proton and electron irradiation than from neutron irradiation at equivalent NRT dose (and dose-rate). Protons are therefore argued to be ill-suited for replicating neutron damage. This might only be the case for primary-damage, however.

Figure 2.17 illustrates the typical differences in average cascade size produced by 1MeV electrons, protons, heavy-ions and neutrons in nickel. The average damage energy, $\bar{T}$, is indicated for each case, as is the fraction of freely migrating primary defects, ε. The freely migrating defects are the point defects left-over after a cascade (those that do not recombine or reside in clusters).

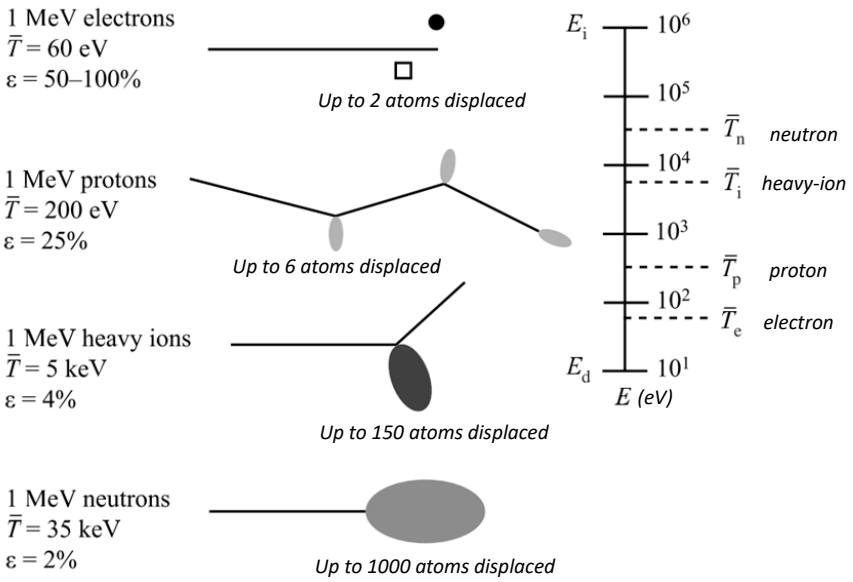

Figure 2.17: Schematic illustration of cascade sizes in nickel for different irradiating particles. $\bar{T}$ is the average damage energy of a cascade (the energy contributing to displacing atoms), and ε is the fraction of the number of displaced atoms that survive as freely migrating point defects, adapted from [17]*. The displacement energy for nickel is 33eV* [121]*.*

Self-ions have been used for decades to study radiation damage in iron and iron-based alloys, and many other materials. Iradiation by self-ions has been used successfully to measure various radiation damage pheonomena, such as threshold dose effects [37,43], primary damage nucleation in cascades [26,122], chromium dependency [20,36–38,54], loop nature [37,54,123], and Burgers vectors [35]. These references are just a few notable examples, but self-ion irradiation has been used for hundreds of studies, spanning many materials. However, the shallow penetration depth of self-ions (up to a few microns) limits the volume of material that can actually be studied, particularly if mechanical properties are sought.

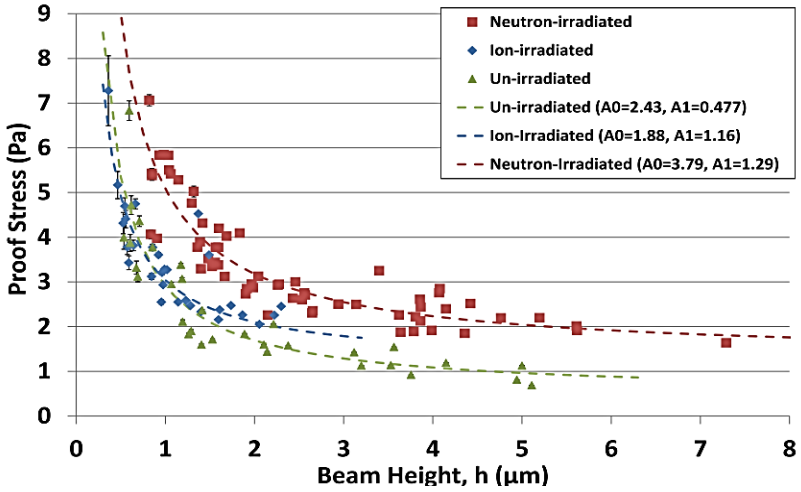

Figure 2.18: Micro-cantilever data of the proof stress in irradiated Fe-6Cr as a function of the size of the cantilever beam. The increase in proof stress at small beam heights is a demonstration of the size-effect. From [124].

Though advances in the field of micromechanics have allowed for radiation hardening, strengthening and embrittlement to be tested [125,126], there are considerable difficulties to conducting such tests. The size-effect is the apparent increase in yield strength of a material as the volume being studied decreases (Figure 2.18) [124]. This makes it difficult to interpret the results on a larger scale, and so the measured mechanical changes brought on by irradiation on the microscale can be unreliable.

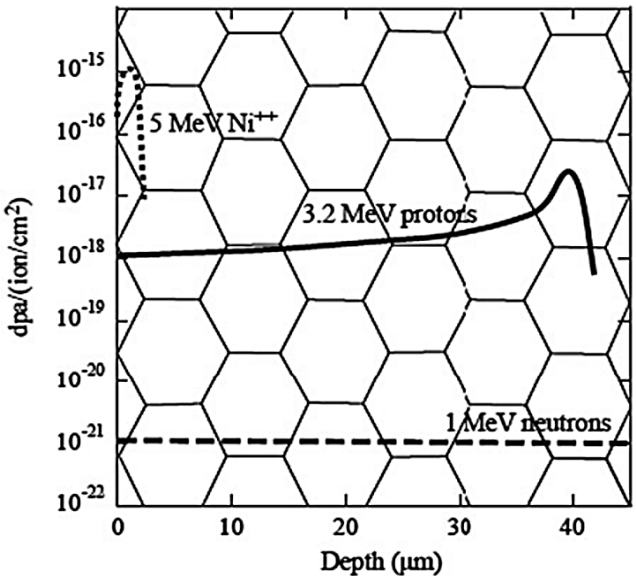

Figure 2.19: Example damage profiles of neutrons, protons and nickel ions in stainless steels. Superimposed is a 10µm grain structure. It is can be seen that a significant portion of the proton damage profile is smooth across a grain. From [17].

Small-scale mechanical tests are also difficult to produce consistently, and so typically a large number of tests are required to improve statistical significance. There is therefore a need for the ability to implant radiation damage over larger volumes, without the use of a nuclear reactor or radioactive-handling facilities.

Proton irradiation is able to produce such damage. Protons penetrate much deeper (typically 10s of microns) than heavy-ions of equivalent energy (typically <1μm), and with a more homogeneous damage profile, unlike the very shallow and inhomogeneous profile of a heavy-ion (Figure 2.19) [17]. The larger penetration depth of protons opens the possibility for micromechanical testing to be used on volumes of material containing several microns of damage, and crucially on volumes where the size-effect is insignificant [124].

Before micromechanical tests can be used reliably on proton-irradiated materials, the microstructural changes must be well-characterised and compared with neutrons and heavy-ions under the same conditions in order to verify that comparable damage is produced. It is futile to conduct such experiments if the dominant mechanisms for hardening are different after proton irradiation than after neutron irradiation.

It should be clarified that charged-particle irradiations are mostly not used with the intention of recreating neutron damage exactly. Instead, they are used to study trends that may otherwise prove too costly or impossible via neutron irradiation. That said, there are efforts to mimic neutron damage using ion beams to the extent that the microstructural and mechanical changes caused by neutrons can be reliably reproduced, including replication of transmutant gases [127–129].

Unfortunately, there is no comprehensive study in the literature comparing the microstructural changes brought on by neutrons, self-ions *and* protons, where each has been used to irradiate under similar conditions and in identical materials.

Gan et al [130] compared austenitic Fe-Cr-Ni alloys irradiated with neutrons and protons from ~300°C to 600°C. It was found that the dislocation loop density and size distribution had similar dose and temperature dependency in proton and neutron-irradiated alloys. Particularly, neutrons irradiated at 275°C and protons irradiated at 360°C showed little difference in irradiated microstructure, despite the temperature difference. The higher temperature was thought to lower the sink strength and promote loop evolution (discussed further in 2.10.3 in relation to the dose-rate effect). The authors suggest this as evidence that the PKA-spectrum differences had no significant effect on the final microstructure. However, their results do not show that proton and neutron irradiation are equivalent, merely that the results follow the same trends for proton and neutron irradiation.

In contrast to what is widely thought from the literature, Souidi et al. [131] suggested that PKA-spectrum differences are not strongly influential on long-term defect evolution. This would justify the use of protons for replicating neutron damage. Monte-Carlo simulations by Souidi et al. showed that at low dose, the dependence of cascade energy on the size distribution of defect clusters is very small. It was suggested that the size distributions from low energy cascades are effective building blocks for the full spectrum of energies obtained under neutron irradiation. Therefore, the energy dependent properties such as cascade size and sub-cascade production should not affect the long-term evolution of defect clusters.

This is supported by work by Yu et al [132] who showed that despite a low PKA-spectrum increasing the proportion of freely migrating defects per NRT-dpa dose, the change in yield strength of an RPV alloy at equivalent dose by electrons, protons and neutrons was similar. Thus, the dominant hardening mechanisms were considered to be unaffected by any PKA-spectrum effects. These authors did not report on the microstructure or microchemistry, so the observed sources of the hardening could be completely different, and the similar changes in yield strength merely coincidental.

An additional factor not yet considered is the fate of the injected particle. For self-ion irradiation, there is an extra interstitial atom near the peak damage region, which may be affecting the evolving microstructure. It has already been discussed in section-2.9 that injected interstitials affect chromium precipitation in Fe-15at.%Cr. There has not been a similar study to determine how dislocation loops are affected by the injected self-interstitials.

The injected atom for proton irradiation is a hydrogen atom, which could become trapped amongst the cascade-generated defects. It is generally assumed that the hydrogen diffuses away from the very small region of interest [93,133]. However, Tanaka et al. [87] has shown it to be highly influential when performing irradiations in-situ with helium implantation. In addition, hydrogen has been shown to be effectively retained in ferritic steels due to trapping at defects and dislocations [134,135], even at high temperature. Jung et al. [134] showed ferritic-martensitic steels show reduced ductility due to hydrogen at concentrations from ~500 to ~1000appm at 350^{o}C. Caution should therefore be taken when irradiating with protons, as the implanted hydrogen is clearly retained, even at high temperature, and this may be playing a more significant role on the defect evolution than is usually supposed. A simple SRIM calculation shows that the injected hydrogen per NRT-dpa is ~10^{2}-10^{3}appm in volumes far from the peak injected material part of the dose profile. This is significantly higher that what can be expected in a DEMO fusion spectrum.

2.10.3 Dose-rate effects

If recoil effects have an insignificant effect on the damage produced from high dose irradiation, then the dominant difference between the neutron and charged-particle irradiation will be due to the extreme differences in damage rate.

Garner et.al. [110] highlighted the influence of dose-rate on the microstructural damage, and argued its influence can dominate over any possible effects from the primary recoil-spectra and transmutation products. The impact of dose-rate is very important since irradiations in the literature can span several orders of magnitude (Table 2.2) [106,135–139], and large differences are unavoidable when attempting to mimic neutron damage with ion beams.

Source of irradiation	**Dose-rate in Fe-based alloys (dpa/s)**	
Fission Reactor Pressure Vessels (RPV)	~10^{-11} - 10^{-10}	[205]
Rotating Target Neutron Source (RNTS-II)	~10^{-10}	[142]
Fast Flux Test Facility	~10^{-8} - 10^{-6}	[142]
DEMO Fusion Reactor	~10^{-8} - 10^{-6}	[206]
Proton implantation	~10^{-7} - 10^{-5}	[145]
Heavy-ion implantation	~10^{-5} - 10^{-3}	[107]
High voltage electron microscopy	~10^{-3}	[207]

Table 2.2: Radiation sources and corresponding dose-rates.

The rate at which point defects interact with sinks and other defects is proportional to the square of their density, and depends on their mobility within the matrix [136]. Their interactions dictate which reaction path they will follow, and their fate has been shown to strongly depend on the dose-rate [137–139].

Defect losses to extended sinks such as surfaces, network dislocations or grain boundaries are described as first-order reaction paths, which do not alter the sink to which they are lost. Second-

order reaction paths cause a change to the intra-granular microstructure. This includes the capture of vacancies or interstitials by loops, voids and clusters, the nucleation of new interstitial or vacancy clusters, and loss by vacancy-interstitial recombination [17,137]. Though network dislocations are described as first order reactions paths, it is wrong to call them this since they experience climb on absorption of defects. Therefore, dislocation sinks can change line length with fluence, and the bias may also change.

The dominant reaction path that determines whether defects are evolving in a sink-dominant or recombination-dominant regime depends on the density of sinks, and the mobility of defects. A sink-dominant regime is explained by there being more defects at higher doses, and therefore more sinks for defects to migrate to. The recombination rate is affected by the temperature and the dose-rate [137] (Figure 2.20). Recombination will be more abundant at high dose-rates, whereas low dose-rates will be characterised by defect loss at grain boundaries and dislocation sinks.

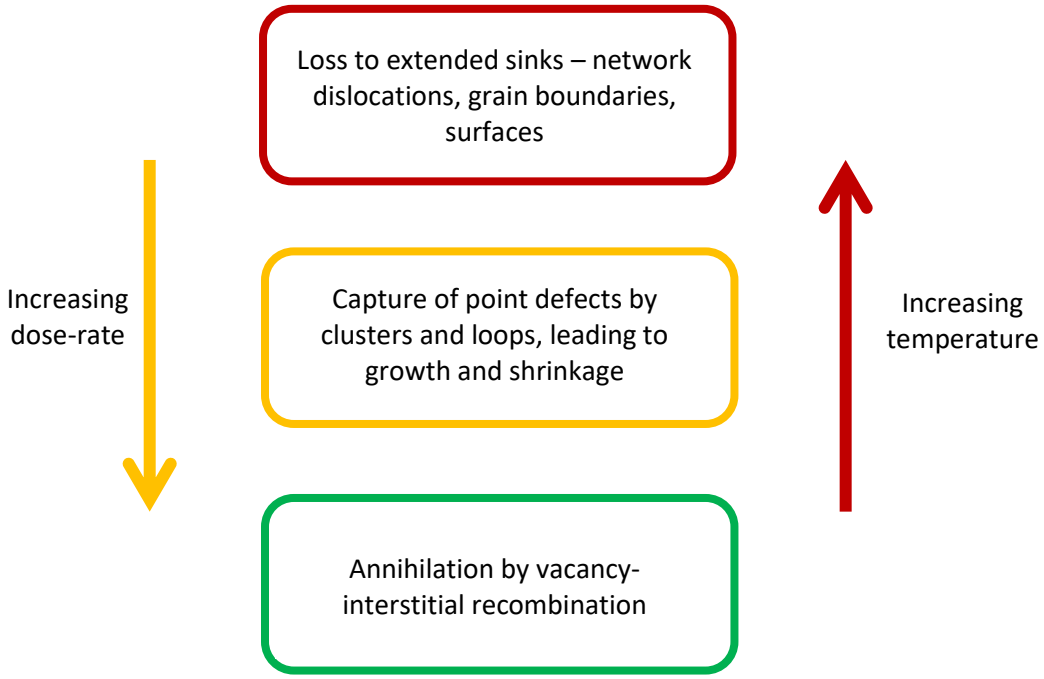

Figure 2.20: Defect behaviour trends with dose-rate and temperature

Vacancy defects generally require a higher energy to migrate than interstitials. In iron, vacancies have a migration energy of 0.67eV whereas interstitials have a migration energy of 0.34eV [50]. Defect migration in iron is strongly subdued by the presence of impurity atoms, such as carbon. Carbon bonds with vacancies to form a strong vacancy-carbon complex with a binding energy of 0.41eV and migration energy of 1.08eV [50], whereas self-interstitials repel carbon [140]. This difference in migration energies can cause a production bias of interstitial or vacancy defects, depending on the temperature [141], and might also cause the production of biased defect sinks [77].

The dose-rate effect on damage evolution was investigated by Muroga et al. [85] who studied Fe-Cr-Ni austenitic alloys. The dislocation loop saturation dose was studied using electrons, fast neutrons and fusion-neutrons to irradiate the alloys, allowing an extremely large range of dose-rates (10^{-9} – 10^{-4}dpa/s) to be probed. Though the alloys used for each irradiation slightly differed, and there was some variation in temperature, a dose-rate dependency was found. With increasing dose-rate, the dislocation loop population increased, as shown by Figure 2.21a.

The electron irradiations were used to observe an extreme difference in PKA-spectrum and study the influence of the spectral differences. Muroga et al. found the defect density from the neutron irradiation experiment was higher than what would be predicted from equivalent dose-rate electron irradiation (as extrapolated by the power-law, with exponent of 0.5), shown in Figure 2.21b.

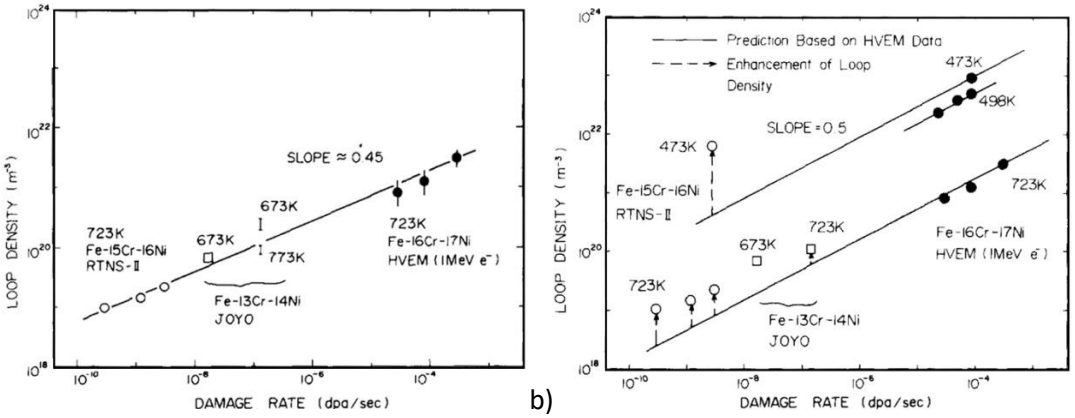

a) b)

Figure 2.21: Saturation loop density dependency on dose-rate using fast spallation neutrons (white circles), fusion-neutrons (white squares) and high voltage electrons (black circles), from [85]*. Graph a) is the best fit trend of dose-rate based on the neutron and electron data. In graph b), the lines are based on the electron data only. The shift from the prediction by the neutrons is suggested to be due to PKA differences.*

It has already been discussed in section-2.10.2 how the proportion of defects that recombine after a cascade increases with PKA-energy (i.e. cascade size) up to ~10keV. Therefore, recoil-spectra differences between neutron (large cascades) and electrons (single Frenkel pairs) should be shown as a lower overall defect density due to neutron irradiation, not an increase as is suggested by Muroga et al.'s results. This is attributed to a PKA-spectrum effect. However, there may also have been differences to the loop sizes (which was not reported), and their interpretation of when "saturation" has been reached (defined by Muroga at al. as when loop density plateaus and loops cease to grow). Additionally, extrapolating the damage-rate trend-line from the high dose-rate electron irradiation to many orders of magnitude lower dose-rates must be accompanied by a significant uncertainty.

The saturation loop density is thought to obey a power-law as dose-rate increases, with a gradient of ~0.5 on a log(dose-rate) vs log(loop density) plot [85,139,142,143]. However, none of these studies use the exact same materials, temperatures, doses or recoil energies, across many orders of magnitude differences in dose-rate. Therefore, there may be deviation from this power-law that is not accounted for in these studies.

Xu investigated the dose-rate effect as part of his DPhil thesis [144], for which he compared self-ion irradiated Fe-5Cr, Fe-10Cr and Fe-14Cr irradiated to the same dpa, at two dose-rates with a factor of 20 difference ($6x10^{-4}$ and $3x10^{-5}$dpa/s). It was shown in each alloy that the interstitial loop number density and sizes increased with increasing dose-rate, as is expected [85]. However, with only two data points differing in dose-rate by a factor of 20, this work is insufficient to estimate a power-law dependency over many orders of magnitude differences in damage rate.

Hardie [124] studied neutron-irradiated Fe-6Cr alloy by micromechanical testing and compared this to the same alloy irradiated with heavy-ions. Despite differences in dose, the work implies the presence of additional hardening mechanisms in the neutron-irradiated material, attributed to differences in dose-rate or PKA-spectra, possibly via differences to the chromium enrichment of grain boundaries, and/or gas embrittlement [124].

The best way to offset the dose-rate effect when using ions or protons is to simply minimise it by irradiating for as long as possible. This is impractical and expensive for most particle accelerators, and so neutron irradiation remains the only source for low dose-rate experiments.

Mansur et al. [138] proposed a means of adjusting the irradiation conditions to compensate the dose-rate effect. Mansur et al. suggested that a shift in temperature could be used to increase the mobility of point defects. This could reduce the timescale over which dislocation loops evolve, change the effective strengths of defect sinks, and ultimately compensate for a dose-rate effect. Such a shift could be used to promote defect evolution in a sink-dominant (Equation 2.7a) or recombination-dominant regime (Equation 2.7b). The former is important for dislocation evolution, and the latter is important for RIS. If dose-rate is to be compensated, ideally both dislocation evolution and RIS will need to be matched.

Equation 2.7

$$a)\ T_2 _ T_1 = \frac{\frac{kT_1^{\,2}}{E_m^v + E_f^v} \times \ln\left(\frac{\varphi_2}{\varphi_1}\right)}{1 - \frac{kT_1}{E_m^v + 2E_f^v} \times \ln\left(\frac{\varphi_2}{\varphi_1}\right)} \qquad b)\ T_2 _ T_1 = \frac{\frac{kT_1^{\,2}}{E_m^v} \times \ln\left(\frac{\varphi_2}{\varphi_1}\right)}{1 - \frac{kT_1}{E_m^v} \times \ln\left(\frac{\varphi_2}{\varphi_1}\right)}$$

$$where \quad T = temperature,\ k = Boltzmann\ constant,$$
$$\varphi = flux\ of\ irradiation,\ E_m^v = migration\ energy\ of\ a\ vacancy,$$
$$E_f^v = formation\ energy\ of\ a\ vacancy$$

This "Mansur shift" is a promising means of offsetting the dose-rate effect and opens the possibility of replicating neutron damage using the high dose-rates of charged-particle irradiation. Though such a temperature shift may be appropriate for use with austenitic materials which only produce <111> dislocation loops during irradiation, it may be less suited to ferritic materials. The Burgers vectors of dislocation loops produced in ferritic materials depends greatly on the temperature [33,35] as was discussed in section-2.4, and possibly dose-rate. The fraction of <111> and <100> loops present in a material could affect the observed radiation hardening [64], so a Mansur shift may struggle to adjust for the dose-rate effect in ferritic materials.

Was et al [145] and Gan et al. [130] used the Mansur equations [138] (Equation 2.7) to estimate a single temperature shift that could compensate both sink-dominant and recombination-dominant regime effects. Was et al. [145] irradiated austenitic steels with neutrons at 275°C and with 3MeV protons at 360°C, and assumed PKA-energy differences had an insignificant effect on the damage produced at >1dpa doses. From this substantial investigation, Was et al. found the radiation induced changes to the steels to be similar for neutron and proton irradiation. The spatial extent of RIS, the microstructure, and even the hardening were similar (for example, Figure 2.22 shows the size distribution of dislocation loops in proton and neutron-irradiated steel from this study [145]).

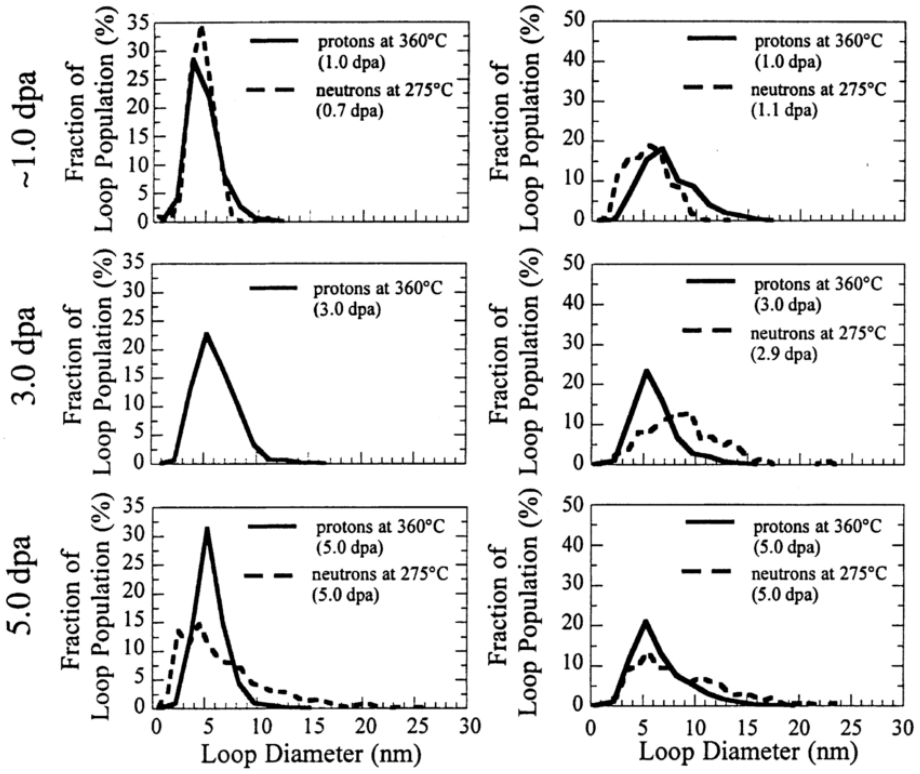

Figure 2.22: Dislocation loop size distribution in 275°C neutron and 360°C proton irradiated austenitic alloys, from [145]*. The loops sizes match up remarkably well.*

However, the results of irradiating at the same temperature in the same alloys was not reported. The temperature shift used by Was et al. [145] and Gan et al. [146] does not correspond to the temperature shift of either Mansur-equation (Equation 5), and instead lies somewhere in the middle. Therefore, it seems there must have been some trial and error involved in finding a temperature shift that worked for their materials.

What is lacking in the literature is a thorough comparison of neutron and proton irradiation at the same temperature, and on the ~MeV proton-energy scale. Victoria et al. [147] irradiated α-iron with 590MeV protons and PWR reactor neutrons at the same temperature of 50°C and to a similar dose of 0.33 and 0.38dpa respectively. At 590MeV, protons will produce recoils up to the MeV-range in iron, so irradiation at these energies is in theory more comparable to a neutron recoil-spectrum [117]. Additionally, their proton irradiation experiment was also only ten-times the dose-rate of their neutron experiment, which is a far smaller difference in dose-rate than is typical for charged-particle irradiations.

Victoria et al. [147] found that the neutron-irradiated iron contained larger dislocation loops than the proton-irradiated sample (5.1nm and 3.3nm mean loop diameter respectively, and ~7nm and ~17nm maximum loop diameter respectively), and contained an approximately three times higher dislocation loop population density. Despite these differences, Victoria et al. claimed the loop sizes were analogous in proton and neutron-irradiated iron. The dislocation loops in both cases were assumed to be interstitial, though this was not measured.

Errors in dose calculations or temperature measurements may be the main source of the differences observed by Victoria et al., though this is not clear. Victoria et al. also claimed that no recoil-spectrum dependency was observed. However, if ~MeV recoil energies are attained by their protons in iron, then the PKA-spectrum should have been comparable to the neutron-induced PKA-spectrum due to cascade splitting [117], hence this statement is not evident from their results.

The work by Was et al. on correlating neutron and proton irradiation damage via a temperature shift to compensate dose-rate differences has been used to justify many more applications of protons as an accurate means of replicating neutron damage (for example [148–155], and Was et al.'s paper on neutron and proton damage [145] has received over 200 citations).

2.11 Summary of key literature elements and thesis goals

- The dislocation loops formed during irradiation of FeCr are similar to those in pure Fe. The loop populations in FeCr are generally reported to be greater than in Fe, and with a smaller size distribution, but there are only minor changes with increasing chromium content. Chromium pins dislocations inhibiting movement and growth, causing FeCr materials to be harder than pure Fe. Chromium also suppresses the population of the <100> loops, and there is still uncertainty over exactly how the <100> loops form, though loop-loop coalescence appears to be the most popular mechanism.

- Dislocation loops can be seen either homogeneously distributed throughout a material, or mostly decorating dislocation lines and/or grain boundaries in iron and FeCr. Though there appears to be a strong influence from the irradiation conditions that can determine the spatial distribution of dislocation loops, the dependency on composition is uncertain.

- Simulating neutron damage using ion beams is advantageous but is accompanied by a large error due to either dose-rate differences, recoil spectrum differences or both. Despite these fundamental differences, there are promising signs that recoil spectra may not be so influential on the evolution of dislocations and voids.

- There are no studies of dose-rate differences with a great enough difference to study the effect sufficiently in the same material. The studies that do analyse the dose-rate effect over many orders of magnitude do so using different irradiating particles, and not the exact same material. The general influence of dose-rate is to increase the loop density, but influence on dislocation loop sizes is not clear.

- The solubility limit of chromium is better known from neutron irradiation studies with analysis by APT, and is thought to lie near 9% at 300°C. There are indications that un-mixing can still occur however in lower chromium compositions via segregation of chromium on dislocation loops.

- Although there are many comparative studies of neutrons, protons and self-ions, none compare all three, nor do they often compare such irradiation at the same temperature. It is becoming increasingly common for a temperature shift to be applied to counter dose-rate differences, however without in-depth comparative studies at equivalent temperature, it is uncertain how influential such shifts really are.

The overall aim from this thesis is to study the microstructure of neutron, self-ion and proton irradiation damage in the same materials in order to assess and highlight the differences produced.

1. How well do protons and self-ions replicate neutron damage if the irradiation conditions are matched as closely as possible? Can it be determined whether dose-rate effects or recoil-spectra (or both) control any differences observed?

2. Do dislocation loop sizes, population, Burgers vector or nature change according to the irradiating particle used to implant the damage? Do the void populations also change? How is the redistribution of chromium impacted by the irradiating particle?

3. Does the dislocation loop homogeneity change when the irradiating particle changes? Is it possible to deduce a mechanism that encourages heterogeneous dislocation loop distributions?

Chapter 3: Experimental methods

3.1 Introduction

In the next few sections, detailed descriptions of the materials used, the sample preparation processes, and the TEM techniques will be outlined. Details of the particular irradiation experiments are described in chapters 4 and 6.

3.2 Material fabrication

The FeCr alloys studied are the same polycrystalline FeCr specimens that were used for early studies of neutron damage effects in FeCr by Gelles et al. [64,91,156] and in more recent neutron studies by Bachhav et al. [97,101,102] and Hardie et al. [124]. Specimens of Fe-6at%Cr and Fe-9at%Cr were used in this thesis in order to examine the post-irradiation microstructure and microchemistry of FeCr at compositions above and below the solubility limit of chromium [101,157] (8-9at%, see section-2.9). From here on, the alloys will be referred to in the text as simply Fe6Cr and Fe9Cr.

The chemical composition of the alloys is shown in Table 3.1 according to the vendor analysis reported by Gelles et al. [91] and next to a more accurate composition taken from the atom-probe analysis by Bachhav et al. [101].

		Cr	C	O_2	N_2	Ni	Si	P	Mn	V
Vendor analysis (at%)	**Fe-6Cr**	6.41	0.03	0.07	0.01	-	-	-	-	-
	Fe-9Cr	10.23	0.01	0.08	0.01	-	-	-	-	-
APT analysis (at%)	**Fe-6Cr**	5.84	0.03	-	-	0.05	0.01	0.01	0.01	0.01
	Fe-9Cr	9.36	0.01	-	-	0.05	0.01	0.01	0.01	0.02

Table 3.1: Chemical compositions of the Fe6Cr and Fe9Cr alloys as reported by Gelles et al. [91] *(vendor analysis) and Bachhav et al.* [101] *(APT analysis)*

A description of the manufacturing process of the alloys is provided by Gelles et al. [91] and repeated here. One hundred pound (~45kg) heats of the Fe6Cr and Fe9Cr alloy were melted at the

Paul D. Merica Research Laboratory, International Nickel Company, New York. The alloys were provided in the form of a 1cm extruded bar, which was then rolled to approximately 0.2cm thick. The material in this form was used for the neutron irradiation experiments by Gelles et al. [64,91,156], which comprised ferritic and ferritic-martensitic microstructures. The materials used for this work originate from this same batch of alloys. The alloys were annealed under an argon atmosphere at 950°C for 15 minutes followed by air cooling, then tempered at 750°C again followed by air-cooling [101,124] to produce a ferritic microstructure with few residual dislocations.

The annealing was performed by my collaborators at UCSB for their 2009 neutron irradiation campaign at the Advanced Test Reactor in Idaho USA [158]. Alloys of Fe6Cr and Fe9Cr from one of these neutron irradiation experiments were studied by TEM as a major part of this thesis. The irradiation experiment is described in detail in section-4.1.

My collaborators at UCSB provided the unirradiated and neutron-irradiated Fe6Cr and Fe9Cr alloys, allowing charged-particle irradiations to be performed on the same materials that were neutron-irradiated. No further heat treatments were applied to the materials. SEM micrographs of the as-received alloys are shown in Figure 3.1. The grains were ferritic, with a grain size 20-30μm for Fe6Cr and 40-60μm for Fe9Cr, though grains as small as 1μm were present in both.

TEM measurements of the foils indicated a clean microstructure with large regions free of dislocations. Figure 3.2 shows example micrographs of the microstructure of the Fe6Cr and Fe9Cr, showing regions with few dislocations that would be ideal for studying irradiation damage. The dislocation density of both the Fe6Cr and Fe9Cr is approximately $6x10^{12}$ m^{-2}, though since the volume of material studied is fairly small, there may be some variation in the dislocation density depending on the grain observed.

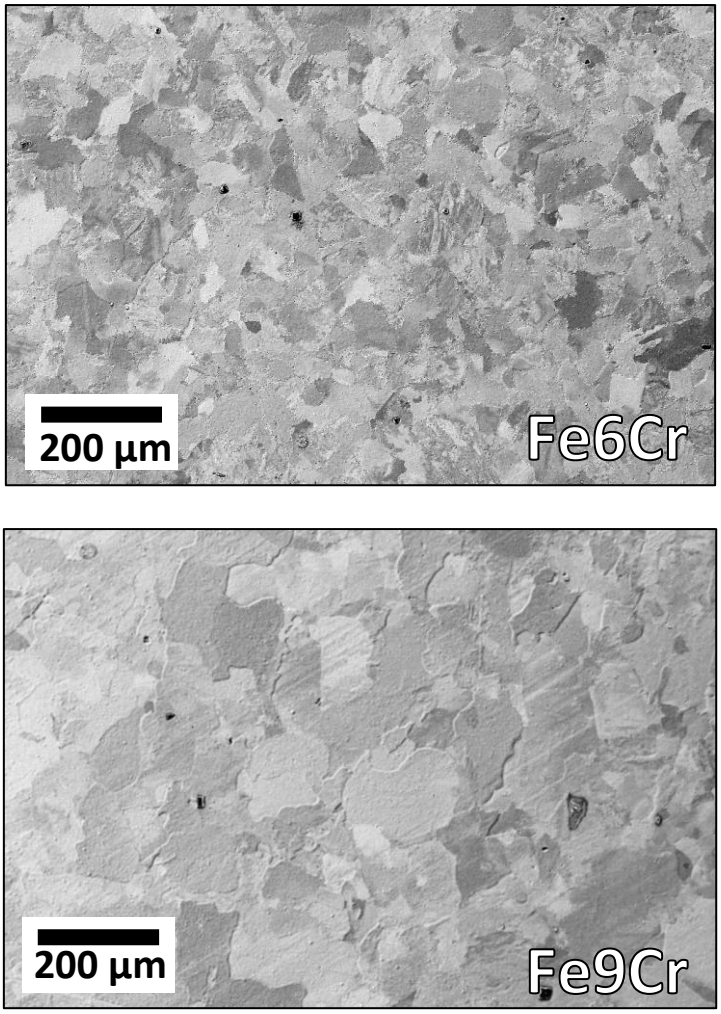

Figure 3.1: SEM micrographs of the grain structures of Fe6Cr and Fe9Cr, as received.

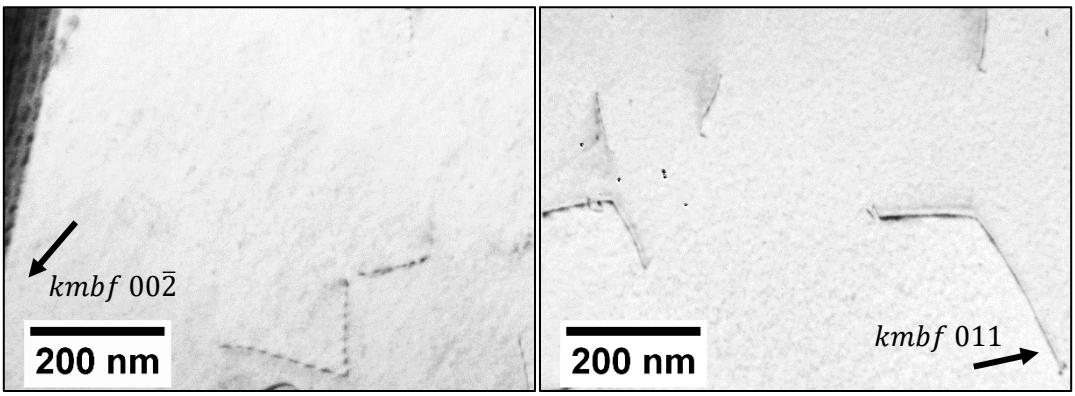

Figure 3.2: TEM micrographs showing large regions with a low dislocation density. Such regions are ideal for studying radiation damage. Micrographs were captured in kinematical bright field conditions (kmbf).

3.3 Irradiation damage experiments and calculations

The work contained in this thesis involves irradiation experiments conducted at the Advanced Test Reactor at Idaho National Laboratory by my collaborators at UCSB [158], as well as my own experiments at the Surrey Ion Beam Centre (a University of Surrey facility) and the Dalton Cumbria Facility (a University of Manchester facility). The details of the irradiation experiments are described in the relevant results chapters (chapters 4 and 6).

Here will be described the two main approaches used to calculate "displacements-per-atom" (dpa), which is the particle-independent dose parameter used for experiments in this thesis (discussed in section-2.10.1).

The SRIM (Stopping Ranges of Ions in Matter) simulation program [110] was used to calculate the dpa and damage profile of the charged-particle irradiations used in this thesis. SRIM uses a binary-collision-approximation (BCA) algorithm to compute the energy losses of ions as they propagate through materials.

Perhaps the most convenient method of calculating dpa is via the VACANCY.TXT output file, which is a prediction of the number of vacancies, v, that are created in generic units of vacancies per ion per angstrom-layer of material. Using Equation 3.1, the displacements-per-atom can be calculated.

Equation 3.1

$$DPA = F \times \frac{v}{V_{atom}}$$

where F is the fluence in ions per unit area, and V_{atom} is the number of atoms contained per angstrom per unit area.

There are two algorithms SRIM can use to simulate the ion; the quick Kinchin-Pease model (K-P) and the Full Cascade model (F-C). The F-C model was presumed to be more accurate until Stoller [18] highlighted that an F-C model generated VACANCY.TXT file differs from the MD-predicted vacancy production and the K-P model VACANCY.TXT file by a factor of ~2. Stoller therefore

recommended that the F-C model be avoided entirely in favour of the K-P model due to flaws in the algorithm.

Stoller also recommended that dpa should not be calculated using the VACANCY.TXT output file. Instead, the damage energy should be calculated, and converted to number-of-vacancies via Equation 3.2. This is the "NRT" method.

Equation 3.2

$$\nu = 0.8 \times \frac{T_{Dam}}{2 \times E_{Disp}}$$

Where E_{Disp} is the displacement threshold energy (40eV for iron)

To calculate the damage-energy, T_{Dam}, it is simplest to first calculate the incident beam-energy, as explained by Stoller [18]. The incident beam-energy is not actually the energy input by the user, but the total energy deposited by the beam for a given event. This is equal to the sum of the energy deposited by the input ion to the target atoms (E2RECOIL.TXT "Energy-from-ions"), the energy deposited by the input ion to the electrons (IONIZ.TXT "Ioniz.-by-ions"), and the energy deposited by the input ion as vibrational-energy (PHONON.TXT "Phonons-by-Ion").

Equation 3.3

$$E_{Incident\ beam} = E_{Deposited\ by\ beam\ to\ target} + E_{Deposited\ by\ beam\ to\ electrons} + E_{Deposited\ by\ beam\ to\ generation\ of\ phonons}$$

The damage energy is then given by the incident beam energy, minus the energy deposited to the electrons by the beam and by the recoil-atoms.

Equation 3.4

$$T_{Dam} = E_{Incident\ beam} - E_{Deposited\ by\ beam\ to\ electrons} - E_{Deposited\ by\ recoils\ to\ electrons}$$

Stoller [18] says the damage-energy can also be calculated as the sum of the beam-energy deposited as phonons (E2RECOIL.TXT "Energy-absorbed-by-target") and the energy deposited as phonons by the recoiling atoms (PHONON.TXT "Phonons-by-recoils"). The file Stoller states should be used for the beam energy deposited as phonons is incorrect (possibly a typographical error), and the correct calculation should use PHONON.TXT "Phonons-by-ion".

Equation 3.5

$$T_{Dam} = E_{Deposited\ by\ beam\ to\ generation\ of\ phonons} + E_{Deposited\ by\ recoils\ to\ generation\ of\ phonons}$$

The calculated "vacancies per ion per angstrom" using the results from Equation 3.2 to Equation 3.5 is shown for 2MeV self-ions and 1.2MeV protons in Figure 3.3. The results are nearly equal for the self-ion simulation, but for 1.2MeV protons, the results differ substantially. This illustrates that SRIM calculations of dpa from proton irradiation has a high degree of uncertainty. This is something that is not acknowledged in the literature with regard to proton irradiation.

For this work, I have used the NRT-method to calculate dpa, using Equation 3.2, Equation 3.3 and Equation 3.4, since this value is roughly equal to the average of all the doses shown for proton irradiation of iron in Figure 3.3. The "calculation-error" for proton irradiation dose calculations was taken to be the standard deviation of the result from all three methods, which equals ±25%.

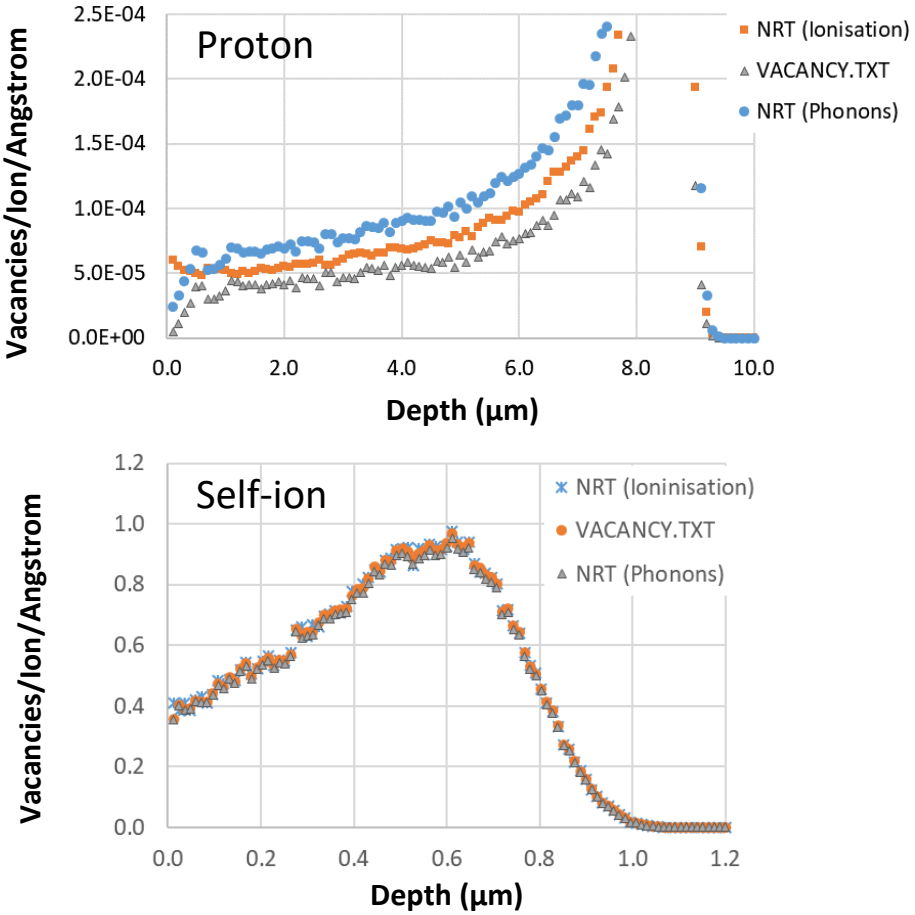

Figure 3.3: A comparison of SRIM profiles for 2MeV self-ion and 1.2 MeV proton irradiation in iron

With guidance from Dr Mark Gilbert, I calculated dpa for the neutron irradiation experiment using the FISPACT-II software package [159], which uses the entire measured energy-spectrum of the neutrons to predict the full range of neutron reactions that take place, including vacancy production and transmutation reactions.

3.4 Sample preparation prior to irradiation

Samples were prepared in the form of 3mm disks because the volume of material available for experiments was very small, and so the unirradiated Fe6Cr and Fe9Cr could only be used in these small quantities.

Samples for the charged-particle irradiations were cut into small pieces that could be thinned using 1200-grade silicon-carbide paper until thin enough to punch into 3mm disks using a TEM-disk punch. These were then polished using SiC paper again with grades 2500 and 4000 in order to remove the imprints from the TEM-disk punch, and then each disk was polished using diamond suspension (grades 3µm, 1µm, 0.25µm and 0.1µm). The final step was to bath-electropolish the samples to remove remaining mechanical deformation.

Electropolishing was conducted using an electrolyte of 5% of the as-received perchloric acid in methanol[7], at <-40°C. Samples were held in place using platinum-tipped tweezers (the anode) in a beaker lined with an aluminium cathode. A magnetic stirrer was used to gently stir the solution during polishing so that the electrolyte could flow over the surface of the sample.

A potential difference of ~30V was applied for 1-second intervals and the sample was checked using an optical microscope after each interval. The potential difference required to produce an acceptable polish could vary by up to ±10V, which could depend on the sample, the age of the electrolyte, the stirring rate, temperature, and even the weather (e.g. humidity or air pressure). In general, good polishing could be reached with this set-up when the current read ~100-120mA.

A relay timer was used to control the duration of the electropolishing. Immediately after electropolishing, it is important to wash the sample using fresh ethanol. First, the sample was dipped into cold ethanol, accompanied by gentle up and down motion (but always keeping it submerged) for ~5 seconds. This removes most of the residual electrolyte from the sample and tweezers. This

[7] Ethanol can also be used.

would be followed by 10 seconds in a second beaker of fresh and cold ethanol, and finally another 10-20 seconds in a beaker of room temperature ethanol. It is important to raise the temperature of the sample gradually through different temperature "washes" in order to prevent condensation on the sample. If the washing has not been thorough enough, or there has been too long between electropolishing and the first washing stage, then the sample can rapidly oxidise and the surface can appear brown within seconds. The set-up used was identical to that used by Yao et al. [160], which is shown in Figure 3.4.

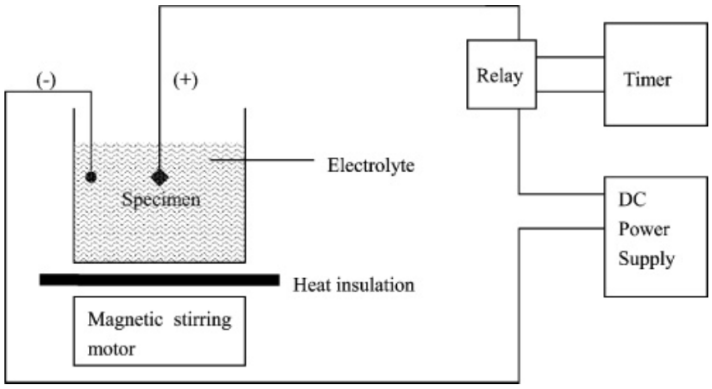

Figure 3.4: Experimental set-up for bath-electropolishing FeCr samples, from [160]

Figure 3.5 shows an SEM image of the interface between a mechanically polished and electropolished surface. Though the mechanically polished surface is flatter, the grains are duller than electropolished side, and some scratches are visible. The grain boundaries in the electropolished side have undergone some pitting, indicating the polishing voltage was slightly too high.

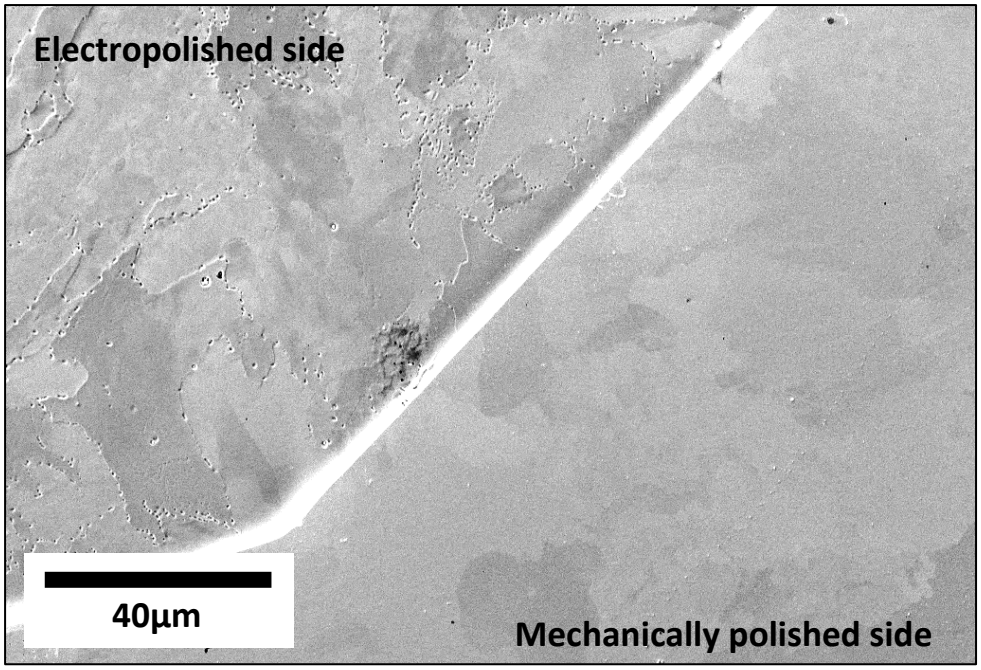

Figure 3.5: Comparison of an electropolished and mechanically polished surface of FeCr

All samples were prepared according to this "recipe" prior to irradiation, except for the neutron-irradiated samples. The neutron-irradiated samples were prepared post-irradiation by staff at INL by mechanical polishing, and a final step of jet-electropolishing (not to electron-transparency) to obtain a deformation-free surface much similar to the electropolished finish shown in Figure 3.5.

3.5 Sample preparation for TEM

The quality of a TEM-foil has a huge influence on the quality of the images obtained in the TEM. The method that produces the highest quality TEM foils, at least for metals, is via jet-electropolishing. When the optimum conditions are used, electropolishing produces many hundreds of square microns of electron-transparent material, whilst introducing no defects to the microstructure that might otherwise reduce the quality of a foil, and no amorphous layer on the surface. Here will be described the method of twin-jet electropolishing, followed by a description of preparation by focussed ion beam (FIB), which was ultimately the method used for foil preparation throughout this thesis.

3.5.1 TEM foil preparation by twin-jet electropolishing

The Struers TenuPol 5 electropolisher uses twin-jets of electrolyte fired at the centre of a 3mm disk, whilst applying a potential difference across the sample. This gently removes material from both sides of a 3mm disk, producing a concave surface on both sides. Eventually, a small hole is formed in the centre, around which the material is thin enough to be transparent to electrons (typically ~100nm thick).

As with the bath-electropolishing used to prepare samples prior to irradiation, the voltage that achieves good polishing is often difficult to establish. As such, it is quite common to find that no single voltage was appropriate for electropolishing, even for identically composed samples. Previous users of these systems, Dr Shuo Xu and Dr Sen Xu, found optimal polishing between 20V and 21.5V [144,161]. However, it was found during this work that optimal polishing could be found at greater than 30V. This is likely due to differences in the resistance of the circuit of the particular apparatus. In practice, it was found that the disks polished best when the current was ~120mA (though even this could vary by ±20mA) and this served as a better guide to finding the correct conditions. Polishing was conducted below -40C to reduce the rate of polish and hence improve control over the process.

Etching of grain boundaries will occur at low voltage, and pitting (small holes 4nm-10nm) across the sample will occur for too high voltage. Somewhere in the middle will be a small window at which ideal polishing will occur. For more information about the process of jet-electropolishing, see reference [162].

Figure 3.6 shows an example micrograph of a successfully electropolished foil of an unirradiated alloy of Fe5Cr. Dislocations are clearly visible with strong contrast against a clean and bright background.

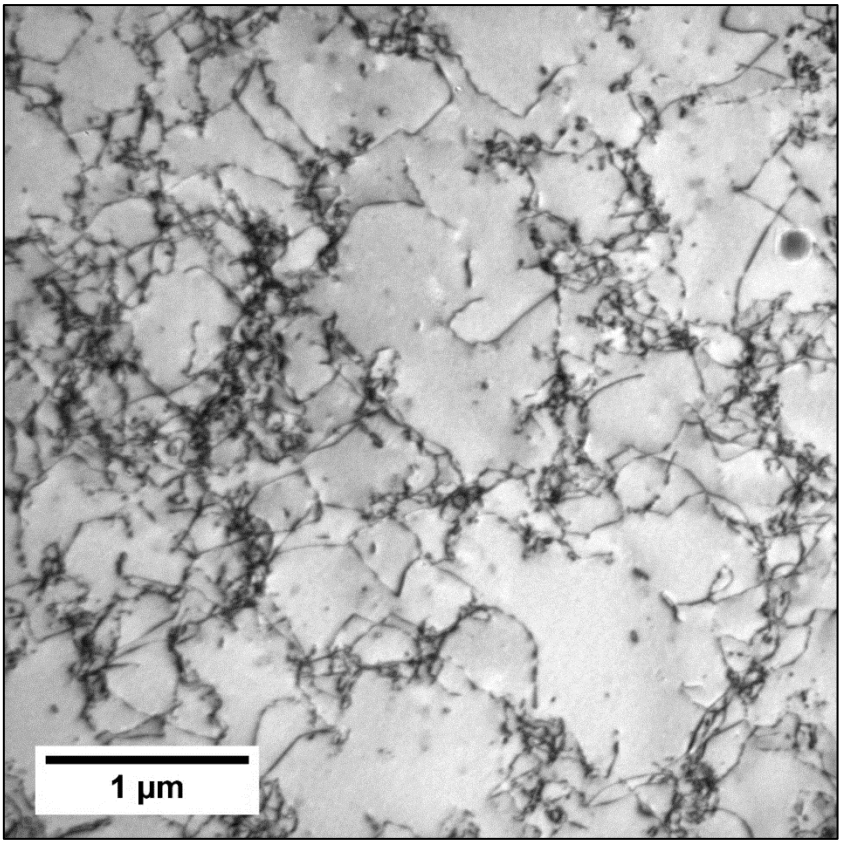

Figure 3.6: Example of a jet-electropolished TEM foil of Fe5Cr.

For charged-particle-irradiated TEM disks, it is required for the sample to be thinned to transparency from the unirradiated side only, else the irradiated layer will be destroyed. If surface effects are to be avoided, then it is also important to remove ~0.5µm from the irradiated layer so the region studied is deeper into the damage profile. This was done by "flash" electropolishing the irradiated side at well-controlled time-intervals to remove material at a controlled rate, and then jet-electropolishing from the unirradiated surface only ("back-thinning"). A description of the method can be found in [160]. Figure 3.7 shows an image of a successfully back-polished foil, which had ~2µm of material removed from the irradiated surface.

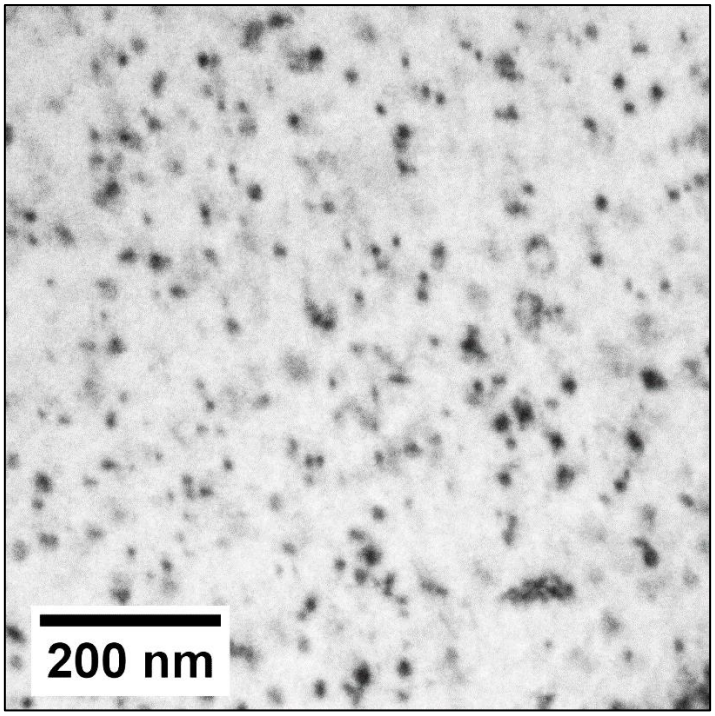

Figure 3.7: Bright field TEM image of a back-thinned sample of Fe5Cr, irradiated with self-ions to 1.8 dpa at 290°C, showing irradiation-induced defects.

In practice, it was found that electropolishing had a very low success rate since the conditions required for the flash-polishing and/or back-thinning could differ substantially from "test" samples. Therefore, many irradiated samples were ruined beyond recovery. Electropolishing was inconsistent, and therefore it was decided not to jet-electropolish the Fe6Cr and Fe9Cr materials. There was only a small volume of each alloy available for irradiation experiments, and so they could not be risked going to waste.

3.5.2 FIB methods for TEM preparation

A focussed-ion-beam microscope (generally referred to as a "FIB") uses a beam of gallium ions to mill out shapes in a material on a micron-scale. Dual-beam FIBs have an SEM column alongside the FIB, allowing for simultaneous milling and imaging. Preparation of TEM foils by FIB is highly advantageous as it is able to mill out foils from carefully selected regions to obtain foils with certain characteristics, e.g. regions containing grain boundaries, cracks, or large precipitates. It produces foils with transparent regions approximately 10-20μm^2 which is a disadvantage (compared to jet-electropolishing) since there is less material to choose from once loaded in the TEM, but is

advantageous because it means many foils can be prepared from the same sample. It also means that magnetic samples have little effect on the electron-beam in the TEM, unlike electropolished disks [160]. The foils produced come from a plane that is typically orthogonal to the sample surface, which is particularly useful for charged-particle irradiations since it is possible to capture the entire damage profile within a foil.

Preparation by FIB is also necessary for most radioactive materials, such as neutron-irradiated material, since it is usually very important to preserve as much of the material as possible so that the same sample can be used for many experiments, not limited to TEM (e.g. micromechanical testing).

Preparation of foils by FIB has a large disadvantage for studying radiation damage. The 30keV gallium ions used in the FIB create a ~50nm layer of radiation damage wherever the beam has been used for milling (or imaging), which can completely overwhelm the visibility of defects produced by neutrons, self-ions or protons. Such a layer is shown in Figure 3.8. It is therefore important to remove or minimise this FIB-damaged layer.

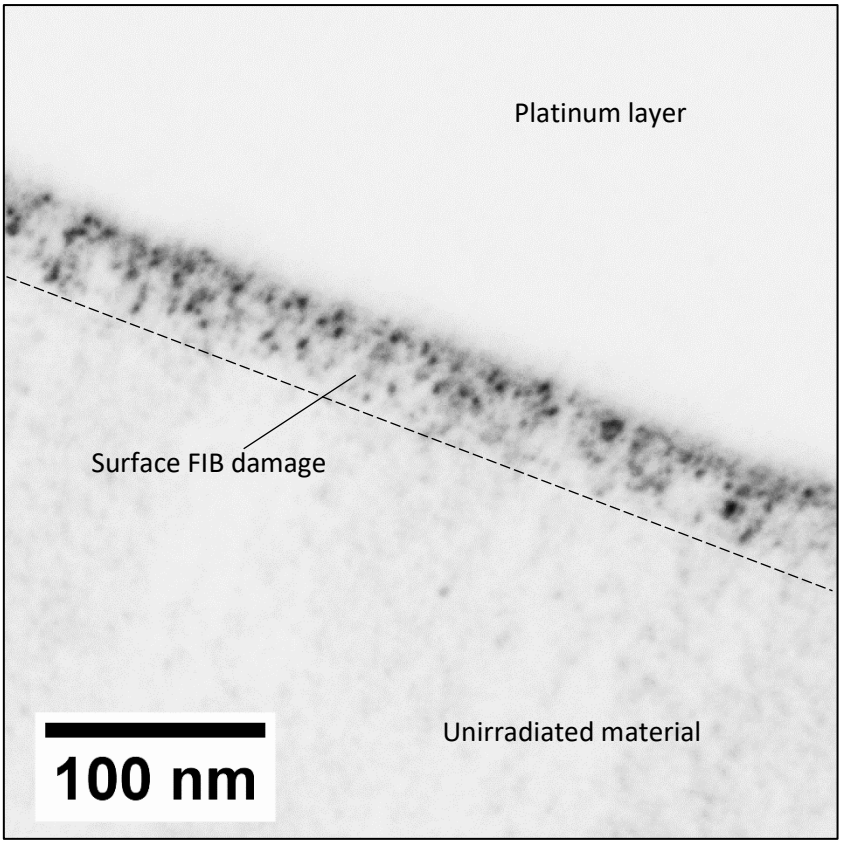

Figure 3.8: Weak-beam micrograph, shown with inverted contrast, of the interface between the platinum layer and the Fe9Cr sample. The interface has a ~50nm region of 30kV FIB damage, while the rest of the foil has been "cleaned" with 2kV FIB.

The initial trench-milling and lift-out method used to prepare cross-sectional TEM foils is a standard technique [163], and so this will not be discussed here. Once a foil has been lifted-out and mounted on a TEM compatible grid, the lamella must be thinned to electron transparency.

The samples were thinned on one side using 30kV Ga+ at 1nA, 600pA and finally 240pA on each side. On one side, two "windows" were milled into the wedge so that the thin regions have thick supports either side. By milling to a shallower depth, the bottom of the lamella also remains thick. This leaves the very thin foil supported on three sides, which helps to maintain the rigidity of foil. Without the windows, foils can be very delicate, and can bend due to magnetic effects inside the TEM.

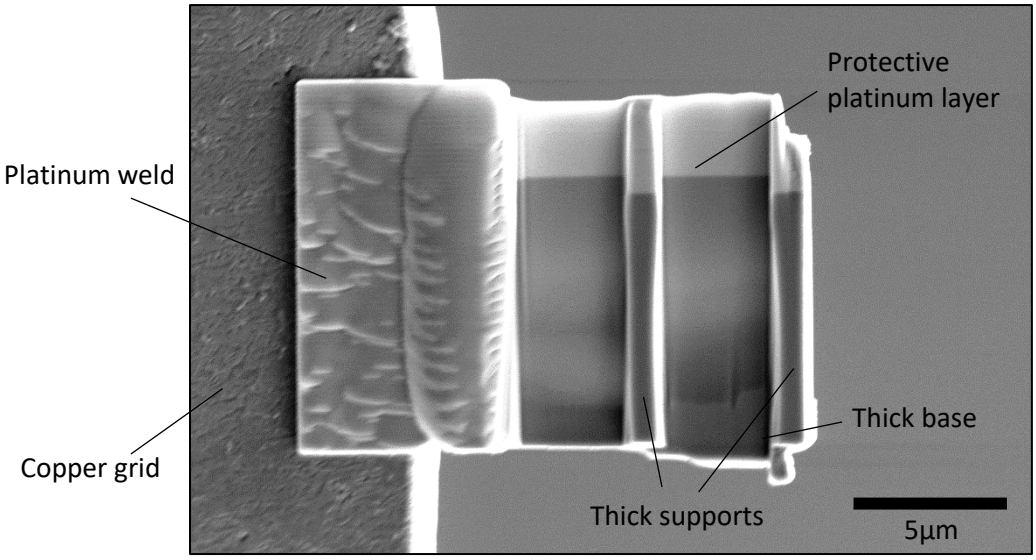

Figure 3.9: TEM lamella during the thinning process. The lamella contains two thin windows supported on three edges by thick supports. This reduces bending when the foil becomes very thin.

Once the foil is translucent when imaged in SEM using 12kV electrons, the foil was ~200nm thick. At least 50nm of material must be removed from both sides of the foil using 2kV Ga+ to remove the 30kV FIB damage. The SRIM profile for 30kV and 2kV Ga into iron is shown in Figure 3.10. The 2kV Ga+ beam produces damage that is confined to within 5nm of the sample surface, and so the majority is lost to the surface-sink, or remains too small to be visible in the TEM.

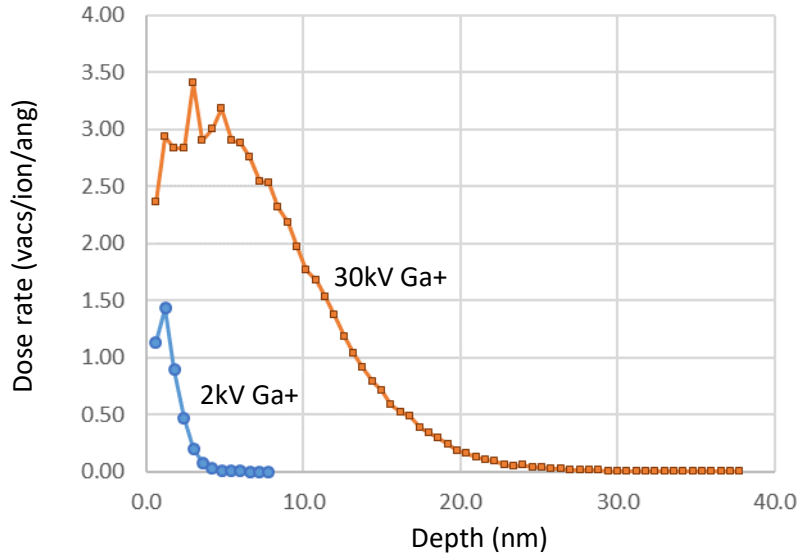

Figure 3.10: SRIM damage profiles for 30kV and 2kV Ga+ into iron [110]

The 2kV Ga+ beam was used to raster each side of the foil, with the FIB beam slightly defocussed. The sample was tilted so that the beam was inclined ~15^{o} with respect to the sample, as shown in Figure 3.11.

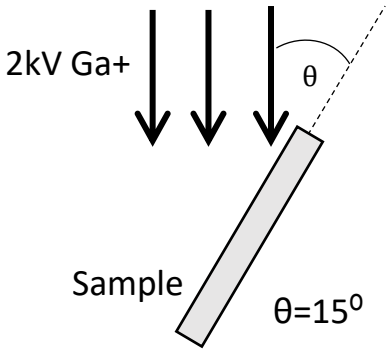

Figure 3.11: Sample orientation with respect to the FIB beam during low energy cleaning

Each side was milled in these conditions for ~10 minutes, and then milling was alternated between sides in 5-minute intervals until the sample appeared translucent in the SEM with 5-7kV electrons. The foil at this stage will be ~100nm thick, which is ideal for diffraction contrast imaging. For electron energy loss spectroscopy (EELS), the samples should be milled further until the samples appear translucent in the SEM with ~3kV electrons, which equates to a foil 20-30nm thick. Examples of a well-prepared and poorly-prepared TEM foil are shown in Figure 3.12.

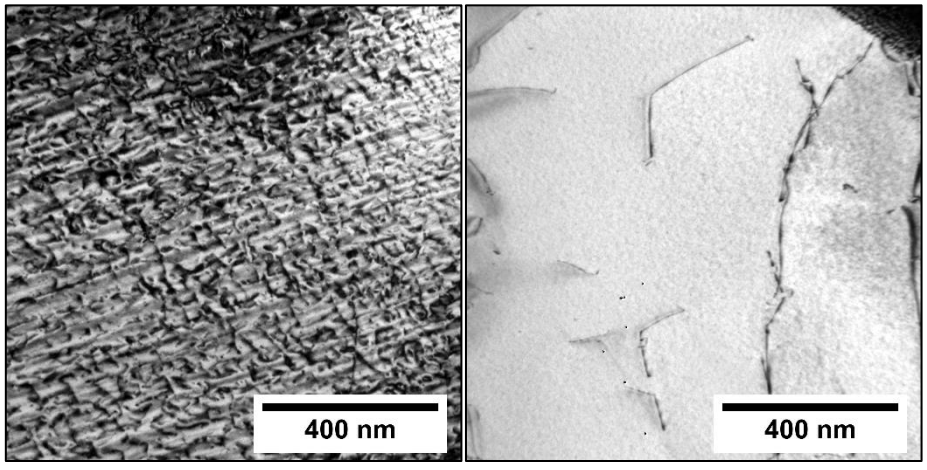

Figure 3.12: Examples of a poorly prepared (left) and well prepared (right) TEM foils using FIB. The poorly prepared foil contains lots of FIB damage and curtaining, which obscures any useful detail.

3.6 Transmission electron microscopy techniques

This section contains a basic overview of the TEM techniques and conventions used throughout this thesis. For detailed explanations, see reference [162] and, for specifically radiation damage characterisation, reference [48]. The majority of the microscopy work in this thesis was performed on a JEOL 2100L microscope with a LaB_6 electron source and 200kV accelerating voltage. Scanning transmission electron microscopy (STEM) and electron energy loss spectroscopy (EELS) were conducted on a JEOL ARM200F with a cold field-emission gun source and 200kV accelerating voltage.

3.6.1 Indexing convention and calibrations

It is important to apply consistent labelling of diffraction patterns when conducting analysis of diffraction contrast images. The software packages CrystalMaker and SingleCrystal [164] were used here to help maintain consistency from experiment to experiment. The diffraction patterns were all captured on a CCD camera, and thus the captured patterns correspond to a view-direction looking down the microscope column. Figure 3.13 illustrates how a typical diffraction pattern was indexed.

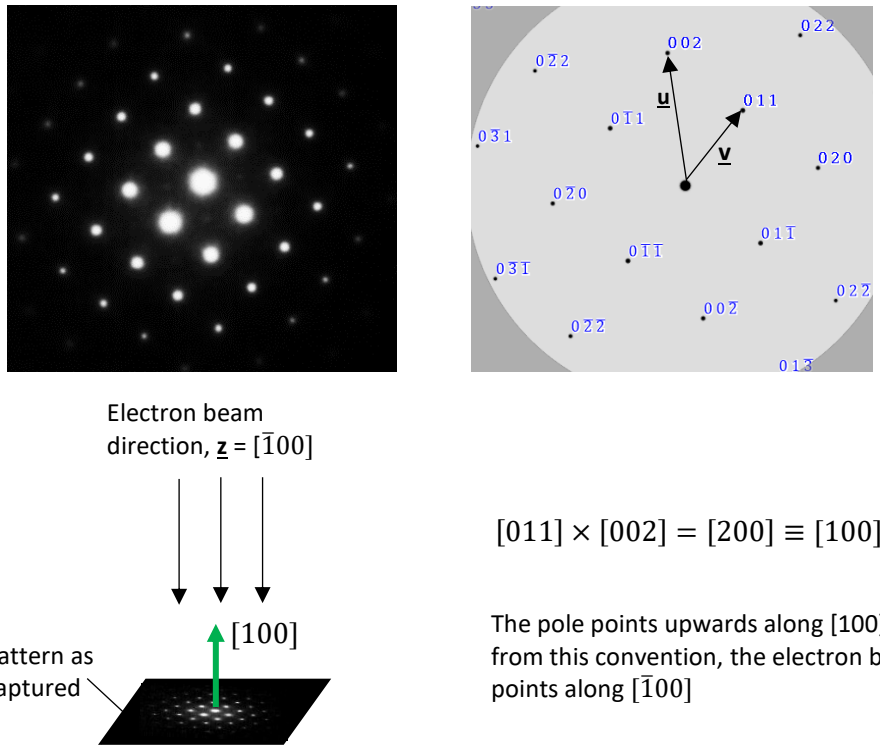

Figure 3.13: Diffraction pattern indexing convention used throughout this thesis. Simulated pattern from [164].

The stereogram that depicts the correct crystal orientation according to the indexed diffraction pattern in Figure 3.13 is shown in Figure 3.14 which shows "north" projected poles. By comparing the stereogram with the Kikuchi-lines in the TEM, the crystallographic orientation can be easily determined. A simulated Kikuchi map is shown alongside the stereogram in Figure 3.14, produced using the package PTC-lab [165]. An important point to note is that the Kikuchi-lines represent the back-projection of the planes and zone axes, i.e. the south-projected poles.

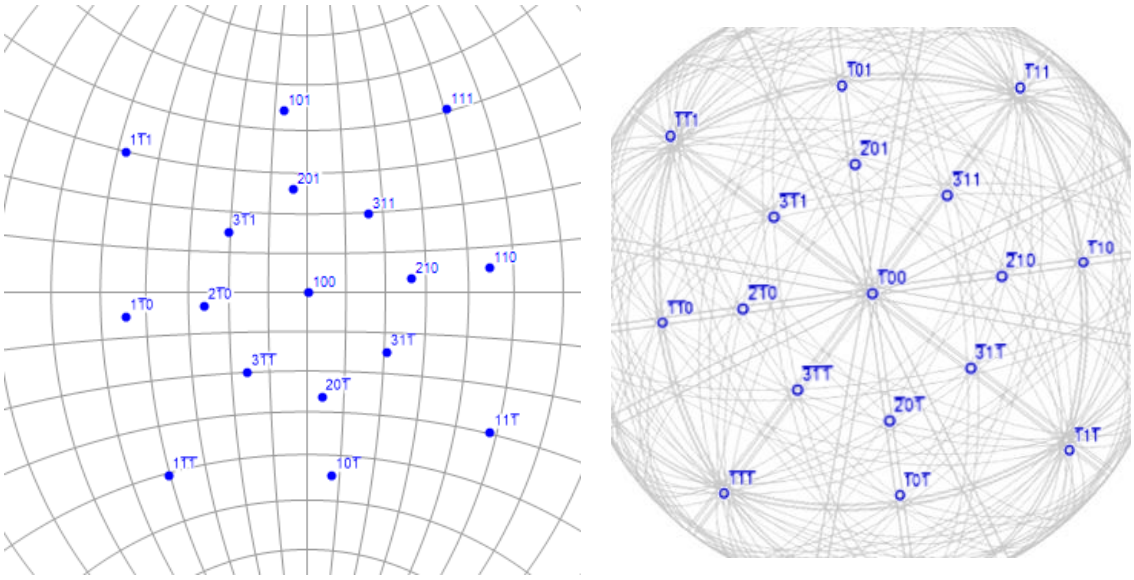

Figure 3.14: Designated crystal orientation to be consistent with the indexing in Figure 3.13, shown as a stereogram (left) generated using SingleCrystal [164] *and as a Kikuchi map (right), generated using PTC-lab* [165]*. The Kikuchi-map corresponds to the back-projection of the stereogram shown.*

With the indexing convention defined, it is then important to consider whether the recorded image and diffraction pattern are rotated with respect to the sample orientation, else the inclination of the sample (and the defects) could be measured incorrectly. In most modern TEMs, the lens arrangement corrects for any rotation between diffraction pattern and image, but there may still be an inversion. The simplest way to check if there is a rotation or inversion between image and diffraction space is to defocus a diffraction pattern until an image is produced within the spots. By correlating distinguishing features in the original image with features in the defocussed diffraction-spot image, the rotation can be deduced. Figure 3.15 shows the calibration conducted on the JEOL 2100L, which follows the method explained by Loretto [166].

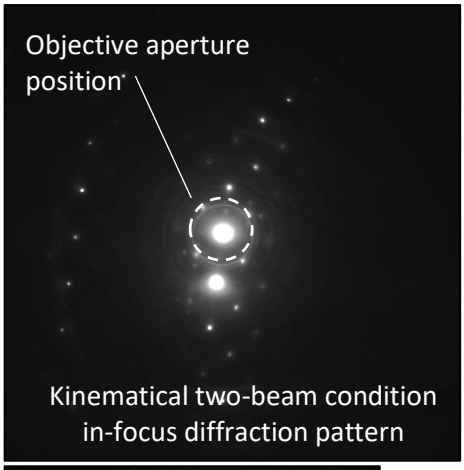

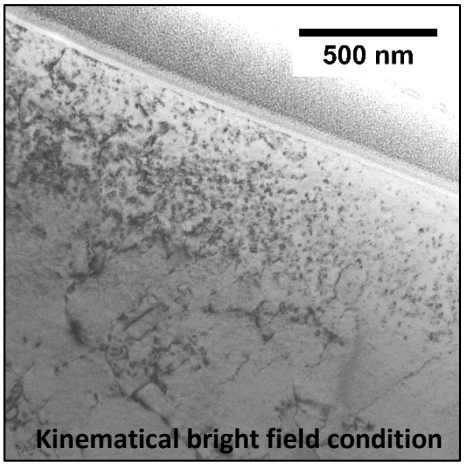

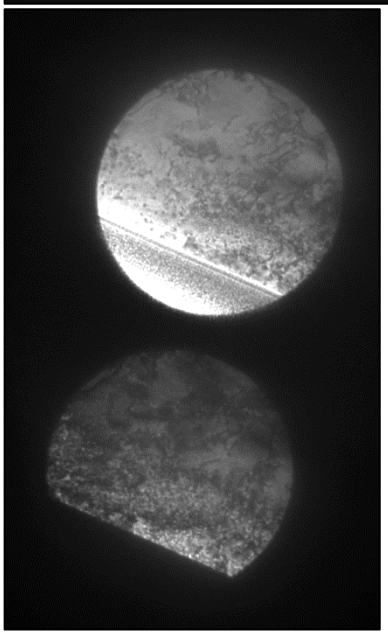

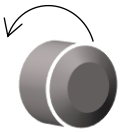

Defocus control anti-clockwise

- Lens strength is reduced
- Cross over point moves below the image plane
- Image viewed in under-focussed spot is rotated 180^{o} from the original image

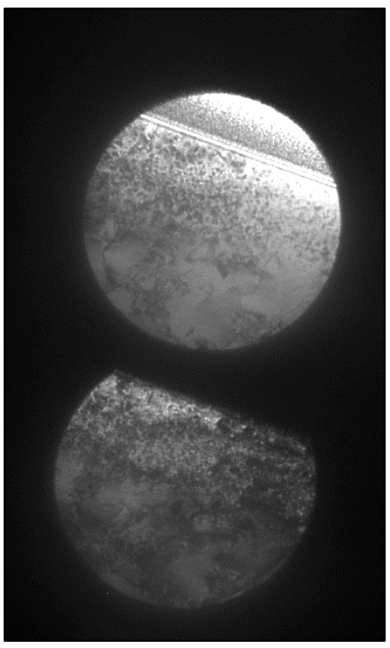

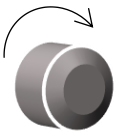

Defocus control clockwise

- Lens strength is increased
- Cross over point moves above the image plane
- Image viewed in over-focussed spot is aligned with the original image

Figure 3.15: Experiment to determine whether an inversion between image and diffraction space exists in the JEOL 2100L.

As explained by Loretto [166], reducing the focus of the diffraction pattern will produce a caustic spot in which can be seen an image of the specimen oriented correctly with respect to the diffraction pattern. From Figure 3.15, the conclusion from the experiment is that the diffraction pattern is rotated 180^{o} with respect to the image captured in "SA mag" mode (real-space). If this was not accounted for, then the direction of a particular **g**-vector will be incorrect by 180^{o}. For most TEM methods, this makes no difference to the imaging or analysis. However, it does make a difference towards the determination of whether a dislocation loop is vacancy or interstitial, as will be discussed in section-3.6.4.

To help understand why an inversion exists, ray-diagrams for the JEOL 2100L are shown in Appendix A alongside an explanation of how the image and diffraction pattern change down the TEM column. The ray-diagrams show that although the image is oriented correctly with respect to the specimen, the diffraction pattern is inverted 180^{o}. This can also be confirmed by comparing the movement of the Kikuchi lines with the stage and rod movement.

3.6.2 Foil thickness measurements

To quantify the irradiation-induced defects, it is important to make a measurement of the foil thickness so that defects can be counted according to their number per unit volume. For the quantification of dislocation loop number density, the foil thickness was determined from convergent beam electron diffraction (CBED) patterns captured in two-beam conditions with the beam converged on the region-of-interest. A description of the CBED method for determining foil thickness can be found in reference [162], and a brief overview is described here.

Viewed in "SA diff" mode (reciprocal space), without any apertures inserted, the pattern will appear as two bright spots (the 000 direct beam and excited reflection, **g**) with a series of parallel fringes contained within the spots (Figure 3.16). The spacing of the fringes is related to the thickness by Equation 3.6.

Equation 3.6

$$a)\ \left(\frac{S_i}{n_i}\right)^2 = -\frac{1}{{\xi_g}^2}\left(\frac{1}{n_i}\right)^2 + \frac{1}{t^2}\,, \qquad b)\ \ S_i = \frac{\lambda}{d^2}\left(\frac{L_i}{L_0}\right)$$

The thickness in equation a) is given by t, ξ_g is the extinction distance of the excited reflection **g,** n_i is an integer, and S_i is the deviation of the i-th minimum from the perfect Bragg condition. In equation b), λ is the electron wavelength, and d is the spacing of the reflecting planes [162]. The values L_0 and L_i are measured directly from the CBED pattern, as indicated in an example CBED pattern in Figure 3.16. The CBED pattern is best captured with a widely-spaced reflection (the example below is a reflection of **g**=130) and using the second-largest condenser aperture to reduce the size of the spots to prevent overlapping.

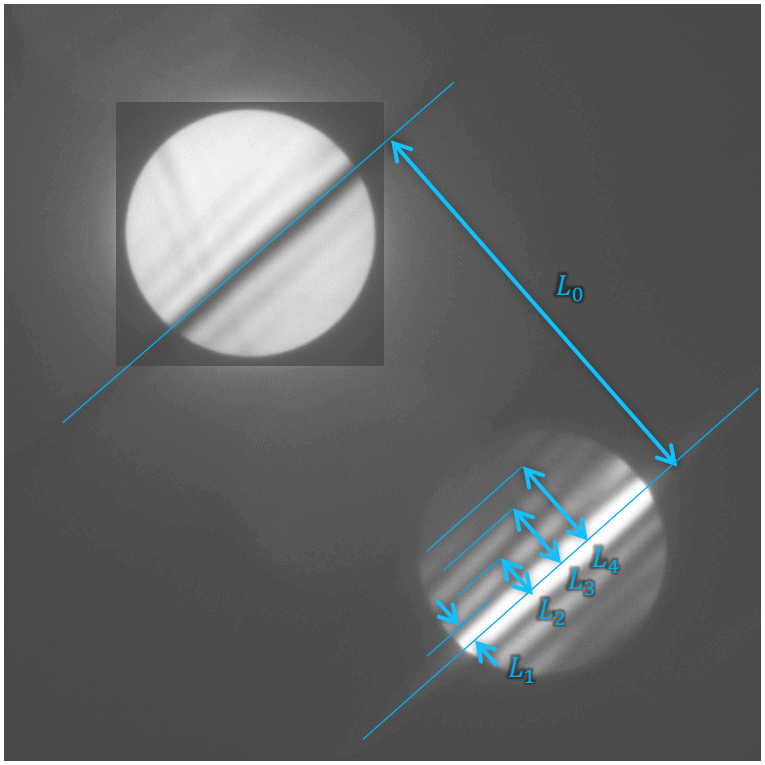

*Figure 3.16: Example CBED pattern using a 130 **g**-reflection. The values of L_i are the length measured from the exact Bragg condition to each successive fringe minimum. The 000 spot is shown with different brightness/contrast settings for display purposes.*

A plot of $\left(\frac{S_i}{n_i}\right)^2$ against $\left(\frac{1}{n_i}\right)^2$ is then produced for n_i = (0, 1, 2, 3…), (1, 2, 3, 4…), (2, 3, 4, 5…) etc. The first set of n_i to produce a straight line with a negative gradient is taken to be the appropriate designation of n_i. This is shown in Figure 3.17. The intercept of the line with the Y-axis is equal to $\frac{1}{t^2}$, and so the thickness can be simply calculated from this intercept.

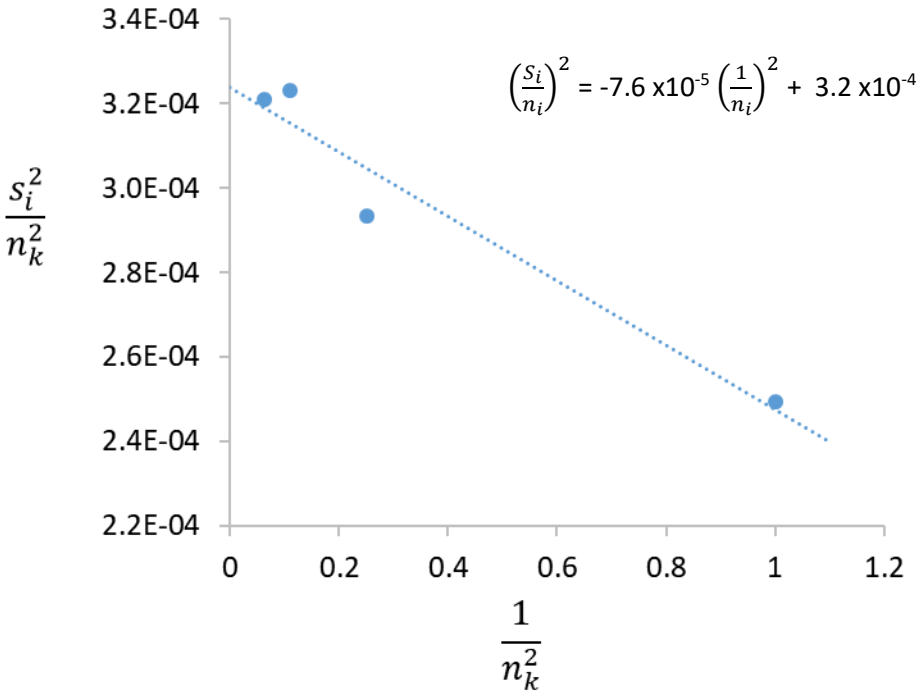

Figure 3.17: Plot used to compute the foil thickness, with i=0. The thickness can be computed from the intercept. The thickness in this case is 54.6nm, with an error from the least-squares line fit of 0.7nm.

The example shown in Figure 3.16 and Figure 3.17 indicates a foil thickness of 55nm. The uncertainty estimated from the least-squares fit of the straight line is 0.7nm, which is ±1% of the measured thickness. This measurement is too small to be a realistic error, as the measured region probably fluctuates in thickness more than this. Radiation damage also broadens the CBED fringes, reducing accuracy of the spacing measurements. A conservative estimate of the uncertainty was therefore assigned as ±10%.

For measurements of foil thickness in regions mapped by EELS, CBED cannot be used because the ~20nm thick foils are too thin to produce CBED fringes. Thickness was instead determined from

the low-loss electron energy spectrum using the Log-Ratio method [167], which is the method used for the "Calculate Thickness" functionality in Digital Micrograph [168]. The thickness was calculated from Equation 3.7.

Equation 3.7

$$t = \lambda \ln\left(\frac{I_t}{I_0}\right)$$

The thickness in Equation 3.7 is given as t, the mean-free path of electrons in the material is λ, I_t is the integrated intensity of the entire electron energy spectrum, and I_0 is the integrated intensity of the low-loss energy spectrum. The spectra were captured in the JEOL ARM200F equipped with a Quantum Gatan image filter (GIF), with convergence and collection half angles of 31.5mrad and 41.0mrad respectively (values taken from recent reference [169]).

The value of λ was calculated by the method described by Malis et al. [167], and implemented using the Digital Micrograph plugin by Mitchell [170]. For Fe6Cr and Fe9Cr, the calculated values of λ are 85.56 and 85.62nm respectively (in practice, the same value of 85.6nm was used for both alloys), with an error of approximately ±10%.

3.6.3 Dislocation loop imaging

Dislocation loops were imaged using the standard diffraction contrast techniques described in references [162], [48] and [171]. Weak beam dark field (WBDF) is the best technique to use for sizing and counting dislocation loops because it can produce high contrast images with sharp dislocation lines that reside very close to the dislocation core [171]. WBDF can be used to image dislocation loops ~1nm in size [172], and can resolve fine loop detail for loops in the 2-5nm range. Kinematical bright field (KMBF) produces images with broader lines (though generally good contrast against the background), but dislocation loops smaller than ~5nm mostly appear as black dots, and little morphology information can be deduced from such spots, and sizing can be less accurate. The broader lines also reduces the resolution, and hence the size limit for loop visibility. Thus, counts and

measured sizes of dislocation loops sized less than in the ~3-5nm range are generally more unreliable than if captured using weak-beam dark field.

It is good practice to assign a minimum dislocation loop size when counting and sizing dislocation loops, and report only counts and sizes above this minimum [171]. This minimises ambiguity associated with designating small contrast features as dislocation loops. This is also particularly important for quantifying dislocation loops in FIB-prepared foils, since 2kV Ga+ damage can remain as <2nm sized defects that may be indistinguishable from irradiation damage, or even surface contaminants such as oxide (e.g. Figure 3.18).

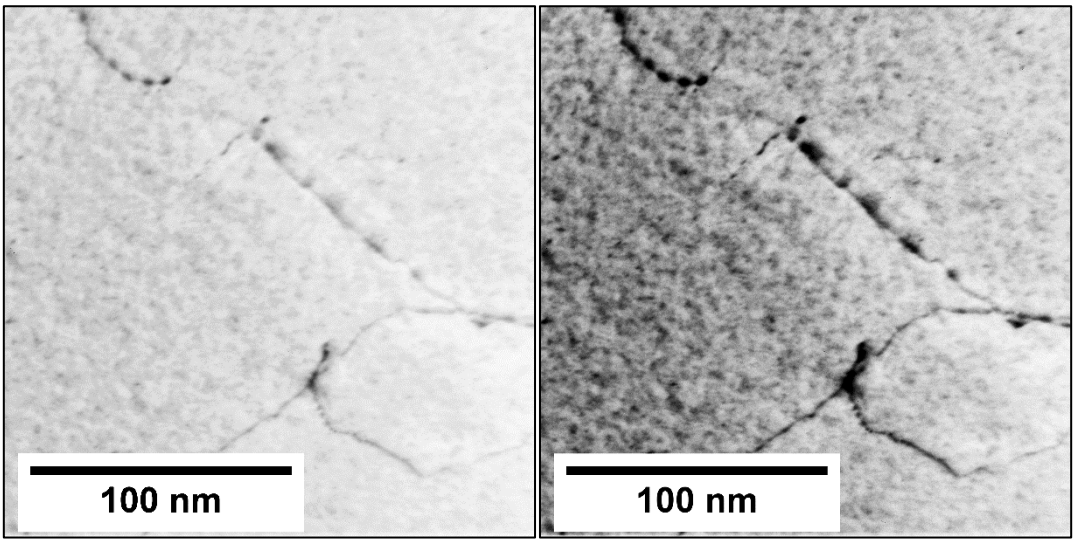

Figure 3.18: Weak beam dark field (shown with inverted contrast) micrographs of unirradiated Fe9Cr. Both micrographs are the same region and imaging condition, but with different brightness/contrast settings. The high contrast image shows the matrix contains many defects less than 1nm in size, which could be FIB damage and/or surface oxide

WBDF was the technique used for all quantitative analysis of dislocation loops used in this thesis, while occasional bright-field images were used as general overview micrographs, or to aid interpretation of WBDF micrographs where contrast is not clear.

A single WBDF condition for each **g**-vector condition generally produces poor-contrast images due to fluctuations in defect contrast as a function of depth for a given condition, and periodic background fluctuations (thickness fringes), e.g. Figure 3.19a. It is best practice to capture several

WBDF conditions with slightly different deviation parameters, and then stack the micrographs to produce one multi-deviation parameter micrograph [171,172]. An example of such a multi-deviation parameter micrograph is shown in Figure 3.19b.

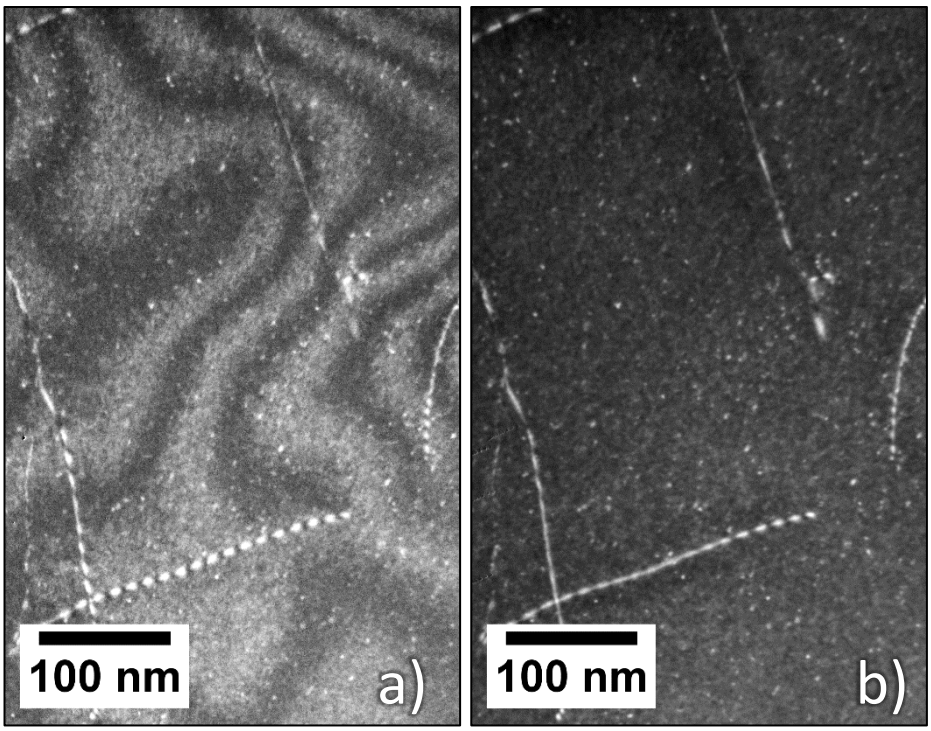

Figure 3.19: Example of extinction-effect intensity oscillations as a function of depth in electropolished Inconel. This is evident in image a) from the periodic intensity of the dislocations, which are inclined in the foil and hence span the entire foil depth. Image b) is the result of stacking multiple WBDF conditions with slightly varying deviation parameter, which cancels the extinction-related intensity oscillations (though not entirely). On a side note, this sample was not irradiated, and was prepared by electropolishing. The white dots are surface contaminants, but look like small dislocation loops.

The deviation parameter can be used as a measure of how "weak" the imaged g-reflection is, and is equal to the reciprocal-space length from the imaged reflection to the Ewald sphere (shown in Figure 3.20, and see reference [162] for detailed explanation). Varying the deviation parameter changes the phase of the intensity oscillations of defects with depth, and the phase of the thickness fringes. Thus, stacking a series of micrographs with slightly different deviation parameters reduces extinction-related defect absences and smooths out background fluctuations. A description of the method can be found in references [171] and [172].

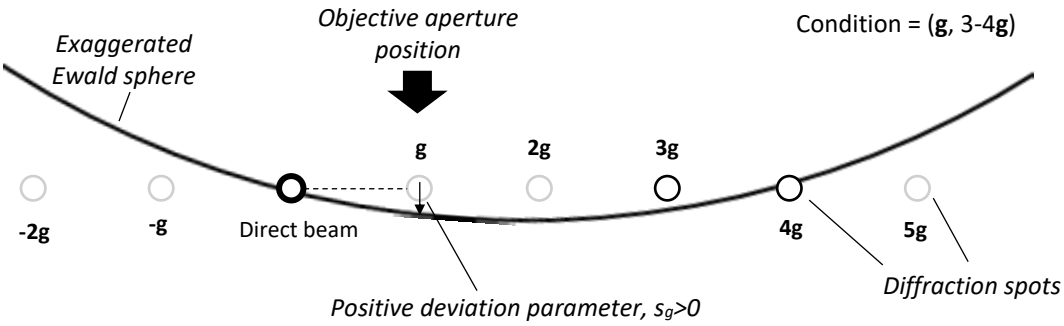

*Figure 3.20: Diagram depicting a weak-beam diffraction condition. The deviation parameter, s_g, is indicated, though usually it is referred to as the multiple of **g** through which the Ewald sphere crosses the reciprocal lattice points, i.e. at zero-**g** (the direct beam) and between 3**g** and 4**g**. The condition is then written as (**g**, 3-4**g**), where the first term refers to the reflection over which the objective aperture is positioned. The deviation parameter could be written more exactly, e.g. 3.5**g**, or 4.25**g**, but since even slight foil bending can change the value of s_g from one side of a micrograph to another, such accuracy was considered inappropriate here.*

Prokhodtseva et al. [172] implemented this method using a script to vary the deviation parameter within the confines of the objective aperture using simple beam-tilt controls. The beam was tilted from one side of the objective aperture to the other, as depicted in Figure 3.21a, allowing automatic and thus faster acquisition of multiple WBDF conditions. An issue with the script by Prokhodtseva et al. is that the tilt direction must be calibrated for each g-vector condition, each grain, and each sample.

To overcome this issue, I have written an alternative acquisition script to control the electron beam using Digital Micrograph [168]. Instead of scanning the beam in one direction with beam-tilt controls, the beam was precessed in a circle within the confines of the objective aperture, as shown in Figure 3.21. Electron beam precession is more commonly used for determining crystallographic information (such as space group) or strain mapping, but also is known to improve dislocation imaging for the purpose of tomography [173].

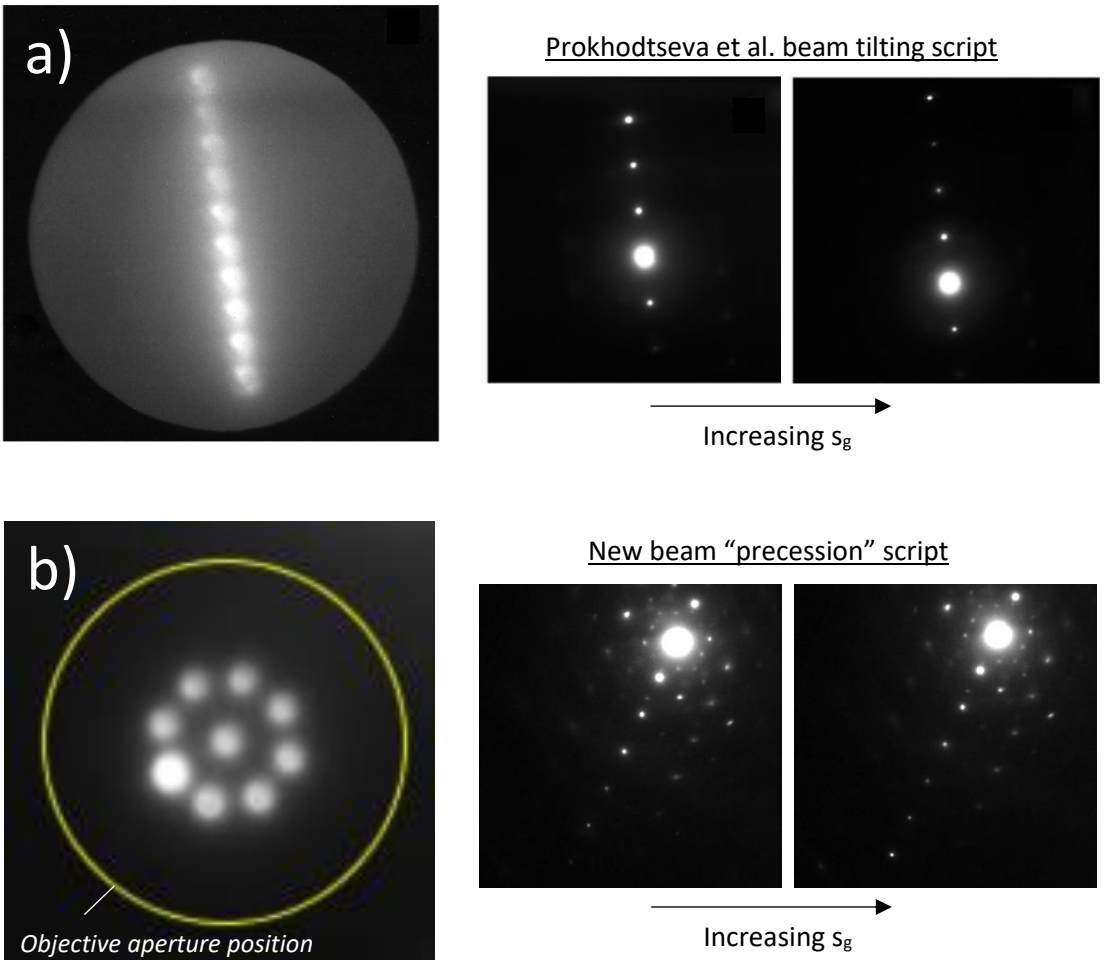

Figure 3.21: Micrographs of diffraction patterns to illustrate automated variation of the deviation parameter via scripted beam tilting. The top example, a), was taken from Prokhodtseva et al. [172] *and shows the position of their beam in the reciprocal plane as the beam is tilted from one side of the objective aperture to the other. The two diffraction patterns top-right show the extremities of the weak beam conditions. The bottom example, b), was captured using the new precession script written as part of this thesis. The beam is tilted in a circle, to avoid having to calibrate a tilt direction. The two diffraction patterns bottom right are the extremities of the weak beam conditions.*

The precession script used is shown in Appendix B. This script allowed the deviation parameter to be varied by up to ~0.02nm^{-1} (limited by the width of the objective aperture). The result is ten WBDF micrographs with a range of deviation parameters. These images were later aligned in ImageJ [174] using a plugin by Tseng [175]. Figure 3.19b was captured via this precession method.

The notation (**g**, n-m**g**) is used to denote a WBDF micrograph that was captured by imaging reflection **g** with an excited **g**-reflection between n**g** and (n+1)**g**, which corresponds to the

approximate location of where the Ewald sphere passes through the diffraction spots of the first Laue zone (see Figure 3.20). All weak-beam images shown throughout this thesis consist of multiple WBDF conditions stacked together, with a deviation parameter range of ~0.02nm^{-1}, which is roughly ½**g** for **g**=011. The measurements of deviation parameter reported throughout this thesis are approximate, as interpreted from the excited **g**-reflections in the diffraction patterns. It should be noted that although a dark field condition is strictly "weak-beam" when s_g>0.2nm^{-1}, s_g was occasionally set as low as 0.1nm^{-1} in order to promote dislocation signal over other features, such as oxide.

All WBDF images captured for this thesis (besides Figure 3.19) are shown with inverted contrast, so defects appear dark on a light background.

3.6.4 Dislocation loop characterisation

Dislocation loop counting and sizing

For every g-vector condition captured in WBDF, the negative g-vector condition was also captured. Dislocation loops were counted by comparing both sets of images, to minimise ambiguous defect contrast due to inside-outside contrast effects. Defects were counted for a particular g-reflection ±g pair if they showed obvious contrast, and/or if they showed inside-outside contrast. The final count reported refers to only dislocation loops sized larger than 2nm, since counts and sizes became highly uncertain for loops below 2nm.

As with counting, dislocation loops were sized by comparing the ±g-vector WBDF micrograph pairs. The dislocation loop image-size can change for the +g and –g conditions, and the direction in which the image appears most elongated can also change by 90^o [176]. Example image contrast of inclined <111> loops are shown in Figure 3.22, as imaged with ±**g**-vector conditions. Figure 3.22a has been taken from Yi's work on irradiated tungsten [86], and shows the simulated loop contrast using TEMACI simulation package by Zhou et al. [176]. Figure 3.22b shows a TEM-captured dislocation

loop from one of the irradiated FeCr alloys studied in this thesis. Although Figure 3.22a and Figure 3.22b are not perfectly comparable since the imaging conditions and materials are different, the examples demonstrate the change in apparent size from reversing the direction of **g**, and the reorientation of the contrast lobes.

Zhou et al. [176] suggested a standard method to deduce an accurate loop size for a given WBDF condition, however this method is inappropriate for most loops since the intensity profile along the major axis of a dislocation loop may actually be close to zero, (as is the case for the larger loop-images in Figure 3.22).

The approach used in this thesis was to draw an elliptical region of interest using standard tools available in ImageJ [174], and designate the major diameter of the elliptical selection as the approximate average size of the defect as viewed in the +**g** and –**g**-vector conditions. More sophisticated measurements of dislocation loop size could in theory be made by considering the 2D intensity profile of a dislocation loop and using a computer-vision approach to compare it with simulated dislocation loop images. Computer vision has already been used successfully to interpret dislocation loops in STEM images [177], but this was not attempted for this thesis.

a)

Simulated loop contrast images from TEMACI. **g**=200.

(Adapted from Yi et al. [178])

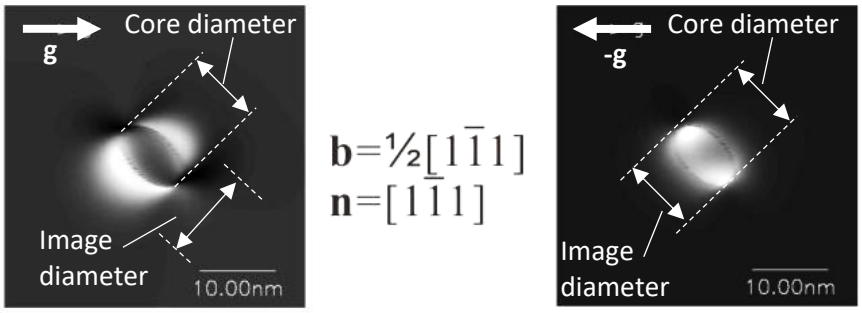

Similar loop contrast, as obtained by TEM, **g**=112, (**g**, 3-4**g**)

b)

(taken from data used for this thesis)

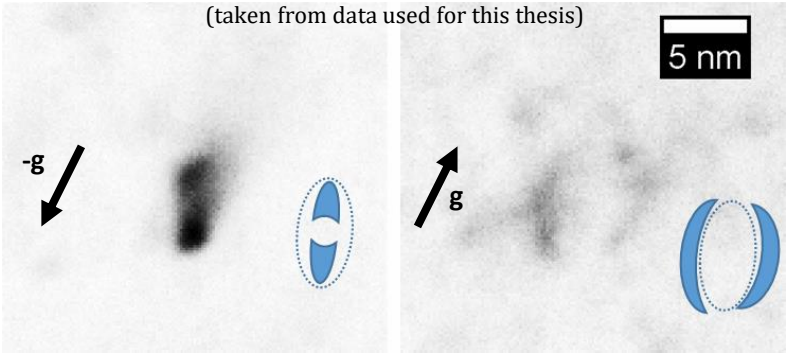

*Figure 3.22: Example image contrast of dislocation loops compared with the size of the dislocation core. a) shows two images of the same loop, viewed with ±**g** vector conditions, as simulated by Yi et al.* [178] *for their work on Tungsten. These images have been adapted to show the true dislocation loop diameter and an example of what might be considered the "image-diameter". b) shows TEM-captured images of a real dislocation loop in irradiated Fe9Cr, also viewed with ±**g** vector conditions (shown with inverted contrast). The dotted circles indicate the best-approximation of the true diameter of the dislocation loop. No attempt was made to accurately quantify the minor-axis.*

Dislocation loop Burgers vector determination

The Burgers vector, **b**, of a dislocation loop can be measured by capturing a series of **g**-vector conditions over the same region, and observing the visibility and invisibility of defects changing with **g**. Comparison to a **g.b** table, such as that shown in Table 3.2, can then be used to deduce the Burgers vector of a dislocation. If only the Burgers vector "family" is required (i.e. <111> or <100>), then fewer micrographs are required than if the exact Burgers vector is required (e.g. [010], $[1\bar{1}\bar{1}]$ etc.). It was assumed that no <110> type dislocation loops existed in the foils. If the invisible-contrast is ambiguous, then the dislocation loop orientation can also be used to aid interpretation of the **g.b** experiment.

		$\boldsymbol{g \cdot b}$ *product*						
Zone axis	$\boldsymbol{g}$ \ $\boldsymbol{b}$	$[100]$	$[010]$	$[001]$	$\frac{1}{2}[111]$	$\frac{1}{2}[1\bar{1}1]$	$\frac{1}{2}[11\bar{1}]$	$\frac{1}{2}[1\bar{1}\bar{1}]$
$[100]$	011	0	1	1	1	0	0	-1
	$01\bar{1}$	0	1	-1	0	-1	1	0
	020	0	1	0	1	-1	1	-1
	002	0	0	1	1	1	-1	-1
$[311]$	$1\bar{1}\bar{2}$	1	-1	-2	-1	0	1	2
	$1\bar{2}\bar{1}$	1	-2	-1	-1	1	0	2
$[210]$	$1\bar{2}1$	1	-2	1	0	2	-1	1
$[110]$	$1\bar{1}2$	1	-1	2	1	2	-1	0

*Table 3.2: Example **g.b** table that could be used to distinguish every <100> and <111> variant of all loops. In practice, it is usually only possible to trace a small fraction of the loops for all conditions.*

In practice, this loop-by-loop correlation method is only possible for reasonably large dislocation loops (>5nm) and on loops with an areal density that is low enough that the dislocation loop images do not overlap significantly. When it is not possible to use loop-loop correlation, the dislocation loop population according to their Burgers vector can be deduced by the statistical analysis method [172]. The total number of loops visible for a given **g**-vector condition, N_{hkl}, can be written in terms of the fractions of visible <100> and <111> dislocation loops. For example, the first three conditions shown in Table 3.2 can be written as a series of simultaneous equations, shown together in Equation 3.8.

Equation 3.8

$$\text{a)} \quad N_{011} = \tfrac{2}{3} L_{<100>} + \tfrac{2}{4} L_{<111>}$$

$$\text{b)} \quad N_{01\bar{1}} = \tfrac{2}{3} L_{<100>} + \tfrac{2}{4} L_{<111>}$$

$$\text{c)} \quad N_{020} = \tfrac{1}{3} L_{<100>} + \tfrac{4}{4} L_{<111>}$$

$L_{<100>}$ and $L_{<111>}$ are the number of <100> and <111> loops that exist in the foil. These simultaneous equations can be written as a matrix equation, shown by Equation 3.9.

Equation 3.9

$$\begin{pmatrix} N_{011} \\ N_{01\bar{1}} \\ N_{020} \end{pmatrix} = \begin{pmatrix} 2/3 & 2/4 \\ 2/3 & 2/4 \\ 1/3 & 4/4 \end{pmatrix} \cdot \begin{pmatrix} L_{<100>} \\ L_{<111>} \end{pmatrix}$$

The values of N_{hkl} are the total number of visible dislocation loops counted for each **g**-vector condition. This can be solved by Equation 3.10.

Equation 3.10

$$\begin{pmatrix} L_{<100>} \\ L_{<111>} \end{pmatrix} = \begin{pmatrix} 2/3 & 2/4 \\ 2/3 & 2/4 \\ 1/3 & 4/4 \end{pmatrix}^{-1} \cdot \begin{pmatrix} N_{011} \\ N_{01\bar{1}} \\ N_{020} \end{pmatrix}$$

This method was first applied to dislocation loop analysis by Prokhodtseva et al. [172], and is known as the "statistical analysis" technique. The result is the least-squares best fit for all measured counts, and is only a "best-fit" estimation due to counting errors. The accuracy of this method improves with loop counts and the number of conditions used. This statistical analysis method was the main technique used in this thesis for determining the overall dislocation loop density ($L_{<100>}$ + $L_{<111>}$), and the fraction of loops present with **b**=<100> and <111>. The standard error was taken as the square root of the total loop population in the measured region (counting error).

Dislocation loop nature determination

The inside-outside contrast method was used to measure the vacancy or interstitial nature of dislocation loops throughout this thesis. This method is well explained in reference [162]. The basic principle of the inside-outside contrast effect can be understood from Figure 3.23a, and relates to whether the planes around a dislocation loop diffract the electron beam on the inside-edge of the dislocation core, or the outside-edge of the dislocation core. Interstitial and vacancy dislocation loops were defined by the Right-Hand Finish-Start (RH-FS) convention [32], as shown by Figure 3.23b.

Whether inside or outside contrast is observed depends on the inclination of the dislocation loop with respect to the beam, the direction of the g-vector, the sign (plus or minus) of the deviation parameter, and the vacancy or interstitial nature of the loop. The inclination of the dislocation loop can be determined via Burgers vector analysis and/or via tilting the specimen to high angles (to observe the change in inclination), and the g-vector and deviation parameter can be well controlled (all weak-beam imaging has been conducted with a positive deviation parameter in this thesis). Formally, outside contrast arises for interstitial loops when (**g.b**)s > 0, and **b.z** < 0, while contrast will be inside for vacancy loops (and vice versa for (**g.b**)s<0 and **b.z**>0) [48].

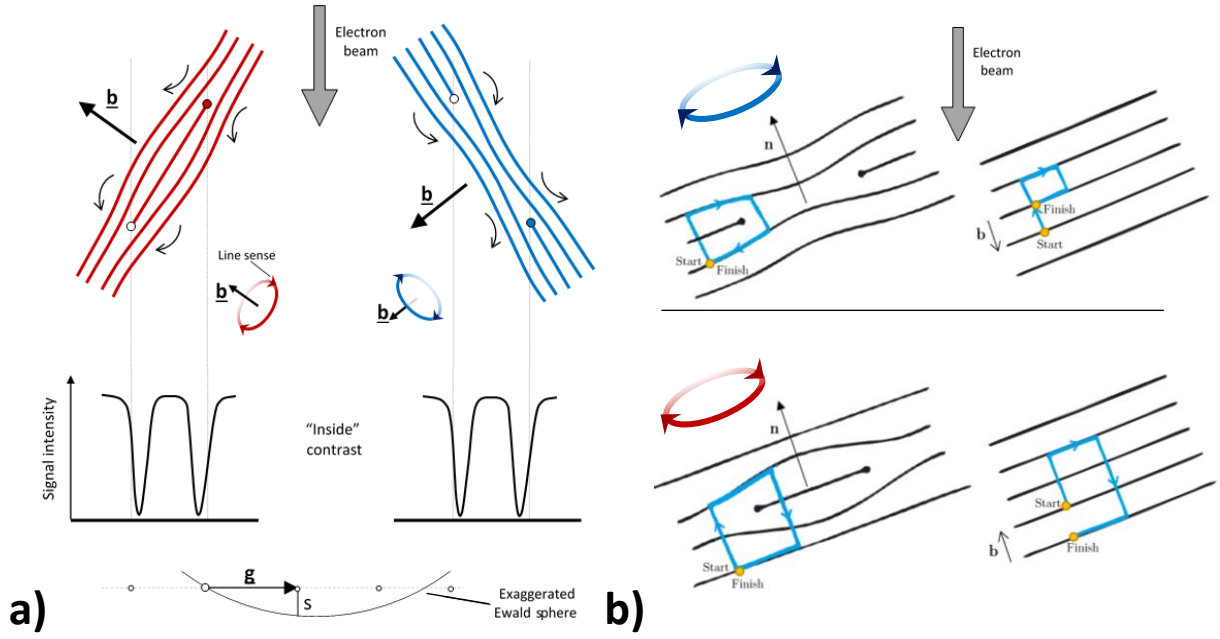

Figure 3.23: a) Diagram illustrating "inside" contrast for a vacancy and interstitial dislocation loop, drawn based on similar diagrams from [71,162,179]*. The "outside" condition would be the reverse inclination, or reverse direction of* ***g****, or sign of s. b) Diagram showing the right-hand finish-start (RH-FS) convention for dislocation loops.*

It is important to be cautious when interpreting inside-outside contrast if the loop inclination has only been determined by the Burgers vector. If the dislocation has a considerable screw component, then it might be lying up to 35° from the prismatic plane [48]. Therefore, the inclination with respect to **z** could be incorrectly determined, and subsequently the nature would be measured incorrectly (see reference [48] for a detailed explanation of how to safely deal with non-edge dislocation loops).

3.7 Imaging voids

Voids were measured in irradiated specimens using the under-over focus technique. This technique is well explained in reference [162]. Voids were captured by tilting the specimen to a kinematical two-beam condition, and then tilting further from the Bragg condition to reduce the intensity of the diffraction contrast. The focal length was then changed from an under-focus condition to an over-focus condition by ±1μm. This was implemented via scripted beam control, which allowed a series of focal lengths to be captured in the range from -1μm to +1μm during which a void will transition from having a dark fringe inside and light fringe outside, to vice versa.

The size most closely corresponding to the actual size of the voids larger than 2nm was found by Ruehle et al. [180] to be the point at which the fringe contrast first crosses the background intensity. For voids below 2nm in diameter, the relationship between fringes and void size is not well established. In this thesis, void-like features sized <2nm in diameter were measured by the same convention as applied to voids >2nm in diameter. It is important to note that small particles (or surface oxide) can also show the same contrast as small voids, and so measurements of such features becomes very ambiguous at and below this length scale [162].

3.8 Electron Energy Loss Spectroscopy

Electron Energy Loss Spectroscopy (EELS) is the practice of measuring the energy distribution of the electrons that pass through the sample in a TEM (or STEM). The electrons can lose energy via inelastic collisions with atomically-bound electrons. This process excites the bound-electron (typically a core-shell electron) to a higher energy state, which then emits an X-ray of characteristic energy to relax back to the initial energy state. The X-rays produced by this process are the X-rays used for energy dispersive X-ray spectroscopy (EDS, or EDX), whereas the inelastically scattered electrons are used for EELS [162].

A typical EDX spectrum contains multiple peaks, corresponding to the flux of X-rays of particular energies that are each indicative of a particular electron energy-state transition. Since

each element has a unique set of energy-quanta that bound electrons can be associated with, the peaks in the X-ray spectra can be used to identify the element that caused a given scattering event. A typical electron energy-loss spectrum will contain peaks that appear as saw-tooth features on an overall decaying electron energy background spectrum (for example, Figure 3.24. These peaks are referred to as “edges”).

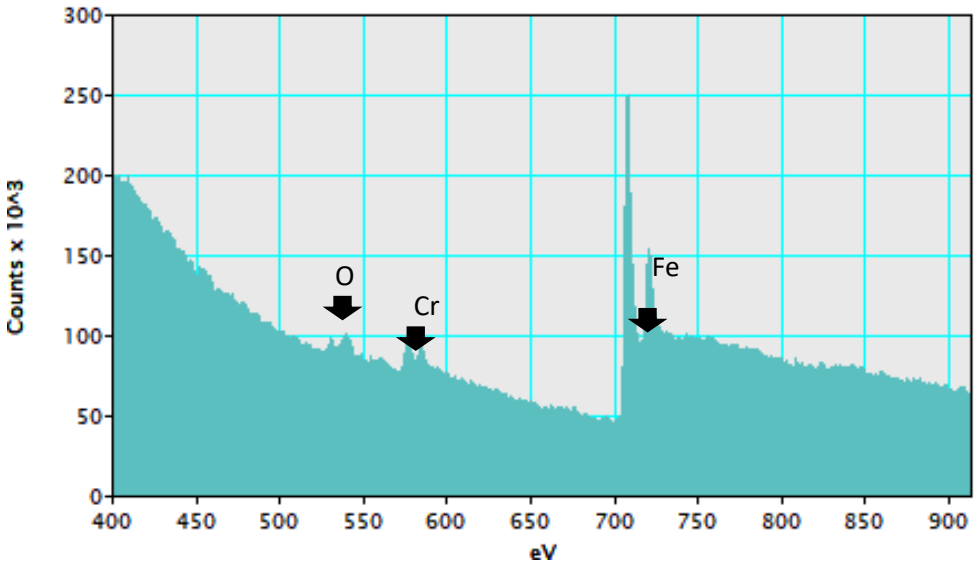

Figure 3.24: Example of a typical EELS spectrum, showing edges for oxygen, chromium and iron

The location of an edge is the minimum energy required to excite a core shell electron and ionise the atom, and the gradual decay after the edge is caused by the reduction in ionisation cross section with increasing energy transfer [162]. Immediately after an edge is a very large spike which decays very quickly. These “fine-structure” parts of the spectrum are known as white-lines and are typical of transition element L-edges.

Like the peaks in EDX, each edge feature is characteristic of a particular element. EELS was used in conjunction with scanning transmission electron microscopy (STEM) so that each pixel of a STEM condition has an associated electron-energy spectrum recorded. This can be used to map the spatial distribution of elements in a material, and is ideal for measuring the redistribution of chromium due to radiation.

EELS has a higher spatial and analytical sensitivity than EDX [162], which is important for identifying subtle changes in chromium concentration in irradiated FeCr. Features such as chromium α' phases may be very small (<2nm) and with a high population density. It is therefore important to have very thin foils to reduce the areal density of such clusters to make them distinguishable from a background chromium concentration. Since EELS demands very thin (ideally 20-30nm thick) foils, it is ideal for quantifying chromium precipitation.

For practical EELS measurements in the JEOL ARM200F, the main edges of interest for this thesis are the high-loss iron and chromium L-edges, where "L" refers to ionisation due to L-shell electrons. These are shown in Figure 3.25. To extract a quantitative signal from such an EELS spectrum, analysis was conducted using the EELS-analysis tools in HyperSpy [181].

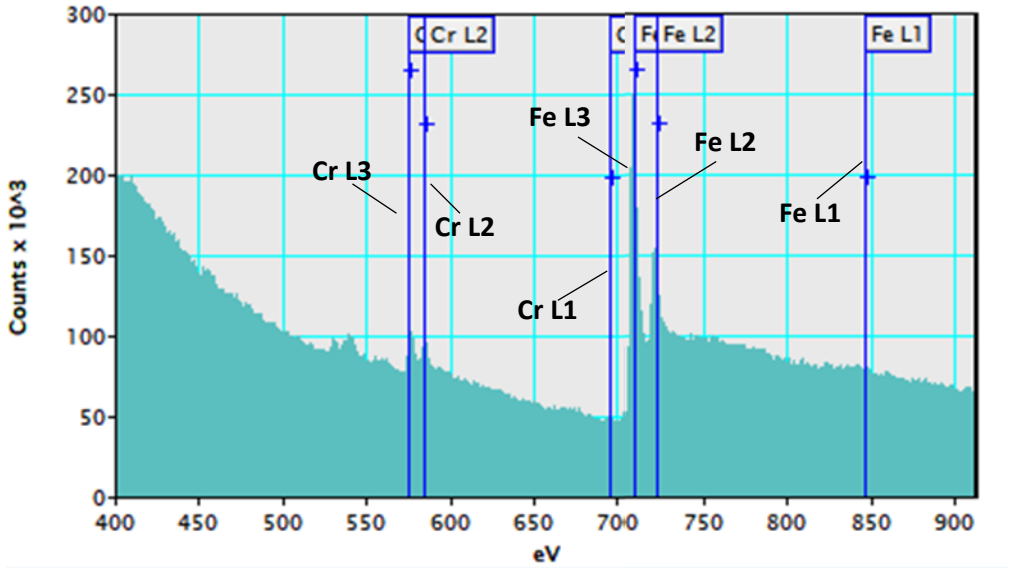

Figure 3.25: The edges of interest for quantifying chromium and iron. Oxygen was also acknowledged in the analysis.

Using Hyperspy, an EELS spectrum-image was aligned so that the zero-loss energy peak is positioned at zero. Then the data had X-ray energy spikes removed from the spectra, and then the data was denoised via the multivariate statistical analysis (MSA) technique known as principal component analysis (PCA). PCA is a standard technique for removing random spectral noise from EELS datasets [182]. PCA was implemented on the EELS maps obtained in this thesis using the built in EELS analysis tools of Hyperspy [181].

Hyperspy was lastly used to fit a model to the spectrum of each pixel using the Hartree-Slater model [181]. Examples of the energy spectra and fitted models are shown for the datasets presented in the experimental results chapters (chapter 4 and chapter 6).

The elemental signals were then taken as the integrated intensity under the modelled edge, and this was converted into atomic-percent by scaling with the extracted signals of other elements. For quantification of FeCr, only the iron and chromium edges were used to compute the composition, though the oxygen signal was included in the model.

The fully processed map is the intensity of chromium in atomic-percent for the region captured. An example chromium map revealing α' chromium phase precipitates is shown in Figure 3.26.

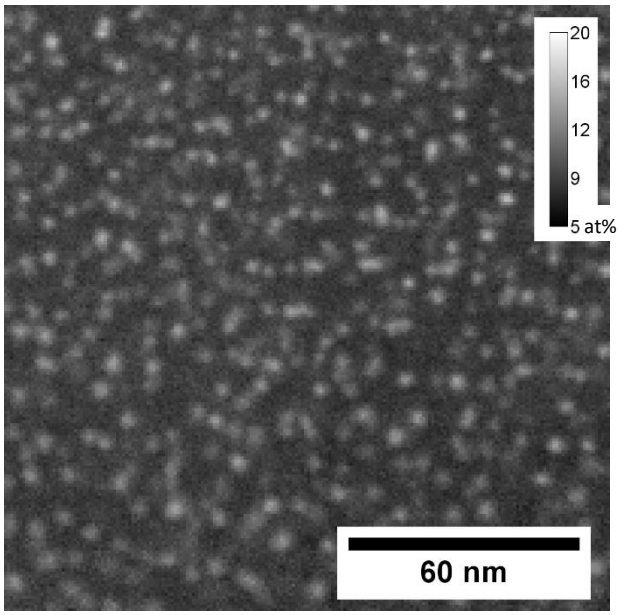

Figure 3.26: Example of an EELS-produced chromium map of chromium precipitates in neutron-irradiatedFe9Cr.

A disadvantage of EELS over an alternative analytical technique such as atom probe tomography (APT) is that the image obtained is two-dimensional, so the composition measured in each pixel represents the mean composition within a column of material through the foil thickness. To estimate the composition of the precipitates, the contribution of signal from the matrix above

and below the precipitate must be estimated. By assuming the distribution of chromium through the precipitate is approximated by a Gaussian function, the composition of the precipitate can be calculated (Figure 3.27). This assumption was applied to all chromium-precipitates analysed in this thesis. The method for removing the background contributions is discussed in detail in Appendix C.

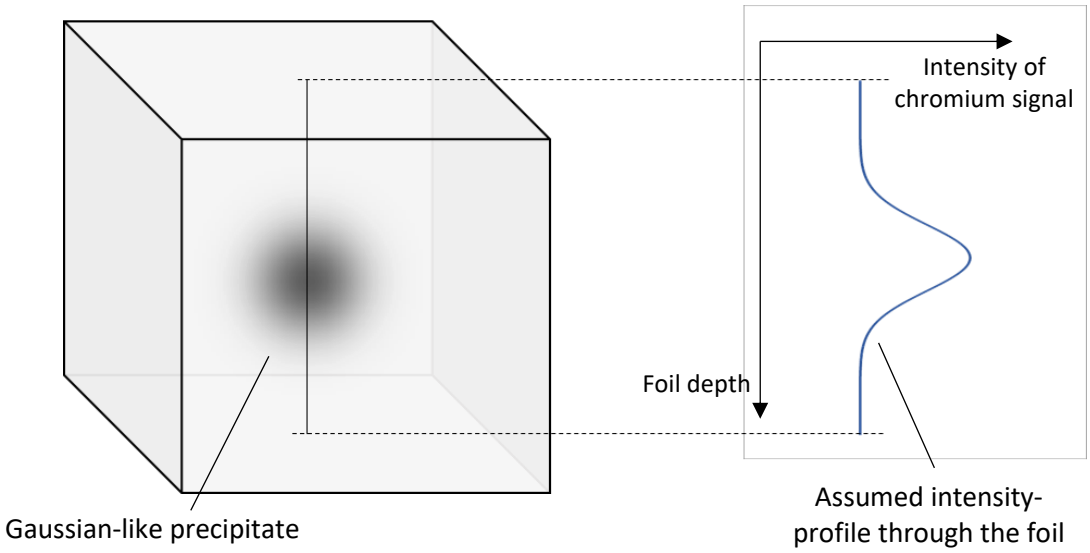

Figure 3.27: Illustration of a precipitate with a Gaussian-like chromium distribution, and the intensity profile through the foil thickness. The mean intensity of the signal through the centre of the precipitate and through foil thickness (shown) is equal to the peak signal measured in a 2D image of the precipitate. If the width of the Gaussian is assumed to be uniform in 3D, an estimation of the intensity profile through the foil (the profile illustrated, right) can be made.

For the EELS-acquired composition maps in this thesis showing redistribution of chromium after irradiation, a ~1nm diameter visibility limit was found for resolving small chromium clusters (for a minimum signal-to-noise ratio of two). An acquisition time of ~15ms per pixel over three frames, and with a probe and pixel size of ~0.3nm were used, followed by PCA denoising. Longer acquisition times will improve the signal-to-noise ratio for small precipitates; however, electron beam damage to the sample can then become severe. Additionally, for sizes <1nm, the definition of a cluster becomes hazy since clusters of that size may simply be due to the random distribution of chromium, rather than any meaningful irradiation-induced clustering.

Chapter 4: Neutron damage in FeCr

4.1 Introduction

In the absence of a dedicated fusion neutron source for materials testing, neutron irradiation inside dedicated fission materials testing reactors is the closest equivalent. In 2009, Professor Robert Odette of the University of California Santa-Barbra conducted a series of irradiation experiments using the Advanced Test Reactor at Idaho National Laboratory, USA. This involved a wide range of materials and irradiation conditions. This chapter will report for the first time the microstructural changes that have occurred in two FeCr alloys from this experiment.

4.2 Irradiation experiment

Alloys of Fe-6Cr and Fe-9Cr were housed in Capsule 1 of the ATR1 experiment [158] (alongside others) and remained inside the ATR through cycles 145A, 145B, 146A, and 146B for 202 days in total. The neutron spectrum for the irradiation is shown in Figure 4.1. Each specimen was in the form of a ~0.1 x 10 mm disk and stacked inside a cylinder measuring 41.9mm in length. Each cylinder of the experiment was stacked together as a rod and inserted into position A-10 of the ATR reactor, as indicated by Figure 4.2. Capsule 1A was positioned furthest from the centre of the core and therefore received the lowest flux.

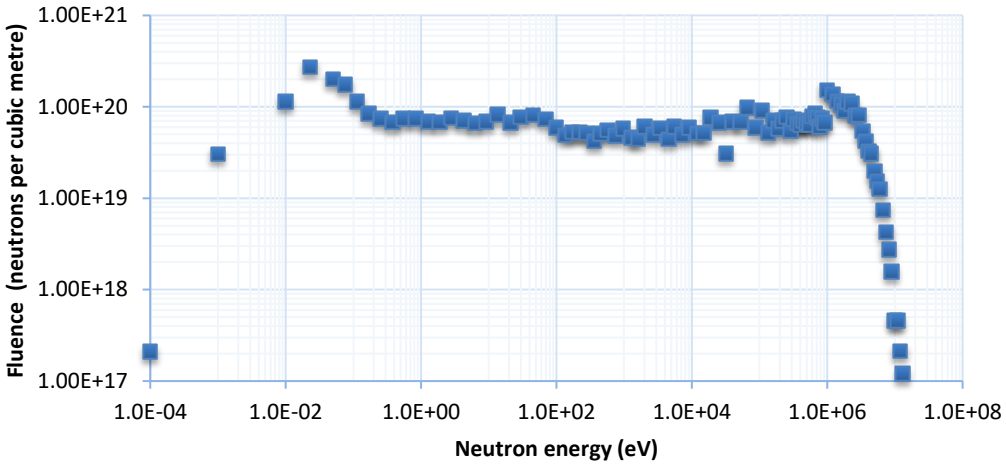

Figure 4.1: Neutron fluence spectrum as received by the FeCr alloys studied in this chapter (from [158]*). The plot is a histogram, where each point is the height of a bin. Note the unequal bin-spacing.*

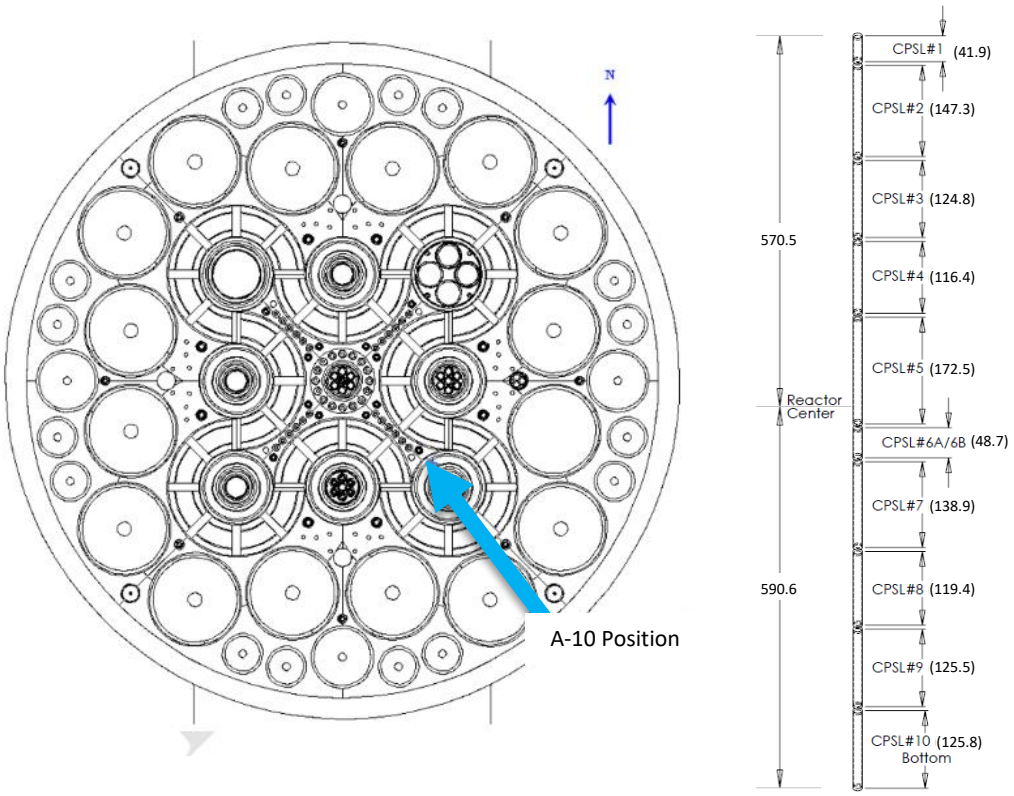

Figure 4.2: Radial cross section view of the ATR core and indicated position of the rod used to hold the samples of this experiment (from [158]*). Lengths are in mm.*

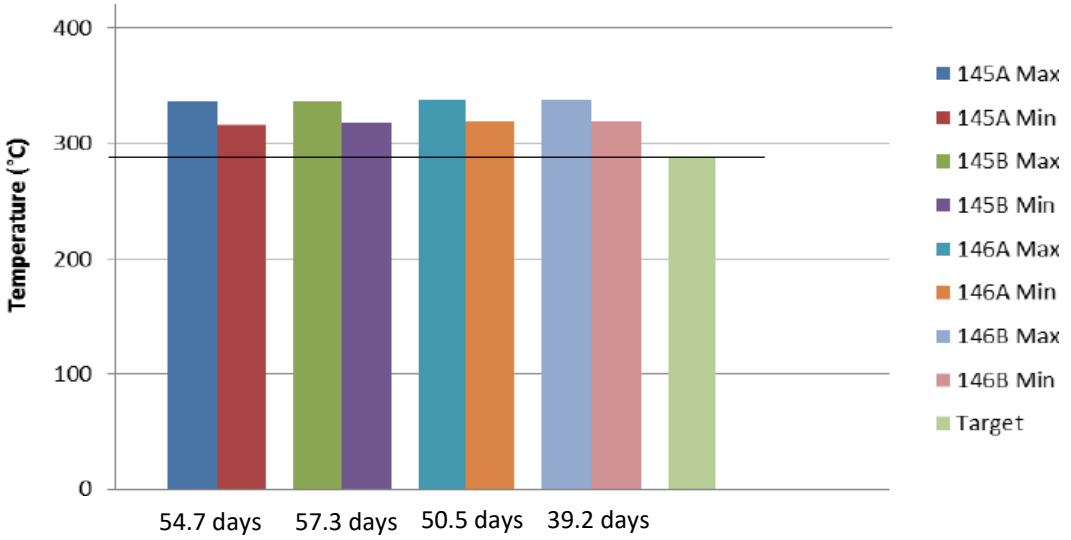

Figure 4.3: Reported temperatures of the FeCr samples during irradiation (after [183]*)*

A finite element steady-state heat transfer analysis for the UCSB test assemblies, basket, primary coolant channel, and adjacent housing was performed using ABAQUS version 6.14-2 by staff-engineers as INL as part of the UCSB experiment. The target temperature was 288°C, which is the same temperature reported by previous researchers that studied materials from this experiment [101,124]. The thermal measurements taken from the thermal analysis report [183] (an internal report) are shown in Figure 4.3. The minimum and maximum temperatures were found to be 315°C to 335°C respectively, which is higher than the target of 288°C.

A package called MCNP (Monte Carlo N-particle transport code) [184] was used by my UCSB collaborators to model and evaluate the experiment at the ATR, as detailed in the as-run experiment report [158]. This used a full 3D model of the core, samples, sample holders and capsules, to predict the flux received by each material. Using the SPECTER neutron cross-section library [185], MCNP predicted a dose of 2.14dpa for the materials in capsule 1.

With assistance from Dr Mark Gilbert, I conducted an alternative approach to the dose calculation using the FISPACT-II software [159] and Tendl-2014 [186] neutron cross-section library. This indicated a lower dose of 1.64dpa using the same neutron-fluence spectrum as predicted by MCNP. This difference in calculated dose will be discussed later in section-6.2.1.

4.3 Sample preparation

Samples were mechanically polished and electropolished by staff at INL to remove any remaining mechanical deformation in the surface layer. The materials were then transferred to the Centre for Advanced Energy Studies (CAES) in Idaho, where TEM foils could be prepared by the FIB lift-out technique as described in chapter 2. I used the CAES facility to prepare a large number of lamella-trenches (Figure 4.4) to remove the majority of the radioactive material around each foil in the CAES "active" FIB microscope. The samples were then transferred to the UK where FIB preparation continued at the Materials Research Facility (MRF) at CCFE, UK. This procedure allowed minimal time to be spent using the costly active handling equipment at the MRF, and also minimised the time between TEM foil preparation and observation in the microscope.

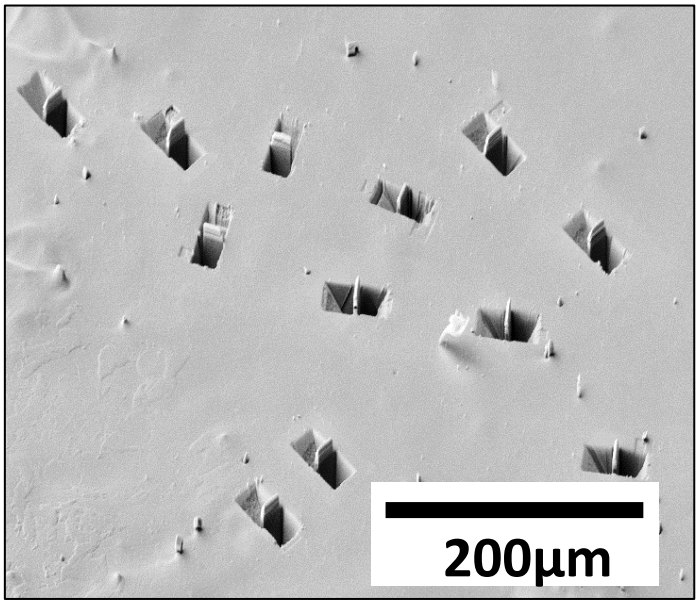

Figure 4.4: A series of TEM lamellae trenches in neutron-irradiated Fe9Cr produced by FIB milling at the CAES facility

EBSD was used at the MRF to identify the orientation of the grains, and only foils with normals close to [100] were selected for lift-out. Microstructural characterisation was performed on the neutron-irradiated Fe6Cr and Fe9Cr foils using mostly weak-beam dark field conditions with a JEOL 2100L TEM. In addition to analyses by diffraction contrast, Election Energy Loss Spectroscopy (EELS) in a JEOL ARM 200F was used to investigate any compositional changes due to the neutron irradiation.

4.4 Microstructure of neutron irradiated Fe6Cr

Figure 4.5 shows a low magnification annular dark field (ADF) image of the microstructure of neutron-irradiated Fe6Cr. This shows that the radiation damage consists of a highly non-uniform distribution of dislocation loops. The majority of dislocation loops are found in the vicinity of linear or helical mixed screw/edge dislocations present in the foil.

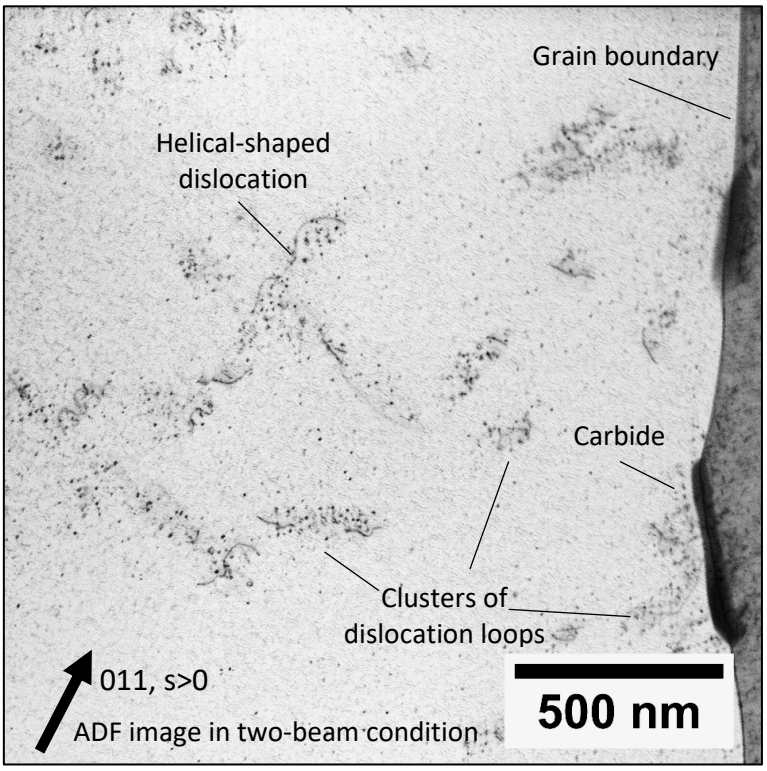

Figure 4.5: Low magnification ADF image of the neutron irradiation damage in Fe6Cr

Figures Figure 4.6 to Figure 4.10 show higher magnification micrographs of various locations in the foil, demonstrating the spatial variation in dislocation loop number density and sizes. In some instances, the dislocations appear to have a helical shape, though it was not possible to analyse these in detail here (a detailed analysis is conducted for similar structures in the neutron-irradiated Fe9Cr in section-3.5.4). Dislocation loops are frequently found clustered around dislocations, either within helical dislocations or confined to one side of a dislocation. The regions between dislocations are much lower in loop density, but small loops of ~2nm diameter are still clearly visible. No clustering of dislocation loops at grain boundaries was seen in this alloy, besides instances where a dislocation is found close to a grain boundary.

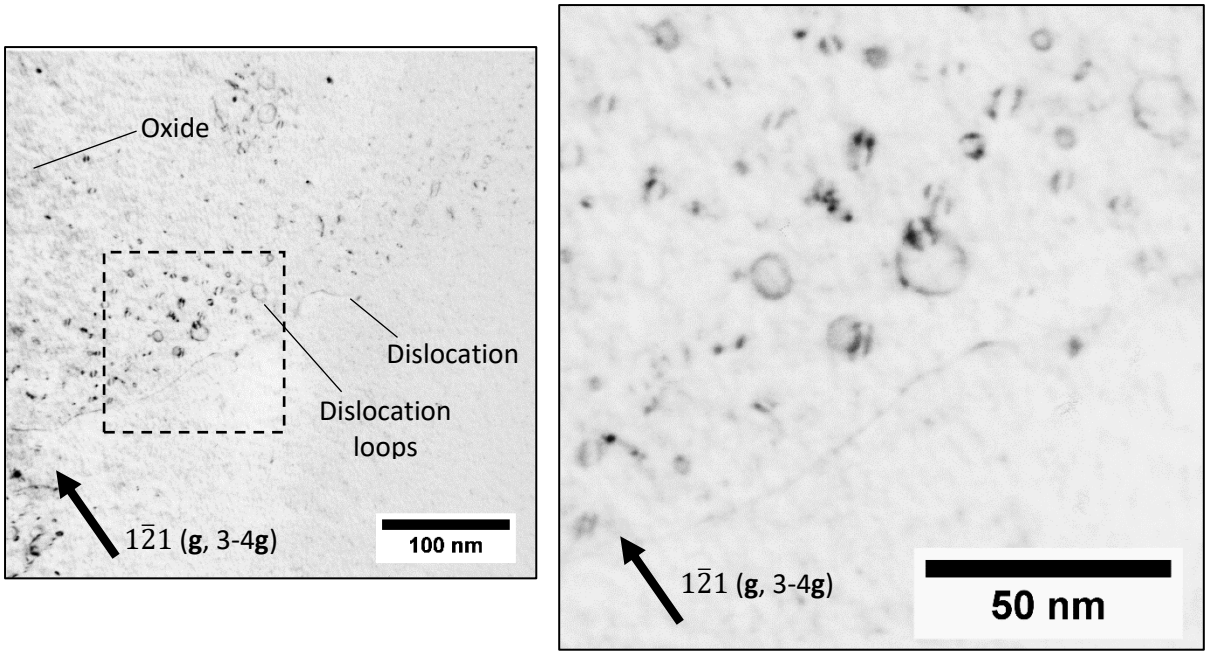

Figure 4.6: Weak-beam micrographs of dislocation loops clustered on one side of a dislocation in neutron irradiated Fe6Cr

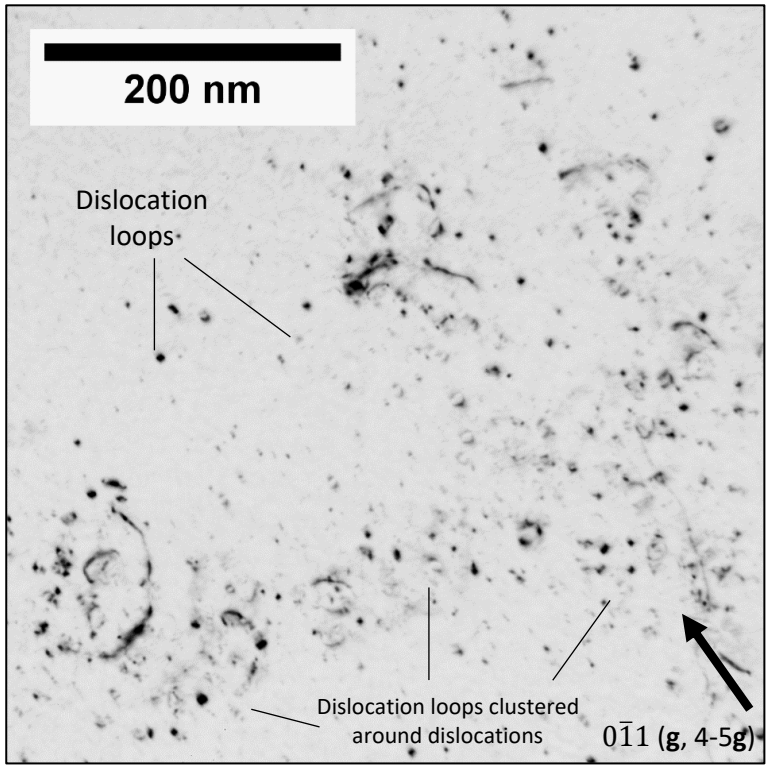

Figure 4.7: Weak beam micrograph of dislocation loops clustered around a network of dislocations in the neutron irradiated Fe6Cr

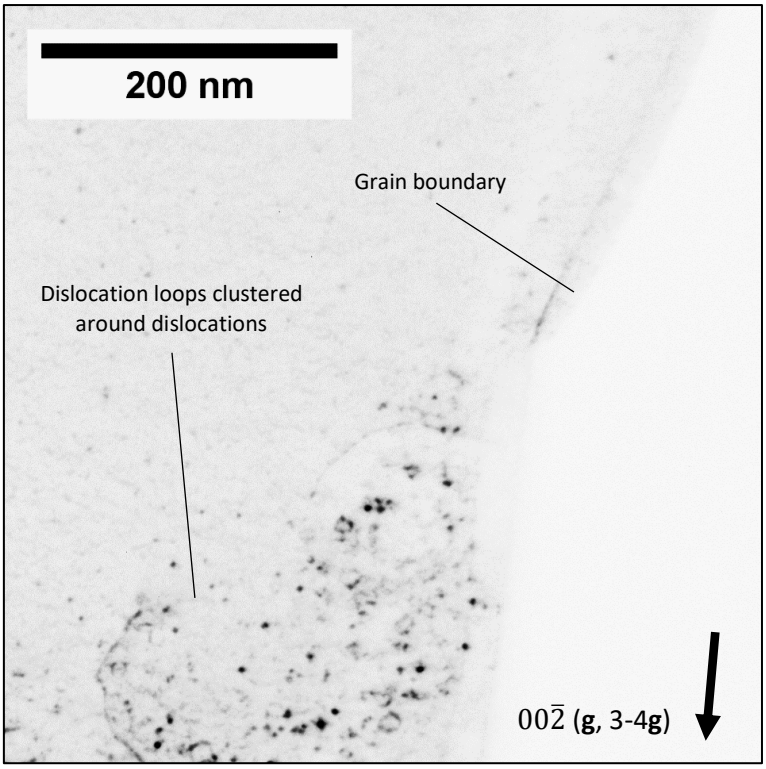

Figure 4.8: Weak-beam micrograph of dislocation loop clustering close to a grain boundary in the neutron irradiated Fe6Cr. Dislocation loops are located preferentially around the dislocation rather than the grain boundary.

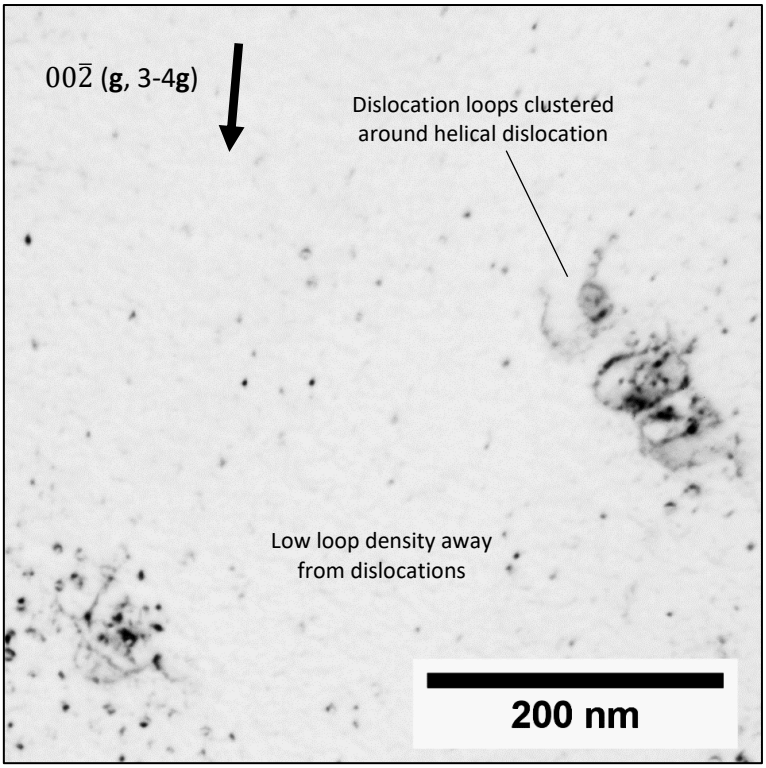

Figure 4.9: Weak-beam micrograph of a region of low density of dislocation loops, and helical dislocation, in the neutron irradiated Fe6Cr.

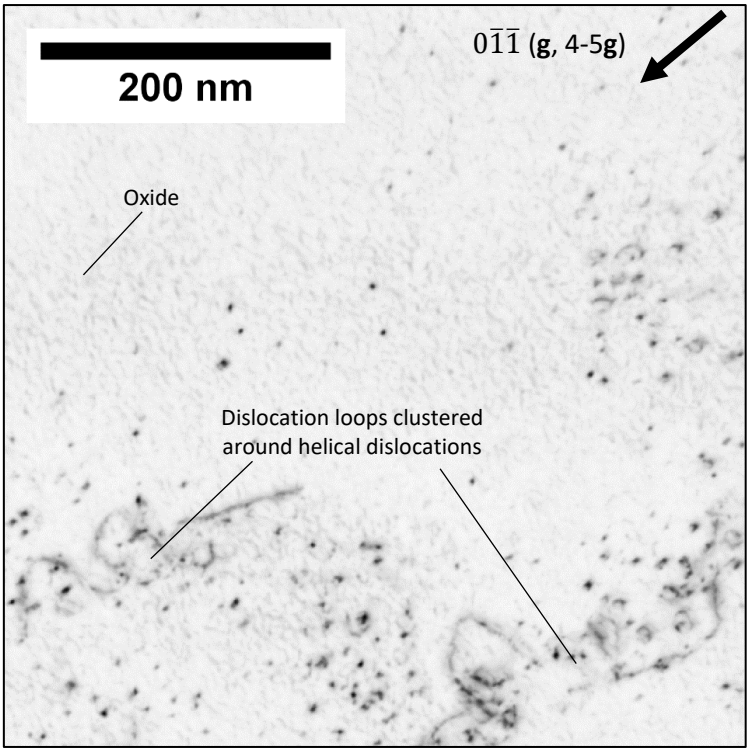

Figure 4.10: Weak beam micrograph showing another region of low density of dislocation loops in the neutron irradiated Fe6Cr. Dislocation loops are seen clustered around helical shaped dislocations.

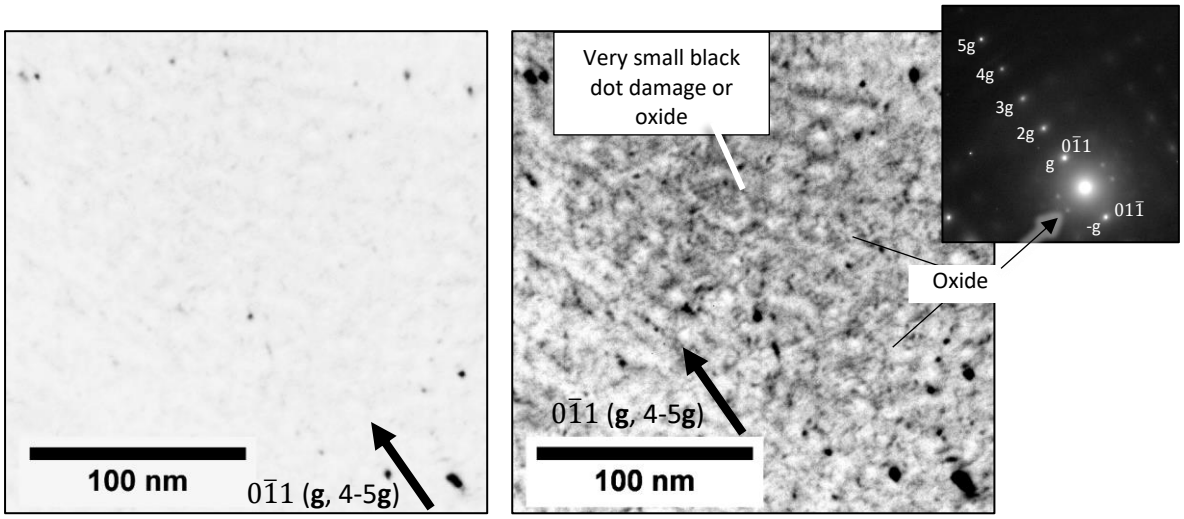

Figure 4.11: Two micrographs of the same region of low loop density in the neutron irradiated Fe6Cr, shown with different contrast settings. The high contrast image shows a rich density of black dots, which may be attributed to neutron damage, FIB damage, or surface oxide. The diffraction pattern for this condition is shown, in which reflections associated with oxide are visible close to the direct beam.

Figure 4.11 shows that a dense population of black dots, mostly <1nm, is present throughout the regions of the foil with an apparent low loop density. Surface-oxide can appear as black dots, in addition to the greyish regions and ripple-like contrast visible in the high contrast micrograph in Figure 4.11. Since the foils were prepared by FIB, the black dots might also be attributed to the remaining 2kV Ga damage. It may also be neutron damage. It was not possible to rule out any of these as a source for the black dot damage in the background. Figure 4.12 shows the interface between a helical dislocation and the matrix. This micrograph shows the dislocation loop density decreases abruptly beyond the neighbourhood of the dislocation.

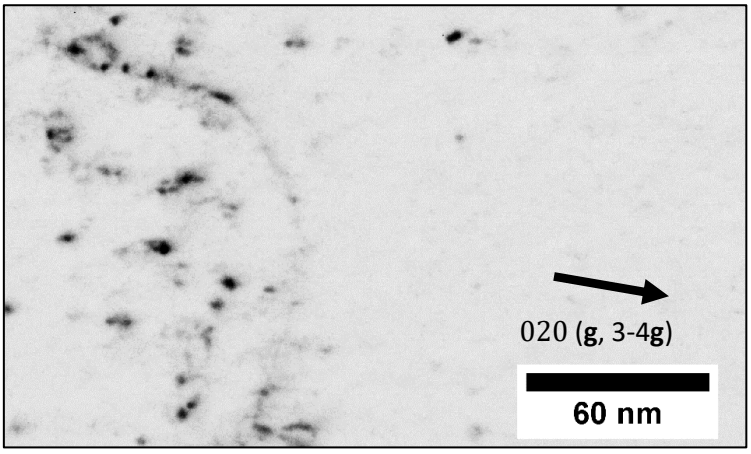

Figure 4.12: The interface between a cluster of loops inside a helical dislocation and the sparsely populated matrix outside the helix.

4.4.1 Burgers vectors and number density of irradiation-induced dislocation loops in the neutron irradiated Fe6Cr

Due to the highly inhomogeneous density of dislocation loops, it is not useful to quote the number density for an arbitrary region of the foil. Instead, the number density was measured for two extremes – a low-density measurement in regions between loop clusters and/or dislocations, and another high-density measurement in regions around a dislocation line.

To determine the Burgers vector of the dislocation loops, micrographs with **g**=±011, $\pm 01\bar{1}$ and ±020 were compared. Loops were counted in conditions **g**=±011 and $\pm 01\bar{1}$ and **g**=±020 by correlating defects in the +**g** and -**g** conditions, and ideally another g-vector micrograph. The statistical analysis method [172] (see section-2.6.4) was then used to extract the probable number of <100> and <111> loops. Figure 4.13 shows an example of the **g**.**b** analysis for selection of <111> and <100> loops that were found in a high-density region. Correlating the same feature across all micrographs was not possible for the smaller loops, so statistical analysis was ultimately used to obtain the relative proportions of <100> and <111> type loops. This was then used to calculate the overall loop number density. Figure 4.14 shows the loop counts as the volume number density of the high and low-density regions, and Figure 4.15 shows the percentage of <111> loops and <100> loops present.

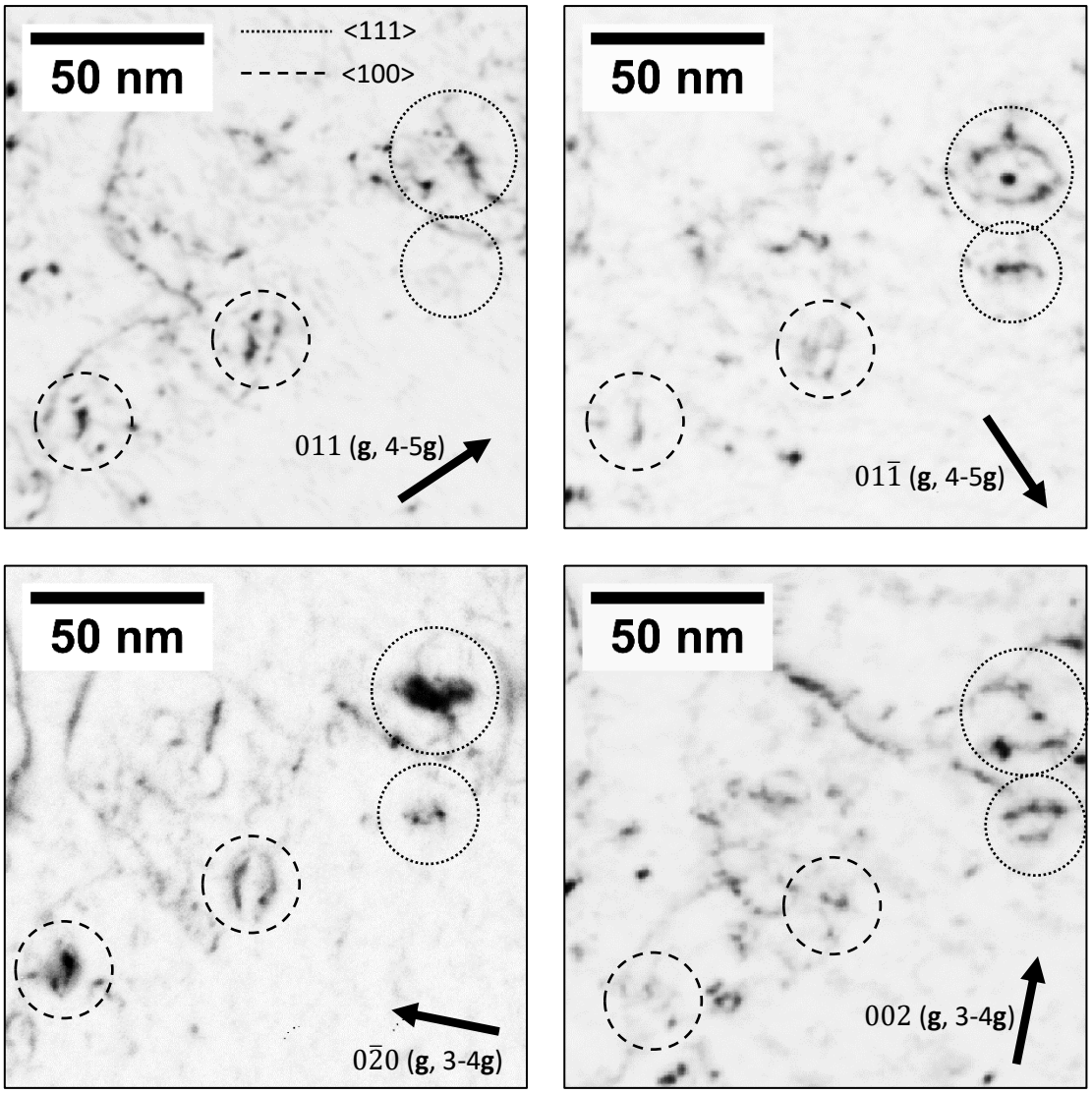

$g \cdot b$ *product*

b \ g	[100]	[010]	[001]	$\frac{1}{2}[111]$	$\frac{1}{2}[1\bar{1}1]$	$\frac{1}{2}[11\bar{1}]$	$\frac{1}{2}[1\bar{1}\bar{1}]$
011	0	1	1	1	0	0	-1
01$\bar{1}$	0	1	-1	0	-1	1	0
0$\bar{2}$0	0	1	0	-1	1	-1	1
020	0	0	1	1	-1	1	-1

*Figure 4.13: Burgers vector analysis revealing the presence of both <111> and <100> type dislocation loops. The **g.b** product table indicates which loops are visible in which condition.*

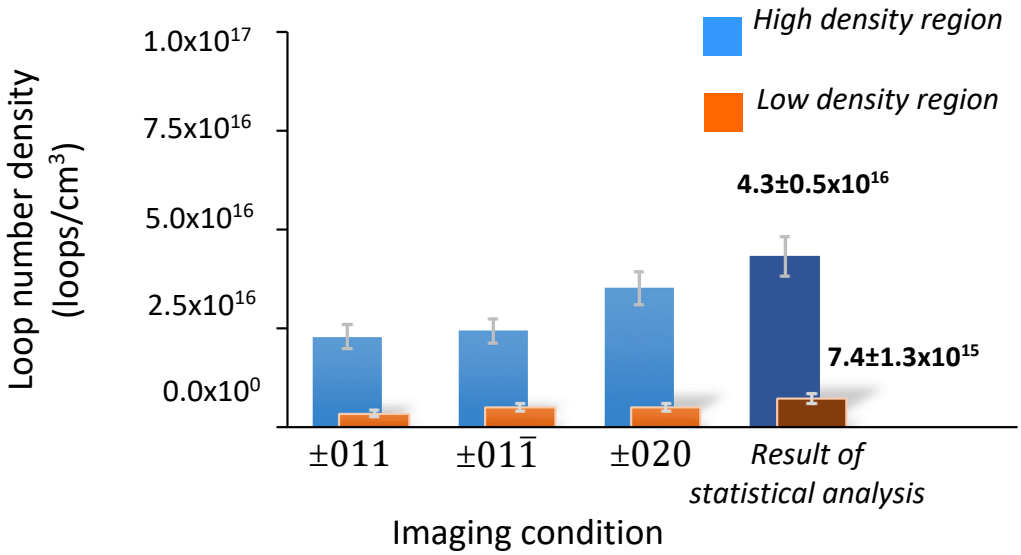

Figure 4.14: Loop volume number density of the dislocation loops. Since the loop density is very heterogeneous, the loops were counted in two regions – a high density and low density region.

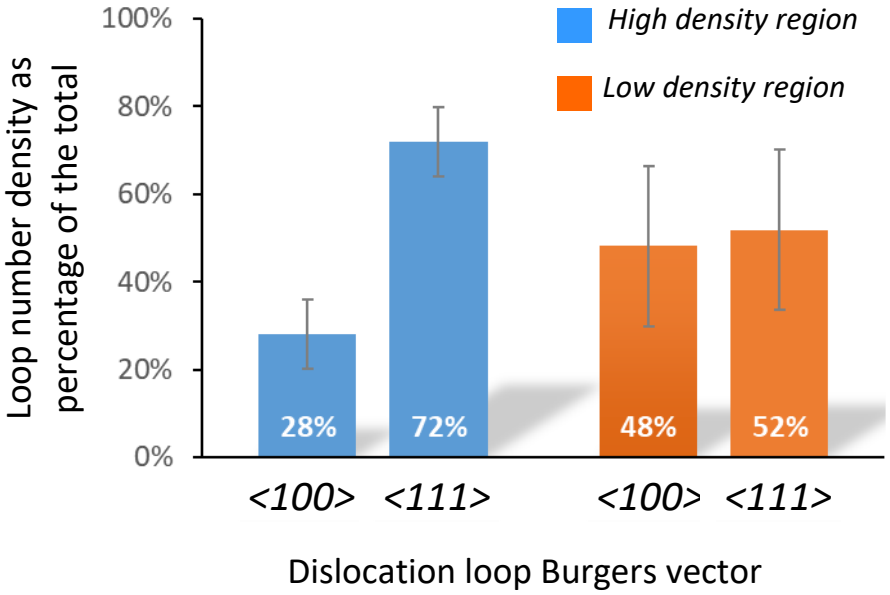

Figure 4.15: The fraction of <100> and <111> loops present in the high and low density regions in the neutron irradiated Fe6Cr.

These plots demonstrate the large change in loop density within the microstructure, with around an order of magnitude difference in visible loop population between the high and low density regions.

The counts used to estimate the loop population and Burgers vectors in the high-density region originate from the area shown in Figure 4.16. The decision to sample this region was arbitrary, but the width of this region corresponds to the maximum diameter of the volume encased by the helical dislocations running through this region. Since the periodicity and diameter of the helix is not uniform, there is some variation in density throughout this region. In addition, the width of the area is ~125nm, which is greater than the thickness of the foil in this region. Therefore, the "dense" volume of dislocation loops was assumed to propagate through the thickness of the foil. The volume considered was then taken to be a series of parallelepipeds, with a thickness of 95±10nm, as indicated by CBED.

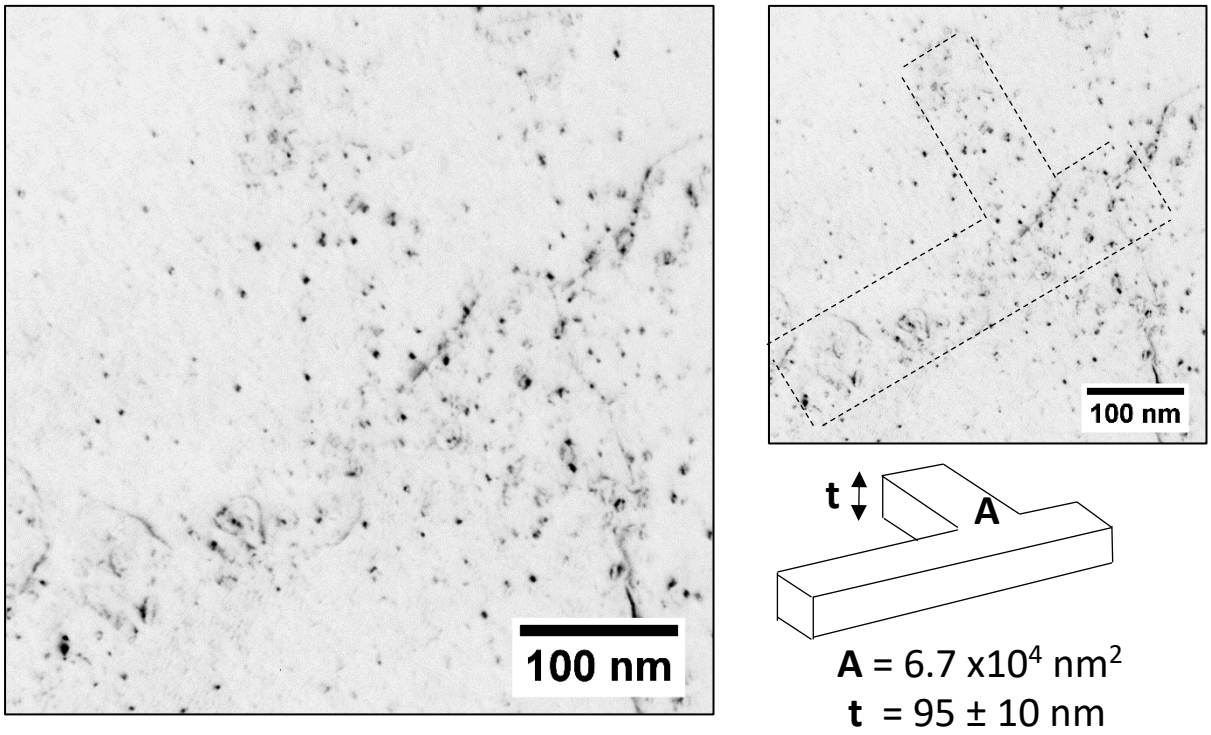

Figure 4.16: Weak beam micrograph of the dense region of dislocation loops in the neutron irradiated Fe6Cr used for counting and sizing the dislocation loops. The shape taken to be the volume of the region is also shown.

Ideally, a cylindrical volume would be used, corresponding to the volume around the dislocation for some radius, but since it was not possible to measure the length of the dislocations here, an appropriate cylindrically-based volume could not be measured. Therefore, the estimation of

loop density for this high density region probably underestimates the true density. Furthermore, the loop population appears to fall gradually beyond the confines of the helical dislocation, so there isn't a fixed edge to this high density region. The intermediate-density region was not analysed.

Section-4.5 shows how the loop density in the Fe9Cr is more locally concentrated around dislocations similar to those studied here in the Fe6Cr, and so a more precise characterisation of the "dense" volume could be made.

4.4.2 Nature analysis of loops in the neutron irradiated Fe6Cr

The loop nature was determined using the inside-outside contrast method [48] (see section-2.6.4). The foil was thinned further to aid cross correlation of loops over several conditions. Figure 4.17 shows a series of micrographs taken under various conditions demonstrating the analysis for a selection of loops. No <100> loops were found in this thinned foil, so the analysis was only done for <111> loops.

The largest loop analysed was ~24nm in diameter, and the smallest was ~5nm in diameter. The oxide presence in the foil limited imaging to stronger (~0.1 nm^{-1}) dark field conditions when imaging g-vectors ±011, ±$01\bar{1}$ and ±020, and kinematical bright field conditions for higher order reflections, with s>0. Bright field micrographs in Figure 4.17 are labelled to distinguish them from the inverted-contrast dark field images. Due to the significant oxide presence, it was difficult to identify the defects through all necessary reflections. For this reason, only seven loops were successfully analysed.

All loops were found to be interstitial.

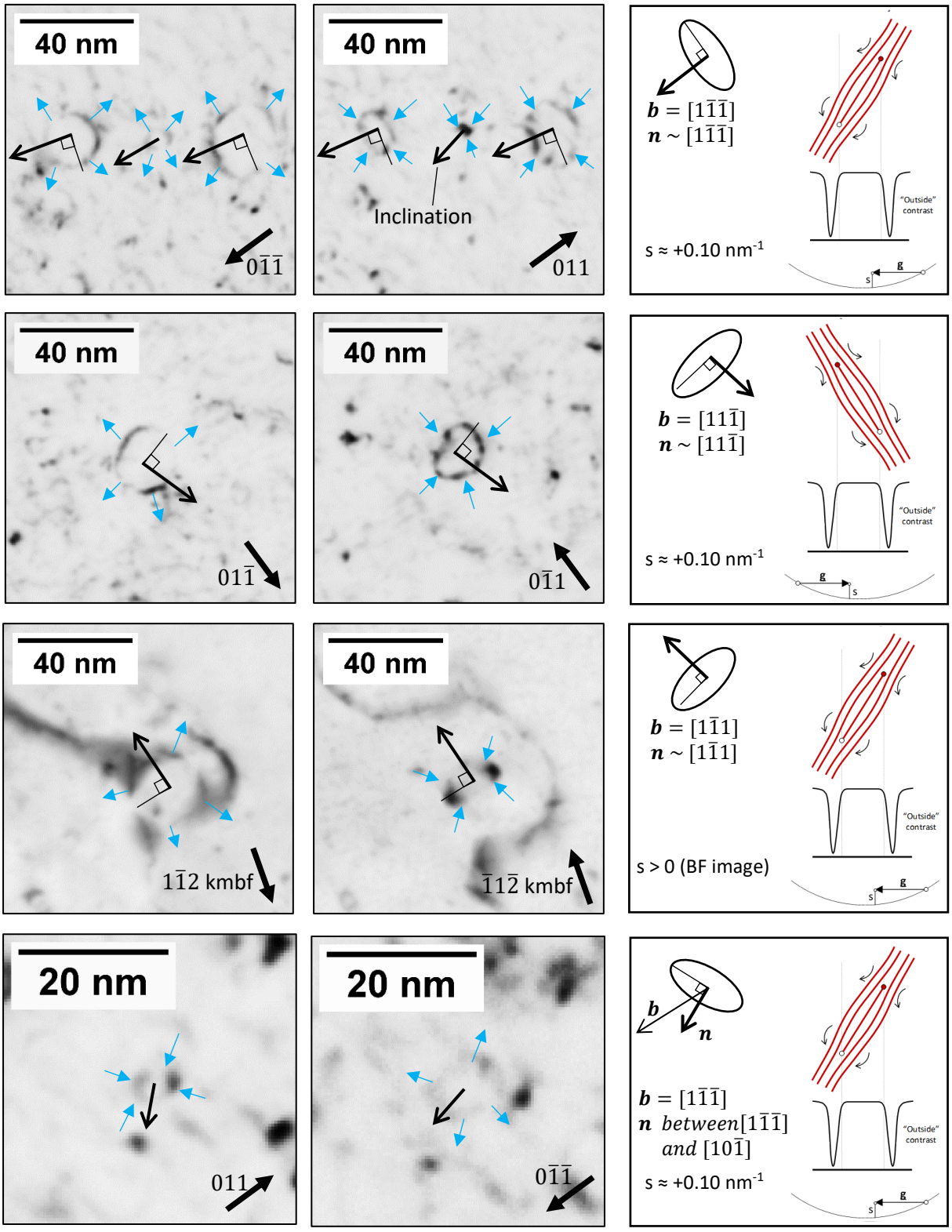

*Figure 4.17: Nature analysis of a selection of dislocation loops in the neutron irradiated Fe6Cr. The Burgers vectors were determined by correlating the same feature through a complete **g.b** series, and observing the invisible conditions. The inclination was inferred from **b** and shape of each loop. All loops were found to be interstitial.*

The precise habit planes of the loops could not be determined from these micrographs, but their projection indicates they lie on close-to-prismatic planes. Two exceptions are the small loop in the first row of micrographs of Figure 4.17, and the loop in the last row of micrographs. In both cases, there appears to be some rotation in the contrast between inside and outside conditions, which confuses the interpretation of the morphology. In both cases, it appears that the habit plane may lie somewhere between a $(1\bar{1}\bar{1})$ plane and $(10\bar{1})$ plane.

4.4.3 Size distributions of loops in the neutron irradiated Fe6Cr

Dislocation loops were counted and sized in three different g-vector conditions with the deviation parameter ~0.14 nm^{-1} on average, which is a stronger condition than a true "weak" beam condition [48]. A stronger condition was used here since the oxide layer overwhelmed any usable signal from the dislocations in the higher deviation parameter conditions. A stronger condition will result in broader dislocation lines, and so the resolution for small defects will be reduced. The effect on the measured size of a loop is expected to be minimal since both +**g** and -**g** conditions were captured.

The size distributions for each ±**g** condition in the high-density region is shown in Appendix D. These show that the mean dislocation loop size does not change significantly with **g**. Figure 4.18 shows the combined size distribution for all measurements, normalised to the loop density of the high and low density regions. The results show that there are significantly more large loops in the high-density region. Since the nature analysis suggests the dislocations are all (or mostly all) interstitial, the size distribution suggests there are significantly more interstitial point defects clustering in the vicinity of dislocations than anywhere else in the microstructure.

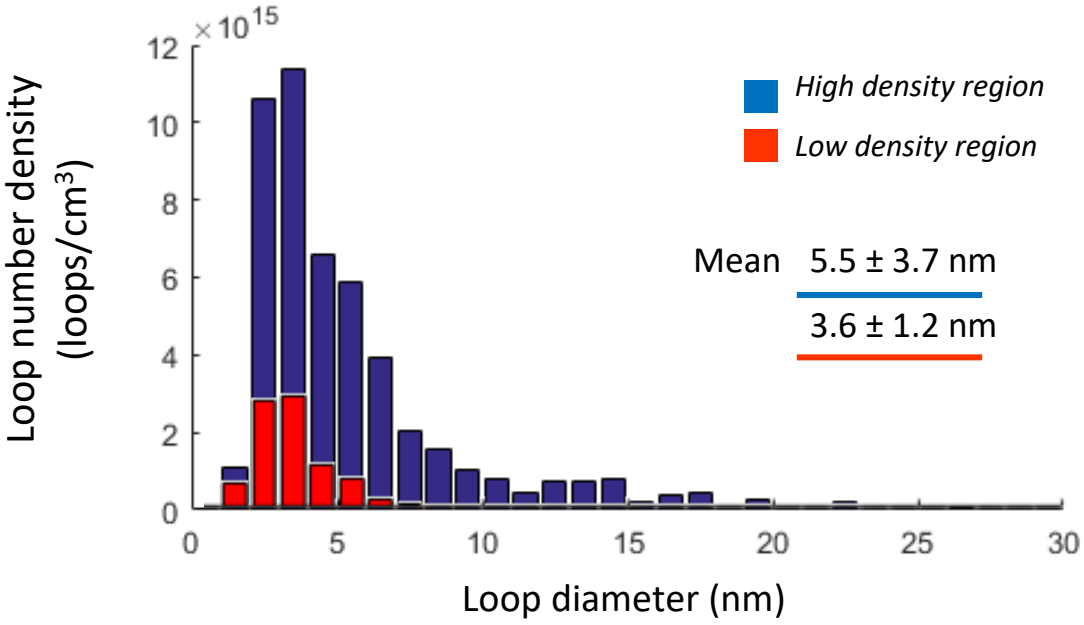

Figure 4.18: Dislocation loop size distribution for the neutron irradiated Fe6Cr, normalised to the loop density in each region.

The size of the dislocation loops can be converted to an atomic volume, but the loop atomic volume as a function of the diameter will be different for different habit planes and Burgers vectors. Since it is not practical to determine the exact Burgers vector and habit plane for every loop, it was assumed that the actual loop volume does not differ substantially from that of a prismatic <111> loop. The atomic volume was calculated from Equation 4.1.

Equation 4.1

$$V_{111} = \sqrt{3}\pi \left(\frac{D}{2a}\right)^2$$

With the atomic volume calculated for each loop, the measurements were then grouped into $0 \leq Y < 0.1$, $0.1 \leq Y < 0.2$, etc. where the atomic volume $N = 10^Y$ atoms. The result is logarithmically spaced bins. Since the bin sizes are unequal, the count from each was then normalised to the width of the respective bin. The result for the high density region is shown as a log-log plot in Figure 4.19, with the Y-axis shown as volume number density. This analysis was not conducted for the low density region due to the low counts. A power-law was fitted to the data for all loops larger than 100 atoms, also shown in Figure 4.19. The limit for the power-law fitting was chosen to be 100 because the data deviates significantly from a power-law for clusters smaller than this.

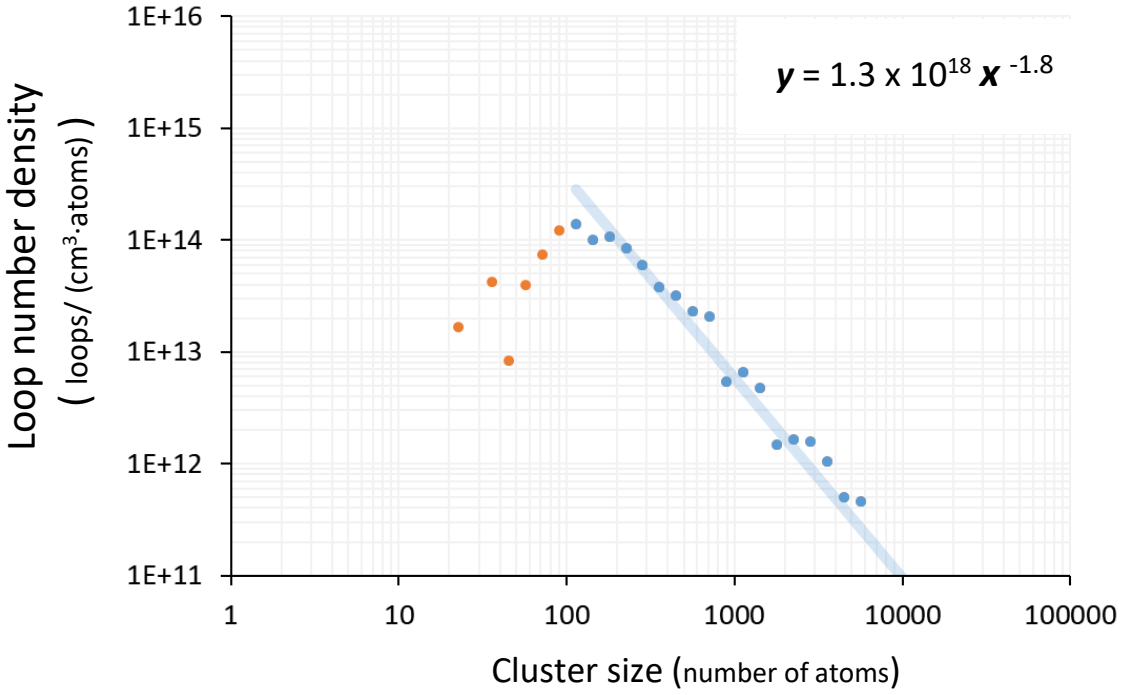

Figure 4.19: Loop size distribution by the atomic volume, shown with logarithmic binning

By assuming the same power-law can be used to extrapolate the dislocation loop distribution for those sized less than 100 atoms in size, then it is possible to estimate the total number of interstitials that are likely to be present, including those invisible to TEM. The error was calculated from the variance in the total interstitial counts of artificial datasets, which were produced using the fitted power-law as a probability distribution function. This process is described in more detail in Appendix D.

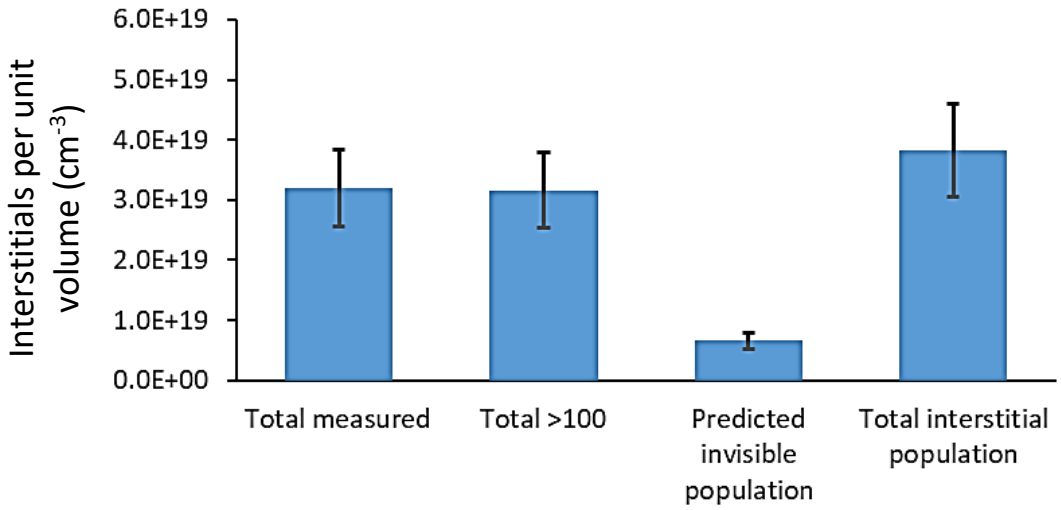

Figure 4.20: Interstitial population estimated in the high density region of the sample.

Figure 4.20 shows that despite Figure 4.19 implying the vast majority of interstitial clusters are smaller than 100 atoms, the majority of interstitials are found in the large clusters. Hence, the predicted population of interstitials in clusters <100 atoms (mostly invisible to TEM) accounts for only a small population of total number of displaced defects; the visible defects contain most of the point defects remaining after irradiation.

4.4.4 Voids in neutron irradiated Fe6Cr

The under-over focus technique was used to investigate whether voids are present in the foil. Micrographs were captured at approximately ±500nm focus. Figure 4.21 shows a 50x50nm area over a cluster of dislocation loops in the under and over focus conditions. Also shown in Figure 4.21 is the sum of one condition with the inverse of the other, which removes the diffraction contrast from the image whilst preserving the Fresnel fringes of the voids. Small features are visible, mostly <2nm, that show the typical light-fringe with dark centre (and vice versa) contrast in the under and over focus conditions.

Features were selected based on whether there is a clear reversal in Fresnel contrast between the under and over focus conditions. The smallest feature that could be resolved was 0.8nm in diameter. It was assumed that these features are voids, however surface oxide and/or surface

craters can also appear with this contrast. It was not possible to distinguish these features apart, and so these results should be treated with caution. More in-depth investigation of the features could be conducted by cross-correlating under-over focus image sets with images obtained by ADF and HAADF STEM, which would help to distinguish cavities from precipitates [171]. Due to time limitations, this additional analysis was not conducted.

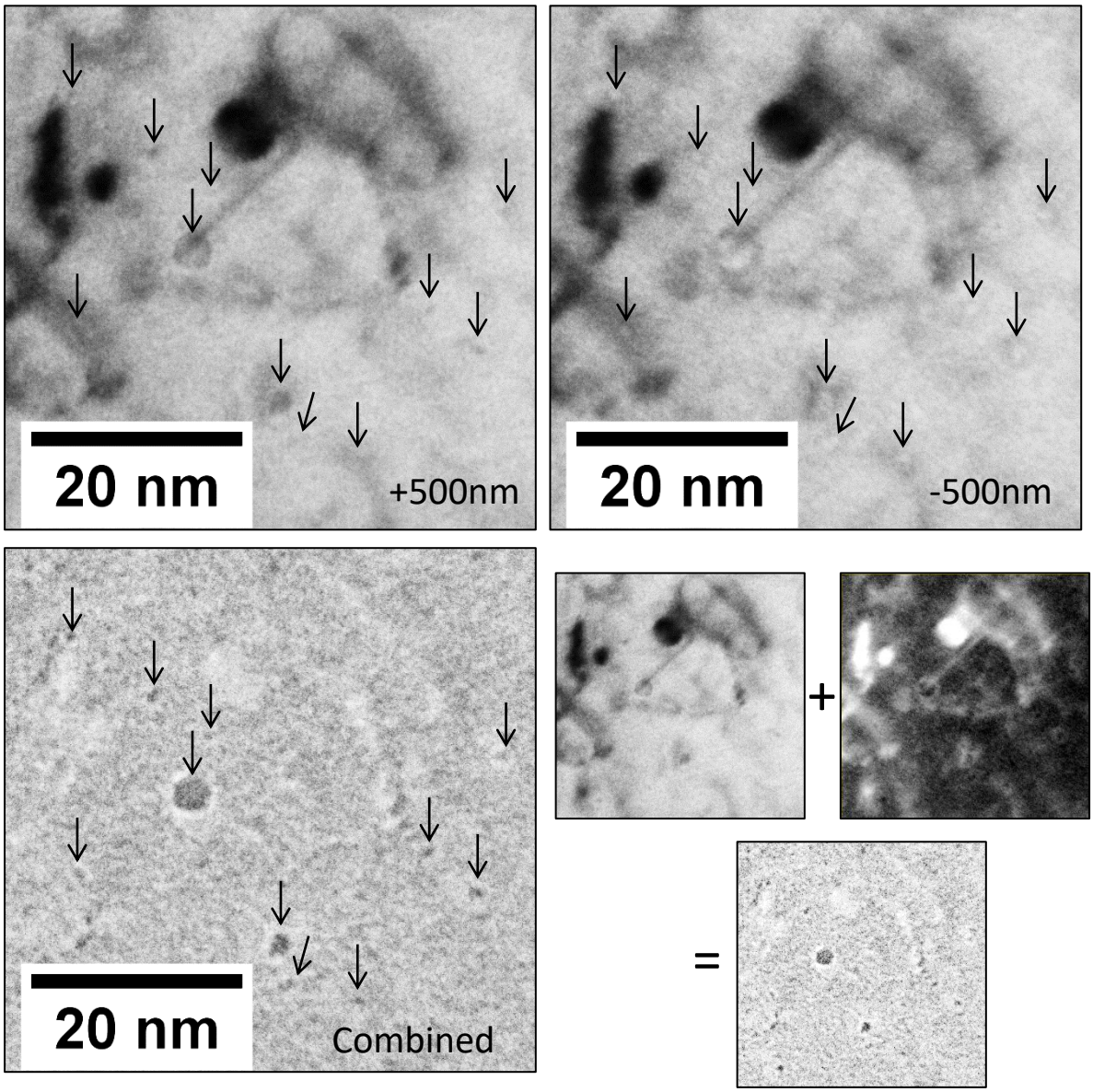

Figure 4.21: Over and under focus micrographs of small void-like features

Figure 4.22 shows a radial line profile for two voids. All voids were measured by the method described in section-3.7. Sizing of voids smaller than 2nm in diameter is more uncertain than those larger than 2nm, and so the criteria by Ruehle [180] may not reflect the true size such features (assuming they are in fact cavities).

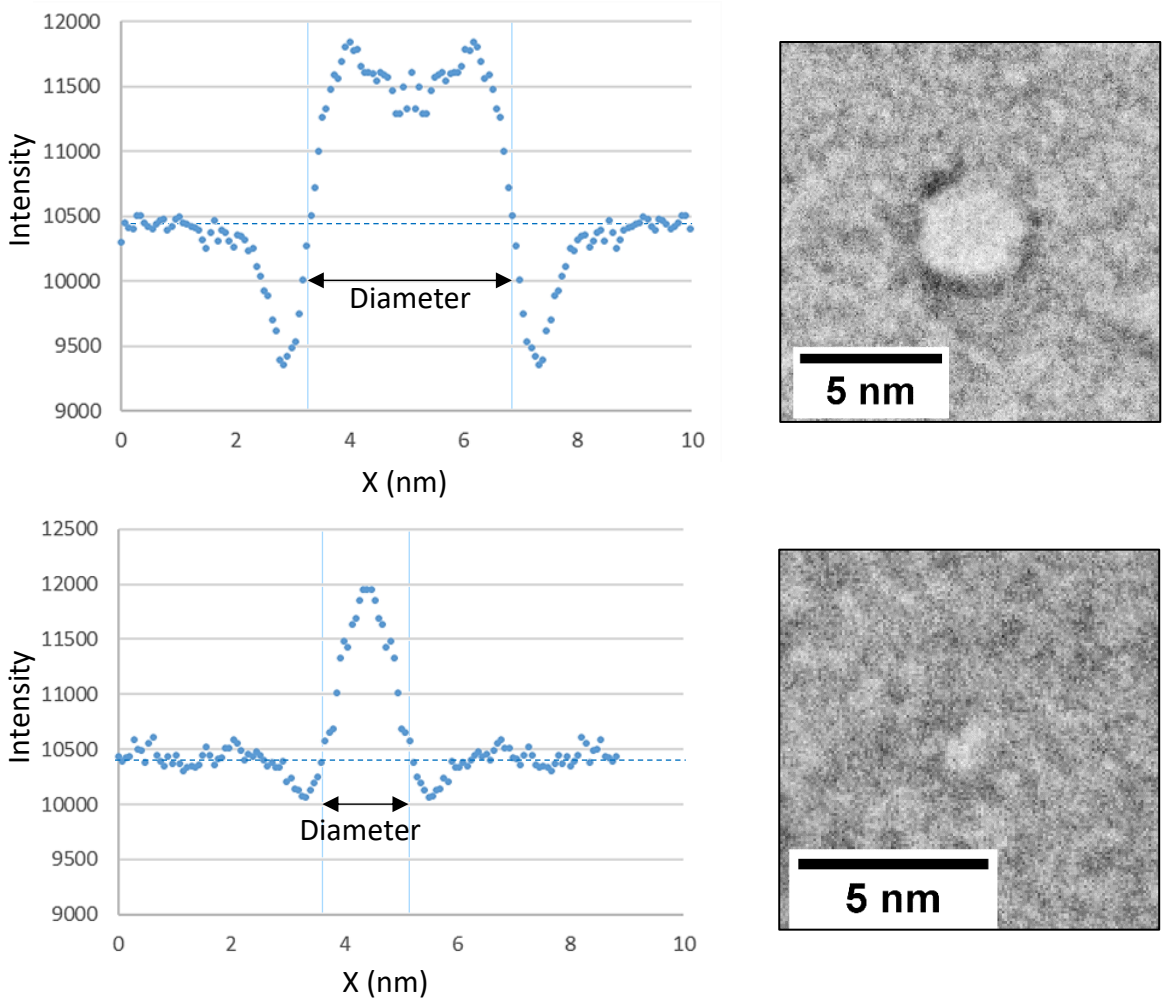

Figure 4.22: Radial line profiles of two possible voids. The micrographs shown are the combined under and over focus images.

Identifying void-like features sized <2nm is difficult, as is clear from the contrast in the second feature of Figure 4.22. This feature was only selected after comparing both over and under-focus conditions and observing a clear reversal in contrast. This does not however rule out the possibility that the feature is actually a surface crater or near-surface void from FIB preparation, or surface

oxide. The largest feature measured (the first line profile in Figure 4.22) is too big to be attributed to oxide or a surface crater, and so is much more likely to be a void than the <2nm features [48,171].

Table 4.1 shows measurements of the number density, mean size, minimum size and maximum size of the voids measured. Due to their small size and weak contrast, only 40 void-like features were measured in total, the majority of which were <2nm. Due to the low density of void features observed, it is likely that there exists a large population of small vacancy clusters that cannot be resolved in the micrographs (since vacancies and interstitials were produced in equal numbers).

	Inside loop cluster	**Outside loop cluster**
Number density (voids cm^{-3})	$4.4 \pm 1.0 \times 10^{16}$ >2nm: $4.2 \pm 3.0 \times 10^{15}$	$4.0 \pm 0.9 \times 10^{16}$ >2nm: $2.1 \pm 2.1 \times 10^{15}$
Mean diameter (nm)	1.5 ± 0.6	1.5 ± 0.4
Maximum diameter (nm)	3.5	2.7
Minimum diameter (nm)	0.8	0.9

Table 4.1: Measurements of density and sizes of the voids in neutron irradiated Fe6Cr

4.4.5 Redistribution of chromium in neutron irradiated Fe6Cr

EELS mapping was used to investigate chromium clustering or precipitation due to the neutron irradiation. A TEM lift out was thinned to ~25nm in thickness using 2kV Ga beam milling in the FIB. The region studied contained a small number of loops that were easily distinguished from FIB damage, though oxide was still an issue.

Inelastically scattered electrons were measured in the energy range from 400 to 912eV with 0.25eV width channels. The edges of interest are discussed in section-3.8. Hyperspy [181] was used to process the EELS data using the methods described in section-3.8. The Hartree-Slater model in Hyperspy was used to fit iron, chromium and oxygen edges to the recorded data and extract the signal contributions from chromium and iron. An example of the model as fitted to a single pixel is shown in Figure 4.23.

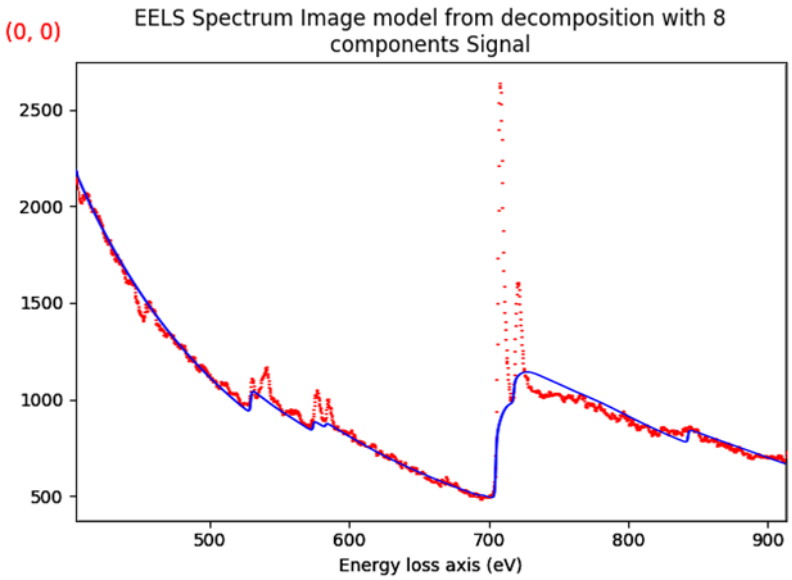

Figure 4.23: EELS spectrum from a single pixel, shown with the fitted model of the edges

Due to time constraints, the method used excludes fine structure in the analysis; hence, only the edges are fitted in the model. The consequence of this is that the extracted chromium composition will not be a good estimate of the true value, although the chromium signal relative to other pixels in the image will be more accurate. The fine structure was fitted using Hyperspy [181] to

the total signal collected from the mapped area to obtain a more accurate measurement of the mean composition, shown in Figure 4.24. This was then used to scale the chromium map to a more accurate composition.

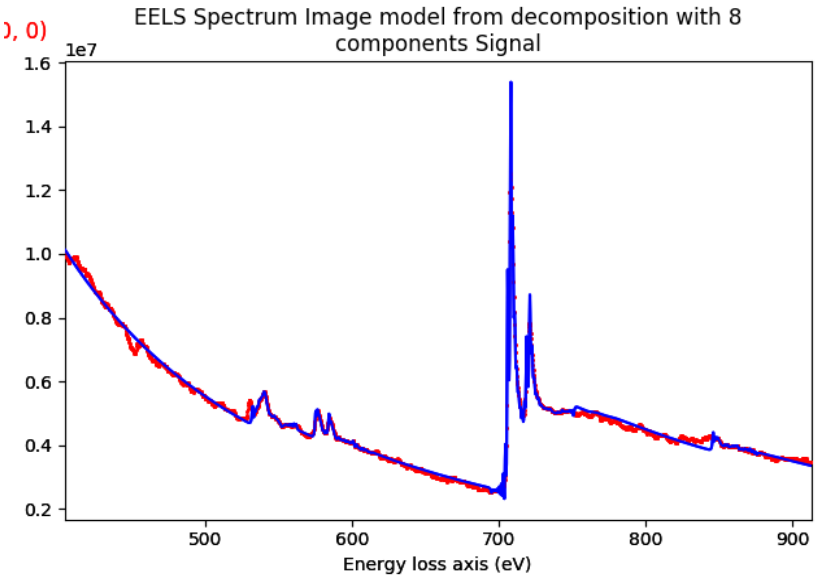

Figure 4.24: EELS spectrum from the entire map, shown with the fitted model of the edge, including fine structure

Figure 4.25 shows a chromium map from a 23nm thick section of the foil. Each pixel is 0.9nm across, and a similarly sized probe was used during EELS acquisition. It was not possible to use a finer probe because the signal was too noisy, and the beam would damage the sample for longer acquisition times. The image shows a population of small chromium clusters barely visible above the background signal.

The clusters were counted, and then each had a Gaussian function fitted to the profile in order to estimate the size of the clusters (e.g., Figure 4.26). The methods described in section-3.8 and Appendix C was then used to estimate the composition of the clusters. Table 4.2: Measurement of density, size and composition of the chromium clusters. The size is twice the standard deviation of the fitted Gaussian function, which contains 63% of the chromium signal. The mean composition is the mean at% of chromium contained within the size defined, and the peak is the amplitude of the

fitted Gaussian function. contains measurements of the density, size and composition of the clusters. A size distribution is not shown since only 23 clusters were measured.

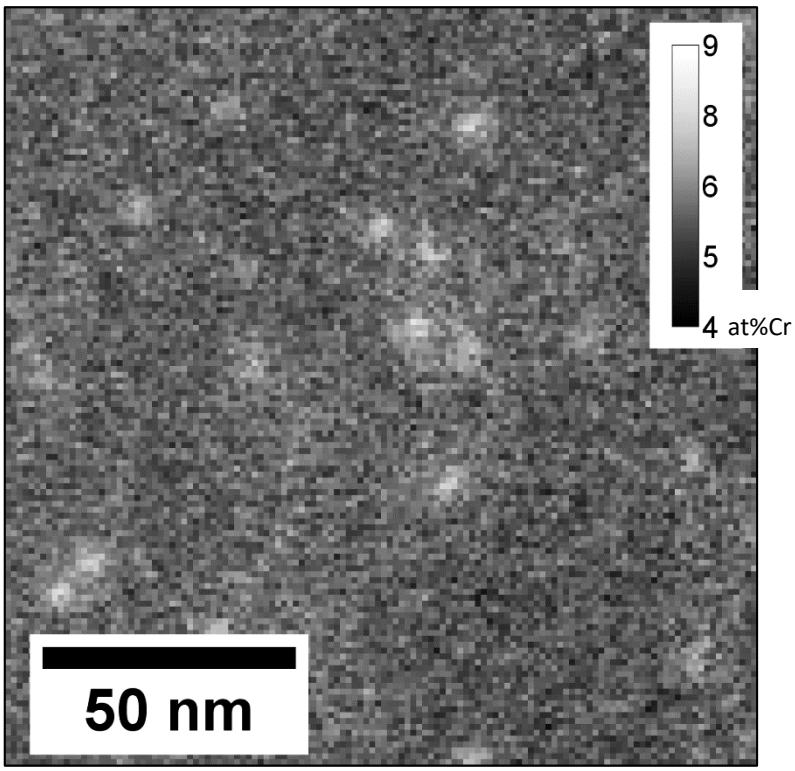

Figure 4.25: Chromium map, showing small clusters distributed throughout the foil

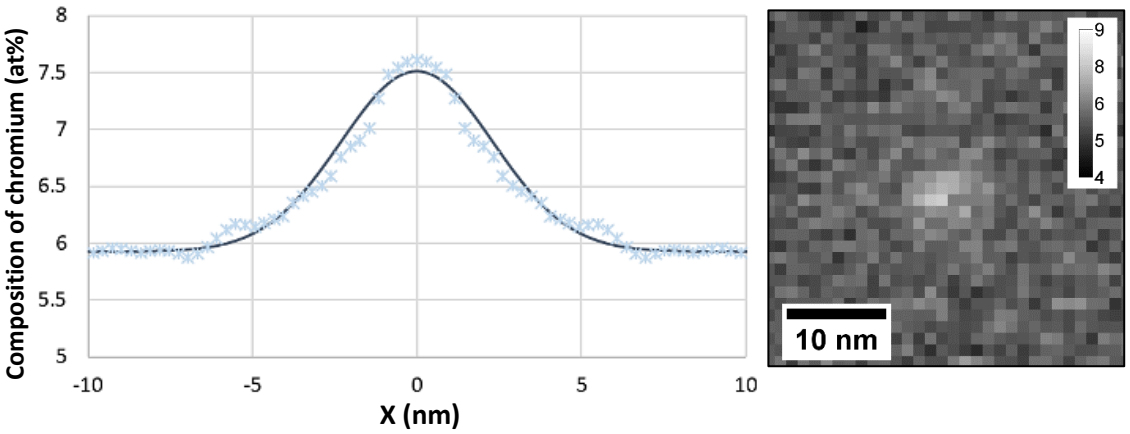

Figure 4.26: Radial line profile through a typical chromium cluster, and the Gaussian function fitted to the profile. The composition indicated includes matrix contributions above and below the cluster.

	Measurement
Number density (clusters cm^{-3})	$4.5 \pm 0.9 \times 10^{16}$
Mean diameter (nm)	4.5 ± 0.9
Maximum diameter (nm)	7.1 nm
Mean composition (at %)	9.6 ± 1.4
Peak composition (at%)	11.1 ± 1.8
Matrix composition (at%)	5.9 ± 0.3

Table 4.2: Measurement of density, size and composition of the chromium clusters. The size is twice the standard deviation of the fitted Gaussian function, which contains 63% of the chromium signal. The mean composition is the mean at% of chromium contained within the size defined, and the peak is the amplitude of the fitted Gaussian function.

The chromium clusters are too low in composition to be designated as α'-prime phases [97,101,104–106,187]. Furthermore, since the composition of the alloy is 2-3at% below the solubility of chromium in iron (~9at% at 300°C [101,187]), this indicates that the clusters are not simply early stage α'-precipitates, and are forming due to some mechanism other than phase separation. Given the density and size of the clusters, it is more likely that the clusters of chromium are where chromium has segregated around dislocation loops [97].

4.5 Microstructure of neutron irradiated Fe9Cr

Figure 4.27 shows a kinematical bright field micrograph of the neutron-irradiated Fe9Cr. The damage structure in the small grain comprises a highly heterogeneous distribution of small (<1nm up to ~20nm) dislocation loops which are clustered around dislocations and low-angle grain boundaries.

The micrographs in Figure 4.28 and Figure 4.29 show the regions labelled A-F in Figure 4.27 at higher magnification. These micrographs show there is no clustering of loops near high-angle grain boundaries, implying either that loop loss at grain boundaries is very efficient, or that the defects have preferentially diffused towards other sinks in the material. There is considerable clustering around the low-angle sub-grain boundaries and dislocations.

Figure 4.30a is a weak beam micrograph of a loop cluster taken near a $[1\bar{1}0]$ pole and shows that loops here are found almost entirely within a zigzag-shaped dislocation. Figure 4.30b shows this same dislocation from a [100] pole, which shows that the dislocation is helical. Helical dislocations can form from screw dislocations that undergo radial climb as they absorb interstitial or vacancy defects [32,78]. Therefore, it is likely that these helical dislocations were created during irradiation. Most dislocation loops appear to be elliptical in projection, implying they are most likely circular in shape, though at least one loop can be seen to have a more complex geometry (e.g. Figure 4.31). This implies that some large loops were able to coalesce. There is a sharp decline in loop density beyond the confines of these helical dislocations (Figure 4.32).

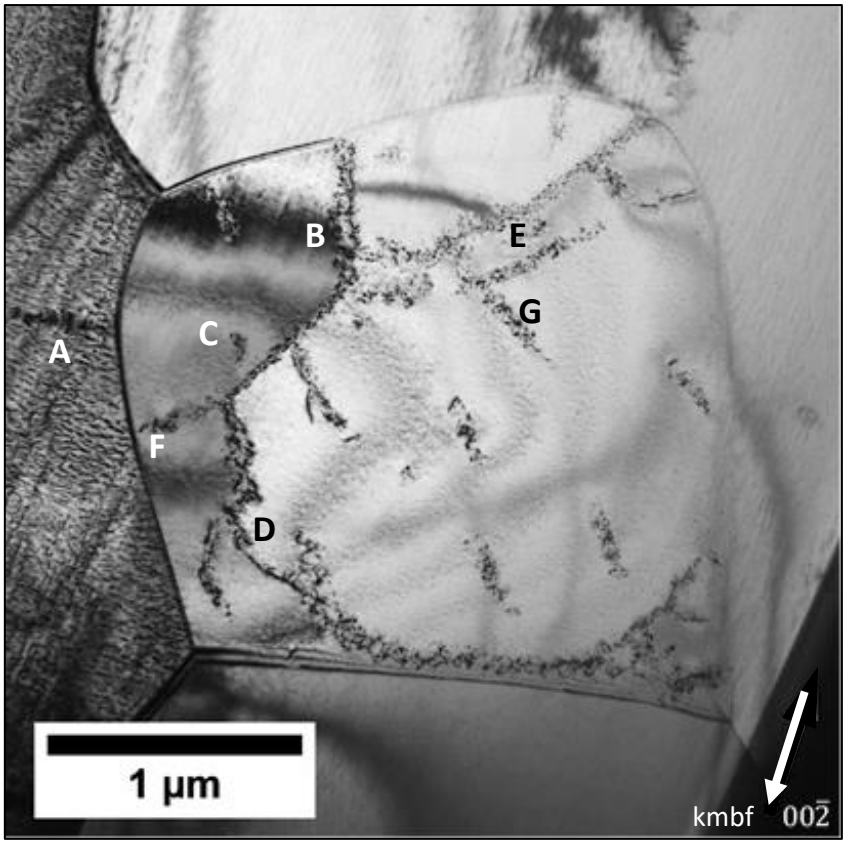

Figure 4.27: Low magnification kinematical bright field micrograph of the neutron irradiation damage in the Fe9Cr

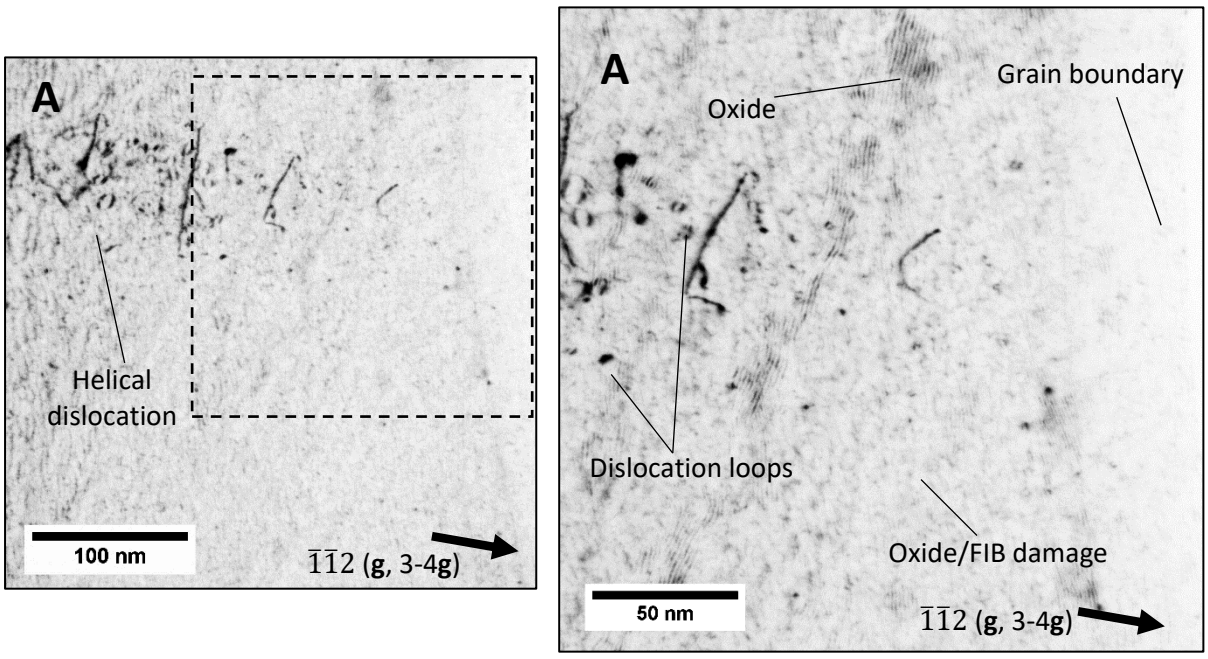

Figure 4.28: Dislocation loops confined to a helical dislocation close to a grain boundary in neutron irradiated Fe9Cr. Captured from region A in Figure 4.27

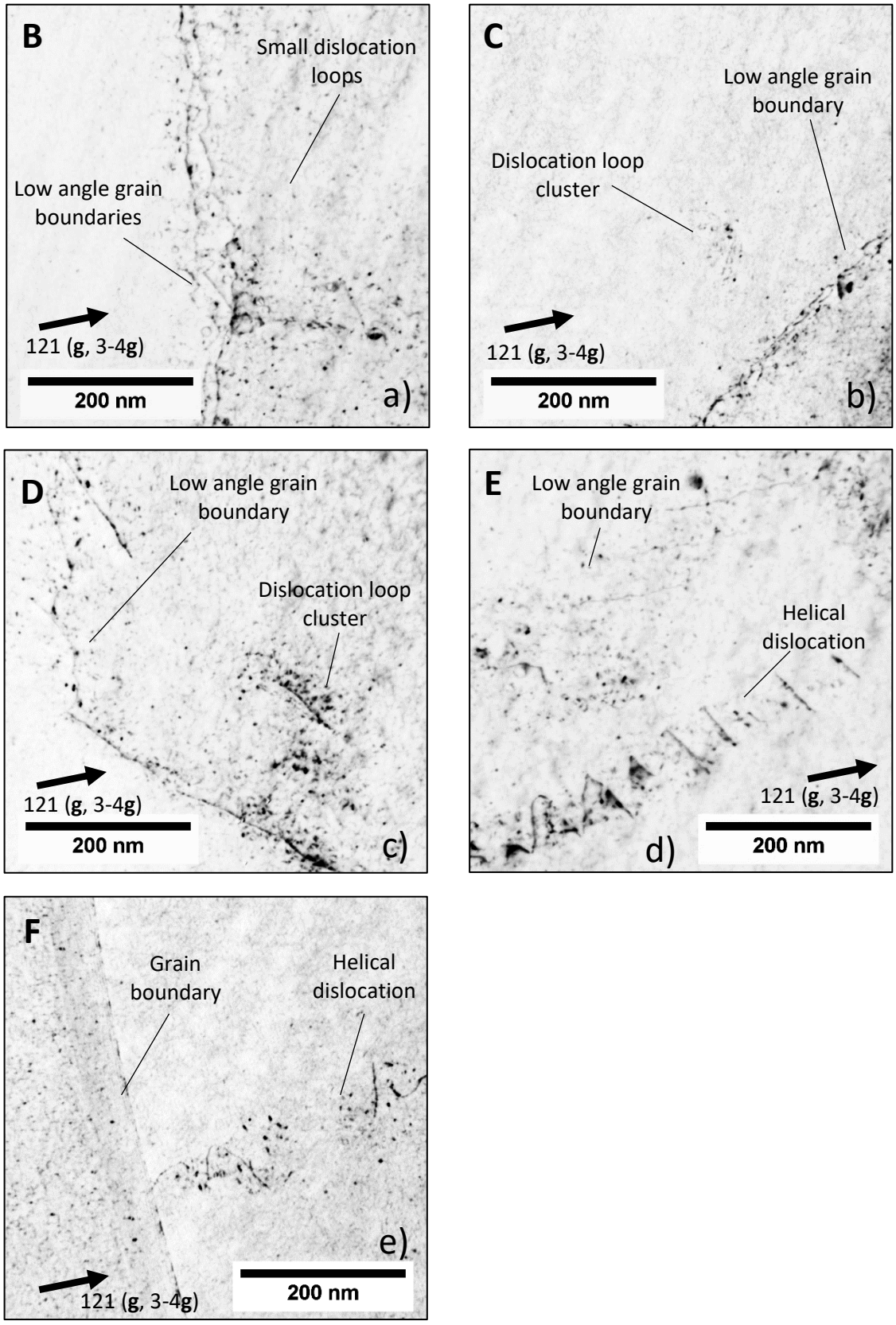

Figure 4.29: Typical micrographs of the microstructure of neutron irradiated Fe9Cr. Micrographs a), b) and c) all contain a low angle grain boundary and show the loop clustering at the boundary and dislocations; micrographs d) and e) contain helical dislocations with dislocation loops confined to the edges of the helix.

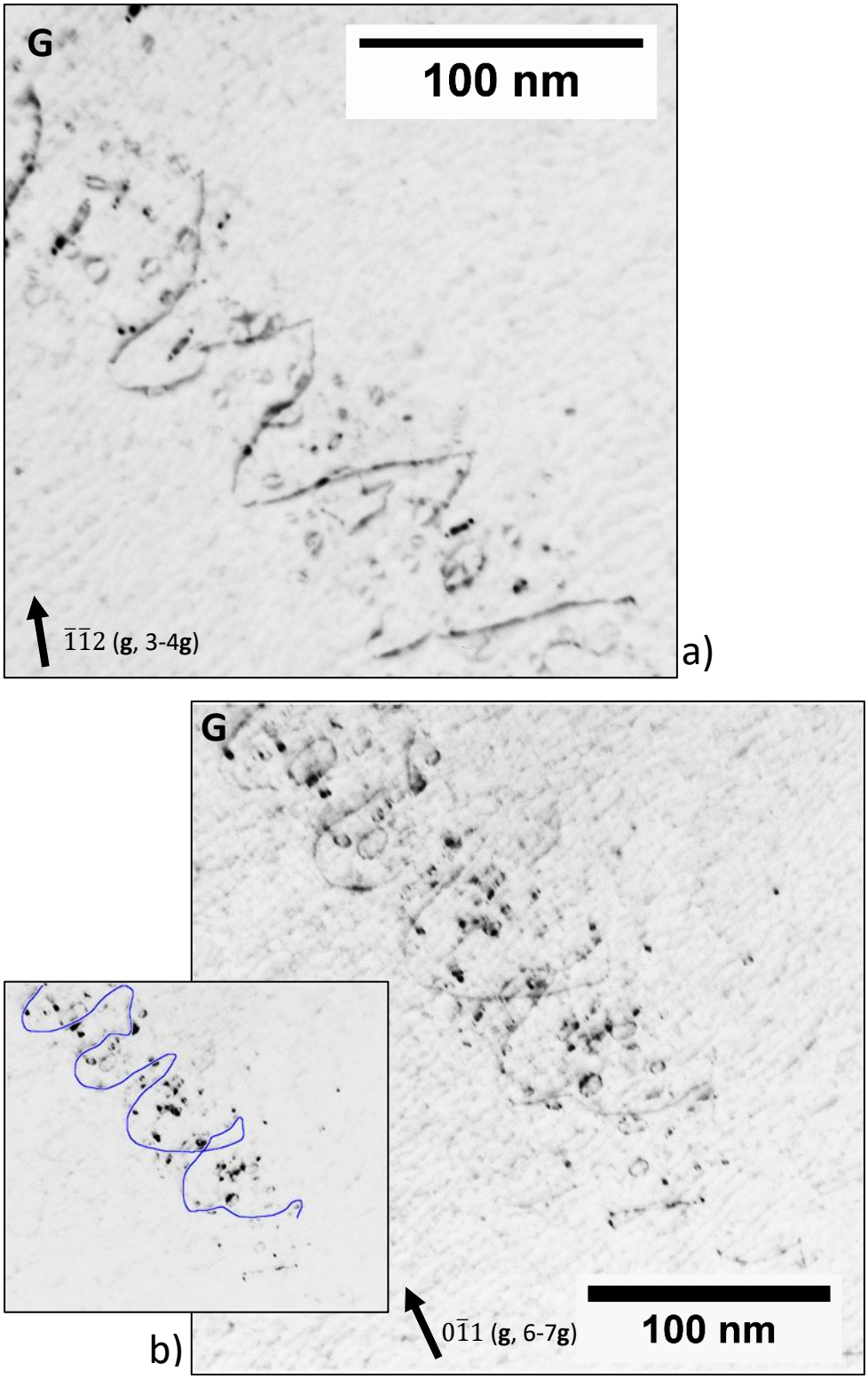

Figure 4.30: Micrographs of neutron irradiated Fe9Cr in region G of Figure 4.27. Micrograph a) shows a helical dislocation from the edge on orientation (close to the $[1\bar{1}0]$ *zone axis), and micrograph b) shows the same dislocation close to a [100] zone axis.*

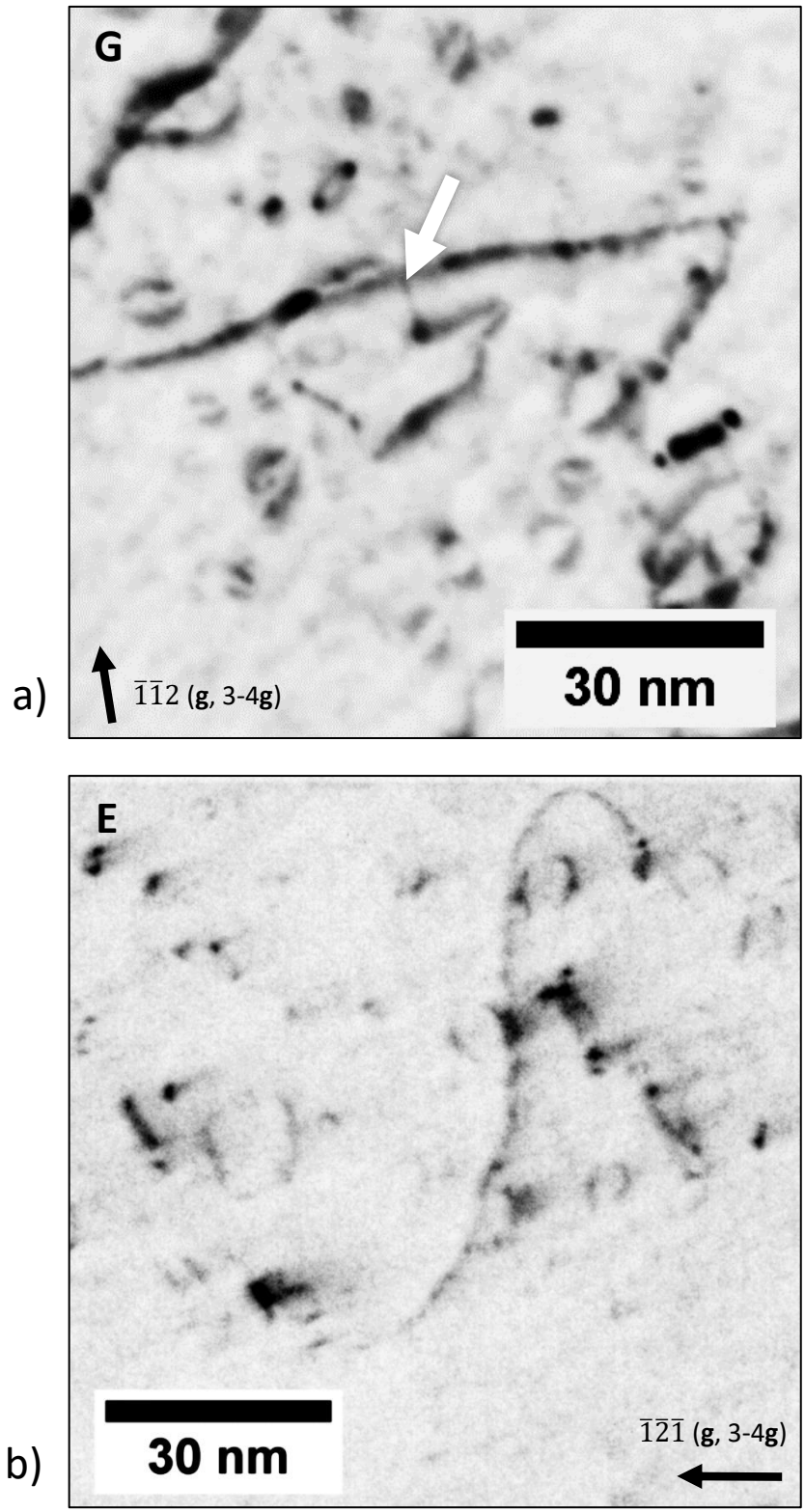

Figure 4.31: High magnification micrographs in neutron irradiated Fe9Cr from regions G and E of Figure 4.27. The helical dislocation has a dense population of dislocation loops within the cylinder encasing the helix. Most loops appear circular, but one exception stands out in micrograph a) which looks like two loops have merged together, indicated by an arrow.

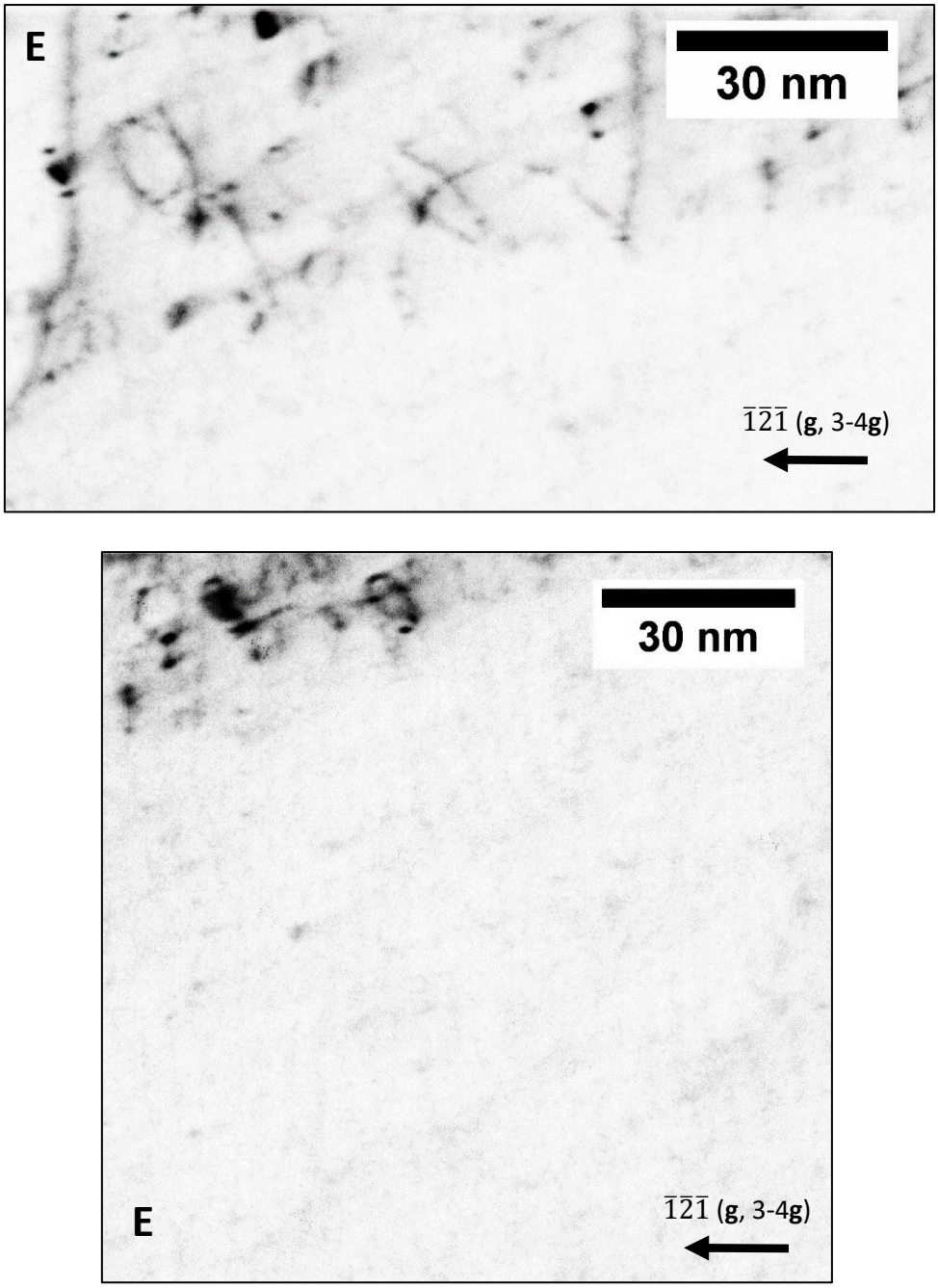

Figure 4.32: Micrographs of the interface between loop cluster and the matrix of neutron irradiated Fe9Cr. The loop density falls very quickly beyond the confines of the helical dislocation.

4.5.1 Burgers vectors and number density of irradiation-induced dislocation loops in the neutron irradiated Fe9Cr

Loop counts were taken from region G in Figure 4.27. Due to time constraints, the dislocation loops at the low-angle grain boundaries were not analysed in detail, and instead the analysis concentrated on dislocation loops bound by the helical dislocation line.

From comparing micrographs with **g**=±011 and g=±$01\bar{1}$ at region G (Figure 4.33), no dislocation loops could be correlated between the two conditions. Dislocation loops with Burgers vector <100> should be present in both conditions (see **g.b** table in Figure 4.13). This suggests that loops with Burgers vector of <111> are present, but there are no loops with a Burgers vector of <100>. This is also evident from the absence of any loops with an edge-on projection close to the [100] pole, nor loops aligned with **g**=002 or 020.

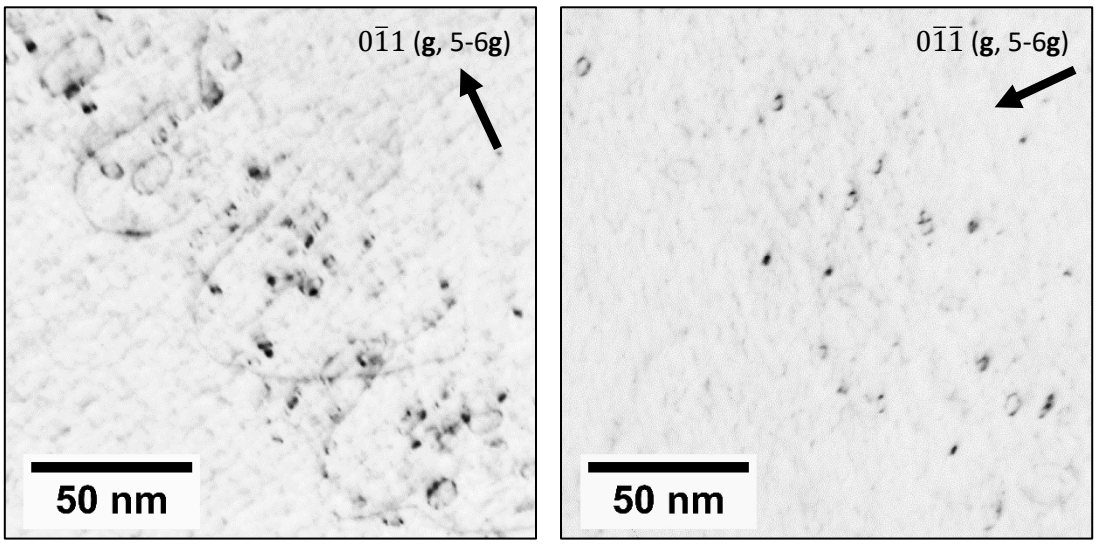

Figure 4.33: Burgers vector analysis showing the absence of <100> loops from the microstructure of neutron irradiated Fe9Cr. The <100> loops would be seen in both $0\bar{1}1$ *and* $0\bar{1}\bar{1}$ *conditions, but none can be identified.*

Figure 4.34 shows a helical dislocation viewed with the Burgers vector close to 90° to the electron beam. Both images are the same, but are shown with different brightness and contrast settings. The higher contrast images shows a significant oxide layer is present, and black dot damage. The radiation damage due to the neutrons is indistinguishable from the FIB damage and oxide outside the helical dislocation, therefore dislocation loops in these regions were not counted. This does not mean no damage exists outside the helix, merely that no damage is distinguishable from FIB damage or oxide.

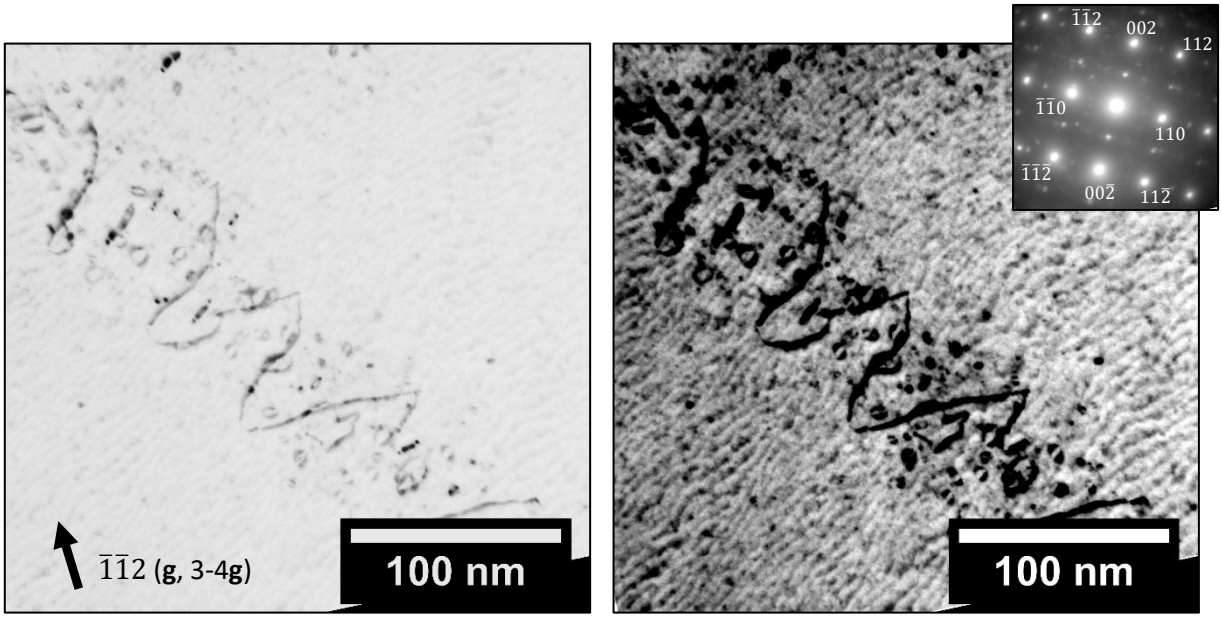

Figure 4.34: A region of neutron irradiated Fe9Cr in the same imaging condition, but shown with two different contrast settings. A large population of small black dots are visible in addition to a strong signal from surface oxide. The black dots could be neutron damage, FIB damage or oxide. A diffraction pattern of the nearby $[1\bar{1}0]$ *zone axis is also shown, in which reflections associated with oxide are visible.*

Extensive imaging of this particular helical dislocation allowed dislocation loops to be counted in conditions g=±$01\bar{1}$, ±011, ±112, ±121, ±$11\bar{2}$ and ±$12\bar{1}$. The total count from the ±011 and ±$01\bar{1}$ is equal to the overall loop population across that volume. The total count from the ±112, ±121, ±$11\bar{2}$ and ±$12\bar{1}$ conditions is equal to 3-times the total loop population across the same volume. Only loops >2nm are included in the overall loop population due to the ambiguity of counting <2nm loops. Figure 4.35 shows the total loop volume number density in each condition, and total loop density according to statistical analysis over all conditions (described in section-3.6.4).

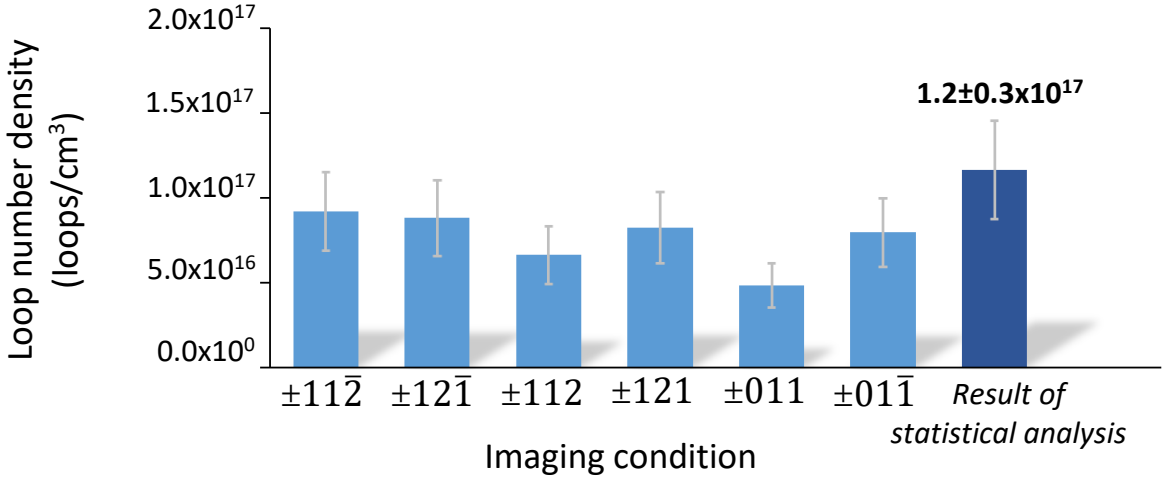

Figure 4.35: Dislocation loop number density in neutron irradiated Fe9Cr for each condition and the result of the statistical analysis from the counts in each condition.

Since the dislocation loops measured all appear to be contained within the helix, the volume was taken as the cylindrical volume contained by 4 turns of the helix, which is easily measured from Figure 4.30a. The length of four turns was measured as 273±3nm, taken as the average of four measurements of the length from different positions on the micrograph. The diameter was measured as 72±5nm, taken as the average of twelve measurements of the diameter from different positions. The volume is then calculated as 1.1±0.1 x10^{-15} cm^3. The error in the loop volume number density is the error propagated from the $\sqrt{N}$ error in the counts.

The loop density outside the helix was not measured in detail due to the very low density of visible dislocation loops. As a rough estimate, an area close to but outside the helix contained only 3 black-dot features that might be dislocation loops larger than 2nm. The area was 680x320nm and was captured in a **g**=$\bar{1}\bar{2}1$ (**g**, 3-4**g**) condition, which makes the loop density in this region an approximate value of 2±1 x10^{14} loops/cm^3 – 1000 times less than the density within the helix. It was not possible to measure with any confidence the densities of dislocation loops smaller than 2nm in diameter.

The statistical analysis method [172] was also used to extract the population of different <111> types. These should be roughly equal if their occurrence is equally likely. Figure 4.36 shows the proportion of each <111> variant. This shows that there are 1.7 times as many $\pm 11\bar{1}$ dislocation loops as the other <111> variants. Since the Burgers vector of the helical dislocation is also $\pm 11\bar{1}$, it is likely that the elastic field of the helical dislocation is affecting the preferred orientation of local dislocation loops.

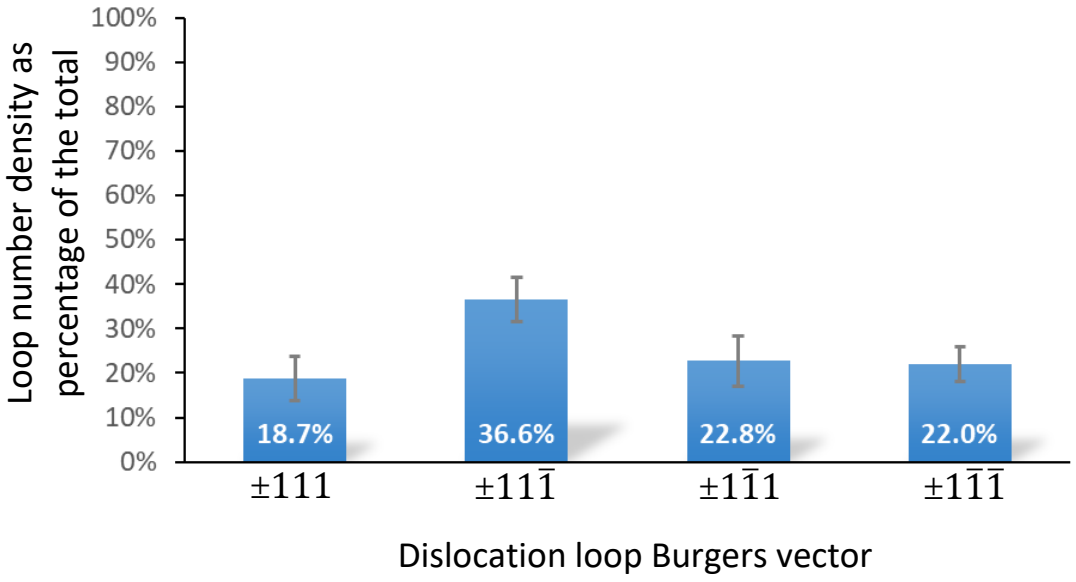

Figure 4.36: The fraction of each <111> Burgers vector variant present in the helical dislocation in the neutron irradiated Fe9Cr microstructure.

4.5.2 Nature analysis of loops in neutron irradiated Fe9Cr

The loop nature was determined using the inside-outside contrast method [48]. The inclination was measured by tilting and/or the likely habit plane based on the Burgers vector. Despite the large number of loops visible in the images, only a handful could reliably correlated through enough micrographs to determine their Burgers vector and/or sense of inclination. This is mainly due to the loop density being very high within the helix, meaning it is easy to confuse one loop with another. In total, 11 loops had their nature determined. The largest was ~25nm and the smallest ~4nm.

All loops were found to be interstitial.

Based on this result, this section continues under the assumption that all loops are interstitial type. Since this analysis is only reliable for loops larger than ~5nm, and large loops are more likely to be interstitial, the analysis is biased towards interstitial types. It is possible that some small vacancy loops are present.

Figure 4.37 shows the inside-outside contrast for a selection of the loops measured. The first two examples are large loops that share their Burgers vector with the helical dislocation. The habit plane of these loops is closer to $(55\bar{4})$ than the prismatic $(11\bar{1})$ plane, and the projection appears to be aligned parallel to the axis of the helical dislocation. The last example in Figure 4.37 depicts a group of smaller loops with the same Burgers vector of [111]. The habit plane of these loops appears to be close to the (110) plane – the same plane on which they are expected to have nucleated [39,62].

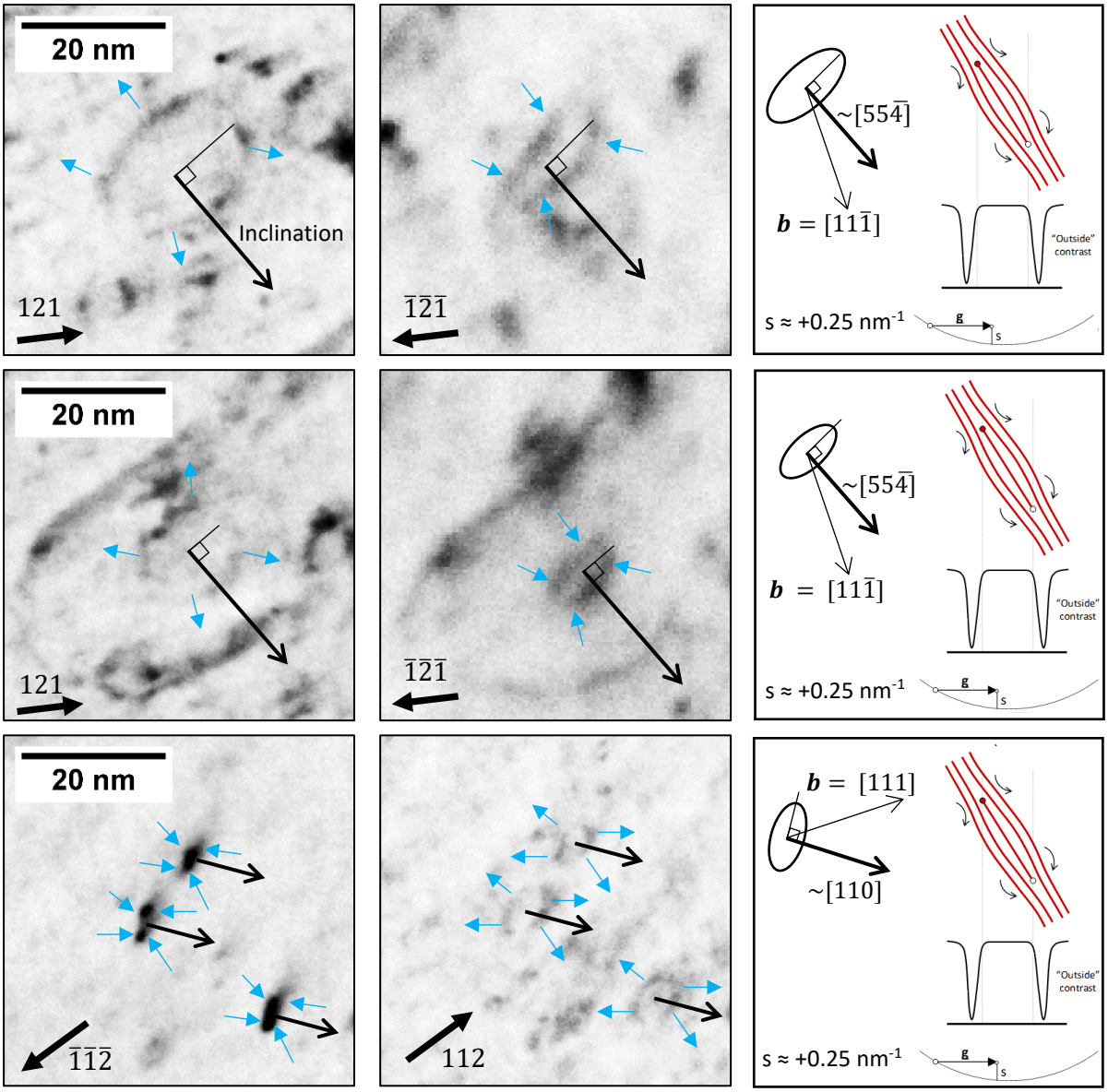

*Figure 4.37: Nature analysis of a selection of dislocation loops in the neutron irradiated Fe9Cr. The Burgers vectors were determined by correlating the same feature through a full **g.b** series and by tilting to observe the inclination. All loops were found to be interstitial.*

4.5.3 Size distributions of loops in the neutron irradiated Fe9Cr

Dislocation loops were counted and sized in five different g-vector conditions with the deviation parameter ~0.2 nm^{-1} on average in each condition. For every **g**-vector condition, the negative **g**-vector was also captured. All micrographs were aligned with a common feature to aid correlating dislocation loops through multiple conditions. Features were designated as being a dislocation loop according to the criteria described in section-2.6.4.

The loop size distribution for each ±**g** pair of micrographs of loops is shown in Appendix D, and corresponds to those measured in a volume of four helical turns. In each condition, ~80-100 loops were counted and the size was taken as the approximate average diameter of the feature in both +**g** and –**g**, and/or another **g**-vector entirely. The mean diameter and standard deviation of dislocation loops larger than 2nm is also shown in Appendix D for each condition.

Figure 4.38 shows the overall loop size distribution of all counted loops. The total count from all micrographs is 503, and is equal to 4 times the total loop population within the measured volume. It was assumed that the size distribution for all measurements is a good approximation for the size distribution of all the loops, though it is worth noting that the distribution shown is constructed from multiple measurements of the same population of loops.

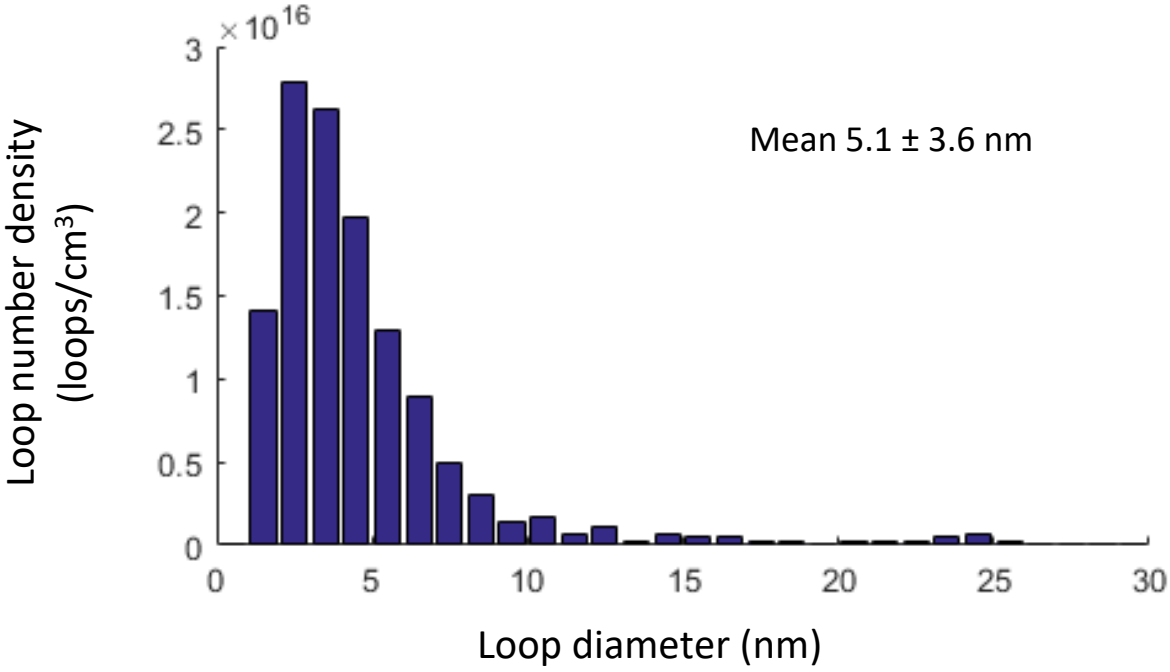

Figure 4.38: Dislocation loop size distribution for all measured loops, and normalised to the loop volume density. Also shown is the mean loop size for loops >2nm in diameter.

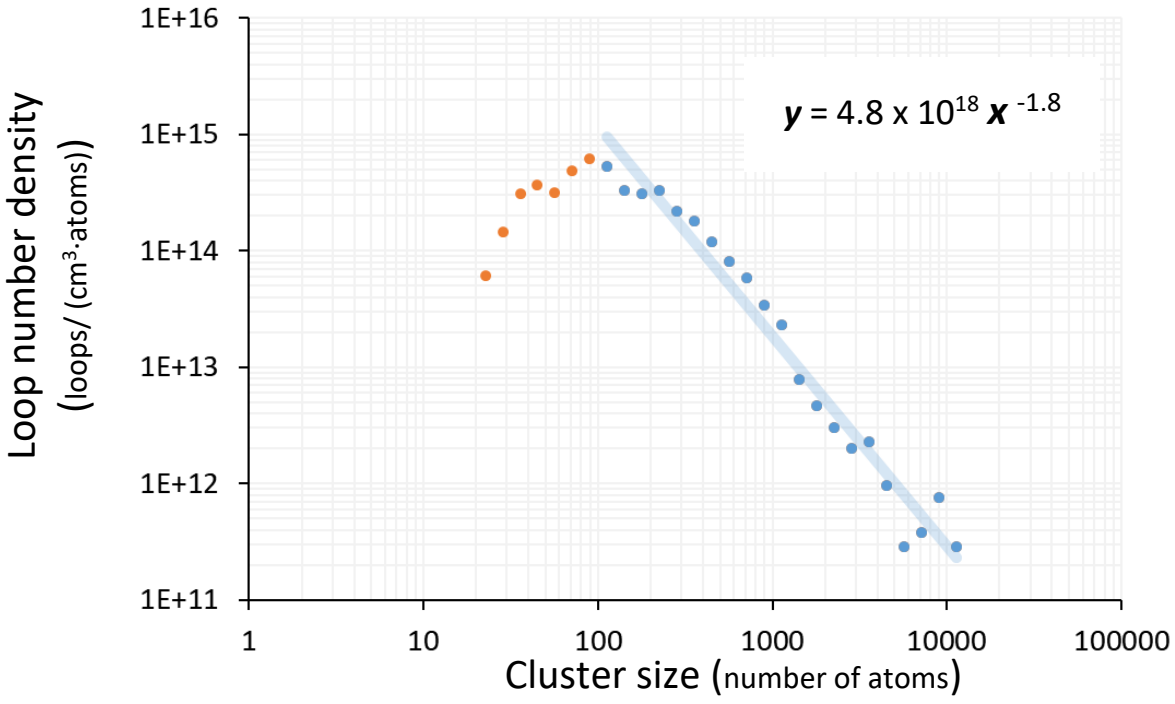

Figure 4.39: Dislocation loop size distribution by atomic volume. The blue points indicate those used to fit the power-law.

The atomic volume of every counted loop was calculated from Equation 4.1. The same method described in section-4.4.3 was then used to produce Figure 4.39. The fitted power-law indicates that dislocation loops larger than 2nm account for only 4% of the cluster population (including isolated point defects), but 83% of all interstitial point defects present, whether in clusters or as isolated point defects. The final defect count is shown in Figure 4.40, which contains error bars calculated by the method described in Appendix E.

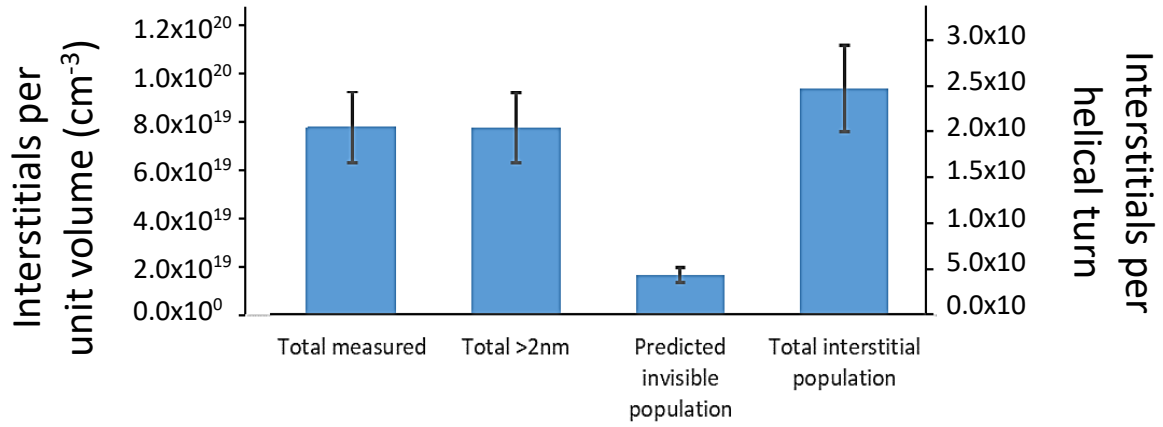

Figure 4.40: Interstitial population estimated within the helical dislocation inside the microstructure of neutron irradiated Fe9Cr

Like the neutron-irradiated Fe6Cr (section-4.4.3), Figure 4.40 suggests that the majority of the interstitial point defects are in the visible (large) dislocation loops. The estimation of the invisible defect population is heavily reliant on the assumption that the power-law fitted to the clusters larger than 2nm in diameter also applies to those less than 2nm in diameter. It is quite possible that the real size distribution deviates significantly from this power-law.

4.5.4 Helical dislocations in neutron irradiated Fe9Cr

Figure 4.41 shows via the invisibility criterion that the Burgers vector of this particular helical dislocation is $\pm[11\bar{1}]$. The inclination this corresponds to is also shown in Figure 4.41, and shows the helix has a left-handed morphology [188]. The helical dislocation is projected in the same direction as the dislocation loops that share a Burgers vector, which is close to the $[55\bar{4}]$ direction.

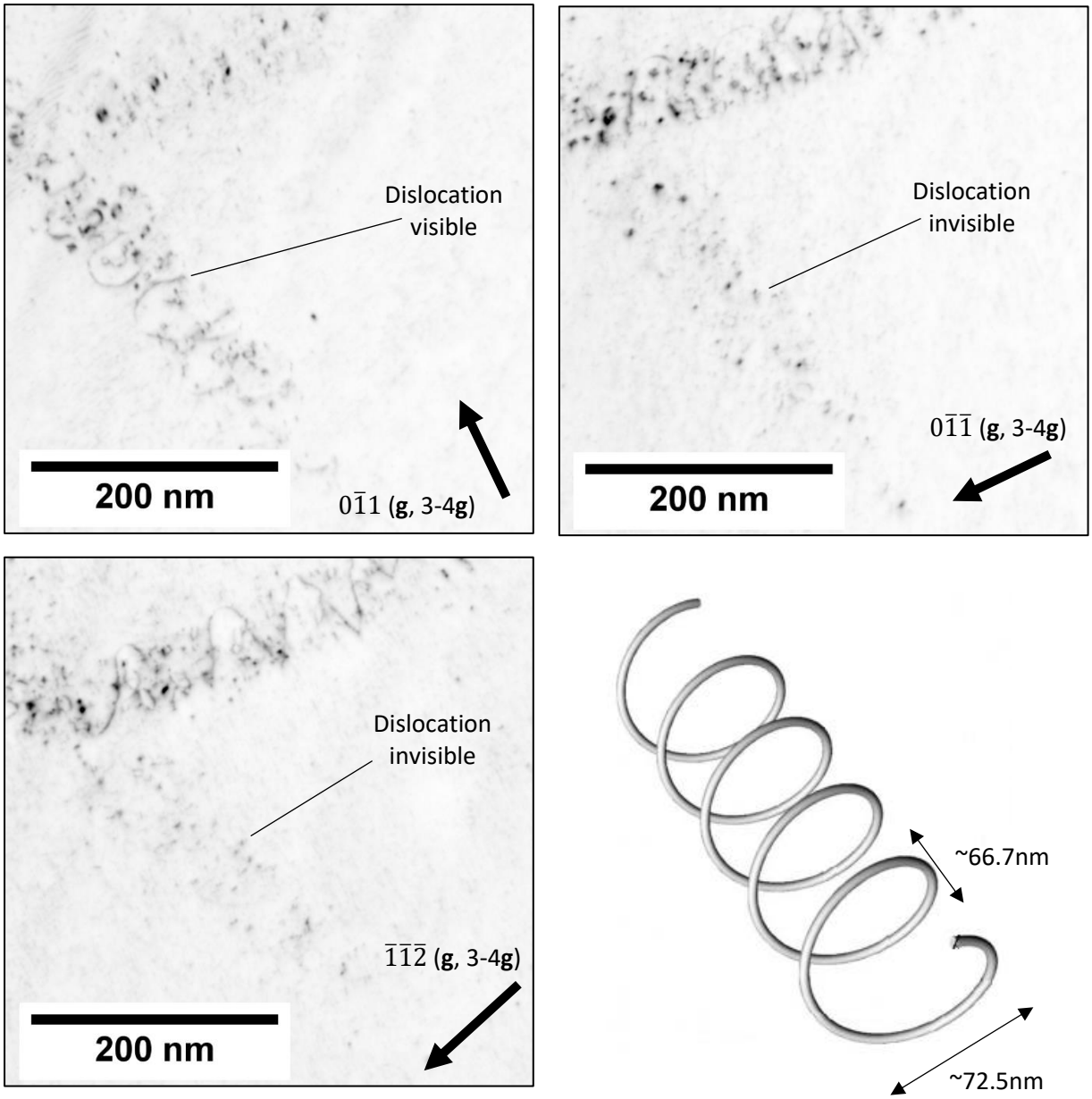

Figure 4.41: Burgers vector analysis of the helical dislocation. The dislocation is invisible when ***g*** *=* $0\bar{1}\bar{1}$ *and* $\bar{1}\bar{1}\bar{2}$*, which from the* ***g.b****=0 criterion, indicates the dislocation has a Burgers vector of* $\pm 11\bar{1}$*.*

Since the helical dislocation is fairly uniform and clear in the micrographs, it is possible to perform inside-outside contrast analysis on the dislocation [189]. From this, it is possible to determine whether the radial climb mechanism that produced the helical-shape was vacancy or interstitial. Figure 4.42a and Figure 4.42b show micrographs with **g=**$\pm 01\bar{1}$, and a segment of the helical dislocation is highlighted in each. The inside and outside conditions are also indicated.

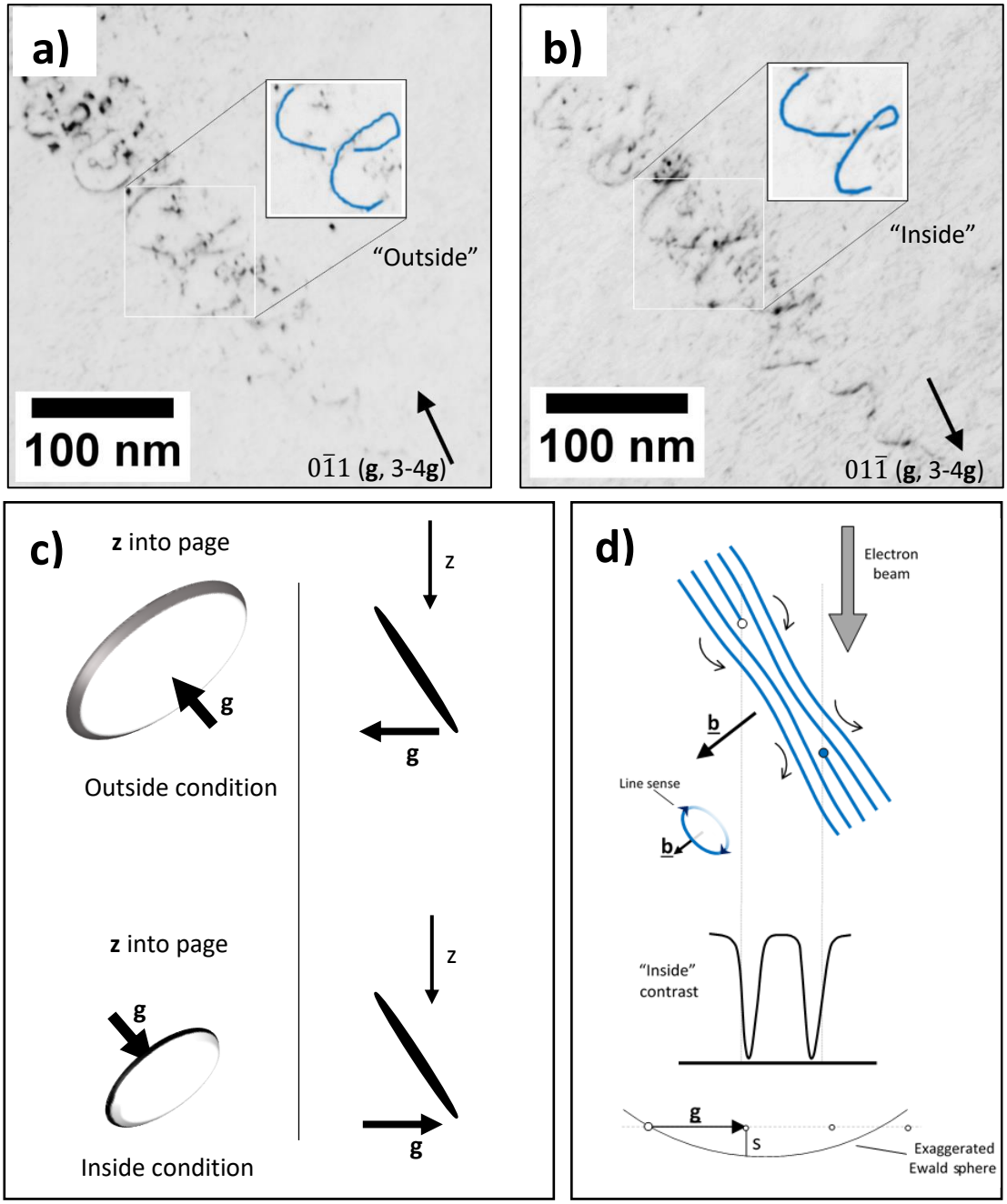

Figure 4.42: a) and b) show the inside-outside contrast of the helical dislocation. c) is a schematic diagram of the inside-outside contrast for an analogous prismatic dislocation loop, and d) is a diagram depicting the "inside" condition for such a loop, drawn based on similar diagrams in [71,162,179]. *This analysis shows the turns of the helical dislocation are akin to a vacancy dislocation loop, so the climb-mechanism that produced the helical dislocation must have been caused by a vacancy flux, not interstitial.*

Figure 4.42c depicts the contrast schematically for an analogous prismatic loop, and by comparing this to Figure 4.42d (as discussed in section-3.6.4), it can be concluded that the helical dislocation must have been produced by vacancy-mediated climb. Since the helical shape was produced by vacancy absorption, and it is a left-handed helix, the initial screw dislocation must also have been left-handed[8] [78,188].

Inside-outside contrast will reverse if the inclination of a loop changes with respect to the direction of **g**. This is the reason for imaging in safe orientations if the inclination is not known [48]. The helical dislocation lies on planes that are not fixed along the length of the dislocation, so the inclination of the "analogous prismatic loop" with respect to **g** changes along the helix. To rule out the possibility of this confusing the final result, the analysis was repeated for a different helical dislocation with a much steeper inclination, as shown in Figure 4.43. As seen from $[31\bar{1}]$, this $\pm 11\bar{1}$ helical dislocation is highly inclined to the electron beam, and the inclination remains the same with respect to the direction of **g** for all of the helix. From this, it can be concluded that this helix formed by absorption of vacancies, in agreement with the analysis in Figure 4.42.

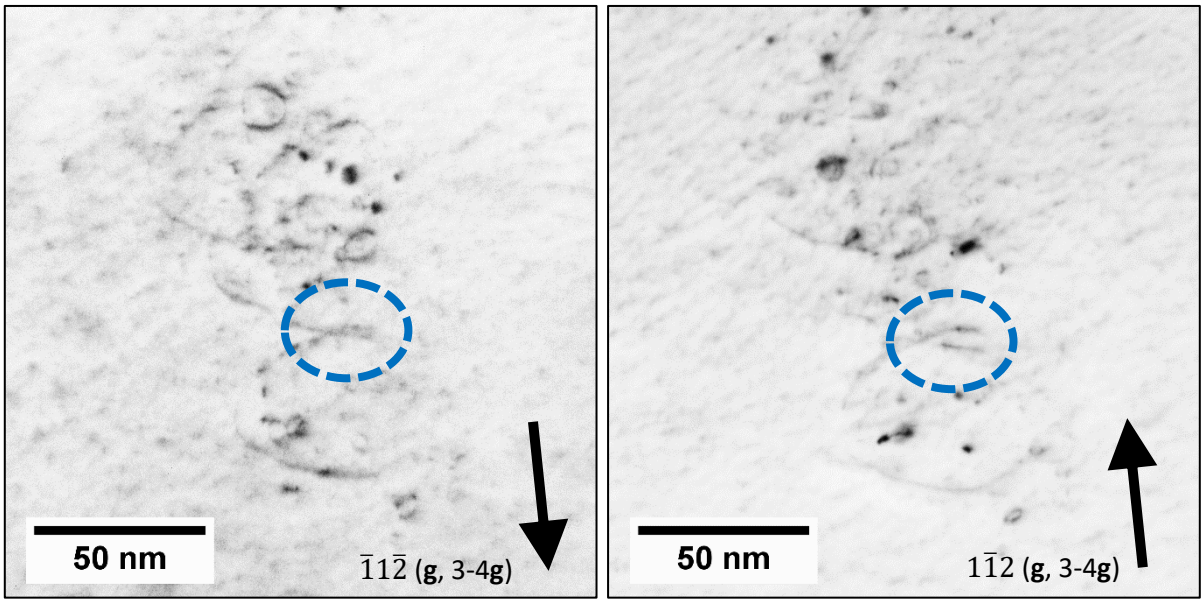

Figure 4.43: Inside-outside contrast of a steeply inclined helical dislocation

[8] Interstitial absorption would produce a helix with the opposite handed-ness of the initial screw dislocation [188].

The results of this analysis show that the dislocations are acting as vacancy-biased sinks, rather than interstitial-biased as has been assumed by previous studies of neutron-irradiated Fe [74] and self-ion irradiated Fe and FeCr [80,172].

The number of vacancies required to produce a helical dislocation with diameter, D, is equal to the number of vacancies contained by a prismatic loop with equal diameter, D, for every period of the helix [188]. For the helix shown in Figure 4.42, the diameter is 72±5nm, which from Equation 4.1 gives a vacancy population of 8.8±1.2 $x10^4$ vacancies per helical turn. The equivalent calculation of the interstitial population indicates that there are 2.5±0.7 $x10^4$ interstitials per helical turn. Due to slight variations in the helix diameter, a large error is assigned to the vacancy count. For the interstitial count, the error was estimated from the variation in total interstitial population as expected if the distribution obeys the fitted power-law, and this was propagated with the error from the volume measurement.

Since interstitials and vacancies were produced in equal quantities, there must exist a large population of interstitials missing from the data, implying there is a substantial population of interstitials that exist as point defects or in clusters too small to be resolved by TEM. This also suggests the fitted power law in section-4.5.3 underestimates the population of interstitials contained by clusters smaller than 2nm by ~$6x10^4$.

4.5.5 Voids in neutron irradiated Fe9Cr

The under-over focus technique was used to search for irradiation-induced voids in the material. Figure 4.44 shows two micrographs of a 50x50nm area close to a helical dislocation, at plus and minus 200nm from the in-focus condition. Also shown is the sum of one image with the inverse of the other, as was done for the Fe6Cr analysis. Very small (<2nm) void-like features are visible in the micrographs, but the contrast is very weak, which made counting very difficult and subjective.

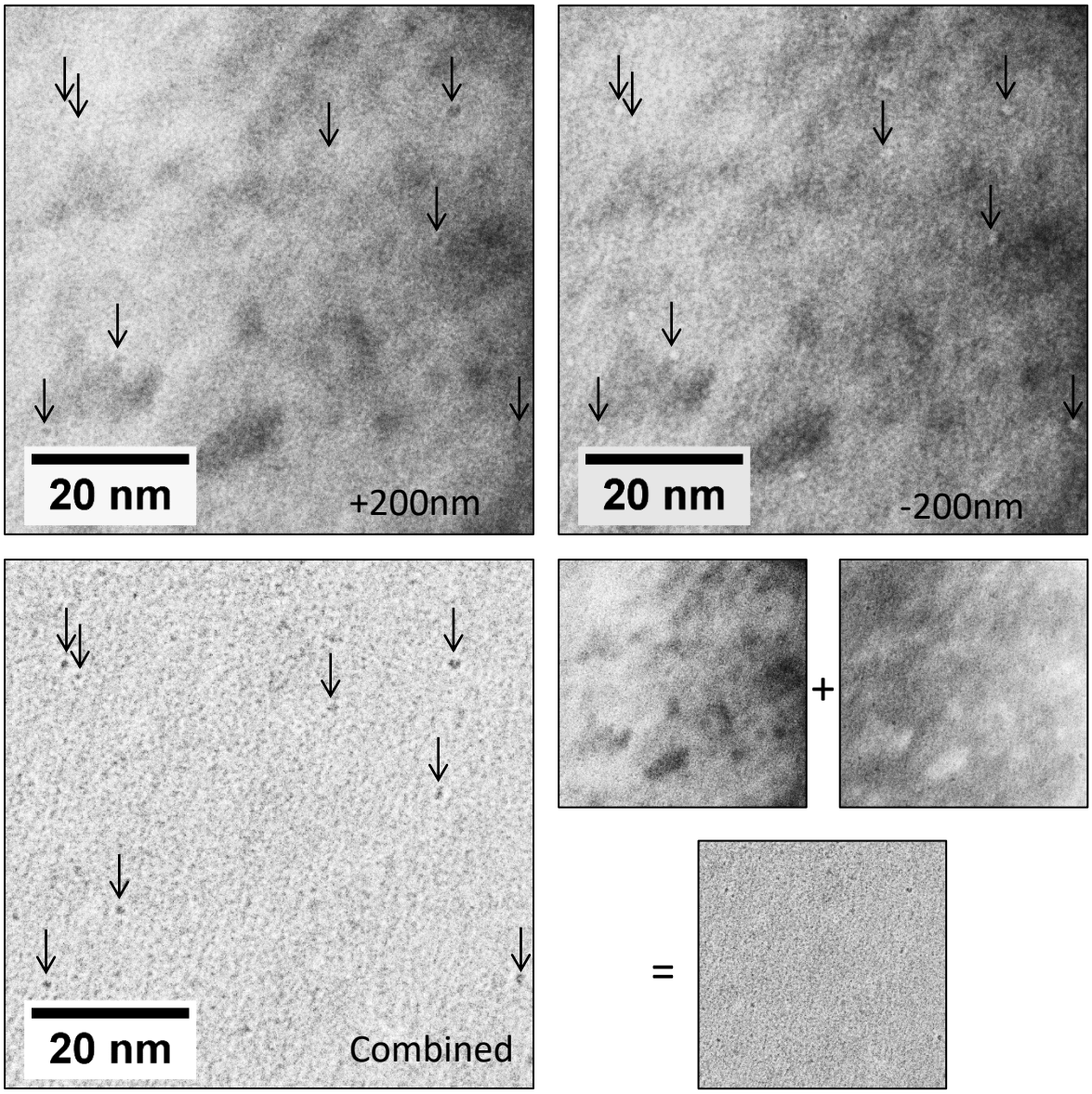

Figure 4.44: Over and under focus micrographs of small void-like features in neutron irradiated Fe9Cr. The inverse of the -200nm focus image was summed with the 200nm focus image to produce the image labelled "combined". The combined image is absent of diffraction contrast.

Figure 4.45 shows the radial line plots from two small void-like features. The micrographs seem to be densely populated by circular features, mostly ~1nm in diameter. These are probably either surface oxide, surface craters, or other surface contaminants on the foil. The features that were selected for counting are those that show definite reversal of contrast in the over and under focus conditions; however it was not possible to rule out the source of this contrast being surface oxide or craters. These micrographs were captured within 24 hours of the foil being thinned, during which time the sample was kept under vacuum storage. In spite of this effort, oxide is known to have formed on the surface during this time from the diffraction pattern (extra reflections not associated with a BCC structure) and weak-beam micrographs (see Figure 4.34 on page 130).

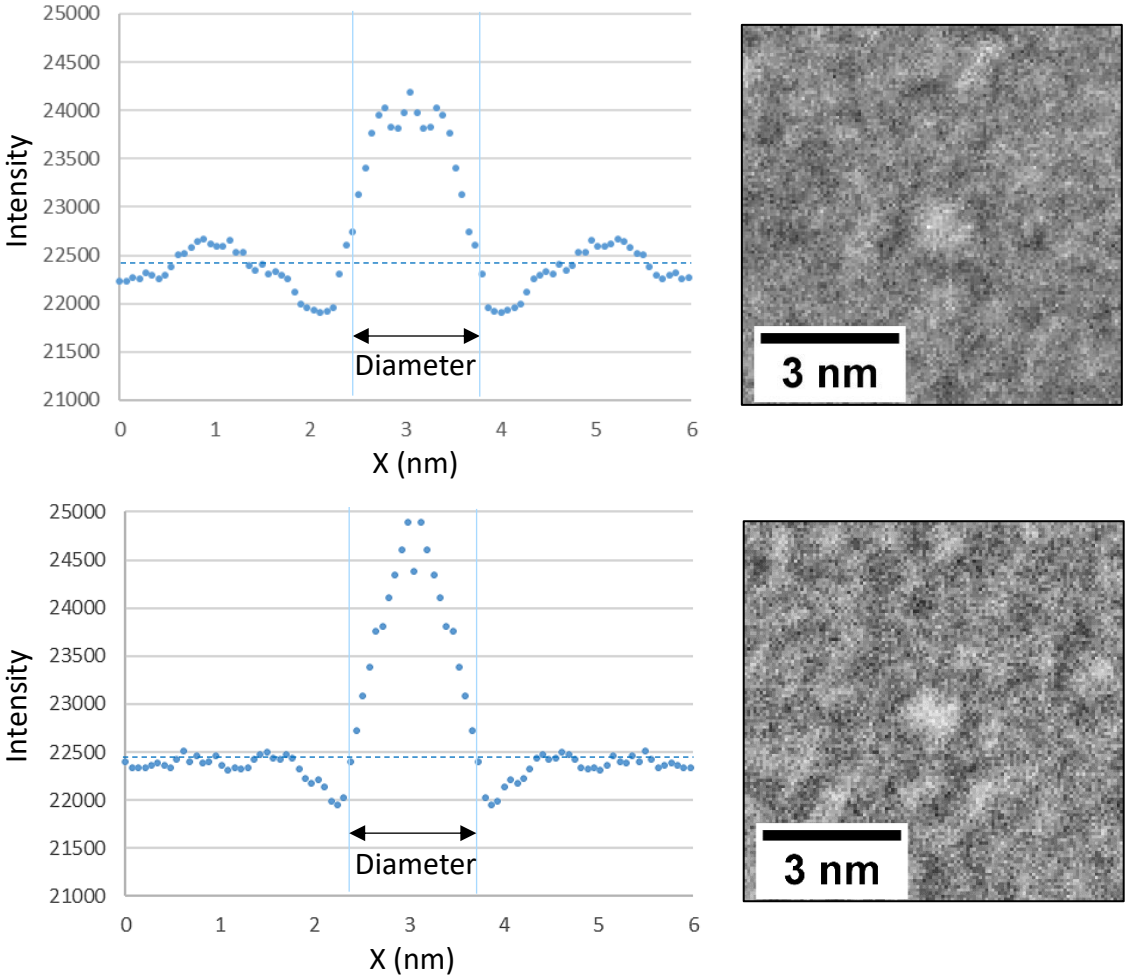

Figure 4.45: Radial line profiles of possible voids

Table 4.3 contains measurements of the number density, mean size, minimum size and maximum size of the void-like features that have been measured. Due to the small size and weak contrast, only 27 features were measured, the majority of which were <2nm. The micrographs suggest that there is probably a large population of vacancy clusters that are too small to be resolved.

	Inside helix	**Outside helix**
Number density (voids cm^{-3})	$1.7 \pm 0.6 \times 10^{16}$ >2nm: $1.9 \pm 1.9 \times 10^{15}$	$1.8 \pm 0.4 \times 10^{16}$ >2nm: 0.0
Mean diameter (nm)	1.2 ± 0.4	1.3 ± 0.3
Maximum diameter (nm)	2.2	1.6
Minimum diameter (nm)	0.8	0.8

Table 4.3: Measurements of density and sizes of the voids

4.5.6 Redistribution of chromium in neutron irradiated Fe9Cr

EELS mapping was used to investigate chromium precipitation due to the neutron irradiation. As with the Fe6Cr in section-3.4.5, a TEM lift out was thinned to ~25nm in thickness using 2kV Ga beam milling in the FIB. No FIB damage was visible in the foil. Unfortunately, I was unable to prepare a foil containing a helical dislocation in a region thin enough for the EELS analysis.

Data was acquired for the same energy range (400-912eV) as the data collected for the Fe6Cr, and processed similarly using Hyperspy [181]. As with the Fe6Cr, the Hartree-Slater model was used to fit known edges to the recorded data and extract the signal contributions from chromium and iron. Figure 4.46 and Figure 4.47 are EELS spectra for a single pixel and a whole map respectively. The former also shows the model as fitted to the edges, whilst the latter shows the model as fitted to the edges and fine structure.

The chromium composition extracted from the fine-structure model was used to calibrate the composition of the whole map, so the mean composition is a more accurate representation of the true composition. Since the first example does not include fine structure, the model fails to include all of the signal from each element, so the relative differences in chromium composition may be underestimated. The extracted chromium maps are shown in Figure 4.48.

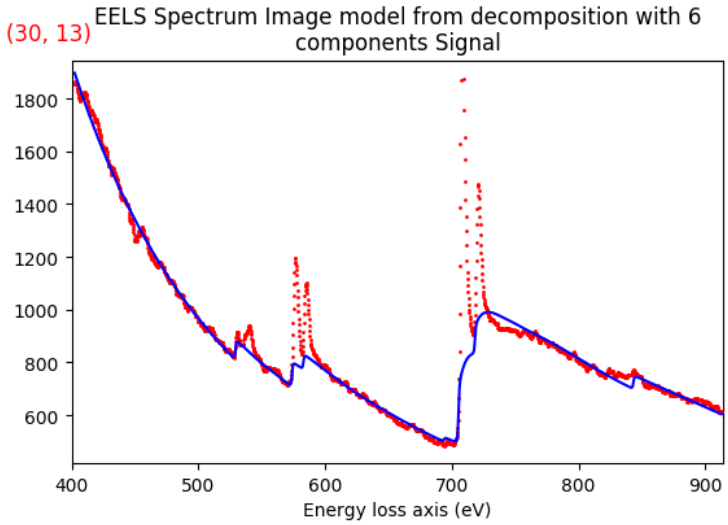

Figure 4.46: EELS spectrum from a single pixel, shown with the fitted model of the edges

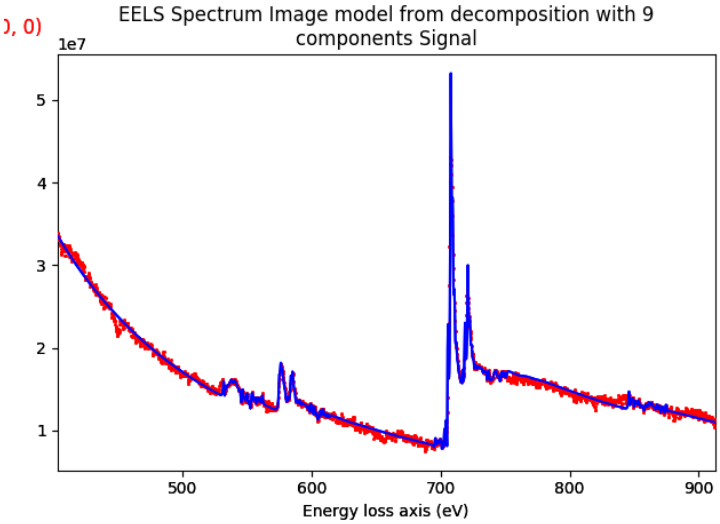

Figure 4.47: EELS spectrum from the entire map, shown with the fitted model of the edge, including fine structure

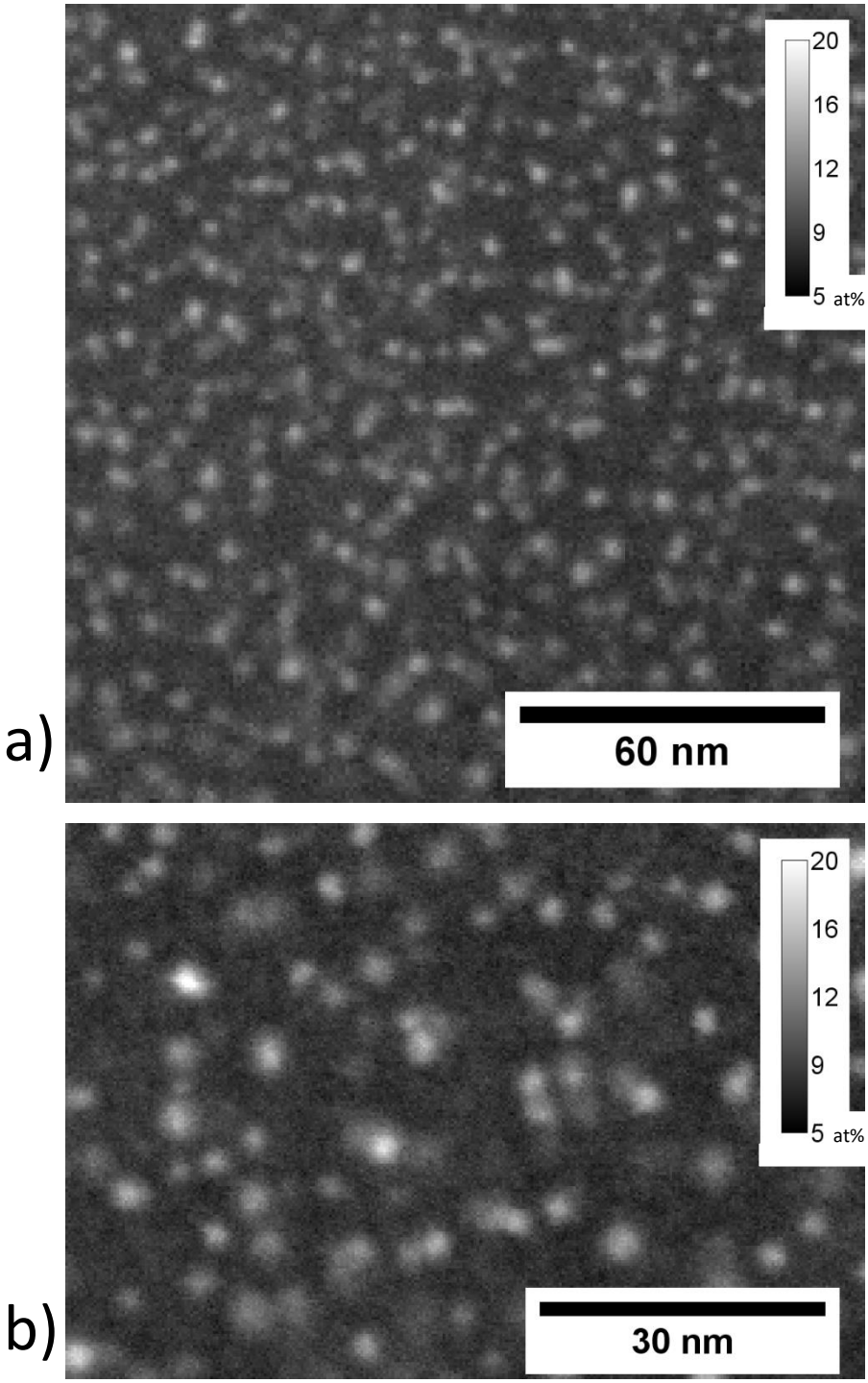

Figure 4.48: Two chromium maps of the Fe9Cr shown at two different magnifications. a) Chromium map with pixel size 0.8nm; b) chromium map with pixel size 0.3nm

Figure 4.48 clearly shows a high density of chromium precipitates is present. Data collection was limited to the thinnest regions of the foil, and it was not possible to investigate chromium clusters around clusters of dislocation loops.

Chromium clusters were counted, and each had a Gaussian fitted to the profile. This is shown for a typical cluster in Figure 4.49. The size and composition were calculated by the same method used for the Fe6Cr (described in Appendix C). In total, 67 clusters were analysed this way, and the results are summarised in Table 4.4.

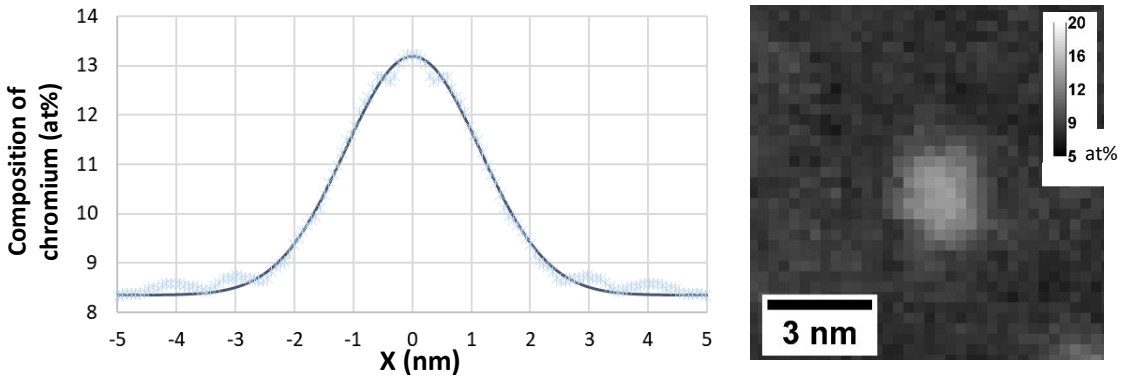

Figure 4.49: Radial line profile through a typical chromium cluster, and the Gaussian function fitted to the profile. The composition indicated includes matrix contributions above and below the cluster.

	Measurement
Number density (clusters cm^{-3})	7.4 ± 0.4 x10^{17}
Mean diameter (nm)	2.1 ± 0.4
Maximum diameter (nm)	3.0
Mean composition (at %)	40.7 ± 16.2
Peak composition (at%)	56.8 ± 21.7
Matrix composition (at%)	8.0 ± 0.6

Table 4.4: Measurement of density, size and composition of the chromium clusters. The size is twice the standard deviation of the fitted Gaussian function, which contains 63% of the chromium signal. The mean composition is the mean at% of chromium contained within the size defined, and the peak is the amplitude of the fitted Gaussian function.

The distributions of the size and compositions of the clusters are shown in Figure 4.50 and Figure 4.51 respectively. It is worth explaining why a few particles appear to have a composition of chromium >100%. In order to calculate the composition of the cluster, it was assumed that the particle is spherical. If there is any elongation of the cluster through the projection, or if there are two or more clusters on top of each other in the foil, then the composition will be overestimated. The tail end of the composition distribution reflects this, and as such may extend beyond 100at% Cr, which is clearly nonsensical. In addition, the high density of clusters means that a fraction of the clusters intercept the foil surface, and so the measured composition will be underestimated in these cases. The peak in the distribution is likely to be more representative of the average composition of the clusters.

A plot of size against mean composition of the clusters is shown in Figure 4.52. The plot indicates there is no correlation between size and composition, although such a trend could be masked due to measurements of clusters intercepting the foil surface (underestimated compositions) and clusters positioned on top of each other in the viewed projection (overestimated compositions).

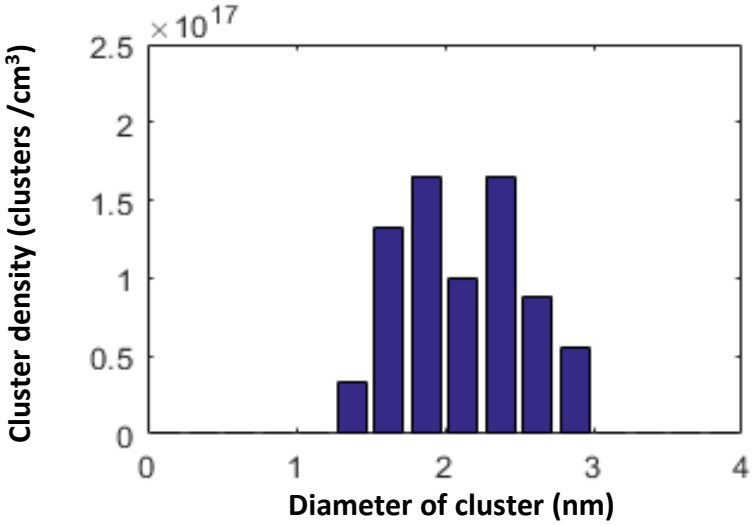

Figure 4.50: Size distribution of chromium clusters in the Fe9Cr. The diameter is taken as twice the standard deviation of the Gaussian function fitted to the intensity profile.

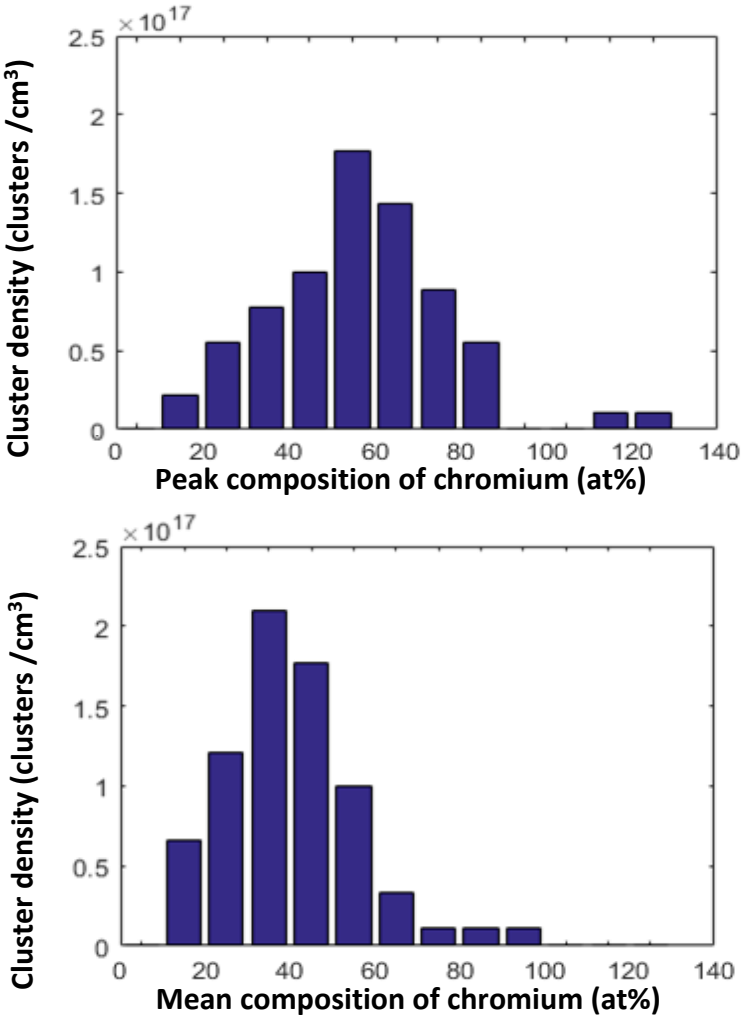

Figure 4.51: Composition distributions of chromium clusters in the Fe9Cr. The peak composition is taken as the amplitude of the Gaussian profile fitted through the foil thickness, and the mean is taken as the mean composition of a cluster within 1 standard deviation of the estimated "Gaussian sphere" (see Appendix C)

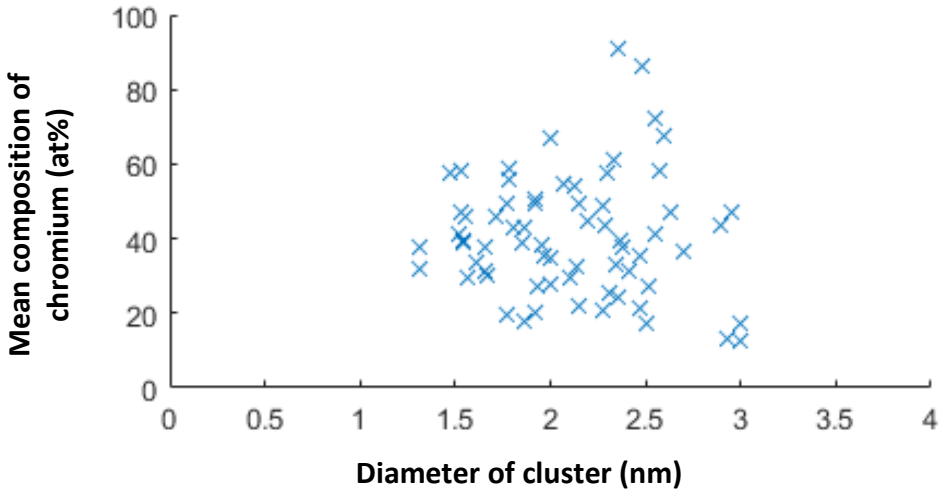

Figure 4.52: Plot of size vs mean cluster composition

4.6 Summary of neutron irradiated FeCr

Table 4.5 contains a summary of the results in the neutron-irradiated FeCr alloys, which will be discussed in chapter 5.

	Fe6Cr		**Fe9Cr**	
Dislocation loop spatial distribution	Heterogeneous		Heterogeneous	
Dislocation loop density - high and low density regions (loops/cm^3)	4.3±0.5 x10^{16}	7.4±1.3 x10^{15}	1.2±0.3 x10^{17}	2±1 x10^{14}
Dislocation loop mean diameter - high and low density regions (nm)	5.5±3.7	3.6±1.2	5.1±3.6	-
Percentage of population with b= <111> - high and low	72±8%	52±18%	100%	-
Interstitial or vacancy?	Interstitial		Interstitial	
Void spatial distribution	Homogeneous		Homogeneous	
Void density - high and low loop density regions (voids/cm^3)	4.4±1.0 x10^{16}	4.0±0.9 x10^{16}	1.7±0.6 x10^{16}	1.8±0.4 x10^{16}
Void mean diameter - high and low loop density regions (nm)	1.2±0.6	1.3±0.4	1.2±0.4	1.3±0.3
Void maximum diameter - high and low loop density regions (nm)	3.5	2.7	2.2	1.6
Chromium cluster distribution	Homogeneous		Homogeneous	
Chromium cluster density (clusters loops/cm^3)	4.5±0.9 x10^{16}		7.4±0.4 x10^{17}	
Chromium cluster mean size (nm)	4.5±0.9		2.1±0.4	
Chromium cluster maximum size (nm)	7.1		3.0	
Chromium cluster mean composition (at%)	11.1±1.8		40.7±16.2	

Table 4.5: Summary of radiation damage found in the neutron irradiated Fe6Cr and Fe9Cr

Chapter 5: Discussion of neutron damage in FeCr

5.1 Introduction

Alloys of Fe6Cr and Fe9Cr were irradiated with neutrons to investigate the hardening mechanisms that can occur inside structural steels used in fission and fusion nuclear reactors. The results from this experiment are presented in chapter 4, summarised in section-4.6, and are discussed in this chapter.

A mixture of dislocation loops, voids and chromium clusters were observed in both the neutron-irradiated Fe6Cr and Fe9Cr. The discussion of these results is divided into two sub-sections; the effect of composition on the radiation damage; and the inhomogeneity of the damage distribution.

5.2 Effect of composition on neutron irradiated FeCr

The two alloys of Fe6Cr and Fe9Cr were selected to investigate how radiation damage is affected in FeCr alloys above and below the solubility limit of chromium in iron (~8-9at% at 300^{o}C [101]). The analysis by weak-beam TEM has shown the visible dislocation loops produced by the neutrons are similar in size, but the population around dislocations in the Fe9Cr is ~2.8x higher than the dense regions in the Fe6Cr. Conversely, in regions far from dislocations, the visible loop density in the Fe6Cr is ~40x higher than the low-density regions of the Fe9Cr. The measurement of the high-density region in the Fe6Cr is within a less well-defined volume than the equivalent measurement in the Fe9Cr, so this may be an underestimate of the density. Nonetheless, the differences in density indicate that the ~3at% difference in chromium content is noticeably affecting the mobility of the radiation-induced defects.

The clustering of loops around the dislocations imply that loops are either diffusing towards the dislocations after nucleation, or there is preferential nucleation occurring at the dislocations. If dislocation loops are nucleating homogeneously and are then attracted to the dislocations, then it would imply that the mobility of defects is higher in the Fe9Cr alloy, as the dislocation would be acting as a more efficient sink for the defects. This is counter-intuitive on the basis that alloying elements should be expected to decrease the dislocation mobility, rather than promote it [20,172].

If instead nucleation were more frequent in the vicinity of dislocations, then it would imply that mobility is lower in the Fe9Cr, since the density around the dislocations falls very rapidly (more so than was observed in the Fe6Cr) beyond the confines of the helical dislocations (i.e. they cannot diffuse away).

Since the low-density regions of the microstructure can extend several hundred nanometres, it is unlikely that the dislocation loops have migrated such a distance to cluster at dislocations. Therefore, the results from chapter 4 support the notion that dislocations are actively promoting the nucleation of visible defects locally to dislocation lines. This will be discussed further in section-4.3 in relation to the observations of helical dislocations.

Regardless of what is happening at the dislocations, it is interesting that very few visible loops were observed elsewhere in the microstructure. Increased visible loop populations were seen at dislocations and low-angle grain boundaries, but between these regions, the visible damage is ~$7x10^{15}$ loops/cm^3 in the Fe6Cr and ~$2x10^{14}$ loops/cm^3 in the Fe9Cr. For the visible loop population to be so low after a dose of 2.1dpa, there must be something preventing the dislocation loops growing to visible sizes. Hernandez-Mayoral et at. [76] also reported a similar microstructure in Fe5Cr and Fe9Cr irradiated with neutrons at 300^{o}C to 0.6dpa, at a similar dose-rate to the experiment in chapter 4. The authors noted that their visible loops were appearing in regions free of chromium precipitates, indicating that chromium clusters inhibit the growth of interstitial clusters to visible sizes. Similar chromium clusters were identified in the neutron-irradiated FeCr studied here

(section-4.4.5 and 4.5.6), which were found far from dislocations or grain boundaries. Unfortunately, it was not possible to take any measurements from the helical dislocations or low-angle grain boundaries for this work (none were present in the ~20nm thick regions of foil).

It is unlikely that all the interstitial defects produced from the cascades have simply recombined with the vacancies at 325°C, as dislocation loops have been identified in purer materials and at smaller doses than were studied here [27,36,47,55,75,91,149]. Therefore, there must be a very high density of <2nm, and even <1nm, defect clusters that are frozen in the matrix and invisible to the TEM (at least in a FIB-prepared foil). Loop mobility is severely reduced by the atmosphere of impurities [190] (in this case, mostly carbon and silicon [97,101]), and segregation of alloying elements to the loops [20,37,104]. For the interstitial clusters to have remained invisible to the TEM, the defects must be pinned in-place by either the impurity elements or alloyed chromium, or both. As explained below, the length of the irradiation experiment is key to understanding the microstructure, and there is a close link between the chromium precipitates and dislocation loops

The EELS observations in section-4.4.5 and 4.5.6 have indicated a chromium precipitate population of ~$5x10^{16}$ and ~$7x10^{17}$ clusters/cm^3 in the Fe6Cr and Fe9Cr respectively. Bachhav et al. [101] studied these same alloys, irradiated with neutrons to a similar dose and temperature, but at a dose-rate approximately four times the dose-rate of the experiment studied here. Bachhav et al. [97,101] studied their alloys by APT, and observed chromium decorated loops only in the Fe6Cr, at a density of ~$3x10^{16}$ /cm^3, and in the Fe9Cr alloy observed a low population of α' phases of ~$9x10^{16}$ /cm^3. The results from the experiment in chapter 4 indicate a higher population of chromium precipitates exist in the lower dose-rate FeCr alloys, particularly in the Fe9Cr in which the density of chromium precipitates is a factor of eight higher than observed by Bachhav et al. [101].

TEM analysis of the faster dose-rate neutron-irradiated FeCr alloys is not published in the literature yet, so it is not possible to make a thorough comparison of the dislocation loops in the faster dose-rate neutron-irradiated FeCr alloys [97,101,124]. Dr Dhriti Bhattacharyya of Australia's

Nuclear Science and Technology Organisation (ANSTO) has conducted microstructural characterisation of the Fe6Cr and Fe9Cr alloys from this faster neutron irradiation experiment, and the results were presented orally at the 2017 TMS Annual Meeting & Exhibition [191]. Visible loops were reported in the matrix of the Fe9Cr, though the population was the lowest of the FeCr alloy set (3%-18%Cr) (as indicated from the TMS abstract [191]).

Reese et al. [157] compared α' phase precipitation in a range of neutron-irradiated FeCr alloys by APT, and suggested that dislocation loops act as nucleation centres for α'. If there is a higher population of visible loops in the matrix of the faster-dose-rate neutron-irradiated FeCr alloys than my observations, this would be strong evidence that chromium precipitates hinder the growth of dislocation loops. Furthermore, it could be argued that this is evidence that the dislocation loops themselves act as nucleation sites for chromium precipitates.

Since there are almost no visible loops in the matrix of the Fe9Cr studied here, then there were in all likelihood no visible loops in the matrix at smaller doses (loops are not expected to have shrunk). This mean that when Bachhav et al.'s rapid irradiation experiment ended, the alloys studied here (which were irradiated at the same time) had only reached ~0.6dpa and the interstitial clusters in the matrix were probably more densely populated, and at below TEM-visible sizes. Working backwards in time, the interstitial cluster population of the low-dose-rate experiment will always have been greater than the interstitial cluster population for a faster dose-rate experiment, if irradiated for the same length of time. Therefore, if the α'-phases require some critical time to nucleate during neutron irradiation, then there will be more nucleation sites for the α' to nucleate in the lower dose-rate experiment. This would give rise to a larger population of α', and a highly immobile interstitial cluster population.

Alternatively, the faster dose-rate may simply be enhancing diffusion by maintaining a higher concentration of non-equilibrium point defects, so interstitial clusters that may otherwise be

immobilised by chromium could be able to glide, climb, and coarsen. This could also give rise to a lower α' population, with a lower interstitial cluster population (but larger visible population).

The lower population of α' phase precipitates in Bachhav et al.'s neutron-irradiated Fe9Cr than what was observed here could also be explained by the higher frequency of large cascades. In Bachhav et al.'s experiment, higher energy cascades could have been destroying chromium-rich regions that might otherwise have gone on to coarsen into α'-phases, and more often than the experiment studied here. This is similar to the argument that ballistic-mixing is the reason α'-phases are rarely reported in heavy-ion irradiated materials [105], and why α'-phases form at high dose-rates under electron irradiation [106].

For the Fe6Cr, visible loops were seen in the matrix, and chromium clustering was also seen. It was not possible to correlate the loops with the chromium clusters. This may imply that the chromium clusters were forming around very small loops (such loops were probably lost to the surface of the ~20nm thick foil during sample preparation). The chromium composition is below the solubility limit (~8-9at%), so α' phase nucleation is not expected in Fe6Cr, and the clusters seen were probably a result of only chromium segregation, with the dislocation acting as the dominant sink for chromium. In the case of the Fe9Cr, the composition is above or close to the solubility limit, so segregation of chromium around dislocation loops probably acted as a catalyst for α' nucleation. Above some particular enrichment of chromium, the chromium cluster itself probably acts as the dominant sink for chromium, rather than the dislocation loop.

5.3 Inhomogeneity of loops in neutron irradiated FeCr

Here is discussed the possible origins of the high loop population in the vicinity of dislocations that were observed in both the Fe6Cr and Fe9Cr.

Sections 4.4 and 4.5 show the microstructures of Fe6Cr and Fe9Cr both have a large visible-loop population in the immediate vicinity of dislocations. In the Fe9Cr, the dislocations are helical, which can form from the agglomeration of interstitial or vacancy defects on majority-screw dislocations. Previous work on dislocation loop decoration, and simulations of helix formation have generally assumed that interstitial defects were responsible for producing the helical dislocation, for example [74,80,82,192]. The analysis in section-4.5.4 shows that the mechanism behind radiation-induced helical dislocation formation in FeCr is actually vacancy-biased, rather than interstitial. This is crucial to understanding the origin of the heterogeneous distribution of dislocation loops in the foil.

Interstitial defects are generally considered to be more mobile in the FeCr system than vacancy defects [50,69]. In pure α-iron, interstitials have a migration energy of 0.30eV while vacancies have a migration energy of 0.67eV [50]. Vacancies are therefore treated as immobile defects compared to highly mobile interstitials. The materials studied here are not pure iron, but an alloy with chromium. Additionally, they are not pure, but contain many impurity elements such as carbon, nitrogen and silicon. It is likely that individual vacancies in these materials form vacancy-carbon complex pairs, which have a migration energy of 1.08eV [50]. Interstitial point defects do not form interstitial-carbon complex pairs [69], but interstitial dislocation loops will gain a significant Cottrell atmosphere of impurities. Such loops in Fe were measured to have a migration barrier of 1.3eV by Arakawa et al. [190]. Chromium may also be segregating to the loops, which will also contribute to impeding their mobility, as discussed in section-4.2. The mobility of both vacancy and interstitial defects are severely restricted by the presence of alloying and impurity atoms, and so it may not be correct to treat one as being significantly more mobile than the other.

A first explanation to consider for the origin of the helical dislocations is whether vacancy defects are being preferentially attracted towards the initial screw dislocation, while interstitials are repelled. Screw dislocations should be a sink for both interstitials and vacancies, though simulations by Sivak et al. [193] indicate screw dislocations are more efficient sinks for interstitials than vacancies. Once a screw dislocation gains some edge-character, it will become a biased sink to whichever defect gives it the edge character [17,188]. Therefore, there must be some mechanism that gives the dislocation the initial edge character from vacancies. Even if the initial vacancy-bias is small, the process will be self-catalysing and accelerate as it continues to gains vacancy-edge character and the vacancy-bias increases.

Defects appear to be highly immobile in both alloys, and more so in the Fe9Cr, which is apparent from the small loop sizes and the sharp drop in loop density outside the helical dislocations. It is therefore unlikely that vacancies have diffused far from their creation point (i.e. the cascade) towards the dislocation-sink; so the helix is probably only affecting defects produced very close to the dislocation line (i.e. the cascade that created the vacancies probably occurred close to, or maybe even on the dislocation line).

For a consistently greater number of vacancies to reach the core of the screw dislocations than the interstitials, the interstitials could be drawn to another sink. There is a second sink-source for the defects in the vicinity of the dislocations; the interstitial clusters themselves. Dislocation loops are very strong sinks for similar-character defects. If a large cascade were to occur close to a dislocation line, then from this cascade, at least one large interstitial loop might nucleate. After the cascade, the loop will quickly develop an impurity atmosphere, which might pin it in the matrix [190] and leave the remaining vacancies to diffuse towards the dislocation line. There may also be other forces preventing the large interstitial loop from merging with the dislocation line. For instance, only loops that share a Burgers vector with the screw dislocation can join together (to conserve the Burgers vector [32,188]). Therefore, loops with a different Burgers vector must rotate Burgers vector

through thermally and/or strain activated changes in order to join the screw dislocation, which a large cluster may not be able to do. Interstitial loops could therefore be pinned close to the dislocation line, unable to combine with the dislocation.

Burgers vector analysis in section-4.5.1 shows there to be a slightly greater population of interstitial loops that share a Burgers vector with the helical dislocation line. Although this shows that the loops have a tendency to rotate early in their evolution to share a common Burgers vector with the line, it indicates that there is still something preventing them from merging with the dislocation line. Alternatively, it might simply imply that such parallel-to-**b** loops formed after the dislocation gained vacancy-helical character.

Nonetheless, it can be deduced that at least some of the interstitial loops that nucleate close to a dislocation line will be pinned close to it, rather than merging with the line. This means a population of pinned interstitial sinks will exist close to the line, before it gains a dominant interstitial or vacancy character. In this situation, the flux of defects reaching the screw-dislocation core might be expected to become biased towards vacancies, since a portion of the interstitials will flow to the pinned dislocation loops instead.

There is evidence in the literature that suggests that although both interstitials and vacancies are attracted to screw dislocations, it is more difficult for interstitials to reach the core. Calculations of the bias factor of various sinks were conducted by Chang et al. [194]. Among their results, they showed that the bias factor for point defects onto a screw dislocation-core in iron is negative – i.e. vacancy biased. The reason described for this bias, as explain by Cheng et al., is that self-interstitials approaching the dislocation core are repelled slightly by the strong compressive fields in the microstructure immediately local to the core. Vacancies are not affected by the compressive field, and yet their attraction to the dislocation is similar to that of a self-interstitial. The resulting effect is that the point-defect flux joining the core is vacancy-biased, whereas the interstitials can only approach the core without joining it. This same reasoning might also apply to dislocation loops

approaching the core, but this was not discussed. This could explain the bias of defects onto the screw dislocations that produced the initial vacancy-edge component.

The discussion has so far focussed on possible explanations for how the helical dislocations were produced and how they came to have vacancy character. The effect this has on the surrounding microstructure will now be discussed.

The screw dislocations act to remove vacancies from the local microstructure that might otherwise be available for interstitial-vacancy annihilation. Since interstitials and vacancies were produced in equal quantities, the local microstructure should be left with a higher density of interstitial defects than regions far from sinks – i.e. the local microstructure is supersaturated with interstitials. It is therefore highly likely that these extra interstitials are the source of the high local-density of interstitial loops around these helical dislocations.

The total interstitial and vacancy populations within the analysed helical dislocation (2.5±0.7 $x10^4$ and 8.8±1.2 $x10^4$ per helical turn, respectively) in the Fe9Cr were estimated based on the diameter of the helical dislocation and the measured sizes of the dislocation-loops. This analysis suggests there are approximately three-times more vacancies "contained" by the helical dislocation than the number of interstitials contained by visible loops. The missing population of interstitials is difficult to explain; there is no other source of vacancies, so it should be expected that the interstitial and vacancy measurements would be equal (or within the margins of error). A prediction of the number of interstitials present as loops too small to be resolved in the TEM was made by assuming the measured cluster-size distribution follows a single power law. However, this estimate also fails to account for the missing population. The conclusion from this is that there must exist an enormous population (~$6x10^4$) of interstitials contained within clusters and/or as lone self-interstitials that follow a steeper cluster-size distribution than was measured here (n=1.8, where the cluster size distribution is satisfied by $N \sim x^{-n}$).

It would be interesting to investigate whether helical dislocations also form during charged particle irradiations, and whether they are also correlated with heterogeneous loop distributions. This is addressed in the next chapter.

Dislocation loop clustering at the low-angle sub-grain boundaries was observed in addition to the clustering at dislocations, but this was not quantitatively analysed. No loop clustering at high-angle grain boundaries was observed, which would indicate that they are either acting as very efficient and unbiased sinks, or that the mobility of the defects is so low in this material and at this temperature that they are not diffusing significantly towards the boundaries. It was not possible to make any definitive conclusions about the role of high-angle grain boundaries in this work.

The low-angle sub-grain boundaries require further investigation. Although explanations about the origins of the loop clustering around dislocations has been discussed extensively, particularly in reference the screw dislocations having a bias towards vacancy defects, it is not possible to say whether a similar mechanism is occurring at the low-angle sub-grain boundaries.

Chapter 6: Replicating neutron damage with heavy ions and protons

6.1 Introduction

The use of materials testing reactors to implant neutron damage is costly, lengthy, and makes samples radioactive, thus complicating the post-irradiation analysis. In attempt to replicate the damage the neutrons produce, materials are often irradiated with surrogate particles in the form of heavy-ions or protons. This chapter explores the damage that protons and self-ions produce in the same FeCr alloys studied after neutron irradiation in the previous chapter, using as similar as possible irradiation parameters to implant the damage. This is the first time such a comparative study of three irradiation types has been performed.

6.2 Irradiation experiments

For this work, unirradiated specimens of the same FeCr alloys that were studied in Chapter 4 were used. This is important to keep the comparison to the neutron-irradiated microstructures fair. The same irradiation parameters were targeted for each irradiation. As a reminder from section-4.1, the neutron-irradiated alloys were irradiated with the following parameters:

- Dose: 2.1dpa (or 1.6dpa calculated using FISPACT-II [159])
- Temperature: Target 290^{o}C. Actual 315-335^{o}C
- Dose rate: 9.3 x10^{-8}dpa/s (200 day irradiation)

The work in this chapter was carried under the apparent knowledge that the neutron-irradiated alloys were irradiated at 290^{o}C, however in the time since much of this work was carried out, it emerged that the alloys were irradiated slightly hotter than intended. The experiments in this chapter therefore had a slightly cooler target temperature than the neutron irradiation temperature.

It is unrealistic to irradiate samples in a particle accelerator for 200 days, which is how long the neutron irradiation lasted. The dose-rate for the experiments reported here were therefore as low as could be reasonably achieved, which equated to 2 days for both the self-ion and proton irradiation experiments.

6.2.1 Irradiation of FeCr alloys with protons

The Dalton Cumbria Facility (DCF) [195] was used for the proton irradiation experiment. This was selected due to DCF's ability to deliver proton beams at the high currents necessary to achieve the target dose in a reasonable time. The facility uses a 2.5MV Pelletron accelerator to accelerate protons up to 2.5MeV in energy. The energy of protons for this experiment was 1.2MeV, which was used for three reasons:

- The accelerator easily maintains a stable beam at this energy
- This energy produces only low-level activity isotopes that decay quickly after irradiation
- The required dose could be implanted with a reasonably uniform dose-profile but with a high enough dose-per-ion to reach the target dose in a realistic time frame.

A summary of the irradiation parameters is shown in Table 6.1, and SRIM [110] calculations of displacements-per-atom (dpa) with depth are presented in Figure 6.1.

Variable	Measurement
Dose at 2-2.5µm depth (dpa)	1.9 (2.0 - 2.5µm)
Fluence (protons/cm^2)	2.8 x10^{19}
Dose rate (dpa/s)	1.0 x10^{-5}
Flux (protons/cm^2/s)	1.6 x10^{14}
Current density (µA/cm^2)	25.5
Length of irradiation (hours)	49
Irradiated area (cm^2)	1.0
Scan frequency (Hz)	520 x 33
Irradiation Temperature (°C)	302

Table 6.1: Irradiation parameters from the proton experiment

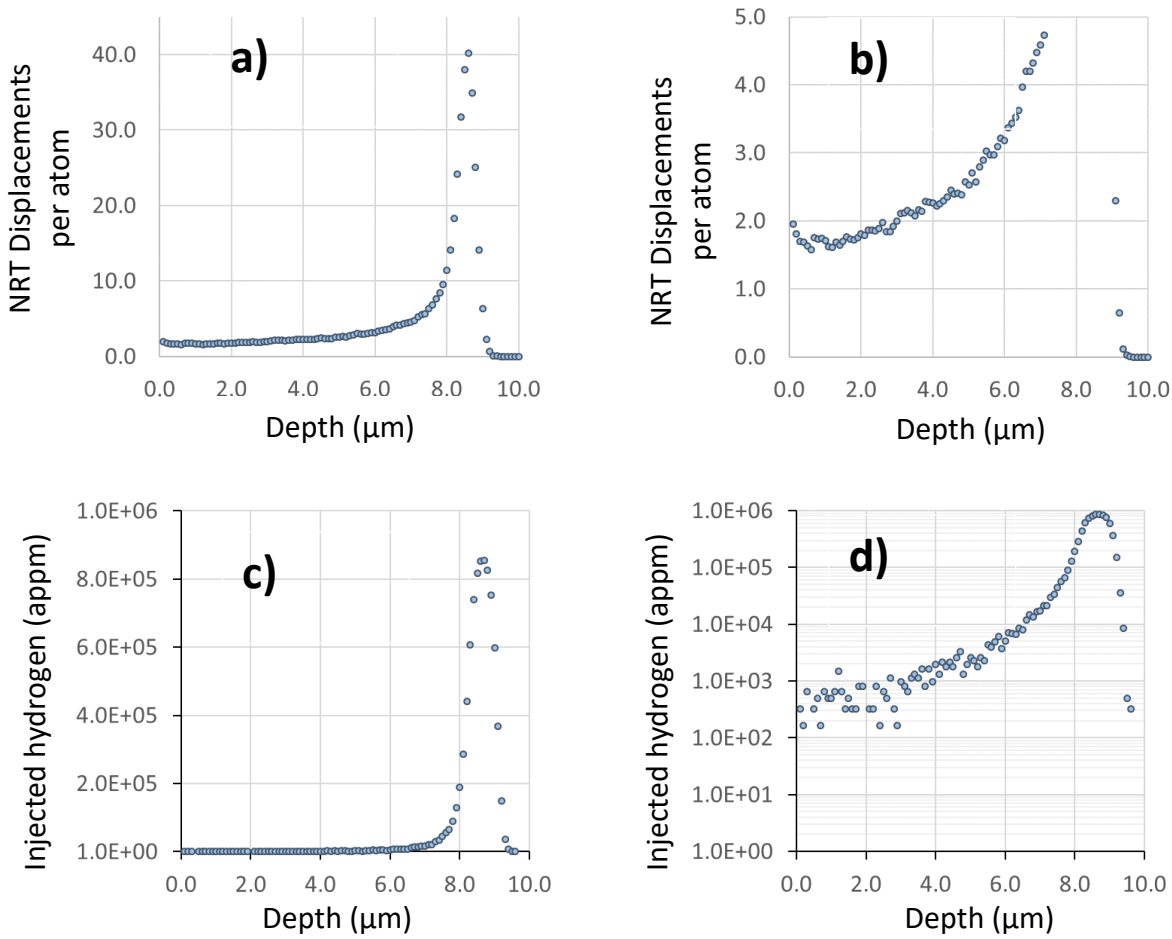

Figure 6.1: Calculated dose and implanted material profiles using SRIM [110] *of the proton irradiation experiment. a) and b) both show the NRT-dpa dose* [18]*, with different y-axis scaling. c) and d) both show the implanted hydrogen profile with linear and log y-axes respectively.*

The irradiated area was controlled by the positions of the last set of Faraday cups before the beam hits the sample. With the beam scanning at a low current, the positions of the four cups were initially all withdrawn so that the Silica glass pieces, shown in Figure 6.2, all glow (since they are exposed to the beam). The Faraday cup positions were then each inserted individually to positions such that the beam is confined to the area indicated by the marked points in Figure 6.2.

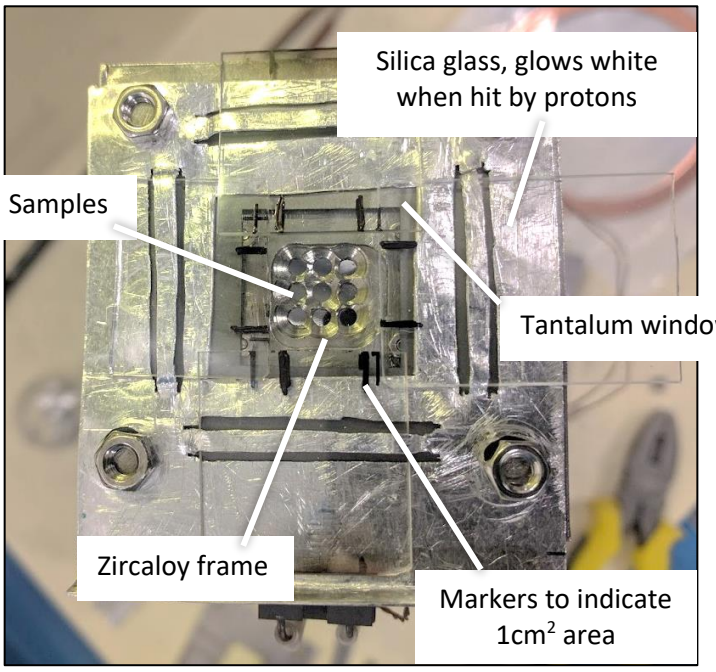

Figure 6.2: Front view of the proton irradiation sample stage

The samples were irradiated as 3mm disks due to the lack of material for larger samples. Each sample was mounted on a copper base with a layer of indium between sample and copper. The samples were then clamped down with a Zircaloy front plate. The indium creates a good thermal contact between the sample and copper base, and the Zircaloy will not produce any long-lived activation products during irradiation of the 1.2MeV protons. The irradiation setup is shown schematically in Figure 6.3.

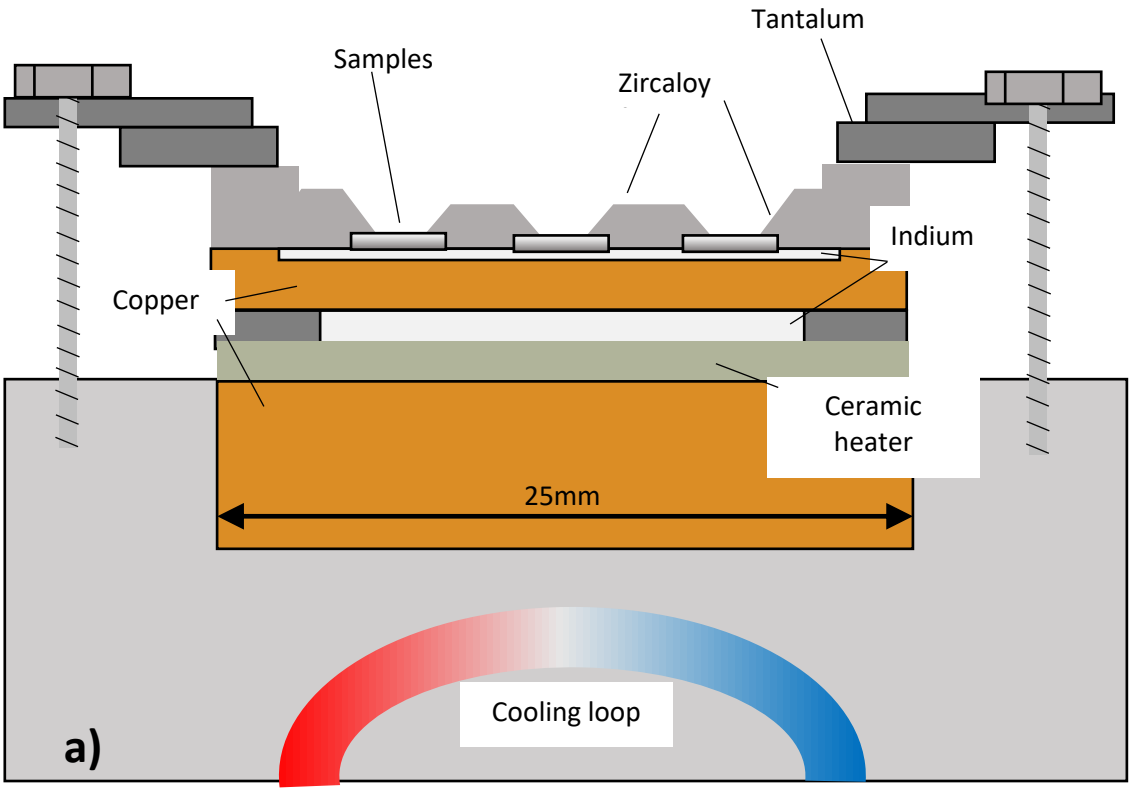

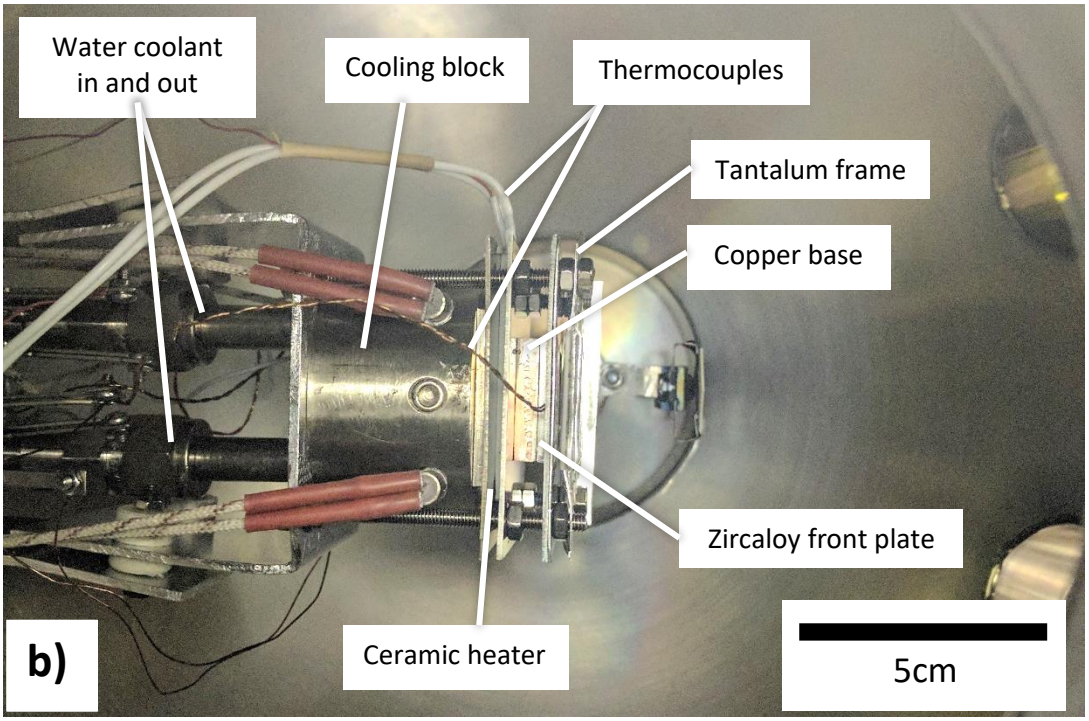

Figure 6.3: a) Schematic diagram of the proton irradiation stage viewed from the side (not to scale). b) photo of the stage mounted inside the target vacuum chamber.

To measure temperature for this experiment, it is not suitable to rely on the read-out from a thermocouple because at the high currents necessary for this work, beam heating is a big problem. The average current density was 11.1μA/cm2, which equates to nearly 20mW/cm^2. The temperature shift this equates to will depend on the material and thermal contact with the cooling block, so the temperature of the samples and the irradiated frame could experience different beam heating. It was not possible to weld thermocouples to the samples themselves due their small size, and furthermore, DCF were unwilling to expose thermocouples directly to the proton beam in order to prevent their activation. Even if it were possible to weld thermocouples onto the samples, protons hitting the thermocouples would cause them to heat-up directly, potentially skewing the measurement.

The routine method to overcome this issue at DCF is to use a thermal camera to monitor the temperature of the samples. Prior to irradiation, the samples are slowly heated to temperature, whilst recording both thermocouple and black body emission from the samples. The thermal emission from each sample is then calibrated according to the thermocouple measurement.

This approach relies very much on the assumption that the temperature during this cycle is uniform across all samples. Since the thermal emissivity of the samples varies with composition, surface finish, oxide layer, and angle with respect to the camera, there can be a noticeable variation in the measured thermal emission of the samples, even at room temperature. The standard deviation of the measured signal from the irradiated samples at temperature is around ~4% of the mean signal (and ~6% at room temperature). This may sound small, but if the assumption of uniform temperature is not valid, then a conservative estimate of the irradiated temperature difference between two samples could be as much as 40^{o}C. The calibration curves recorded are shown in Figure 6.4.

With the emission calibrated to the thermocouple-measured temperature, the samples were then exposed to the beam. The samples experienced ~60°C of beam heating during the experiment, but the temperature on the samples remained stable-throughout the irradiation.

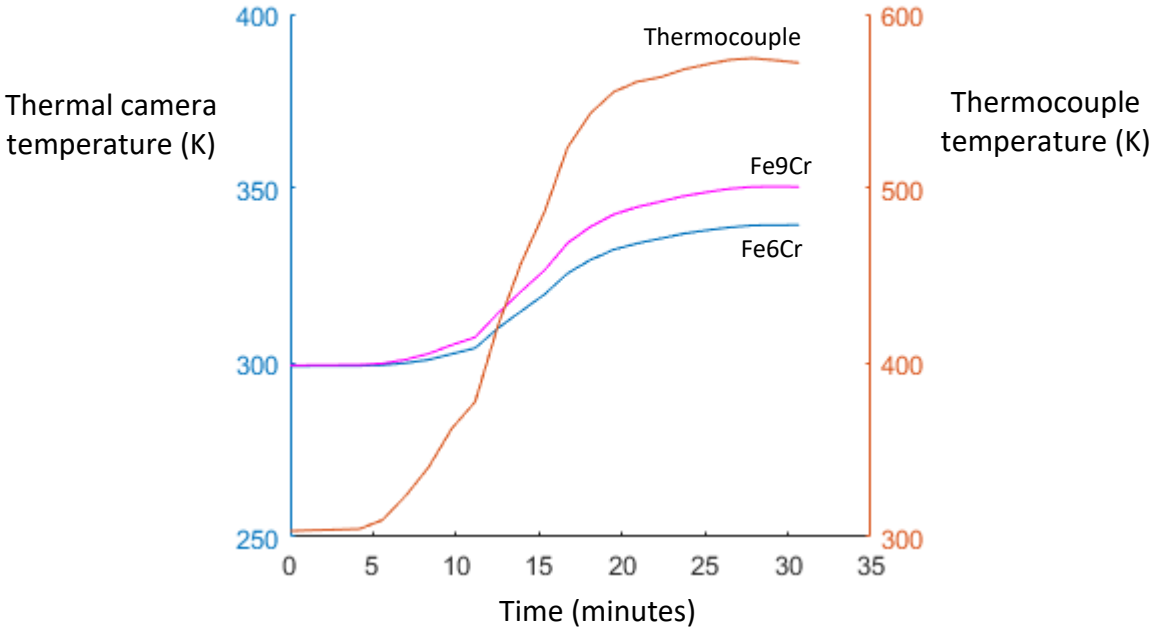

Figure 6.4: Calibration curves for measuring the temperature of the disks by the thermal camera. The pink and blue curves are the uncalibrated temperature as measured by the thermal camera (left-hand axis) while the temperature measured by thermocouple is also shown (right-hand axis).

Figure 6.5 shows the calibrated temperature, read out from the Fe6Cr and Fe9Cr during the experiment. The dose on the sample was calculated from the deposited charge on the stage, accounting for a dark current of -0.025 μA. The dose as a function of time is shown in Figure 6.6. The dose is expected to be uniform over the sample since the beam was rastered using a focussed probe (<7mm FWHM[9]), and over-scan of ~5-10mm. A static defocussed beam was considered for this work, but preliminary experiments indicated the dose profile over the irradiated area would have to be very non-uniform for an appreciable dose to be obtained.

[9] The beam was focussed using the scintillating silica glass to monitor the beam width. This could only be done at low current and saturates the webcam, so the measurement of spot size is only a rough estimate.

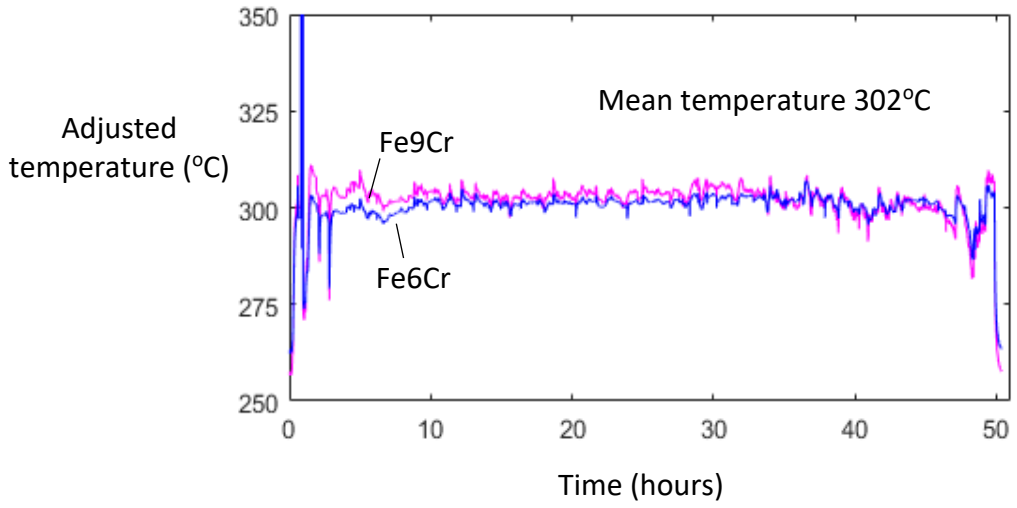

Figure 6.5: Calibrated temperature of each disk throughout the course of the irradiation

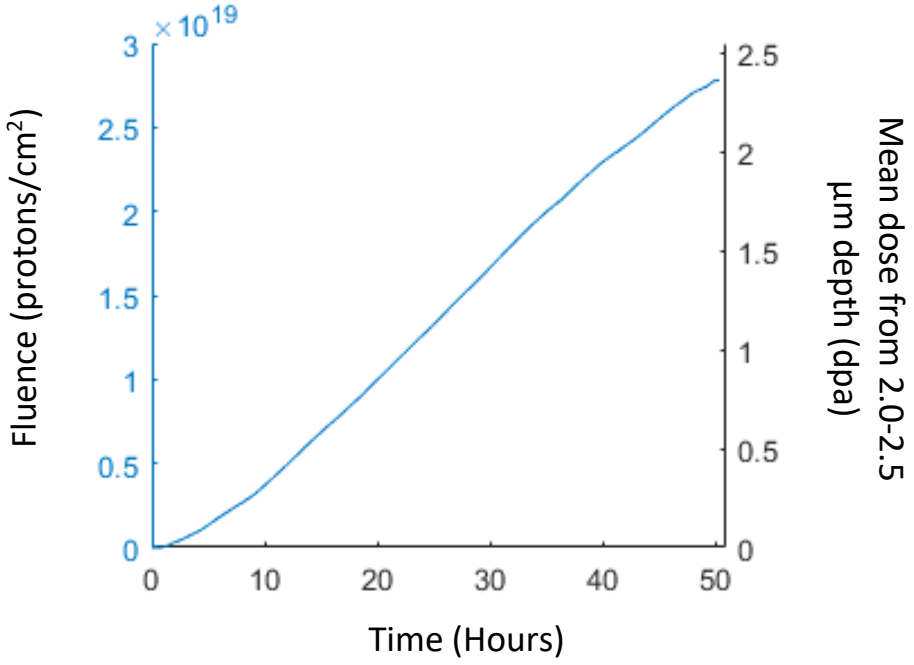

Figure 6.6: Fluence and dpa-dose as a function of time during proton irradiation

6.2.2 Irradiation by self-ions

The Surrey Ion Beam Centre was used for self-ion implantation. The facility was selected due to Surrey's ability to run a stable heavy-ion beam for long periods, which was necessary to match the proton irradiation dose-rate. Fe+ ions with energy 2MeV were used for this implantation, which produced the deepest damage layer that was achievable with this set-up.

A thorough breakdown of current and temperature as a function of time was not provided, and so the feedback from the irradiation is not as well documented as the proton irradiation. The temperature was monitored by thermocouple only, but this temperature is expected to be more reliable than for the proton irradiation since the effect of beam heating is negligible for self-ion irradiation at the flux used [133]. The flux was reported to have fluctuated by ±20% over the course of the irradiation. The temperature, and fluence are shown in Table 6.2. The SRIM [110] calculated dpa and injected material profiles are shown in Figure 6.7. The irradiation set-up is shown in Figure 6.8.

Variable	Measurement
Dose at Bragg peak (dpa)	2.2
Fluence (ions/cm^2)	1.9 x10^{15}
Dose rate (dpa/s)	1.2 x10^{-5}
Flux (ions/cm^2/s)	1.1 x10^{10}
Current density (nA/cm^2)	1.8
Length of irradiation (hours)	48
Irradiated area (cm^2)	4.9
Scan frequency (Hz)	0 (static beam)
Temperature (^{o}C)	290

Table 6.2: Irradiation parameters of the self-ion experiment

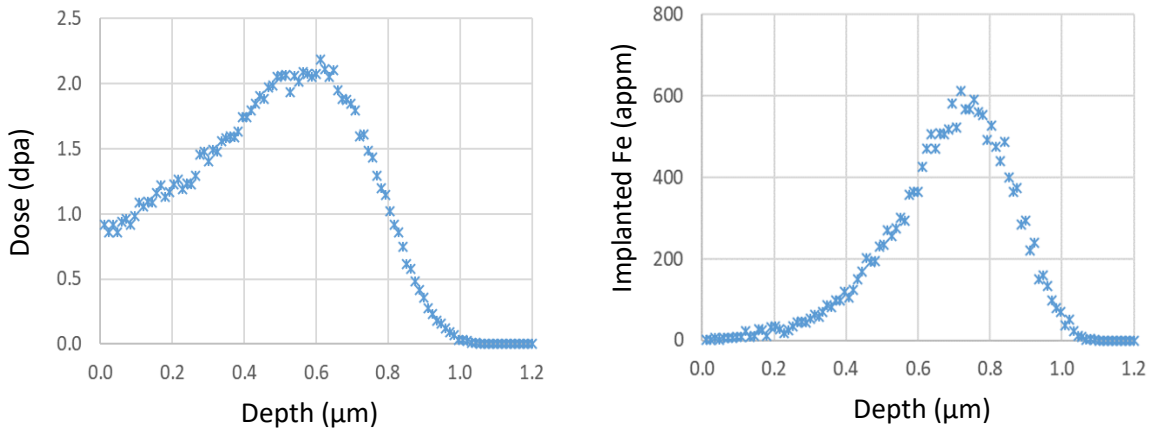

Figure 6.7: Calculated dose and implanted material profiles of the self-ion irradiation experiment using SRIM.

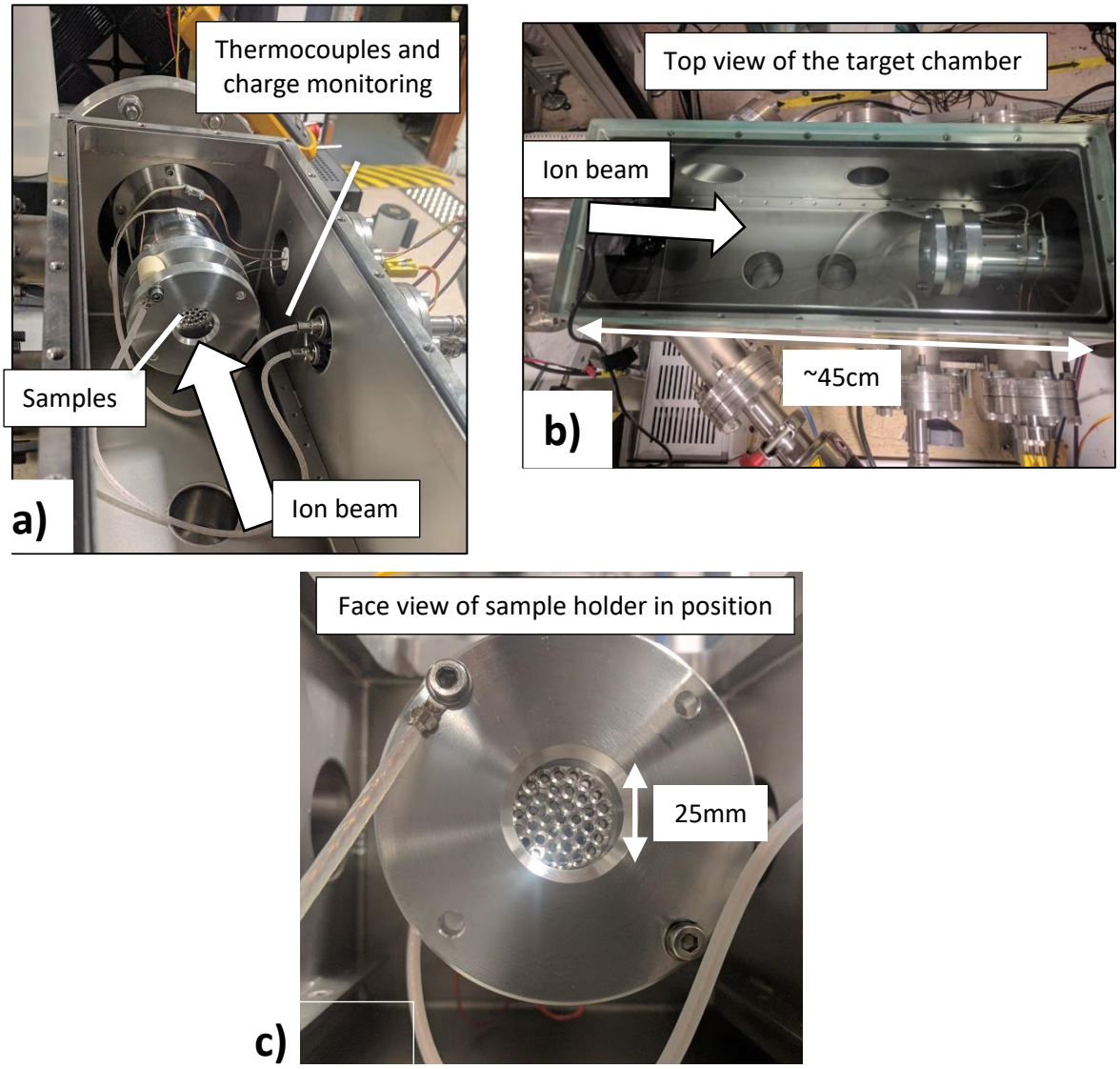

Figure 6.8: Various photos of the set-up for self-ion implantation. a) was captured from above the aperture through which the ion-beam enters the target chamber. b) is captured from above the target chamber. c) was captured directly in-front of the sample mount.

6.3 Microstructure of proton and ion irradiated Fe6Cr

Figure 6.9 and Figure 6.10 show low magnification micrographs of the proton-irradiated and self-ion irradiated Fe6Cr, respectively. The low magnification image of the proton-irradiated sample is taken from a region at 2.0-2.5µm depth, equating to an average dose of 1.9dpa.

The ion-irradiated sample received a dose that peaks at 2.2dpa at 600nm depth. The region analysed is indicated on Figure 6.10, which is shallower in the profile than the Bragg peak, and corresponds to an average dose of 1.8dpa. The region in which the Bragg peak is expected seems appears to have less damage than the regions at shallower depths. The region of maximum dpa should contain the maximum damage, so this could be an indication that the electron beam is not close to normal to the foil surface. Taking the peak-damage to be ~500nm depth, rather than ~600nm depth, the foil would have to be tilted ~33° from normal to have moved the apparent position of the Bragg peak 100nm, which is unlikely. The damage in the self-ion irradiated sample at depths shallower than 500nm appears to be fairly uniform, besides a small selection of loop clusters.

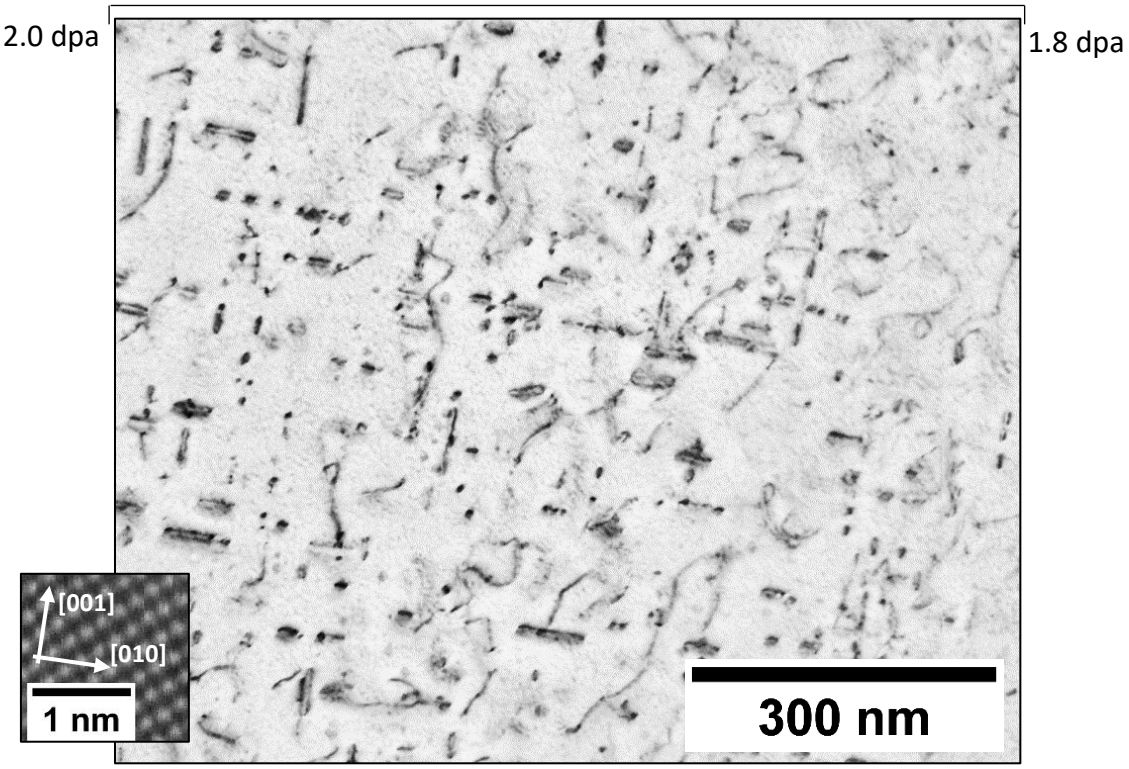

Figure 6.9: ADF image (inverted contrast) captured down a <100> zone axis of proton irradiated Fe6Cr, with atomic resolution image shown to illustrate unit cell orientation.

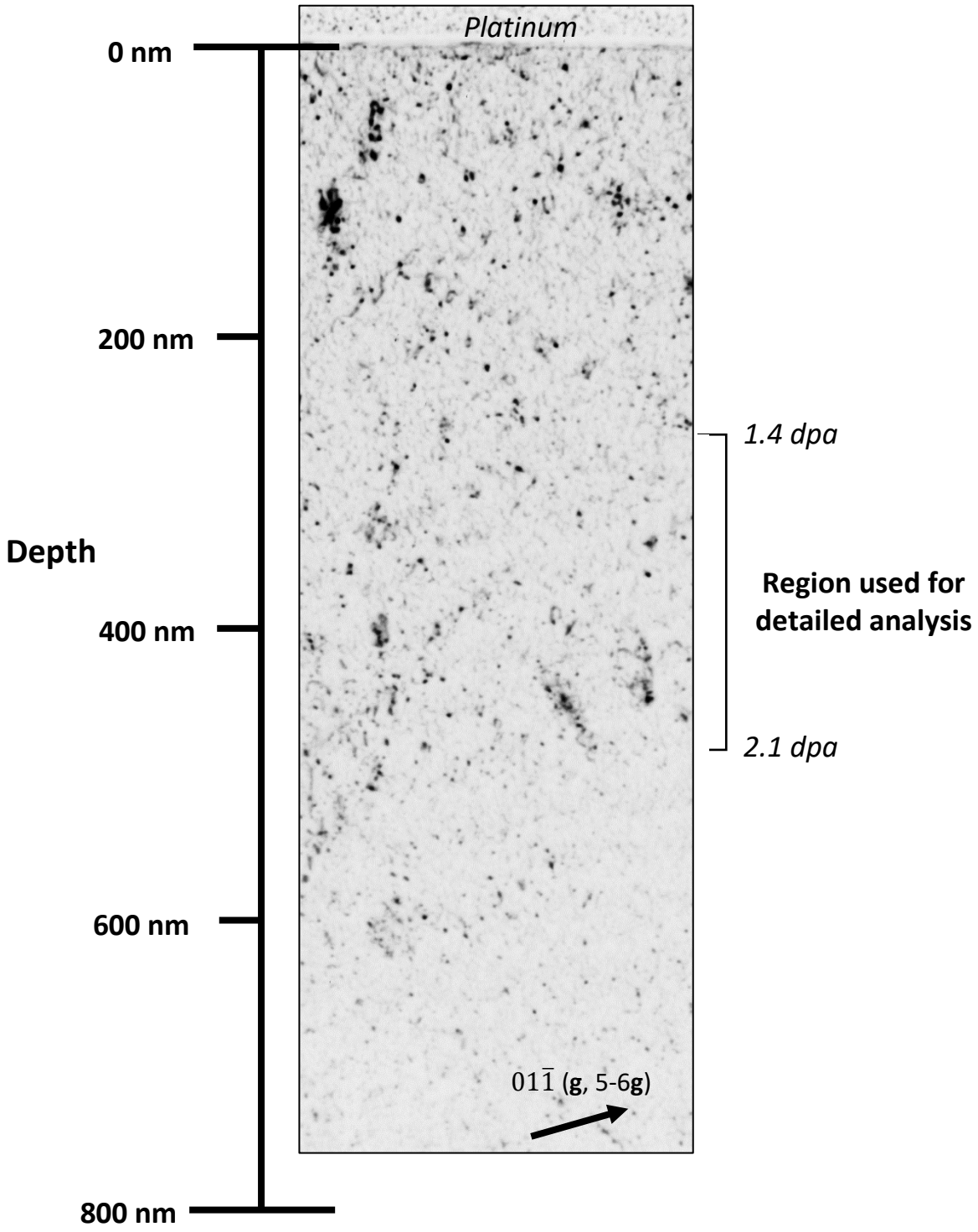

Figure 6.10: Low magnification weak beam image of the self-ion irradiated Fe6Cr

It is immediately apparent that the damage is very different between the proton and ion-irradiated samples. The proton-irradiated Fe6Cr contains mostly large (>20nm) edge-on dislocation loops (the long and thin loops), residing on planes 90^{o} to each other, with only a small population of loops that do not appear with this morphology. The loops appear uniformly distributed throughout the region. The ion-irradiated sample contains many small <10nm dislocation loops, with some denser clusters visible, but mostly distributed homogeneously throughout the foil. The damage appears to be roughly uniform throughout the majority of the dose profile, indicating that the defects have moved and evolved over a length scale on the same order of magnitude as the implantation profile.

Figure 6.11 to Figure 6.17 show higher magnification micrographs of the proton and ion-irradiated samples. The proton-irradiated sample does not appear to contain any obvious helical dislocations similar to those seen in the neutron-irradiated material. The dislocations that are present are shorter. Although some do appear “wavey”, it was not possible to confirm these as helical dislocations. The dislocations may actually be large loops that intersect the surface, and are thus open loops.

The self-ion irradiated sample does contain dislocations similar to the neutron-irradiated helical dislocations (e.g. Figure 6.14), but they are not well defined and there does not appear to be any loop clustering around them. Some loop clusters are visible as rafts.

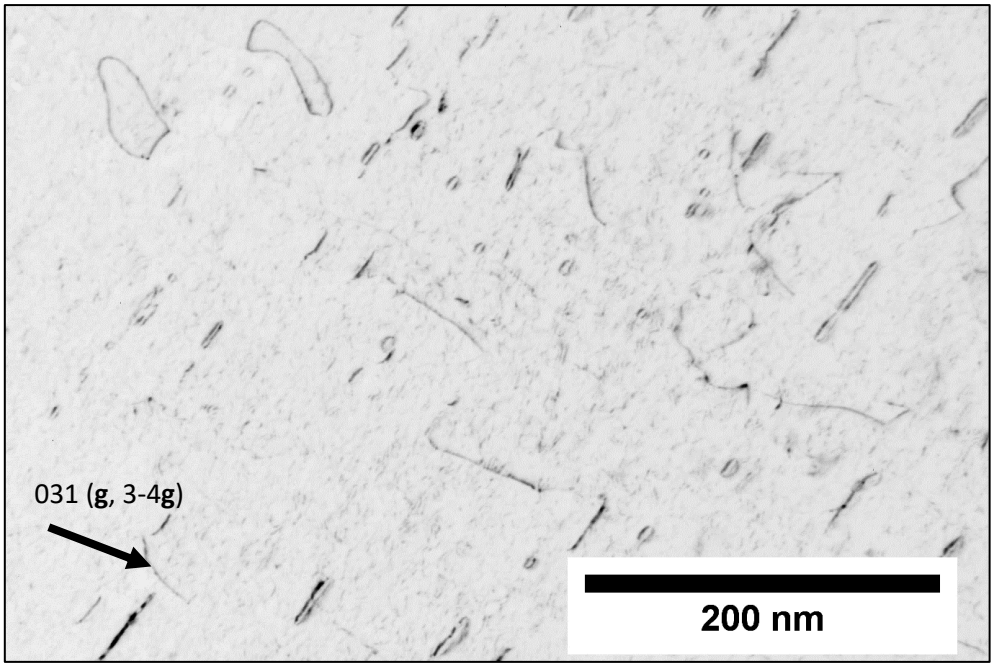

Figure 6.11: Weak beam micrograph of proton irradiated Fe6Cr showing mostly edge loops, and two examples of larger inclined loops in the top left of the micrograph

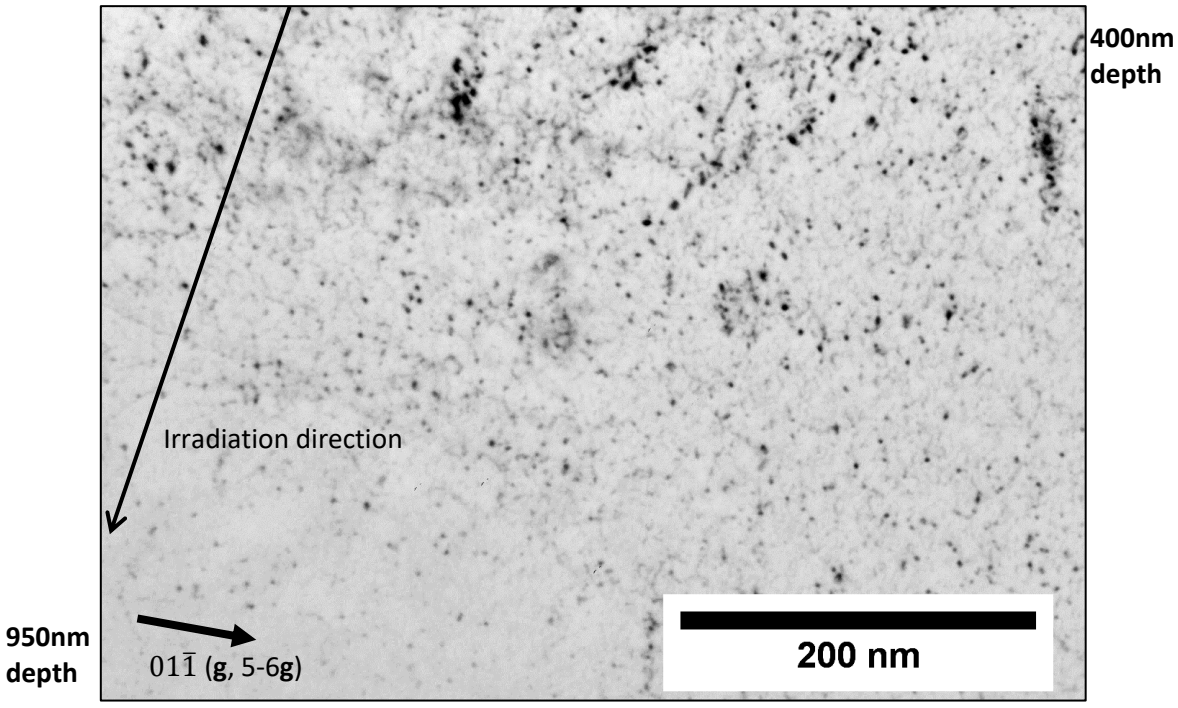

Figure 6.12: Weak beam micrograph of the self-ion irradiated Fe6Cr at the end of the damage profile. A raft of loops is visible in the top right of the micrograph, and the loop population declines in the direction of irradiation.

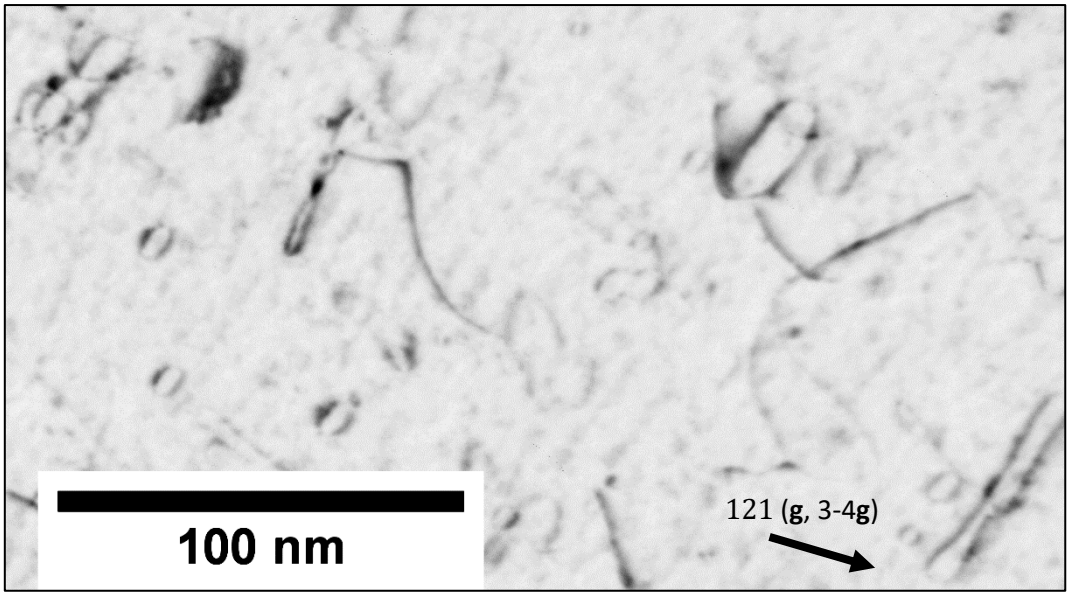

Figure 6.13: Higher magnification weak-beam micrograph of proton irradiated Fe6Cr, captured close to the $[2\bar{1}0]$ *pole.*

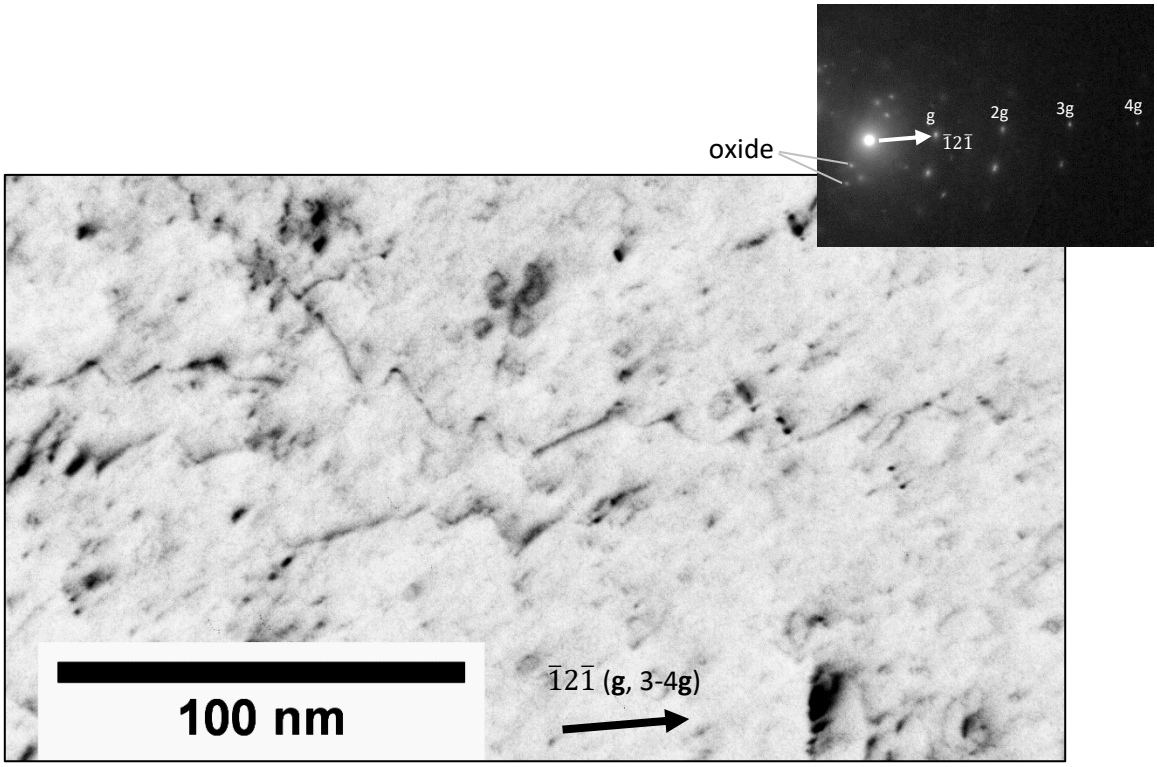

Figure 6.14: Higher magnification weak-beam micrograph of the self-ion irradiated Fe6Cr, captured close to the $[31\bar{1}]$ *pole. A selection of dislocations are visible, possibly helical, running from left to right across the micrograph. The diffraction pattern for this condition is also shown, in which some oxide reflections are visible.*

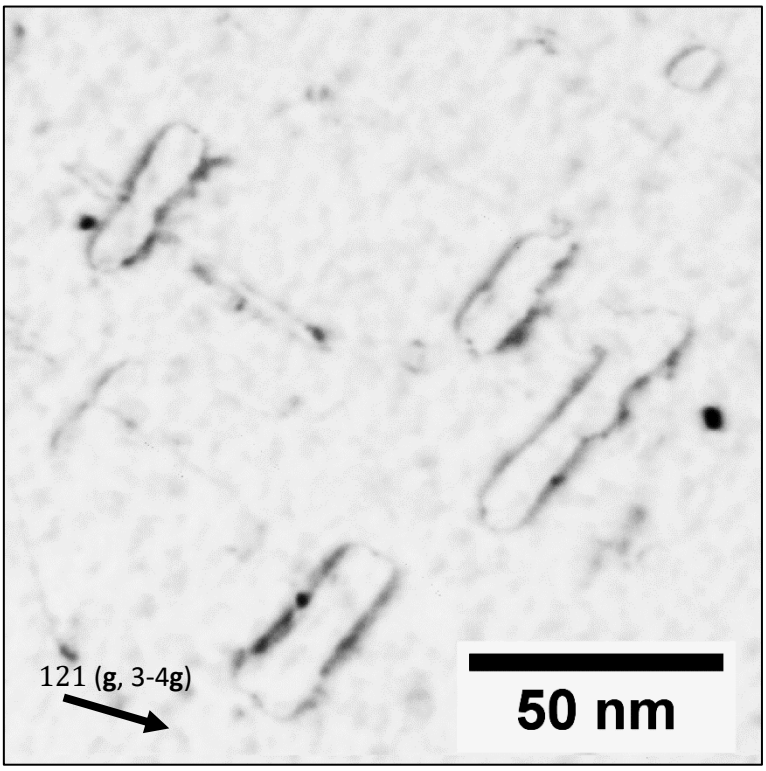

Figure 6.15: High magnification weak-beam micrograph of <100> type dislocation loops in proton irradiated Fe6Cr, captured close to a $[2\bar{1}0]$ *pole.*

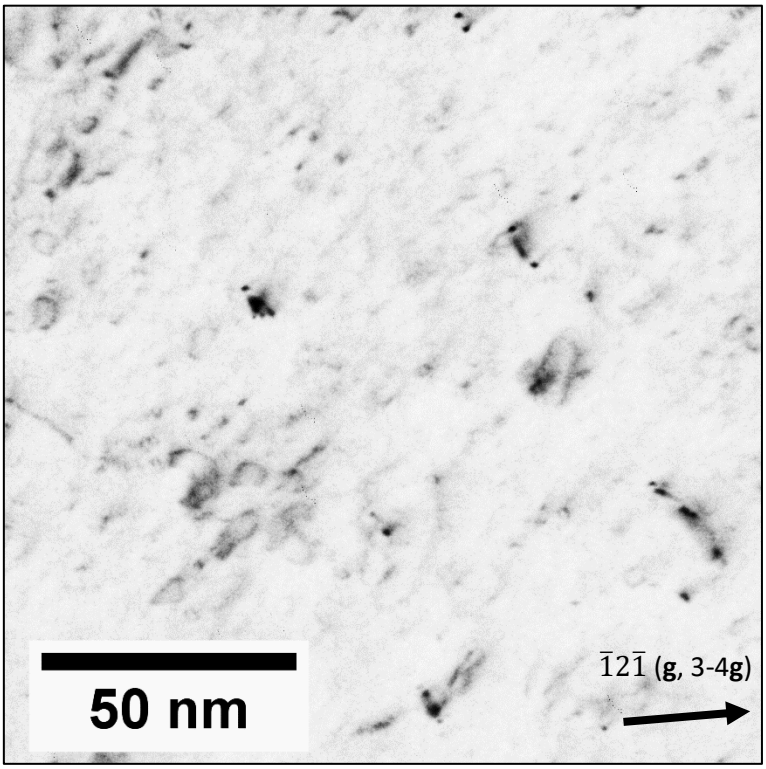

Figure 6.16: High magnification weak-beam micrograph of dislocation loops in self-ion irradiated Fe6C, showing a mix of <100> and <111> type loops.

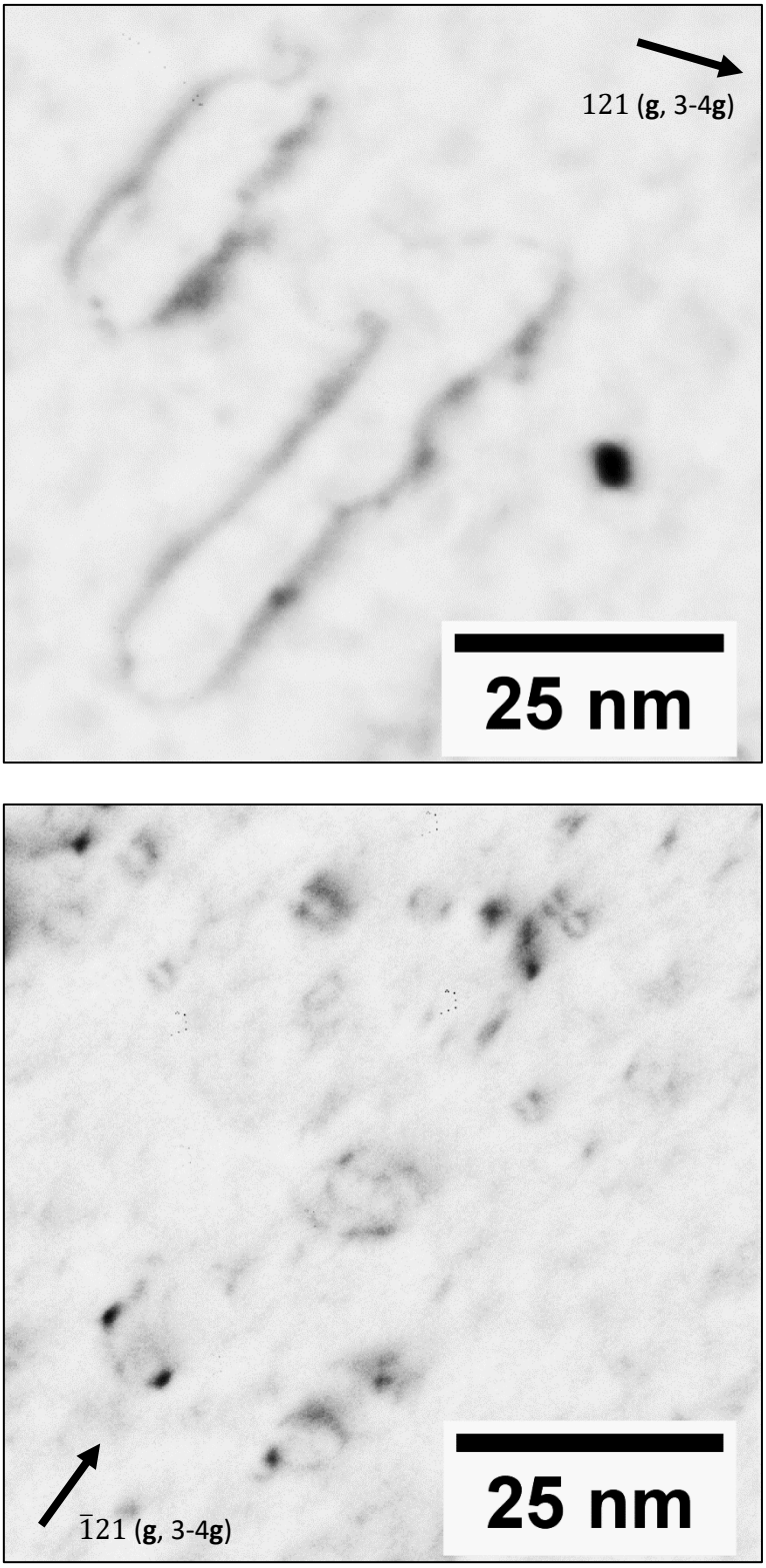

Figure 6.17: High magnification micrographs of loops in proton (top) and self-ion irradiated Fe6Cr. The self-ion irradiated Fe6Cr contains many small dislocation loops, whereas the Fe6Cr are large, and appear non-uniform, suggesting they were produced from the coalescence of large dislocation loops.

6.3.1 Burgers vectors and number density of irradiation-induced dislocation loops in proton and self-ion irradiated Fe6Cr

Proton-irradiated sample

A thin region (52nm thick) of the proton-irradiated foil at ~2.5μm depth into the damage profile was used for quantitative analysis. Thicker regions were imaged, but the large sizes and dense population of loops made the images very complicated and difficult to count.

Since the loops in the proton-irradiated Fe6Cr were so large, it was simple enough to use cross correlation through **g**.**b** conditions to completely determine the Burgers vector of the loops. Additionally, the loops are mostly edge-on to the beam when viewed from a [100] zone axis, and lie on (010) and (001) planes. This strongly implies the majority of loops are <100> type.

Micrographs of 013 type were used in place of 011, 020 etc. type reflections since the significant oxide layer present on this foil rendered such conditions unusable. The 013 type reflections had much less oxide interference, and so were preferred when imaging around the [100] zone axis. For determining the Burgers vector of the loops, it would appear that since **g**.**b**≠0 for all possible Burgers vectors (except [100]), it would not be possible to use the visibility of the loops to determine the Burgers vector. However, the product of **g.b** for 001 and 010 loops is different (Table 6.3), and hence the amplitude of the contrast is noticeably different. The visibility of one variant is reduced enough to be able to deduce the Burgers vector, as can be seen from Figure 6.18.

Also in Figure 6.18 is a composite micrograph equal to the sum of an $0\bar{1}\bar{3}$ and $0\bar{3}\bar{1}$ weak-beam condition, which reveals all variants of the loop Burgers vectors with good contrast (besides **b**=[100]), similar to a STEM image captured down a <100> zone axis [196]. Figure 6.18 also shows the diffraction pattern of the [100] zone axis, which the foil was oriented close to. From this, it is can be seen that edge-on loops align with the 002 and 020 g-reflections. Also visible are in-plane [100] dislocation loops, which should normally be invisible according to **g**.**b**.

$\boldsymbol{g \cdot b}$ *product*

Zone axis	g \ b	$[100]$	$[010]$	$[001]$	$\frac{1}{2}[111]$	$\frac{1}{2}[1\bar{1}1]$	$\frac{1}{2}[11\bar{1}]$	$\frac{1}{2}[1\bar{1}\bar{1}]$
$[100]$	$0\bar{1}\bar{3}$	0	-1	**-3**	-2	-1	1	2
	$0\bar{3}\bar{1}$	0	**-3**	-1	-2	1	-1	2
	$0\bar{3}1$	0	**-3**	1	-1	2	-2	1

Table 6.3: ***g.b*** *product table for some 031-type conditions. The product is proportional to the amplitude of the signal observed in a micrograph.*

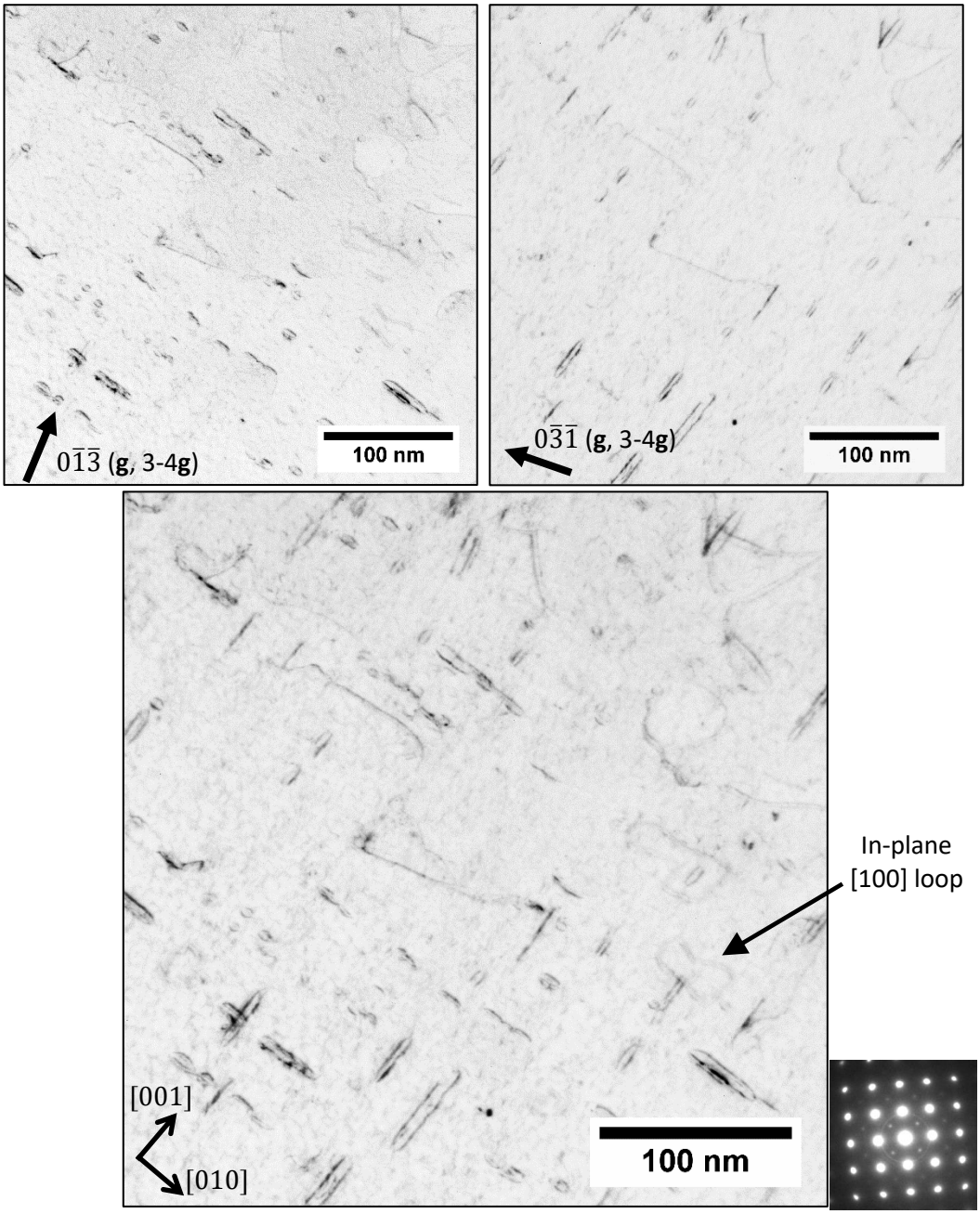

Figure 6.18: Weak-beam micrographs of proton irradiated Fe6Cr using a) ***g****=*$0\bar{1}\bar{3}$*, b)* ***g****=*$0\bar{3}\bar{1}$*, and c) both conditions combined. The combined micrograph shows all visible Burgers vectors, and even some in-plane [100] loops. The [100] zone axis diffraction pattern is shown, which is close to the weak-beam conditions used here.*

Using this nearly-invisible **g.b** method in addition to observing the plane the loops appear to lie on, it was shown that all 150 loops in Figure 6.18 are <100> type, at a loop density of $2.6\pm0.3\times10^{16}$ loops/cm^3 in this region. The micrograph of the proton-irradiated Fe6Cr in Figure 6.11 (page 174) shows two large loops in the top left corner that have good visibility and are not edge-on. These loops are most likely <111> type, which indicates a small population of <111> loops are present in the proton-irradiated sample, despite none being observed in the region of Figure 6.18. This would indicate a <111> population of ~10^{14} loops/cm^3. The large size of these loops indicate it is possible that a large number of <111> loops intersect the foil surface, and may appear as "open" loops. Throughout the foil, a large population of short dislocation lines can be seen. These may simply be open loops with **b**=<111>, in which case the population of <111> loops would be closer to 10^{15} loops/cm^3. From this, we have estimated lower and upper bounds for the fraction of the total loop population made up of <111> loops. These are 0.5% and 4.5% of the total population, which is within the statistical error of the total count.

It is surprising that the loops have grown so much larger in the proton-irradiated sample than the neutron-irradiated sample because the larger size is typical of higher temperature irradiations [35,54]. This result may indicate that the temperature of the sample ran higher than the target temperature for at least some of the irradiation. This will be discussed further later.

Self-ion irradiated sample

The self-ion-irradiated sample also had a considerable oxide layer, which made counting loops very difficult. Comparison of the weak-beam micrographs to kinematical bright-field micrographs aided counting and deduction of the Burgers vectors, which revealed a mixed population of <111> and <100> loops in the sample. Figure 6.19 shows weak-beam micrographs of the microstructure, and a series of loops are highlighted. The invisibility of the loops can be traced across each condition to show the mixed <100> and <111> loop population, aided by Table 6.4. For the vast majority of defects in the foil, it was not possible to trace them from one condition to another.

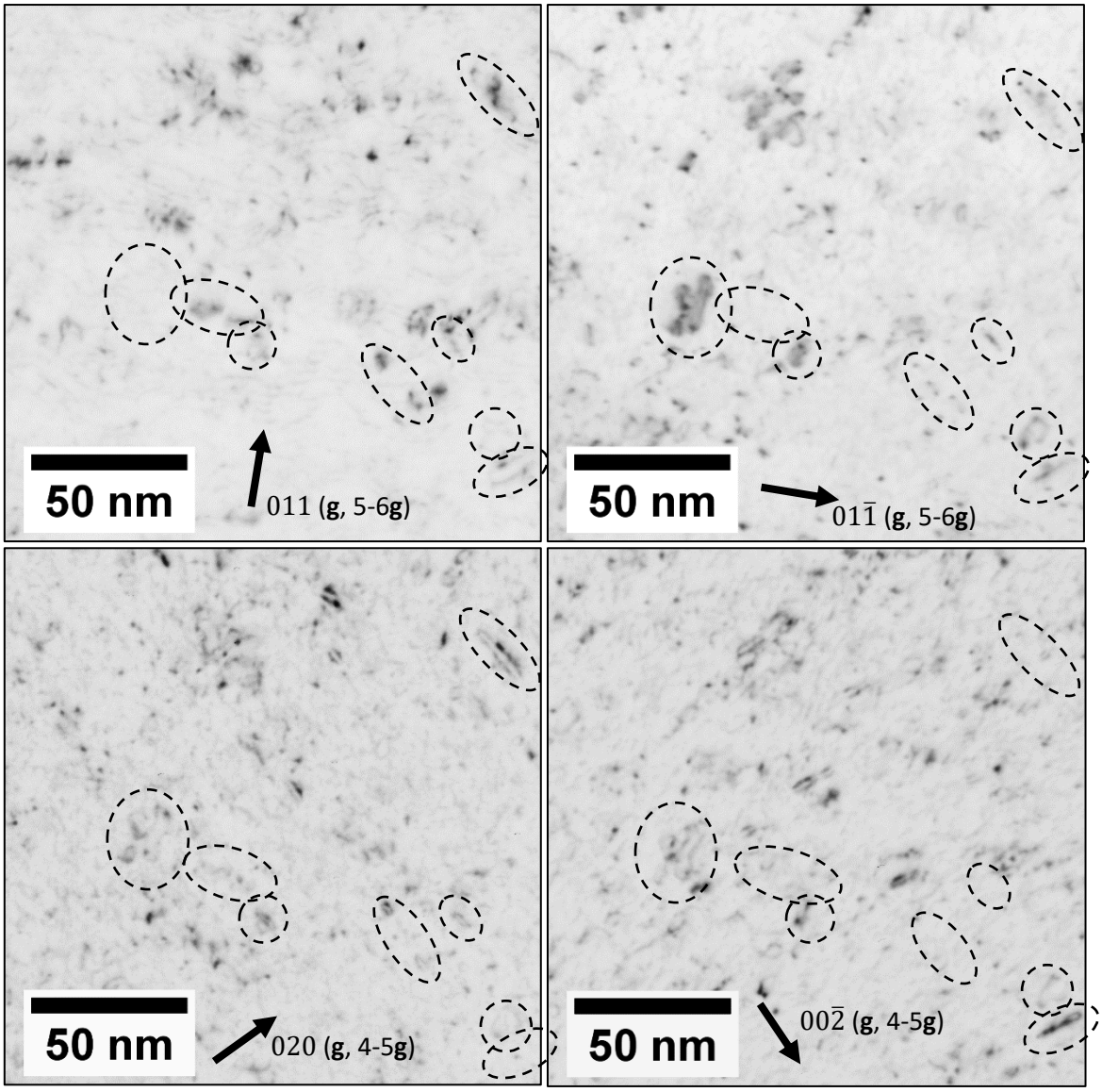

*Figure 6.19: Weak-beam micrographs of self-ion-irradiated Fe6Cr, using various g-vectors to demonstrate **g.b** analysis to identify the loop Burgers vectors. Example <111> and <100> loops are circled, and identifiable by comparing to Table 6.4. Due to the difficulty in tracing the same loops from one condition to another, the overall fraction of <100> and <111> type loops was determined using the statistical analysis method* [172].

		$\boldsymbol{g \cdot b}$ *product*						
Zone axis	g \ b	$[100]$	$[010]$	$[001]$	$\frac{1}{2}[111]$	$\frac{1}{2}[1\bar{1}1]$	$\frac{1}{2}[11\bar{1}]$	$\frac{1}{2}[1\bar{1}\bar{1}]$
$[100]$	011	0	1	1	0	0	0	-1
	$01\bar{1}$	0	1	-1	0	-1	1	0
	020	0	1	0	1	-1	1	-1
	$00\bar{2}$	0	0	1	1	1	-1	-1

*Table 6.4: **g.b** product table for some 011-type and 002-type conditions. A product of zero indicates an "invisible" condition.*

The overall fraction of <111> and <100> loops present in the foil was determined by the statistical analysis method [172], which also includes counts from weak-beam micrographs captured using g=±112, 121 etc. The counts from each micrograph are shown in Figure 6.20. The number of loops counted in each condition ranged from 150 to 210, amounting to over 1000 loops sized counted overall. The volume used for the images captured near the $[31\bar{1}]$ and $[210]$ zone axes accounts for the ~25° tilt from the foil normal (close to $[100]$). The error bars shown for the counts are the statistical $\sqrt{N}$ counting error propagated with the error in the thickness measurement.

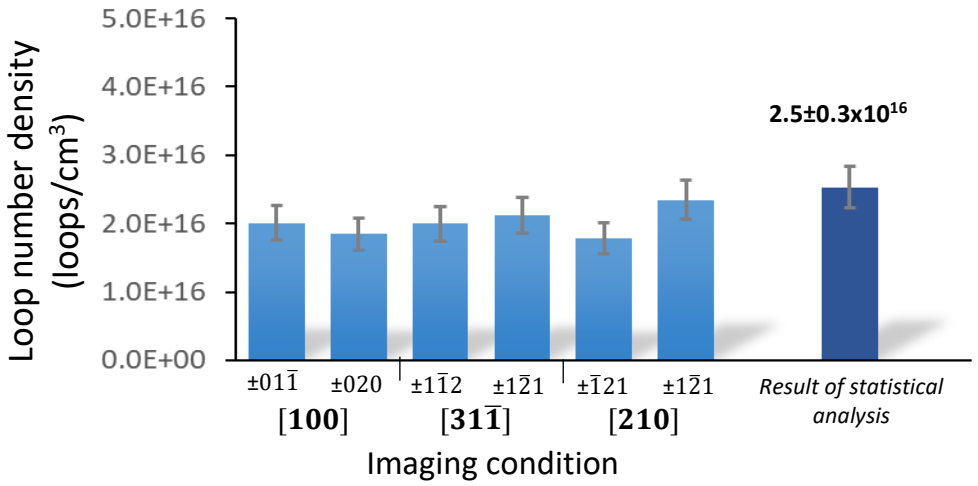

Figure 6.20: Dislocation loop density of the self-ion irradiated Fe6Cr, as determined by the statistical analysis method [172]*. The visible density in each condition is shown.*

6.3.2 Comparison of loop number density and Burgers vectors of neutron, proton and self-ion irradiated Fe6Cr

The number density for the self-ion irradiated Fe6Cr for each condition and overall is shown in Figure 6.20, and this is compared with the number density in the proton-irradiated and neutron-irradiated Fe6Cr in Figure 6.21. The Burgers vector of the loops is shown in Figure 6.22 as a percentage of the total population. From this we see the majority of loops in the proton irradiated samples are <100> type, but the majority of loops in the self-ion and neutron-irradiated samples are <111> type. Despite the loops being so much larger in the proton-irradiated sample, the population of loops is similar to the self-ion irradiated sample. This implies far more point defects make up the visible clusters in the proton-irradiated Fe6Cr than the self-ion irradiated Fe6Cr.

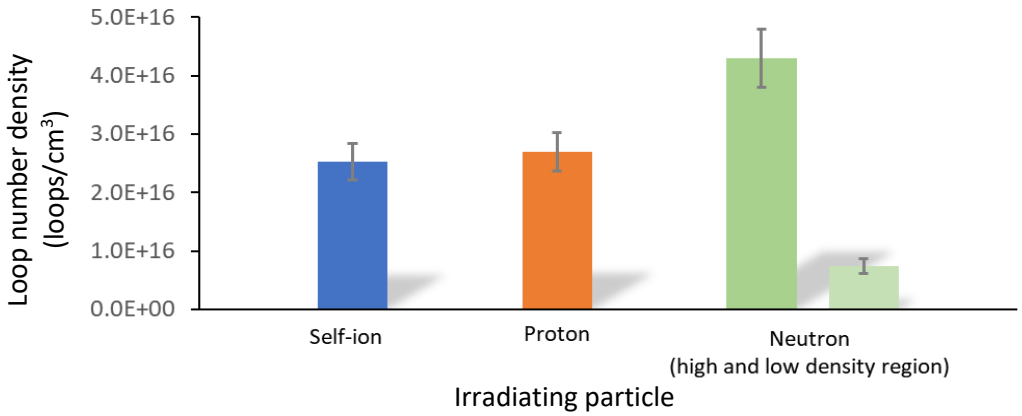

Figure 6.21: Dislocation loop number densities for self-ion, proton and neutron irradiated Fe6Cr

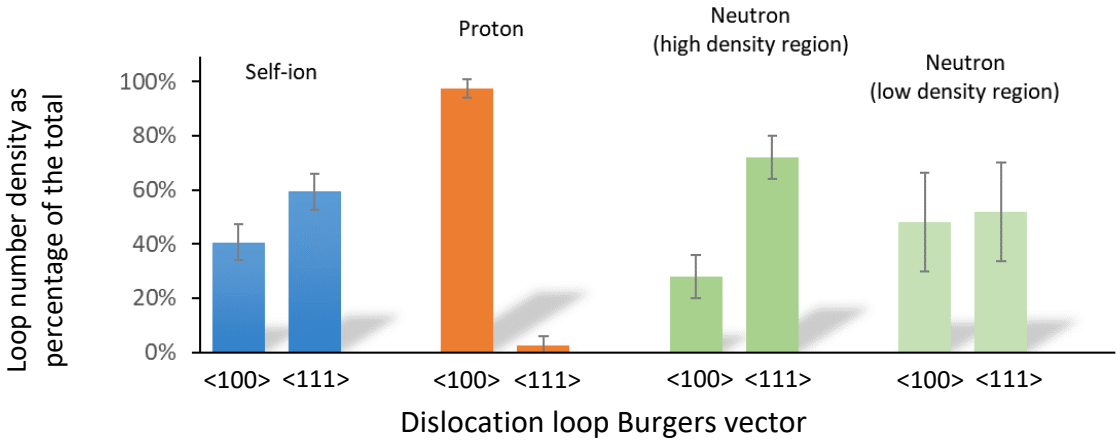

Figure 6.22: Fraction of <100> and <111> loops present in self-ion, proton and neutron irradiated Fe6Cr

6.3.3 Nature analysis of loops in proton and self-ion irradiated Fe6Cr

Loop nature was determined using the inside-outside contrast method [48]. Due to the large size of the loops in the proton-irradiated sample, it is easy to identify the <100> loops from the [100] zone axis. It was found that all [010] loops have a minor image-diameter that increases when the sample is tilted to the $[2\bar{1}0]$ zone axis, implying they are all inclined the same direction with respect to the beam. Some [100] loops were also visible as in-plane loops in Figure 6.18. Figure 6.23 shows the inside-outside contrast analysis for a selection of loops. In total, 32 loops were analysed in the proton-irradiated sample. All loops were found to be interstitial.

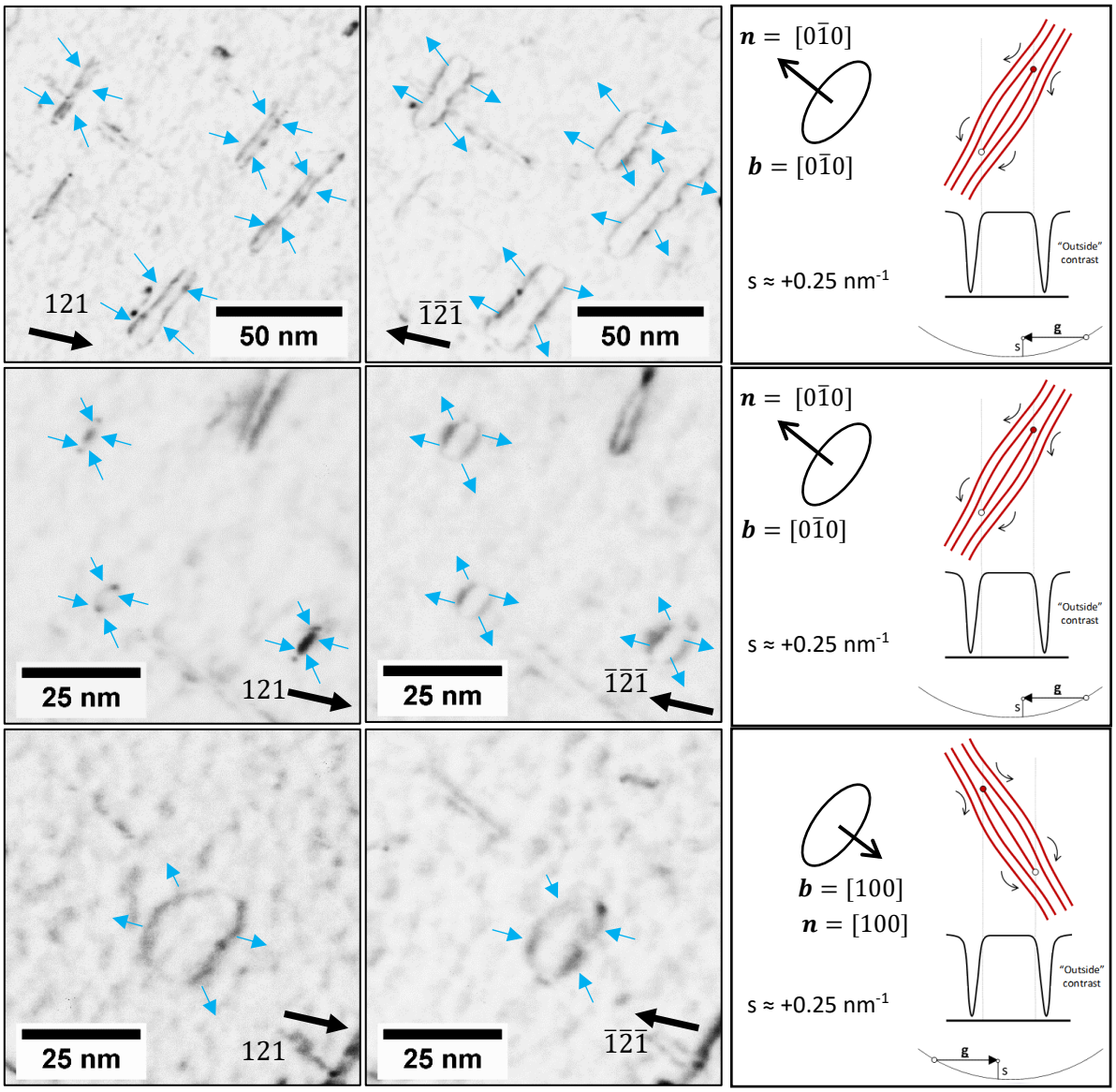

Figure 6.23: Nature analysis of dislocation loops in the proton irradiated Fe6Cr. The Burgers vector was inferred from the orientation of the loops. Inclination was determined by tilting from $[100]$ *to* $[2\bar{1}0]$. *All loops were found to be interstitial-type.*

It was difficult to determine the nature of loops in the self-ion irradiated sample due to the poor contrast from the loops. This made it difficult to verify an invisibility condition when correlating loops through multiple imaging conditions. The <100> type loops were easier to analyse since their Burgers vector can be inferred from their edge-on projection near the [100] zone axis, as was the case for the proton-irradiated sample. It was more difficult to determine the nature of <111> loops, which required more extensive **g.b** analysis to verify their inclination. Figure 6.24 shows the analysis for a selection of the loops.

The last example in Figure 6.24 is a cluster of four irregularly-shaped loops (which may alternatively be a larger number of small loops in close proximity to each other). The analysis of this cluster shows why nature determination (and counting) was very difficult here; the loops in the outside contrast condition are invisible for this example, or at least indistinguishable from surface oxide. The outside contrast condition usually exhibits a weaker signal than the inside condition, so in this case, the signal is similar or less than the contrast from the oxide layer. The loops all appeared narrower when viewed from the [100] zone axis, and are invisible in both plus and minus **g**=$1\bar{2}\bar{1}$ conditions. They are also invisible when **g**=± 011, and visible in **g**=$\bar{1}1\bar{2}$. This gives a strong indication that the loops have **b**=$\pm[11\bar{1}]$. Their habit plane is difficult to determine due to their irregular shape, but from their appearance, it seems they lie close to a $(11\bar{1})$ plane.

In total, 9 <111> and 6 <100> loops were analysed in the self-ion irradiated sample. All loops were found to be vacancy. This is unusual, and the result will be discussed at length in section-7.3.

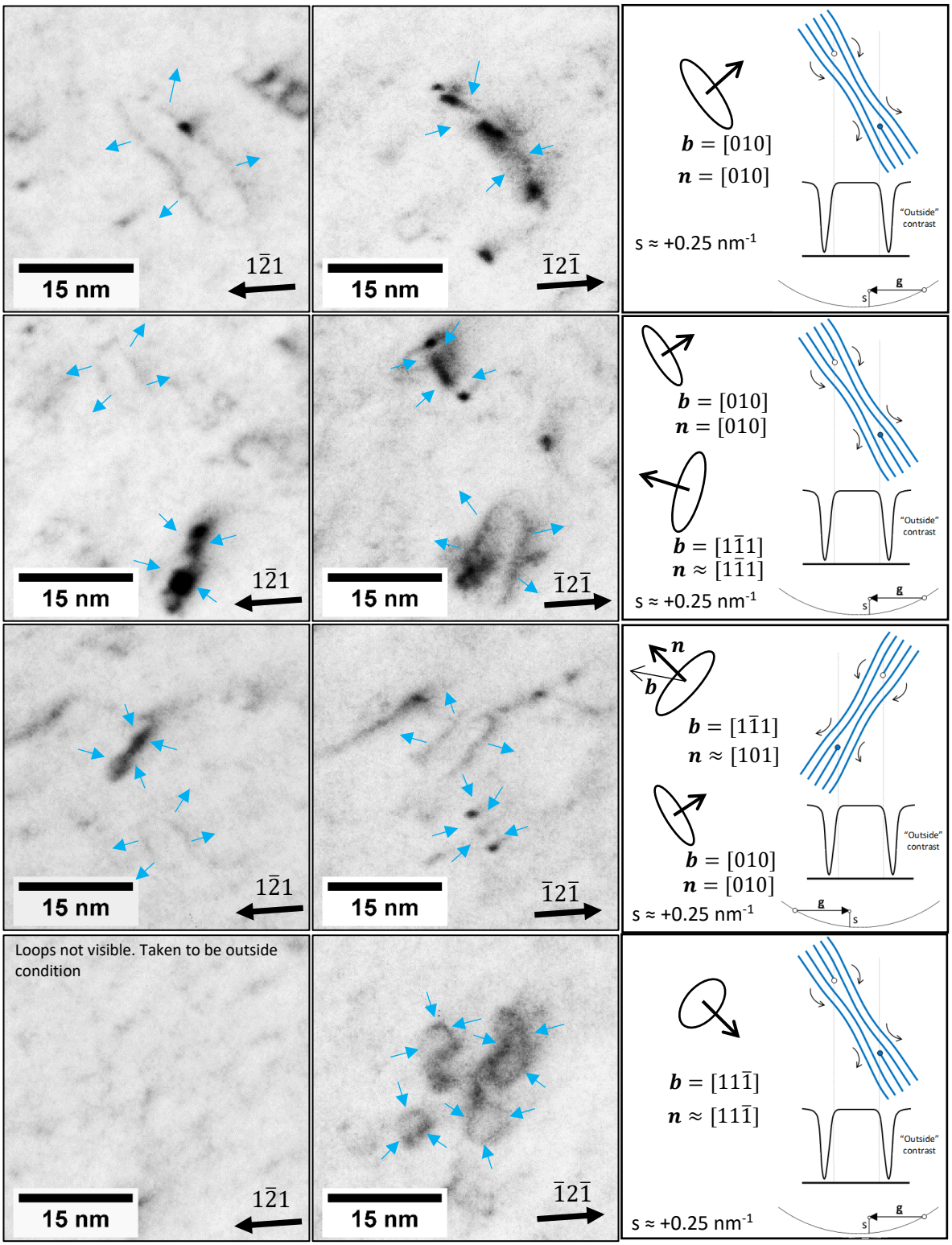

*Figure 6.24: Nature analysis of dislocation loops in the self-ion irradiated Fe6Cr. The Burgers vectors were determined by the **g.b** invisibility criterion, and from the orientation of the loop images. All 9 dislocation loops analysed were found to be vacancy-type.*

6.3.4 Size distributions of loops in proton and self-ion irradiated Fe6Cr

Dislocation loops were counted and sized using a range of g-vector conditions and foil orientations. Each micrograph is a summation of micrographs with slightly different deviation parameters and close to 0.2nm^{-1} on average, though for some conditions the deviation parameter was less than 0.2nm^{-1} in order to promote the signal from dislocations over the signal from surface oxide. For every g-vector condition captured, the negative-g condition was also captured to aid counting and accurate sizing. The size measured was taken as approximately the average image size of a loop as seen in the plus- and minus-g conditions.

The size distribution of dislocation loops in the self-ion irradiated Fe6Cr is shown in Figure 6.25 and in the proton-irradiated Fe6Cr in Figure 6.26. The size distributions for each condition used are shown in Appendix D.

To compare the loop sizes for different irradiating particle, the loop sizes were plotted as box and whisker diagrams in Figure 6.27. The red line in each box indicates the median loop size, which is a better measure of the average loop size than the mean here, since the loop sizes are not normally distributed.

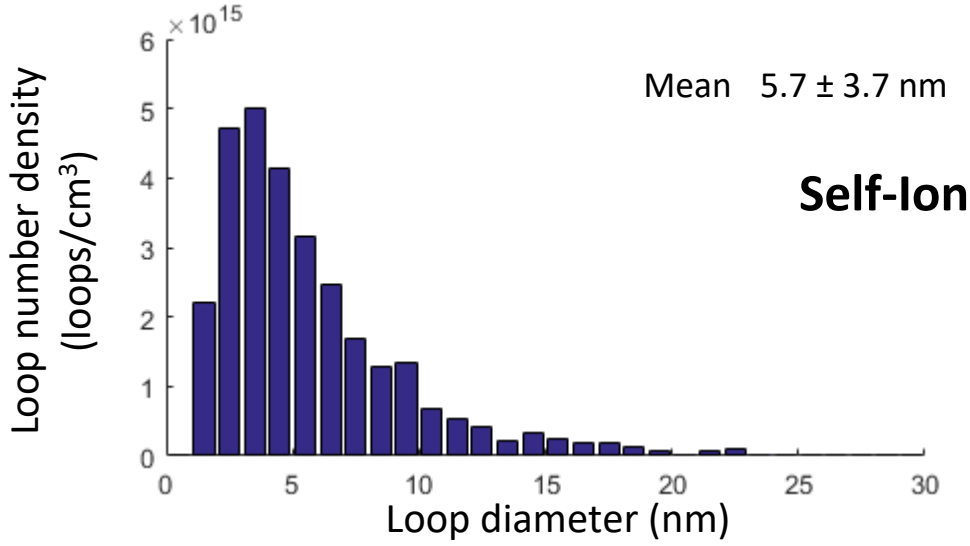

Figure 6.25: Overall size distribution for dislocation loops in the self-ion irradiated Fe6Cr

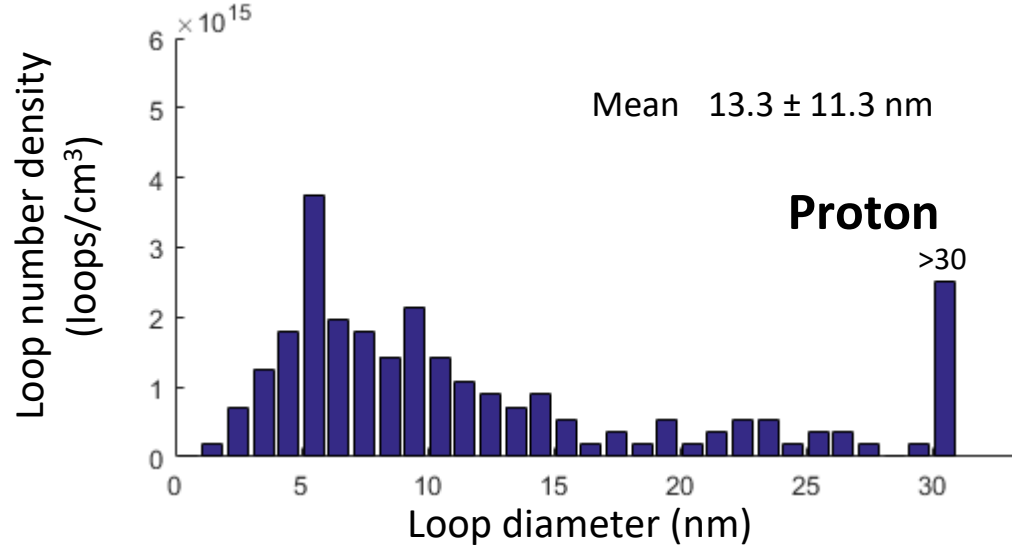

Figure 6.26: Overall size distribution for dislocation loops in the proton-irradiated Fe6Cr

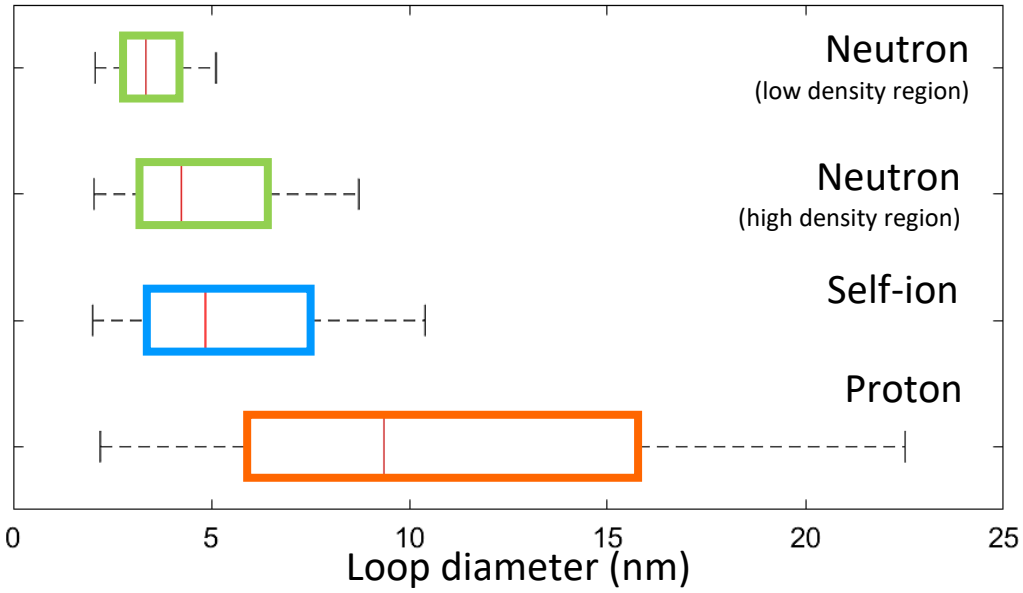

Figure 6.27: Box and whisker plots of the dislocation loop sizes in Fe6Cr irradiated with neutrons, self-ions and protons. The whiskers, box and red line on the plot from left to right indicate the 5th, 25th, 50th, 75th and 95th percentiles.

Figure 6.27 shows that the dislocation loops have slightly larger sizes in the self-ion irradiated sample than the high-density regions of the neutron-irradiated Fe6Cr. The loops in the proton-irradiated sample are overwhelmingly larger than those in the self-ion and neutron-irradiated samples.

To estimate the number of point defects contained within visible loops, the loop sizes were converted to atomic volume, and then plotted as a histogram again. For the self-ion irradiated sample, the total atomic volume was weight-averaged according to the <100> and <111> loop counts, using Equation 6.1 and Equation 6.2 to convert diameter to atomic volume.

Equation 6.1: $$V_{100} = 2\pi \left(\frac{D}{2a}\right)^2$$

Equation 6.2: $$V_{111} = \sqrt{3}\pi \left(\frac{D}{2a}\right)^2$$

This assumes the fraction of <111> and <100> loops does not change with size, which may not be true. It was also assumed that all loops can be treated as being circular, and that the atomic

volume of the irregularly shaped loops does not differ substantially from that of a circular loop with diameter equal to the size measured. The volume of a prismatic <100> loop of equivalent diameter to a <111> prismatic loop contains ~17% more point defects, so this estimate should be within ~20% of the actual total.

Since the majority of loops in the proton-irradiated Fe6Cr are <100> type, it would seem the calculation of atomic volume should be more reliable. However, Figure 6.28 shows that many of the loops are not circular, so it is inaccurate to simply convert this to a loop-area using πr^2. The loops in Figure 6.28 look like they were created from the coalescence of two or several smaller loops, so the true atomic volume of a loop is not necessarily correlated with the measured "diameter"[10].

Also, given that there is also a large population of loops with a measured size that is larger than half the foil thickness (and some larger than the full foil thickness), it is likely that some of the loops have shrunk or fragmented as the foil was thinned.

These factors lead to considerable uncertainty in estimations of the interstitial volume of the loops present in the proton-irradiated Fe6Cr. As a compromise, an estimate of lower and upper bounds of the interstitial total was made that accounts for these factors, making a large series of assumptions about the morphology of the loops in the process. The process and assumptions made are described in Appendix F.

[10] What has been measured as a size is not necessarily the diameter of a circle.

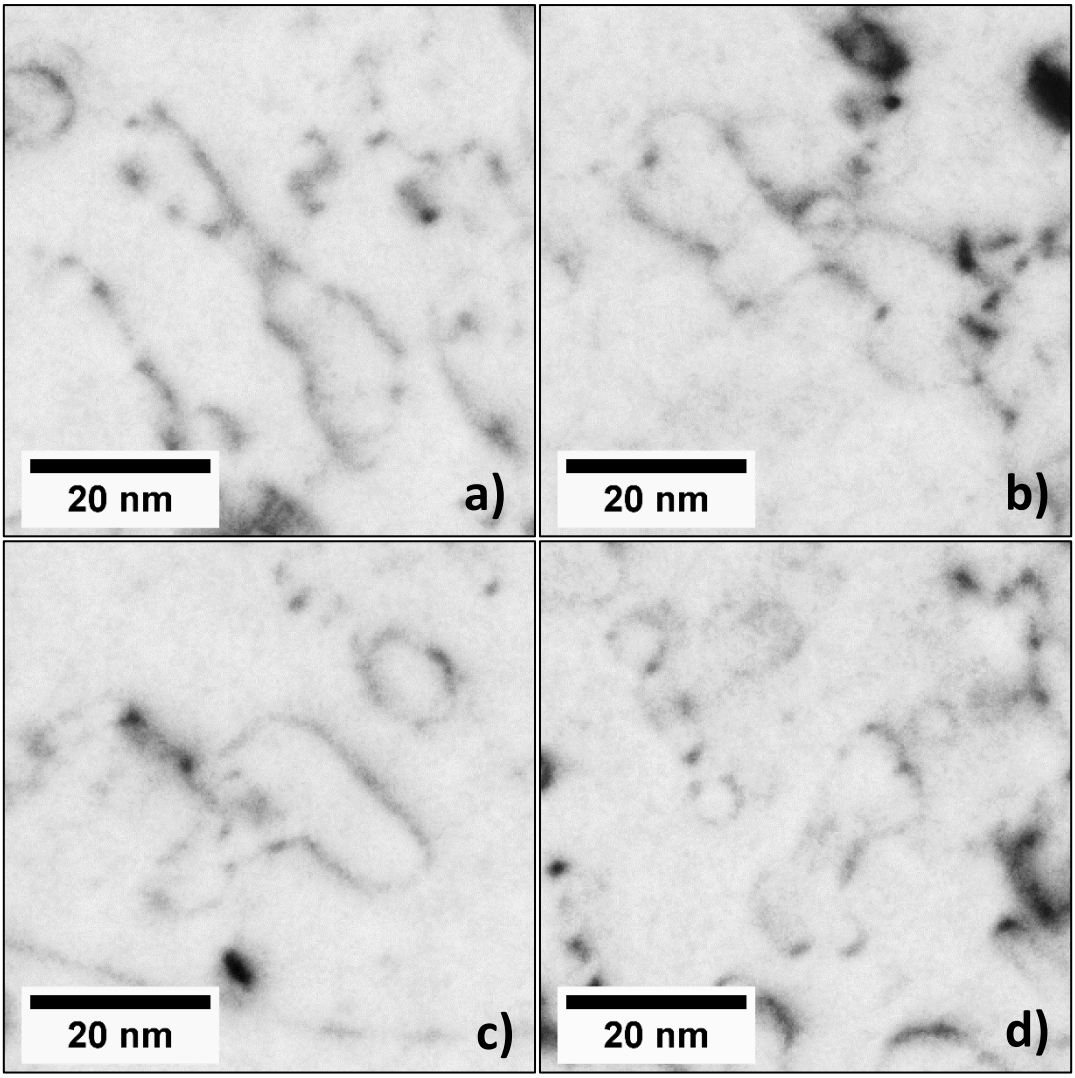

Figure 6.28: A selection of high magnification weak-beam micrographs in proton irradiated Fe6Cr showing irregularly shaped dislocation loops.

The total atomic volume of visible loops are shown in Figure 6.29 for the proton, self-ion and neutron-irradiated material. I have decided to show the estimates without any prediction of an invisible population of interstitials or vacancies from extending a power law to smaller cluster sizes. It was shown in sections 3.4.3 and 3.5.3 that this method contributes little to the overall total, and since the invisible limit should be approximately the same here as for the neutron-irradiated sample, it was considered to add an unnecessary layer of complexity to an already complicated and uncertain estimation of the populations.

The size distributions of the loops by atomic volume in the self-ion and proton-irradiated Fe6Cr, from which power laws were derived, are shown in Appendix G. The error bars added to the counts were calculated by the same method used in section-4.5.3, described in Appendix E.

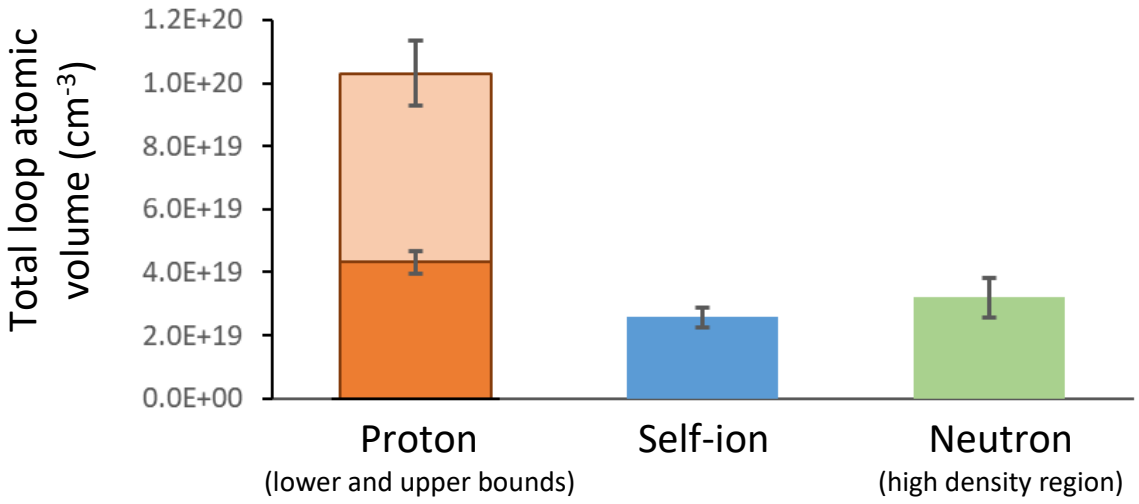

Figure 6.29: Comparison of the total number of point defects contained by visible dislocation loops produced by proton, self-ion and neutron irradiation. In section-6.3.3, only vacancy loops were found in the self-ion irradiated Fe6Cr, but only interstitials in the proton and neutron irradiated Fe6Cr.

Figure 6.29 shows that the self-ion irradiated sample contains slightly fewer point defects in visible loops than the high-density regions of the neutron-irradiated material. The interstitial count was not estimated for the low-density region of the neutron-irradiated sample due to the low counts. The total interstitial population of the proton-irradiated sample appear to be larger than the neutron irradiated sample, despite the large errors in the calculation of the interstitial population within the proton-irradiated sample.

6.3.5 Voids in proton and self-ion irradiated Fe6Cr

The under-over focus technique was used to look for voids in the ion and proton-irradiated Fe6Cr. The self-ion irradiated sample contained a selection of very small void-like features that had very weak contrast in the foil. Example under and over-focus micrographs are shown in Figure 6.30, which were captured from a thin region ~200nm into the damage profile, corresponding to a dose of ~1.2dpa.

Some of the features visible in Figure 6.30 appear facetted on {100} planes. The voids were counted and sized according to the criteria given by Ruehle et al. [180] and described in section-3.7. Example measurements are shown in Figure 6.31, and the results are summarised in Table 6.5.

By treating the measured void diameters as the diameter of a sphere, the total volume occupied by vacancies can be estimated, and the total number of vacancies contained. From this method, the total number of vacancies in the foil was found to be 1.4×10^{20} vacancies/cm^3. This value is an overestimate, since many of the voids appear facetted, so will have a volume smaller that of an equivalent diameter sphere. This value is also greater than the upper-estimate of the interstitials contained by visible loops (2.6×10^{19} interstitials), calculated in section-6.3.4.

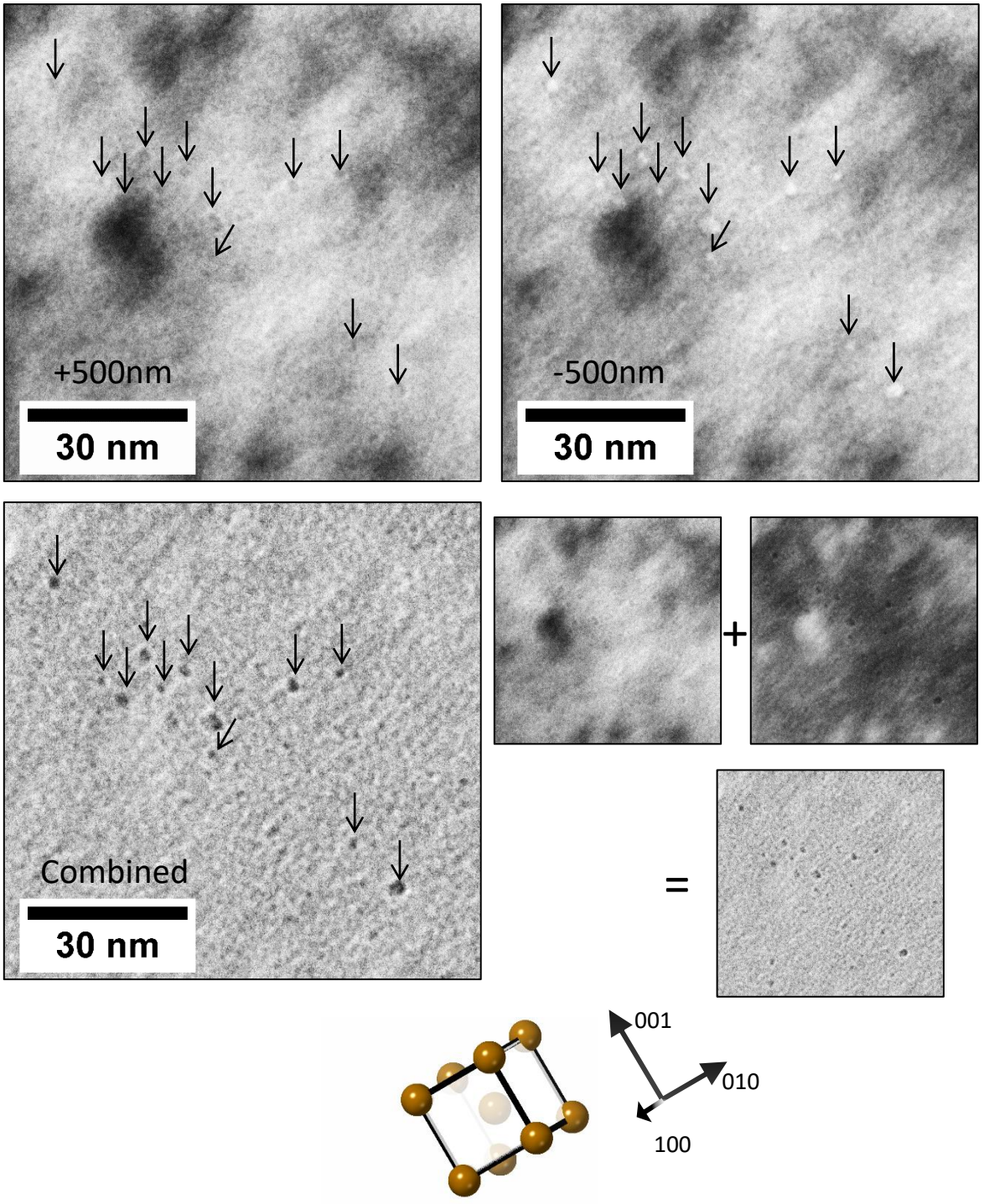

Figure 6.30: Micrographs of self-ion irradiated Fe6Cr, captured using the under-over focus technique to reveal voids in the microstructure. Example voids are indicated by arrows. A correctly-oriented image of a unit-cell with respect to the micrographs is also shown.

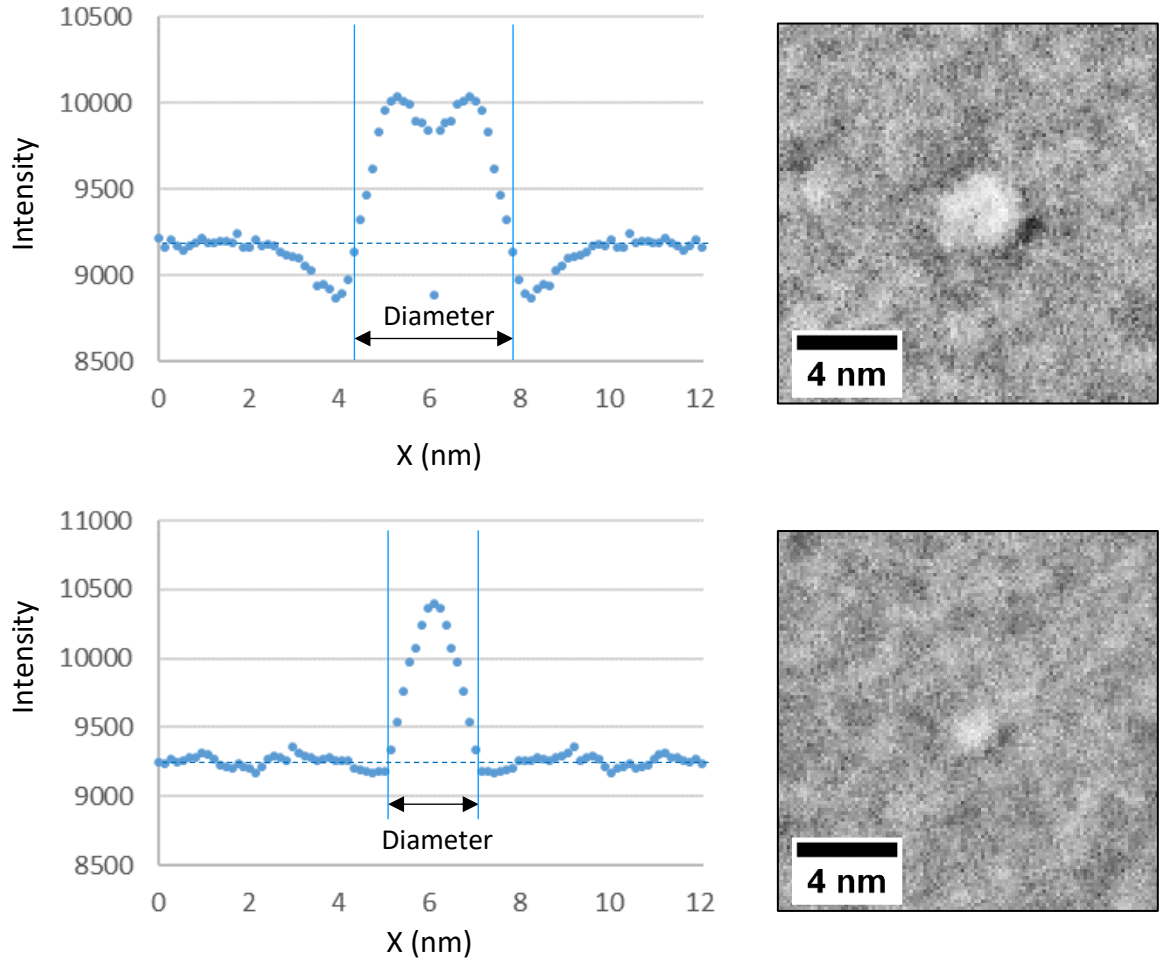

Figure 6.31: Examples of voids observed in the self-ion irradiated Fe6Cr

	Self-ion irradiated
Number density (voids cm^{-3})	1.0 ± 0.1 x10^{16} >2nm: 7.0 ± 1.2 x10^{15}
Mean diameter (nm)	2.4 ± 0.7
Maximum diameter (nm)	6.0
Minimum diameter (nm)	1.6

Table 6.5: Summary of voids in self-ion irradiated Fe6Cr

The proton-irradiated Fe6Cr contains a large population of large voids, as shown in Figure 6.32 using the under-over focus method. The voids have grown to much larger sizes (typically >5nm in diameter) than have been seen in the ion or neutron-irradiated samples (typically ~2nm). The voids appear mostly uniformly distributed throughout the matrix, though there are some instances of void chains visible, an example of which is visible in Figure 6.32 and shown at higher magnification in Figure 6.33.

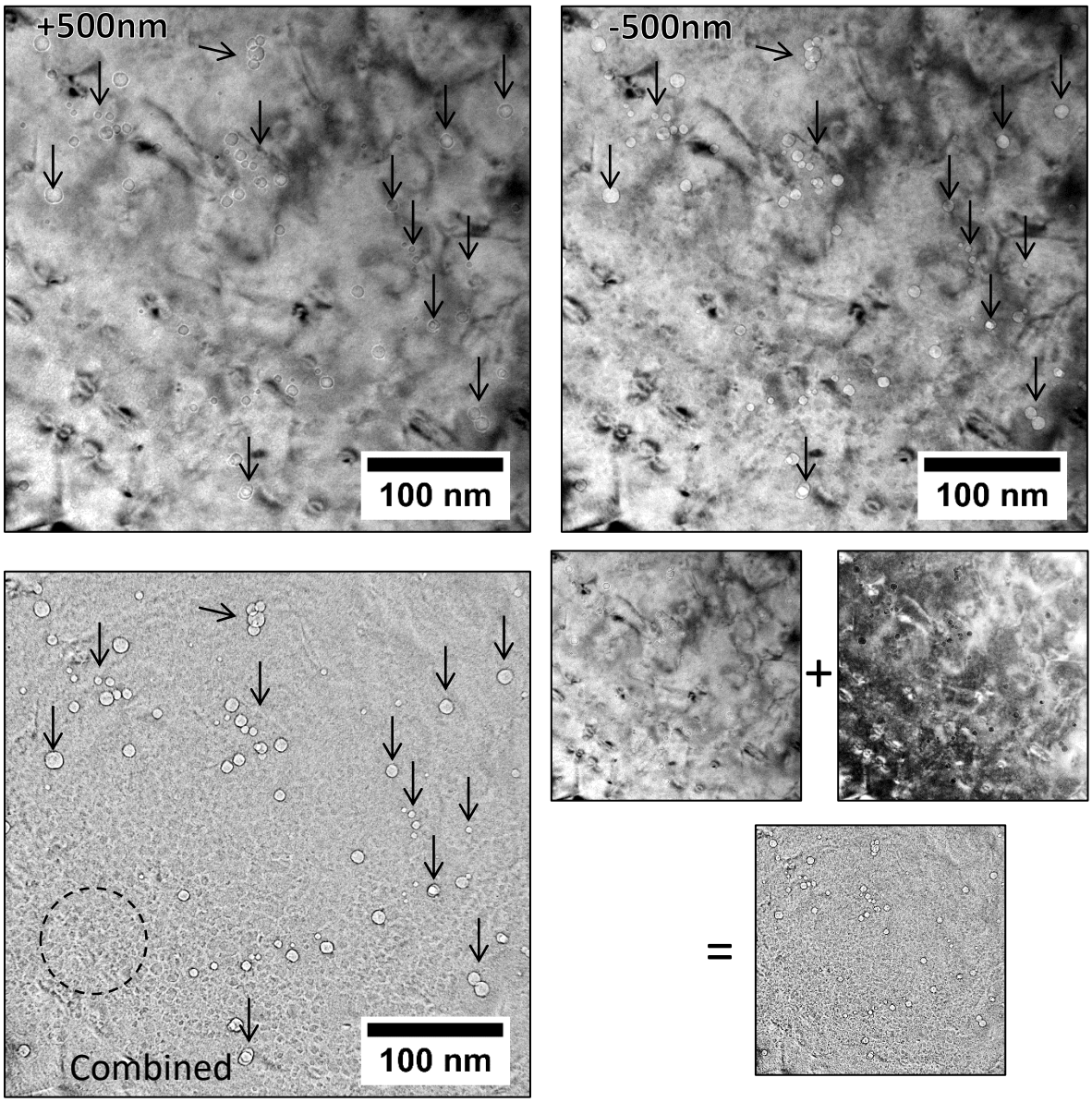

Figure 6.32: Micrographs of proton irradiated Fe6Cr, images using the under-over focus technique to reveal voids in the microstructure. The dotted circle in the combined image indicates a region rich in surface contaminants (possibly oxide). Example voids are indicated by arrows.

Since the Fe6Cr was irradiated with protons, it is possible that hydrogen is retained inside these cavities. The distinction between a bubble and void is hazy; Was [17] states that if the cavity is spherical, rather than facetted, it is more likely to be pressurised and should be designated as a bubble. This definition is just conjecture however. To observe the edge of the voids with more clarity, the under-over focus method was used with a smaller difference in focus of ±250nm to minimise the width of the Fresnel fringes. Contrast is reduced, but the shape of the voids becomes clearer.

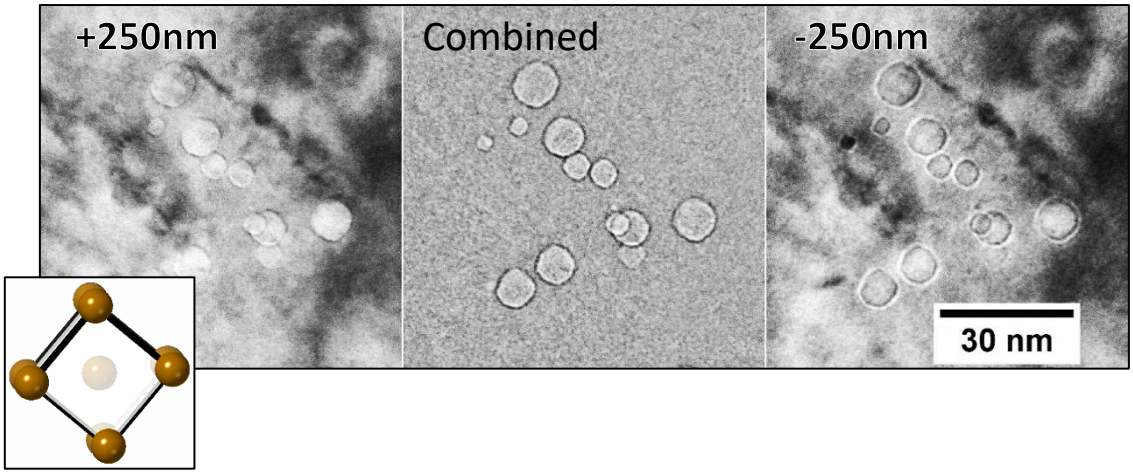

Figure 6.33: Higher magnification micrographs of a chain of voids in the proton irradiated Fe6Cr. A correctly-oriented unit cell with respect to the micrographs is shown. The voids are not exactly spherical, but neither do they have well-defined facets as might be expected of empty-cavities [17,197].

The out-of-focus images were captured with the foil tilted slightly away from a [100] pole, and this is depicted as a unit cell as part of Figure 6.33. From Figure 6.33, it can be seen than though the voids are not exactly spherical, they do not have well defined facets either. Some straight edges are visible for some voids, which line up with approximately {100} planes, but many appear to have a more complicated geometry, possibly with a combination of {100} and {110} (close-packed) facets. Very large voids will tend towards a spherical size [17] (though cubic-shaped voids are often seen in iron alloys over 10nm in diameter [197,198]), but at these sizes (<10nm) the facets observed here would be expected to be clearer if the cavities did not contain any gas [197,198]. This might indicate that hydrogen is contained by the cavities, and could be changing the surface energy of the cavity-

walls. However, a clearer assessment of the facetted/un-facetted nature of voids and bubbles across various materials is required to be conclusive of hydrogen's impact here.

The role of hydrogen has not been investigated further as part of this thesis, but future work could involve measuring the pressure inside the cavity, and/or looking to measure the hydrogen directly via EELS (both of which are very difficult things to measure on features at this scale).

Two example measurements of the voids are shown in Figure 6.34, and a summary of the measurements is shown in Table 6.6.

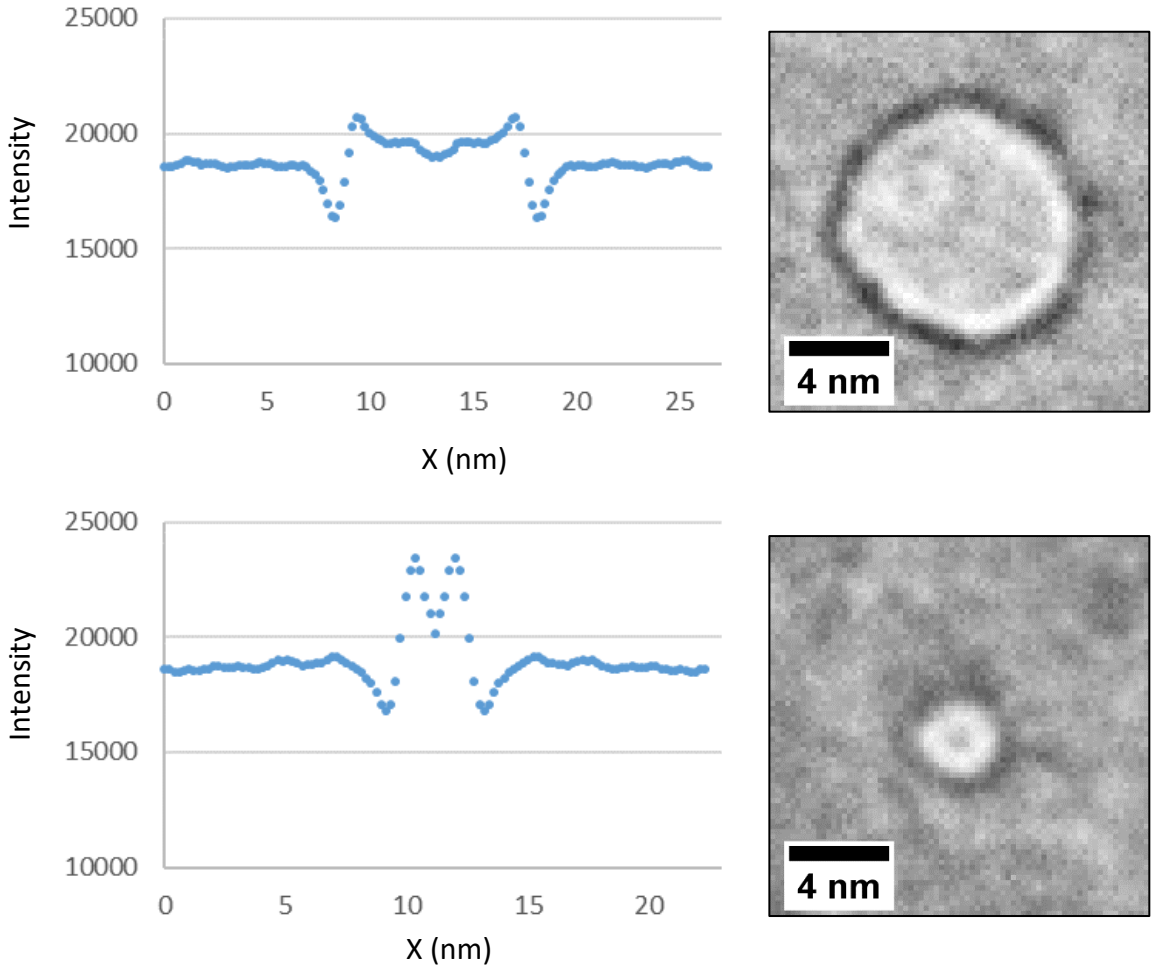

Figure 6.34: Examples of voids observed in the proton irradiated Fe6Cr

	Proton irradiated
Number density (voids cm^{-3})	1.1 ± 0.1 x10^{16} >2nm: 1.0 ± 0.1 x10^{16}
Mean diameter (nm)	5.7 ± 2.5
Maximum diameter (nm)	12.2
Minimum diameter (nm)	1.2

Table 6.6: Summary of voids in proton irradiated Fe6Cr

Figure 6.35 shows a comparison of the void populations in the Fe6Cr after neutron, self-ion and proton irradiation, and Figure 6.36 shows the same for the void sizes. These plots show that the measured void population in the neutron-irradiated sample is much higher; however, if only voids larger than 2nm are considered, the neutron-irradiated sample has the fewest. Since the measurement of <2nm voids can become very ambiguous due to the resolution and poor contrast of such features, and since these features are easily mistaken for FIB damage, oxide or other small particle contaminants, it is not possible to make reliable conclusions about <2nm voids.

Figure 6.36 shows what is clear from the micrographs – the voids in the proton-irradiated sample are much larger than those in the neutron and self-ion irradiated Fe6Cr. The smallest voids are contained by the neutron-irradiated sample, which implies vacancy diffusion is enhanced during proton irradiation and self-ion irradiation.

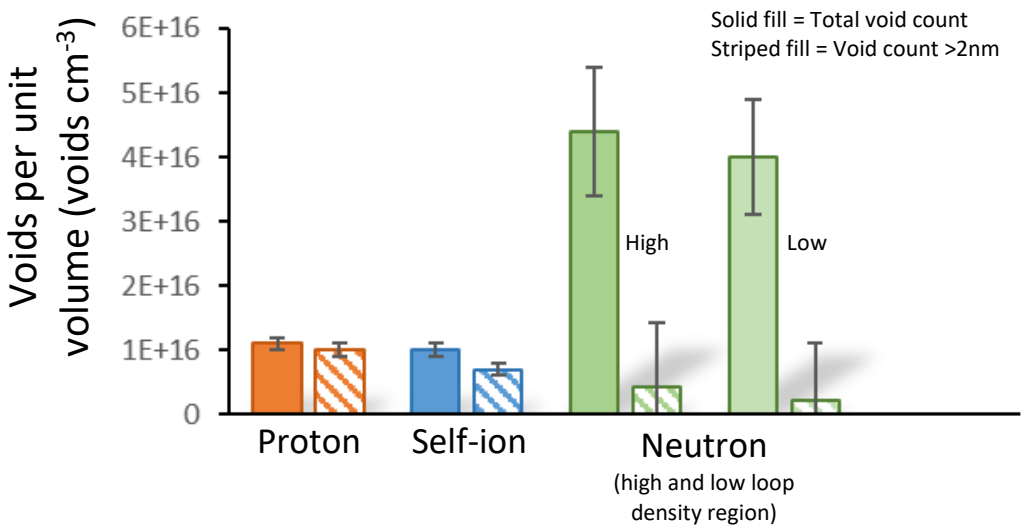

Figure 6.35: Void populations in Fe6Cr after proton, self-ion and neutron irradiation

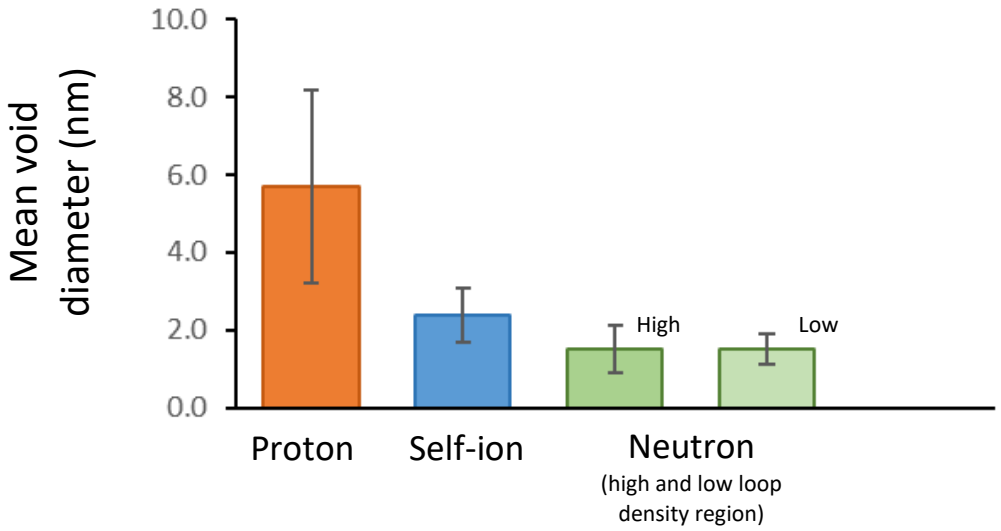

Figure 6.36: Void sizes in Fe6Cr after proton, self-ion and neutron irradiation

6.3.6 Redistribution of chromium in proton and self-ion irradiated Fe6Cr

EELS analysis of the ion-irradiated Fe6Cr was not attempted. The Fe9Cr, presented in the second half of this chapter, was actually studied before the Fe6Cr. EELS analysis was conducted on the Fe9Cr, in which were found no chromium precipitates of any kind. This will be shown in section-6.4.5. Since precipitation of chromium in the Fe6Cr has already been shown to be far less severe than the Fe9Cr from the results of the neutron-irradiated samples (sections 3.4.5 and 3.5.5), it was decided not to spend time looking for such precipitation in the ion-irradiated Fe6Cr sample.

EELS analysis of the proton-irradiated Fe6Cr is presented here. Since the dislocation loops and voids were much larger than those seen in the self-ion or neutron-irradiated samples, it was possible to conduct in-depth analysis of the chromium distribution around such features.

Figure 6.37 and Figure 6.38 show the edge model fitted to a pixel of an EELS map of various defects (Figure 6.39) and the edge model fitted to the whole image, with fine structure included in the fit. The composition was scaled to the extracted composition from the fine structure model.

Figure 6.39 shows a HAADF (high-angle annular dark field) micrograph of a region of the foil containing various dislocations loops and voids. Also shown is the extracted chromium map of the same region, in which there is a clear inhomogeneous distribution of chromium throughout the region. All regions of enrichment appear to correlate with a defect in the HAADF image. Due to the varying shapes, sizes and types of defects, and the fact that the distribution of chromium could be non-uniform around loops, no attempt was made to deduct the matrix contributions to the measured chromium signal, and so the analysis here is mostly qualitative.

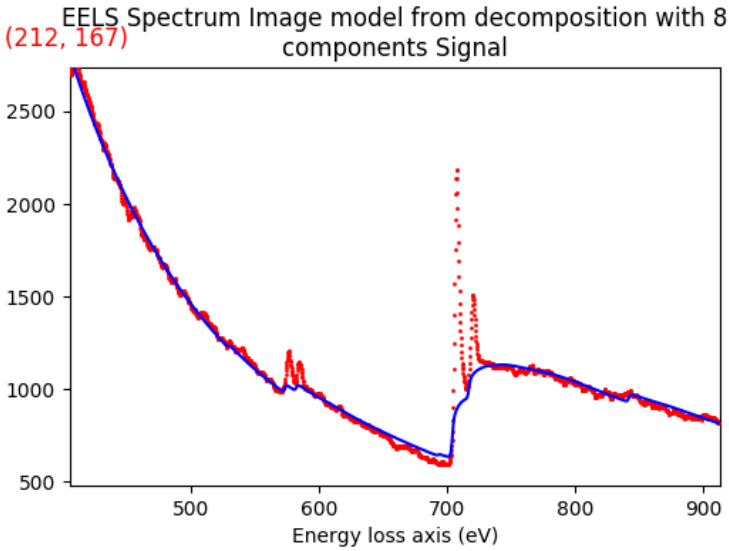

Figure 6.37: EELS spectrum from a single pixel the mapped proton-irradiated Fe6Cr, shown with the fitted model of the edges.

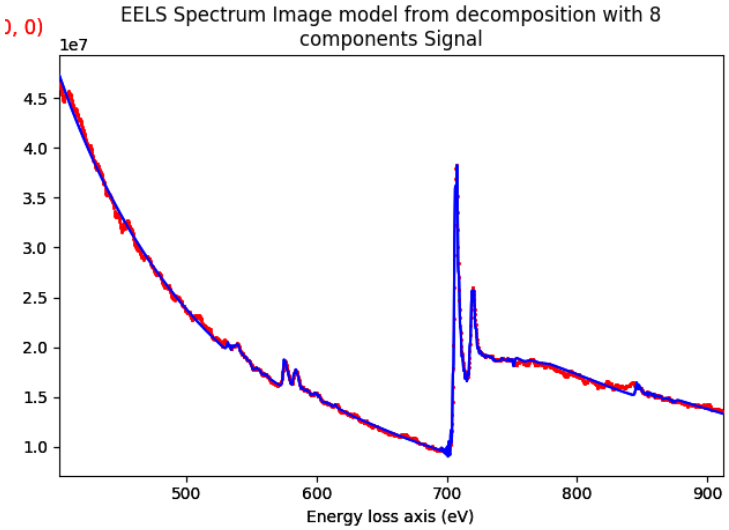

Figure 6.38: EELS spectrum from the whole region shown in Figure 6.39, with fine structure included in the fitted model of the edges

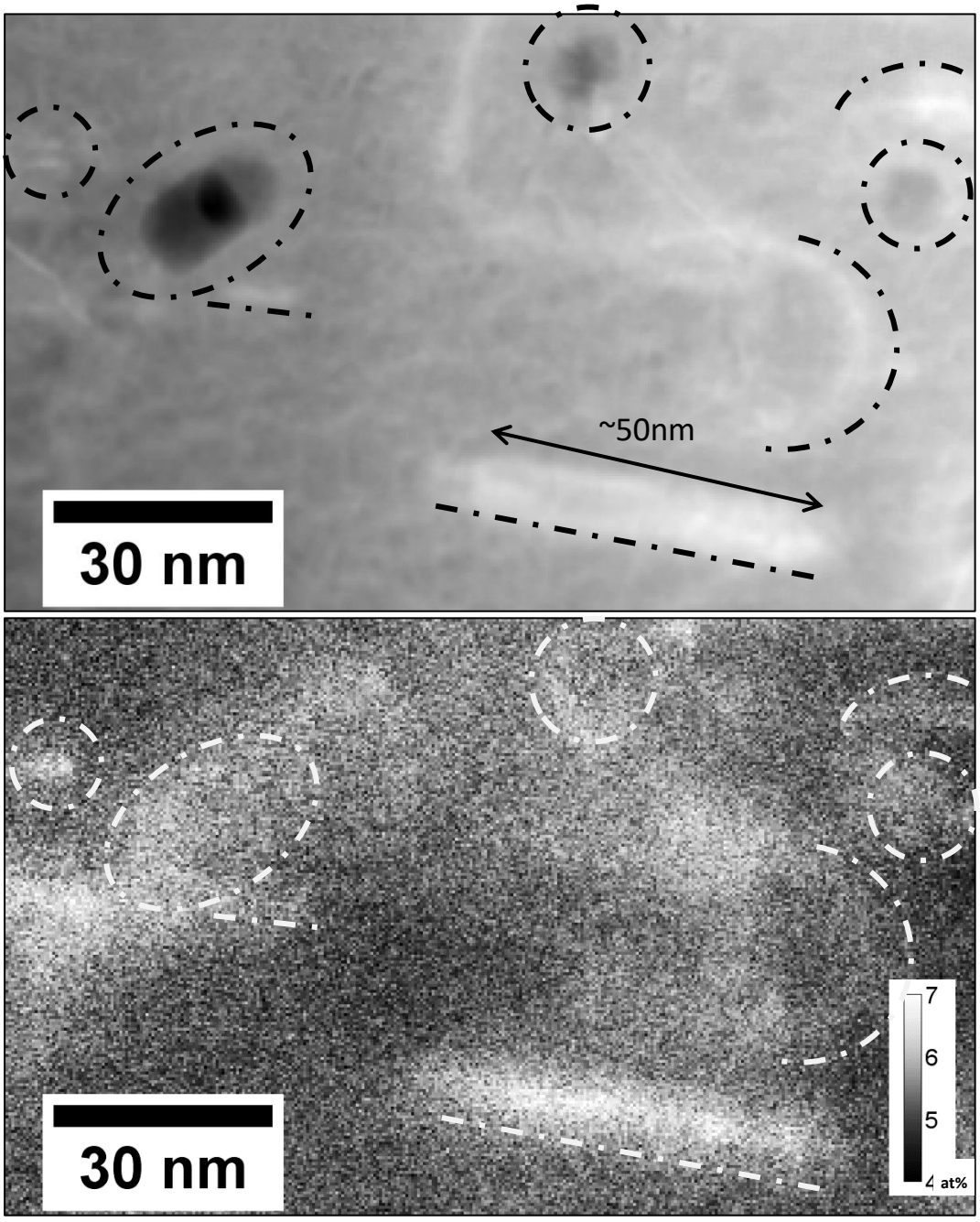

Figure 6.39: HAADF micrograph of proton irradiated Fe6Cr, (a) showing dislocations, dislocation loops and voids in the proton irradiated Fe6Cr, and (b) is the accompanying EELS-produced chromium map, showing enrichment of the defects visible in a).

The edge-on loops contain the highest signal of chromium in the map since the chromium is probably segregated evenly all around the dislocation core of the loop. Hence, there should be more chromium through the thickness of the foil for the edge loops than single dislocation lines. The large "S" shaped dislocation line visible in the HAADF image could be a segment of a dislocation (possibly helical), or one or more dislocation loops intersecting the foil surface. The chromium map shows there is slight enrichment of chromium on this dislocation, but the signal is very weak and masked by the chromium signal from other loops for most of the line length.

The voids also appear to be enriched with chromium, although every void is in close proximity to a dislocation defect, which may have contributed to the enrichment.

Figure 6.40 shows the chromium composition line profile of an edge loop both axially and across the plane of the loop. The profile across the plane was assumed to have a profile well approximated by a Wigner semi-circle distribution, and the profile through the axis of the loop was assumed to follow a Gaussian distribution.

The distribution fitted across the plane suggests a diameter of 60nm, which is larger than the diameter of 50nm measured from the HAADF image. This suggests the chromium profile extends radially beyond the dislocation core.

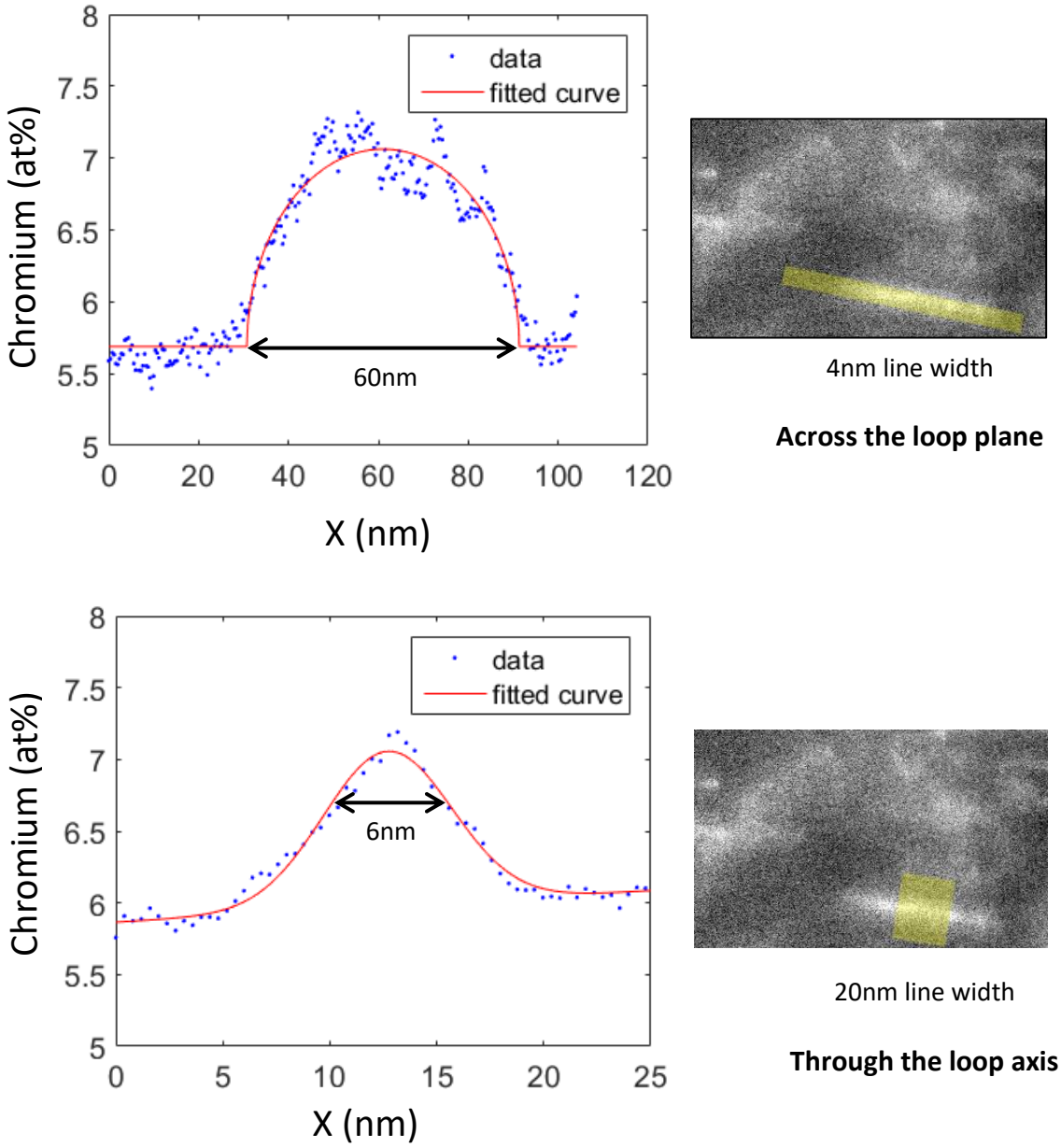

Figure 6.40: Chromium profiles from a dislocation loop in proton irradiated Fe6Cr, taken parallel and perpendicular to the plane of the dislocation loop. This shows the distribution of chromium around the dislocation loop.

It was assumed that chromium is segregated locally around the core of the dislocation, and so the profile of chromium through the foil thickness cannot be approximated as a single Gaussian function, as was done in sections 3.4.5 and 3.5.5, but should instead be approximated as the sum of two equal width Gaussian functions. When the chromium profile was approximated for the clusters in sections 3.4.5 and 3.5.5, it was assumed that the width of the profile was the same through the foil as the width we measured in the plane of the foil.

For this large dislocation loop, the chromium distribution may be different in the plane of the loop to the distribution in the direction orthogonal to the habit plane. Figure 6.41 shows this conundrum schematically. To quantify the enrichment of chromium around the core of the dislocation, atom probe tomography is a better technique since the reconstructed atom maps are three-dimensional. For EELS mapping, a tilt series is ideally required, but this was not performed due to time constraints. No attempt was made to quantify the chromium content around this loop any further.

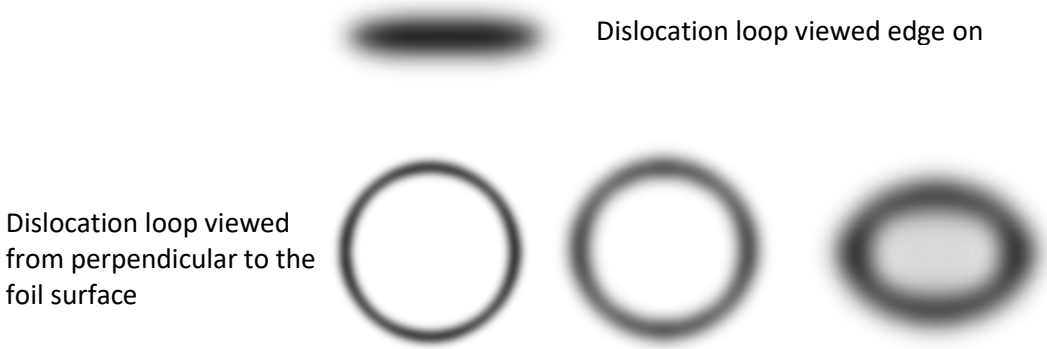

Figure 6.41: Various chromium profiles that may exist for a dislocation loop. Since the loop is only imaged from one orientation, the profile in the plane of this loop can only be speculated.

Figure 6.42 shows a HAADF micrograph of the proton-irradiated Fe6Cr captured with the specimen oriented down the [100] zone axis, in which an in-plane loop can be seen. The loop would usually be invisible in this condition from the **g.b** criterion, but this criterion is relaxed in STEM mode, allowing contrast to be seen either side of the dislocation core. Also shown in Figure 6.42 is a chromium map of the same region, and the intensity maps from the iron and chromium. It can be seen from these images that chromium has segregated on the dislocation loop. The core of the dislocation probably lies somewhere between the inside and outside bands of contrast, visible in the HAADF image.

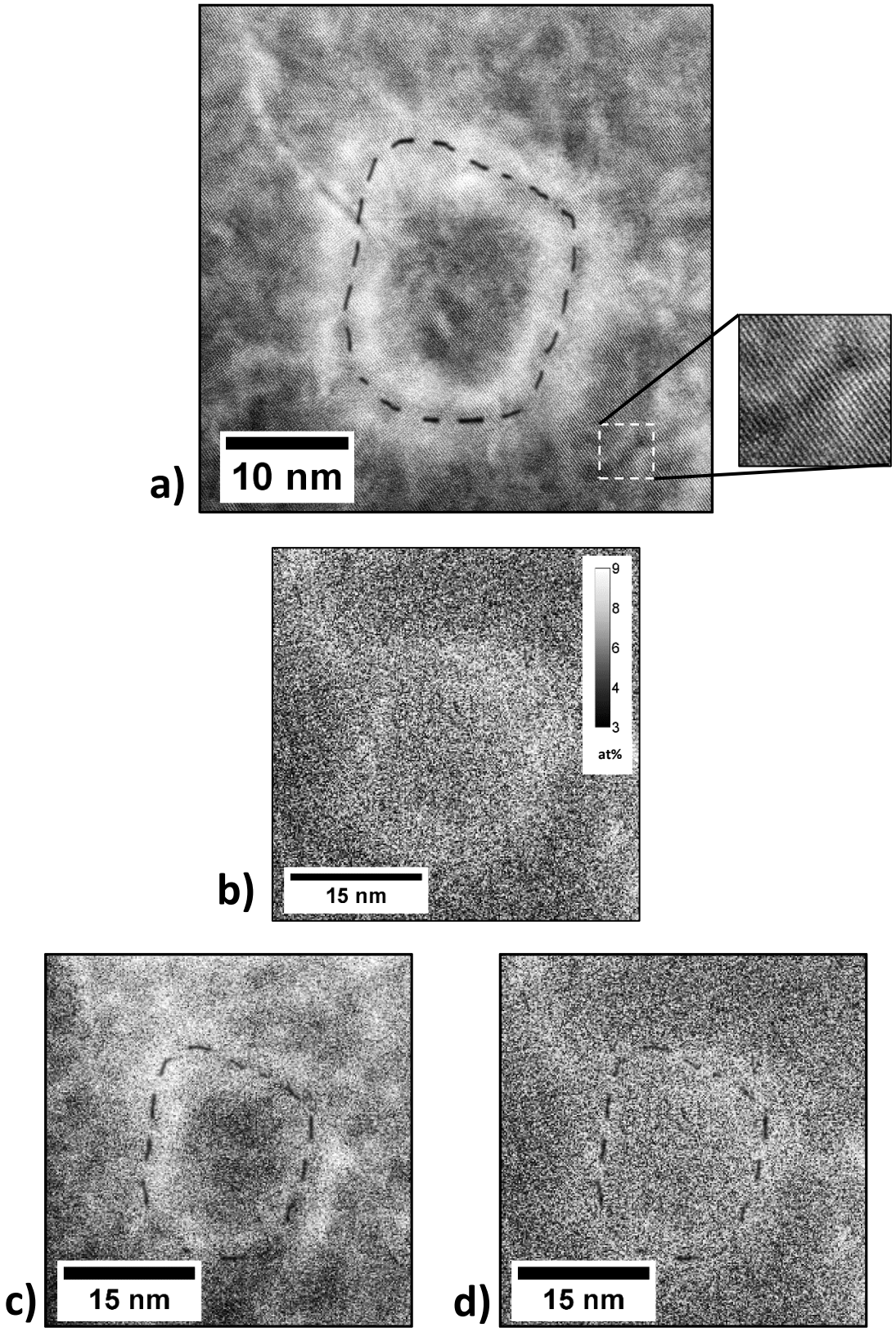

Figure 6.42: Various STEM and EELS maps obtained from an in-plane dislocation loop in the proton irradiated Fe6Cr. a) is HAADF image of the dislocation loop on the (100) plane; b) is the chromium map as atomic-percent of the volume imaged; c) and d) are the iron and chromium signal extracted from the EELS spectra, normalised to display similar contrast. The approximate location of the core is depicted by a dashed line in a), c) and d).

Figure 6.43 shows line profiles from the chromium, iron and HAADF signals (where the HAADF signal has been normalised to similar levels for display purposes). Also shown is the chromium composition as atomic-percent, with the HAADF signal also shown (again, normalised for display purposes). Lines have been added to the plots to indicate the rough position of the dislocation core, which was taken as the half-way point between the maxima of the inside and outside bands in the HAADF image.

These images and profiles show that the maxima in chromium composition coincide well with positions where the dislocation core is expected to lie. Figure 6.43 also shows that the inside of the dislocation loop has ~0.4at% more measured-chromium than outside of the loop. This suggests that the plane of interstitials that make up the dislocation loop is enriched with chromium, in addition to the enrichment immediately local to the dislocation core.

It is also apparent from Figure 6.43 that there is a gradient to the chromium composition profile across the image, which could originate from a non-uniform thickness over the mapped region. It is also a possibility for the gradient to be caused by other defects in the vicinity of the loop, e.g. there appear to be small chromium clusters to the right-hand side of the dislocation loop in Figure 6.42.

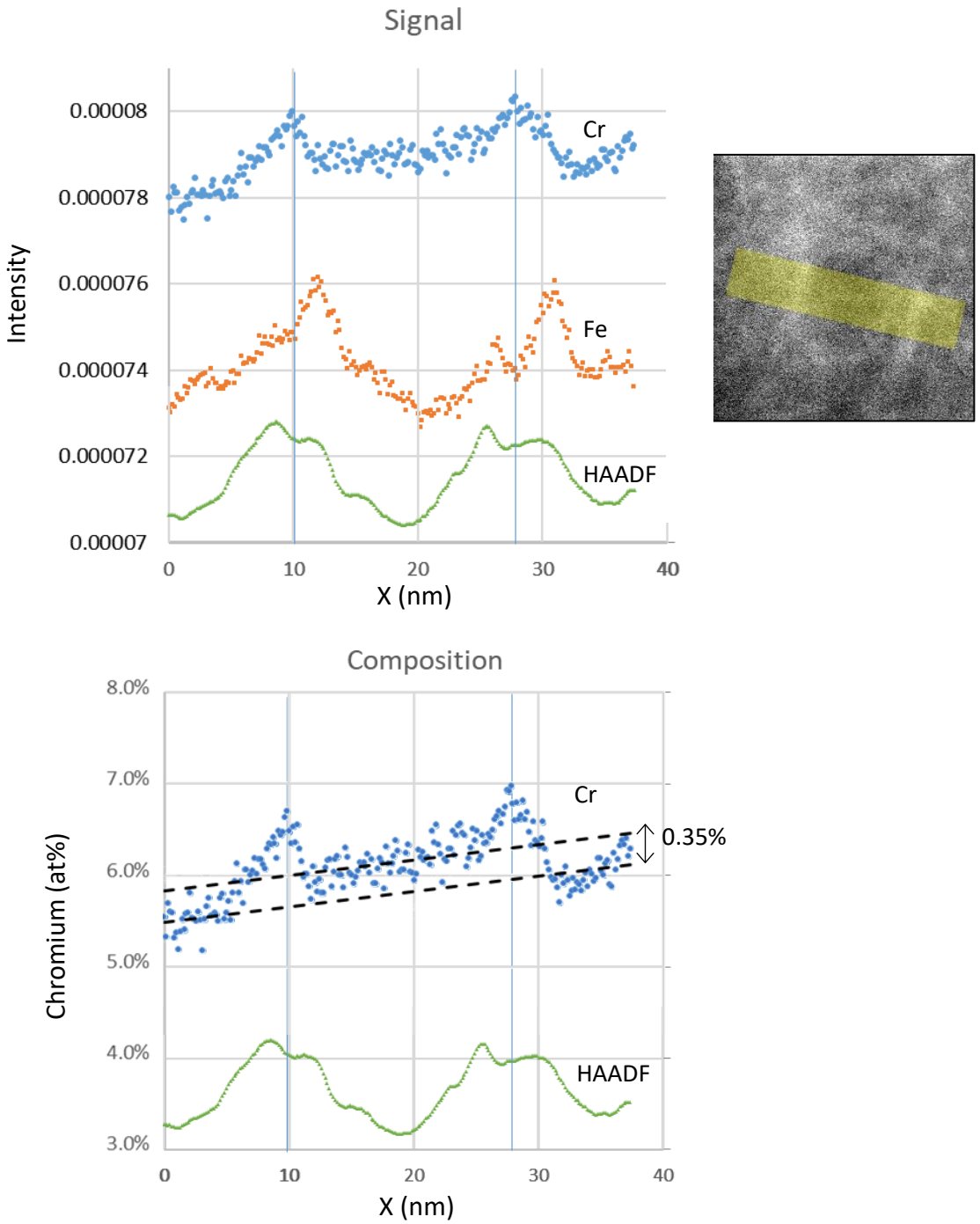

Figure 6.43: Extracted profiles of the iron, chromium and HAADF signals across the in-plane dislocation loop in the proton irradiated Fe6Cr, normalised to a similar mean intensity for display purposes. The corresponding chromium profile as atomic-percent is also shown. The HAADF signal in both plots has been normalised for display purposes.

To make a rough estimate of the actual chromium composition around the core (without any matrix contribution), the chromium distribution through the foil depth must be guessed. From the measurement of the edge loop in Figure 6.39, the chromium profile in the axial direction of the loop was found to have a Gaussian-like distribution with σ=3.0nm (where σ is the standard deviation of the fitted Gaussian function). Gaussian functions were also fitted to the chromium profiles around the two maxima in Figure 6.43, which were found to have σ=1.6nm.

It was then assumed that the chromium distribution through the foil thickness and core of the dislocation is well approximated by a Gaussian function with σ somewhere between 1.6 and 3.0nm.

The peak chromium composition of each maximum in the profile shown in Figure 6.43 was taken to be equal to the average composition of a Gaussian-like chromium profile through the foil thickness. Table 6.7 shows the measurements used for this analysis, and the end result. The rough estimate implies the chromium composition peaks at the core somewhere between 12 and 17at%.

The number density for chromium clusters in this material was not measured since the area analysed is quite small, and the chromium enriched regions seen all correlate with defects visible in the HAADF signal. It is probably fair to say that all dislocations, dislocation loops and voids in the proton-irradiated Fe6Cr have some local enrichment of chromium. This is something that was not possible to confirm in the neutron-irradiated Fe6Cr.

	Peak 1	Peak 2
Measured peak Cr composition (at%)	6.7	7.0
2x standard deviation of fitted Gaussian function - $2\sigma_p$ (nm)	3.1	3.1
Foil thickness at peak (nm)	42.9	42.0
Estimate of Cr composition near core (at%)	11.6-16.9	11.7-16.8

Table 6.7: Chromium composition close to the dislocation core of the in-plane dislocation loop in the proton irradiated Fe6Cr. The table includes the measured value, and an estimation of the enrichment when matrix contributions to the signal are removed.

The thickness used for these calculations was extracted from the low-loss spectrum map using the method described in section-3.6.2. This map is shown in Figure 6.44, which shows that the inside of the loop is ~1nm thicker than the outside. This is too much extra thickness to be attributed to the extra atomic planes[11] that make up the dislocation loop (0.286nm thick). When accounting for the variance in mean-free path of electrons due to the variance in chromium composition over the map, the thickness of the foil through the loop is on average 0.85nm thicker than regions outside the loop, equal to close to 5 atomic planes. The thicker region does not take-up the full area projected by the loop, so the extra thickness may simply be random fluctuations in thickness which coincidentally align with a dislocation loop. Further imaging and EELS mapping of in-plane dislocation loops is required to verify this, but this was not done as part of this thesis due to time constraints.

[11] A prismatic [100] dislocation loop in bcc consists of a platelet of two extra 200 planes.

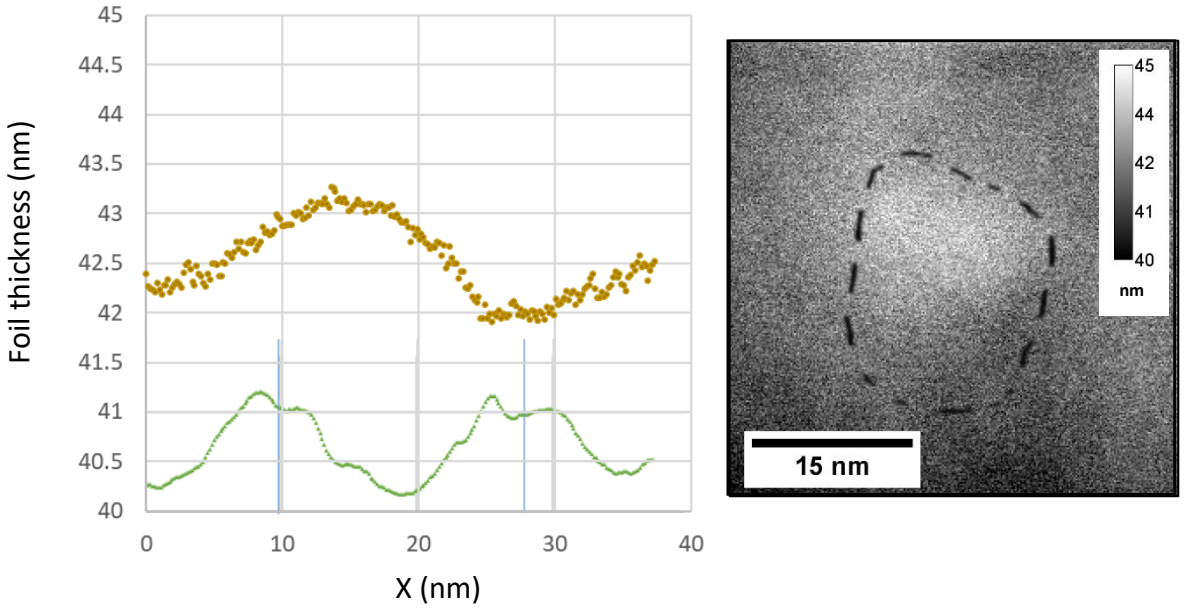

Figure 6.44: Thickness map of the region containing the in plane dislocation loop in the proton irradiated Fe6Cr. The column of material passing through the centre of the loop is thicker than the columns of material outside the loop.

6.4 Microstructure of proton and ion irradiated Fe9Cr

Figure 6.45, Figure 6.46 and Figure 6.47 show low magnification micrographs of the proton and self-ion irradiated Fe9Cr. Like the proton-irradiated Fe6Cr, the low magnification image of the proton-irradiated Fe9Cr was taken from a region at 2.0-2.5µm depth, equating to an average dose of 1.9dpa. The self-ion irradiated sample had the same peak dose of 2.2dpa as the ion-irradiated Fe6Cr, with an average dose in the region indicated in Figure 6.47 of 1.8dpa.

Figure 6.48 to Figure 6.55 show the typical microstructure of the proton and self-ion irradiated Fe9Cr. The proton-irradiated sample contains a heterogeneous distribution of defects, with higher-density regions found close to helical-dislocations, much like the neutron-irradiated Fe9Cr (section-4.5). The self-ion irradiated Fe6Cr contains more homogeneously-distributed damage prior to a decline in visible damage at depths beyond the Bragg-peak. Though some “wavey” dislocations are visible in the self-ion-irradiated microstructure, it is not clear whether these are helical.

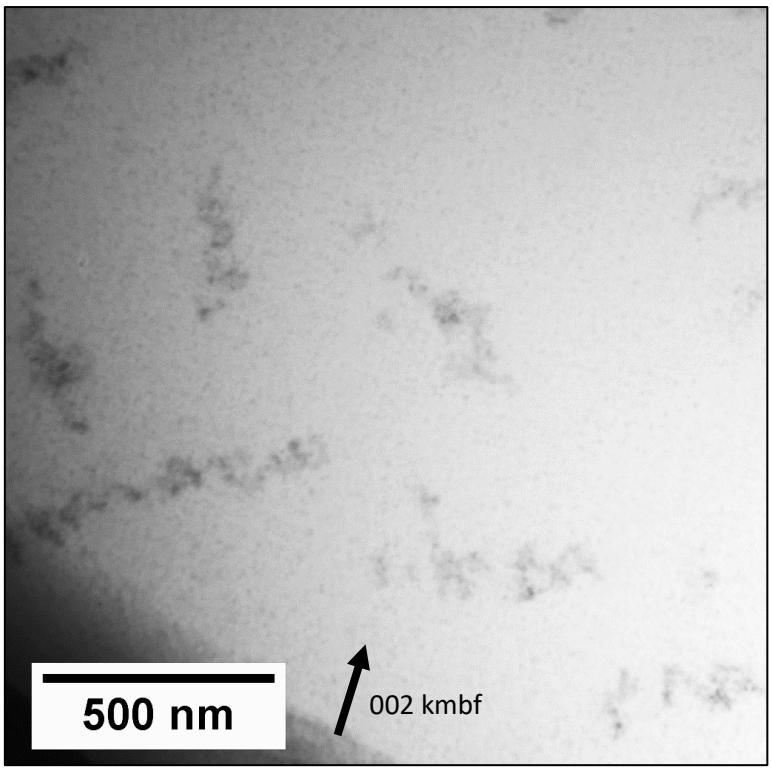

Figure 6.45: Kinematical bright field micrograph of the proton irradiated Fe9Cr

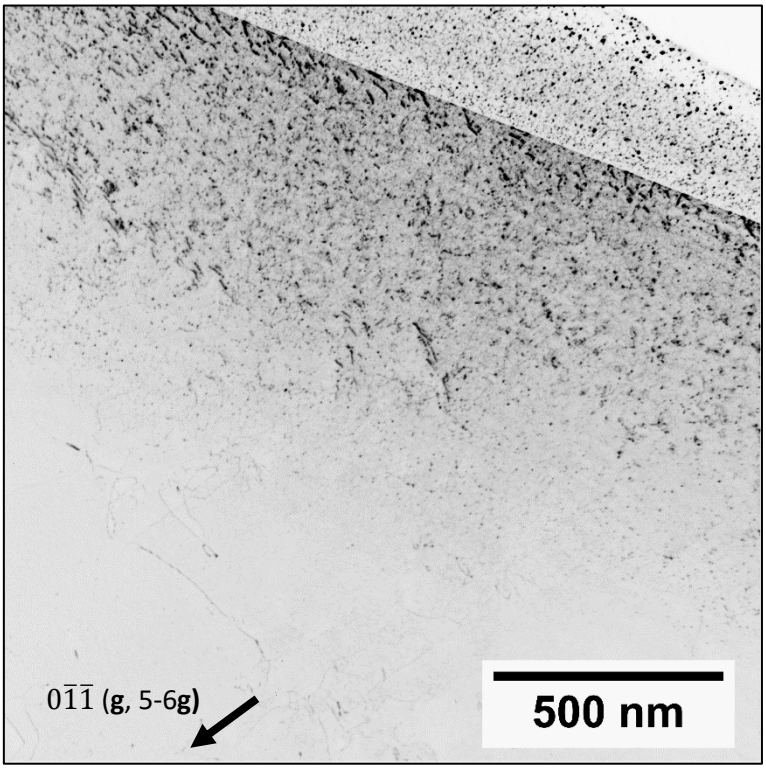

Figure 6.46: Weak beam micrograph of the self-ion irradiated Fe9Cr

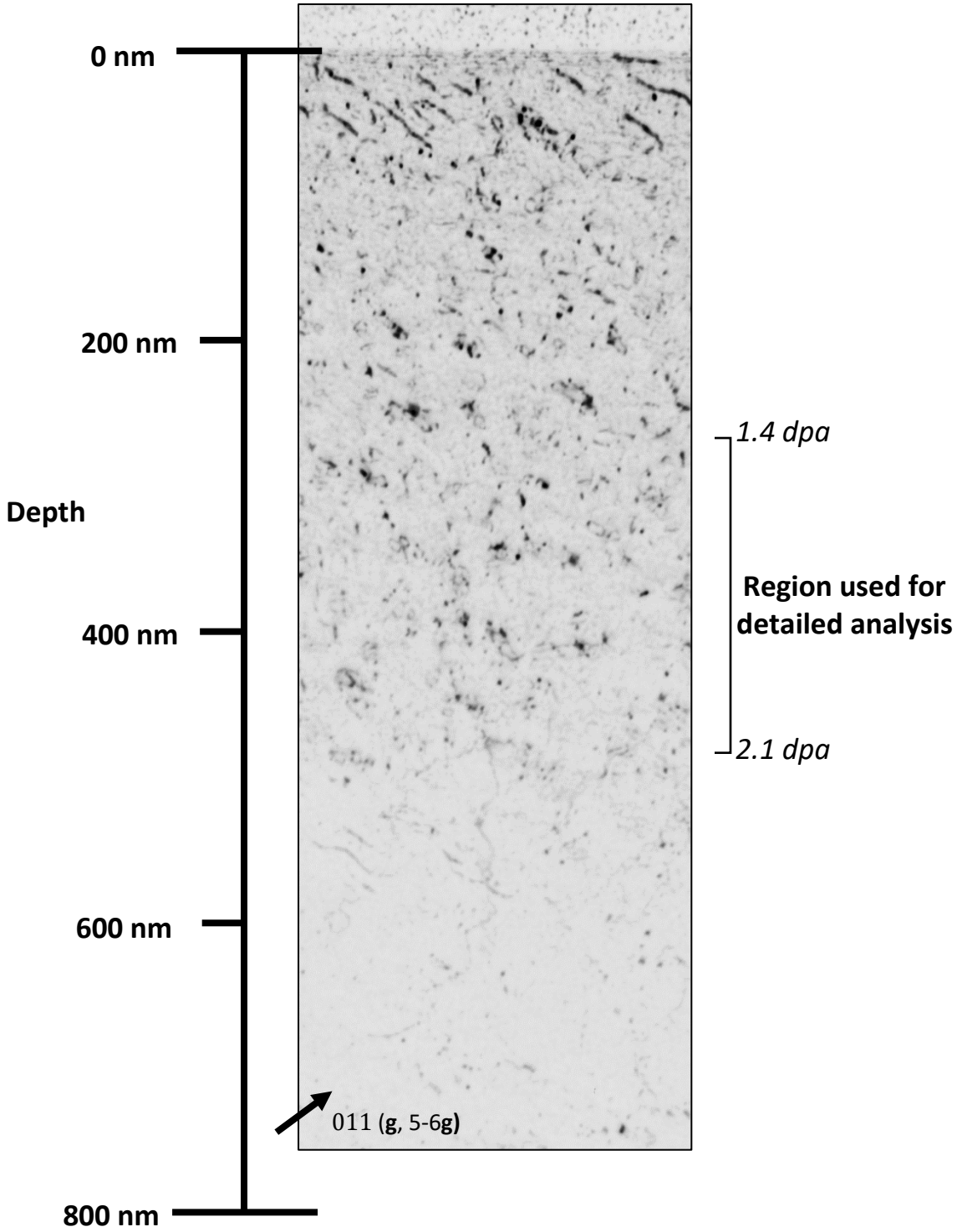

Figure 6.47: Low magnification weak beam image of the self-ion irradiated Fe9Cr

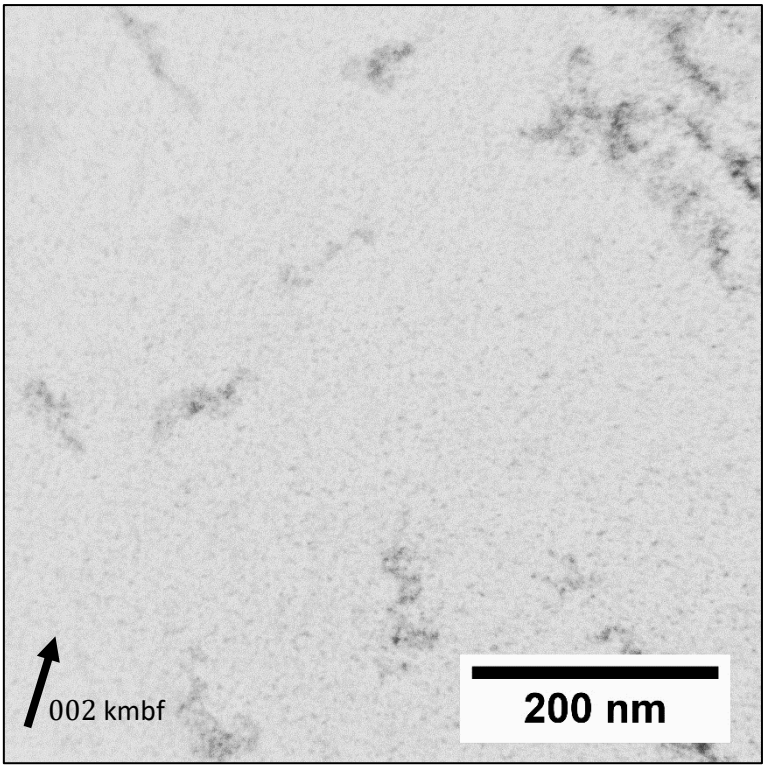

Figure 6.48: Kinematical bright field micrograph of the proton irradiated Fe9Cr. The original micrograph had a considerable contrast gradient, so the background has been subtracted for display purposes using ImageJ [174].

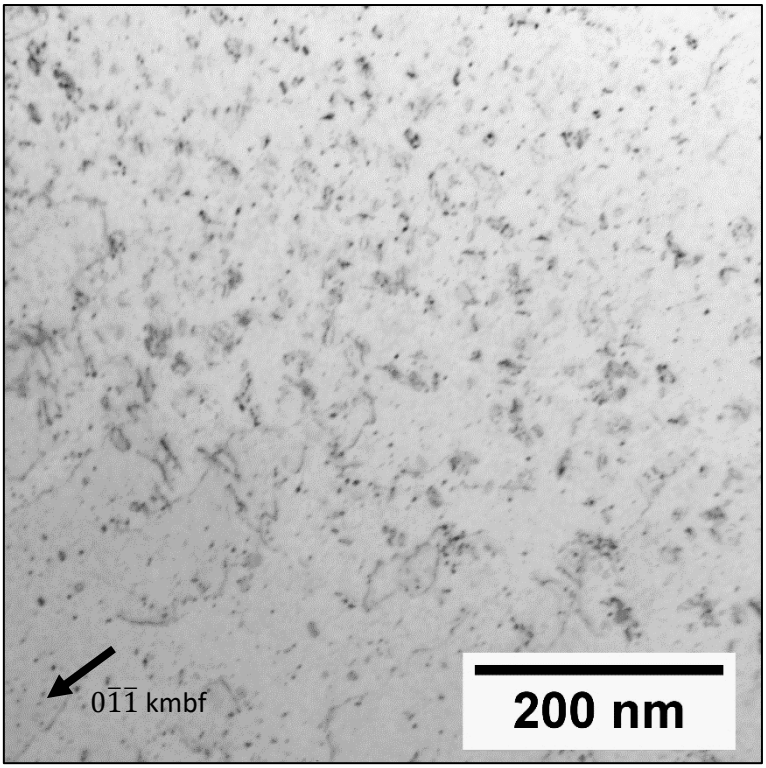

Figure 6.49: Kinematic bright field micrograph of the self-ion irradiated Fe9Cr

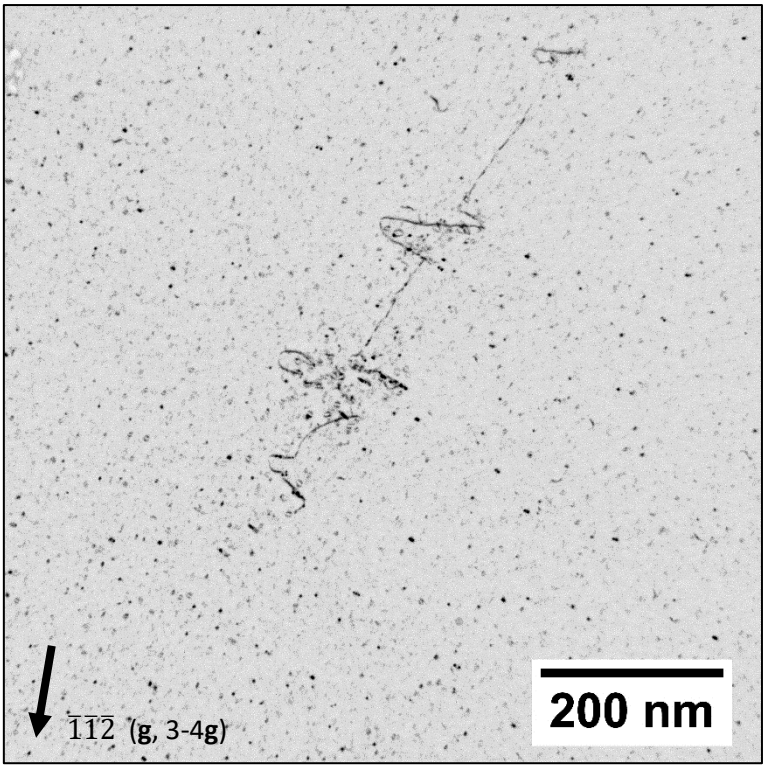

Figure 6.50: Weak-beam micrograph of a typical dislocation in the proton irradiated Fe9Cr

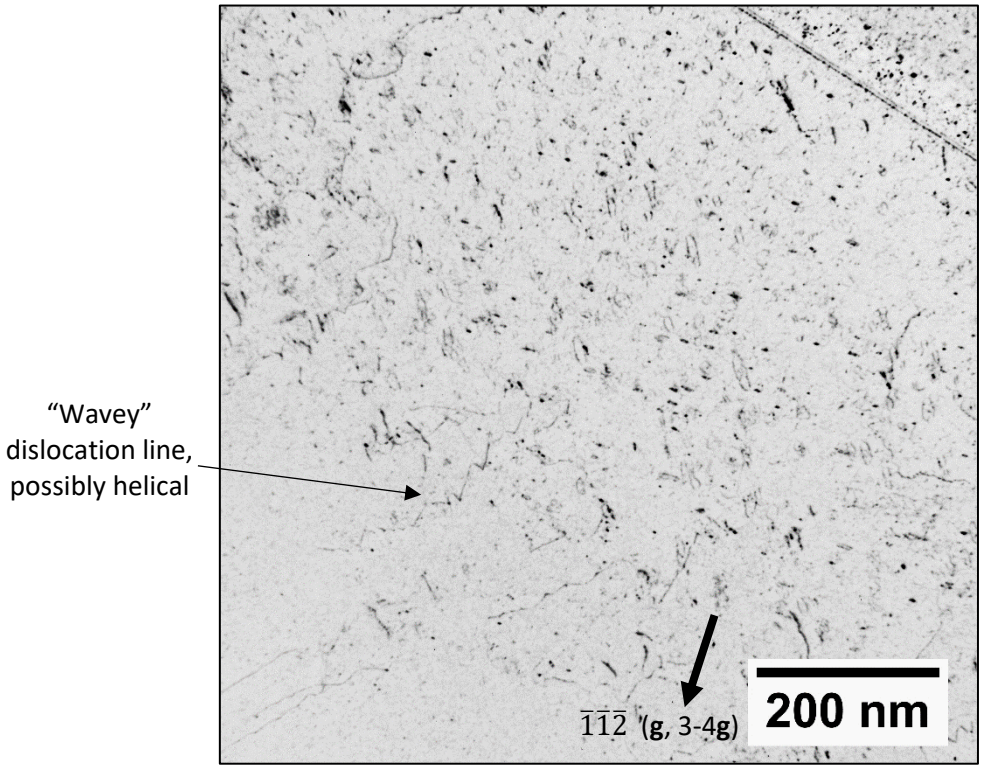

Figure 6.51: Weak beam micrograph of the irradiation layer in the self-ion irradiated Fe9Cr

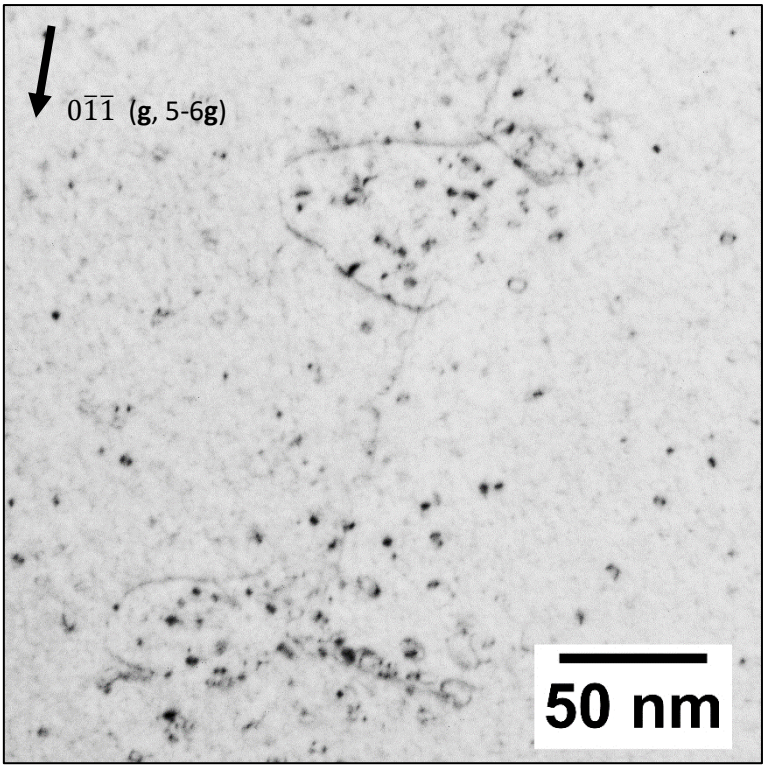

Figure 6.52: Higher magnification weak beam micrograph of an inclined dislocation in the proton irradiated Fe9Cr, captured with the foil oriented close to $[31\bar{1}]$*. The dislocation consists of straight and helical segments.*

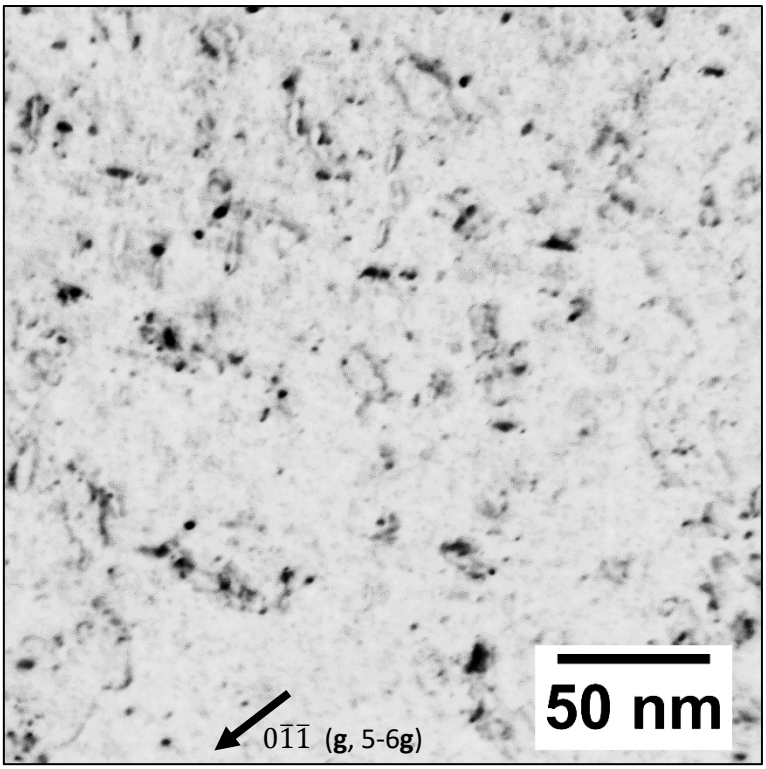

Figure 6.53: Higher magnification weak beam micrograph of the self-ion irradiated Fe9Cr

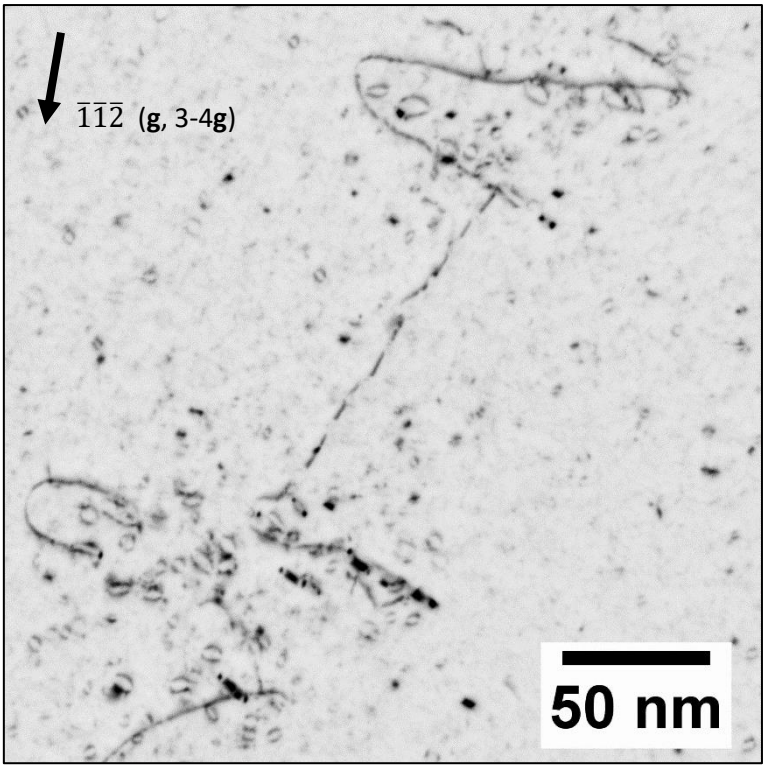

Figure 6.54: Weak beam micrograph of a dislocation in the proton irradiated Fe9Cr, captured with the foil oriented close to $[3\bar{1}\bar{1}]$*. The loop population is greater in regions confined by helical segments.*

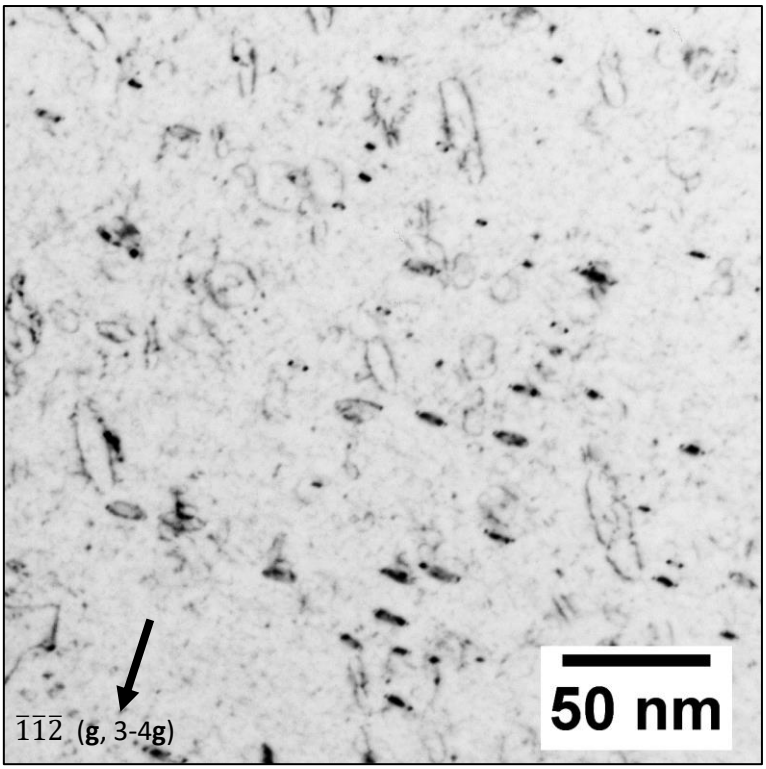

Figure 6.55: Weak-beam micrograph of the self-ion irradiated Fe9Cr, showing a selection of large (>20nm) dislocation loops.

6.4.1 Burgers vectors and number density of irradiation-induced dislocation loops in proton and self-ion irradiated Fe9Cr

Dislocation loops were imaged and counted in the proton and self-ion irradiated samples using a wide range of imaging conditions and foil orientations. Figure 6.56 shows an example of **g**.**b** analysis for the self-ion irradiated sample. The analysis of the ion-irradiated sample shows that a mixed population of <100> and <111> type loops is present.

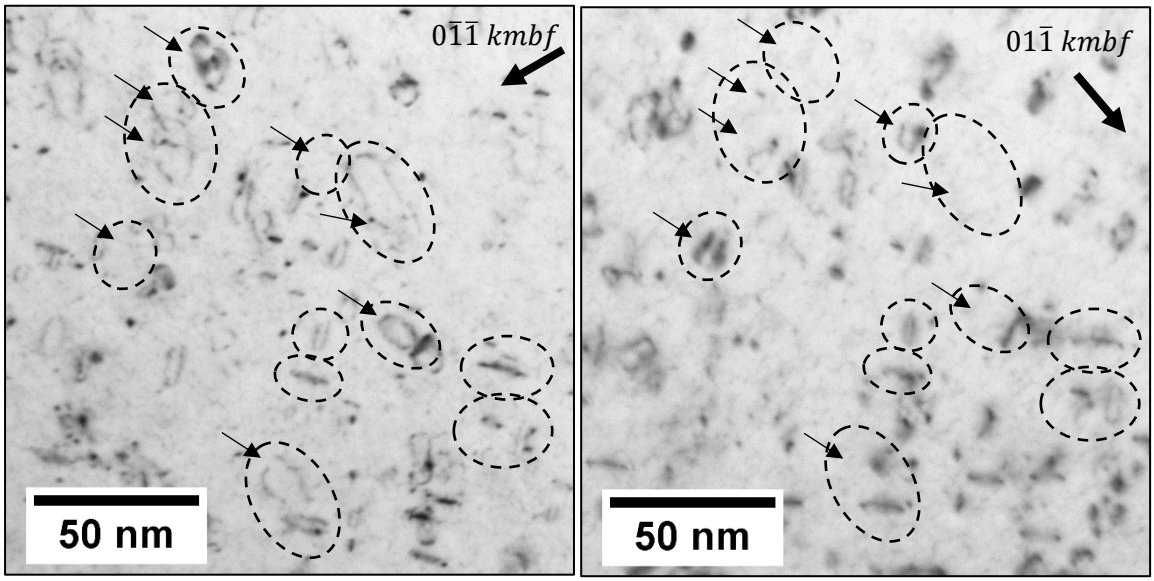

*Figure 6.56: Kinematical bright field images of the same region in the self-ion irradiated Fe9Cr using **g**-vectors $0\bar{1}\bar{1}$ and $01\bar{1}$. Dotted circles indicate a selection of <111> and <100> loops. Loops with an arrow shown are loops visible in only one condition (i.e. <111> type). The other loops are visible in both conditions, so are <100> type.*

Figure 6.57 shows **g.b** analysis of the proton-irradiated Fe9Cr around one of the helical dislocation segments. It was not possible to trace most of the loops in the $0\bar{1}\bar{1}$ condition with loops in the $0\bar{1}1$ condition due to the densely packed loops and the large tilt between conditions (~35 degrees). The overall fraction of <111> and <100> loops present in the self-ion irradiated and proton-irradiated Fe9Cr was ultimately determined by the statistical analysis method [172] (described in section-3.6.4).

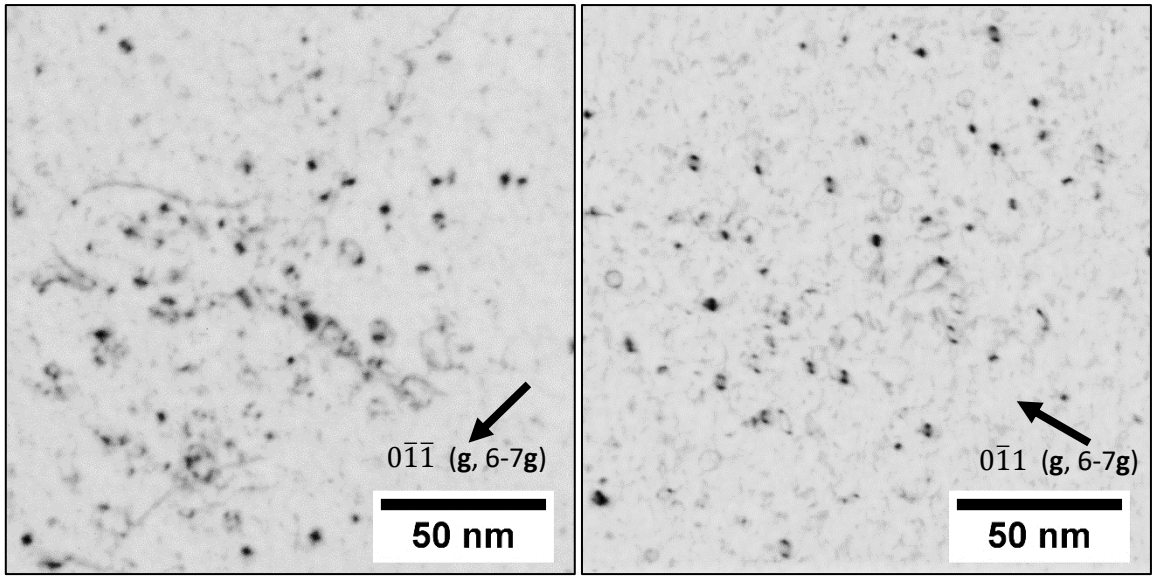

*Figure 6.57: Weak-beam dark field micrographs of the same region in the proton irradiated Fe9Cr using **g**-vectors $0\bar{1}\bar{1}$ and $0\bar{1}1$. The $0\bar{1}\bar{1}$ condition was captured close to the $[31\bar{1}]$ zone axis, and the $0\bar{1}1$ condition was captured close to the $[3\bar{1}\bar{1}]$ zone axis. To reduce the movement of the projected position of the loops, the images were rotated in order to align the dislocation.*

The visible loop density from each condition for the proton and self-ion irradiated Fe9Cr is shown in Figure 6.58, alongside the total loop density as calculated via the statistical analysis method. The counts were taken from the matrix far from dislocations, and also regions within a helical dislocation-segment, to produce measurements of the loop density from a high-density and low-density region.

A comparison of the proton, self-ion and the neutron-irradiated Fe9Cr dislocation loop number densities and Burgers vectors are shown in Figure 6.59 and Figure 6.60 respectively. These figures show that the neutron-irradiated Fe9Cr contains the highest loop-density regions of any of the samples, but also the lowest loop-density regions. The self-ion irradiated sample had a lower loop-density than the high-density regions of the neutron-irradiated Fe9Cr, but the loops were homogeneously distributed, so the overall visible-defect density is probably much higher.

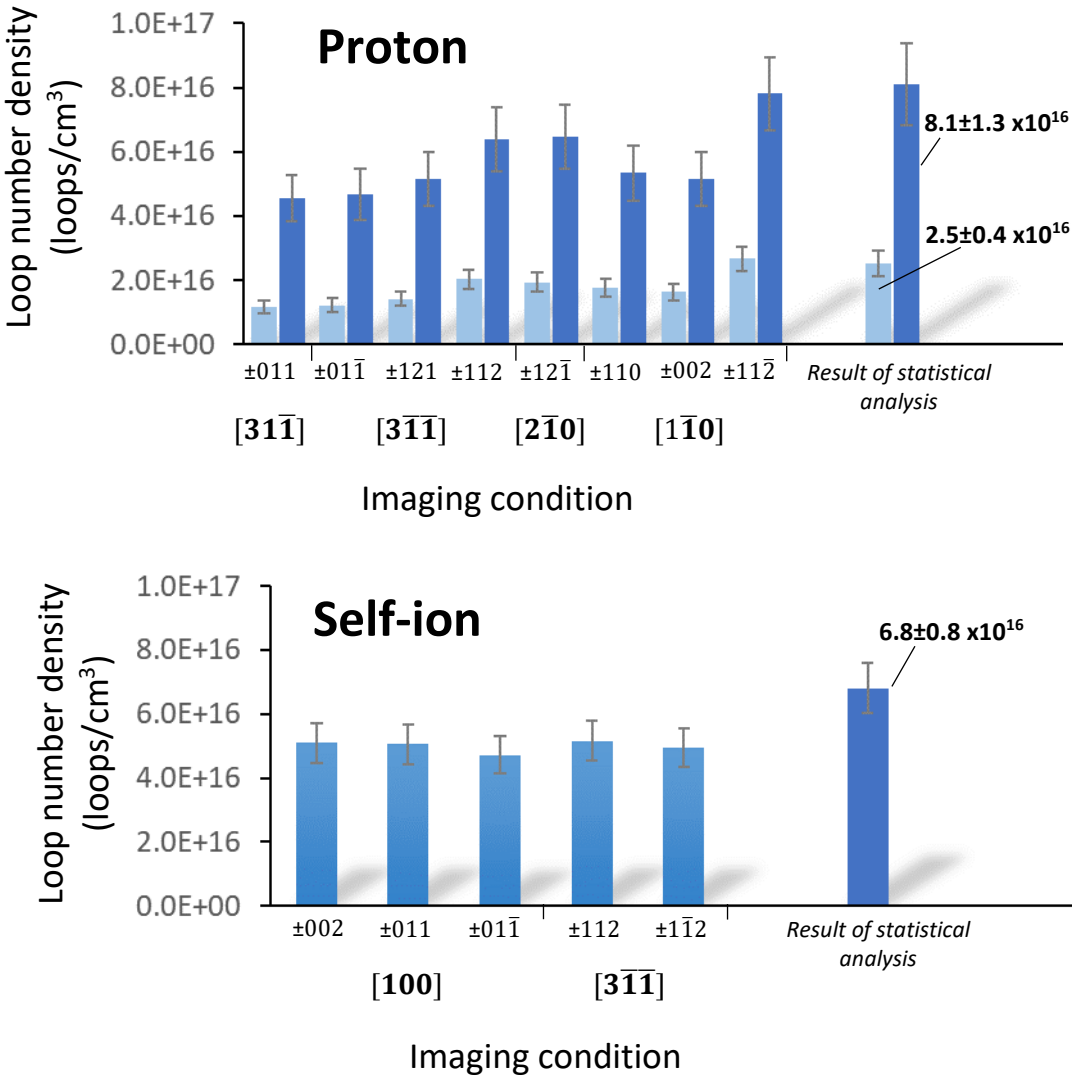

Figure 6.58: Dislocation loop density of the proton and self-ion irradiated Fe9Cr, as determined by the statistical analysis method [172]. *The visible density in each condition is shown.*

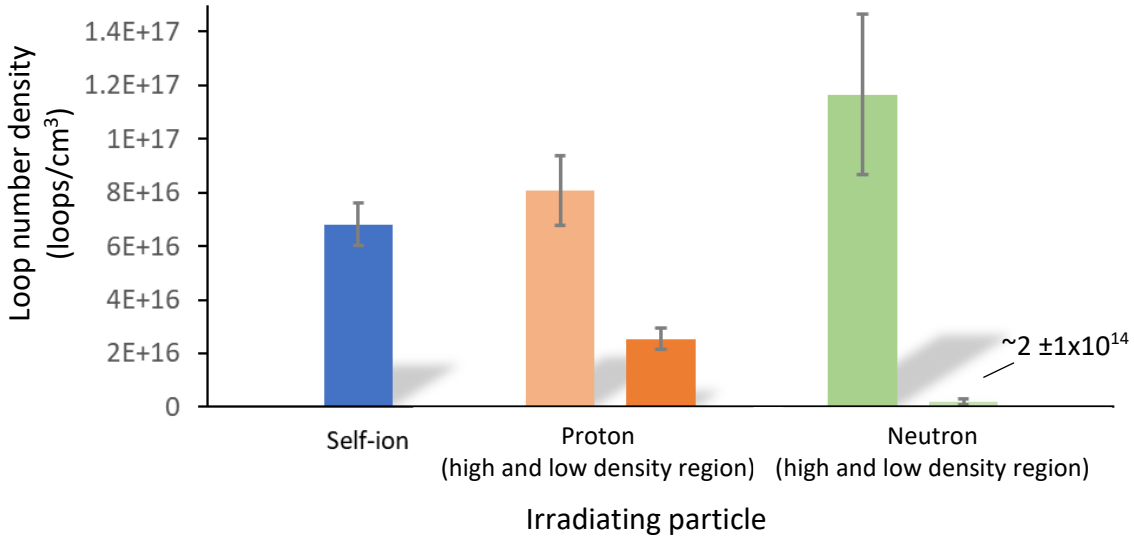

Figure 6.59: Dislocation loop number densities for self-ion, proton and neutron irradiated Fe9Cr

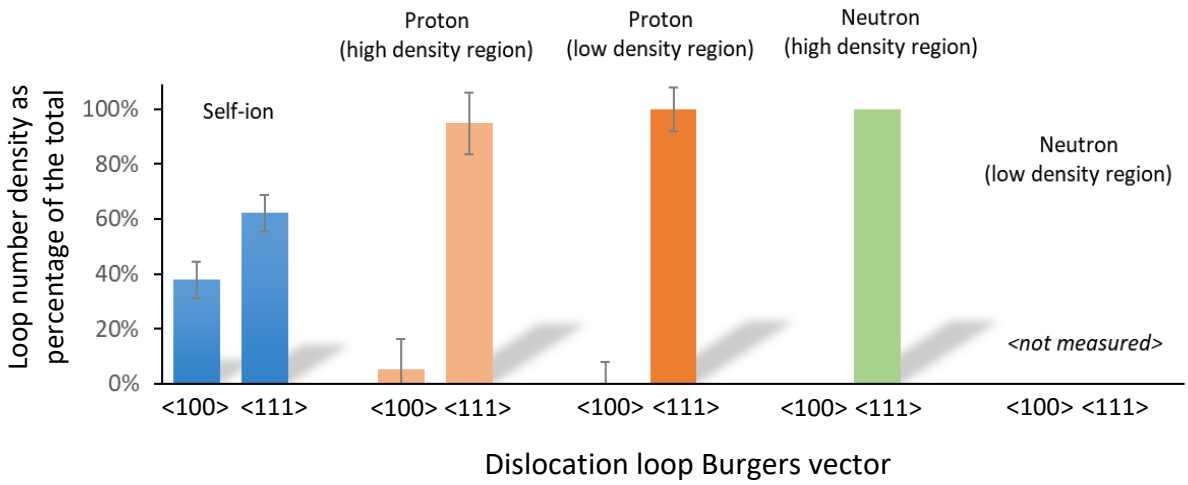

Figure 6.60: Fraction of <100> and <111> loops present in self-ion, proton and neutron irradiated Fe9Cr

6.4.2 Nature analysis of loops in proton and self-ion irradiated Fe9Cr

The nature of dislocation loops in the proton and ion-irradiated Fe9Cr was determined by the inside-outside contrast method [48]. Figure 6.61 shows this analysis for a selection of loops in the proton-irradiated sample. Only the largest loops could be reliably identified, the smallest of which was ~5nm in diameter. In total, 8 loops were analysed, all of which were <111> type loops. All loops were found to be interstitial.

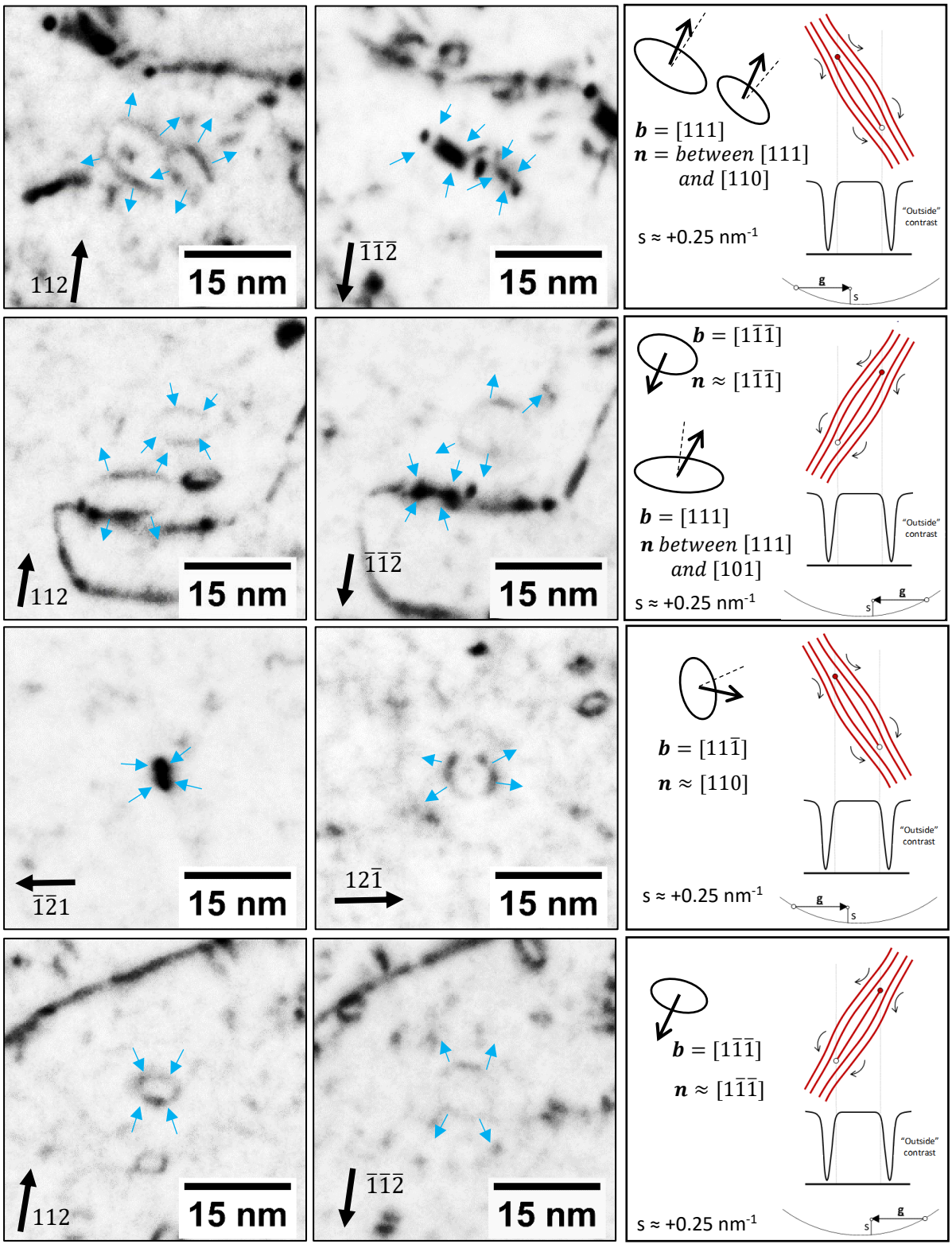

*Figure 6.61: Nature analysis of dislocation loops in the proton irradiated Fe9Cr. The Burgers vectors were determined by the **g.b** analysis method, and from the approximate habit plane the loops appear to lie on. All 8 loops analysed were found to be interstitial.*

The self-ion irradiated sample contains much larger loops than the proton-irradiated samples, which made determining the nature easier. It was decided to show more detail in the nature analysis of the ion-irradiated Fe9Cr because, like the Fe6Cr, it was found to contain mostly vacancy-type loops. This is unusual for the FeCr system, and so the detailed analysis shown as part of Figure 6.62 and Figure 6.63 has been shown so that each step of the process can be carefully checked to ensure no errors were made.

Figure 6.62 follows a selection of loops as the sample is tilted along the 112 Kikuchi band from the $[11\bar{1}]$ pole to the $[1\bar{1}0]$ pole, passing through the $[20\bar{1}]$ and $[3\bar{1}\bar{1}]$ poles. At each condition, the orientation of the sample is shown, and the projected directions on a correctly oriented unit cell is shown. From the change in shape of the loops, it was found that the Burgers vector of loop 1 is ±[001] and loops 2 and 3 are ±[111]. The Burgers vector does not actually matter for this analysis, providing the inclination with respect to **g** is correct, which the tilt experiment has determined. The index assigned to **g** is also not necessary for this analysis, providing the direction of **g** is correct.

Figure 6.63 shows the plus and minus g-vector conditions, and the orientation of the loops with respect to **g**. This step confirms that Burgers vector, **b**, must point in roughly the opposite direction to the loop normal, **n,** (i.e. **b.n**<0) for all loops analysed in Figure 6.63, and hence the loops must be vacancy [48]. As a reminder, the microscope does have an inversion in the diffraction pattern, and this has been corrected for here (see section-3.6.1).

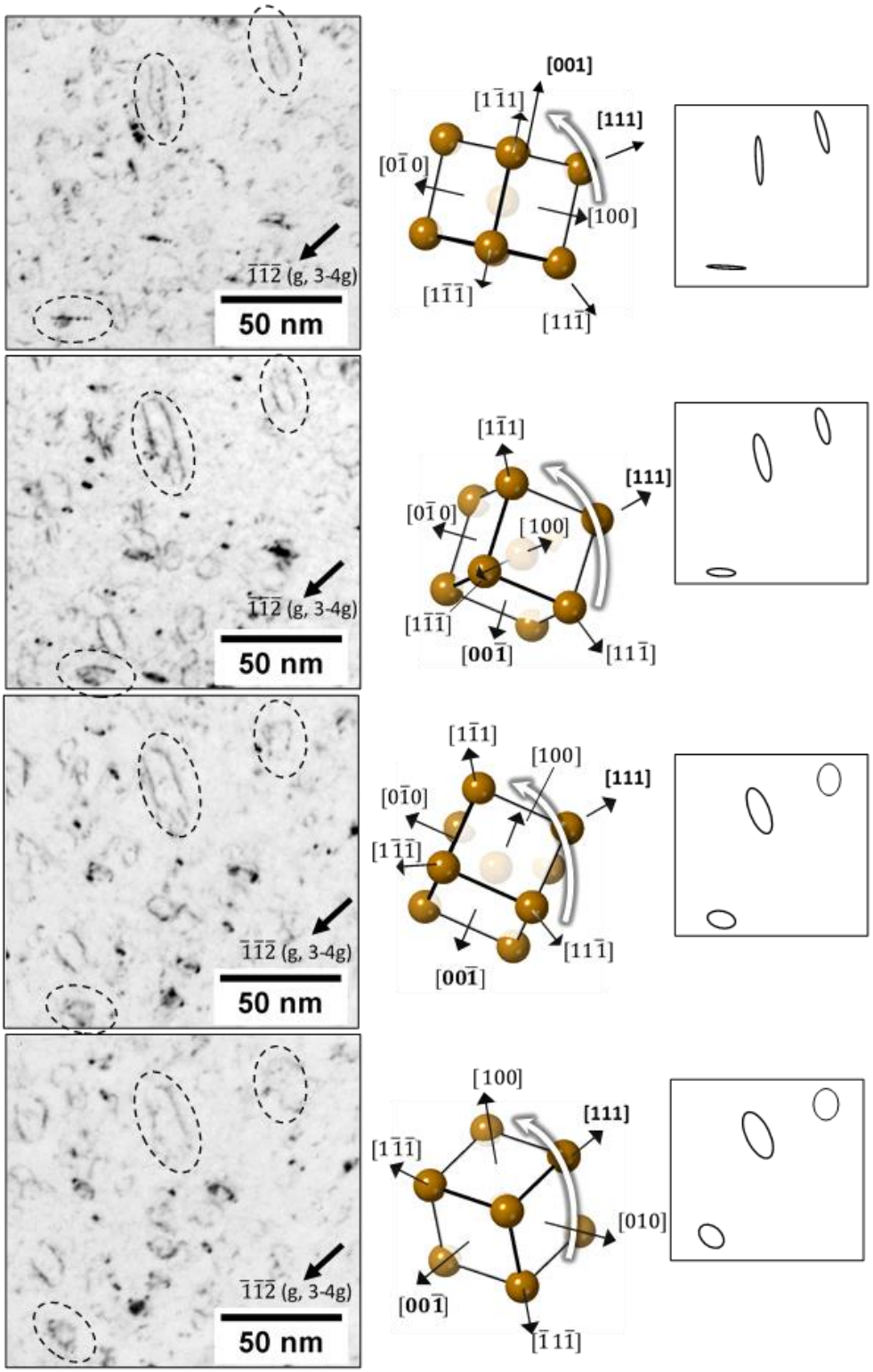

Figure 6.62: Tilt series along a 112 Kikuchi band, from the $[1\bar{1}0]$ *pole to the* $[11\bar{1}]$ *pole, showing the change in projection of large dislocation loops in the self-ion irradiated Fe9Cr. A selection of loops are indicated by dotted circles that increase in minor image-diameter as the foil is tilted from* $[1\bar{1}0]$ *to* $[11\bar{1}]$*. Unit cell orientations were produced using* [164]*.*

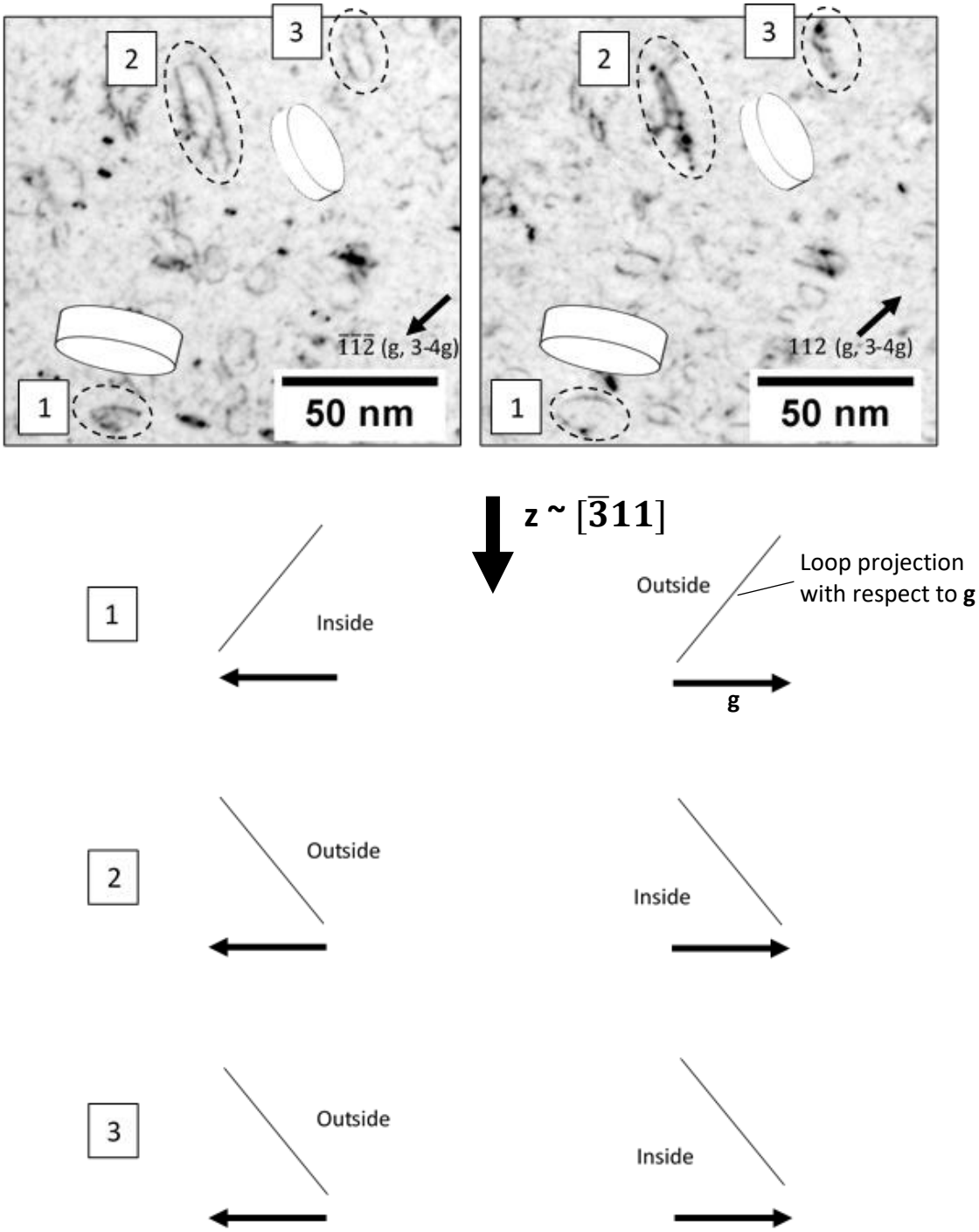

*Figure 6.63: Inside-outside contrast analysis of the dislocation loops labelled 1, 2 and 3. Shown next to each loop is an image of a cylinder to show the inclination. Beneath the micrographs is a diagram showing the inclination of the loops with respect to **g**, as viewed from the direction orthogonal to **g** and **z**. The inside-outside contrast is consistent with vacancy-type loops.*

A second set of loops ~5nm in size and further into the damage profile were also analysed, shown in Appendix H. These loops were also vacancy.

It is easy to confirm at least 20 of the [001] loops are vacancy-type, and at least 10 of the [111] loops are also vacancy. In total, 33 vacancy loops from ~5nm to ~30nm in major-diameter were identified. The other variants of the <100> loops were not measured here due to their poor visibility here.

As with the self-ion irradiated Fe6Cr, this result is very unusual, and possible mechanisms that might lead to this observation are discussed in chapter 7.

6.4.3 Size distributions of loops in proton and self-ion irradiated Fe9Cr

Dislocation loops in the proton and self-ion irradiated Fe9Cr were counted and sized using a range of g-vector conditions and foil orientations. A full list of the g-vector conditions is shown in Figure 6.58. For every g-vector condition captured, the negative-g condition was also captured to aid counting and accurate sizing. The size measured was taken as approximately the average image size of a loop as seen in the plus- and minus-g conditions, as described in section-3.6.4.

The size distribution of dislocation loops in the proton-irradiated Fe9Cr is shown in Figure 6.64 and in the self-ion irradiated Fe9Cr in Figure 6.65. The size distributions for each condition used are shown in Appendix D. The size distribution for the proton-irradiated Fe9Cr shows the loop sizes for a region of high-loop density (inside a helical dislocation segment) and for a region in the matrix, far from dislocations or grain-boundaries.

To compare the loop sizes for different irradiating particle, the measured loop sizes in the Fe9Cr were plotted as box and whisker diagrams in Figure 6.66. The red line in each box indicates the median loop size.

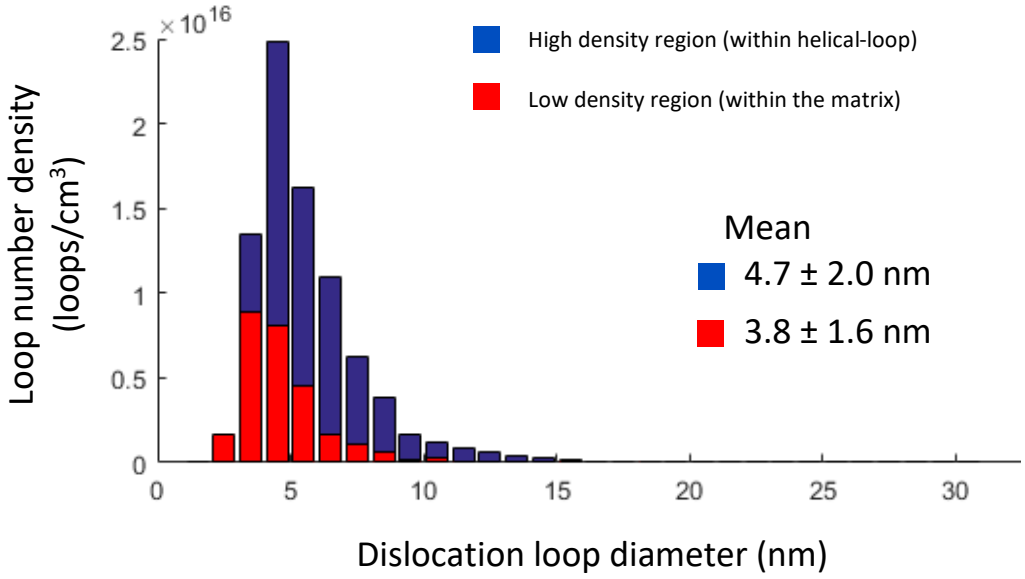

Figure 6.64: Overall size distributions for the proton irradiated Fe9Cr in the matrix and within a helical-dislocation segment

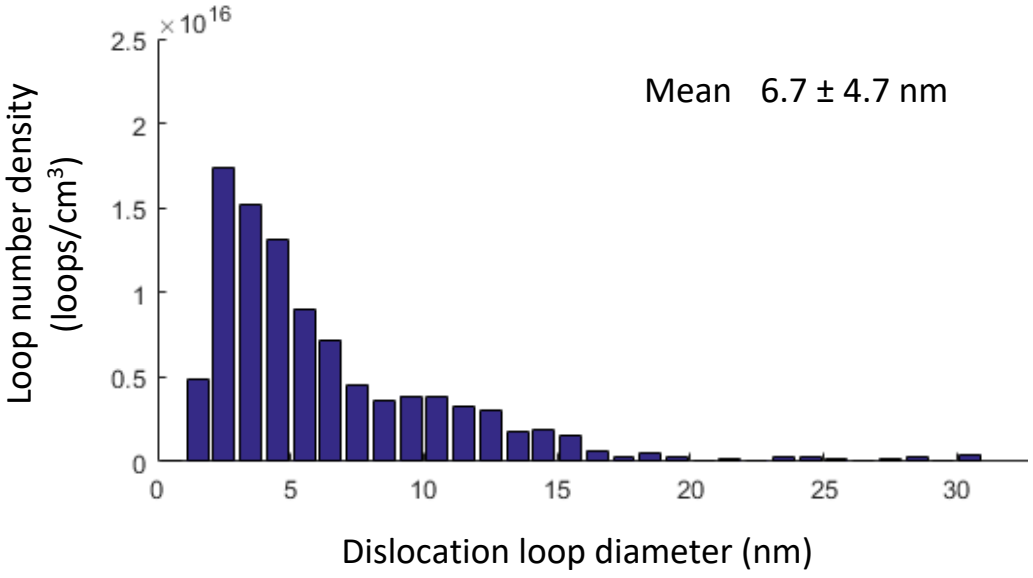

Figure 6.65: Overall size distributions for the self-ion irradiated Fe9Cr

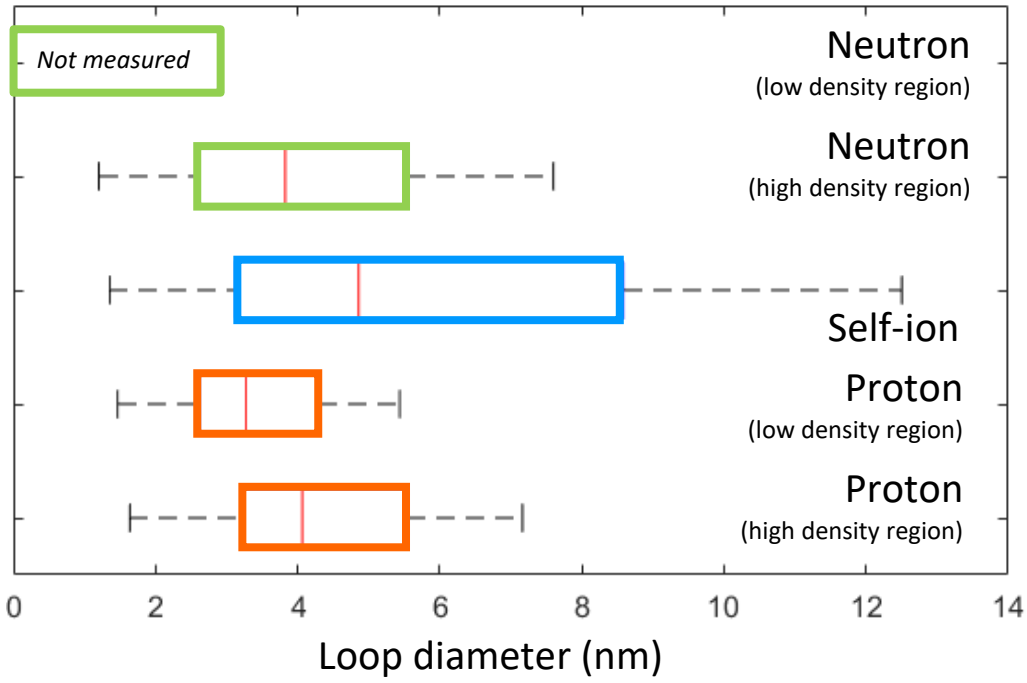

Figure 6.66: Box and whisker plots of the dislocation loop sizes in Fe9Cr irradiated with neutrons, self-ions and protons. The whiskers, box and red line on the plot from left to right indicate the 5th, 25th, 50th, 75th and 95th percentiles.

Figure 6.66 shows the largest loops were found in the self-ion irradiated Fe9Cr, whereas the smallest were found in the matrix of the proton-irradiated Fe9Cr. However, since the neutron-irradiated Fe9Cr contained large regions absent of visible dislocation loops, it can be assumed that the matrix of the neutron-irradiated sample actually contained the smallest defect clusters. To recap, the proton-irradiated Fe6Cr contained larger loops than the self-ion irradiated Fe6Cr, whereas the opposite is observed here in the Fe9Cr.

The total atomic volume of the loops in the self-ion and proton-irradiated Fe9Cr was estimated by treating the loops as circular prismatic loops, and using Equation 6.1 and Equation 6.2 to convert the measured diameter to a volume. Since only vacancy loops were found in the self-ion irradiated Fe9Cr, the estimate of atomic volume is the volume occupied by vacancies, rather than interstitials. The size distributions according to their atomic-volume are shown in Appendix F.

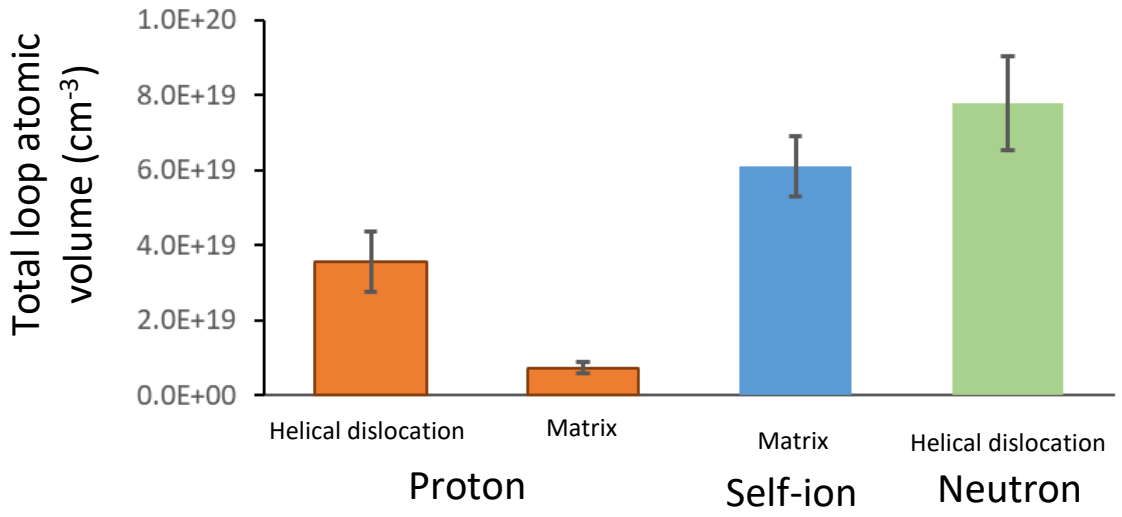

Figure 6.67: Comparison of the total atomic volume of dislocation loops produced by proton, self-ion and neutron irradiation in Fe9Cr. In section-6.4.2, only vacancy loops were found in the self-ion irradiated Fe9Cr, but only interstitials in the proton and neutron irradiated Fe9Cr.

Figure 6.67 shows that the densest population of interstitials is within the helical dislocations inside the neutron-irradiated Fe9Cr. Fewer interstitials were contained by the helical segment of the proton-irradiated Fe9Cr, even though the helical dislocation diameter (~130nm) is much larger than the helical dislocation in the neutron-irradiated Fe9Cr (~70nm). With a diameter of 130nm, the helical dislocation segment in the proton-irradiated Fe9Cr is intersecting the foil surface, so the estimate of the volume containing the loops in the proton-irradiated is probably an overestimate, and hence the density may be underestimated.

6.4.4 Voids in proton and self-ion irradiated Fe9Cr

The under-over focus technique was used to look for voids in the ion and proton-irradiated Fe9Cr. The ion-irradiated sample contained a selection of very small void-like features that had very weak contrast in the foil. Example under and over focus micrographs are shown in Figure 6.68, which were captured from a thin region ~200nm into the damage profile, corresponding to a dose of ~1.2dpa. The region contains many ~1nm diameter features that are dark when focus is positive and light when focus is negative. The features are barely distinguishable from the background

fluctuations, and so it is difficult to say with any confidence that any of these features are voids, rather than simply surface oxide or contaminants.

Analysis of the most distinctive of these features is provided; however it is highly uncertain that they are voids, and there is ambiguity over which features to include and which to discard as background. An example of the analysis is shown in Figure 6.69, and the results are summarised in Table 6.8. As with the previous sections, the "void" diameter was taken to be the width of the image where the intensity first falls below background.

Despite the ambiguity over the origin of the features indicated in Figure 6.68, it is possible to confirm from this analysis that no large voids are produced from the ion-irradiation in the Fe9Cr at these doses. This is typically what is observed in previous ion-irradiation studies of similar alloys [35,36,38]. It has already been found that a large population of the dislocation loops in the foil are vacancy type (section-6.4.2), so it would make sense that the void population is small or zero.

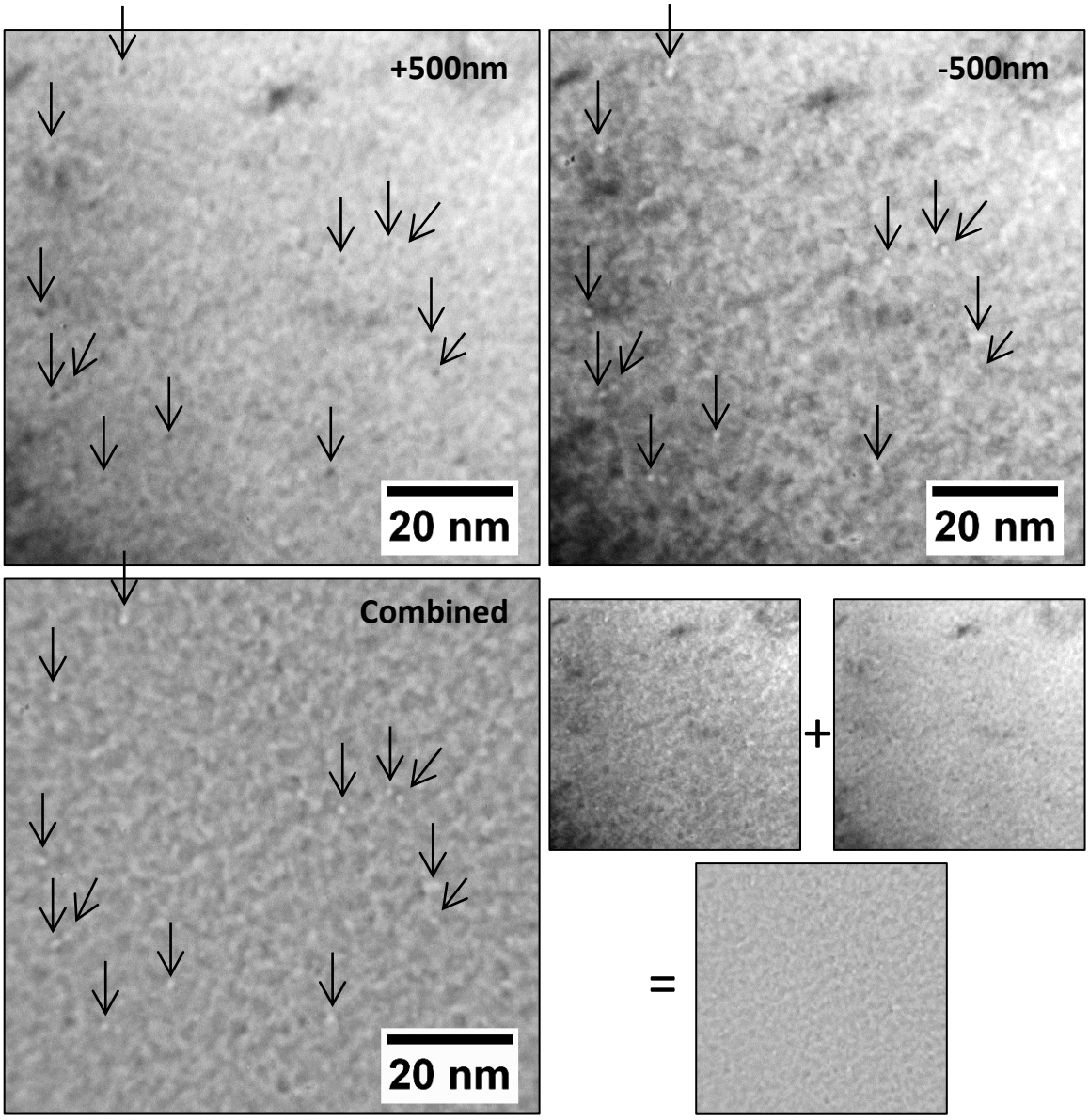

Figure 6.68: Micrographs of self-ion irradiated Fe9Cr, images using the under-over focus technique to reveal voids in the microstructure. Examples of features that might be small voids are indicated by an arrow

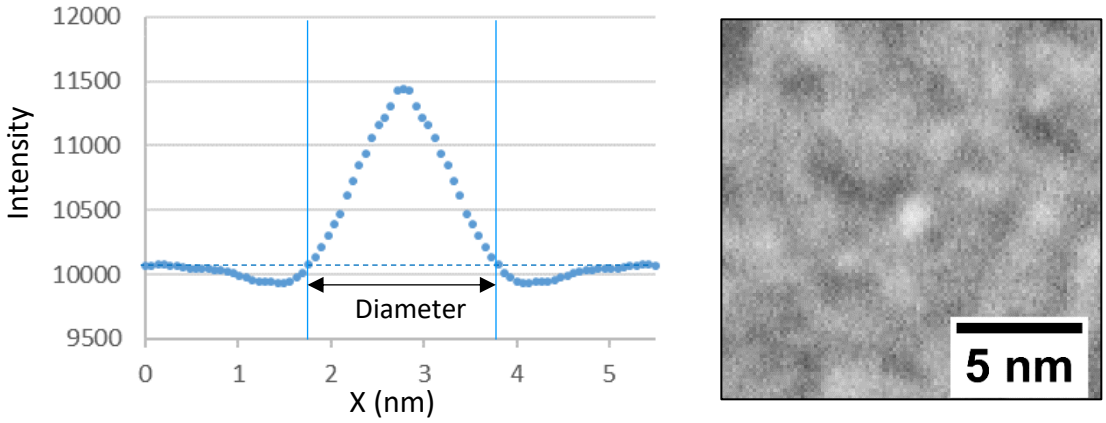

Figure 6.69: Example of the radial-intensity profile of voids observed in the self-ion irradiated Fe9Cr

	Self-ion irradiated
Number density (cm^{-3})	$2.2 \pm 0.6 \times 10^{16}$ >2nm: $9.4 \pm 3.8 \times 10^{15}$
Mean diameter (nm)	1.9 ± 0.4
Maximum diameter (nm)	2.6
Minimum diameter (nm)	1.2

Table 6.8 Summary of voids in self-ion irradiated Fe9Cr

Figure 6.70 shows over and under focus of a region of the proton-irradiated Fe9Cr that contains a dislocation with helical segments. In Figure 6.71, a combined over-under focus image was added to a weak-beam micrograph, captured with the same foil orientation. The result is a single image showing clearly the dislocation and dislocation loop contrast next to the Fresnel contrast of the voids.

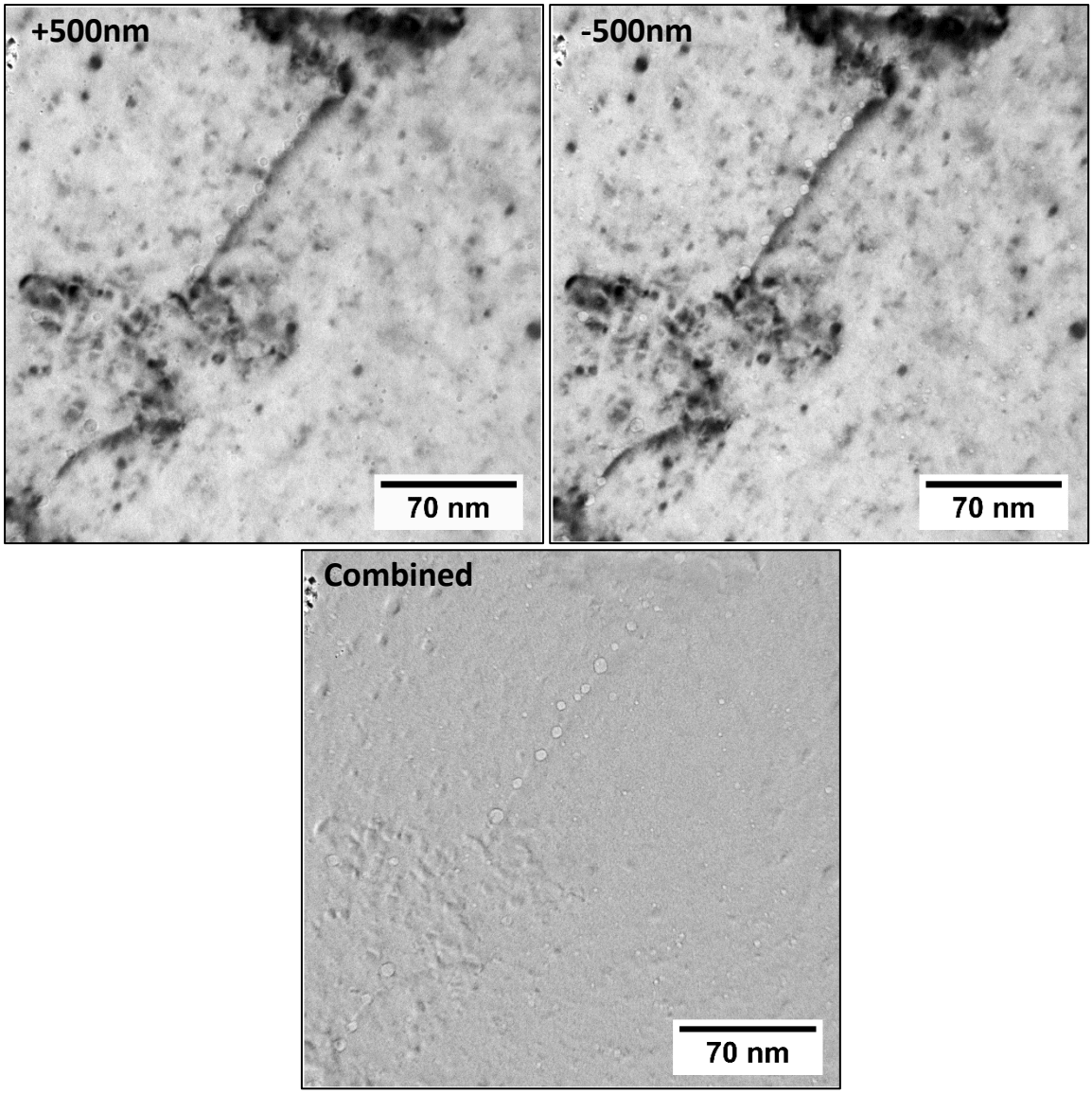

Figure 6.70: Micrographs of proton irradiated Fe9Cr, images using the under-over focus technique to reveal voids in the microstructure

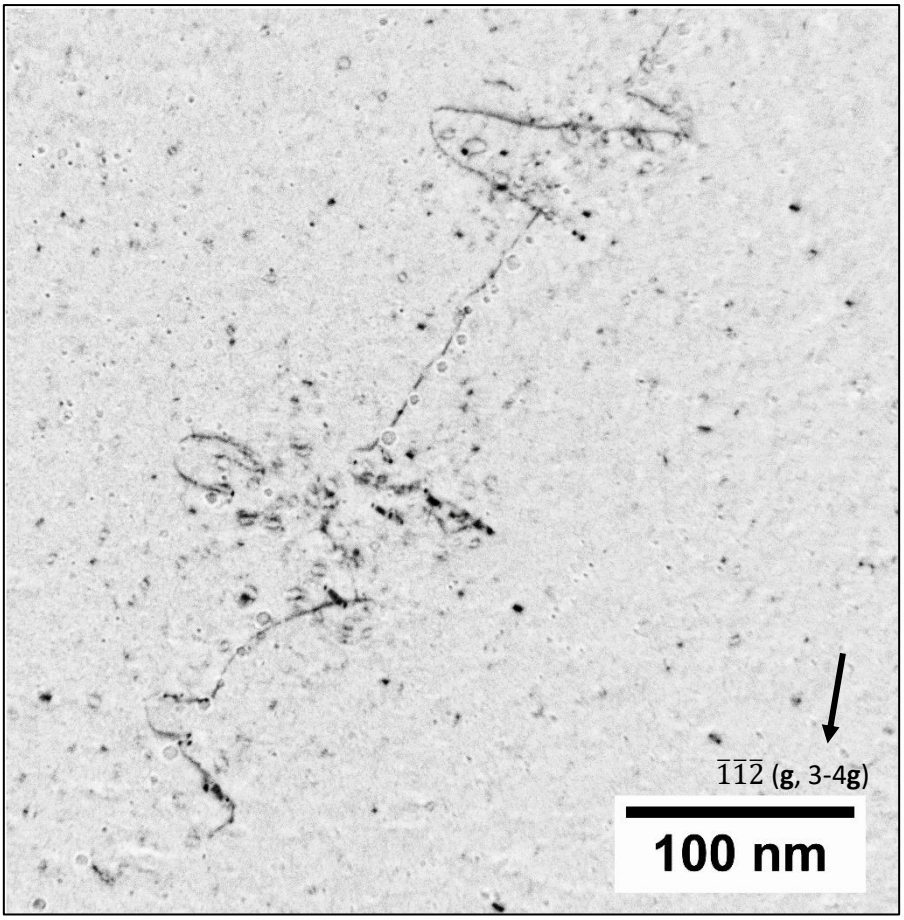

Figure 6.71: Combined weak-beam and under-over focus micrographs of the proton irradiated Fe9Cr, to show both voids and dislocations.

These images show that large voids reside on or near the dislocation line, except for the helical segments. The helical segments of the dislocation contain fewer and smaller voids. Close to the dislocation line, and within the helical segments, the void population is smaller and the sizes smaller (typically ~2nm). Regions further from the dislocation line appear to have a larger population of larger voids (typically >5nm) than in regions directly next to the dislocation, indicating a depletion zone around the dislocation exists. The void distribution in the matrix seems otherwise homogeneous, though at least one instance of a void cluster that does not coincide with any defects in the weak-beam micrograph is visible in Figure 6.72.

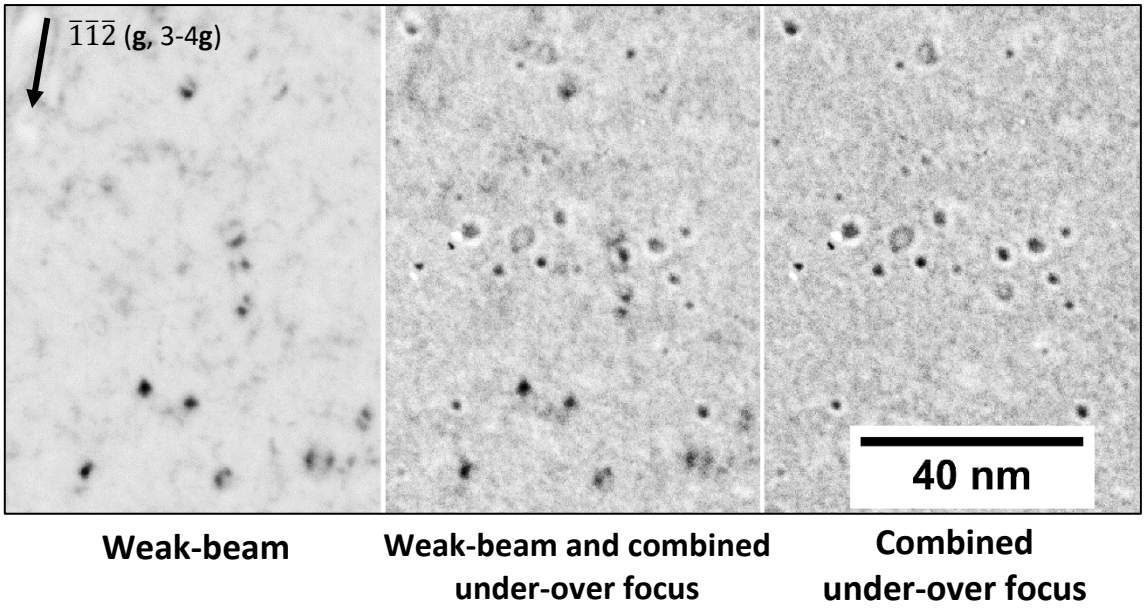

Figure 6.72: Small cluster of voids visible in the combined over-under focus image. Shown next to a weak-beam condition to reveal the dislocation loops in the vicinity, and the combination of both images in the centre. The voids do not appear to correlate with any features in the weak-beam condition (nor any features in other g-vector conditions).

The large sizes and high contrast strongly suggest the features visible from the under-over focus micrographs are cavities, rather than oxide or surface contaminants (as may be the case for the ion-irradiated Fe9Cr). Since the samples were irradiated with protons, it is possible that hydrogen is retained inside the cavities. The distinction between a bubble and void is stated by Was [17] that if the cavity is spherical, rather than facetted, it is more likely to be pressurised, and should be designated as a bubble. This definition is just conjecture and has not been rigorously tested. The smaller cavities (<2nm) will appear spherical anyway due to resolution limits, but the larger cavities can be studied to see if they are facetted.

The under-over focus technique was used again with a smaller difference in focus to keep the Fresnel fringes narrow and reveal the shape of the features with more clarity. Figure 6.73 shows a selection of facetted voids in the proton-irradiated microstructure, indicating that if there is hydrogen gas inside, it is not causing the void to take a spherical shape, and is probably not under pressure. Figure 6.73 shows the approximate orientations of the facets, which seem to agree well with a cubic shape, although some appear less uniform.

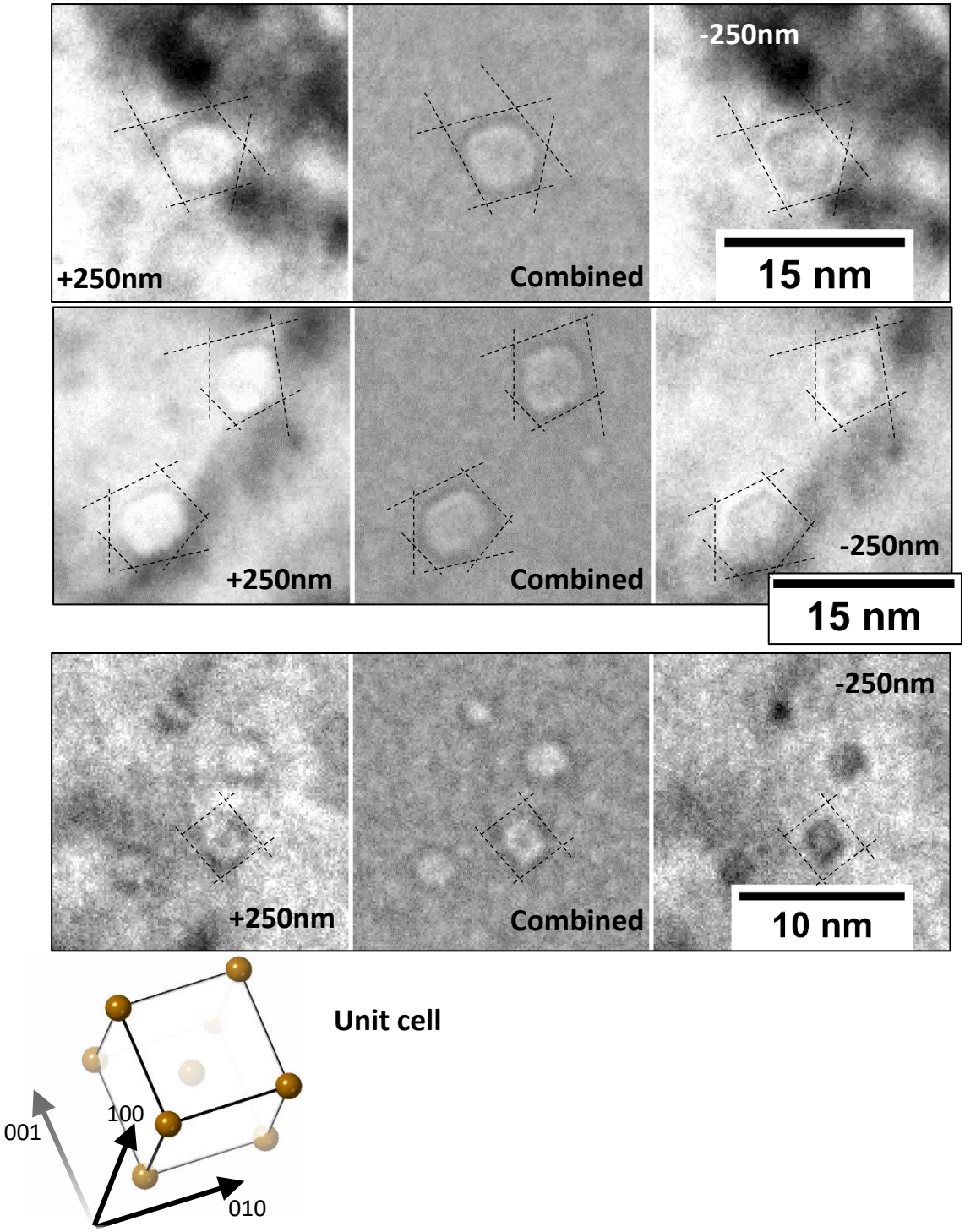

Figure 6.73: Higher magnification micrographs of voids in the proton irradiated Fe6Cr. A correctly oriented unit cell is shown, and approximate orientation of facets are shown.

Since the population of voids in the sample is not uniformly distributed throughout the foil, measurements of the void population and sizes were made in various regions, shown in Figure 6.74 to Figure 6.77. Alongside each Figure is a Table summarising the measurements from the corresponding region. These measurements show the void population ranges from 2.3×10^{16} to 5.7×10^{16} voids/cm^3, and a mean size from 1.7 to 4.5nm.

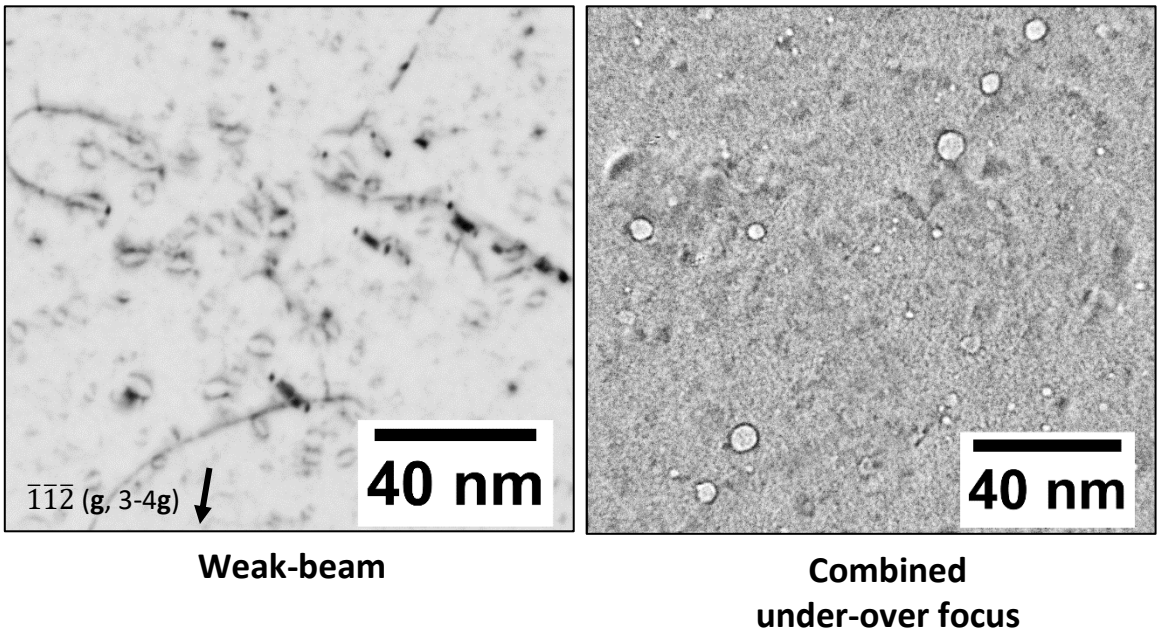

Figure 6.74: Weak beam micrograph and under-over focus image of helical dislocation segment in proton irradiated Fe9Cr. The voids were sized and counted, and these measurements are summarised in Table 6.9.

	Proton irradiated, inside helical segment
Number density (voids cm^{-3})	$2.4 \pm 0.6 \times 10^{16}$ >2nm: $1.3 \pm 0.4 \times 10^{16}$
Mean diameter (nm)	2.4 ± 1.2
Maximum diameter (nm)	5.4
Minimum diameter (nm)	1.1

Table 6.9: Summary of voids within the helical segment of the dislocation shown in Figure 6.74.

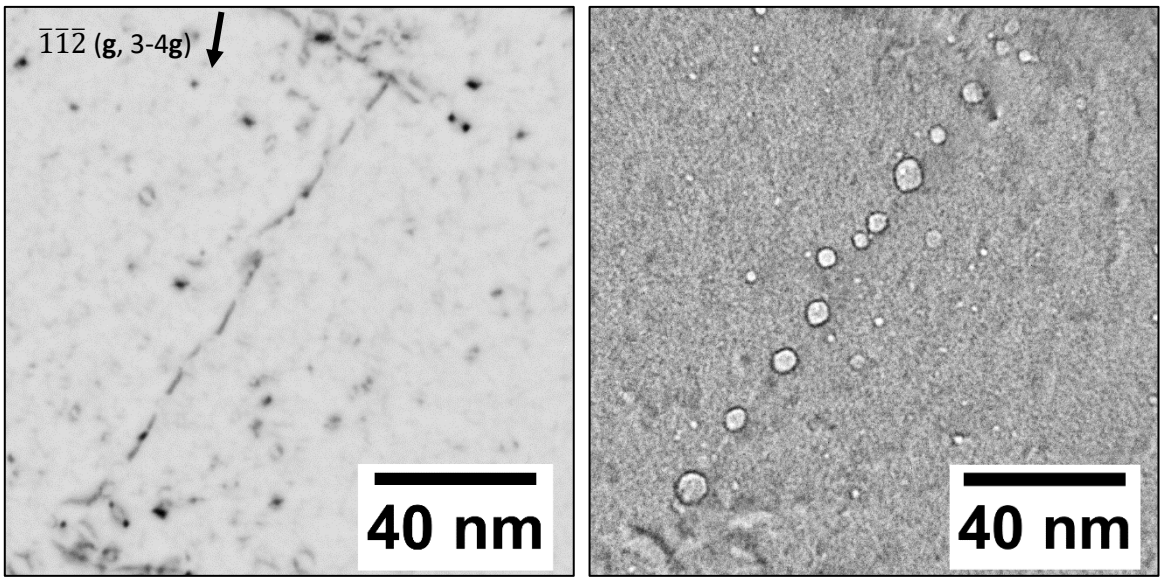

Figure 6.75: Weak beam micrograph and under-over focus image of straight segment of dislocation in proton irradiated Fe9Cr. The voids were sized and counted, and these measurements are summarised in Table 6.10.

	Proton irradiated, on dislocation line
Number density	7.9 ± 2.3 voids/100nm 2.4 ± 0.7 x10^{18} voids/cm^3
Mean diameter (nm)	4.5 ± 1.1
Maximum diameter (nm)	6.5
Minimum diameter (nm)	3.3

Table 6.10: Summary of voids aligned along the straight segment of the dislocation shown in Figure 6.75. The volume density quoted here is the number of voids contained by a cylinder with diameter equal to the largest void in the chain, and length equal to the dislocation line length that contains all voids in the chain.

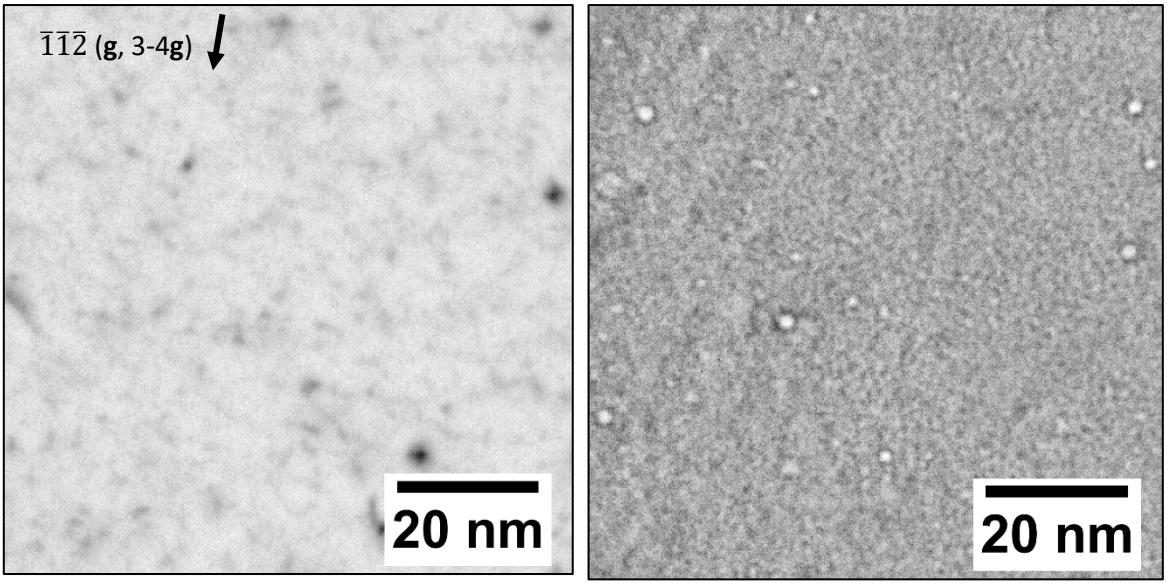

Figure 6.76: Weak beam micrograph and under-over focus image of region immediately next to a straight dislocation segment in proton irradiated Fe9Cr. The voids were sized and counted, and these measurements are summarised in Table 6.11.

	Proton irradiated, close to dislocation
Number density (voids cm^{-3})	2.3 ± 0.6 x10^{16} >2nm: 1.4 ± 1.4 x10^{15}
Mean diameter (nm)	1.7 ± 0.3
Maximum diameter (nm)	2.4
Minimum diameter (nm)	1.1

Table 6.11: Summary of voids next to the straight segment of the dislocation shown in Figure 6.76

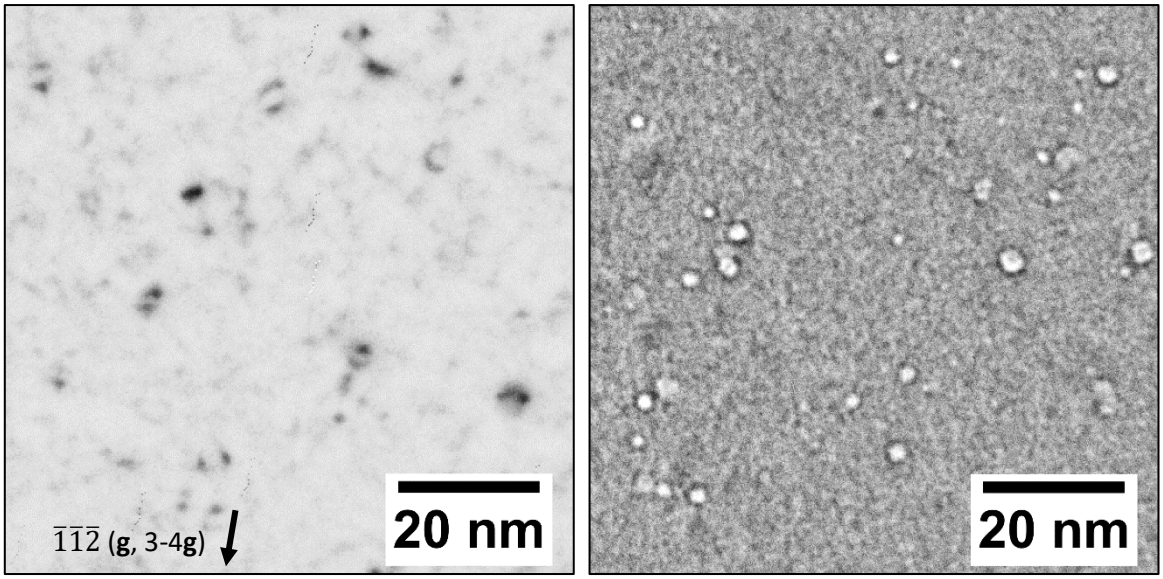

Figure 6.77: Weak beam micrograph and under-over focus image of the matrix in proton irradiated Fe9Cr. The voids were sized and counted, and these measurements are summarised in Table 6.12.

	Proton irradiated matrix
Number density (voids cm^{-3})	5.7 ± 0.9 x10^{16} >2nm: 2.2 ± 0.6 x10^{16}
Mean diameter (nm)	2.0 ± 0.6
Maximum diameter (nm)	3.5
Minimum diameter (nm)	1.1

Table 6.12: Summary of voids within the matrix of the dislocation shown in Figure 6.78

Figure 6.78 shows the radial profiles of two example voids. The smaller example measures <2nm, but the contrast is still very high, and much higher than similar features found in the ion-irradiated sample, despite the proton-irradiated foil being thicker. This would indicate that the features analysed in the self-ion irradiated sample are more likely to be surface contaminants, such as oxide, than voids.

Figure 6.79 shows a comparison of the measured void populations in the proton, self-ion and neutron-irradiated Fe9Cr, and Figure 6.80 shows the measured sizes of the voids. These figures show that the proton-irradiated Fe9Cr contains the largest population of voids, and largest in size.

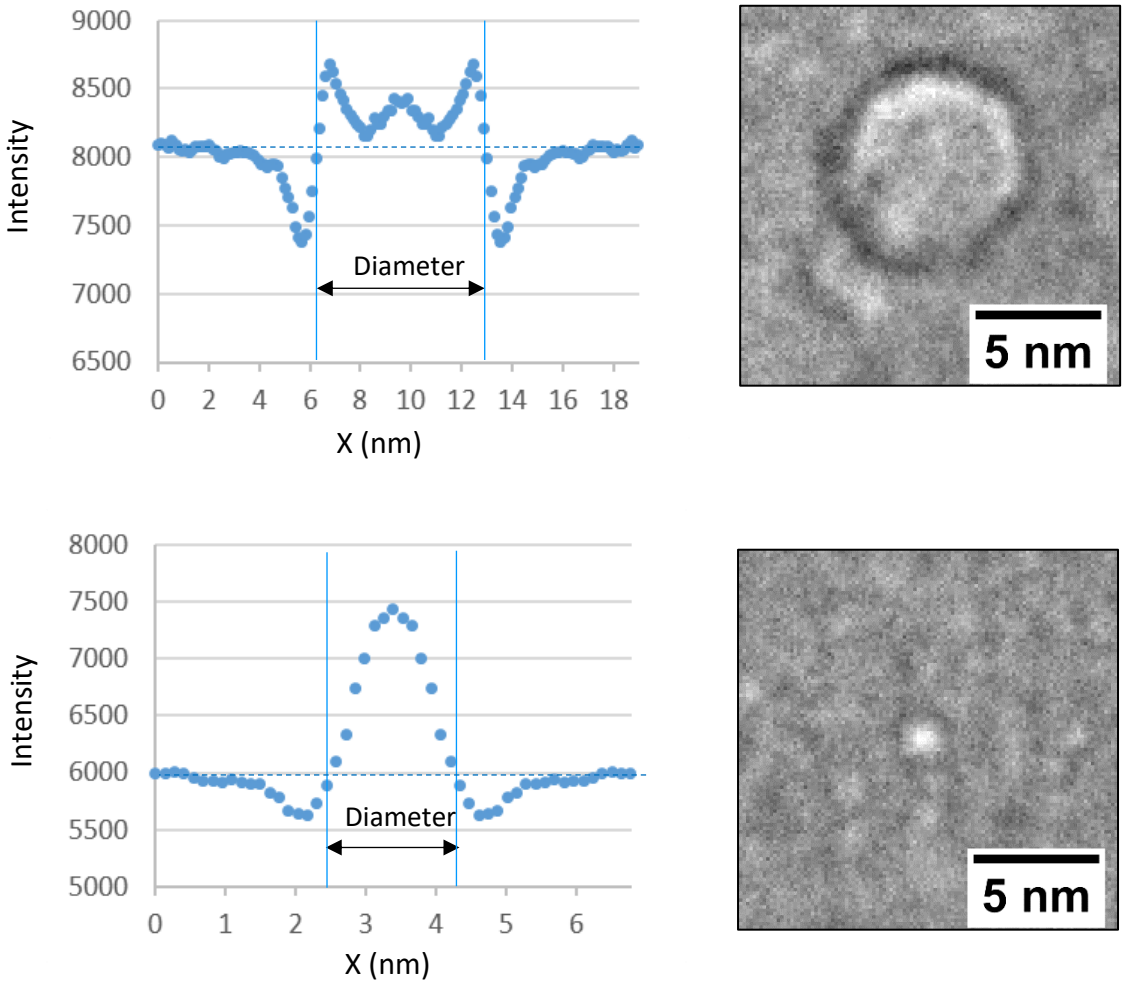

Figure 6.78: Examples of the radial-intensity profiles of voids observed in the proton irradiated Fe9Cr

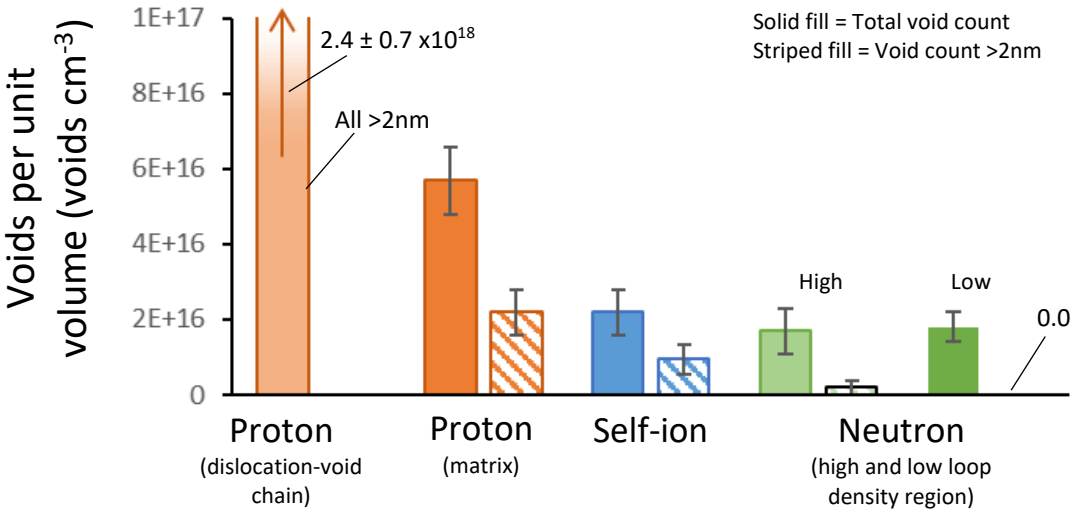

Figure 6.79: Void populations in Fe9Cr after proton, self-ion and neutron irradiation

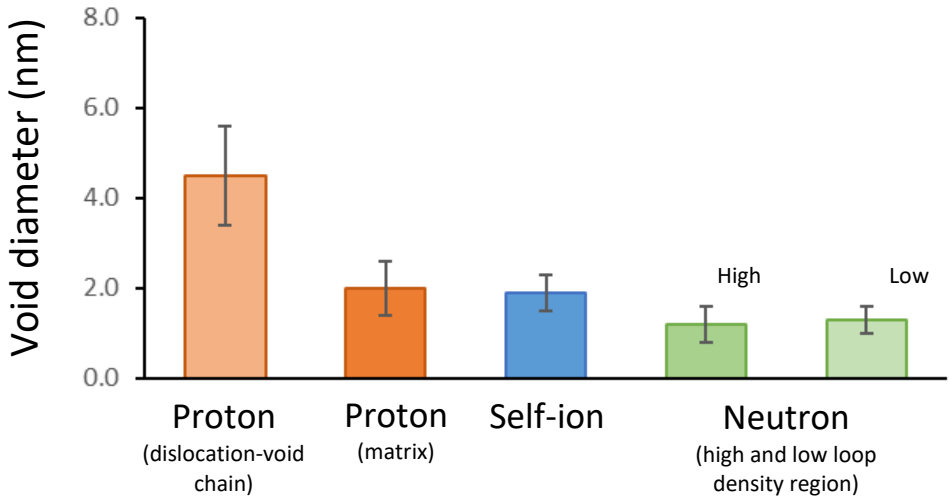

Figure 6.80: Void sizes in Fe9Cr after proton, self-ion and neutron irradiation

6.4.5 Redistribution of chromium in proton and self-ion irradiated Fe9Cr

EELS analysis of the ion-irradiated Fe9Cr was conducted in thin regions of the foil at 200-300nm depth into the damage profile, corresponding to a dose of ~1.3dpa . Figure 6.81 and Figure 6.82 show the Hartree-Slater models fitted to the electron energy spectrum, with and without fine structure fitting. The fine structure measurement was taken as a single spectra from the whole region, and was used to calibrate the composition.

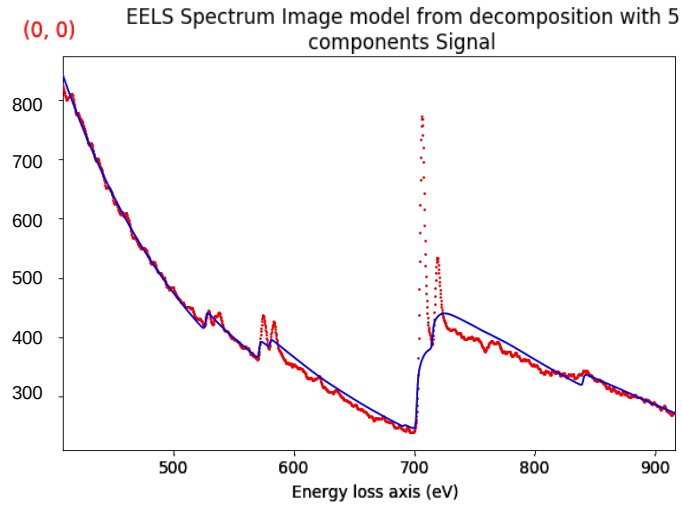

Figure 6.81: EELS spectrum from a single pixel, captured from the self-ion irradiated Fe9Cr, and shown with the fitted model of the edges

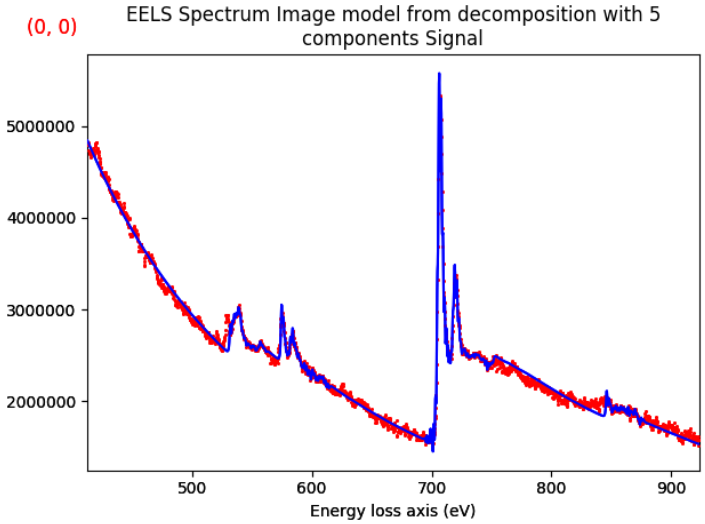

Figure 6.82: EELS spectrum from the whole region shown by the chromium map of the self-ion irradiated Fe9Cr, shown in Figure 6.83. Fine structure was included in the fitted model of the edges

An example chromium map extracted from the EELS spectra is shown in Figure 6.83. The thickness in this region was ~23nm. This analysis suggests there is no visible chromium precipitation in the ion-irradiated Fe9Cr, or if there is, it is not visible via EELS. Atom Probe Tomography is an alternative technique that may be able to detect subtle chromium clustering, or segregation on dislocation loops if any exists in this material, but this was not pursued here as part of this thesis.

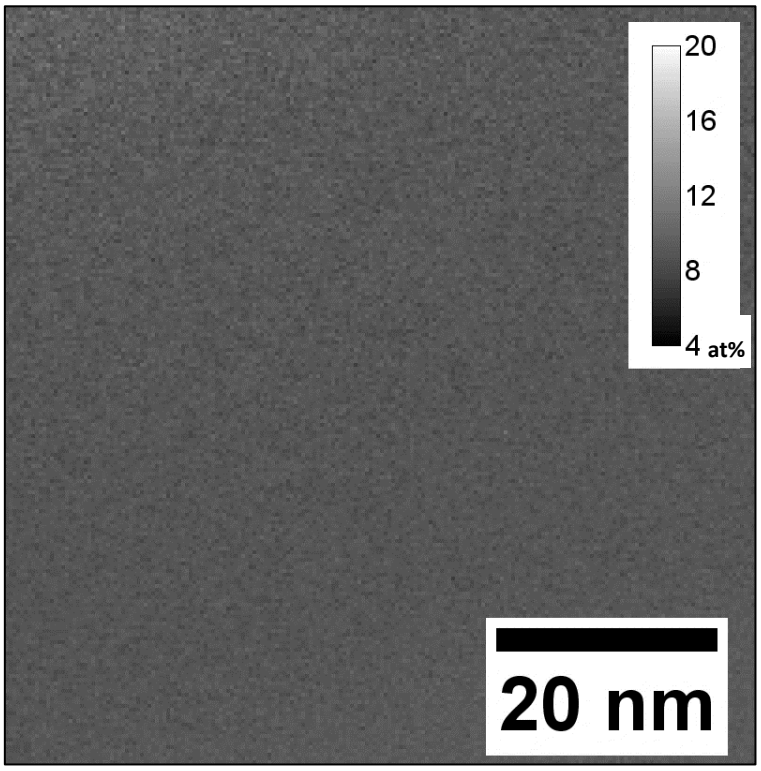

Figure 6.83: Chromium map of the self-ion irradiated Fe9Cr in a region ~23nm thick, at around 1.3 dpa. There is no visible detail in the map, implying the chromium is still in solution.

EELS maps were obtained from the proton-irradiated Fe9Cr at a region ~2.5µm depth. The image model fitted to the spectrum with and without fine structure is shown in Figure 6.84 and Figure 6.85. As with previous EELS analysis, the fine-structure was fitted to the signal from the whole micrograph, and the extracted composition was used to scale the composition determined from the model without fine structure. The result is a more accurate composition measurement, but the relative increase in chromium may be underestimated.

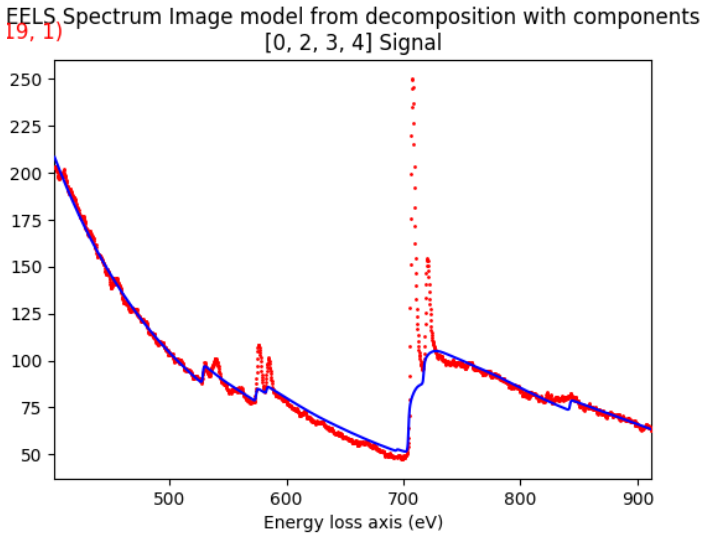

Figure 6.84: EELS spectrum from a single pixel, captured from the proton irradiated Fe9Cr, and shown with the fitted model of the edges

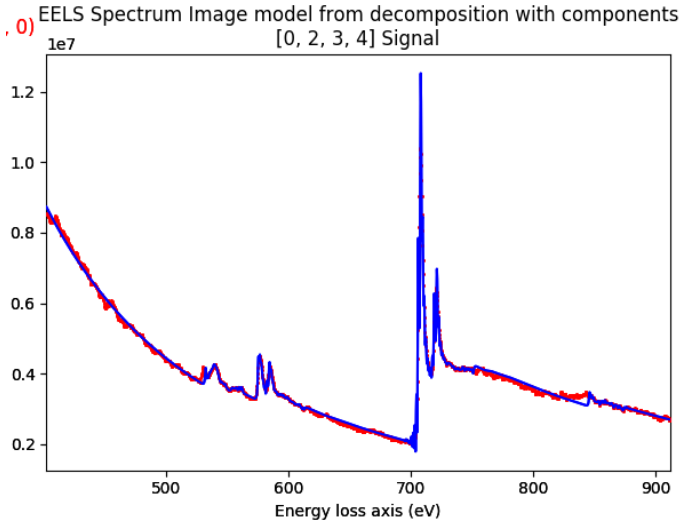

Figure 6.85: EELS spectrum from the whole region shown by the chromium map of the proton irradiated Fe9Cr, shown in Figure 6.86. Fine structure was included in the fitted model of the edges

Figure 6.86 shows a chromium map extracted from the EELS spectra, which shows a rich density of chromium precipitates distributed through the foil. Figure 6.87 shows the radial profile of chromium for two example clusters. Each cluster had a Gaussian function fitted to the profile, and this was used to estimate the chromium profile through the foil-thickness, and subsequently the overall cluster composition without contributions from the matrix. This same method was applied to similar chromium clusters observed in the neutron-irradiated material, and is discussed in more detail in section-3.4.5. Table 6.13 summarises the results from this analysis.

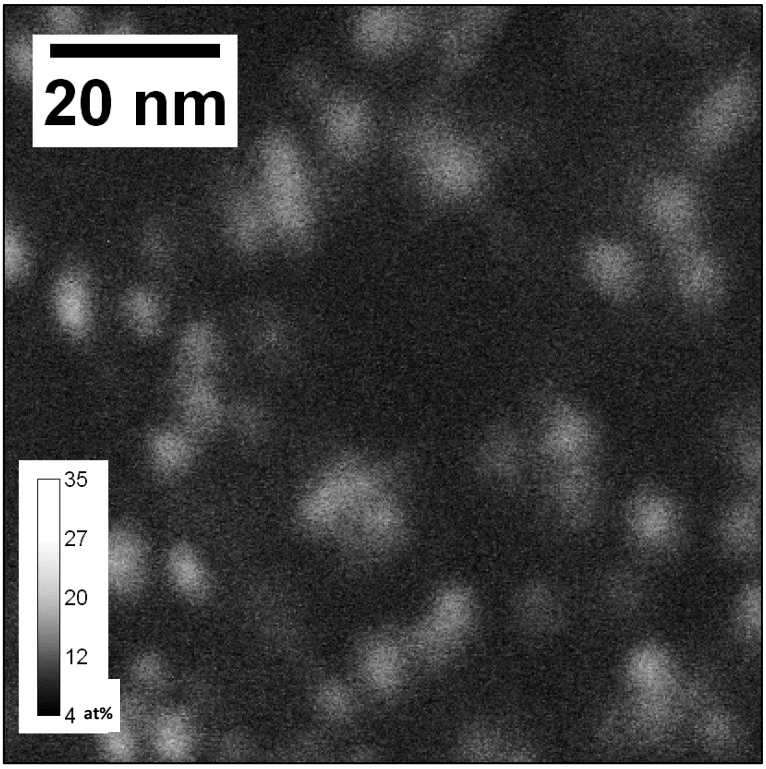

Figure 6.86: Chromium map of the proton irradiated Fe9Cr in a region ~26nm thick, at around 1.8dpa.

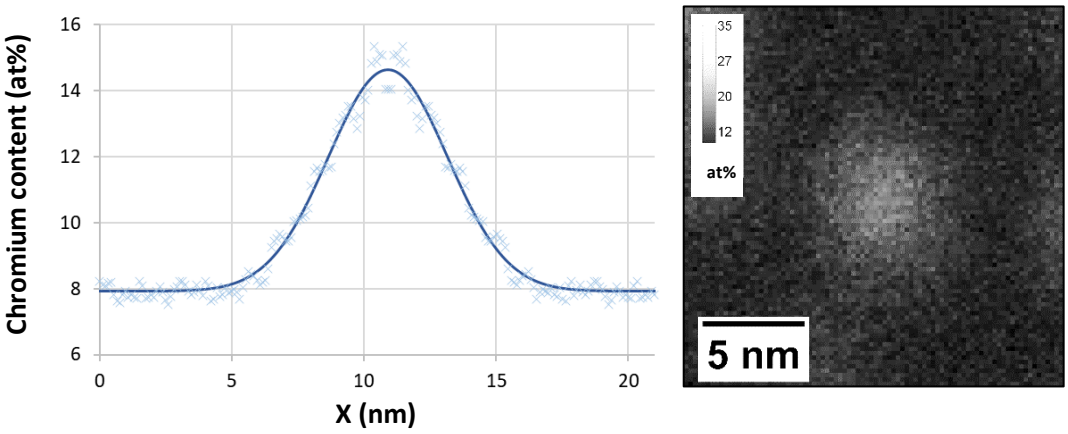

Figure 6.87: Example radial profile of a chromium cluster in the proton irradiated Fe9Cr

	Measurement
Number density (clusters cm^{-3})	$2.5 \pm 0.3 \times 10^{17}$
Mean diameter (nm)	4.4 ± 1.0
Maximum diameter (nm)	6.9 nm
Mean composition (at %)	25.2 ± 6.8
Peak composition (at%)	30.9 ± 8.5
Matrix composition (at%)	7.9 ± 1.2

Table 6.13: Summary of measurements of chromium clusters in proton irradiated Fe9Cr

To investigate the clusters further, a second EELS map was collected from the proton-irradiated Fe9Cr at much higher magnification than shown in Figure 6.86. Figure 6.88 shows the corresponding higher magnification chromium map of the proton-irradiated Fe9Cr. The image was captured down a <100> zone axis and using an atomic resolution probe size (though the EELS map is not atomic resolution due to sample drift during acquisition).

The precipitates in Figure 6.88 appear smaller and have a higher chromium content than those in Figure 6.86. Efforts were made to keep the probe sizes approximately equal to the pixel width in both cases to ensure most of the chromium signal collected comes from the column of that pixel. However, there will always be some signal contribution from outside this column due to the beam tails, which will lead to reduced spatial resolution of the EELS map, and reduced relative changes in composition. In Figure 6.86, the probe size was probably larger than the pixel width, so the precipitates appear larger and lower in composition than those visible in Figure 6.88. Ideally, the EELS maps would always be collected at the resolution of Figure 6.88, but this is not always practical or possible due to sample and time limitations. Figure 6.89 shows the radial profile from one of these precipitates.

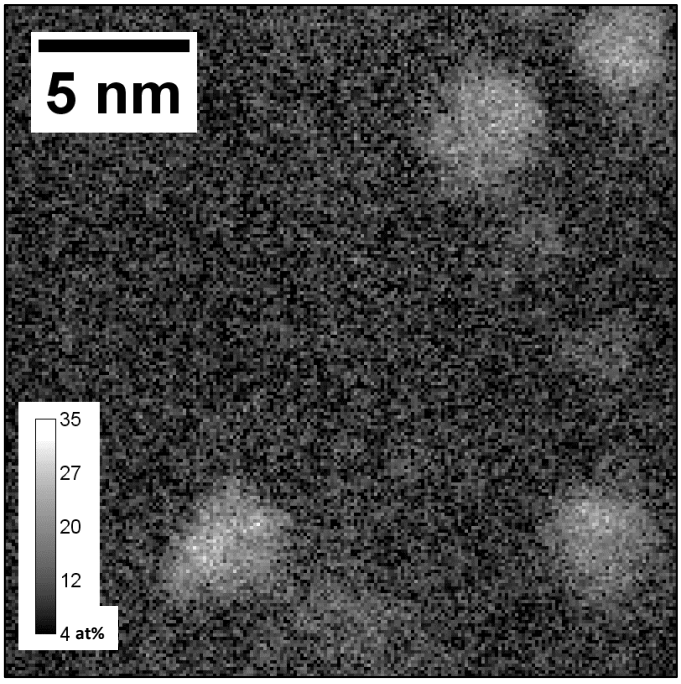

Figure 6.88: Chromium map of the proton-irradiated Fe9Cr, captured at a higher magnification and resolution than Figure 6.86. Chromium precipitates are visible with much greater clarity, allowing for a more accurate determination of their size and composition.

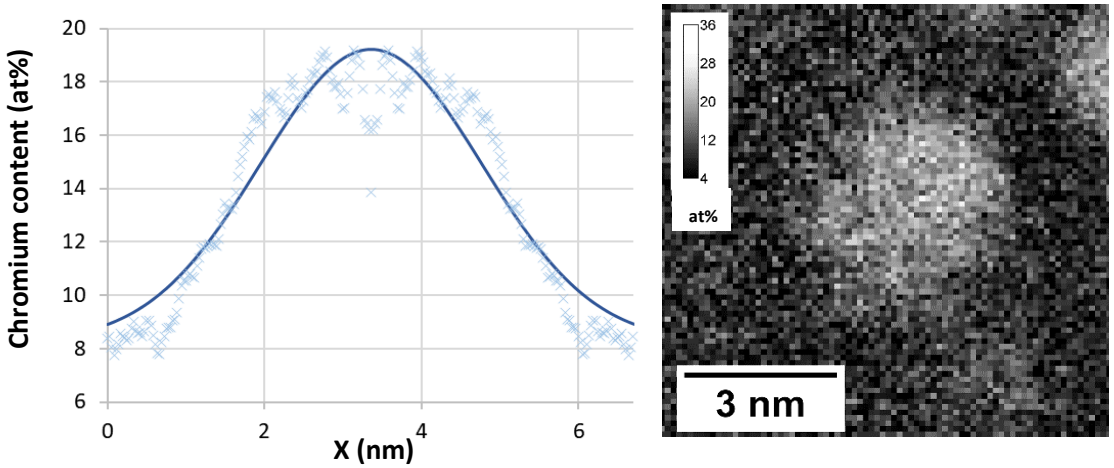

Figure 6.89: Radial line profile from a chromium cluster in the proton irradiated Fe9Cr, captured at high magnification and resolution.

Applying the same analysis as applied to the clusters in Figure 6.86, the composition of the cluster without matrix contributions was estimated. This particular cluster was found to have a mean chromium content of 45at% and peaks at 69at%. However, the fitted function (shown as part of Figure 6.89) doesn't appear to fit the profile well. The profile seems to be more similar to a semi-circle distribution function, implying that the cluster has a chromium profile that is constant for at least some of its volume.

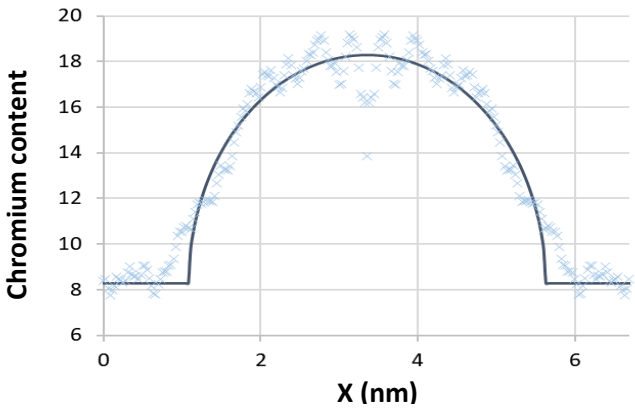

Figure 6.90: Radial profile of the chromium cluster in Figure 6.89 and fitted Wigner semi-circle distribution

Figure 6.90 shows the same data as Figure 6.69, but with a fitted Wigner semi-circle function. The diagram in Figure 6.91 illustrates how the composition of the cluster can be extracted if it is assumed that the composition is constant through the cluster, rather than Gaussian-like. Solving this for the cluster in Figure 6.88, the composition was found to be 52at% with a diameter of 4.5nm.

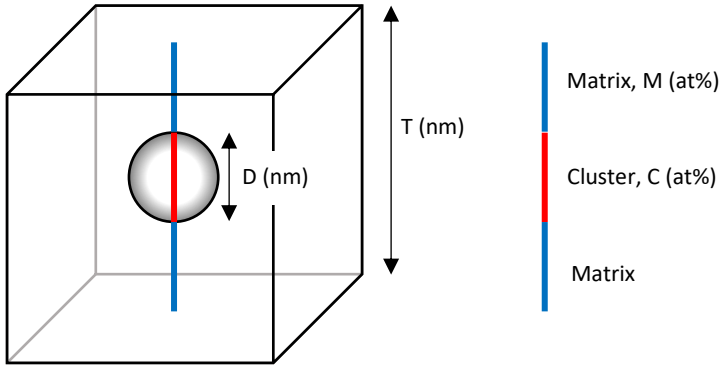

Average composition along line, $\bar{A} = \frac{C \times D + M \times (T - D)}{T}$

Figure 6.91: Diagram illustrating how to calculate the composition of a solid sphere as measured through a column of TEM foil. The average composition along the line, $\bar{A}$, is the peak value in the measured composition profile.

6.5 Summary of proton and self-ion irradiated FeCr

Table 6.14 contains a summary of the results in the proton and self-ion irradiated Fe6Cr alloy. The equivalent results from the Fe9Cr alloy are summarised in Table 6.14. These results are discussed in chapter 7. For convenience, the table summarising the results from the neutron-irradiated alloys (Table 4.5) is repeated here as Table 6.16.

Fe6Cr	**Proton**	**Self-ion**
Dislocation loop spatial distribution	Homogeneous	Mostly homogeneous
Dislocation loop density (loops/cm^3)	2.7±0.3 x10^{16}	2.5±0.3 x10^{16}
Dislocation loop mean diameter (nm)	13.3±11.3	5.7±3.7
Percentage of population with b= <111> - high and low	3%	59%
Interstitial or vacancy?	Interstitial	Interstitial
Void spatial distribution	Homogeneous	Homogeneous
Void density (voids/cm^3)	1.1±0.1 x10^{16}	1.0±0.1x10^{16}
Void mean diameter (nm)	5.7±2.5	2.4±0.7
Void maximum diameter (nm)	12.2	6.0
Chromium cluster distribution	Homogeneous (Segregation of dislocation loops)	*Not measured*
Chromium cluster density (clusters loops/cm^3)	Assumed equal to loop density	-
Chromium cluster mean size (nm)	-	-
Chromium cluster maximum size (nm)	-	-
Chromium cluster mean composition (at%)	Estimated 12 - 17	-
Chromium cluster mean peak composition (at%)	-	-

Table 6.14: Summary of radiation damage found in the proton and self-ion irradiated Fe6Cr

Fe9Cr	**Proton**		**Self-ion**
Dislocation loop spatial distribution	Heterogeneous		Homogeneous
Dislocation loop density - high and low (loops/cm^3)	8.1±1.2 x10^{16}	2.5±0.4 x10^{15}	6.8±0.8 x10^{16}
Dislocation loop mean diameter - high and low (nm)	4.7±2.0	3.8±1.6	6.7±4.7
Percentage of population with b= <111> - high and low	100%	95%	62%
Interstitial or vacancy?	Interstitial		Vacancy
Void spatial distribution	Heterogeneous		Homogeneous
Void density - high and low (voids/cm^3)	2.4±0.7 x10^{18} On dislocation lines	4.0±0.9 x10^{16} Matrix	2.2±0.6x10^{16} Poor contrast, possibly surface contaminants
Void mean diameter - high and low (nm)	4.5±1.1 On dislocation lines	2.0±0.6 Matrix	1.9±0.4
Void maximum diameter - high and low (nm)	6.5	3.5	2.6
Chromium cluster distribution	Homogeneous		None
Chromium cluster density (clusters loops/cm^3)	2.5±0.3 x10^{17}		-
Chromium cluster mean size (nm)	4.4±1.0 (4.5)		-
Chromium cluster maximum size (nm)	6.9 (-)		-
Chromium cluster mean composition (at%)	25.2±6.8 (52)		-
Chromium cluster mean peak composition (at%)	30.9±8.5 (-)		-

Table 6.15: Summary of radiation damage found in the proton and self-ion irradiated Fe9Cr. The chromium cluster results shown in brackets refer to the higher magnification measurements of a particular cluster, which may be more representative of the true compositions of the clusters.

Neutron	**Fe6Cr**		**Fe9Cr**	
Dislocation loop spatial distribution	Heterogeneous		Heterogeneous	
Dislocation loop density - high and low density regions (loops/cm^3)	4.3±0.5 x10^{16}	7.4±1.3 x10^{15}	1.2±0.3 x10^{17}	2±1 x10^{14}
Dislocation loop mean diameter - high and low density regions (nm)	5.5±3.7	3.6±1.2	5.1±3.6	-
Percentage of population with b= <111> - high and low	72±8%	52±18%	100%	-
Interstitial or vacancy?	Interstitial		Interstitial	
Void spatial distribution	Homogeneous		Homogeneous	
Void density - high and low loop density regions (voids/cm^3)	4.4±1.0 x10^{16}	4.0±0.9 x10^{16}	1.7±0.6 x10^{16}	1.8±0.4 x10^{16}
Void mean diameter - high and low loop density regions (nm)	1.2±0.6	1.3±0.4	1.2±0.4	1.3±0.3
Void maximum diameter - high and low loop density regions (nm)	3.5	2.7	2.2	1.6
Chromium cluster distribution	Homogeneous		Homogeneous	
Chromium cluster density (clusters loops/cm^3)	4.5±0.9 x10^{16}		7.4±0.4 x10^{17}	
Chromium cluster mean size (nm)	4.5±0.9		2.1±0.4	
Chromium cluster maximum size (nm)	7.1		3.0	
Chromium cluster mean composition (at%)	11.1±1.8		40.7±16.2	

Table 6.16: Summary of radiation damage found in the neutron irradiated Fe6Cr and Fe9C (repeat of Table 4.5)

Chapter 7: Discussion of the differences between neutron, proton and self-ion irradiation

7.1 Introduction

Alloys of Fe6Cr and Fe9Cr were irradiated with self-ions and with protons to replicate the neutron damage in the same alloys. The results of the neutron experiment are presented in chapter 4 and discussed in chapter 5. The results from the self-ion and proton irradiation experiments are presented in chapter 6.

I have shown that the microstructure of FeCr after neutron irradiation differs significantly from the microstructure of the same materials after proton and self-ion irradiation. Differences were observed in the dislocation loop population and homogeneity, the sizes of the loops, the Burgers vector of the loops, the nature of the loops, the void population and sizes, and the formation of chromium α'-phases. Here will be discussed these results, and the mechanisms that could be responsible.

The discussion is split into four sub-sections; the irradiation and TEM experiments that were conducted and how comparable they actually are; the differences to irradiation-induced dislocation loops, the voids, and finally the redistribution of chromium.

7.2 Discussion of the as-conducted experiments and the effects of systematic errors on the results

It is important to consider whether the differences observed between neutron, proton and self-ion damage are simply due to uncertainties in the experimental parameters. Although I have tried to keep the dose and temperature the same for all experiments, there are systematic errors in

each of these which may or may not have had noticeable effects on my observations. The dose-rate and recoil energy effects will also be discussed.

7.2.1 Discussion of dose-measurement errors

To recap, the dose received by the samples after neutron irradiation was calculated by my collaborators at UCSB using the MCNP [184] package to model the ATR core and sample assembly. This package was able to predict the neutron spectrum received by the samples in each capsule, and from the SPECTER neutron cross section library [185], calculated the number of neutron-PKA reactions to expect, and hence the dpa the material received. The neutron flux was not measured directly, and instead was calculated from the reported lobe power history of the reactor. This was used to scale the MCNP simulation of the core to predict the corresponding heat and neutron flux. The dpa was then calculated using the SPECTER dpa-cross section library which is the 2013-ASTM standard for irradiations of iron-based materials, and so has been widely used previously. The SPECTER library is out-dated though; the currently recommended alternative is the TENDL library [186].

FISPACT-II [159] is a neutron transport package that was developed to accurately predict the neutron reactions that take place when a material is exposed to a neutron-flux. FISPACT was used to calculate the dpa-dose received by the neutron-irradiated samples using the same neutron energy spectrum predicted by MCNP, but using the TENDL-2014 library. Using this, I calculated a dose of 1.6dpa, which is lower than the 2.1dpa calculated using the SPECTER library.

It was not expected that these doses would result in substantially different microstructures however. It is important to remember that 1dpa is a very large dose, literally indicating that on average, every atom in the microstructure has been displaced from its lattice site once. Above ~1dpa, it should be expected that more of the new point defects will flow to existing sinks (loops, voids, helical dislocations etc.) than will agglomerate as a new defect. Therefore, the visible defect evolution should be mostly coarsening, and defect nucleation will be in decline [199]. There might

be some observable changes to the population between 1.6 and 2.1dpa, and the loops will be smaller at 1.6dpa, but I would not expect a difference large enough to dominate the differences observed between the neutron, self-ion and proton damage.

The dose received by the self-ion irradiated sample had a peak of 2.2dpa, calculated using SRIM [110] to predict the energy lost via elastic collisions, phonons, and ionisation in pure iron. This was then scaled by the fluence, which was calculated from the charge deposited on the sample stage. The samples are electrically insulated from the final aperture in front of the stage, and so the charge deposited over the irradiated area can be accurately measured by monitoring the electrical current from the stage and integrating over time. The last aperture prior to the samples is positioned 1-2cm centimetres in front of the samples.

The largest margin of error in the dose comes in the TEM measurements. The irradiation profile of 2MeV self-ions is highly inhomogeneous (see Figure 6.7 in section-6.2.2), and so the dose in the regions that were analysed varies from one side of a micrograph to another. The measurements of loop size and density came from a region of foil that differed in dose by up to 0.5dpa over ~300nm, just prior to the Bragg peak. The effect of this difference is expected to be negligible, and the captured micrographs do not indicate a noticeable change in microstructure from one side of a micrograph to another.

It is worth mentioning that the approximate regions of maximum damage in the self-ion irradiated alloys did not correspond to the region of maximum dpa, even accounting for slight variations in the orientation of the foil with respect to the beam. This could indicate that SRIM [110] is overestimating the damage depth, or that the injected interstitials are suppressing loop growth, or that the difference in recoil energies with depth is more significant than first thought. The damage was not analysed in detail at various depths, doses and injected-Fe concentrations, but the micrographs suggest there could be important differences worth investigating in the future.

The proton irradiation dose was calculated in much the same way as for the self-ion irradiation. The dpa-dose was calculated using SRIM [110] to predict proton energy losses as they travel through the sample, and then the calculated displacements were scaled to the fluence. However, as noted in section-3.3, the number of vacancies predicted by SRIM for the proton irradiation experiment differs by up to 1dpa depending on the method used to calculate it. It was decided to use the NRT-dpa [18] as calculated by subtracting the ionisation-energy losses from the beam energy, since this is approximately equal to the average of the three methods, as described in section-3.3. The calculated dpa for the proton irradiation experiment could therefore be incorrect by up to ~0.5dpa.

The change in dose from one side of a micrograph to another (due to the dose-profile) should be insignificant, since the dpa changes by only ~0.2dpa over ~700nm. The fluence should be uniform over the irradiated area, since the beam was rastered. However, the "tails" of the beam profile could result in a higher overall dose received by the sample in the centre (in this case, the Fe6Cr). Although over-scanning the irradiated area and focussing the beam should minimise the variation in dose from sample to sample, it is possible that the centre-most sample received a slightly higher dose.

Overall, it is unlikely the dpa-dose received by the examined regions of the various samples are exactly the same for neutron, proton and self-ion irradiated samples. However, the doses received should not be substantially different. The largest difference there might be is between a TENDL-2014 [186] calculated neutron dose of 1.6dpa, and a phonon-energy loss calculated proton dose of ~2.4dpa.

7.2.2 Discussion of temperature measurement errors

The temperature of the neutron-irradiated samples, like the dose, was predicted from the lobe power history of the ATR whilst the samples were inside the reactor core. The result of finite element modelling indicated a minimum temperature of 315°C and maximum temperature of 335°C.

It is not known whether the temperature was at 335°C for a day, week, month or longer. Similarly, it is not known if the temperature constantly cycled between 315°C and 335°C. It is known, however, that the samples were in the reactor for four cycles. Between the cycles, the rod containing the capsules must have been removed to change out other capsules, and hence the temperature lowered. The thermal history of any neutron irradiation experiment is complex and difficult to accurately control, so these subtle changes could have changed the microstructure noticeably.

The temperature of the self-ion irradiation was cooler than the minimum temperature of the neutron irradiation since, at the time of the irradiation, only the target temperature of the neutron irradiation (290°C) was known. The same is true for the proton irradiation experiment. A cooler irradiation will typically result in smaller loops and higher density. However, in all the charged particle irradiations, the dislocation loops were on average larger than the loops in the neutron-irradiated materials. From this, I conclude that the source of the larger loops in the charged particle irradiations was not because the irradiation temperature was cooler, and so the effect of the cooler target temperature for the charged particle irradiations had an insignificant effect on the microstructural differences.

I have no reason to believe that the self-ion irradiation temperature was hotter than intended, but the proton irradiation may have run hotter than the indicated temperature. I discussed in section-5.2.1 that the temperature measurement by thermal camera had flaws, and could lead to an uncertain measured temperature.

The microstructure of the proton-irradiated Fe6Cr is a strong indication that the sample was hotter during irradiation than the measurements suggested, since the loops were very large (mostly >20nm) and almost entirely <100> type. Additionally, there was a substantial population of >5nm diameter voids. These observations are typical of higher-temperature irradiations, so it is important to consider how the temperature could have been higher. The correction applied to the thermal camera measurement relied on the assumption that the stage assembly was in thermal equilibrium

when each calibration-measurement was made. The emissivity of each sample was calibrated to the temperature read out by a thermocouple, which was positioned on the back of the sample holder (it was not possible to weld the thermocouple to the front plate, nor directly on the samples). Since the back of the sample holder was positioned closer to the ceramic heater than the samples, the temperature of the thermocouple could have been hotter than the samples during calibration of the thermal camera if the assembly were not in thermal equilibrium. However, this would lead to an overestimate of the sample temperature, rather than an underestimate. Therefore, it is unlikely that a miscalibration of the thermal camera is responsible for the anomalously large loops and voids in the proton-irradiated Fe6Cr.

Although the energy of the protons used was partly selected because the DCF beam was stable at this energy, there were occasional intense current bursts. These were caused by the ion-source occasionally releasing a larger number of ions than usual. The result was a brief spike in the current on the sample, which then dropped to zero before stabilising again. An event such as this happened within a fraction of a second. The temperature and current data were recorded every 2.2 seconds, so such events were missed from the logged-data. A current spike will be accompanied by a spike in temperature. Such temperature spikes might give enough energy for two loops to merge, or for a loop to transition from <111> type to <100>, or a vacancy cluster to reassemble as a void. This is only speculative however. It would require more extensive irradiations by protons at various facilities and thermal cycling experiments to confirm whether such temperature spikes have any significant effect on the microstructure. This would not explain why the microstructure of the proton-irradiated Fe9Cr consists of much smaller loops than the proton-irradiated Fe6Cr.

Overall, the temperature is a variable that is difficult to control in irradiation experiments, although less-so for self-ion irradiations. Accurate temperature control during proton irradiation is a considerable obstacle to overcome, and is probably the largest source of error in such experiments.

Further experiments should be conducted to investigate whether the observations of large loops and voids are an isolated anomaly, or a real consequence of the proton irradiation.

7.2.3 Discussion of recoil spectra and dose rate effects

If the differences in dose and temperature are not substantial, then the differences in microstructure should be dominated by recoil and dose-rate effects. The recoil-energy is the energy deposited by an irradiating particle into a PKA, and controls the size of the cascade, and the number of defects and defect-clusters produced from a collision event. To compare these effects, the PKA-energy spectra of the self-ion and proton irradiation experiments were calculated using SRIM [110]. These are shown as cumulative frequency plots in Figure 7.1, alongside the recoil spectrum from the neutron experiment, as calculated from the neutron energy spectrum by Dr Mark Gilbert.

It can be argued that self-ion irradiation doesn't have a PKA "spectrum". Rather, the implanted ion can be treated as the PKA, and hence the PKA energy is just the implantation energy. It is wrong to treat a proton as a PKA though, so using the PKA spectrum predicted by SRIM [110] is more appropriate. SRIM was therefore also used for the self-ion irradiation for consistency.

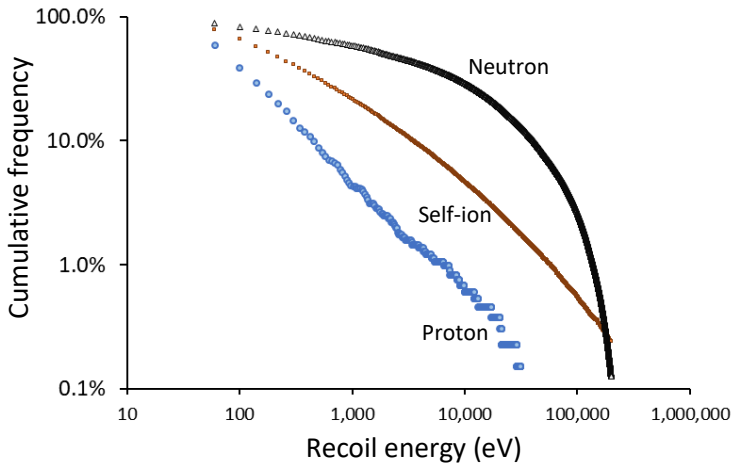

Figure 7.1: Recoil spectra in iron caused by the ATR neutrons, 1.2 MeV protons and 2 MeV self-ions, shown as cumulative frequency plots, ignoring PKAs less than 40eV. The Y-axis indicates the fraction of recoils above the recoil energy on the X-axis. The recoil spectra of the self-ions and protons were computed using SRIM [110]*. The recoil spectrum of the ATR neutrons was computed by Dr Mark Gilbert using the neutron energy-spectrum.*

These plots show how the protons produce a much higher fraction of low recoil energies than both self-ions and neutrons. The neutrons from the ATR produce PKA energies up to ~200keV, with 90% of PKAs having energy greater than 80eV (above which more than one Frenkel pair can be produced), and 58% above 1keV. Below 40eV (the displacement energy of iron), no defects can be produced. Between 40eV and 80eV, only 1 defect can be produced, and above 80eV, the average number of defects produced will scale linearly with the damage energy, up to some critical energy [17] (~10keV), above which electronic-losses will dominate and vacancy generation will saturate. For the large cascades, those with a recoil energy greater than 1keV occur 4% and 21% of the time for proton and self-ion irradiation respectively.

Figure 7.2 shows the median PKA energy for each irradiating particle, excluding PKAs below 40eV. This shows that nearly half of all recoils due to proton irradiation produce only single Frenkel pairs. The self-ion damage is dominated by larger cascades, but the neutron-generated cascades far exceed the energy of both self-ion and proton induced recoils, with a median PKA energy of almost 3keV. It is important to remember that above ~5-10keV [19,116–118] (or maybe even as high at 500keV [119]), sub-cascade branching occurs. A better treatment of the recoil spectrum would be to re-calculate the spectrum of recoils for all PKAs above this sub-cascade branching energy. This was not done here, since it requires much more extensive SRIM calculations, and an appropriate value for the minimum PKA energy at which the cascades will (on average) consist of many smaller sub-cascade branches.

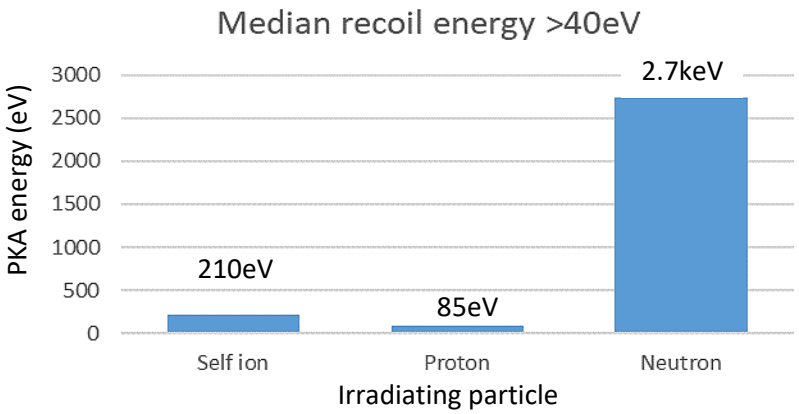

Figure 7.2: Median recoil energy in iron due to 2 MeV self-ion, 1.2 MeV proton and ATR neutron irradiation, as calculated by SRIM (proton and self-ion) and as calculated by Dr Mark Gilbert (ATR neutron).

The differences in PKA-spectra of the neutron, proton and self-ion irradiation are accounted for in the calculation of dpa, so the number of displacements the irradiations have produced should be similar. However, the type of primary defect produced by a proton, self-ion or neutron could be affected by the PKA energy, since small cascades produce freely-migrating defects more "efficiently" [17]. This suggests that radiation-enhanced diffusion is more significant during proton irradiation than during neutron or self-ion irradiation (since more mobile defects are produced), which will favour the redistribution of chromium and the flow of defects to sinks (such as grain boundaries, dislocations, and loops).

The last factor to discuss is the dose-rate. It was impractical to conduct proton and self-ion irradiations at the same dose-rate as the neutron-irradiation. Instead, charged particle irradiations were carried out at a dose-rate ~100x faster than the neutron dose-rate. This will promote loop nucleation due to the frequent cascades causing cascade overlap to occur earlier, preventing the microstructure from recovering post-cascade [17]. The dose-rate effect could be the prime reason for my observations of more visible loops in matrix-regions of the charged particle irradiations than the matrix regions of the neutron-irradiated samples.

7.3 The effect of irradiating particle on the irradiation-induced dislocation loops

The vast majority of the dislocation loops in the neutron-irradiated Fe9Cr were presumed to exist as clusters too small to see in the TEM. Both the Fe6Cr and Fe9Cr contain large areas (several hundred nanometres) with a very low density of visible loops (as low as ~10^{14} loops/cm^3 in the Fe9Cr), with the majority of the visible damage clustered around dislocations and low-angle grain boundaries. This observation is consistent with similar observations of neutron damage in FeCr by Hernandez-Mayoral et al. [76]. I have observed a large density of visible loops in the matrix of both self-ion and proton-irradiated FeCr. This indicates that a faster dose-rate could promote growth, a finding that is also supported by the self-ion dose-rate experiments by Xu [144]. I await publication of the results of Bhattacharyya et al [191] to make a comparison of dislocation loops produced by faster dose-rate neutron irradiation.

The self-ion irradiated microstructure is very different to the neutron-irradiated microstructures. Although some loops were clustered together, the damage was much more homogeneous throughout the first 600nm of the foil, after which the loop population declined with depth. The loops in the Fe6Cr had similar sizes to the high loop-density regions of the neutron-irradiated sample, but the loops in the self-ion irradiated Fe9Cr were much larger than those in the neutron and proton-irradiated Fe9Cr.

The largest difference between the self-ion irradiated samples and the rest of the samples is that the loops were vacancy in nature. Vacancy loops are rarely reported in ferritic materials, and usually only in situations where there is a large interstitial sink close by (e.g. the foil surface). This is because interstitials exhibit a much larger strain field on the matrix, and thus migrate easily and "see" other interstitials more easily than vacancies. Interstitials clusters therefore coarsen more quickly than vacancy clusters, leading to the majority of visible dislocation loops being interstitial. Therefore, the most likely explanation for my observations of vacancy loops is that interstitials are being lost to some interstitial sink. The only interstitial sink visible from my micrographs is the

surface of the sample. If interstitials are being lost to the sample surface during irradiation, then this would leave a supersaturation of vacancies in the matrix, which are able to cluster as dislocation loops. This would suggest the interstitial defects are able to migrate hundreds of nanometres to reach the surface during irradiation.

Interstitial loops can glide very easily, and if there is a clear path, will move towards sinks such as a grain boundary or free surface very quickly. However, movement over hundreds-of-nanometres would require an extremely ultra-high purity alloy, because only small amounts of impurities are able to pin a dislocation loop in its glide path. For instance, Arakawa et al. [190] studied the diffusion of dislocation loops in ultra-high purity iron (<1wt-ppm of carbon) during simple heating experiments, and observed dislocation loops hopping along their glide cylinder up to 200nm per "hop" at a temperature of 300^{o}C. The dislocation loops would hop back and forth rapidly between two points in the glide cylinder (where the impurities lie).

The alloys I have studied are much less pure than the iron sample Arakawa et al. observed (see section-3.1 for compositional analysis of my alloys). This would suggest that interstitial diffusion to a free surface during self-ion irradiation should affect only a small fraction of the microstructure. However, from my observation of vacancy loops in regions ~300 to 500nm from the irradiation surface, this suggests that interstitials are diffusing over a much greater distance than expected. A question that must be considered is whether this faster diffusion of interstitial dislocation loops is due to the material or the irradiation. As a reminder, we have seen only interstitial loops in the proton and neutron irradiated alloys. Detailed analysis of the near-surface damage in the proton-irradiated samples was not conducted.

If the increase in interstitial loop diffusivity is a material effect, then one might consider the absence of loops in the neutron-irradiated Fe9Cr to also be because of increased diffusion (to the grain boundaries). However, this is unlikely since I have not observed any vacancy loops in the neutron irradiated alloys as I have in the self-ion irradiated alloys, and the discrepancy between

interstitial and vacancy defects in the helical dislocations strongly implies that there is a large population of small interstitial defects that are not visible from my analysis. This would also require the interstitials to be capable of gliding for microns, rather than hundreds-of-nanometres as seems to be the case for the self-ion irradiated alloys.

The more likely explanation is that the high frequency of large cascades during self-ion irradiation increases diffusion enough to substantially extend the glide range of an interstitial defect. The effects of cascades occurring close to or on top of a pre-existing dislocation loop are still poorly understood. In-situ observations of loop hopping in impure α-iron has been studied by Satoh et al. [200] during high energy electron irradiation. Satoh et al. suggested that electrons cause de-trapping of dislocation loops, allowing them to glide further distances. Like the electrons in Satoh et al.'s experiment, self-ion cascades could also be disrupting the trapping site of dislocation loops, allowing them to glide further, and eventually reach the free surface or a grain boundary. An in-situ irradiation experiment dedicated to studying loop glide during irradiation in varying purity materials at different dose rates would be helpful towards understanding my results.

My observations have large implications for self-ion irradiation, as the damage is often assumed to be interstitial, and representative of neutron damage; for my alloys, the damage is actually vacancy, and so the hardening mechanisms are very different to neutron damage. Further investigations with higher and lower chromium containing alloys should be conducted to evaluate the loop nature effects in more detail, and also higher-energy irradiations to allow for a deeper irradiation damage layer.

The self-ion irradiated Fe6Cr and Fe9Cr both contained a higher proportion of <100> loops than the neutron-irradiated samples (the Fe6Cr contained 41±7% and 28±8% <100> loops, while the Fe9Cr contained 39±7% and 0% <100> loops after self-ion and neutron irradiation respectively). The <100> loops are produced either by loop-loop coalescence or via rotation of the loop habit plane while it is small, or both. The observation of a greater number of <100> loops is usually correlated

with higher loop mobility [47]. It can therefore be concluded that the loops produced during self-ion irradiation were more mobile than loops produced during neutron irradiation. This could be an effect of the frequent bombardment of the matrix with large cascades, amounting to ballistic mixing of the atoms, which will enhance their diffusion to defect sinks (such as already nucleated loops). Ballistic mixing is also a proposed explanation for the reduced chromium precipitation that occurs during self-ion irradiation experiments [105,106] (discussed in section-6.4).

At the fast dose-rate of the self-ion and proton irradiations, the cascades are frequent and close together, which will promote defect clustering, resulting in larger loops early on. Such loops will act as sinks in the matrix for more defects, so coarsening will occur at lower doses than the low dose-rate neutron irradiation. This is already backed up by the dose-rate observations by Xu [144]. Frequent cascades may also facilitate the transition of a <111> loop to a <100> loop, but this is only speculation.

The Fe6Cr contained mostly larger <100> loops, which as discussed in section-6.2.2 is typical higher temperature irradiations [35]. If the temperature was not significantly different from the irradiation temperature of the neutron experiment, then these results signify that proton irradiation is significantly promoting diffusion of the defects, leading to coarsening of the loops, and the promotion of <100> loop formation.

Although most loops analysed in the proton, self-ion and neutron-irradiated Fe6Cr and Fe9Cr were close to pure-edge type, several examples of loops with non-prismatic habit planes were found. Examples were found in all studied samples, besides the proton-irradiated Fe6Cr, of loops with habit planes lying closer to a {110} type plane than {111}. It has been suggested by [39] that <111> dislocation loops evolve by nucleating on {110} planes, then rotating towards {111}, then rotating to {211}, and finally {100}, transitioning Burgers vector at some point between the last stages. No {211}-plane loops were found in the neutron, proton or ion-irradiated samples.

Within the helical dislocation inside the neutron-irradiated Fe9Cr, a greater number of loops had habit planes that matched the orientation of the helical dislocation, indicating that the dislocation loop planes are influenced by the local strain field of the dislocation, and other defects in their vicinity. This is observation is supported by previous observations of dislocation loops in the vicinity of other defects or free surfaces [37,38].

7.4 The effect of irradiating particle on the irradiation induced voids

The void populations and sizes in the proton-irradiated materials were substantially greater than those seen in the neutron and self-ion irradiated materials. The voids in the proton-irradiated sample were ~5nm in diameter on average, whereas the self-ion and neutron-irradiated samples contained mostly <2nm voids.

Voids are rarely seen in self-ion irradiated microstructures at ~1dpa doses (see section-2.8), but this may be in part due to the difficulty in distinguishing small voids from surface oxide or any other surface contaminant, or small particle. A slightly higher density and mean size of voids in the self-ion irradiated Fe6Cr were recorded than in the neutron-irradiated alloy. The error bars are large for both sets of measurements, so it is appropriate to say that the voids in the neutron-irradiated Fe6Cr are fairly well replicated by the self-ion irradiation. Although many examples of defects with void-like contrast were visible in the self-ion irradiated Fe9Cr, they all had very poor contrast compared to similar-sized voids in the proton-irradiated Fe9Cr, so these features might actually be surface contaminants. If these features are voids, then their density is low, which would normally indicate that the vacancy defects mostly exist as clusters too small to identify from surface oxide and/or contaminants. However, a substantial population of the dislocation loops in the self-ion irradiated Fe9Cr are vacancy type, which may explain why no larger voids are visible from the under-over focus technique, although the self-ion irradiated Fe6Cr also contained vacancy loops.

As with the dislocation loops, the voids in the proton-irradiated Fe6Cr are much larger (up to 12nm in diameter) than the self-ion and neutron-irradiated Fe6Cr (up to 6nm and 3nm respectively).

Such large voids are typically observed at higher temperatures (since vacancies are more mobile), and high dose [138,156]. However, since a large population of large voids exists in the proton-irradiated Fe9Cr (up to 7nm), and in materials studied in preliminary proton-irradiation experiments, I can conclude that proton irradiation enhances void growth.

It is unlikely that the implanted hydrogen is causing bubbles to nucleate independently of the vacancy population, since hydrogen is highly mobile in iron and steel. Implanted hydrogen is often not considered to be influential during proton irradiation [145], since the majority of the hydrogen is deposited beyond the Bragg peak, several microns from where measurements are conducted. However, as shown in Figure 5.1, the implanted hydrogen at shallow depths of the proton-irradiated alloys is between 500 and 1000appm. Considering that hydrogen is easily trapped at defects like vacancy clusters, it is highly probable that hydrogen remains in the microstructure during and after irradiation, or at least long enough to affect the vacancy-defects.

Although some voids in the proton-irradiated Fe6Cr appear misshapen, they do not appear to be uniformly circular either. This indicates that they are not pressurised, but may still contain hydrogen. It is not possible to be very conclusive about the role of hydrogen here, since direct measurements (e.g. via EELS) were not made. However, the results do indicate that hydrogen does affect the evolution of vacancy defects during proton irradiation. A more in-depth investigation of implanted hydrogen on the resulting microstructure, with dose as an independent variable, would be useful for verifying hydrogen's influence during proton irradiation.

The voids in the proton-irradiated materials have been observed to be produced in chains, which in the Fe9Cr are situated on top of screw dislocations. Helical dislocations were found in the proton-irradiated Fe9Cr, but many examples consist of straight and helical segments. The helical segments are absent of these void-chains, which would support the earlier result that these helical dislocations are produced by vacancy-mediated climb, rather than interstitial (section-4.5.4). Hence, vacancies were removed from the local microstructure, so voids did not form. It is not clear why

void-chains formed in some places, and helical dislocations formed in others. It could be an indication that the irradiation temperature is very close to the temperature at which it is preferable for vacancies to gather as voids, rather than on the dislocation. The dislocations would therefore contain a mixture of void-chains and helical segments. There would still be a flux of vacancies towards the dislocation (due to the vacancy-bias), which would lead to void nucleation close to the dislocation core.

7.5 The effect of irradiating particle on the redistribution of chromium

Electron energy-loss spectroscopy was used to determine whether, in response to neutron, proton or self-ion irradiation, α' phase chromium precipitates have formed, and/or whether chromium has segregated on irradiation induced defects. Chromium precipitates were found to be present in the matrix of the neutron-irradiated Fe6Cr and Fe9Cr, and the matrix of the proton-irradiated Fe9Cr. No such precipitation or segregation was identified in the self-ion irradiated Fe9Cr, and the Fe6Cr was not measured.

The analysis of chromium clusters in the neutron and proton-irradiated Fe9Cr indicates the core of the clusters exceed 50at% chromium in both cases, which is typical of α'-phases (though there is not a well-defined threshold composition of chromium that defines when a cluster is α'-phase, rather than simply a cluster). Furthermore, there is inconsistency in the literature over how a cluster is defined, with various isosurfaces used as a threshold for defining clustered regions in APT data [101,187]. This makes it difficult to reliably compare the chromium compositions measured from different experiments. The measurements of the core composition in the neutron and proton-irradiated Fe9Cr are similar to the APT measurements by Kuksenko et al. [187] on similar FeCr alloys neutron-irradiated to a lower dose. This supports my designation of these clusters as α'-phases.

The chromium precipitates in the proton-irradiated Fe9Cr were fewer in number by approximately a third than those in the neutron-irradiated alloy, and had an average composition of ~20at% Cr, whereas the neutron-irradiated precipitates had an average composition of ~40at%. The

measurements of the clusters in the proton-irradiated sample probably underestimate the composition of chromium due to the larger STEM beam width, with a subsequent measurement using an atomic-resolution probe indicating a higher mean composition of ~50at% Cr.

The neutron-irradiated Fe9Cr alloy I have studied is from the same batch of materials as the Fe9Cr alloy studied by Bachhav et al. [101], which was irradiated to a similar dose and at a similar temperature but at a dose-rate that was roughly four-times faster. The population of α' precipitates I measured in the neutron-irradiated Fe9Cr alloy ($7.4x10^{17}cm^{-3}$) is nearly an order of magnitude higher than that which Bachhav et al. recorded ($8.5x10^{16}cm^{-3}$). The population of precipitates in the proton-irradiated alloy was ~3x the population measured by Bachhav et al. [101].

It was discussed earlier in section-5.2 how the increase in α'-precipitate population in the neutron-irradiated Fe9Cr over the Bachhav et al. measurements could be due to the large population of very small interstitial clusters invisible to TEM that are (probably) present in my alloy. This observation is probably connected to the dose-rate effect, hence a lower population of α' was seen in Bachhav et al.'s faster dose-rate experiment. However, the proton irradiation experiment was a hundred-times faster than the neutron irradiation experiment. This suggests that although dose-rate may be acting to suppress α' formation, proton irradiation enhances α' to such a degree that it overcomes any dose-rate effects acting to suppress it.

Accelerated chromium precipitation can only be attributed to accelerated diffusion of chromium during irradiation. Proton irradiation appears to enhance defect mobility in relation to void and loop growth, and so it is reasonable to expect chromium diffusion to also be enhanced. This would be expected from the increased fraction of freely-migrating defects produced by proton-induced cascades.

The flow of interstitials and vacancies leads to the redistribution of the matrix atoms over time, which can cause a local concentration of chromium to exceed the solubility limit [201–203], and cause a new α' phase to form. This will then continue to grow and become further enriched.

Since no such precipitation was seen in the self-ion irradiated Fe9Cr, I can conclude that either the large cascades, the injected iron-atoms, or both suppress this process. A very large cascade might be able to disrupt a local concentration of chromium that may otherwise become α'. Frequent bombardment of the lattice by such large cascades would mean this process occurs often. Therefore, α' precipitates would struggle to nucleate. Large cascades from protons are rarer, which may allow time for a chromium cluster to coarsen and become further enriched, leading to the observed microstructure.

Large and frequent cascades (e.g. from ion or neutron irradiation) may also disrupt the flow of chromium towards sinks such as dislocation loops. If dislocation loops do act as nucleation centres of α' precipitates, then the lack of such precipitates may explain why the loops in the self-ion irradiated Fe9Cr were able to grow much larger (although, the self-ion irradiated Fe6Cr contained smaller loops than the Fe9Cr, in which it is presumed no chromium redistribution occurred).

Chromium was found to be enriched around the large dislocation loops in the proton-irradiated Fe6Cr. The large loops present allowed for investigation of where chromium lies in relation to the dislocation core. It was not possible to see the dislocation core, but chromium seemed to peak in concentration close to where the core was expected to lie (from the diffraction-contrast). The inside of the loop was also enriched with chromium in comparison to the matrix, indicating that chromium is becoming trapped in and/or near the interstitial planes of the dislocation loop.

Chromium clustering was also seen in the neutron-irradiated Fe6Cr, which like the proton-irradiated Fe6Cr, I expect is associated with dislocation loops (though it was not possible to verify this). This demonstrates that irradiation can cause chromium to cluster at concentrations below the solubility limit via segregation of irradiation-induced defects. The proton irradiation had a very different distribution of chromium in the matrix to the neutron-irradiated alloy, but this is due to the large loops also present.

Chapter 8: Conclusions

8.1 Summary of key results

Alloys of Fe6Cr and Fe9Cr were irradiated with neutrons, self-ions and protons to a dose of ~2dpa and at temperatures in the region of 300°C. The key findings are listed below.

1- Neutron irradiation of Fe6Cr and Fe9Cr produced a highly heterogeneous distribution of small (~5nm) interstitial dislocation loops, mostly with a Burgers vector of <111> (section-4.4.1 and 4.5.1). High densities of dislocation loops were present around helical dislocations. These helical dislocations were initially straight near-pure screw dislocations which, during irradiation, experienced radial climb in response to a vacancy-biased flux onto the dislocation core (section-4.5.4). The results indicate that the removal of vacancies by the dislocations causes a supersaturation of interstitials in the local microstructure, leading to the high density ($4.3x10^{16}$ and $1.2x10^{17}$ loops/cm^3 in the high-density regions of the Fe6Cr and Fe9Cr respectively) of visible loops close to the helical dislocations.

2- The matrix of neutron-irradiated Fe6Cr and Fe9Cr contained a rich density of chromium clusters ($4.5x10^{16}$ and $7.4x10^{17}$/cm^3 in the Fe6Cr and Fe9Cr respectively), which in the Fe9Cr were identified as α'-phases. The density of chromium clusters in the Fe9Cr was ~10x higher than the density of clusters reported by Bachhav et al. [101] in the same alloy irradiated with neutrons at a 4x faster dose-rate. These results suggest that chromium precipitates impede loop mobility and growth to visible sizes. The dose-rate effect is shown to be significant for only a factor of four difference for neutron irradiation, possibly due to the ballistic dissolution of newly formed chromium clusters at high dose-rates.

3- Irradiation to a similar dose and at a similar temperature by self-ions and by protons produces damage that is inconsistent with the neutron damage observations. The ion-

irradiated Fe6Cr (section-4.3) contained a mostly homogeneous distribution of vacancy dislocation loops, but the loops were similar in size (~5nm) to the interstitial loops in the high-density regions of the neutron irradiated Fe6Cr. The ion-irradiated Fe6Cr also contained a higher fraction of <100>-type loops than the neutron-irradiated sample (41% and 28% in the ion and neutron-irradiated Fe6Cr respectively). Homogeneously distributed dislocation loops were found in the proton-irradiated Fe6Cr. They were mostly <100>, all interstitial, and were much larger (~13nm in diameter) than those in the neutron and self-ion irradiated alloys (~6nm in both). These results suggest that defect mobility was greatly enhanced during proton irradiation, more so than during self-ion or neutron irradiation, leading to a coarser population of loops. This is also implied by the larger (>5nm) population of voids distributed throughout the proton irradiated Fe6Cr.

4- The dislocation loops in the self-ion irradiated Fe9Cr were homogeneously distributed, and larger (~7nm in diameter) than those in the neutron and proton-irradiated alloys (~5nm in both). The loops in the self-ion irradiated Fe9Cr were mostly vacancy-type, whereas loops in the neutron and proton-irradiated Fe9Cr were all interstitial. Voids, mostly <2nm in size, were identified in the self-ion irradiated Fe6Cr and Fe9Cr, but these were less clear and possibly surface oxide in the Fe9Cr. The dislocation loops in the proton-irradiated Fe9Cr were heterogeneously distributed through the foil, similar to the neutron-irradiated alloy, with higher loop densities close to helical-shaped dislocations.

5- Proton irradiation of the Fe6Cr and Fe9Cr produced a large population of voids (~$1x10^{16}$ and $4x10^{16}$ voids/cm^3 respectively) throughout the microstructure. In the Fe9Cr, larger voids ~5nm were found aligned in chains alongside or through screw dislocations. The line dislocations comprised straight sections (with the void-chains) and helical segments, containing fewer voids and smaller voids ~2nm in size. The helical segments, like the helical dislocation in the neutron irradiated Fe9Cr, were also produced by a vacancy-biased defect

flux. Since the voids in the self-ion and neutron irradiated Fe6Cr and Fe9Cr were much smaller (~2nm), the large void population of the proton-irradiated alloys may be evidence that injected hydrogen is stabilising void growth.

6- Chromium α'-precipitates were identified in the neutron and proton-irradiated Fe9Cr, but not the self-ion irradiated Fe9Cr. The dose-rate of the proton and self-ion irradiation experiments were similar, which suggests that injected interstitials and/or large cascades of the self-ion irradiation were disrupting early stage chromium clusters, which may otherwise have gone on to form α' phases.

8.2 On the use of protons and self-ions for replicating neutron damage

Table 8.1 summarises the irradiation induced changes produced by the charged-particle irradiations and the implications these have in relation to recreating neutron damage.

	Irradiation-induced change	Implications for replicating neutron damage
Protons	Cavity formation	Hydrogen is probably retained in proton-irradiated material (section-6.3.4 and 6.4.4), which will accelerate void-swelling and possibly embrittlement, even in regions prior to the Bragg peak.
	Chromium redistribution	This is well-approximated by protons (section-6.4.5), with similar α'-phases forming under proton irradiation. Diffusion is enhanced during proton irradiation compared with neutron irradiation, so temperature shifts to offset dose-rate may be different for proton irradiation.
	Dislocation loop production	Interstitial dislocation loops similar to neutron-induced loops can be produced by protons (section-6.4), but for some alloys they may grow to much larger sizes (section-6.3). Temperature fluctuations during irradiation may enhance growth of such defects, and enhance the transition to <100> type.
Self-ions	Cavity formation	Very small voids, or none, are produced at doses up to 2dpa (section-6.3.4 and 6.4.4). Neutron irradiation produced similar cavities, but these similarities are less certain due to ambiguities over measuring such small features.
	Chromium redistribution	Chromium was only seen in solution after self-ion irradiation (section-6.4.5). Lower dose-rates (lower than 10^{-5}dpa/s) may be necessary for chromium redistribution to be significant. Self-ions are not well-suited for replicating radiation-induced segregation or precipitation.
	Dislocation loop production	Neutron-induced dislocation loops were poorly recreated by self-ion irradiation (section-6.3 and 6.4). Homogeneous damage distribution should be expected at dose rates ~10^{-5}dpa/s. Self-ion irradiation can favour a high population of large vacancy loops in some materials (section-6.3.3 and 6.4.2) and irradiation conditions, which will affect the hardening mechanisms at play. Nature analysis should always be performed where possible to assess the role of vacancy loops in self-ion damage.

Table 8.1: Summary of how well protons and self-ions to replicate neutron damage

8.3 Future work

There are several areas that required further investigation, and several results that leave open-ended questions regarding radiation damage and the application of charged particles for replicating neutron damage in FeCr.

1- The differences that have been observed in the microstructures of FeCr after neutron, proton and self-ion irradiation may be reflected in changes to mechanical properties. A study to link the microstructure and mechanical properties of each irradiation-type would be useful.

2- It would be an interesting experiment to irradiate a sample with the intent to nucleate dislocation loops without any chromium precipitates (for example, using high dose-rate heavy-ion irradiation), and then hold the sample at temperature for days, weeks and/or months. If dislocation loops are acting as the nucleation sites for α' formation, then they might still nucleate, despite the absence of dynamic effects of the radiation. It would also be interesting to investigate higher chromium compositions.

3- The observation of large voids in the proton-irradiated alloys suggests vacancy diffusion was enhanced in comparison to neutron irradiation. A temperature dependence study would help to identify the effects of beam heating and hydrogen on the resulting void structures.

4- Many facilities exist that can be used for ion or proton implantation of materials to replicate neutron damage. To verify the consistency of irradiation experiments, it would be useful to compare the results from same experiment repeated at several facilities.

5- It is important that extensive nature analysis be conducted on dislocation loops in self-ion irradiated alloys with various chromium contents. Such experiments would help to explain the origin of the vacancy loops found in the self-ion irradiated Fe9Cr.

References

[1] UNFCCC, Adoption of the Paris agreement - Proposal by the President. Draft Decision -/CP.21, (2015). http://unfccc.int/resource/docs/2015/cop21/eng/l09r01.pdf (accessed December 15, 2015).

[2] P.M. Vitousek, Beyond Global Warming: Ecology and Global Change, Ecology. 75 (1994) 1861. doi: https://doi.org/10.2307/1941591

[3] S.J. Zinkle, Fusion materials science: Overview of challenges and recent progress, Phys. Plasmas. 12 (2005) 58101. doi: https://doi.org/10.1063/1.1880013

[4] S.J. Zinkle, J.T. Busby, Structural materials for fission & fusion energy, Mater. Today. 12 (2009) 12–19. doi: https://doi.org/10.1016/S1369-7021(09)70294-9

[5] M. Kikuchi, K. Lackner, M. Quang, Fusion Physics, International Atomic Energy Agency, Vienna, 2012. https://www-pub.iaea.org/MTCD/Publications/PDF/Pub1562_web.pdf

[6] D. Maisonnier, I. Cook, S. Pierre, B. Lorenzo, D.P. Luigi, G. Luciano, N. Prachai, P. Aldo, DEMO and fusion power plant conceptual studies in Europe, Fusion Eng. Des. 81 (2006) 1123–1130. doi: https://doi.org/10.1016/j.fusengdes.2005.08.055

[7] ITER Project, http://www.iter.org, Accessed 12-01-2016

[8] Large Helical Device Project, National Institute for Fusion Science, https://www-lhd.nifs.ac.jp/pub/index_e.html (accessed September 21, 2018)

[9] Wendelstein 7-X | Max-Planck-Institut für Plasmaphysik, https://www.ipp.mpg.de/w7x (accessed September 21, 2018)

[10] Compact Fusion | Lockheed Martin, https://www.lockheedmartin.com/en-us/products/compact-fusion.html (accessed September 21, 2018)

[11] R. Betti, O.A. Hurricane, Inertial-confinement fusion with lasers, Nat. Phys. 12 (2016) 435–448. doi: https://doi.org/10.1038/nphys3736

[12] A.K. Suri, N. Krishnamurthy, I.S. Batra, Materials issues in fusion reactors, J. Phys. Conf. Ser. 208 (2010) 12001. doi: https://doi.org/10.1088/1742-6596/208/1/012001

[13] J.L. Boutard, A. Alamo, R. Lindau, M. Rieth, Fissile core and Tritium-Breeding Blanket: structural materials and their requirements, Comptes Rendus Phys. 9 (2008) 287–302. doi: https://doi.org/10.1016/j.crhy.2007.11.004

[14] A. Kohyama, A. Hishinuma, D.S. Gelles, R.L. Klueh, W. Dietz, K. Ehrlich, Low-activation ferritic and martensitic steels for fusion application, J. Nucl. Mater. 233–237 (1996) 138–147. doi: https://doi.org/10.1016/S0022-3115(96)00327-3

[15] Eurofer | The European Steel Association, http://www.eurofer.org/ (accessed September 21, 2018)

[16] R. Lindau, A. Möslang, M. Rieth, M. Klimiankou, E. Materna-Morris, A. Alamo, A.A.F. Tavassoli, C. Cayron, A.M. Lancha, P. Fernandez, N. Baluc, R. Schäublin, E. Diegele, G. Filacchioni, J.W. Rensman, B.V. d. Schaaf, E. Lucon, W. Dietz, Present development status of EUROFER and ODS-EUROFER for application in blanket concepts, Fusion Eng. Des. 75–79 (2005) 989–996. doi: https://doi.org/10.1016/j.fusengdes.2005.06.186

[17] G.S. Was, Fundamentals of Radiation Materials Science, Springer, 2007. doi: https://doi.org/10.1007/978-3-540-49472-0

[18] R.E. Stoller, M.B. Toloczko, G.S. Was, A.G. Certain, S. Dwaraknath, F.A. Garner, On the use of SRIM for computing radiation damage exposure, Nucl. Instruments Methods Phys. Res. Sect. B Beam Interact. with Mater. Atoms. 310 (2013) 75–80. doi: https://doi.org/10.1016/j.nimb.2013.05.008

[19] R. Dierckx, The Importance of the PKA Energy Spectrum for Radiation Damage Simulation, J. Nucl. Mater. 144 (1987) 214–227. doi: https://doi.org/10.1016/0022-3115(87)90034-1

[20] K. Arakawa, M. Hatanaka, H. Mori, K. Ono, Effects of chromium on the one-dimensional motion of interstitial-type dislocation loops in iron, J. Nucl. Mater. 329–333 (2004) 1194–1198. doi: https://doi.org/10.1016/j.jnucmat.2004.04.263

[21] M. Biget, R. Rizk, P. Vajda, A. Bessis, On the spontaneous recombination volume of Frenkel defects in irradiated b.c.c. metals, Solid State Commun. 16 (1975) 949–952. doi: https://doi.org/http://dx.doi.org/10.1016/0038-1098(75)90901-1

[22] J.A. Horak, T.H. Blewitt, Fast neutron irradiation induced resistivity in metals, Phys. Status Solidi. 9 (1972) 721–730. doi: https://doi.org/10.1002/pssa.2210090238

[23] M.R. Gilbert, J. Marian, J.C. Sublet, Energy spectra of primary knock-on atoms under neutron irradiation, J. Nucl. Mater. 467 (2015) 121–134. doi: https://doi.org/10.1016/j.jnucmat.2015.09.023

[24] M.R. Gilbert, S.L. Dudarev, P.M. Derlet, D.G. Pettifor, Structure and metastability of mesoscopic vacancy and interstitial loop defects in iron and tungsten, J. Phys. Condens. Matter. 20 (2008) 345214. doi: https://doi.org/10.1088/0953-8984/20/34/345214

[25] W. Hoffelner, Handbook of Damage Mechanics, Springer Nature, New York, 2014. doi: https://doi.org/10.1007/978-1-4614-5589-9

[26] X. Yi, A.E. Sand, D.R. Mason, M.A. Kirk, S.G. Roberts, K. Nordlund, S.L. Dudarev, Direct observation of size scaling and elastic interaction between nano-scale defects in collision cascades, EPL (Europhysics Lett. 110 (2015) 36001. doi: https://doi.org/10.1209/0295-5075/110/36001

[27] A. De Backer, A.E. Sand, K. Nordlund, L. Luneville, D. Simeone, S.L. Dudarev, Subcascade formation and defect cluster size scaling in high-energy collision events in metals, EPL (Europhysics Lett. 115 (2016) 26001. doi: https://doi.org/10.1209/0295-5075/115/26001

[28] A.E. Sand, D.R. Mason, A. De Backer, X. Yi, S.L. Dudarev, K. Nordlund, Cascade fragmentation: deviation from power law in primary radiation damage, Mater. Res. Lett. 5 (2017) 357–363. doi: https://doi.org/10.1080/21663831.2017.1294117

[29] A.E. Sand, S.L. Dudarev, K. Nordlund, High-energy collision cascades in tungsten: Dislocation loops structure and clustering scaling laws, EPL (Europhysics Lett. 103 (2013) 46003. doi: https://doi.org/10.1209/0295-5075/103/46003

[30] F. Ferroni, X. Yi, K. Arakawa, S.P. Fitzgerald, P.D. Edmondson, S.G. Roberts, High temperature annealing of ion irradiated tungsten, Acta Mater. 90 (2015) 380–393. doi: https://doi.org/10.1016/J.ACTAMAT.2015.01.067

[31] W.K. Brown, K.H. Wohletz, Derivation of the Weibull distribution based on physical principles and its connection to the Rosin–Rammler and lognormal distributions, J. Appl. Phys. 78 (1995) 2758–2763. doi: https://doi.org/10.1063/1.360073

[32] D. Hull, D.J.J. Bacon, Introduction to Dislocations, Fifth Edit, Elsevier BH, 2011. doi: https://doi.org/10.1016/B978-0-08-096672-4.00019-0

[33] S.L. Dudarev, R. Bullough, P.M. Derlet, Effect of the alpha-gamma Phase transition on the stability of dislocation loops in bcc iron, Phys. Rev. Lett. 100 (2008) 1–4. doi: https://doi.org/10.1103/PhysRevLett.100.135503

[34] I.M. Robertson, A study of the irradiation damage structure in alpha-iron, Univ. Oxford DPhil Thesis. (1981)

[35] Z. Yao, M.L. Jenkins, M. Hernández-Mayoral, M.A. Kirk, The temperature dependence of heavy-ion damage in iron: A microstructural transition at elevated temperatures, Philos. Mag. 90 (2010) 4623–4634. doi: https://doi.org/10.1080/14786430903430981

[36] S. Xu, Z. Yao, M.L. Jenkins, TEM characterisation of heavy-ion irradiation damage in FeCr alloys, J. Nucl. Mater. 386–388 (2009) 161–164. doi: https://doi.org/10.1016/j.jnucmat.2008.12.078

[37] Z. Yao, M. Hernández-Mayoral, M.L. Jenkins, M.A. Kirk, Heavy-ion irradiations of Fe and Fe–Cr model alloys Part 1: Damage evolution in thin-foils at lower doses, Philos. Mag. 88 (2008) 2851–2880. doi: https://doi.org/10.1080/14786430802380477

[38] M. Hernández-Mayoral, Z. Yao, M.L. Jenkins, M.A. Kirk, Heavy-ion irradiations of Fe and Fe–Cr model alloys Part 2: Damage evolution in thin-foils at higher doses, Philos. Mag. 88 (2008) 2881–2897. doi: https://doi.org/10.1080/14786430802380477

[39] N. Gao, J. Chen, R.J. Kurtz, Z.G. Wang, R.F. Zhang, F. Gao, New understanding of nano-scale interstitial dislocation loops in BCC iron, J. Phys. Condens. Matter. 29 (2017) 455301. doi: https://doi.org/10.1088/1361-648X/aa8a47

[40] V.G. Kapinos, D.J. Bacon, Influence of ion-electron interaction on the formation mechanism of depleted zones in displacement cascades in metals, Phys. Rev. B. 50 (1994) 13194–13203. doi: https://doi.org/10.1103/PhysRevB.50.13194

[41] B.N. Singh, M. Eldrup, S.J. Zinkle, S.I. Golubov, On Grain Size Dependent Void Swelling in Pure Copper Irradiated with Fission Neutrons, Philos. Mag. A. 82:6 (2002) 1137–1158. doi: https://doi.org/10.1080/01418610208240021

[42] I.M. Robertson, M.L. Jenkins, C.A. English, Low-dose neutron-irradiation damage in α-iron, J. Nucl. Mater. 108–109 (1982) 209–221. doi: https://doi.org/10.1016/0022-3115(82)90489-5

[43] C.A. English, M.L. Jenkins, Heavy Ion Damage in Solids, Treatise Heavy Ion Sci. 6 (1985) 325–356. doi: https://doi.org/10.1007/978-1-4615-8103-1

[44] R. V. Hesketh, The formation of dislocation loops in copper during neutron irradiation, Philos. Mag. 7 (1962) 519–521. doi: https://doi.org/10.1080/14786436208212184

[45] A. Dunlop, B.M. Pande, K. Böning, P. Rosner, H.E. Schaefer, The negative curvature phenomenon of resistivity damage rate observed in some metals neutron irradiated at 4.6 K, J. Nucl. Mater. 108–109 (1982) 83–94. doi: https://doi.org/10.1016/0022-3115(82)90475-5

[46] I.M. Robertson, M.A. Kirk, W.E. King, Formation of dislocation loops in iron by self-ion irradiations at 40K, 18 (1984) 317–320. doi: https://doi.org/10.1016/0036-9748(84)90444-7

[47] R. Schäublin, B. Décamps, A. Prokhodtseva, J.F. Löffler, On the origin of primary ½ a0 and a0 loops in irradiated Fe(Cr) alloys, Acta Mater. 133 (2017) 427–439. doi: https://doi.org/10.1016/J.ACTAMAT.2017.02.041

[48] M.L. Jenkins, M. Kirk, Characterization of Radiation Damage by Transmission Electron Microscopy, IOP Publishing Ltd, Bristol and Philadelphia, 2001

[49] K.M. Miller, Dislocation bias and point-defect relaxation volumes, J. Nucl. Mater. 84 (1979) 167–172. doi: https://doi.org/10.1016/0022-3115(79)90160-0

[50] S.L. Dudarev, J.L. Boutard, R. Lässer, M.J. Caturla, P.M. Derlet, M. Fivel, C.-C. Fu, M.Y. Lavrentiev, L. Malerba, M. Mrovec, D. Nguyen-Manh, K. Nordlund, M. Perlado, R. Schäublin, H. Van Swygenhoven, D. Terentyev, J. Wallenius, D. Weygand, F. Willaime, The EU programme for modelling radiation effects in fusion reactor materials: An overview of recent advances and future goals, J. Nucl. Mater. 386–388 (2009) 1–7. doi: https://doi.org/10.1016/j.jnucmat.2008.12.301

[51] X. Yi, M.L. Jenkins, M.A. Kirk, Z. Zhou, S.G. Roberts, In-situ TEM studies of 150 keV W+ ion irradiated W and W-alloys: Damage production and microstructural evolution, Acta Mater. 112 (2016) 105–120. doi: https://doi.org/10.1016/j.actamat.2016.03.051

[52] G.W. Groves, A. Kelly, Interstitial Dislocation Loops in Magnesium Oxide, Philos. Mag. 6 (1961) 1527–1529. doi: https://doi.org/10.1080/00318086.1961.11643281.

[53] G. Groves, A. Kelly, Erratum, Philos. Mag. 7 (1962) 892–892. doi: https://doi.org/10.1080/14786436208212678

[54] M.L. Jenkins, Z. Yao, M. Hernández-Mayoral, M.A. Kirk, Dynamic observations of heavy-ion damage in Fe and Fe-Cr alloys, J. Nucl. Mater. 389 (2009) 197–202. doi: https://doi.org/10.1016/j.jnucmat.2009.02.003

[55] A.E. Sand, M.J. Aliaga, M.J. Caturla, K. Nordlund, Surface effects and statistical laws of defects in primary radiation damage: Tungsten vs. iron, EPL (Europhysics Lett. 115 (2016) 36001. doi: https://doi.org/10.1209/0295-5075/115/36001

[56] F. Wan, Q. Zhan, Y. Long, S. Yang, G. Zhang, Y. Du, Z. Jiao, S. Ohnuki, The behavior of vacancy-type dislocation loops under electron irradiation in iron, J. Nucl. Mater. 455 (2014) 253–257. doi: https://doi.org/10.1016/J.JNUCMAT.2014.05.048

[57] J. Gao, Y. Du, S. Ohnuki, F. Wan, Evolution of dislocation loops in annealed iron pre-irradiated with hydrogen ion in high-voltage electron microscope, J. Nucl. Mater. 481 (2016) 81–87. doi: https://doi.org/10.1016/J.JNUCMAT.2016.09.008

[58] K. Arakawa, M. Hatanaka, E. Kuramoto, K. Ono, H. Mori, Changes in the burgers vector of perfect dislocation loops without contact with the external dislocations, Phys. Rev. Lett. 96 (2006) 1–4. doi: https://doi.org/10.1103/PhysRevLett.96.125506

[59] B.L. Eyre, A.F. Bartlett, An electron microscope study of neutron irradiation damage in alpha-iron, Philos. Mag. 12 (1965) 261–272. doi: https://doi.org/10.1080/14786436508218869

[60] B.C. Masters, Dislocation loops in irradiated iron, Philos. Mag. 11 (1965) 881–893. doi: https://doi.org/10.1080/14786436508223952

[61] L.L. Horton, J. Bentley, K. Farrell, A TEM study of Neutron Irradiated Iron, J. Nucl. Mater. 109 (1982) 222–233. doi: https://doi.org/10.1016/0022-3115(82)90490-1

[62] B.L. Eyre, R. Bullough, On the formation of interstitial loops in b.c.c. metals, Philos. Mag. 12 (1965) 31–39. doi: https://doi.org/10.1080/14786436508224943

[63] R.E. Stoller, G.R. Odette, B.D. Wirth, Primary damage formation in bcc iron, J. Nucl. Mater. 251 (1997) 49–60. doi: https://doi.org/10.1016/S0022-3115(97)00256-0

[64] D.S. Gelles, R.E. Schäublin, Post-irradiation deformation in a Fe-9 % Cr alloy, Mater. Sci. 310 (2001) 82–86. doi: https://doi.org/10.1016/S0921-5093(00)01772-X

[65] J. Marian, B.D. Wirth, J.M. Perlado, Mechanism of Formation and Growth of Interstitial Loops in Ferritic Materials, Phys. Rev. Lett. 88 (2002) 255507. doi: https://doi.org/10.1103/PhysRevLett.88.255507

[66] J. Marian, B.D. Wirth, J.M. Perlado, Mechanism of Formation and Growth of Interstitial Loops in Ferritic Materials, Phys. Rev. Lett. 88 (2002) 255507. doi: https://doi.org/10.1103/PhysRevLett.88.255507

[67] H. Xu, R.E. Stoller, Y.N. Osetsky, D. Terentyev, Solving the puzzle of 100 Interstitial Loop Formation in bcc Iron, Phys. Rev. Lett. 110 (2013) 1–5. doi: https://doi.org/10.1103/PhysRevLett.110.265503

[68] J.C. Haley, S.A. Briggs, P.D. Edmondson, K. Sridharan, S.G. Roberts, S. Lozano-Perez, K.G. Field, Dislocation loop evolution during in-situ ion irradiation of model FeCrAl alloys, Acta Mater. 136 (2017) 390–401. doi: https://doi.org/10.1016/J.ACTAMAT.2017.07.011

[69] D. Nguyen-Manh, A.P. Horsfield, S.L. Dudarev, Self-interstitial atom defects in bcc transition metals: Group-specific trends, Phys. Rev. B. 73 (2006) 20101. doi: https://doi.org/10.1103/PhysRevB.73.020101

[70] Q. Li, C.M. Parish, K. a. Powers, M.K. Miller, Helium solubility and bubble formation in a nanostructured ferritic alloy, J. Nucl. Mater. 445 (2014) 165–174. doi: https://doi.org/10.1016/j.jnucmat.2013.10.048

[71] M.L. Jenkins, Characterisation of radiation-damage microstructures by TEM, J. Nucl. Mater. 216 (1994) 124–156. doi: https://doi.org/10.1016/0022-3115(94)90010-8

[72] D.H. Thompson, Three-dimensional dislocation dynamics modelling of particle-reinforced ferrous alloys for nuclear applications, Univ. Oxford DPhil Thesis. (2015)

[73] D.J. Bacon, F. Gao, Y.N. Osetsky, Primary damage state in fcc, bcc and hcp metals as seen in molecular dynamics simulations, J. Nucl. Mater. 276 (2000) 1–12. doi: https://doi.org/10.1016/S0022-3115(99)00165-8

[74] C.A. English, Low-dose neutron irradiation damage in FCC and BCC metals, J. Nucl. Mater. 108–109 (1982) 104–123. doi: https://doi.org/10.1016/0022-3115(82)90477-9

[75] W.-Y. Chen, Y. Miao, J. Gan, M.A. Okuniewski, S.A. Maloy, J.F. Stubbins, Neutron irradiation effects in Fe and Fe-Cr at 300 °C, Acta Mater. 111 (2016) 407–416. doi: https://doi.org/10.1016/J.ACTAMAT.2016.03.060

[76] M. Hernández-Mayoral, C. Heintze, E. Oñorbe, Transmission electron microscopy investigation of the microstructure of Fe–Cr alloys induced by neutron and ion irradiation at 300 °C, J. Nucl. Mater. 474 (2016) 88–98. doi: https://doi.org/10.1016/j.jnucmat.2016.03.002

[77] M. Horiki, T. Yoshiie, M. Iseki, M. Kiritani, Invisible and visible point defect clusters in neutron irradiated iron, J. Nucl. Mater. 271–272 (1999) 256–260. doi: https://doi.org/10.1016/S0022-3115(98)00744-2

[78] S. Amelinckx, W. Bontinck, W. Dekeyser, F. Seitz, On the formation and properties of helical dislocations, Philos. Mag. 2 (1957) 355–378. doi: https://doi.org/10.1080/14786435708243825

[79] M. Wen, N.M. Ghoniem, B.N. Singh, Dislocation decoration and raft formation in irradiated materials, Philos. Mag. 85 (2005) 2561–2580. doi: https://doi.org/10.1080/14786430500154281

[80] R. Schaeublin, D. Gelles, M. Victoria, Microstructure of irradiated ferritic/martensitic steels in relation to mechanical properties, J. Nucl. Mater. 307–311 (2002) 197–202. doi: https://doi.org/10.1016/S0022-3115(02)01034-6

[81] T. Yoshiie, Y. Satoh, Q. Xu, Analysis of defect structural evolution in fcc metals irradiated with neutrons under well defined boundary conditions, J. Nucl. Mater. 329–333 (2004) 81–87. doi: https://doi.org/10.1016/J.JNUCMAT.2004.04.006

[82] A. Prokhodtseva, B. Décamps, R. Schäublin, Comparison between bulk and thin foil ion irradiation of ultra high purity Fe, J. Nucl. Mater. 442 (2013) S786–S789. doi: https://doi.org/10.1016/j.jnucmat.2013.04.032

[83] H. Trinkaus, B.N. Singh, A.J.E. Foreman, Mechanisms for decoration of dislocations by small dislocation loops under cascade damage conditions, J. Nucl. Mater. 249 (1997) 91–102. doi: https://doi.org/10.1016/S0022-3115(97)00230-4

[84] H. Trinkaus, B.N. Singh, A.J.E. Foreman, Segregation of cascade induced interstitial loops at dislocations: possible effect on initiation of plastic deformation, J. Nucl. Mater. 251 (1997) 172–187. doi: https://doi.org/10.1016/S0022-3115(97)00246-8

[85] T. Muroga, H. Watanabe, N. Yoshida, Correlation of fast neutron, fusion neutron and electron irradiations based on the dislocation loop density, J. Nucl. Mater. 174 (1990) 282–288. doi: https://doi.org/10.1016/0022-3115(90)90241-E

[86] X. Yi, Electron Microscopy Study of Radiation Damage in Tungsten and Alloys, Univ. Oxford DPhil Thesis. (2013)

[87] T. Tanaka, K. Oka, S. Ohnuki, S. Yamashita, T. Suda, S. Watanabe, E. Wakai, Synergistic effect of helium and hydrogen for defect evolution under multi-ion irradiation of Fe-Cr ferritic alloys, J. Nucl. Mater. 329–333 (2004) 294–298. doi: https://doi.org/10.1016/j.jnucmat.2004.04.051

[88] J.L. Straalsund, R.W. Powell, B.A. Chin, An overview of neutron irradiation effects in LMFBR materials, J. Nucl. Mater. 108–109 (1982) 299–305. doi: https://doi.org/10.1016/0022-3115(82)90499-8

[89] F.. Garner, M.. Toloczko, B.. Sencer, Comparison of swelling and irradiation creep behavior of fcc-austenitic and bcc-ferritic/martensitic alloys at high neutron exposure, J. Nucl. Mater. 276 (2000) 123–142. doi: https://doi.org/10.1016/S0022-3115(99)00225-1

[90] E.A. Little, D.A. Stow, Effects of chromium additions on irradiation-induced void swelling in α-iron, Met. Sci. 14 (1980) 89–94. doi: https://doi.org/10.1179/030634580790426265

[91] D.S. Gelles, Microstructural examination of neutron-irradiated simple ferritic alloys, J. Nucl. Mater. 108–109 (1982) 515 26-515 26. doi: https://doi.org/10.1016/0022-3115(82)90523-2

[92] D.M. Stewart, Y.N. Osetsky, R.E. Stoller, S.I. Golubov, T. Seletskaia, P.J. Kamenski, Atomistic studies of helium defect properties in bcc iron: Comparison of He-Fe potentials, Philos. Mag. 90 (2010) 935–944. doi: https://doi.org/10.1080/14786430903270650

[93] Y. Dai, Y. Foucher, M.R. James, B.M. Oliver, Neutronics calculation, dosimetry analysis and gas measurements of the first SINQ target irradiation experiment, STIP-I, J. Nucl. Mater. 318 (2003) 167–175. doi: https://doi.org/10.1016/S0022-3115(03)00099-0

[94] M. Matijasevic, A. Almazouzi, Effect of Cr on the mechanical properties and microstructure of Fe–Cr model alloys after n-irradiation, J. Nucl. Mater. 377 (2008) 147–154. doi: https://doi.org/10.1016/j.jnucmat.2008.02.061

[95] S.I. Porollo, A.M. Dvoriashin, A.N. Vorobyev, Y. V Konobeev, The microstructure and tensile properties of Fe–Cr alloys after neutron irradiation at 400°C to 5.5–7.1 dpa, J. Nucl. Mater. 256 (1998) 247–253. doi: https://doi.org/10.1016/S0022-3115(98)00043-9

[96] Y.V. Konobeev, A.M. Dvoriashin, S.I. Porollo, F.A. Garner, Swelling and microstructure of pure Fe and Fe–Cr alloys after neutron irradiation to ~26dpa at 400°C, J. Nucl. Mater. 355 (2006) 124–130. doi: https://doi.org/10.1016/j.jnucmat.2006.04.011

[97] M. Bachhav, L. Yao, G. Robert Odette, E.A. Marquis, Microstructural changes in a neutron-irradiated Fe–6at.%Cr alloy, J. Nucl. Mater. 453 (2014) 334–339. doi: https://doi.org/10.1016/j.jnucmat.2014.06.050

[98] C. Pareige, V. Kuksenko, P. Pareige, Behaviour of P, Si, Ni impurities and Cr in self ion irradiated Fe–Cr alloys – Comparison to neutron irradiation, J. Nucl. Mater. 456 (2015) 471–476. doi: https://doi.org/10.1016/j.jnucmat.2014.10.024

[99] G. Bonny, D. Terentyev, L. Malerba, On the α–α' miscibility gap of Fe–Cr alloys, Scr. Mater. 59 (2008) 1193–1196. doi: https://doi.org/10.1016/j.scriptamat.2008.08.008

[100] L. Malerba, A. Caro, J. Wallenius, Multiscale modelling of radiation damage and phase transformations: The challenge of FeCr alloys, J. Nucl. Mater. 382 (2008) 112–125. doi: https://doi.org/10.1016/j.jnucmat.2008.08.014

[101] M. Bachhav, G. Robert Odette, E.A. Marquis, α' precipitation in neutron-irradiated Fe–Cr alloys, Scr. Mater. 74 (2014) 48–51. doi: https://doi.org/10.1016/j.scriptamat.2013.10.001

[102] M. Bachhav, G. Robert Odette, E.A. Marquis, Microstructural changes in a neutron-irradiated Fe–15at.%Cr alloy, J. Nucl. Mater. 454 (2014) 381–386. doi: https://doi.org/10.1016/j.jnucmat.2014.08.026

[103] A. Caro, M. Caro, E.M. Lopasso, D.A. Crowson, Implications of ab initio energetics on the thermodynamics of Fe-Cr alloys, Appl. Phys. Lett. 89 (2006) 2006–2008. doi: https://doi.org/10.1063/1.2354445

[104] C. Pareige, V. Kuksenko, P. Pareige, Behaviour of P, Si, Ni impurities and Cr in self ion irradiated Fe–Cr alloys – Comparison to neutron irradiation, J. Nucl. Mater. 456 (2015) 471–476. doi: https://doi.org/10.1016/j.jnucmat.2014.10.024

[105] O. Tissot, C. Pareige, E. Meslin, B. Décamps, J. Henry, Influence of injected interstitials on α' precipitation in Fe–Cr alloys under self-ion irradiation, Mater. Res. Lett. 5 (2017) 117–123. doi: https://doi.org/10.1080/21663831.2016.1230896

[106] O. Tissot, C. Pareige, E. Meslin, B. Decamps, J. Henry, Kinetics of α' precipitation in an electron-irradiated Fe15Cr alloy, Scr. Mater. 122 (2016) 31–35. doi: https://doi.org/10.1016/j.scriptamat.2016.05.021

[107] C.D. Hardie, C.A. Williams, S. Xu, S.G. Roberts, Effects of irradiation temperature and dose rate on the mechanical properties of self-ion implanted Fe and Fe-Cr alloys, J. Nucl. Mater. 439 (2013) 33–40. doi: https://doi.org/10.1016/j.jnucmat.2013.03.052

[108] S.J. Zinkle, A. Möslang, Evaluation of irradiation facility options for fusion materials research and development, Fusion Eng. Des. 88 (2013) 472–482. doi: https://doi.org/10.1016/j.fusengdes.2013.02.081

[109] M.J. Norgett, M.T. Robinson, I.M. Torrens, A proposed method of calculating displacement dose rates, Nucl. Eng. Des. 33 (1975) 50–54. doi: https://doi.org/10.1016/0029-5493(75)90035-7

[110] J.F. Ziegler, M.D. Ziegler, J.P. Biersack, SRIM - The stopping and range of ions in matter (2010), Nucl. Instruments Methods Phys. Res. Sect. B Beam Interact. with Mater. Atoms. 268 (2010) 1818–1823. doi: https://doi.org/10.1016/j.nimb.2010.02.091

[111] F.A. Garner, H.L. Heinisch, R.L. Simons, F.M. Mann, Implications of neutron spectrum and flux differences on fission-fusion correlations at high neutron fluence, Radiat. Eff. Defects Solids. 113 (1990) 229–255. doi: https://doi.org/10.1080/10420159008213068

[112] D.J. Mazey, Fundamental aspects of high-energy ion-beam simulation techniques and their relevance to fusion materials studies, J. Nucl. Mater. 174 (1990) 196–209. doi: https://doi.org/10.1016/0022-3115(90)90234-E

[113] M.B. Lewis, N.H. Packan, G.F. Wells, R.A. Buhl, Improved techniques for heavy-ion simulation of neutron radiation damage, Nucl. Instruments Methods. 167 (1979) 233–247. doi: https://doi.org/10.1016/0029-554x(79)90011-9

[114] S. Ishino, P. Schiller, A. Rowcliffe, Need for and requirements for a neutron irradiation facility for fusion materials testing, J. Fusion Energy. 8:147 (1989). doi: https://doi.org/10.1007/BF01051645

[115] M.R. Gilbert, J.C. Sublet, Neutron-induced transmutation effects in W and W-alloys in a fusion environment, Nucl. Fusion. 51 (2011) 43005. doi: https://doi.org/10.1088/0029-5515/51/4/043005

[116] R.E. Stoller, G.R. Odette, B.D. Wirth, Primary damage formation in bcc iron, J. Nucl. Mater. 251 (1997) 49–60. doi: https://doi.org/10.1016/S0022-3115(97)00256-0

[117] R.E. Stoller, Role of cascade energy and temperature in primary defect formation in iron, J. Nucl. Mater. 276 (2000) 22–32. doi: https://doi.org/10.1016/S0022-3115(99)00204-4

[118] R.M. More, J.A. Spitznagel, Primary recoil spectra and subcascade effects in ion bombardment experiments, Radiat. Eff. 60 (1982) 27–33. doi: https://doi.org/10.1080/00337578208242772

[119] E. Zarkadoula, S.L. Daraszewicz, D.M. Duffy, M.A. Seaton, I.T. Todorov, K. Nordlund, M.T. Dove, K. Trachenko, The nature of high-energy radiation damage in iron., J. Phys. Condens. Matter. 25 (2013) 125402. doi: https://doi.org/10.1088/0953-8984/25/12/125402

[120] C.A. English, Recoil effects in radiation damage, Radiat. Eff. Defects Solids. 113 (1990) 15–28. doi: https://doi.org/10.1080/10420159008213052

[121] A.Y. Konobeyev, U. Fischer, Y.A. Korovin, S.P. Simakov, Evaluation of effective threshold displacement energies and other data required for the calculation of advanced atomic displacement cross-sections, Nucl. Energy Technol. 3 (2017) 169–175. doi: https://doi.org/10.1016/J.NUCET.2017.08.007

[122] D.R. Mason, A.E. Sand, X. Yi, S.L. Dudarev, Direct observation of the spatial distribution of primary cascade damage in tungsten, Acta Mater. 144 (2018) 905–917. doi: https://doi.org/10.1016/J.ACTAMAT.2017.10.031

[123] M.L. Jenkins, C.A. English, B.L. Eyre, Heavy-ion irradiation of α-iron, Philos. Mag. A. 38 (1978) 97–114. doi: https://doi.org/10.1080/01418617808239220

[124] C.D. Hardie, G.R. Odette, Y. Wu, S. Akhmadaliev, S.G. Roberts, Mechanical properties and plasticity size effect of Fe-6%Cr irradiated by Fe ions and by neutrons, J. Nucl. Mater. 482 (2016) 236–247. doi: https://doi.org/10.1016/j.jnucmat.2016.10.028

[125] C.D. Hardie, Micro-Mechanics of Irradiated Fe-Cr Alloys for Fusion Reactors, Univ. Oxford DPhil Thesis. (2013)

[126] D.E.J. Armstrong, Measuring Elastic, Plastic and Fracture Properties using Micro-Cantilever Testing, Univ. Oxford DPhil Thesis. (2009)

[127] G.S. Was, Z. Jiao, E. Getto, K. Sun, A.M. Monterrosa, S.A. Maloy, O. Anderoglu, B.H. Sencer, M. Hackett, Emulation of reactor irradiation damage using ion beams, Scr. Mater. 88 (2014) 33–36. doi: https://doi.org/10.1016/j.scriptamat.2014.06.003

[128] Z. Jiao, J. Michalicka, G.S. Was, Self-ion emulation of high dose neutron irradiated microstructure in stainless steels, J. Nucl. Mater. 501 (2018) 312–318. doi: https://doi.org/10.1016/J.JNUCMAT.2018.01.054

[129] S. Taller, D. Woodley, E. Getto, A.M. Monterrosa, Z. Jiao, O. Toader, F. Naab, T. Kubley, S. Dwaraknath, G.S. Was, Multiple ion beam irradiation for the study of radiation damage in materials, Nucl. Instruments Methods Phys. Res. Sect. B Beam Interact. with Mater. Atoms. 412 (2017) 1–10. doi: https://doi.org/10.1016/J.NIMB.2017.08.035

[130] J. Gan, G.S. Was, Microstructure evolution in austenitic Fe-Cr-Ni alloys irradiated with protons: comparison with neutron-irradiated microstructures, J. Nucl. Mater. 297 (2001). doi: https://doi.org/10.1016/S0022-3115(01)00615-8

[131] A. Souidi, M. Hou, C.S. Becquart, L. Malerba, C. Domain, R.E. Stoller, On the correlation between primary damage and long-term nanostructural evolution in iron under irradiation, J. Nucl. Mater. 419 (2011) 122–133. doi: https://doi.org/10.1016/j.jnucmat.2011.08.049

[132] Q. Yu, G.S. Was, L.M. Wang, R. Odette, D.E. Alexander, Hardening and Microstructure of Model Reactor Pressure Vessel Steel Alloys Using Proton Irradiation, MRS Proc. 650 (2011) R6.2. doi: https://doi.org/10.1557/PROC-650-R6.2

[133] G.S. Was, Challenges to the use of ion irradiation for emulating reactor irradiation, J. Mater. Res. (2015) 1–25. doi: https://doi.org/10.1557/jmr.2015.73

[134] P. Jung, C. Liu, J. Chen, Retention of implanted hydrogen and helium in martensitic stainless steels and their effects on mechanical properties, J. Nucl. Mater. 296 (2001) 165–173. doi: https://doi.org/10.1016/S0022-3115(01)00545-1

[135] A.J. Kumnick, H.H. Johnson, Deep trapping states for hydrogen in deformed iron, Acta Metall. 28 (1980) 33–39. doi: https://doi.org/10.1016/0001-6160(80)90038-3

[136] S.L. Dudarev, M.R. Gilbert, K. Arakawa, H. Mori, Z. Yao, M.L. Jenkins, P.M. Derlet, Langevin model for real-time Brownian dynamics of interacting nanodefects in irradiated metals, Phys. Rev. B - Condens. Matter Mater. Phys. 81 (2010) 1–15. doi: https://doi.org/10.1103/PhysRevB.81.224107

[137] C. Abromeit, Aspects of simulation of neutron damage by ion irradiation, J. Nucl. Mater. 216 (1994) 78–96. doi: https://doi.org/10.1016/0022-3115(94)90008-6

[138] L.K. Mansur, Correlation of neutron and heavy-ion damage. II. The predicted temperature shift if swelling with changes in radiation dose rate, J. Nucl. Mater. 78 (1978) 156–160. doi: https://doi.org/10.1016/0022-3115(78)90514-7

[139] T. Okita, T. Sato, N. Sekimura, F.A. Garner, L.R. Greenwood, The primary origin of dose rate effects on microstructural evolution of austenitic alloys during neutron irradiation, J. Nucl. Mater. 307–311 (2002) 322–326. doi: https://doi.org/10.1016/S0022-3115(02)01202-3

[140] C. Domain, C.S. Becquart, J. Foct, Ab initio study of foreign interstitial atom (C, N) interactions with intrinsic point defects in α -Fe, Phys. Rev. B. 69 (2004) 144112. doi: https://doi.org/10.1103/PhysRevB.69.144112

[141] C.H. Woo, B.N. Singh, The Concept of Production Bias and Its Possible Role in Defect Accumulation under Cascade Damage Conditions, Phys. Status Solidi. 159 (1990) 609–616. doi: https://doi.org/10.1002/pssb.2221590210

[142] M. Kiritani, Radiation rate dependence of microstructure evolution, J. Nucl. Mater. 169 (1989) 89–94. doi: https://doi.org/10.1016/0022-3115(89)90524-2

[143] T. Okita, T. Sato, N. Sekimura, T. Iwai, F.A. Garner, The synergistic influence of temperature and displacement rate on microstructural evolution of ion-irradiated Fe–15Cr–16Ni model austenitic alloy, J. Nucl. Mater. 367–370 (2007) 930–934. doi: https://doi.org/10.1016/j.jnucmat.2007.03.061

[144] S. Xu, A Study of Irradiation Damage in Iron and Fe-Cr Alloys, Univ. Oxford DPhil Thesis. (2013)

[145] G.S. Was, J.T. Busby, T. Allen, E.A. Kenik, A. Jensson, S.M. Bruemmer, J. Gan, A.D. Edwards, P.M. Scott, P.L. Andreson, Emulation of neutron irradiation effects with protons: Validation of principle, J. Nucl. Mater. 300 (2002) 198–216. doi: https://doi.org/10.1016/S0022-3115(01)00751-6

[146] J. Gan, G.S. Was, R.E. Stoller, Modeling of microstructure evolution in austenitic stainless steels irradiated under light water reactor condition, 299 (2001) 53–67. doi: https://doi.org/10.1016/S0022-3115(01)00673-0

[147] M. Victoria, N. Baluc, C. Bailat, Y. Dai, M.I. Luppo, R. Schaublin, The microstructure and associated tensile properties of irradiated fcc and bcc metals, 276 (2000) 114–122. doi: https://doi.org/10.1016/S0022-3115(99)00203-2

[148] G.S. Was, M. Hash, R.G. Odette, Hardening and microstructure evolution in proton-irradiated model and commercial pressure-vessel steels, Philos. Mag. 85 (2005) 703–722. doi: https://doi.org/10.1080/14786430412331319974

[149] C. Xu, G.S. Was, Proton irradiation creep of FM steel T91, J. Nucl. Mater. 459 (2015) 183–193. doi: https://doi.org/10.1016/j.jnucmat.2015.01.023

[150] Z. Jiao, A.N. Ham, G.S. Was, Microstructure of helium-implanted and proton-irradiated T91 ferritic/martensitic steel, J. Nucl. Mater. 367–370 (2007) 440–445. doi: https://doi.org/10.1016/J.JNUCMAT.2007.03.118

[151] G. Gupta, Z. Jiao, A.N. Ham, J.T. Busby, G.S. Was, Microstructural evolution of proton irradiated T91, J. Nucl. Mater. 351 (2006) 162–173. doi: https://doi.org/10.1016/j.jnucmat.2006.02.028

[152] Z.W. Zhang, C.T. Liu, X.L. Wang, M.K. Miller, D. Ma, G. Chen, J.R. Williams, B.A. Chin, Effects of proton irradiation on nanocluster precipitation in ferritic steel containing fcc alloying additions, Acta Mater. 60 (2012) 3034–3046. doi: https://doi.org/10.1016/J.ACTAMAT.2012.02.008

[153] K.G. Field, B.D. Miller, H.J.M. Chichester, K. Sridharan, T.R. Allen, Relationship between lath boundary structure and radiation induced segregation in a neutron irradiated 9 wt.% Cr model ferritic/martensitic steel, J. Nucl. Mater. 445 (2014) 143–148. doi: https://doi.org/10.1016/J.JNUCMAT.2013.10.056

[154] T.R. Allen, J.I. Cole, E.A. Kenik, G.S. Was, Analyzing the effect of displacement rate on radiation-induced segregation in 304 and 316 stainless steels by examining irradiated EBR-II components and samples irradiated with protons, J. Nucl. Mater. 376 (2008) 169–173. doi: https://doi.org/10.1016/J.JNUCMAT.2008.01.025

[155] K.J. Stephenson, G.S. Was, Comparison of the microstructure, deformation and crack initiation behavior of austenitic stainless steel irradiated in-reactor or with protons, J. Nucl. Mater. 456 (2015) 85–98. doi: https://doi.org/10.1016/j.jnucmat.2014.08.021

[156] D.S. Gelles, Void swelling in binary FeCr alloys at 200 dpa, J. Nucl. Mater. 225 (1995) 163–174. doi: https://doi.org/10.1016/0022-3115(95)00053-4

[157] E.R. Reese, M. Bachhav, P. Wells, T. Yamamoto, G. Robert Odette, E.A. Marquis, On α' precipitate composition in thermally annealed and neutron-irradiated Fe- 9-18Cr alloys, J. Nucl. Mater. 500 (2018) 192–198. doi: https://doi.org/10.1016/J.JNUCMAT.2017.12.036

[158] J.W. Nielsen, As-Run Physics Analysis for the UCSB--1 Experiment in the Advanced Test Reactor, Idaho Falls, ID (United States), 2015. doi: https://doi.org/10.2172/1235196

[159] J.C. Sublet, J.W. Eastwood, J.G. Morgan, M.R. Gilbert, M. Fleming, W. Arter, FISPACT-II: An Advanced Simulation System for Activation, Transmutation and Material Modelling, Nucl. Data Sheets. 139 (2017) 77–137. doi: https://doi.org/10.1016/J.NDS.2017.01.002

[160] Z. Yao, S. Xu, M.L. Jenkins, M.A. Kirk, Preparation of TEM samples of ferritic alloys, J. Electron Microsc. (Tokyo). 57 (2008) 91–94. doi: https://doi.org/10.1093/jmicro/dfn004

[161] S. Xu, TEM Characterisation of Heavy-Ion Irradiation Damage in Fe-Cr Alloys, Univ. Oxford DPhil Thesis. (2009)

[162] D.B. Williams, C.B. Carter, Transmission Electron Microscopy: A Textbook for Materials Science, 2nd Edit., Springer, 2009. doi: https://doi.org/10.1007/978-0-387-76501-3

[163] R.M. Langford, A.K. Petford-Long, Preparation of transmission electron microscopy cross-section specimens using focused ion beam milling, J. Vac. Sci. Technol. A Vacuum, Surfaces, Film. 19 (2001) 2186–2193. doi: https://doi.org/10.1116/1.1378072

[164] CrystalMaker Software: Crystal & Molecular Structures Modelling and Diffraction, http://crystalmaker.com/index.html (accessed September 3, 2018)

[165] X.. Gu, T. Furuhara, W.. Zhang, PTCLab: free and open-source software for calculating phase transformation crystallography, J. Appl. Cryst. 49 (2016) 1099–1106. doi: https://doi.org/10.1107/S1600576716006075

[166] M.H. Loretto, Electron Beam Analysis of Materials, Springer Netherlands, Dordrecht, 1984. doi: https://doi.org/10.1007/978-94-009-5540-0

[167] T. Malis, S.C. Cheng, R.F. Egerton, EELS log-ratio technique for specimen-thickness measurement in the TEM, J. Electron Microsc. Tech. 8 (1988) 193–200. doi: https://doi.org/10.1002/jemt.1060080206

[168] Gatan, Gatan Digital Microscopy Suite Software 2.3, http://www.gatan.com/products/tem-analysis/gatan-microscopy-suite-software (accessed September 3, 2018)

[169] Z. Shen, K. Arioka, S. Lozano-Perez, A mechanistic study of SCC in Alloy 600 through high-resolution characterization, Corros. Sci. 132 (2018) 244–259. doi: https://doi.org/10.1016/J.CORSCI.2018.01.004

[170] D.R.G. Mitchell, Mean Free Path Estimator for Digital Micrograph, (2012). http://www.dmscripting.com/meanfreepathestimator.html (accessed September 3, 2018)

[171] M. Kirk, X. Yi, M. Jenkins, Characterization of irradiation defect structures and densities by transmission electron microscopy, J. Mater. Res. 30 (2015) 1195–1201. doi: https://doi.org/10.1557/jmr.2015.19

[172] A. Prokhodtseva, B. Décamps, A. Ramar, R. Schäublin, Impact of He and Cr on defect accumulation in ion-irradiated ultrahigh-purity Fe(Cr) alloys, Acta Mater. 61 (2013) 6958–6971. doi: https://doi.org/10.1016/j.actamat.2013.08.007

[173] S. Nicolopoulos, D. Bultreys, Precession electron diffraction and TEM applications, . www.nanomegas.com (accessed September 5, 2018)

[174] J. Schindelin, I. Arganda-Carreras, E. Frise, V. Kaynig, M. Longair, T. Pietzsch, S. Preibisch, C. Rueden, S. Saalfeld, B. Schmid, J.-Y. Tinevez, D.J. White, V. Hartenstein, K. Eliceiri, P. Tomancak, A. Cardona, Fiji: an open-source platform for biological-image analysis, Nat. Methods. 9 (2012) 676–682. doi: https://doi.org/10.1038/nmeth.2019

[175] Q. Tseng, Template Matching and Slice Alignment - ImageJ Plugins, (2011). doi: https://doi.org/10.1073/pnas.1106377109

[176] Z. Zhou, M.L. Jenkins, S.L. Dudarev, A.P. Sutton, M.A. Kirk, Simulations of weak-beam diffraction contrast images of dislocation loops by the many-beam Howie-Basinski equations, Philos. Mag. 86 (2006) 4851–4881. doi: https://doi.org/10.1080/14786430600615041

[177] W. Li, K.G. Field, D. Morgan, Automated defect analysis in electron microscopic images, Npj Comput. Mater. 4 (2018) 36. doi: https://doi.org/10.1038/s41524-018-0093-8

[178] X. Yi, M.L. Jenkins, M. Briceno, S.G. Roberts, Z. Zhou, M.A. Kirk, In situ study of self-ion irradiation damage in W and W–5Re at 500 °C, Philos. Mag. 93 (2013) 1715–1738. doi: https://doi.org/10.1080/14786435.2012.754110

[179] P.B. Hirsch, A. Howie, R.B. Nicholson, D.W. Pashley, M.J. Whelan, L. Marton, Electron microscopy of thin crystals, R.E. Krieger Pub. Co, 1977

[180] M. Ruehle, M. Wilkens, Defocusing contrast of cavities, Cryst. Lattice Defects. 6 (1975) 129–140. https://inis.iaea.org/search/search.aspx?orig_q=RN:8303085 (accessed August 23, 2018)

[181] F. de la Peña, T. Ostasevicius, V.T. Fauske, P. Burdet, E. Prestat, P. Jokubauskas, M. Nord, M. Sarahan, K.E. MacArthur, D.N. Johnstone, J. Taillon, J. Caron, V. Migunov, T. Furnival, A. Eljarrat, S. Mazzucco, T. Aarholt, M. Walls, T. Slater, F. Winkler, B. Martineau, G. Donval, R. McLeod, E.R. Hoglund, I. Alxneit, I. Hjorth, T. Henninen, L.F. Zagonel, A. Garmannslund, HyperSpy 1.3.1, (2018). doi: https://doi.org/10.5281/ZENODO.1221347

[182] M. Bosman, M. Watanabe, D.T.L. Alexander, V.J. Keast, Mapping chemical and bonding information using multivariate analysis of electron energy-loss spectrum images, Ultramicroscopy. 106 (2006) 1024–1032. doi: https://doi.org/10.1016/J.ULTRAMIC.2006.04.016

[183] As-Run Thermal Analysis for the UCSB-1 Experiment in the Advanced Test Reactor - Project No. 29607, Engineering Calculations and Analysis Report, Idaho National Laboratory, 2015

[184] Los Alamos National Laboratory: MCNP Home Page, https://mcnp.lanl.gov/ (accessed August 23, 2018)

[185] L.R. Greenwood, R.K. Smither, SPECTER: neutron damage calculations for materials irradiations, Argonne, IL, 1985. doi: https://doi.org/10.2172/6022143

[186] D.R. and A.J.K. M. Fleming, J.C. Sublet, J. Kopecky, Probing experimental and systematic trends of the neutron-induced TENDL-2014 nuclear data library, 2015. https://tendl.web.psi.ch/bib_rochman/UKAEA-R(15)29_30.9.15.pdf

[187] V. Kuksenko, C. Pareige, P. Pareige, Cr precipitation in neutron irradiated industrial purity Fe–Cr model alloys, J. Nucl. Mater. 432 (2013) 160–165. doi: https://doi.org/10.1016/J.JNUCMAT.2012.07.021

[188] P.M. Anderson, J.P. Hirth, J. Lothe, Theory of dislocations, 3rd Edit., Cambridge University Press, Cambridge, 2017

[189] G. Wagner, V. Gottschalch, Helical dislocations in Sn-doped GaP epitaxial layers and their characterization by transmission electron microscopy, Philos. Mag. A Phys. Condens. Matter, Struct. Defects Mech. Prop. 52 (1985) 395–406. doi: https://doi.org/10.1080/01418618508237634

[190] K. Arakawa, K. Ono, M. Isshiki, K. Mimura, M. Uchikoshi, H. Mori, Observation of the one-dimensional diffusion of nanometer-sized dislocation loops., Science. 318 (2007) 956–9. doi: https://doi.org/10.1126/science.1145386

[191] D. Bhattacharyya, P. Wells, M. Bachhav, A. Xu, E. Marquis, G.R. Odette, Effect of Neutron Irradiation on the Microstructure of a Series of Fe-Cr Alloys, Oral presentation at the 2017 TMS Annual Meeting & Exhibition: Microstructural Processes in Irradiated Materials, in: San Diego, 2017. http://www.programmaster.org/PM/PM.nsf/ApprovedAbstracts/25022C71AE7436EF85257FF2000648B7?OpenDocument (accessed August 23, 2018)

[192] D. Kaoumi, J. Adamson, M. Kirk, Microstructure evolution of two model ferritic/martensitic steels under in situ ion irradiation at low doses (0–2 dpa), J. Nucl. Mater. 445 (2014) 12–19. doi: https://doi.org/10.1016/j.jnucmat.2013.10.047

[193] A.B. Sivak, P.A. Sivak, V.A. Romanov, V.M. Chernov, Dislocation sinks efficiency for self-point defects in iron and vanadium crystals, Inorg. Mater. Appl. Res. 6 (2015) 105–113. doi: https://doi.org/10.1134/S2075113315020161

[194] Z. Chang, D. Terentyev, N. Sandberg, K. Samuelsson, P. Olsson, Anomalous bias factors of dislocations in bcc iron, J. Nucl. Mater. 461 (2015) 221–229. doi: https://doi.org/10.1016/J.JNUCMAT.2015.03.025

[195] P.T. Wady, A. Draude, S.M. Shubeita, A.D. Smith, N. Mason, S.M. Pimblott, E. Jimenez-Melero, Accelerated radiation damage test facility using a 5 MV tandem ion accelerator, Nucl. Instruments Methods Phys. Res. Sect. A Accel. Spectrometers, Detect. Assoc. Equip. 806 (2016) 109–116. doi: https://doi.org/10.1016/J.NIMA.2015.09.088

[196] C.M. Parish, K.G. Field, A.G. Certain, J.P. Wharry, Application of STEM characterization for investigating radiation effects in BCC Fe-based alloys, J. Mater. Res. 30 (2015) 1275–1289. doi: https://doi.org/10.1557/jmr.2015.32

[197] K. Yabuuchi, R. Kasada, A. Kimura, Effect of alloying elements on irradiation hardening behavior and microstructure evolution in BCC Fe, J. Nucl. Mater. 442 (2013) S790–S795. doi: https://doi.org/10.1016/J.JNUCMAT.2013.04.035

[198] R. Nakai, K. Yabuuchi, S. Nogami, A. Hasegawa, The effect of voids on the hardening of body-centered cubic Fe, J. Nucl. Mater. 471 (2016) 233–238. doi: https://doi.org/10.1016/J.JNUCMAT.2015.09.048

[199] M.A. Kirk, I.M. Robertson, M.L. Jenkins, C.A. English, T.J. Black, J.S. Vetrano, The collapse of defect cascades to dislocation loops, J. Nucl. Mater. 149 (1987) 21–28. doi: https://doi.org/10.1016/0022-3115(87)90494-6

[200] Y. Satoh, H. Matsui, T. Hamaoka, Effects of impurities on one-dimensional migration of interstitial clusters in iron under electron irradiation, Phys. Rev. B. 77 (2008) 94135. doi: https://doi.org/10.1103/PhysRevB.77.094135

[201] F. Soisson, T. Jourdan, Radiation-accelerated precipitation in Fe–Cr alloys, Acta Mater. 103 (2016) 870–881. doi: https://doi.org/10.1016/j.actamat.2015.11.001

[202] O. Senninger, F. Soisson, E. Martínez, M. Nastar, C.-C. Fu, Y. Bréchet, Modelling radiation induced segregation in iron–chromium alloys, Acta Mater. 103 (2016) 1–11. doi: https://doi.org/10.1016/J.ACTAMAT.2015.09.058

[203] R. Cauvin, G. Martin, Solid solutions under irradiation. I. A model for radiation-induced metastability, Phys. Rev. B. 23 (1981) 3322–3332. doi: https://doi.org/10.1103/PhysRevB.23.3322

[204] JEOL, JEM-2100 Electron Microscope Manual, Printed in Japan, 2004. http://www.jeol.co.jp (accessed September 3, 2018)

[205] E.E. Bloom, S.J. Zinkle, F.W. Wiffen, Materials to deliver the promise of fusion power - Progress and challenges, J. Nucl. Mater. 329–333 (2004) 12–19. doi: https://doi.org/10.1016/j.jnucmat.2004.04.141

[206] M.R. Gilbert, S. Zheng, R. Kemp, L.W. Packer, S.L. Dudarev, Comparative Assessment of Material Performance in Demo Fusion Reactors, Fusion Sci. Technol. (2014) 9–17. doi: https://doi.org/10.13182/FST13-751

[207] G.S. Was, T.R. Allen, Intercomparison of microchemical evolution under various types of particle irradiation, J. Nucl. Mater. 205 (1993) 332–338. doi: https://doi.org/10.1016/0022-3115(93)90097-I

List of figures reprinted with permissions

Figure 1.1: The experimental reactor, ITER, from [7]*. When complete it will be the largest Magnetic Confinement Fusion (MCF) device in the world, with an aim of generating more fusion energy than the energy it consumes.*

The ITER Organization provides images and videos on its public website free of charge for educational and institutional use, www.iter.org

Figure 1.2: Overview of operating temperatures and neutron dose regimes for structural materials in current generation II and potential generation IV fission plants, plus fusion devices ITER and DEMO [4].

Reprinted from Mater. Today, Vol. 12, S.J. Zinkle, J.T. Busby, Structural materials for fission & fusion energy, Copyright (2009), with permission from Elsevier

Figure 1.3: Effect of chromium content on the change in DBTT of RA steels and alloys by neutron irradiation, from [14].

Reprinted from J. Nucl. Mater. Vol. 233–237, A. Kohyama, A. Hishinuma, D.S. Gelles, R.L. Klueh, W. Dietz, K. Ehrlich, Low-activation ferritic and martensitic steels for fusion application, 138–147, Copyright (1996) with permission from Elsevier

Figure 1.4: Calculated decay of surface dose-rate in iron and ferritic–martensitic steels after irradiation (12.5 MW/m^2) in a first wall DEMO spectrum [16].

Reprinted from Fusion Eng. Des. Vol. 75–79, R. Lindau, A. Möslang, M. Rieth, M. Klimiankou, E. Materna-Morris, A. Alamo, A.A.F. Tavassoli, C. Cayron, A.M. Lancha, P. Fernandez, N. Baluc, R. Schäublin, E. Diegele, G. Filacchioni, J.W. Rensman, B.V. d. Schaaf, E. Lucon, W. Dietz, Present development status of EUROFER and ODS-EUROFER for application in blanket concepts, 989–996, Copyright (2005) with permission from Elsevier

Figure 2.1: Number of vacancies created in a cascade as a function of the damage energy [17].

Reprinted with permission from Springer Nature, Fundamentals of Radiation Materials Science, G.S. Was, Copyright (2007)

Figure 2.2: Damage energy as a function of PKA energy, from [19].

Reprinted from J. Nucl. Mater. Vol. 144, R. Dierckx, The Importance of the PKA Energy Spectrum for Radiation Damage Simulation, 214–227, Copyright (1987) with permission from Elsevier

Figure 2.3: a) Neutron energy spectra for a nuclear fusion DEMO first wall, and for a Fission pressurised water reactor (PWR) from [23]*. b) The PKA energy spectra for the various neutron-PKA reactions in iron exposed to a DEMO neutron spectrum* [23]*. The spectra for (n, elastic) is for hard-sphere ballistic displacements, whereas (n, inelastic) is the spectrum for all reactions involving transmutation.*

Reprinted from , J. Nucl. Mater. Vol. 467, M.R. Gilbert, J. Marian, J. C. Sublet, Energy spectra of primary knock-on atoms under neutron irradiation, 121–134, Copyright (2015) with permission from Elsevier

Figure 2.4: Diagram of a collision cascade occurring. A vacancy rich region forms in the centre and interstitials at the edge of the cascade, from [25].

Reprinted with permission from Springer Nature, Handbook of Damage Mechanics, W. Hoffelner, Copyright (2014)

Figure 2.5: Cluster size distribution of primary interstitial defects, for various PKA energies in tungsten, from [27].

Reprinted from Europhysics Lett. Vol. 115, A. De Backer, A.E. Sand, K. Nordlund, L. Luneville, D. Simeone, S.L. Dudarev, Subcascade formation and defect cluster size scaling in high-energy collision events in metals, 26001, Copyright (2016) with permission from IOP Publishing

Figure 2.6: Formation of prismatic dislocation loops. a) represents a crystal with a large number of vacancies dispersed throughout the matrix. In b) the vacancies have migrated on to a common plane, and in c) the matrix has collapsed to form a pure edge dislocation loop. d) is an interstitial dislocation loop formed by an equivalent process. From [32].

Reprinted with permissions from Elsevier BH, Introduction to Dislocations Fifth Edit, D. Hull, D.J.J. Bacon, Copyright (2011)

Figure 2.7: Dislocation loop habit planes and the proposed transformation from <100> to <111> Burgers vector, from [39].

Reprinted from J. Phys. Condens. Matter. Vol. 29, N. Gao, J. Chen, R.J. Kurtz, Z.G. Wang, R.F. Zhang, F. Gao, New understanding of nano-scale interstitial dislocation loops in BCC iron, 455301, Copyright (2017) with permission from IOP Publishing

Figure 2.8: Prediction of the ratio of energies required to form a/2<111> and a<100> loops in iron (red lines), a prediction based on a different simulation method (light lines) and a prediction "best fit" in relation to experimental observations (black lines), from [33].

Reprinted from Phys. Rev. Lett. Vol. 100, S.L. Dudarev, R. Bullough, P.M. Derlet, Effect of the alpha-gamma Phase transition on the stability of dislocation loops in bcc iron, 1–4 (2008) with permission from the American Physical Society

Figure 2.9: Experimental observations by Yao et al. [35] *of changes in populations of interstitials in a<100> and a/2<111> loops in iron.*

Reprinted from Philos. Mag. Vol. 90, Z. Yao, M.L. Jenkins, M. Hernández-Mayoral, M.A. Kirk, The temperature dependence of heavy-ion damage in iron: A microstructural transition at elevated temperatures, 4623–4634, Copyright (2010) with permission from Taylor & Francis

Figure 2.10: Bright field micrographs of homogeneous and heterogeneous dislocation loop damage in FeCr irradiated with neutrons to 0.6 dpa at 300^{o}C. a) Fe2.5Cr and b) Fe5Cr, from [76].

Reprinted from J. Nucl. Mater. Vol. 474, M. Hernández-Mayoral, C. Heintze, E. Oñorbe, Transmission electron microscopy investigation of the microstructure of Fe–Cr alloys induced by neutron and ion irradiation at 300 °C, 88–98, Copyright (2016) with permission from Elsevier

Figure 2.11: A series of video frames of a recording of loops coalescing into long finger-like structures.in ultra-high purity iron, from ~3dpa (far left) to ~5dpa (far right), from [38].

Reprinted from Philos. Mag. Vol. 88, M. Hernández-Mayoral, Z. Yao, M.L. Jenkins, M.A. Kirk, Heavy-ion irradiations of Fe and Fe–Cr model alloys Part 2: Damage evolution in thin-foils at higher doses, 2881–2897, (2008) with permission from Taylor & Francis

Figure 2.12: Austenitic stainless steel unirradiated and irradiated with neutrons, from [88].

Reprinted from J. Nucl. Mater., 108–109, J.L. Straalsund, R.W. Powell, B.A. Chin, An overview of neutron irradiation effects in LMFBR materials, 299–305, Copyright (1982) with permission from Elsevier

Figure 2.13: Fe-Cr phase diagram, from [100].

Reprinted from J. Nucl. Mater. 382, L. Malerba, A. Caro, J. Wallenius, Multiscale modelling of radiation damage and phase transformations: The challenge of FeCr alloys, 112–125, Copyright (2008) with permission from Elsevier

Figure 2.14: Atom Probe Tomography data showing chromium distribution in FeCr alloys neutron irradiated to 1.8 dpa at 325^{o}C . a) Fe-3Cr, b) Fe-6Cr, c) Fe-9Cr, d) Fe-12Cr, e) Fe-15Cr, f) Fe-18Cr. α' precipitates (the dense clusters of chromium) form in Fe-9Cr, but not in Fe-6Cr, implying a solubility limit between 6 and 9at%. From [101].

Reprinted from Scr. Mater. Vol. 74, M. Bachhav, G. Robert Odette, E.A. Marquis, α' precipitation in neutron-irradiated Fe–Cr alloys, 48–51, Copyright (2014) with permission from Elsevier

Figure 2.15: Atom Probe Tomography data showing chromium distribution in an ultra-high purity Fe-5Cr alloy irradiated at 400°C with heavy ions at 0.6dpa [107].

Reprinted from J. Nucl. Mater. Vol. 439, C.D. Hardie, C. A. Williams, S. Xu, S.G. Roberts, Effects of irradiation temperature and dose rate on the mechanical properties of self-ion implanted Fe and Fe-Cr alloys, 33–40, Copyright (2013)

Figure 2.16: Neutron spectra for various DEMO concepts, a typical pressurised water reactor (PWR) and the HIFR experimental fission reactor, from [23].

Reprinted from , J. Nucl. Mater. Vol. 467, M.R. Gilbert, J. Marian, J. C. Sublet, Energy spectra of primary knock-on atoms under neutron irradiation, 121–134, Copyright (2015) with permission from Elsevier

Figure 2.17: Schematic illustration of cascade sizes in nickel for different irradiating particles. T is the average damage energy of a cascade (the energy contributing to displacing atoms), and ε is the fraction of the number of displaced atoms that survive as freely migrating point defects, adapted from [17]. *The displacement energy for nickel is 33eV* [121].

Reprinted with permission from Springer Nature, Fundamentals of Radiation Materials Science, G.S. Was, Copyright (2007)

Figure 2.18: Example damage profiles of neutrons, protons and nickel ions in stainless steels. Superimposed is a 10μm grain structure. It is can be seen that a significant portion of the proton damage profile is smooth across a grain. From [17].

Reprinted with permission from Springer Nature, Fundamentals of Radiation Materials Science, G.S. Was, Copyright (2007)

Figure 2.19: Micro-cantilever data of the proof stress in irradiated Fe-6Cr as a function of the size of the cantilever beam. The increase in proof stress at small beam heights is a demonstration of the size-effect. From [124].

Reprinted from J. Nucl. Mater. Vol. 482, C.D. Hardie, G.R. Odette, Y. Wu, S. Akhmadaliev, S.G. Roberts, Mechanical properties and plasticity size effect of Fe-6%Cr irradiated by Fe ions and by neutrons, 236–247, Copyright (2016) with permission from Elsevier

Figure 2.21: Saturation loop density dependency on dose-rate using fast spallation neutrons (white circles), fusion-neutrons (white squares) and high voltage electrons (black circles) [85]. *Graph a) is the best fit trend of dose-rate based on the neutron and electron data. In graph b), the lines are based on the electron data only. The shift from the prediction by the neutrons is suggested to be due to PKA differences.*

Reprinted from J. Nucl. Mater. Vol. 174, T. Muroga, H. Watanabe, N. Yoshida, Correlation of fast neutron, fusion neutron and electron irradiations based on the dislocation loop density, 282–288, Copyright (1990) with permission from Elsevier

Figure 2.22: Dislocation loop size distribution in 275°C neutron and 360°C proton irradiated austenitic alloys [145]*. The loops sizes match up remarkably well.*

Reprinted from J. Nucl. Mater. Vol. 300, G.S. Was, J.T. Busby, T. Allen, E.A. Kenik, A. Jensson, S.M. Bruemmer, J. Gan, A.D. Edwards, P.M. Scott, P.L. Andreson, Emulation of neutron irradiation effects with protons: Validation of principle, 198–216, Copyright (2002) with permission from Elsevier

Figure 3.4: Experimental set-up for bath-electropolishing FeCr samples, from [160]

Reprinted from J. Electron Microsc Vol. 57, Z. Yao, S. Xu, M.L. Jenkins, M.A. Kirk, Preparation of TEM samples of ferritic alloys, 91–94, Copyright (2008) with permission from Oxford University Press

Figure 3.21: Micrographs of diffraction patterns to illustrate automated variation of the deviation parameter via scripted beam tilting. The top example, a), was taken from Prokhodtseva et al. [172] *and shows the position of their beam in the reciprocal plane as the beam is tilted from one side of the objective aperture to the other. The two diffraction patterns top-right show the extremities of the weak beam conditions.*

Reprinted from Acta Mater. Vol. 61, A. Prokhodtseva, B. Décamps, A. Ramar, R. Schäublin, Impact of He and Cr on defect accumulation in ion-irradiated ultrahigh-purity Fe(Cr) alloys, 6958–6971, Copyright (2013) with permission from Elsevier

*Figure 3.22: Example image contrast of dislocation loops compared with the size of the dislocation core. a) shows two images of the same loop, viewed with ±**g** vector conditions, as simulated by Yi et al.* [178] *for their work on Tungsten. These images have been adapted to show the true dislocation loop diameter and an example of what might be considered the "image-diameter".*

Reprinted from Philos. Mag. Vol. 93, X. Yi, M.L. Jenkins, M. Briceno, S.G. Roberts, Z. Zhou, M.A. Kirk, In situ study of self-ion irradiation damage in W and W–5Re at 500 °C, 1715–1738, (2013) with permission from Taylor & Francis

Figure 4.2: Radial cross section view of the ATR core and indicated position of the rod used to hold the samples of this experiment (from [158]*). Lengths are in mm.*

Reprinted from J.W. Nielsen, As-Run Physics Analysis for the UCSB--1 Experiment in the Advanced Test Reactor (2015), Idaho Falls, ID (United States) with permission from the US Department of Energy

Figure A.1: Ray diagram for a JEOL 2100L microscope, from [204].

Reprinted from JEM-2100 Electron Microscope Manual (2004) with permission from JEOL

APPENDIX A

Ray diagrams for a JEOL 2100L TEM microscope to demonstrate why an inversion exists

Figure A.1 was taken from the JEOL 2100L manual [204] which depicts simplified ray diagrams in "SA mag" mode (used for diffraction contrast imaging in real-space) and "SA diff" mode (used for capturing selected-area diffraction patterns in reciprocal-space). The blue arrow represents the orientation of the specimen and the subsequent orientation of the specimen-images at various positions down the TEM column. The first diagram shows that the blue arrow is oriented in the same direction at the "Film" position (where the image is captured) as the arrow in the "Specimen" position. The second diagram shows that the direction in which red spot lies at the "Film" position is opposite to direction immediately below the "Specimen" position. Therefore, the captured diffraction pattern is oriented 180° to the specimen, but the captured specimen-image is oriented correctly.

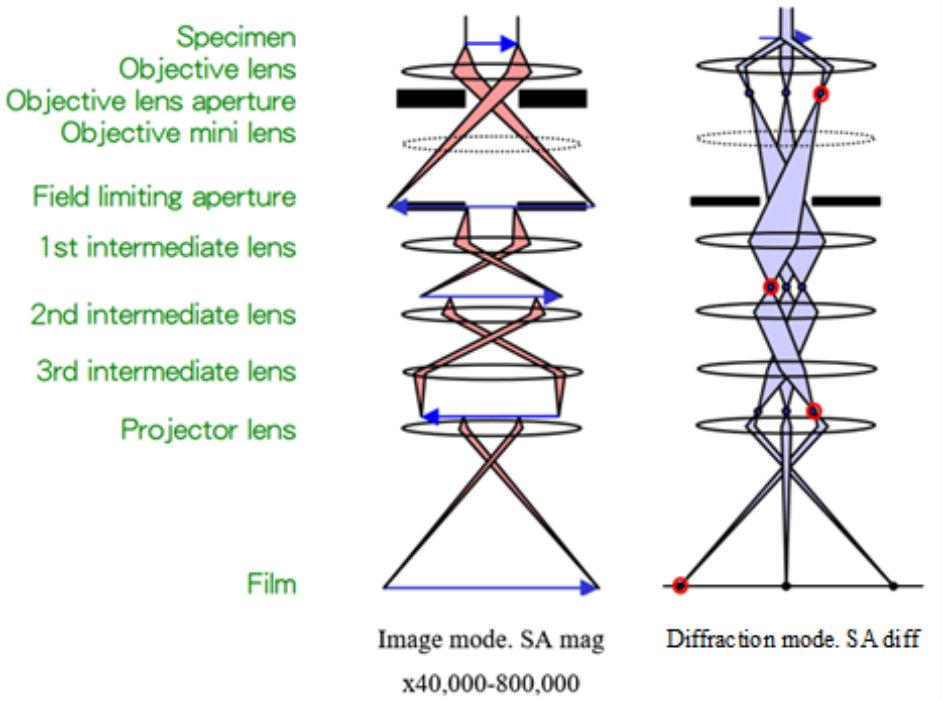

Figure A.1: Ray diagram for a JEOL 2100L microscope, from [204]

APPENDIX B

Electron beam precession script

Figure B.1 and Figure B.2 show the script used to precess the electron beam during acquisition of weak-beam micrographs, written in Gatan Microscopy Suite - Digital Micrograph version 2.3 [168]. Lines 1-89 are mostly introducing variables, initialising parameters and configuring the script to automatically label the images with the correct imaging condition. The part of the script that precesses the beam is shown in lines 90-120 in Figure B.2.

```
1
2  // ---------------                                                                  ----------------------------------
3  // ---------------                    ELECTRON BEAM PRECESSION TOOL                 ----------------------------------
4  // ---------------                                                 v 2.0            ----------------------------------
5  // ------------------------------------------------------------------------------------------------------------------
6  //                                                                                  BY JACK HALEY
7
8
9  // This DM script was designed to subtly vary the deviation parameter when imaging in weak-beam dark field conditions, though
10 // it can also be used for other experiments that require such precession.
11 // It is designed to be configured according to a pre-defined deviation parameter "radius", though this can also be set-up
12 // to respond according to a pre-defined precession angle.
13
14
15 // Changes in this version:
16 //     - A Beam shift correction has been added so that higher precession angles can be used without the beam deviating from the
17 //       centre of the column. (Experimental and still not working correctly)
18 //     - More thorough comments and layout adjusted to be more intuitive
19
20
21 // ----------------------Defined Variables-------------------------------------------------------------
22
23 number x0, y0, x1, y1, r0, th, camID, exposure, frame, deviation_cal,deviation_radius, xs0, ys0, xs1, ys1, rs0, tilt_shift_cal
24 image stack, img
25 number processing,xbin, ybin, deg, angle, rotations, th0
26 string filename, ImName, path0, sample, record
27
28
29
30
31
32
33 // ----------------------User set parameters-----------------------------------------------------------
34
35 xbin=1   // camera binning
36 ybin=1
37 th0=0.786 // this is the change in precession rotation-angle between each image
38 exposure=6  // camera exposure
39
40 tilt_shift_cal = 0.656618  // this is the factor we multiply to correct the beam tilt with beam shift
41 deviation_cal=0.000105     // this is the factor we multiply with to turn a deviation parameter into a raw beam tilt number
42
43 deviation_radius = 0.01    // this is the maximum deviation parameter change, related to the precession angle
44 rotations = 1               // set the number of full rotations of the precession to perform
45
46 // Set up the directory to save into and the filename, including imaging condition
47 path0="Z:\\Jack Haley\\nb3sn again\\"
48 sample="nb3sn_n_irrad_df_sg3_100k_condl_large_grain_"
49
50 record = "yes"
51
52 // --------------------Some initial values-----------------------------------------------------------
53
54 frame=0
55 angle=0
56 processing = CameraGetGainNormalizedEnum( )
57 camID=CameraGetActiveCameraID()
58
59 EMGetBeamTilt(x0, y0)   // get the starting conditions so we can revert to them at the end
60 EMGetBeamShift(xs0, ys0)
61
62 r0=deviation_radius/deviation_cal   // calculate the raw values for the tilt radius and shift radius
63 rs0 = r0*tilt_shift_cal
64
65 filename=sample+"dev_radius_0_"
66
67 rotations=rotations*6.27
68
69
```

Figure B.1: Lines 1-69 of the beam precession script, written in Digital micrograph [168]

```
70
71  // ---------------------Record the starting condition image-------------------------------------------------------------------
72
73  if (record=="yes") {
74
75      img := CameraAcquire(camID,exposure,xbin, ybin, processing)
76      stack=img // we create a stack to keep adding the images to. It will look blurry because of the image movement.
77
78      SetName(img, (filename))
79      ImName=(path0+filename)
80      Result("\n"+ImName)
81      SaveAsGatan3(img, ImName)
82
83
84      //Filename now changes to reflect that we have tilted away from the initial condition. Recorded as angle and radius
85      filename=sample+"dev_radius_"+deviation_radius+"_dev_angle_"
86
87  }
88
89
90  // ----------------------Start Precessing-----------------------------------------------------------------------------------------
91
92  th=-th0 // so the first condition in the while loop is 0
93
94  if (record=="yes"){      // if you want to record images at each precession point
95  while (th<rotations){      // while we our within a single 360 degree circuit of the precession
96      th=th+th0
97      deg=360*(th/6.28) // convert to radians
98      deg=round(deg)
99      Result("\n"+"th="+th+"  degrees="+deg) // output current angle
100
101
102     // use polar coordinates to calculate the new beam tilt and the beam shift needed to correct the beam movement on the screen
103     xl=x0+r0*cos(th)
104     yl=y0+r0*sin(th)
105
106     xsl= xs0+rs0*cos(th)
107     ysl= ys0+rs0*sin(th)
108
109     EMSetBeamTilt(xl,yl) // change the beam tilt to the new position
110     EMSetBeamShift(xsl,ysl) // shift the beam to correct movement on screen and through objective aperture (This feature does not work
111
112     img := CameraAcquire(camID,exposure, xbin, ybin, processing)
113
114     // Add to the stack and save the image
115     stack=stack+img
116     SetName(img, (filename+deg))
117     ImName=(path0+filename+deg)
118     SaveAsGatan3(img, ImName)
119
120     frame=frame+1 // move on to next condition
121 }
122 }
123
124 if (record=="no"){      // If we don't want record, and just want to precess the beam and observe on the green-screen
125 while (th<rotations){      // while we our within a single 360 degree circuit of the precession
126     th=th+th0
127     deg=360*(th/6.28) // convert to radians
128     deg=round(deg)
129
130     // use polar coordinates to calculate the new beam tilt and the beam shift needed to correct the beam movement on the screen
131     xl=x0+r0*cos(th)
132     yl=y0+r0*sin(th)
133
134     xsl= xs0+rs0*cos(th)
135     ysl= ys0+rs0*sin(th)
136
137     EMSetBeamTilt(xl,yl) // change the beam tilt to the new position
138     EMSetBeamShift(xsl,ysl) // shift the beam to correct movement on screen and through objective aperture
139
140     frame=frame+1 // move on to next condition
141 }
142 }
143
144 // --------------- Return to the inital beam/shift positions ------------------------------------------------------------
145
146 EMSetBeamTilt(x0, y0)
147 EMSetBeamShift(xs0, ys0)
148
149 if (record=="yes"){
150 ShowImage(stack)
151 }
152
153 // -------------------- END ---------------------------------------------------------------------------------------------------
```

Figure B.2: Lines 70-153 of the beam precession script, written in Digital micrograph [168]

APPENDIX C

Removal of matrix contributions from EELS-captured chromium-precipitates

Here is explained how to estimate the composition of a Gaussian-like precipitate from a two-dimensional chromium map. Figure C.1 shows schematically such a precipitate in a 3D volume (e.g. a TEM foil). Also shown is what a 2D composition-map of this precipitate might look like.

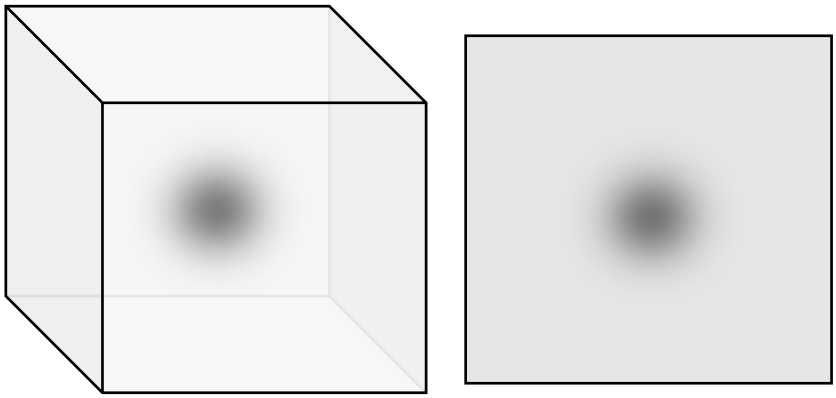

Figure C.1: Schematic illustration of a precipitate or cluster of atoms in a volume (i.e. a TEM foil) and an illustration of the 2D image that might be obtained from an EELS (or EDS) map.

By fitting a Gaussian-function (Equation C.1) to the line profile over such a precipitate recorded in a 2D composition-map, values of the amplitude, A1, and width of the distribution, 2σ, can be calculated. The amplitude is equal to the mean composition of the column of specimen that passes through the centre of the precipitate (Figure C.2). Assuming the precipitate is spherical, the values of A1 and 2σ can then be used to estimate the composition profile through this column of material (Figure C.3).

Equation C.1

$$I = I0 + A1\ exp\left(\frac{-(x-\mu)^2}{2\sigma^2}\right)$$

where I is the intensity, I0 is the background intensity, A1 is the amplitude, x is the position in the profile, μ is the position of the peak-intensity, and σ is the standard-deviation of the function

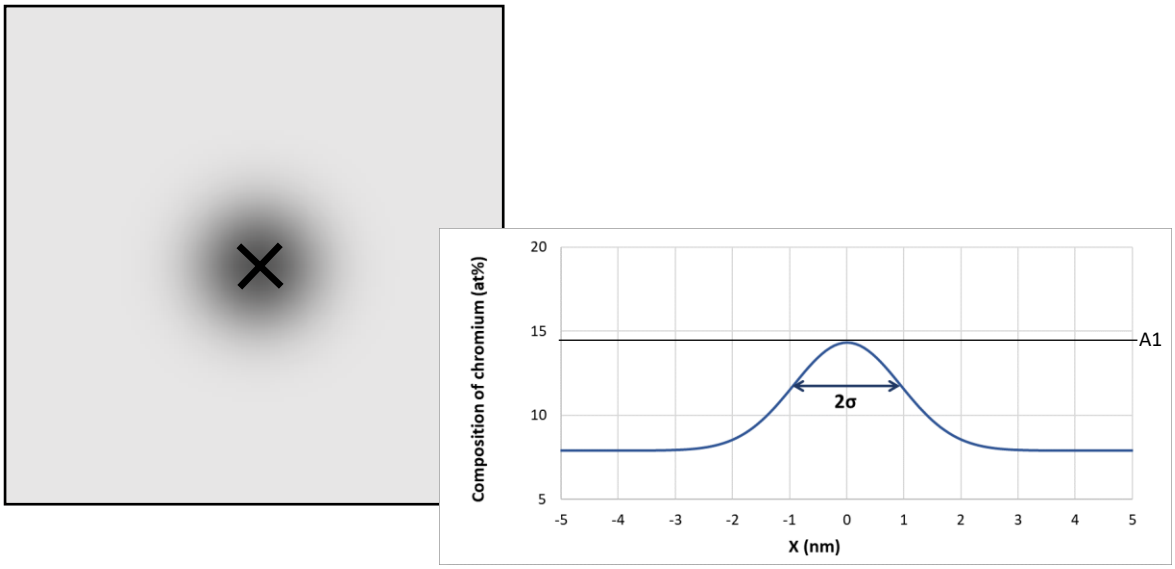

Figure C.2: The compositional line profile over the 2D-mapped precipitate or cluster, which is Gaussian-like. Fitting Equation C.1 to the profile produces values for A1 and 2σ. A1 is then the average composition through the column of specimen passing through the centre of the precipitate.

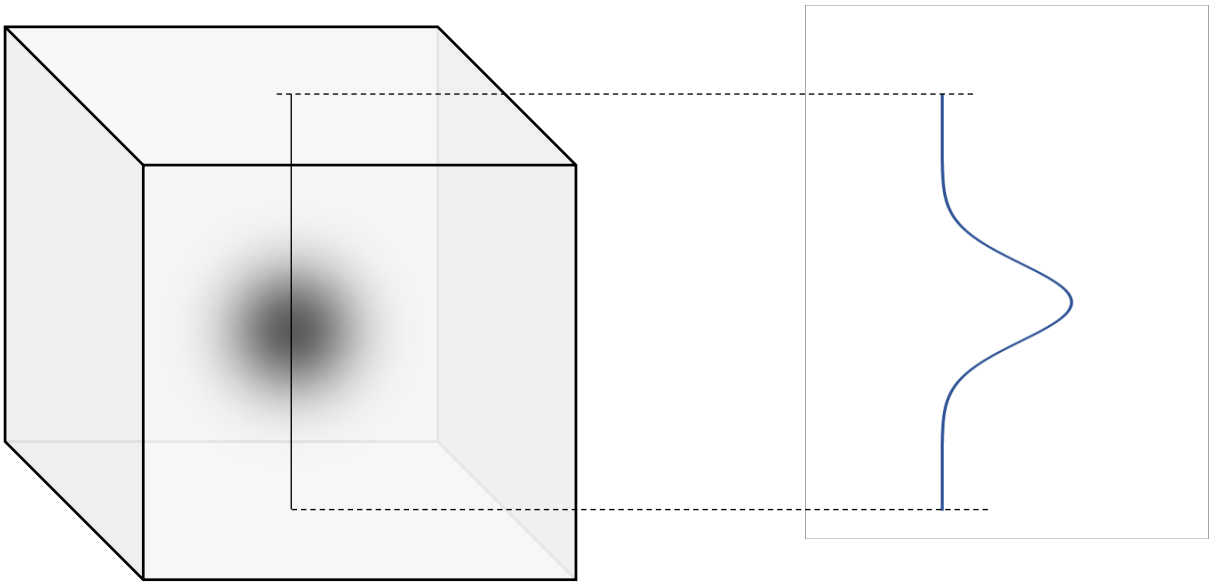

Figure C.3: Composition distribution through the column of specimen. The mean of this distribution over the foil thickness is equal to A1.

The mean *composition* along the indicated line in Figure C.3 equals the peak composition in the projected profile (this is different to the mean that is referred to in the Equation C.1, μ, which refers to the position of the peak in the profile). It was assumed that the signal measured from the precipitate is equal to the signal if precipitate were positioned exactly half-way through the foil. This follows from the assumption that the particle is entirely contained by the foil.

A generic Gaussian-curve was then plotted from zero to the foil thickness, T, with a curve-width of 2σ (equal to the width of the first Gaussian-function). This new Gaussian-curve would then be normalised so the mean intensity of the curve from zero to T is one, and then multiplied by the mean composition through the foil thickness (the amplitude of the first Gaussian-function, A1). The resulting distribution will be the final estimation of how the composition changes through the centre of the Gaussian-line precipitate. This is method is depicted in Figure C.4.

The amplitude of the Gaussian function through the foil thickness (through the precipitate), A2, will correspond to the peak-composition of the particle. The mean composition of the particle was taken as the mean composition contained by a three-dimensional Gaussian-object with amplitude A2 and width 2σ (Equation C.2).

Equation C.2:

$$I = I0 + A2\ exp\left(\frac{-(x-\mu)^2}{2\sigma^2}\right) + A2\ exp\left(\frac{-(y-\mu)^2}{2\sigma^2}\right) + A2\ exp\left(\frac{-(z-\mu)^2}{2\sigma^2}\right)$$

where I is the intensity, I0 is the background intensity, A2 is the amplitude, x, y and z are the positions in the 3D profile, μ is the position of the peak-intensity, and σ is the standard-deviation of the function

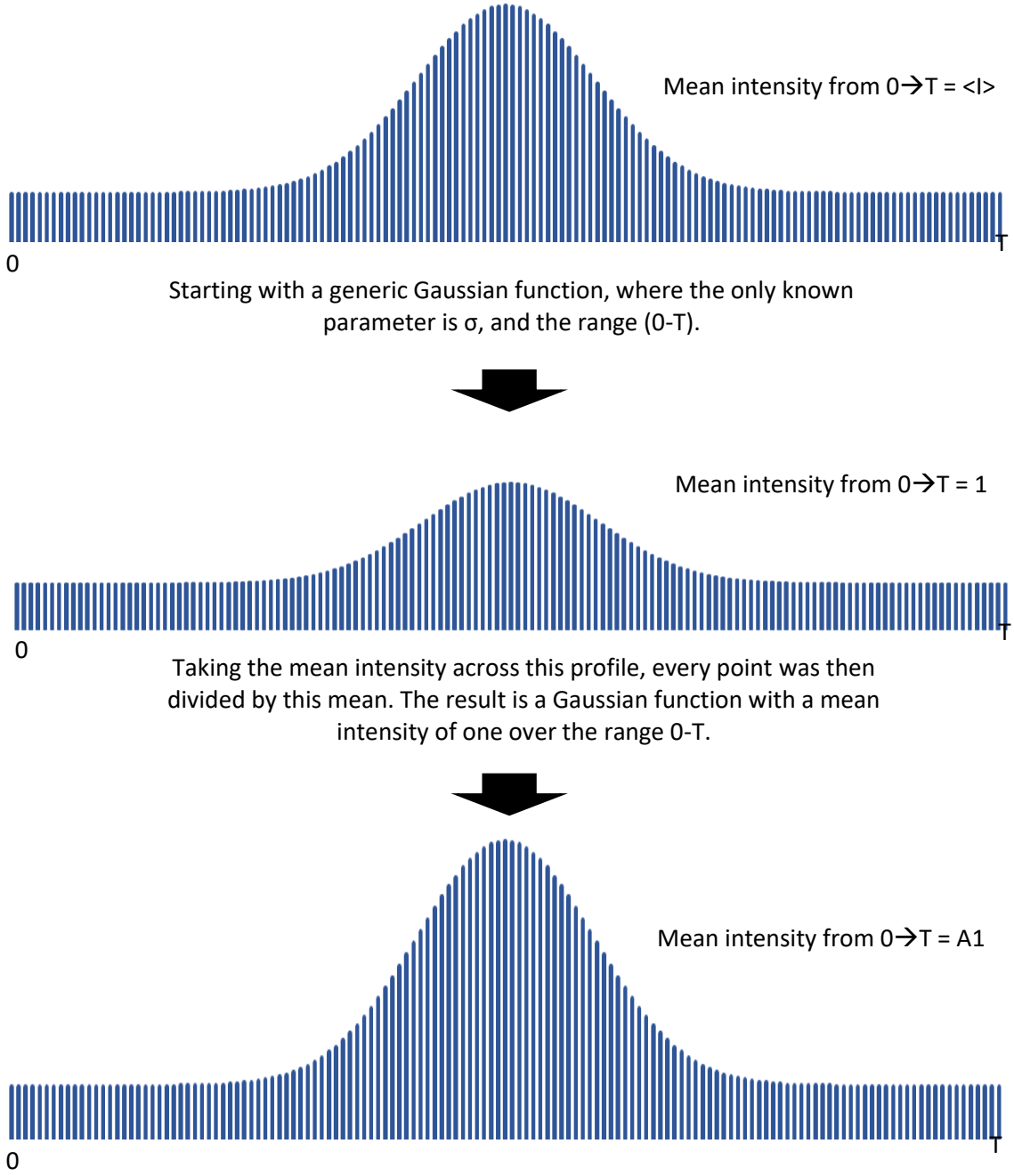

Figure C.4: Method for estimating the composition distribution through the centre of a precipitate after A1 and 2σ have been calculated from the 2D-composition map.

APPENDIX D

Dislocation loop size distributions for each imaging condition

Here are shown the size distributions by imaging condition for the irradiated materials, rather than the combined size-distributions shown in the main text.

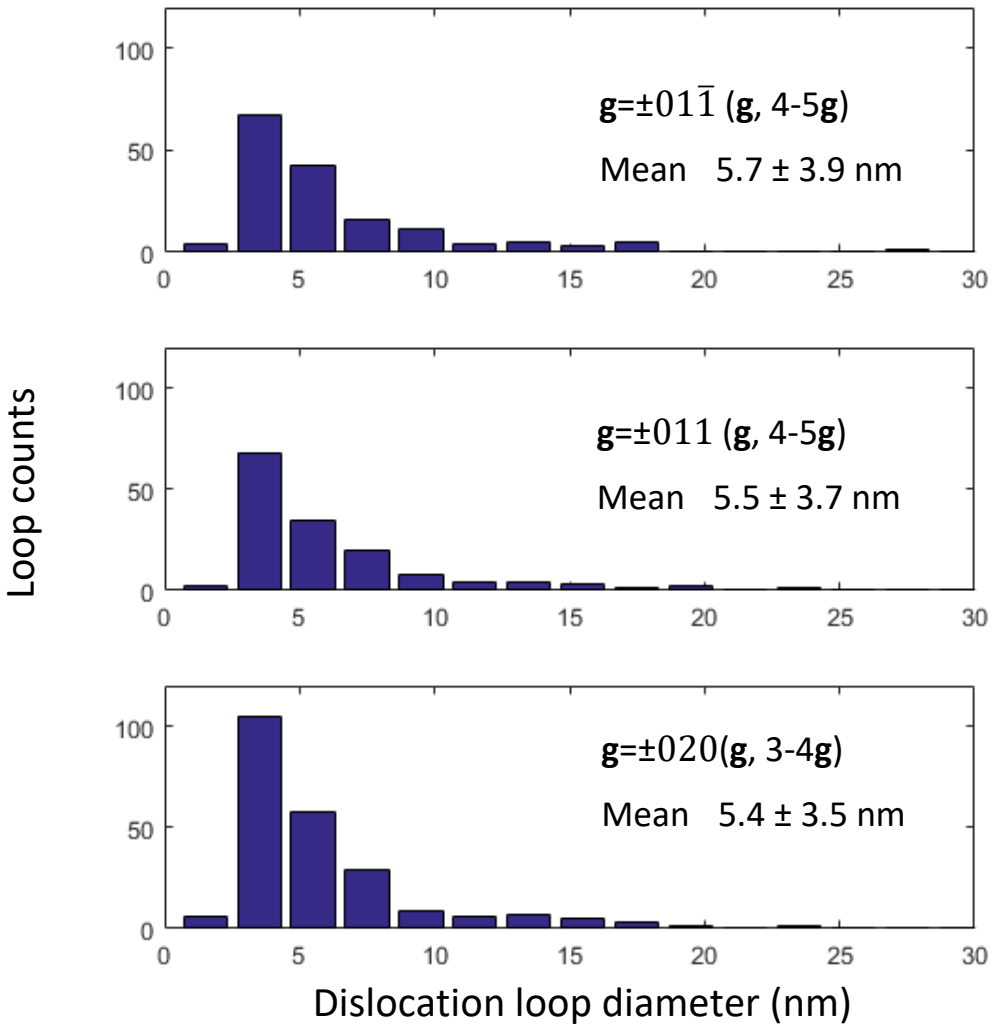

Figure D.1: Size distributions for dislocation loops in neutron-irradiated Fe6Cr, for each imaging condition.

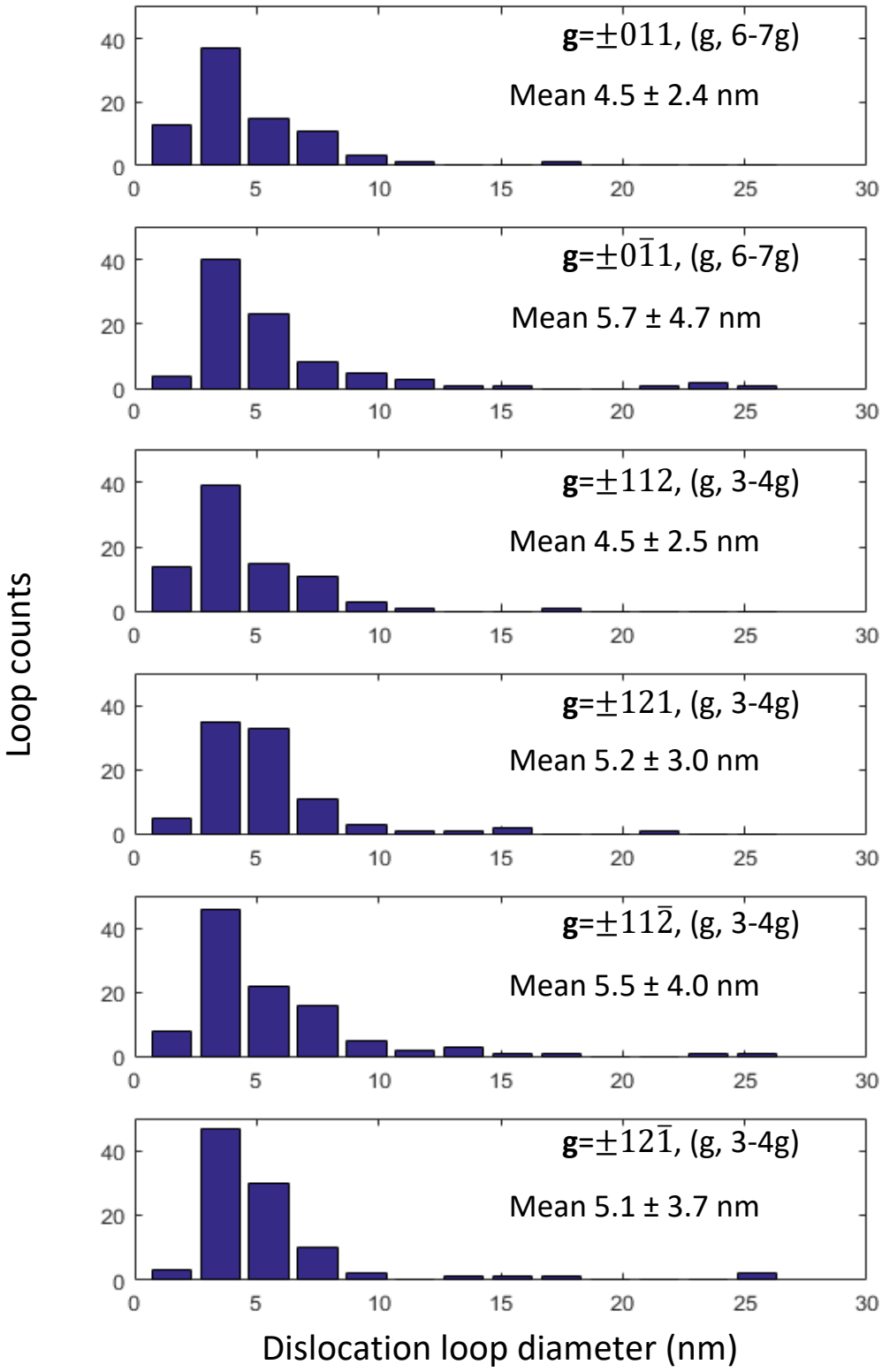

Figure D.2: Size distributions for dislocation loops in neutron-irradiated Fe9Cr, for each imaging condition.

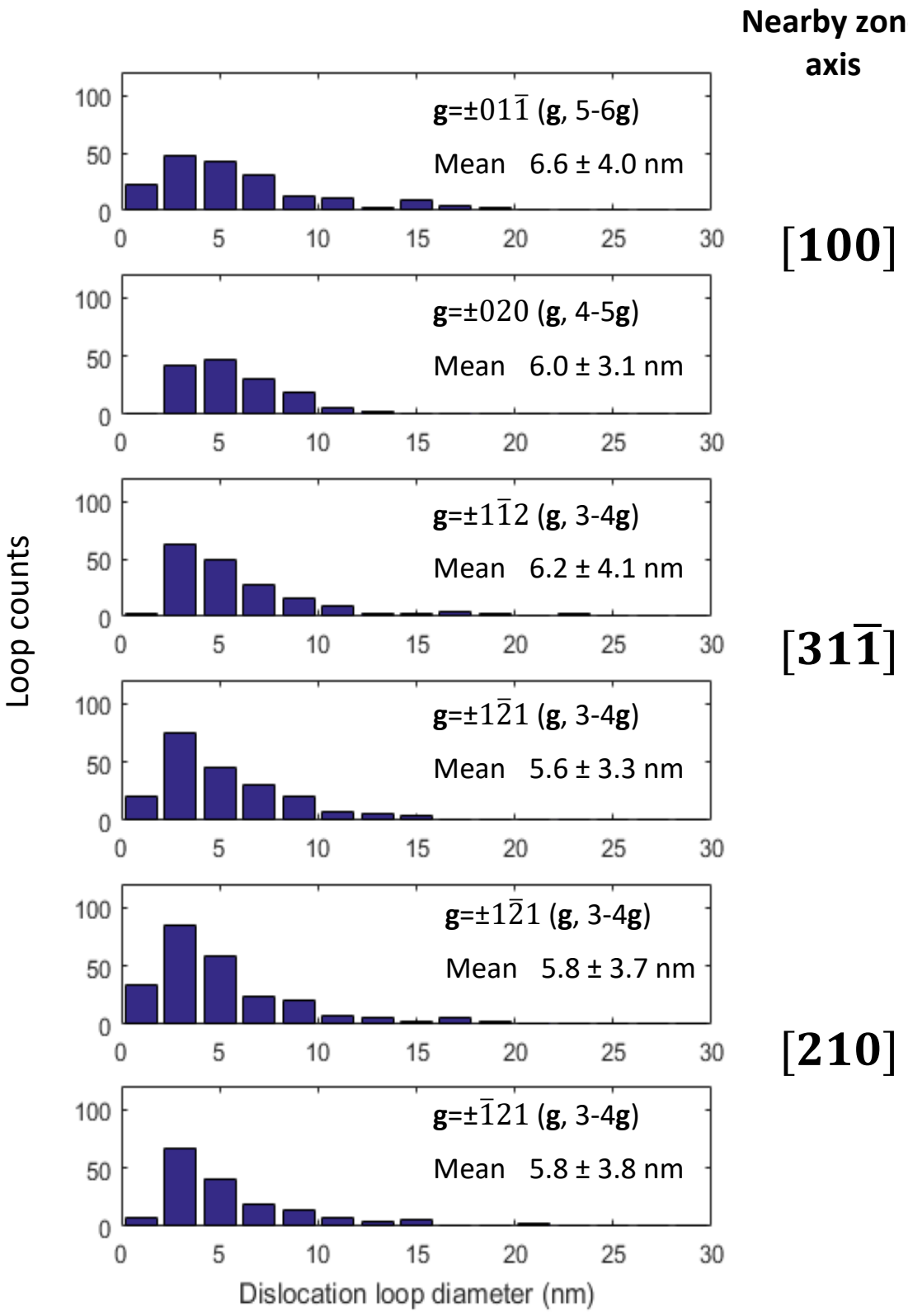

Figure D.3: Size distributions for dislocation loops in self-ion irradiated Fe6Cr, for each imaging condition.

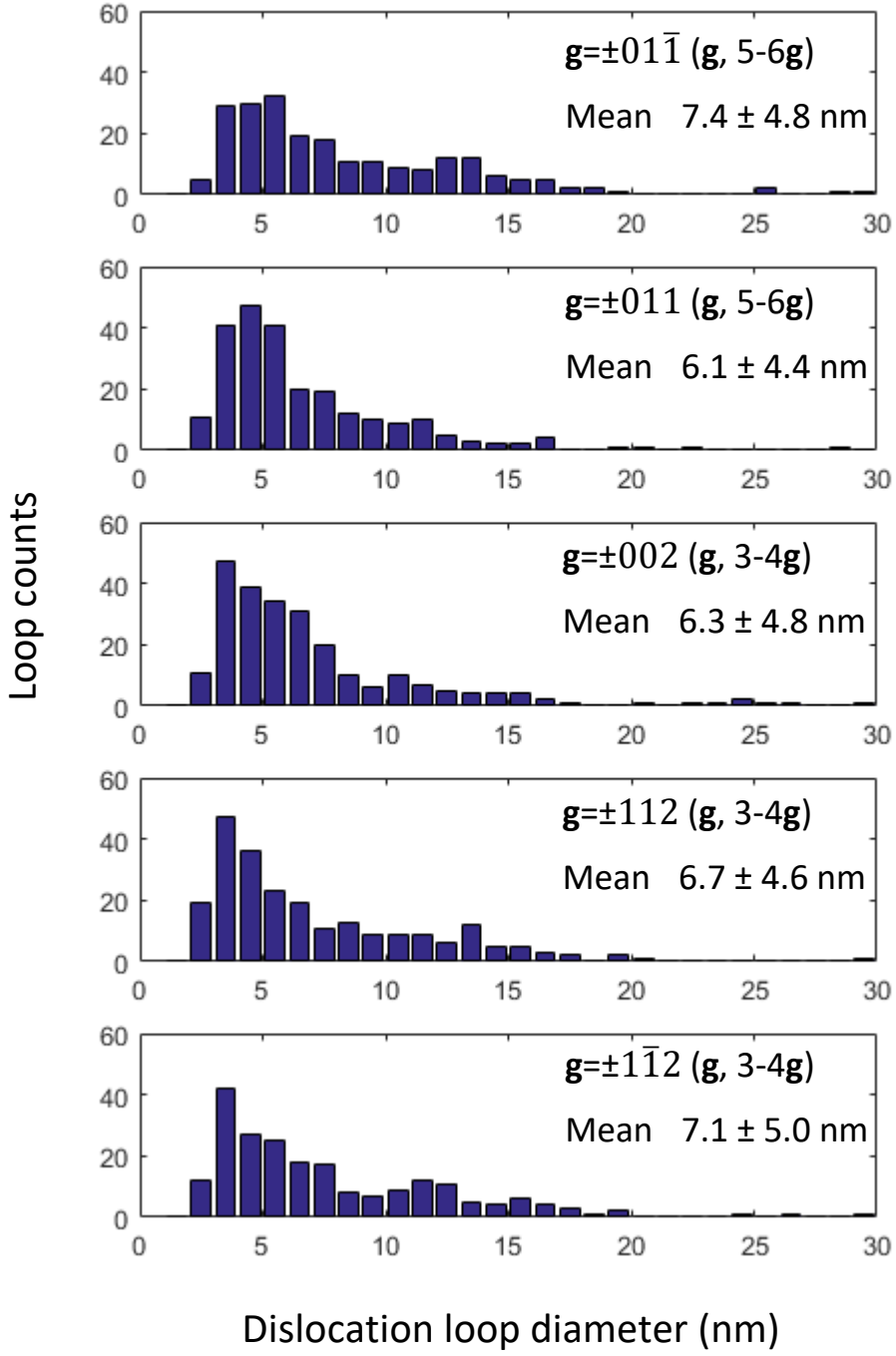

Figure D.4: Size distributions for dislocation loops in self-ion irradiated Fe9Cr, for each imaging condition.

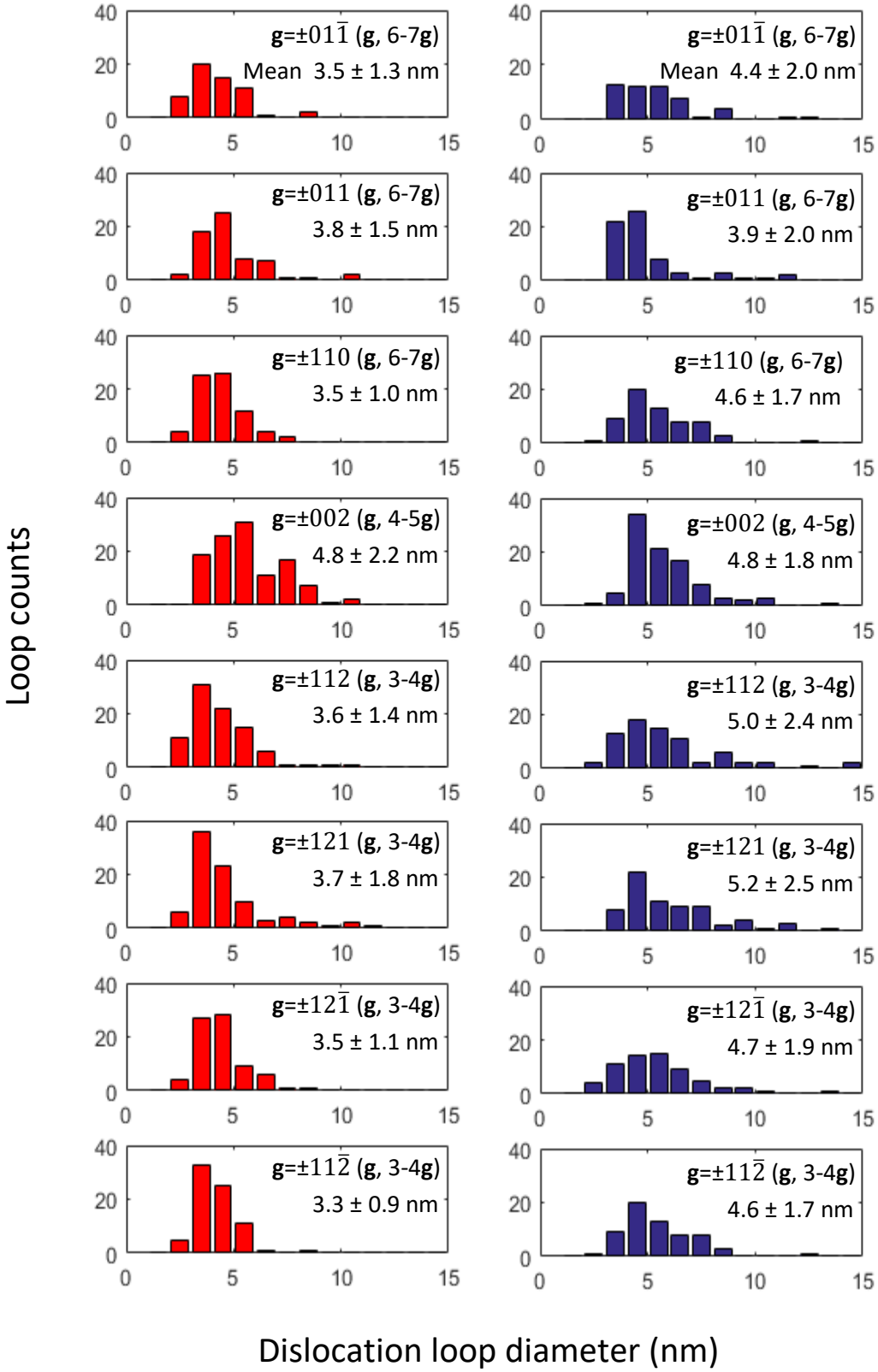

Figure D.5: Size distributions for dislocation loops in proton-irradiated Fe9Cr, for each imaging condition.

APPENDIX E

Error estimation of interstitial counts

The process used to calculate errors in the estimation of the total number of interstitials contained by dislocation loops is described below.

1) Power laws fitted to the cluster-size distribution were taken to be the probability distribution of finding a loop of a given size from each irradiation, and from this, the fraction of clusters containing less than 100 atoms were determined.
2) With the fraction missing calculated, 100 data sets were then simulated in batches containing the same number of clusters counted containing >100 atoms, plus the missing defect population calculated from the fraction in the last step. Each data set was scaled so the population of clusters sized >100 atoms equalled the measured count.
3) The error in the count of interstitials was then taken as the standard deviation in the total defect count from all datasets. The result is a statistical error that acknowledges the un-measured clusters.

This method was applied to all estimations of the total number of point defects contained by the dislocation loop population.

APPENDIX F

Assumptions involved in estimating the interstitial volume of loops in the proton irradiated Fe6Cr

The upper bound estimate of the estimation of interstitials contained by dislocation loops in the proton-irradiated Fe6Cr assumes all measured loop sizes correspond to the diameter of a circle. This is the only assumption made, so the estimate of interstitial counts will definitely overestimate the true count.

For the lower bound, a larger set of assumption were made. First, it was assumed that all foil depths are equally likely to contain a loop. Second, it was assumed that only edge-on [010] or [001] loops were measured (i.e., the low population of <111> loops were ignored). Third, it was assumed that at least half of a loop must reside in the foil for it to resist being pulled out of the foil by surface forces. Loops will be initially treated as having a circular shape, and the shape of the loop intersecting the surface were segments of a circle (Figure F.1).

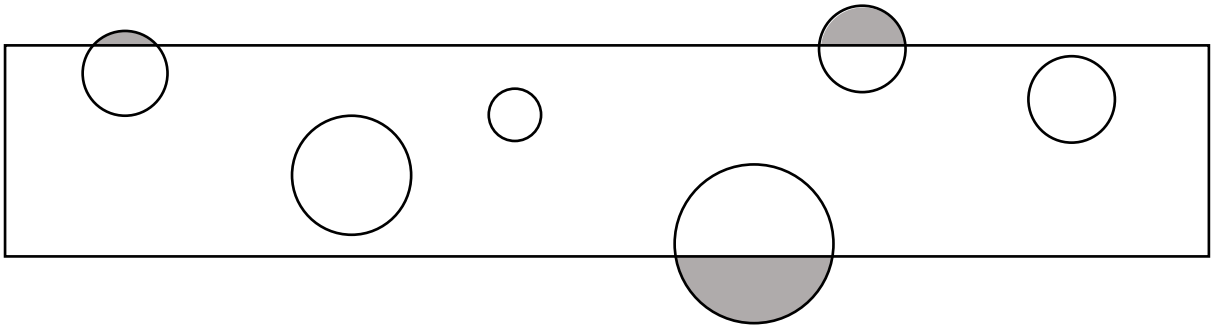

Figure F.1: Diagram illustrating the problem of calculating loop volume if a significant fraction of the loops intersect the foil surface.

If a loop has a diameter larger than the foil thickness, then the probability of it intersecting a foil surface is 100%. If a loop has a diameter that is half the foil thickness, then the probability of it intersecting a foil surface is 50%. If a loop has a diameter, D, and D<T, then the probability of it intersecting the foil surface will be D/T, where T is the foil thickness.

For every loop, the probability of it intersecting the surface was calculated, and a random number generator was applied to designate certain loops as intersecting the surface. Those that were designated as not intersecting the surface have their area taken to be the area of a circle with diameter D.

Of the loops that do intersect the surface, the loop area was calculated as the area of a circle with diameter, D, minus the product of half the area with a random number from 0→0.5 (i.e. a random area up to half the area of the loop is subtracted).

The atomic volume was then calculated based on the area measured for each loop. This calculation was repeated 1000 times and the average atomic volume is taken to be the result.

Up to this point, all loops have been treated as being circular, except for when they intersect the foil surface. Figure 6.28 shows that this is not the case. It was therefore assumed that the frequency of circular loops falls to zero above some critical size in this sample, and the coalescence of large loops into elongated shapes dominates loop growth above this critical size. Additionally, it was assumed that two loops above this critical size will form an elongated loop with major diameter approximately equal to twice the diameter of the smaller loops (in reality, it may be slightly shorter than this) (Figure F.2). The histogram of the measured loop "diameters" suggests that the frequency of loops might have two peaks in the distribution, with a smaller second peak somewhere between 20 and 25nm. The noise in the distribution here makes it difficult to confirm this. A second peak would support the argument that the frequency of coalescence into elongated loops becomes more frequent above some critical size, which would lead to an increase in the frequency of measured large "diameters".

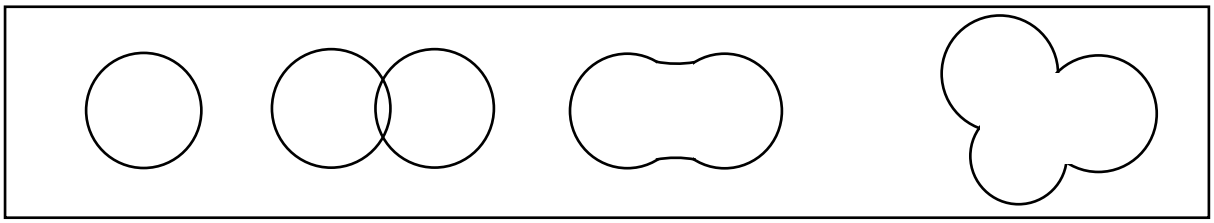

Figure F.2: Diagram illustrating the problem of calculating loop volume if the loop geometry resembles coalesced dislocation loops.

The critical diameter was taken to be the group in the histogram that roughly corresponds to the minima between the two peaks, taken to be 19nm. Loops larger than 19nm had their volume calculated as the volume of two loops with diameters equal to half the measured diameter. Loops larger than 38nm had their volume calculated as the volume of three loops, and larger than 57nm as for four loops.

Due to the large number of assumptions and approximations made in calculating the interstitial loop volume in the proton-irradiated Fe6Cr, the end result is highly uncertain. However, but calculating upper and lower bounds, a reasonable comparison to the other irradiation-conditions can be made.

APPENDIX G

Size distribution of loops in self-ion and proton irradiated Fe6Cr and Fe9Cr as atomic volume

Figure G.1 and Figure G.2 show the cluster-size distribution analysis for the proton and self-ion irradiated Fe6Cr and Fe9Cr respectively, and the power laws fitted to each. The histograms were constructed via the same method used in section-4.4.3. The plot for the proton-irradiated Fe6Cr contains the upper and lower bound estimates of the distribution.

The power exponent of the proton-irradiated Fe6Cr is between 1.1 and 1.4, which is much lower than the exponent for the self-ion irradiated material (~1.7) and the neutron-irradiated sample (~1.8). In addition to low population of small loops, this shows that loop growth is probably dominated by loop-loop coalescence of larger loops, rather than coarsening via the absorption of small interstitial clusters. The difference between the exponents of the ion and neutron-irradiated samples are within 0.1 of each other, which is the approximate error assigned to these values

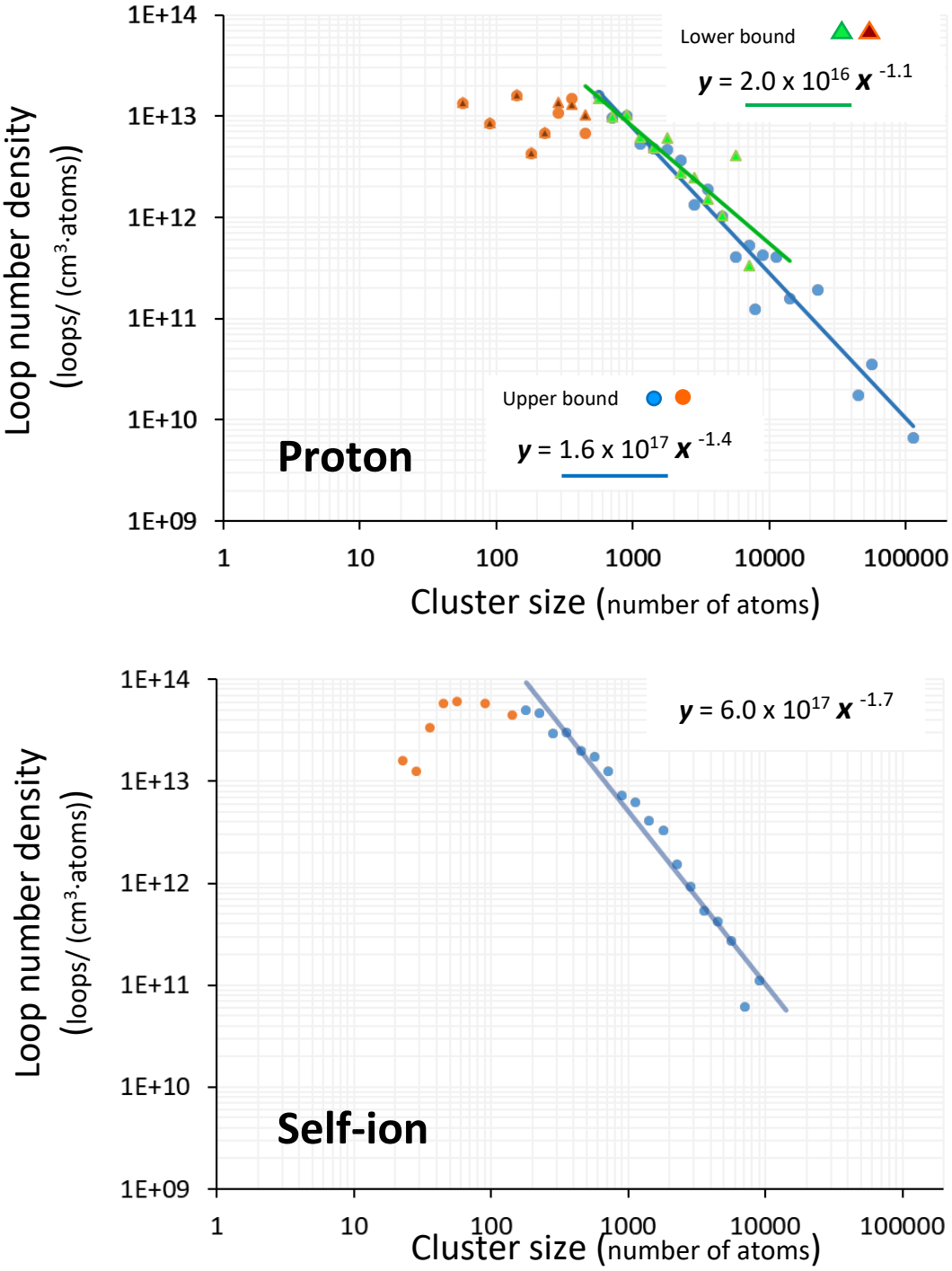

Figure G.1: Loop size distributions by atomic volume of the proton and self-ion irradiated Fe6Cr.

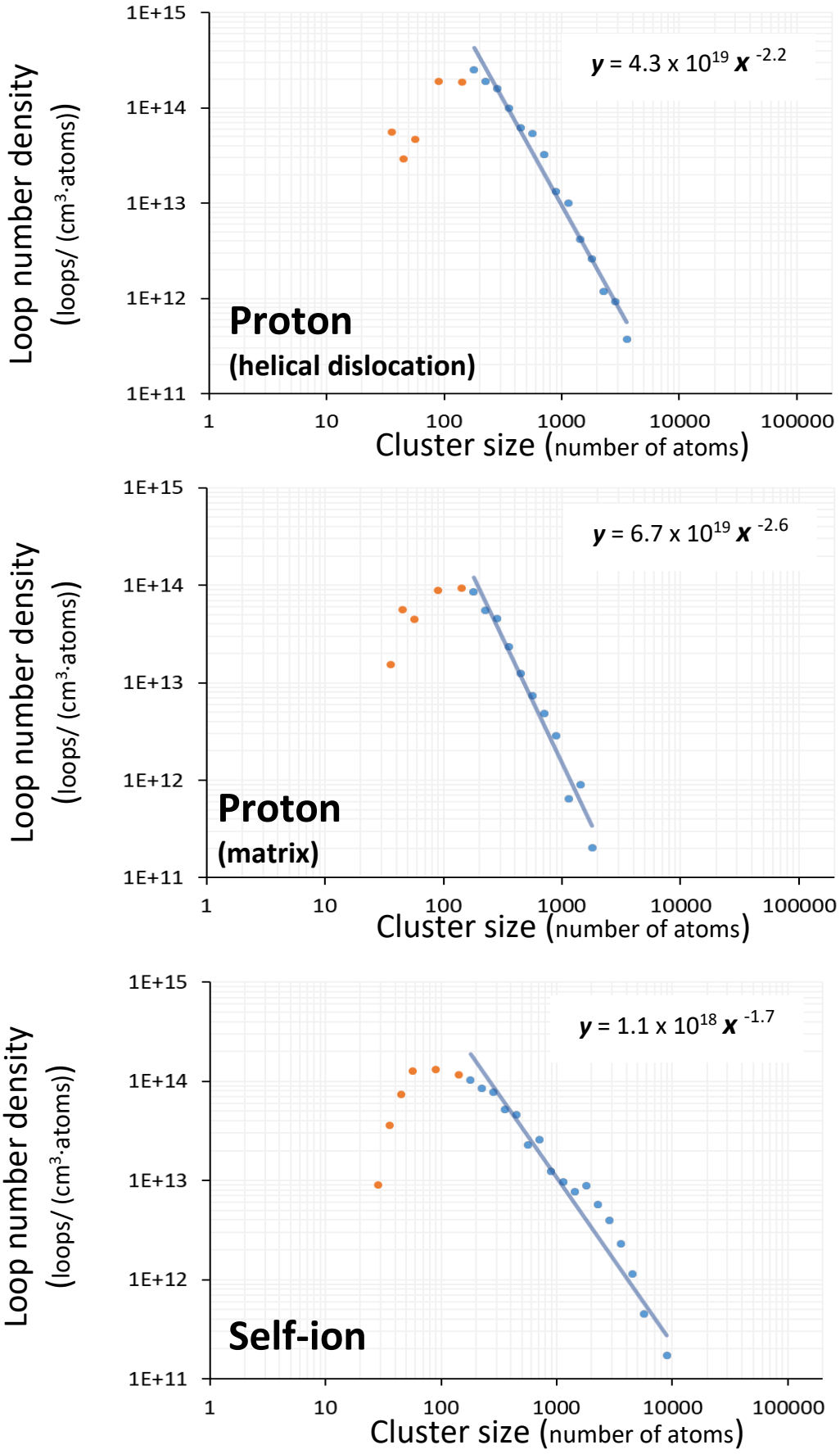

Figure G.2: Loop size distributions by atomic volume of the proton and self-ion irradiated Fe9Cr.

APPENDIX H

Nature analysis of small loops in ion irradiated Fe9Cr

Figure H.1 and Figure H.2 show the nature-analysis for a second set of loops in the same ion-irradiated foil of Fe9Cr as the loops analysed in section-6.4.2. These loops are smaller than those analysed in section-6.4.2 (Figure 6.62 and Figure 6.63, and reside further into the damage profile. From the same tilting experiment, the inclination of the loops and their Burgers vectors were determined. Loop 1 (indicated in Figure H.1) was found to have a projection consistent with a loop with Burgers vector ±[001] and the cluster of loops (labelled "2" in Figure H.1) are consistent with having a Burgers vector of $[1\bar{1}\bar{1}]$. Figure H.2 shows the plus- and minus-g vector conditions for this set of loops, and the orientation of the loops with respect to g. The cluster of loops lose visibility in the 112 condition, which was taken as the "outside" condition. From this, it was found that all loops were vacancy.

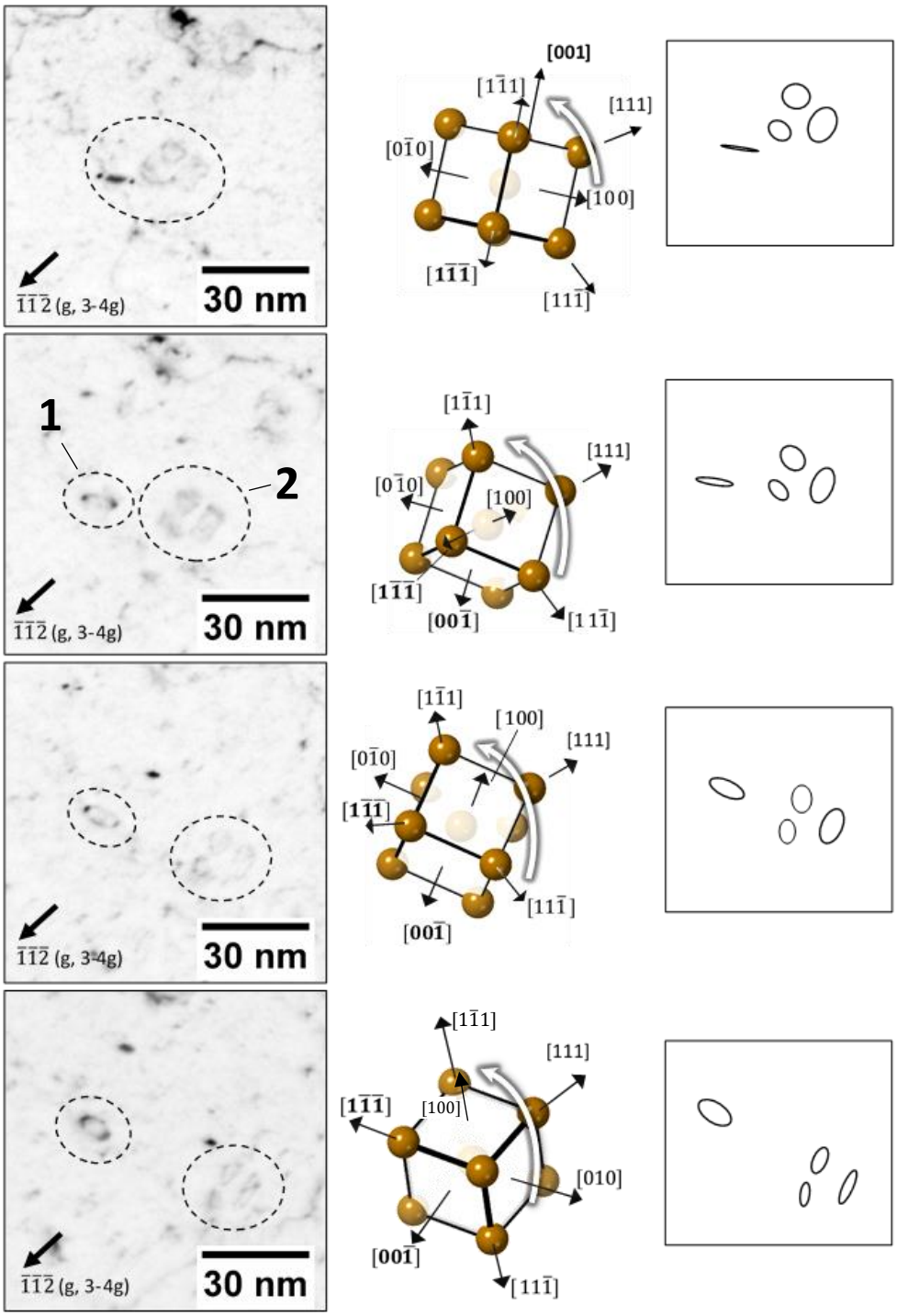

Figure H.1: Tilt series along a 112 Kikuchi band, from the $[1\bar{1}0]$ *pole to the* $[11\bar{1}]$ *pole, showing the change in projection of small dislocation loops in the self-ion irradiated Fe9Cr. A selection of loops are indicated by dotted circles. The loop in the left-hand dotted circle increases in minor image-diameter as the foil is tilted from* $[1\bar{1}0]$ *to* $[11\bar{1}]$*, whereas the loops in the right-hand dotted circle decrease in minor image-diameter.*

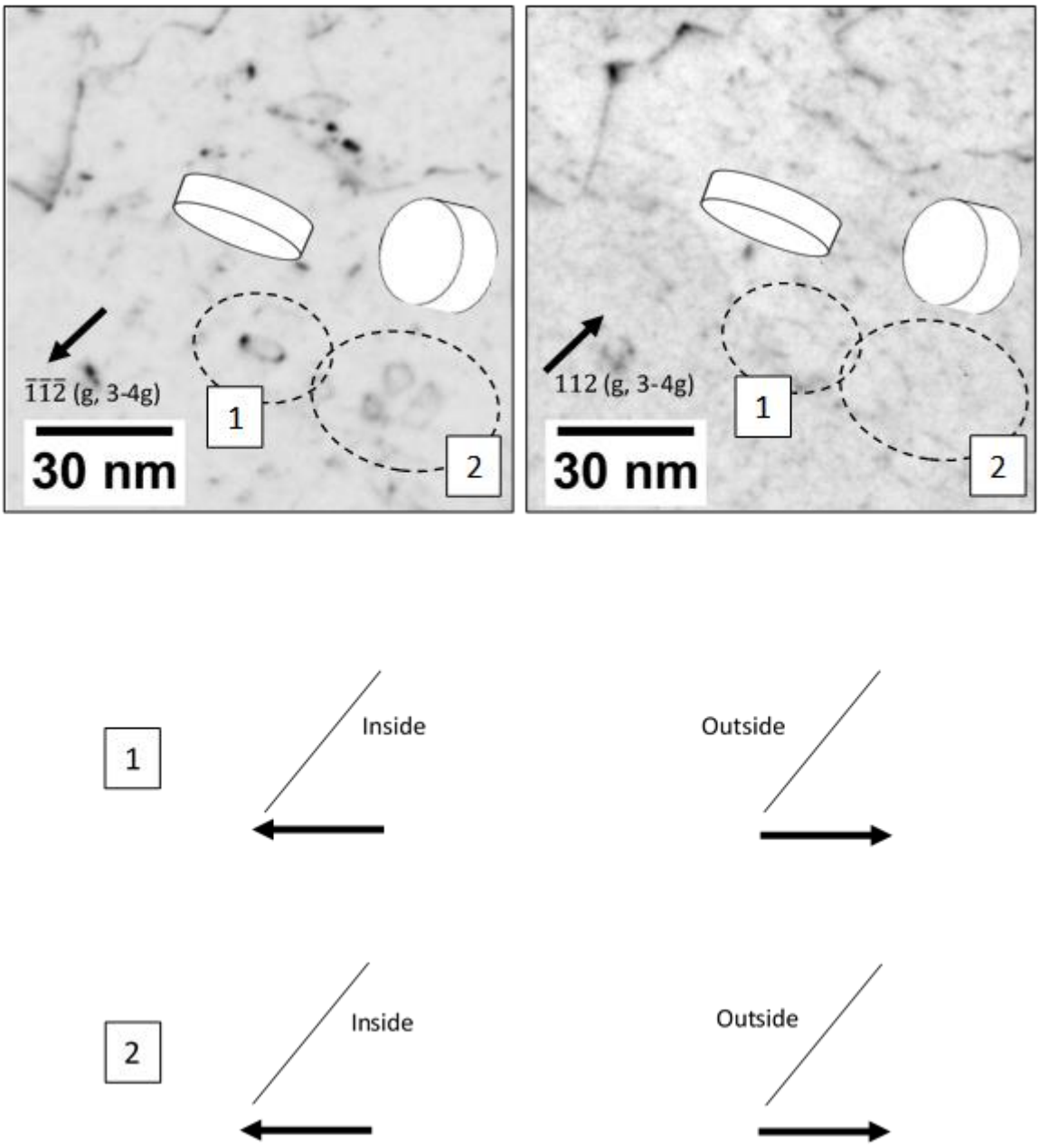

*Figure H.2: Inside-outside contrast analysis of the dislocation loops labelled 1 and 2. Shown next to each loop is an image of a cylinder to show the inclination. Beneath the micrographs is a diagram showing the inclination of the loops with respect to **g**, as viewed from the direction orthogonal to **g** and **z**. Although loop 1 has a different habit plane to loop(s) 2, the inclination with respect to g is the same for these conditions. The inside-outside contrast is consistent with vacancy-type loops.*